ELECTROCARDIOGRAPHIC IMAGING

EDITED BY: Maria S. Guillem, Carlos Figuera and Linwei Wang
PUBLISHED IN: Frontiers in Physiology

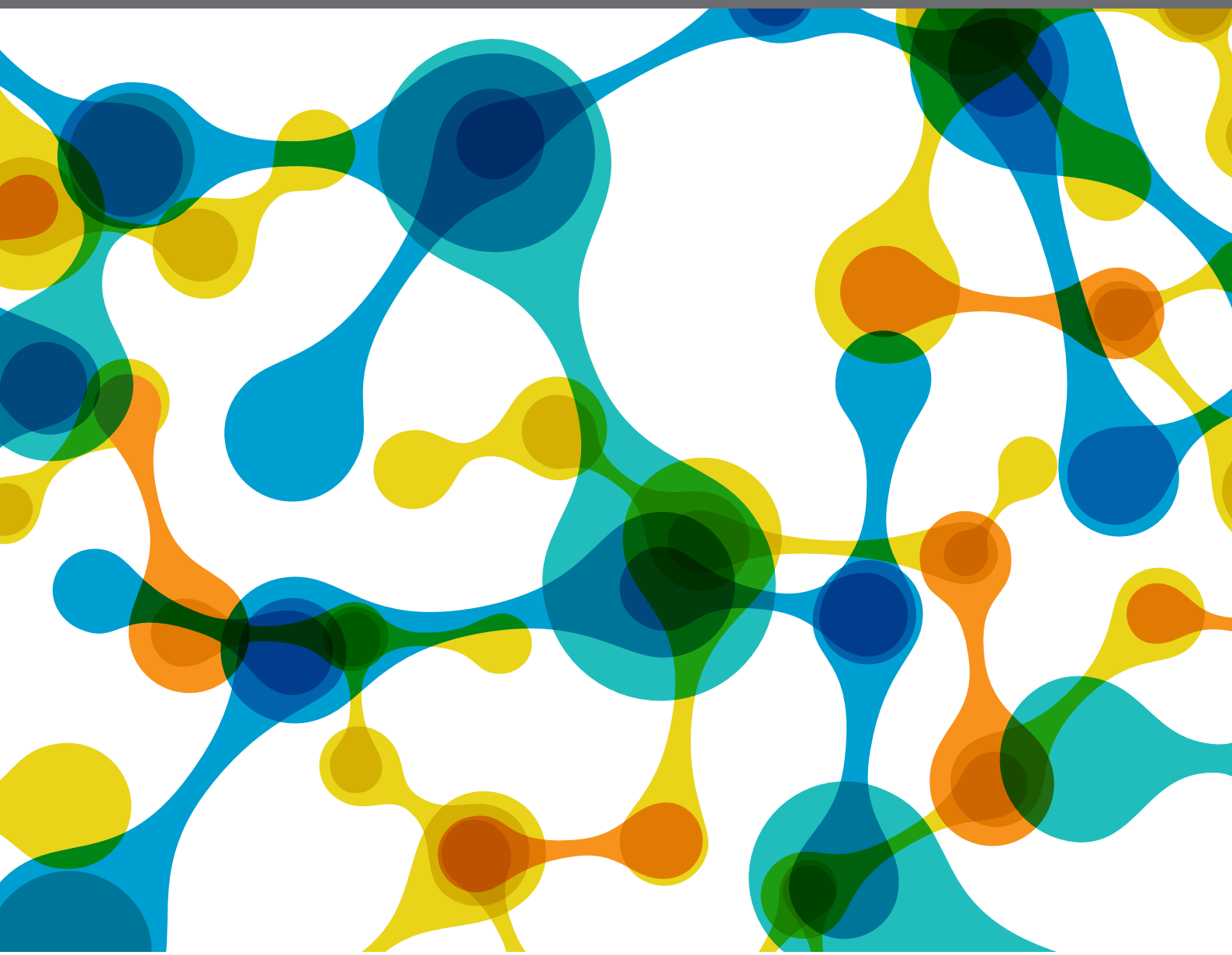

frontiers Research Topics

ISSN 1664-8714
ISBN 978-2-88963-671-6
DOI 10.3389/978-2-88963-671-6

About Frontiers

Frontiers is more than just an open-access publisher of scholarly articles: it is a pioneering approach to the world of academia, radically improving the way scholarly research is managed. The grand vision of Frontiers is a world where all people have an equal opportunity to seek, share and generate knowledge. Frontiers provides immediate and permanent online open access to all its publications, but this alone is not enough to realize our grand goals.

Frontiers Journal Series

The Frontiers Journal Series is a multi-tier and interdisciplinary set of open-access, online journals, promising a paradigm shift from the current review, selection and dissemination processes in academic publishing. All Frontiers journals are driven by researchers for researchers; therefore, they constitute a service to the scholarly community. At the same time, the Frontiers Journal Series operates on a revolutionary invention, the tiered publishing system, initially addressing specific communities of scholars, and gradually climbing up to broader public understanding, thus serving the interests of the lay society, too.

Dedication to Quality

Each Frontiers article is a landmark of the highest quality, thanks to genuinely collaborative interactions between authors and review editors, who include some of the world's best academicians. Research must be certified by peers before entering a stream of knowledge that may eventually reach the public - and shape society; therefore, Frontiers only applies the most rigorous and unbiased reviews.
Frontiers revolutionizes research publishing by freely delivering the most outstanding research, evaluated with no bias from both the academic and social point of view. By applying the most advanced information technologies, Frontiers is catapulting scholarly publishing into a new generation.

What are Frontiers Research Topics?

Frontiers Research Topics are very popular trademarks of the Frontiers Journals Series: they are collections of at least ten articles, all centered on a particular subject. With their unique mix of varied contributions from Original Research to Review Articles, Frontiers Research Topics unify the most influential researchers, the latest key findings and historical advances in a hot research area! Find out more on how to host your own Frontiers Research Topic or contribute to one as an author by contacting the Frontiers Editorial Office: researchtopics@frontiersin.org

ELECTROCARDIOGRAPHIC IMAGING

Topic Editors:
Maria S. Guillem, Universitat Politècnica de València, Spain
Carlos Figuera, Rey Juan Carlos University, Spain
Linwei Wang, Rochester Institute of Technology, United States

Electrical activity in the myocardium coordinates the contraction of the heart, and its knowledge could lead to a better understanding, diagnosis, and treatment of cardiac diseases. This electrical activity generates an electromagnetic field that propagates outside the heart and reaches the human torso surface, where it can be easily measured. Classical electrocardiography aims to interpret the 12-lead electrocardiogram (ECG) to determine cardiac activity and support the diagnosis of cardiac pathologies such as arrhythmias, altered activations, and ischemia. More recently, a higher number of leads is used to reconstruct a more detailed quantitative description of the electrical activity in the heart by solving the so-called inverse problem of electrocardiography. This technique is known as ECG imaging.

Today, clinical applications of ECG imaging are showing promising results in guiding a variety of electrophysiological interventions such as catheter ablation of atrial fibrillation and ventricular tachycardia. However, in order to promote the adoption of ECG imaging in the routine clinical practice, further research is required regarding more accurate mathematical methods, further scientific validation under different preclinical scenarios and a more extensive clinical validation

Citation: Guillem, M. S., Figuera, C., Wang, L., eds. (2020). Electrocardiographic Imaging. Lausanne: Frontiers Media SA. doi: 10.3389/978-2-88963-671-6

Table of Contents

04 ***Electrocardiographic Imaging Using a Spatio-Temporal Basis of Body Surface Potentials—Application to Atrial Ectopic Activity***
Steffen Schuler, Andreas Wachter and Olaf Dössel

17 ***Validation and Opportunities of Electrocardiographic Imaging: From Technical Achievements to Clinical Applications***
Matthijs Cluitmans, Dana H. Brooks, Rob MacLeod, Olaf Dössel, María S. Guillem, Peter M. van Dam, Jana Svehlikova, Bin He, John Sapp, Linwei Wang and Laura Bear

36 ***Reducing Error in ECG Forward Simulations With Improved Source Sampling***
Jess Tate, Karli Gillette, Brett Burton, Wilson Good, Brian Zenger, Jaume Coll-Font, Dana Brooks and Rob MacLeod

52 ***Evaluation of Fifteen Algorithms for the Resolution of the Electrocardiography Imaging Inverse Problem Using* ex-vivo *and* in-silico *Data***
Amel Karoui, Laura Bear, Pauline Migerditichan and Nejib Zemzemi

66 ***Tracking the Position of the Heart From Body Surface Potential Maps and Electrograms***
Jaume Coll-Font and Dana H. Brooks

78 ***Impact of the Endocardium in a Parameter Optimization to Solve the Inverse Problem of Electrocardiography***
Gwladys Ravon, Yves Coudière, Mark Potse and Rémi Dubois

91 ***Solving the Inverse Problem of Electrocardiography on the Endocardium Using a Single Layer Source***
Alexander Kalinin, Danila Potyagaylo and Vitaly Kalinin

104 ***ECG Imaging to Detect the Site of Ventricular Ischemia Using Torso Electrodes: A Computational Study***
Vinay Kara, Haibo Ni, Erick Andres Perez Alday and Henggui Zhang

120 ***Corrigendum: ECG Imaging to Detect the Site of Ventricular Ischemia Using Torso Electrodes: A Computational Study***
Vinay Kara, Haibo Ni, Erick Andres Perez Alday and Henggui Zhang

121 ***Optical Imaging of Ventricular Action Potentials in a Torso Tank: A New Platform for Non-Invasive Electrocardiographic Imaging Validation***
Laura R. Bear, Richard D. Walton, Emma Abell, Yves Coudière, Michel Haissaguerre, Olivier Bernus and Rémi Dubois

132 ***ECG Adapted Fastest Route Algorithm to Localize the Ectopic Excitation Origin in CRT Patients***
Danila Potyagaylo, Mikhail Chmelevsky, Peter van Dam, Margarita Budanova, Stepan Zubarev, Tatjana Treshkur and Dmitry Lebedev

145 ***Considering New Regularization Parameter-Choice Techniques for the Tikhonov Method to Improve the Accuracy of Electrocardiographic Imaging***
Judit Chamorro-Servent, Rémi Dubois and Yves Coudière

163 ***Effects of Heart Rate and Ventricular Wall Thickness on Non-invasive Mapping: An* in silico *Study***
Erick Andres Perez Alday, Dominic G. Whittaker, Alan P. Benson and Michael A. Colman

frontiers in Physiology

ORIGINAL RESEARCH
published: 22 August 2018
doi: 10.3389/fphys.2018.01126

Electrocardiographic Imaging Using a Spatio-Temporal Basis of Body Surface Potentials—Application to Atrial Ectopic Activity

Steffen Schuler, Andreas Wachter and Olaf Dössel*

Institute of Biomedical Engineering, Karlsruhe Institute of Technology, Karlsruhe, Germany

Electrocardiographic imaging (ECGI) strongly relies on a priori assumptions and additional information to overcome ill-posedness. The major challenge of obtaining good reconstructions consists in finding ways to add information that effectively restricts the solution space without violating properties of the sought solution. In this work, we attempt to address this problem by constructing a spatio-temporal basis of body surface potentials (BSP) from simulations of many focal excitations. Measured BSPs are projected onto this basis and reconstructions are expressed as linear combinations of corresponding transmembrane voltage (TMV) basis vectors. The novel method was applied to simulations of 100 atrial ectopic foci with three different conduction velocities. Three signal-to-noise ratios (SNR) and bases of six different temporal lengths were considered. Reconstruction quality was evaluated using the spatial correlation coefficient of TMVs as well as estimated local activation times (LAT). The focus localization error was assessed by computing the geodesic distance between true and reconstructed foci. Compared with an optimally parameterized Tikhonov-Greensite method, the BSP basis reconstruction increased the mean TMV correlation by up to 22, 24, and 32% for an SNR of 40, 20, and 0 dB, respectively. Mean LAT correlation could be improved by up to 5, 7, and 19% for the three SNRs. For 0 dB, the average localization error could be halved from 15.8 to 7.9 mm. For the largest basis length, the localization error was always below 34 mm. In conclusion, the new method improved reconstructions of atrial ectopic activity especially for low SNRs. Localization of ectopic foci turned out to be more robust and more accurate. Preliminary experiments indicate that the basis generalizes to some extent from the training data and may even be applied for reconstruction of non-ectopic activity.

Keywords: ECG, inverse problem, spatio-temporal regularization, basis vectors, body surface potentials, atrial ectopic beats

OPEN ACCESS

Edited by:
Linwei Wang,
Rochester Institute of Technology,
United States

Reviewed by:
Nejib Zemzemi,
Institut National de Recherche en Informatique et en Automatique (INRIA), France
Rafael Sebastian,
Universitat de València, Spain
Peter Johnston,
Griffith University, Australia

****Correspondence:***
Steffen Schuler
publications@ibt.kit.edu

Specialty section:
This article was submitted to Cardiac Electrophysiology, a section of the journal Frontiers in Physiology

Received: *21 May 2018*
Accepted: *27 July 2018*
Published: *22 August 2018*

Citation:
Schuler S, Wachter A and Dössel O (2018) Electrocardiographic Imaging Using a Spatio-Temporal Basis of Body Surface Potentials—Application to Atrial Ectopic Activity. Front. Physiol. 9:1126. doi: 10.3389/fphys.2018.01126

1. INTRODUCTION

Reconstructing the heart's electrical activity from non-invasively measured body surface potentials (BSP) is known as the inverse problem of electrocardiography (Pullan et al., 2010). The ill-posedness of this problem can be overcome by introducing additional information—a technique called regularization. Classical regularization methods such as Tikhonov regularization add the

"information" that the solution must be of small signal energy or smooth in space or time. However, they do not complement the measurements with physiological information about the spread of cardiac excitation, which could greatly improve the uniqueness of the solution. For example, ambiguities can arise between sources on two different regions oriented in parallel, when body surface potentials are projected back onto the heart. Incorporating information about the spatio-temporal coherence of excitation spread, i.e., taking into account that excitation waves can only gradually propagate across connected regions, is expected to help resolve ambiguities. Several approaches have been proposed to incorporate electrophysiological knowledge (van Oosterom, 1999; Messnarz et al., 2004; Ghodrati et al., 2006; Wang et al., 2010; Potyagaylo et al., 2014, 2016a; Cluitmans et al., 2018). Cluitmans et al. (2017) reconstructed potentials on the ventricular epicardium as sparse combinations of spatial source basis vectors generated from simulations of many paced beats. In this work, we use a related approach. However, we suggest to create a basis of body surface potential patterns instead of source patterns to condense the information to what can possibly be measured on the body surface. Corresponding basis patterns in source space are then obtained and combined to express reconstructions. Furthermore, we use a spatio-temporal basis instead of a spatial-only one, as we believe this reduces ambiguities and increases the robustness to noise. We demonstrate the method in an application to atrial ectopic activity.

2. METHODS

The outline of this study is illustrated in **Figure 1**. First, fast marching simulations of 200 ectopic foci are performed and forward calculated to create basis vectors. Reconstructions are then performed using these basis vectors for another set of 100 ectopic foci simulations. Here, the monodomain model is used with three different conduction velocities (CV) and forward calculated BSPs are corrupted with three different levels of noise. Finally, reference reconstructions are obtained using the Tikhonov-Greensite method and the same metrics are calculated for both reconstruction methods.

2.1. Geometries

Figure 2 shows the geometries used for forward and inverse calculations. They are the same as in Schuler et al. (2017), which in turn are based on Figuera et al. (2016). The surface meshes of the atria and torso consist of 4,800 and 844 nodes and have an average edge length of 3.4 and 27.0 mm, respectively. A subset of 173 torso nodes have been selected as electrodes (blue spheres). Much finer tetrahedral meshes of the atria were used for excitation simulations (142 k nodes, average edge length: 0.9 mm). Blue and red spheres on the atria mark evenly distributed pacing locations used for fast marching and monodomain simulations, respectively. Note that pacing locations for both sets of simulations do generally not coincide.

2.2. Fast Marching Simulations

For creating basis vectors, fast marching simulations of 200 paced beats were performed. First, local activation times (LAT) t_a were computed by solving the eikonal equation with the fast marching method (Pernod et al., 2011):

$$\|\nabla t_a\|_2 = \frac{1}{c}$$

The CV was homogeneously set to $c = 0.8\,\mathrm{m/s}$. A TMV template was then aligned with LATs. Experiments with a template based on the Courtemanche et al. cell model and a step-function-like template (**Figure 3**) showed that basis vectors created as described in section 2.5.1 are mainly determined by the depolarization upstroke and it is not necessary to include the repolarization. Therefore, we decided to use the step-function-like template. The temporal sampling period was chosen to be 2 ms.

2.3. Monodomain Simulations

As activity to be reconstructed, 100 paced beats were simulated using the monodomain model:

$$\nabla \cdot (\sigma_{mono} \nabla V_m) = \beta \left(C_m \frac{\partial V_m}{\partial t} + I_{ion} \right)$$

The monodomain conductivity σ_{mono} was chosen homogeneous and isotropic and, together with the surface-to-volume ratio β, was adjusted to obtain the desired CV. In order to study what happens, if a wrong CV is assumed for the creation of basis vectors, we varied the CV by ±50% of its baseline value. Therefore, three different CVs were used for monodomain simulations: 0.4, 0.8, and 1.2 m/s. Ionic currents I_{ion} across the cell membrane were defined according to Courtemanche et al. (1998). As for fast marching simulations, the temporal resolution is 2 ms.

2.4. Forward Calculation

According to bidomain theory, extracellular potentials ϕ are related to volumetric TMVs V_m by:

$$\nabla \cdot ((\boldsymbol{\sigma}_i + \boldsymbol{\sigma}_e) \nabla \phi) = -\nabla \cdot (\boldsymbol{\sigma}_i \nabla V_m) \tag{1}$$

In this work, we assume isotropic, i.e., scalar intra- and extracellular conductivities $\boldsymbol{\sigma}_i$ and $\boldsymbol{\sigma}_e$, respectively. As this is a special case of equal intra- and extra-cellular anisotropy ratios, volumetric TMVs may be replaced by TMVs on the myocardial surface (Yamashita and Geselowitz, 1985). For a homogeneous torso with the same bulk conductivity as the heart σ, the potential ϕ at an observation point can be calculated from surface TMVs V_m by (Simms and Geselowitz, 1995):

$$\phi = -\frac{1}{4\pi\sigma} \int_{S_H} \sigma_i V_m \, d\Omega_H - \frac{1}{4\pi} \int_{S_B} \phi_B \, d\Omega_B \tag{2}$$

S_H and S_B are the surfaces bounding the myocardium and torso, respectively. $d\Omega_H$ and $d\Omega_B$ are the solid angles subtended by an area element on the corresponding surface as seen from an

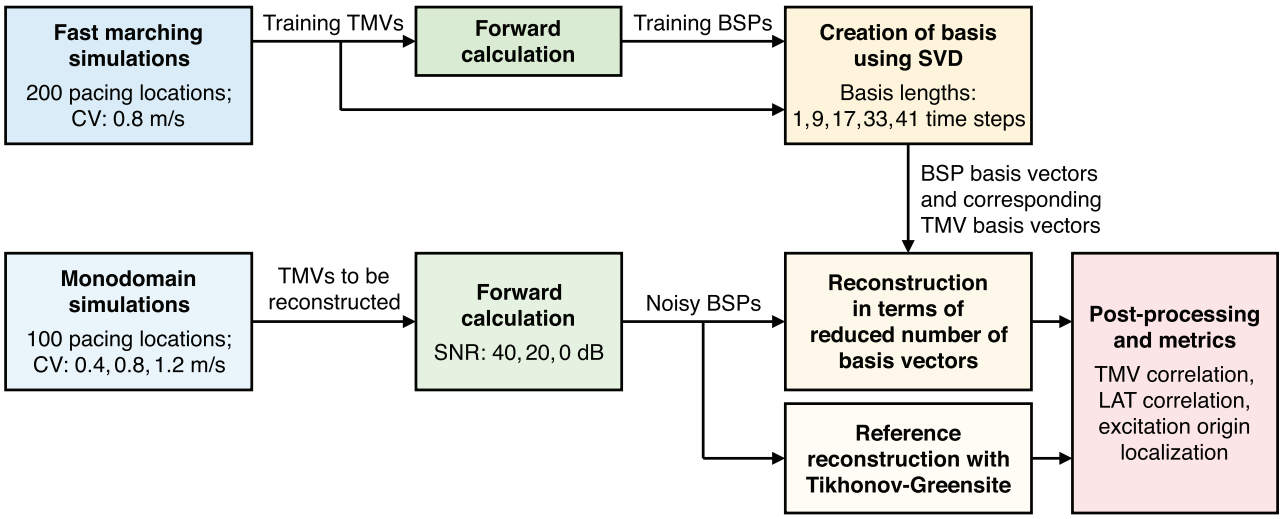

FIGURE 1 | Flowchart illustrating the outline of this study.

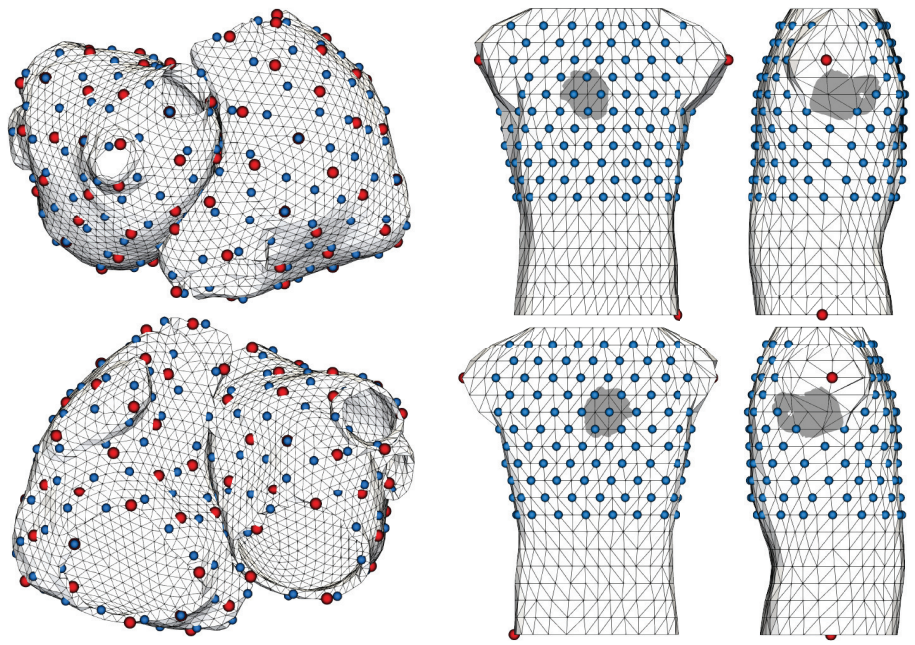

FIGURE 2 | Meshes of the atria and torso used for forward and inverse calculations. Blue spheres on the atria indicate 200 pacing locations used to create basis vectors, while red spheres indicate 100 pacing locations used for monodomain simulations to be reconstructed. Torso electrodes are shown in blue. Red spheres on the torso mark reference nodes.

observation point. By applying the boundary element method to solve (2) for BSPs $\phi = \phi_B$, a lead field matrix $\mathbf{A}$ is obtained that transforms surface TMVs to BSPs. Intracellular and bulk conductivities are set to $\sigma_i = 0.05\,\mathrm{S/m}$, and $\sigma = 0.2\,\mathrm{S/m}$ and potentials are referenced to Wilson's central terminal. We assume the following linear forward model:

$$\mathbf{b}_k = \mathbf{A}\mathbf{x}_k + \boldsymbol{\varepsilon}_k$$

where $\mathbf{b}_k$, $\mathbf{x}_k$ and $\boldsymbol{\varepsilon}_k$ are BSPs, TMVs, and white Gaussian noise for all nodes at a time step k, respectively. For fast marching simulations used to create basis vectors, we do not add any noise. For monodomain simulations, we consider three different signal-to-noise ratios (SNRs): 40, 20, and 0 dB. It is assumed that each electrode is affected by the same absolute noise power, which is set to the average signal power of all electrodes divided by the SNR. For solving the inverse problem, we assume perfect knowledge

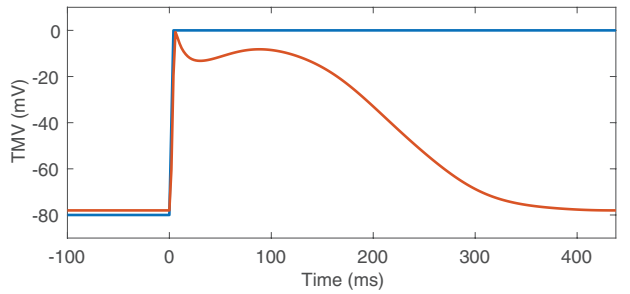

FIGURE 3 | TMV templates based on the Courtemanche et al. cell model (red) and the step function (blue).

of **A** and thus neglect errors due to imperfect geometries and conductivities.

2.5. Reconstruction Using Spatio-Temporal BSP Basis

The following identifiers and terminology will be used in this section:

N	Number of atria nodes
M	Number of torso electrodes
K	Total number of time steps in training data (here: 200) or to be reconstructed
L	Basis length: odd number of time steps in each basis vector (here: 1, 9, 17, 25, 33, 41)
P	Basis dimension: number of basis vectors used for reconstruction

2.5.1. Creation of Basis Vectors

As in Cluitmans et al. (2017), we use the singular value decomposition (SVD) to create basis vectors. In order to get a spatio-temporal basis, we define an observation as the column-wise concatenation of values at all nodes for all time steps within a time window of length L. As we do not know the time delay between the activity to be reconstructed and the activities used to create the basis, we include all possible delays by continuously time-shifting the window by a single time step. This way, a total of $K-L+1$ observations are generated for each simulation. Row-wise concatenation of all observations (all time shifts of all simulations) then yields a data matrix $\mathbf{D}$. Using $\mathbf{x}_k$ to denote TMVs for all nodes at a time step k, the TMV data matrix $\mathbf{D_x}$ is thus given as:

$$\mathbf{D_x} = \begin{bmatrix} \begin{pmatrix} \mathbf{x}_1^\mathsf{T} & \mathbf{x}_2^\mathsf{T} & \cdots & \mathbf{x}_L^\mathsf{T} \\ \mathbf{x}_2^\mathsf{T} & \mathbf{x}_3^\mathsf{T} & \cdots & \mathbf{x}_{L+1}^\mathsf{T} \\ \vdots & \vdots & & \vdots \\ \mathbf{x}_{K-L+1}^\mathsf{T} & \mathbf{x}_{K-L+2}^\mathsf{T} & \cdots & \mathbf{x}_K^\mathsf{T} \end{pmatrix} \\ \vdots \\ \text{(repeat for all simulations)} \end{bmatrix}$$

By replacing $\mathbf{x}$ with $\mathbf{b}$, a BSP data matrix $\mathbf{D_b}$ can be constructed in exactly the same way. From $\mathbf{A}\mathbf{x}_k = \mathbf{b}_k$, it follows that the whole TMV data matrix can be forward calculated using a block diagonal lead field matrix $\widetilde{\mathbf{A}}$:

$$\widetilde{\mathbf{A}}\,\mathbf{D_x}^\mathsf{T} = \mathbf{D_b}^\mathsf{T} \quad \Leftrightarrow \quad \mathbf{D_b} = \mathbf{D_x}\,\widetilde{\mathbf{A}}^\mathsf{T} \quad \text{with} \quad \widetilde{\mathbf{A}} = \mathbf{I}_L \otimes \mathbf{A} \tag{3}$$

$\mathbf{I}_L$ is the $L \times L$ identity matrix and $\otimes$ denotes the Kronecker product.
We now perform an SVD of the BSP data matrix:

$$\mathbf{D_b} = \mathbf{U}\mathbf{S}\mathbf{V_b}^\mathsf{T} \tag{4}$$

The columns of $\mathbf{V_b}$ are spatio-temporal basis vectors of BSPs. We now want to find the corresponding TMV basis vectors $\mathbf{V_x}$, for which holds:

$$\mathbf{V_b} = \widetilde{\mathbf{A}}\,\mathbf{V_x} \tag{5}$$

Substituting (3) and (5) in (4) yields:

$$\mathbf{D_x}\,\widetilde{\mathbf{A}}^\mathsf{T} = \mathbf{U}\mathbf{S}\mathbf{V_x}^\mathsf{T}\,\widetilde{\mathbf{A}}^\mathsf{T} \quad \Leftrightarrow \quad \mathbf{V_x}^\mathsf{T} = (\mathbf{U}\mathbf{S})^+\,\mathbf{D_x} = \mathbf{S}^+\mathbf{U}^\mathsf{T}\,\mathbf{D_x}$$

$(\cdot)^+$ denotes the Moore–Penrose pseudoinverse. This shows that the TMV basis can directly be calculated from the TMV data matrix using an inversion of **US**, the scores matrix obtained from the SVD of the BSP data matrix. An inversion of $\widetilde{\mathbf{A}}$ is not required.

2.5.2. Reconstruction in Terms of Basis Vectors

Now the BSPs of a patient show up. They will be called $\mathbf{B} = [\mathbf{b}_1, \mathbf{b}_2, \ldots, \mathbf{b}_K]$ in the following. Here, K is the total number of time steps to be reconstructed. To reconstruct TMVs in terms of a reduced number P of basis vectors, we first perform a least-squares regression using BSP basis vectors. This results in the optimal basis vector weights $\mathbf{W}$:

$$\mathbf{W} = \arg\min_{\mathbf{W}} \left\| \mathbf{V_b}(:, 1{:}P)\,\mathbf{W} - \widetilde{\mathbf{B}} \right\|_F^2 \tag{6}$$

$\|\cdot\|_F$ denotes the Frobenius norm and $\widetilde{\mathbf{B}}$ are the "measured" BSPs reshaped into the format of basis vectors. Using MATLAB notation, they are given by:

$$\widetilde{\mathbf{B}}(:, k) = \text{reshape}\big(\mathbf{B}(:, k{:}k+L-1),\, LM,\, 1\big) \quad \text{for} \quad k = 1, 2, \ldots, K-L+1$$

Since the columns of $\mathbf{V_b}$ form an orthonormal basis, the solution to (6) is given by:

$$\mathbf{W} = \mathbf{V_b}(:, 1{:}P)^\mathsf{T}\,\widetilde{\mathbf{B}} \tag{7}$$

This can be seen as filtering the BSPs by projecting them onto the P most important BSP basis vectors. The weights $\mathbf{W}$ are now used to obtain the reconstructed TMVs $\widetilde{\mathbf{X}}_r$ as linear combination of corresponding TMV basis vectors:

$$\widetilde{\mathbf{X}}_r = \mathbf{V_x}(:, 1{:}P)\,\mathbf{W}$$

Each column of $\widetilde{\mathbf{X}}_r$ contains the row-wise concatenation of all time windows with length L. As final solution $\mathbf{X}_r$, we therefore extract the central time step of each window:

$$\mathbf{X}_r = \mathbf{V_x}\left(\tfrac{L-1}{2}N+(1{:}N),\ 1{:}P\right)\mathbf{W}$$

Corresponding BSPs can be obtained in the same manner:

$$\mathbf{B}_r = \mathbf{V_b}\left(\tfrac{L-1}{2}M+(1{:}M),\ 1{:}P\right)\mathbf{W} = \mathbf{A}\,\mathbf{X}_r$$

We would like to point out that creating the basis vectors in BSP space instead of in source space, i.e., calculating the SVD of $\mathbf{D_b}$ instead of $\mathbf{D_x}$, is the key step which makes it possible to perform an unregularized least-squares regression without additional constraints. If the basis vectors were created in source space, they may still contain redundant information with respect to BSPs and therefore a regularized regression would be necessary: $\mathbf{W} = \arg\min_{\mathbf{W}} \left\{ \left\| \widetilde{\mathbf{A}}\,\mathbf{V_x}(:,\ 1{:}P)\,\mathbf{W} - \widetilde{\mathbf{B}} \right\|_F^2 + \lambda \left\| \mathbf{R}\,\mathbf{V_x}(:,\ 1{:}P)\,\mathbf{W} \right\|_F^2 \right\}$, where $\mathbf{R}$ is a regularization matrix. This would require inverting a $P{\times}P$ matrix for every combination (P, λ), while only a fast matrix multiplication (7) has to be computed for each P when using the BSP basis.

2.5.3. Choice of Basis Dimension

Following the concept of the L-curve, the "optimal" basis dimension is determined from the log-log graph of the residual norm $\|\mathbf{B}_r - \mathbf{B}\|_F$ versus the corresponding basis dimension P (left diagram in **Figure 4**). Instead of the maximal curvature, which is not very pronounced in the resulting "L-curves," we found that the minimal absolute slope (blue circles) of a smoothing spline fit is a good criterion for selecting the basis dimension. To ensure that solutions are not underregularized, we set the basis dimension 10% lower than at the point of minimal absolute slope (red circles). The right diagram in **Figure 4** shows that the resulting basis dimension for one specific SNR depends linearly on the basis length L.

2.6. Reference Reconstruction With Tikhonov-Greensite

For comparison, reconstructions with the Tikhonov-Greensite method (TikhGS) are performed (Greensite and Huiskamp, 1998). While standard Tikhonov methods regularize each time step individually, TikhGS performs Tikhonov regularization for the p most important temporal singular vectors of BSPs, which helps to eliminate noise and generally leads to better reconstructions, given the number of singular vectors used is chosen appropriately. We apply the epi-endo projection described in Schuler et al. (2017), which further improves the solution. TikhGS is then used with simultaneous zero- and second-order constraints:

$$\mathbf{B} = \mathbf{U}\mathbf{S}\mathbf{V}^{\mathsf{T}}, \quad \overline{\mathbf{V}} = \mathbf{V}(:,\ 1{:}p)$$

$$\mathbf{X}\overline{\mathbf{V}} = \arg\min_{(\mathbf{X}\overline{\mathbf{V}})} \left\{ \|\mathbf{A}(\mathbf{X}\overline{\mathbf{V}}) - \mathbf{B}\overline{\mathbf{V}}\|_F^2 + \lambda\|\mathbf{L}(\mathbf{X}\overline{\mathbf{V}})\|_F^2 + \eta\|\mathbf{X}\overline{\mathbf{V}}\|_F^2 \right\}$$

$$\mathbf{X} = (\mathbf{X}\overline{\mathbf{V}})\overline{\mathbf{V}}^{\mathsf{T}}$$

In order to provide the reference method with the best possible parameters, p was varied between 3 and 13 and regularization parameters λ and η were optimized for each case individually to maximize the mean of spatial TMV correlation with the ground truth over the period of depolarization. The downhill simplex method was used for optimization.

2.7. Post-processing and Metrics

2.7.1. Transmembrane Voltages

To assess the quality of reconstructed TMVs, the Pearson correlation coefficient between reconstructions and the ground truth is computed separately for each time step across all nodes (spatial CC). As we want to quantify, how good the depolarization is being reconstructed, we only calculate the spatial CC for time steps between the first and the last activation of each simulation, as defined by the ground truth.

2.7.2. Local Activation Times

Local activation times represent one of the most important characteristic of cardiac excitation spread and are therefore estimated from reconstructed TMVs. We use the "global activation time" approach described in Dubois et al. (2012), which is based on cross-correlating signals of nearby nodes to find their time delay. The method has further been advanced in Duchateau et al. (2017) to combine delay-based and deflection-based activation times. In this work, however, we stick with the delay-only formulation. The procedure is illustrated in **Figure 5**. First, TMVs are oversampled to allow for a precise alignment in time. As signal for cross-correlation, we then use a Gaussian filtered version of the magnitude of the surface gradient of TMVs: $\|\nabla V_m(t)\|_2$. Using a lowpass filtered time derivative as described in Duchateau et al. (2017) yielded unsatisfactory results for both TikhGS and the BSP basis reconstruction. This might be explained by the fact that the spatial gradient of TMVs is the source of body surface potentials according to (1). LATs are finally estimated from the delays using least-squares regression of a linear model. As LAT metric, we calculate the spatial CC between LATs estimated for reconstructions and the ground truth.

2.7.3. Ectopic Focus Localization

BSPs are directly proportional to the solid angle at a measurement point subtended by the depolarization wavefront, which separates regions of low and high TMVs (see Equation 2). For a given noise level, the instantaneous SNR therefore rises with the size of the depolarization wavefront and the excitation origin cannot reliably be determined from the small signal at the very onset of excitation. If the depolarization wavefront spreads too far from the origin, however, the uncertainty of localizing the origin within the depolarized region increases as well. As the CV is not known beforehand, we therefore do not base the focus localization on one specific time step, but use the temporal mean of many time steps after excitation onset. If the TMV waveform was a Heaviside step function, the TMV time integral (and thus also its temporal mean) would be proportional to reversed activation times. For other TMV waveforms, the temporal mean still yields a valid activation "sequence," as long

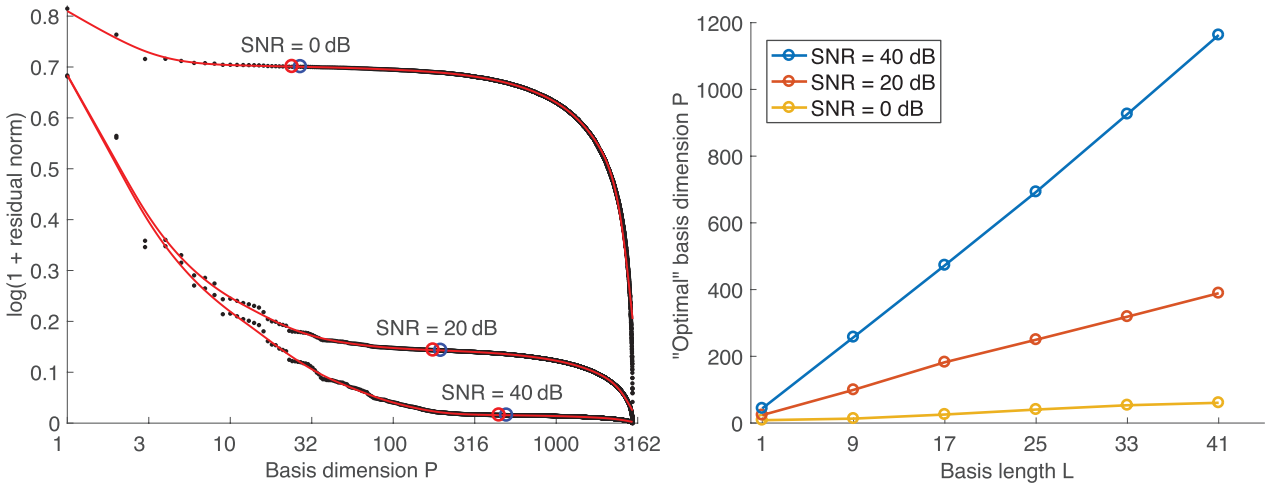

FIGURE 4 | (Left) Exemplary "L-curves" for a basis length of $L = 17$. Black dots: original data points. Red curves: smoothing spline fits. Blue circles: Points of min. absolute slope. Red circles: Points 10% left of min. slope points. **(Right)** Dependency of basis dimension on basis length.

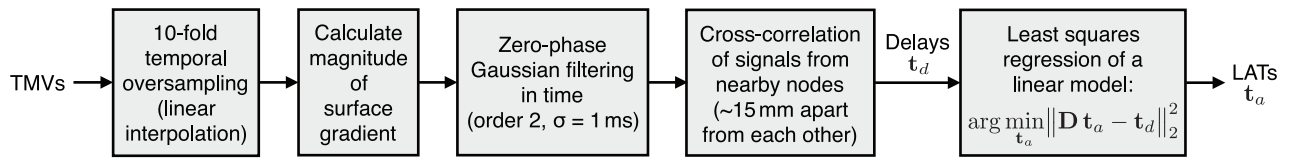

FIGURE 5 | Delay-based LAT estimation. **D** is a difference matrix to obtain pair-wise delays from LATs.

as the TMV time integral is increasing (Schulze, 2015). Based on the TMV waveform of the Courtemanche et. al. model (**Figure 3**), we chose to calculate the mean over 200 ms after excitation onset. In general, this time should not be chosen larger than the effective refractory period. In this work, the time of excitation onset is assumed to be known. In practice, it would have to be determined as the P wave onset. Having obtained activation sequences, a template matching approach is employed to detect the focus location: For every mesh node, the zero-mean normalized correlation (ZNC) of the temporal mean of TMVs $\overline{V_m}$ and the reversed geodesic distance field, originating from the respective node and truncated at 3 cm, is calculated. As the ZNC only measures similarity in shape, not magnitude, the result is further weighted with $(\overline{V_m} - \min\{\overline{V_m}\})$. The maximum of this "focus measure" is finally detected as focus. The method is illustrated in **Figure 6** for both BSP basis and TikhGS reconstructions. Correlating with the geodesic distance fields can also be seen as a transformation to find the center of mass of the TMV distribution on a curved surface.

As localization error, the geodesic distance between the true and reconstructed focus is evaluated. In contrast to the Euclidean distance, this metric correctly yields large errors for nearby points that are not directly connected via the geometry, such as two points on the opposite side of the interatrial region.

3. RESULTS

3.1. Basis Vectors and Singular Values

Figure 7 (left) depicts 3 time steps of exemplary TMV basis vectors for a basis length of $L = 17$. It can be seen that the spatial and/or temporal frequency increases with the basis vector number and that spatial patterns evolve over time. The diagram on the right shows that the larger the basis length, the more basis vectors are needed to represent the same proportion of information contained within all basis vectors.

3.2. Robustness to Noise

Metrics for reconstructions of monodomain simulations with the same CV as used for basis creation are shown in **Figure 8**. For all noise levels considered, BSP basis reconstructions perform consistently better than TikhGS. Even a spatial-only basis ($L = 1$) leads to an improvement. Increasing the basis length further increases the correlation coefficients for both TMVs and LATs, especially for low SNRs. This can also be seen from **Figure 9**, where LATs for an ectopic focus near the left inferior pulmonary vein are shown for different SNRs and basis lengths. While the LAT map for $L = 1$ and 40 dB already looks much like the ground truth, basis lengths of at least $L = 9$ and $L = 17$ are needed for 20 and 0 dB, respectively.

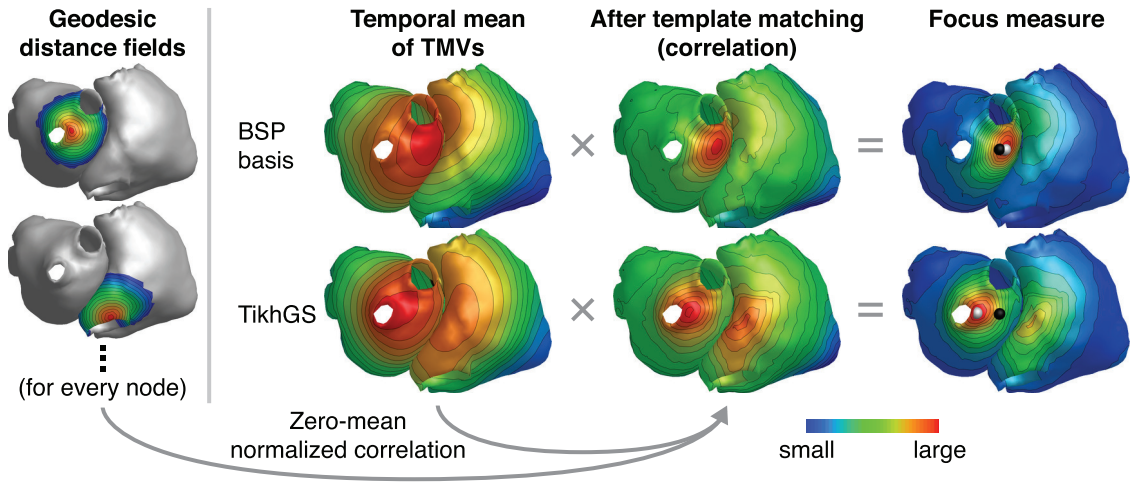

FIGURE 6 | Ectopic focus localization illustrated for exemplary reconstructions with the BSP basis ($L = 33$) and TikhGS. CV = 0.8 m/s. SNR = 0 dB. Black spheres: true focus, white spheres: reconstructed focus. Geodesic distance fields shown on the left are reversed and truncated at 3 cm (dark blue). Gray areas are not taken into account for correlation.

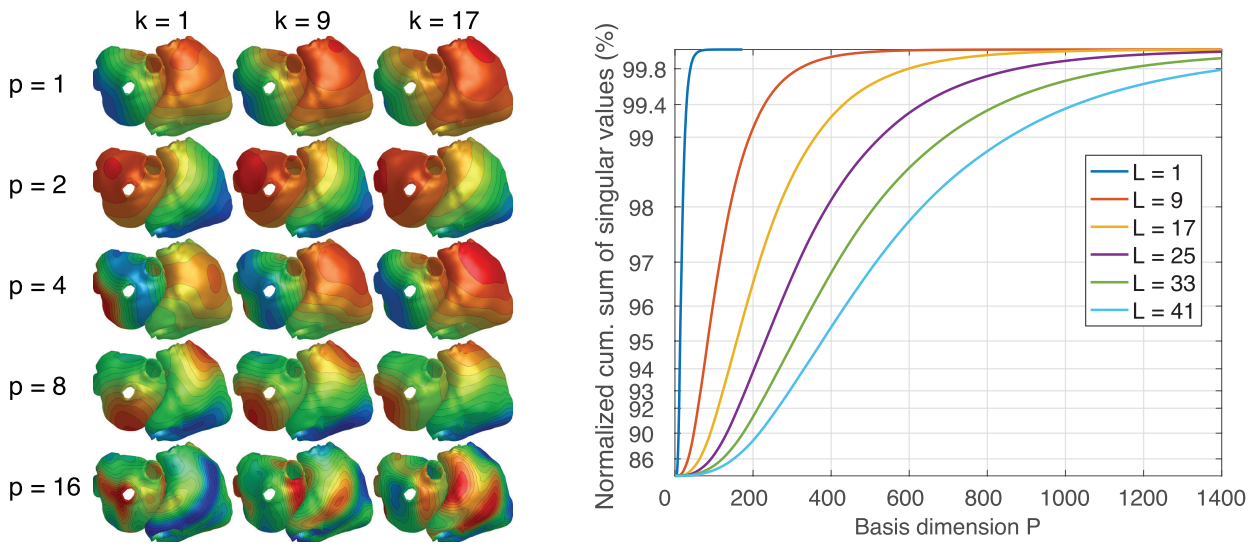

FIGURE 7 | (Left) Examples of TMV basis vectors for $L = 17$. p: basis vector number. k: time step. Colors only visualize spatial morphology. **(Right)** Cumulative sum of singular values for different basis lengths L.

3.3. Influence of Conduction Velocity

In theory, errors in the spatial dimension, i.e., the position of the wavefront, increase linearly with time for a mismatch of CV. Therefore it is expected that the reconstruction quality deteriorates for large basis lengths if the CV used to create basis vectors deviates from the actual CV. **Figures 10A,B** show the metrics for a CV of 0.4 and 1.2 m/s, respectively, while the CV assumed for basis vectors remains at 0.8 m/s. It can be seen that there is now indeed an upper limit for the improvement with increasing basis lengths. Results show a clear tradeoff between the error due to a wrong CV for large basis lengths and the error due to lower robustness to noise for small basis lengths. Although the BSP basis reconstruction still outperforms TikhGS in every case, it can be seen from comparison of both figures that overestimating the true CV during basis creation seems to be less problematic than underestimating it. **Figure 11** shows another interesting effect of wrong CVs. If the CV is overestimated (top row), LATs estimated from reconstructions with large basis lengths are smaller than true LATs, suggesting a larger than actual CV. To a lesser extent, the opposite effect can be seen for an underestimation (bottom row).

3.4. Ectopic Focus Localization

Localization errors are shown in **Figure 12**. The mean error decreases with increasing basis length, even for CVs different from 0.8 m/s. For $L = 41$, it is approximately halved compared to TikhGS (see **Table 1**). Another important improvement is the reduction of the maximum localization error. While errors for TikhGS range up to 90 mm, the maximum error for $L = 41$ is 34 mm. For a CV of 0.4 m/s, however, there is an outlier for $L = 25$ and $L = 33$. This case is illustrated on the right of **Figure 12C**. For this ectopic focus at the orifice of the inferior vena cava, the reconstruction first shows a false activity on the nearby left atrium. Only after the excitation has further increased in size, the reconstruction continues to show the activity at the correct location. A better localization thus would have been obtained for a later (or longer) time window used for calculating the temporal mean.

In general, the BSP basis reconstruction largely resolves ambiguities. In **Figure 13A**, this is demonstrated for a focus on the anterior-septal wall of the left atrium. TikhGS and a purely spatial basis fail to recover the activity at the correct spot and show multiple activities on the right and left atrium instead. Using a spatio-temporal basis, however, leads to a reconstruction at the correct spot. Increasing the basis length progressively increases the uniqueness of the solution. An even better impression on where ambiguities arise between sources can be obtained by taking a look at the distributions of localization errors across the atria, as shown in **Figure 13B**. For TikhGS, the largest errors occur at the interatrial region, where left and right atrial surfaces are very close to each other and oriented in parallel. Using a BSP basis of sufficient length greatly reduces these errors.

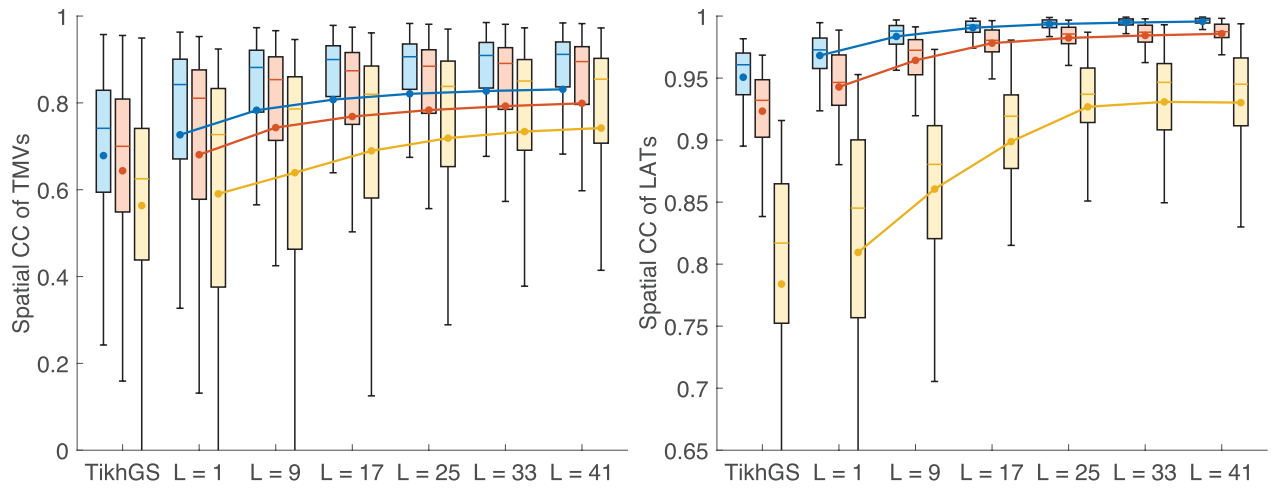

FIGURE 8 | Metrics for a CV of 0.8 m/s. Colors represent different SNRs. Blue: 40 dB, red: 20 dB, yellow: 0 dB. Boxes: 25–75th percentile. Whiskers: 1.5 inter-quartile range. Filled circles and lines represent the mean. **(Left)** Spatial CC of TMVs. **(Right)** Spatial CC of LATs.

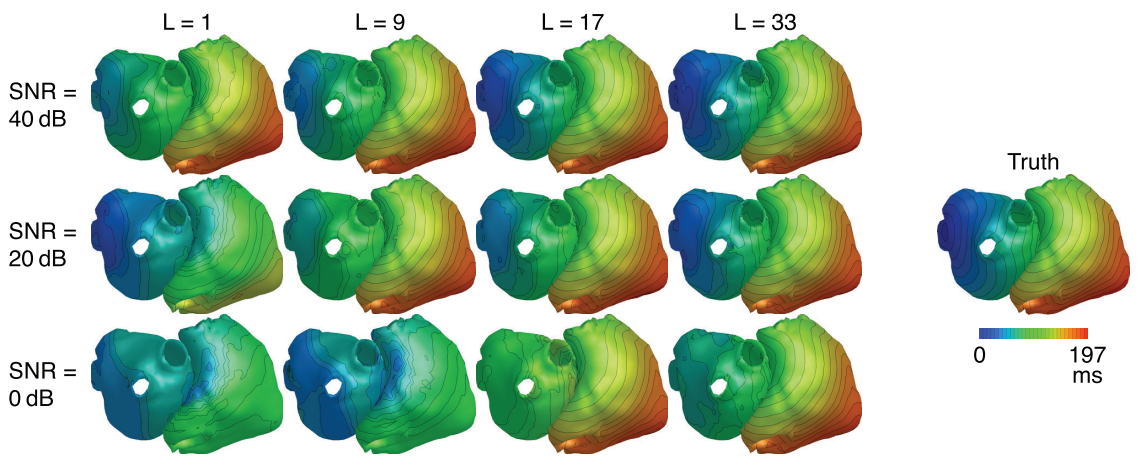

FIGURE 9 | LATs for different SNRs and basis lengths L. CV = 0.8 m/s.

3.5. Effect of Non-conducting Region

In order to test, how much the reconstruction relies on the excitation patterns in the training data, we added a non-conducting scar region to one simulation. For that purpose, the monodomain conductivity was set to zero in a circular region with a diameter of 4 cm on the right atrium. The results are shown in **Figure 14**. It can be seen that the reconstructed wavefront propagates around the non-conducting region on the

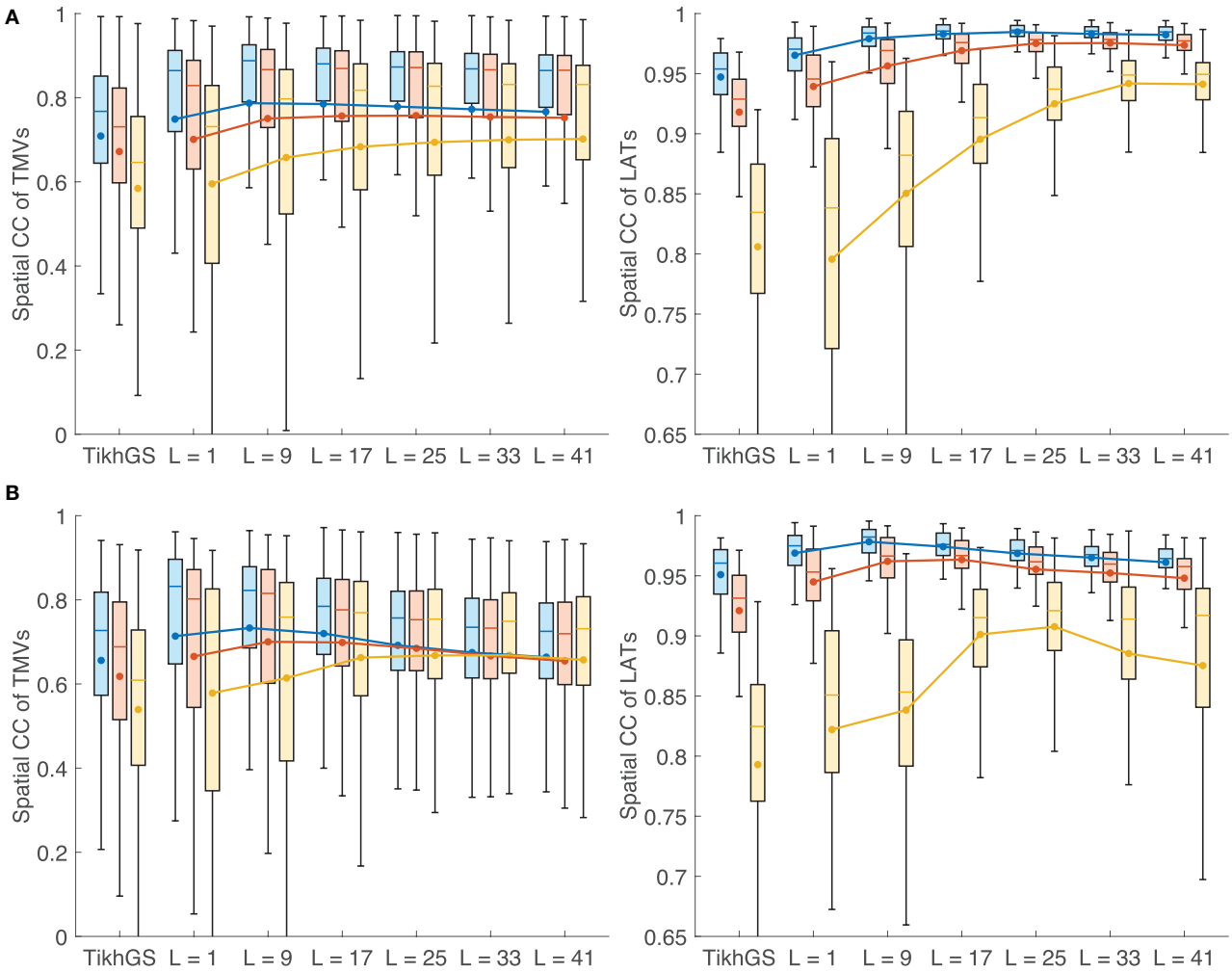

FIGURE 10 | (A) Metrics for a CV of 0.4 m/s. **(B)** Metrics for a CV of 1.2 m/s. See caption of **Figure 8** for details.

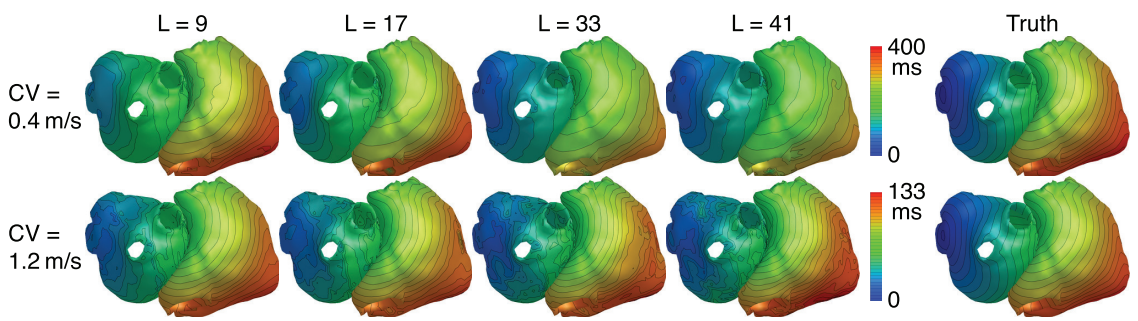

FIGURE 11 | LATs for different CVs and basis lengths *L*. SNR = 40 dB.

right atrium, even though the training data did not include such a pattern. The basis created by including all time shifts of excitation patterns in the data matrix therefore generalizes from individual patterns.

4. DISCUSSION

We demonstrated that using a spatio-temporal basis of BSPs to reconstruct TMVs improves the robustness to noise, resolves ambiguities between sources and leads to better localization of atrial ectopic foci than TikhGS. Of all possible solutions fitting to measured BSPs, the proposed method selects the one which is most probable with regard to the training data used to create basis vectors. This approach allows us to reconstruct hidden sources as well, given they occur in conjunction with other, visible sources. Compared to simply correlating measured BSPs with BSPs of many simulated beats (Potyagaylo et al., 2016b), the new method has two main

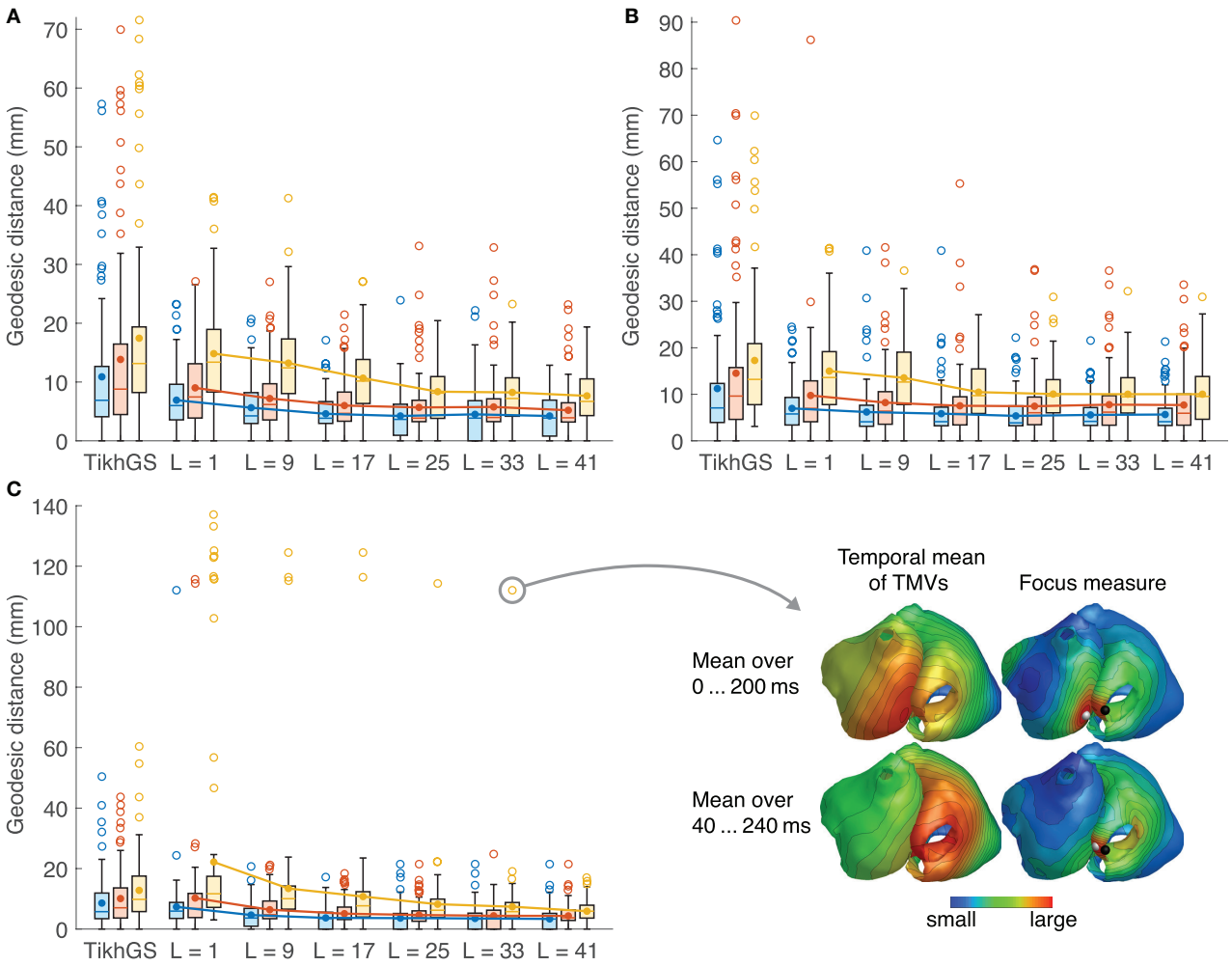

FIGURE 12 | Localization errors for all 100 ectopic foci. See caption of **Figure 8** for colors and markers. Outliers are shown as empty circles. **(A)** CV = 0.8 m/s. **(B)** 1.2 m/s. **(C)** 0.4 m/s. The outlier for CV = 0.4 m/s and $L = 33$ is depicted on the bottom right. Black sphere: true focus, white sphere: reconstructed focus.

TABLE 1 | Localization errors in mm.

	CV = 0.4 m/s				CV = 0.8 m/s				CV = 1.2 m/s			
	TikhGS		L = 41		TikhGS		L = 41		TikhGS		L = 41	
SNR (dB)	20	0	20	0	20	0	20	0	20	0	20	0
Mean	10.1	12.8	4.4	5.9	13.8	17.5	5.2	7.6	14.5	17.3	7.7	10.0
90th percentile	19.9	23.5	8.3	10.9	33.6	35.0	10.0	13.1	36.4	31.1	17.3	18.4
Maximum	43.7	60.4	21.5	17.0	69.9	71.6	23.2	19.4	90.4	69.9	33.6	30.9

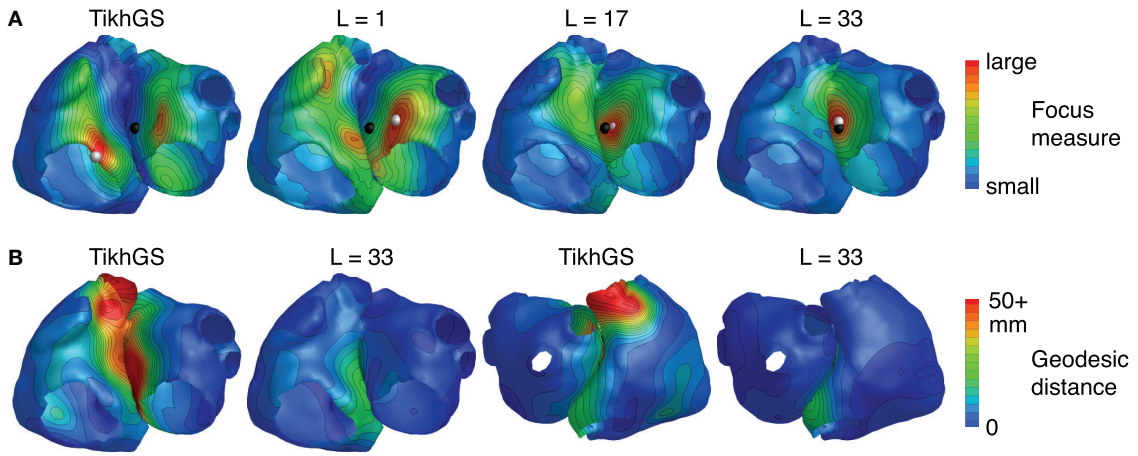

FIGURE 13 | (A) Focus measure for a focus on the anterior-septal wall of the left atrium (CV = 0.8 m/s, SNR = 0 dB). Black sphere: true focus, white sphere: reconstructed focus. **(B)** Distribution of localization errors across the atria for TikhGS and the BSP basis reconstruction (CV = 0.8 m/s, SNR = 20 dB, results for 0 dB are qualitatively similar). Values were interpolated by minimizing the Laplacian at all nodes (Oostendorp et al., 1989).

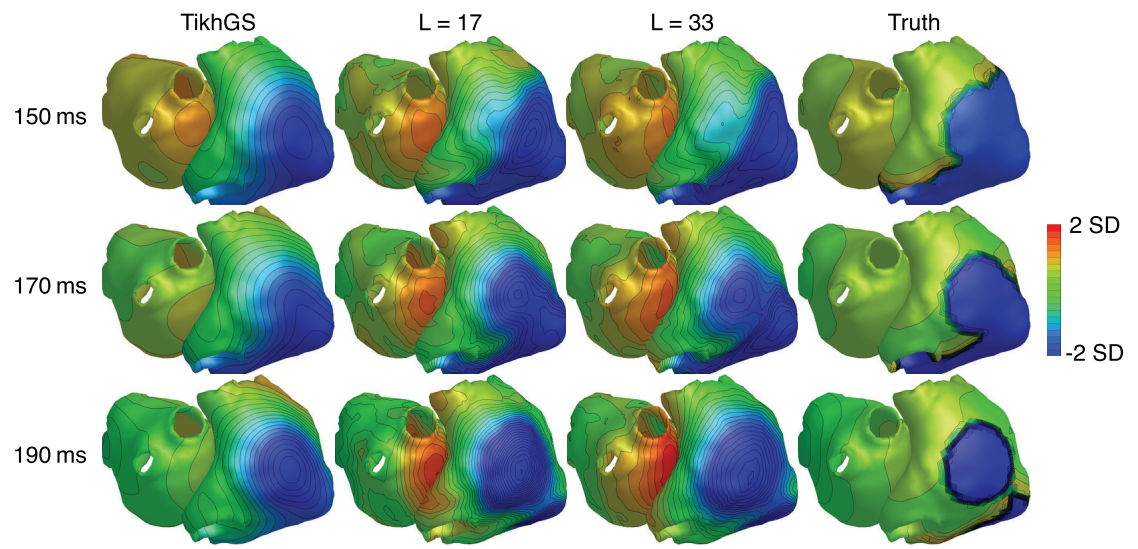

FIGURE 14 | TMVs for a simulation containing a non-conducting scar region on the right atrium. SNR = 20 dB. CV = 0.8 m/s. Each time step was normalized by subtracting the spatial mean and dividing by the spatial standard deviation (SD).

advantages: First, the basis generalizes to some extent from the individual activities used as input and thus also allows us to represent excitation patterns that were not among the training data. Second, measured and simulated BSPs do not have to be aligned in time, as the basis contains all time shifts. Localization results obtained by correlating with all BSP patterns in the training data and finding the one with the maximum correlation coefficient are included in the **Supplementary Material**. Although this approach works comparably well if the CV matches the CV in the training data, it performs considerably worse than the BSP basis reconstruction for non-matching CVs.

One remaining question regarding the creation of basis vectors is how to best set up the training data, so that each basic activation pattern occurs equally often in the data matrix. In the current geometry, the left and right atrium are only connected by one bridge representing the Bachmann's bundle. This results in almost the same activation pattern on the opposite atrium, once the excitation has passed the bridge. This activation pattern (corresponding to pacing at the bridge) occurs disproportionately often in the data matrix and will therefore best be represented by the resulting basis vectors. Reconstructions might therefore be biased toward this specific pattern. In geometries with multiple bridges, this effect is not

as pronounced. Limiting the information in the data matrix to a time window around the beginning of excitations is expected to optimize the basis for better reconstructions near the excitation origin.

4.1. Limitations

There are several limitations of this study that need to be acknowledged. The most important one is that atrial conductivities were assumed to be homogeneous and isotropic. Although we think this is a logical first step in evaluating the new reconstruction method systematically, its performance has to be studied with atrial anisotropy and several atrial geometries. This has to be done in a future work. However, exemplary reconstructions for four ectopic foci in a highly anisotropic model of the atria are included in the **Supplementary Material**. These results indicate that the method improves reconstructions over TikhGS for anisotropic spread of excitation as well, although the reconstruction quality does decrease compared to the isotropic case. Another aspect not considered is fibrosis, which may hamper the localization of atrial ectopic foci (Godoy et al., 2018). Finally, further studies are needed to evaluate the sensitivity to imperfect geometries and conductivities.

4.2. Outlook

We are planning to study the new reconstruction method with clinical measurements during (focal) ventricular tachycardia. We hope to make use of scar-related information from late gadolinium enhancement MRI during the creation of basis vectors. For non-focal arrhythmias, it would be interesting to see whether including non-focal activities in the basis is beneficial.

AUTHOR CONTRIBUTIONS

SS developed the BSP basis reconstruction method, designed and conducted the simulation study and wrote the manuscript. AW created atrial fiber orientations for the simulations in the **Supplementary Material**. OD provided technical expertise and contributed during study design and manuscript preparation.

FUNDING

This study was supported by the German Research Foundation (DFG) under the grant DO 637/21-1.

SUPPLEMENTARY MATERIAL

The Supplementary Material for this article can be found online at: https://www.frontiersin.org/articles/10.3389/fphys.2018.01126/full#supplementary-material

Movies of atrial ectopic foci reconstructions and exemplary reconstructions of rotational activity (simple atrial fibrillation from Figuera et al., 2016) can be found in the **Supplementary Material**.

REFERENCES

Cluitmans, M., Karel, J., Bonizzi, P., Volders, P., Westra, R., and Peeters, R. (2018). Wavelet-promoted sparsity for non-invasive reconstruction of electrical activity of the heart. *Med. Biol. Eng. Comput*. doi: 10.1007/s11517-018-1831-2. [Epub ahead of print].

Cluitmans, M. J. M., Clerx, M., Vandersickel, N., Peeters, R. L. M., Volders, P. G. A., and Westra, R. L. (2017). Physiology-based regularization of the electrocardiographic inverse problem. *Med. Biol. Eng. Comput.* 55, 1353–1365. doi: 10.1007/s11517-016-1595-5

Courtemanche, M., Ramirez, R. J., and Nattel, S. (1998). Ionic mechanisms underlying human atrial action potential properties: insights from a mathematical model. *Am. J. Physiol.* 275(1 Pt 2), H301–H321.

Dubois, R., Labarthe, S., Coudière, Y., Hocini, M., and Haïssaguerre, M. (2012). "Global and directional activation maps for cardiac mapping in electrophysiology," in *Computing in Cardiology* (Kraków), 349–352.

Duchateau, J., Potse, M., and Dubois, R. (2017). Spatially coherent activation maps for electrocardiographic imaging. *IEEE Trans. Biomed. Eng.* 64, 1149–1156. doi: 10.1109/TBME.2016.2593003

Figuera, C., Suárez-Gutiérrez, V., Hernández-Romero, I., Rodrigo, M., Liberos, A., Atienza, F., et al. (2016). Regularization techniques for ECG imaging during atrial fibrillation: a computational study. *Front. Physiol.* 7:466. doi: 10.3389/fphys.2016.00466

Ghodrati, A., Brooks, D., Tadmor, G., and MacLeod, R. (2006). Wavefront-based models for inverse electrocardiography. *IEEE Trans. Biomed. Eng.* 53, 1821–1831. doi: 10.1109/TBME.2006.878117

Godoy, E. J., Lozano, M., García-Fernández, I., Ferrer-Albero, A., MacLeod, R., Saiz, J., et al. (2018). Atrial fibrosis hampers non-invasive localization of atrial ectopic foci from multi-electrode signals: a 3D simulation study. *Front. Physiol.* 9:404. doi: 10.3389/fphys.2018.00404

Greensite, F., and Huiskamp, G. (1998). An improved method for estimating epicardial potentials from the body surface. *IEEE Trans. Biomed. Eng.* 45, 98–104.

Messnarz, B., Tilg, B., Modre, R., Fischer, G., and Hanser, F. (2004). A new spatiotemporal regularization approach for reconstruction of cardiac transmembrane potential patterns. *IEEE Trans. Biomed. Eng.* 51, 273–281. doi: 10.1109/TBME.2003.820394

Oostendorp, T. F., van Oosterom, A., and Huiskamp, G. (1989). Interpolation on a triangulated 3d surface. *J. Comput. Phys* 80, 331–343.

Pernod, E., Sermesant, M., Konukoglu, E., Relan, J., Delingette, H., and Ayache, N. (2011). A multi-front eikonal model of cardiac electrophysiology for interactive simulation of radio-frequency ablation. *Comput. Graph.* 35, 431–440. doi: 10.1016/j.cag.2011.01.008

Potyagaylo, D., Cortés, E. G., Schulze, W. H. W., and Dössel, O. (2014). Binary optimization for source localization in the inverse problem of ECG. *Med. Biol. Eng. Comput.* 52, 717–728. doi: 10.1007/s11517-014-1176-4

Potyagaylo, D., Dossel, O., and van Dam, P. (2016a). Influence of modeling errors on the initial estimate for nonlinear myocardial activation times imaging calculated with fastest route algorithm. *IEEE Trans. Biomed. Eng.* 63, 2576–2584. doi: 10.1109/TBME.2016.2561973

Potyagaylo, D., Loewe, A., van Dam, P., and Dössel, O. (2016b). "ECG imaging of focal atrial excitation: evaluation in a realistic simulation setup," in *Computing in Cardiology, Vol. 43* (Vancouver, BC), 113–116.

Pullan, A. J., Cheng, L. K., Nash, M. P., Ghodrati, A., MacLeod, R., and Brooks, D. H. (2010). "The inverse problem of electrocardiography," in *Comprehensive Electrocardiology*, eds P. MacFarlane, A. van Oosterom, O. Pahlm, P. Kligfield, M. Janse, and J. Camm (London: Springer), 299–344.

Schuler, S., Potyagaylo, D., and Dssel, O. (2017). "ECG imaging of simulated atrial fibrillation: imposing epi-endocardial similarity facilitates the reconstruction of transmembrane voltages," in *Computing in Cardiology, Vol. 44* (Rennes).

Schulze, W. H. W. (2015). *ECG Imaging of Ventricular Activity in Clinical Applications*. Ph.D. thesis, Institute of Biomedical Engineering, Karlsruhe Institute of Technology.

Simms, H. D. J., and Geselowitz, D. B. (1995). Computation of heart surface potentials using the surface source model. *J. Cardiovasc. Electrophysiol.* 6, 522–531.

van Oosterom, A. (1999). The use of the spatial covariance in computing pericardial potentials. *IEEE Trans. Biomed. Eng.* 46, 778–787.

Wang, L., Zhang, H., Wong, K. C., Liu, H., and Shi, P. (2010). Physiological-model-constrained noninvasive reconstruction of volumetric myocardial transmembrane potentials. *IEEE Trans. Biomed. Eng.* 57, 296–315. doi: 10.1109/TBME.2009.2024531

Yamashita, Y., and Geselowitz, D. B. (1985). Source-field relationships for cardiac generators on the heart surface based on their transfer coefficients. *IEEE Trans. Biomed. Eng.* 32, 964–970.

Conflict of Interest Statement: The authors declare that the research was conducted in the absence of any commercial or financial relationships that could be construed as a potential conflict of interest.

frontiers in Physiology

REVIEW
published: 20 September 2018
doi: 10.3389/fphys.2018.01305

Validation and Opportunities of Electrocardiographic Imaging: From Technical Achievements to Clinical Applications

Matthijs Cluitmans[1], Dana H. Brooks[2], Rob MacLeod[3], Olaf Dössel[4], María S. Guillem[5], Peter M. van Dam[6], Jana Svehlikova[7], Bin He[8], John Sapp[9], Linwei Wang[10] and Laura Bear[11]**

[1] Department of Cardiology, Cardiovascular Research Institute Maastricht Maastricht University, Maastricht, Netherlands, [2] Department of Electrical and Computer Engineering, Northeastern University, Boston, MA, United States, [3] Biomedical Engineering Department, Scientific Computing and Imaging Institute (SCI), and Cardiovascular Research and Training Institute (CVRTI), The University of Utah, Salt Lake City, UT, United States, [4] Karlsruhe Institute of Technology, Karlsruhe, Germany, [5] ITACA, Universitat Politècnican de València, Valencia, Spain, [6] Donders Institute for Brain, Cognition and Behaviour, Radboud University Nijmegen Medical Center, Nijmegen, Netherlands, [7] Institute of Measurement Science, Slovak Academy of Sciences, Bratislava, Slovakia, [8] Department of Biomedical Engineering Carnegie Mellon University, Pittsburgh, PA, United States, [9] QEII Health Sciences Centre and Department of Medicine, Dalhousie University, Halifax, NS, Canada, [10] Rochester Institute of Technology, Rochester, NY, United States, [11] IHU LIRYC, Fondation Bordeaux Université, Inserm, U1045 and Université de Bordeaux, Bordeaux, France

OPEN ACCESS

Edited by:
Bas J. Boukens, University of Amsterdam, Netherlands

Reviewed by:
Ruben Coronel, University of Amsterdam, Netherlands
Thom Oostendorp, Radboud University Nijmegen Medical Centre, Netherlands

***Correspondence:**
Matthijs Cluitmans
m.cluitmans@maastrichtuniversity.nl
Laura Bear
laura.bear@ihu-liryc.fr

Specialty section:
This article was submitted to Cardiac Electrophysiology, a section of the journal Frontiers in Physiology

Received: *19 May 2018*
Accepted: *29 August 2018*
Published: *20 September 2018*

Citation:
Cluitmans M, Brooks DH, MacLeod R, Dössel O, Guillem MS, van Dam PM, Svehlikova J, He B, Sapp J, Wang L and Bear L (2018) Validation and Opportunities of Electrocardiographic Imaging: From Technical Achievements to Clinical Applications. Front. Physiol. 9:1305. doi: 10.3389/fphys.2018.01305

Electrocardiographic imaging (ECGI) reconstructs the electrical activity of the heart from a dense array of body-surface electrocardiograms and a patient-specific heart-torso geometry. Depending on how it is formulated, ECGI allows the reconstruction of the activation and recovery sequence of the heart, the origin of premature beats or tachycardia, the anchors/hotspots of re-entrant arrhythmias and other electrophysiological quantities of interest. Importantly, these quantities are directly and non-invasively reconstructed in a digitized model of the patient's three-dimensional heart, which has led to clinical interest in ECGI's ability to personalize diagnosis and guide therapy. Despite considerable development over the last decades, validation of ECGI is challenging. Firstly, results depend considerably on implementation choices, which are necessary to deal with ECGI's ill-posed character. Secondly, it is challenging to obtain (invasive) ground truth data of high quality. In this review, we discuss the current status of ECGI validation as well as the major challenges remaining for complete adoption of ECGI in clinical practice. Specifically, showing clinical benefit is essential for the adoption of ECGI. Such benefit may lie in patient outcome improvement, workflow improvement, or cost reduction. Future studies should focus on these aspects to achieve broad adoption of ECGI, but only after the technical challenges have been solved for that specific application/pathology. We propose 'best' practices for technical validation and highlight collaborative efforts recently organized in this field. Continued interaction between engineers, basic scientists, and physicians remains essential to find a hybrid between technical achievements, pathological mechanisms insights, and clinical benefit, to evolve this powerful technique toward a useful role in clinical practice.

Keywords: ECG imaging, validation, electrocardiography, electrophysiology, experiment

INTRODUCTION

Electrocardiographic imaging (ECGI) reconstructs the electrical activity of the heart from a dense array of body-surface electrocardiograms and a patient-specific heart-torso geometry. Depending on how the problem is formulated, ECGI allows the reconstruction of the activation and recovery sequence of the heart, the origin of premature beats or tachycardia, the anchors/hotspots of re-entrant arrhythmias and other electrophysiological quantities of interest. Importantly, these quantities are directly and non-invasively reconstructed in a digitized model of the patient's three-dimensional heart, which allows personalized diagnosis and localized therapy guidance.

Over the past four decades, ECGI has seen considerable development, from purely analytical studies (Rudy et al., 1979; Figuera et al., 2016; Svehlikova et al., 2018), to torso tank (Oster et al., 1997, 1998; Ramanathan and Rudy, 2001; Shome and Macleod, 2007; Bear et al., 2018a) and large animal models (Liu et al., 2012; Oosterhoff et al., 2016; Cluitmans et al., 2017; Bear et al., 2018b) and finally application in humans (Ghanem et al., 2005; Horáček et al., 2011; Haissaguerre et al., 2014; Schulze, 2015; Punshchykova et al., 2016). It is now increasingly used for academic research and in clinical practice. Despite this progress, validation of ECGI remains a significant challenge.

Mathematically, ECGI solves the inverse problem of electrocardiography (i.e., to determine the cardiac electrical source for a given body-surface potential distribution), a problem fundamentally hindered by the fact that a multitude of patterns of cardiac electrical activity can produce similar body-surface potentials. The majority of these "inverse solutions" are physically and physiologically unlikely; therefore, additional constraints are imposed to stabilize the problem and select a more realistic solution, a process that is called "regularization." Regularization that is based on physical and physiological *a priori* information significantly improves the solvability and robustness of inverse solutions from ECG recordings. ECGI is thus strongly dependent on implementation choices, such as the cardiac source model and the method of regularization. Both these components need to be taken into account by the validation approach, which is not always straightforward. A second aspect that makes ECGI validation challenging is the difficulty in obtaining highly detailed and localized invasive ground-truth data in *in vivo* animals or humans. Finally, ECGI is strongly dependent on the specific clinical application of interest, as each application will yield a need for different quantitative parameters and their validation.

The aims of this paper are:

(1) To review the current status of validation of ECGI, as recent overviews on this topic are lacking (Sections Forms of Validation, Cardiac Source Models, Technical Validation, Pathological Validation, and Clinical (and Socioeconomic) Validation);
(2) To highlight which challenges in ECGI validation remain to facilitate clinical adoption; this includes commercial and socioeconomic challenges (Section Clinical (and Socioeconomic) Validation);
(3) To provide a consensus on the "best" ways to perform ECGI validation in the future (Section Consensus on Designing a Validation Study).

FORMS OF VALIDATION

Given the increased clinical use of ECGI over the recent past, there is an associated need for ECGI validation. Validation studies come in three different forms: technical, pathological, or clinical validation (see **Figure 1**).

The first form evaluates the **technical** accuracy and performance of ECGI for reconstructing the value of specific electrophysiological quantities. The relevant quantities include transmembrane voltage, electrograms, activation and recovery times, and related features that can be quantified. The accuracy of these features is not only influenced by the inverse or regularization methods that are used, but also by the pre-processing (e.g., techniques that filter or average the recorded body-surface potentials or improve the geometrical accuracy, methods to deal with poor quality signals, etc.) and post-processing methods that are used to extract features that are not directly available from inverse solutions (e.g., the calculation of activation time or other temporal fiducials from a reconstructed electrogram, or the use of phase mapping for rotor detection). Technical validation studies seek to evaluate these quantifiable features, generally irrespective of the underlying disease or clinical setting.

The second category of ECGI validation studies is to define the **pathological** accuracy and performance of ECGI, i.e., its capability to extract features applicable to a specific pathology or arrhythmia. For example, determining the origin of a premature ventricular complex (PVC) requires a different approach than determining the fractionation of local electrograms in myocardial infarction, or determining the region of large repolarization gradients in patients susceptible to ventricular fibrillation (VF). For each of these types of validation, the exact value of the reconstructed quantities may not be as important as their ability to separate healthy from diseased states. For example, it may matter less whether ECGI can determine the exact value of the steepness of a repolarization gradient (which, for example, may depend on mesh coarseness) as long as it can reliably differentiate a proarrhythmic gradient from a normal gradient (Vijayakumar et al., 2014).

The third category of validation studies evaluates the **clinical** accuracy and performance of ECGI, i.e., its benefit in daily clinical practice. The main focus of these studies is not the accuracy of reconstructed or post-processed parameters, but their influence on clinical decision making. For example, ECGI might provide improved therapy outcomes in atrial fibrillation (AF) ablation, improved workflow in the cardiac electrophysiology laboratory, reduced radiation burden or procedural times, etc.

Although we divide validation into three distinct categories, there is often overlap between them, particularly in the case of "pathological" and "clinical" validation. Here we used these categories to emphasize the difference between using ECGI to investigate disease mechanisms (in which validation may

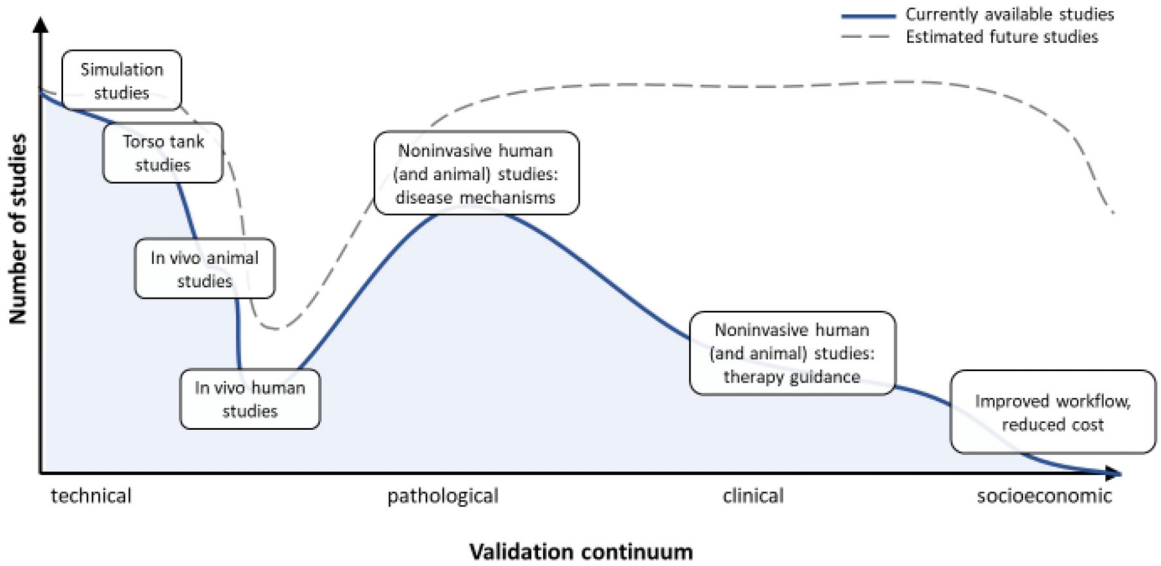

FIGURE 1 | Describes the validation continuum, from purely technical studies to pathological/clinical validation and socioeconomic benefit studies. Whereas the technical validation of ECGI is extensive, as is its use in disease mechanisms studies and validation of the true clinical benefit is still lacking.

focus on parameters directly reconstructed by ECGI) and using ECGI for clinical applications (in which validation may focus on indirect parameters such as patient outcome and reduced procedure costs).

Each validation form has different requirements in terms of data, metrics and analysis (**Figure 1**). In the remainder of this review, we assess the current status of each validation form, discuss the different issues surrounding validation, and provide a consensus as to the best approach to overcome these challenges to arrive at clinically relevant studies and applications.

CARDIAC SOURCE MODELS

Validating an ECGI formulation begins by defining the cardiac source to be reconstructed. Many of the original ECGI formulations approximated the cardiac source as either a single or multiple equivalent dipoles (Bayley and Berry, 1962; Rudy and Messinger-Rapport, 1988) or equivalent dipole layer (van Oosterom, 2004). Despite these source models being "equivalent" to the "ground truth" cardiac electrical activity they represent (in the sense that the models each fully represent cardiac electrical activity from a biophysical standpoint), there are no obvious physiological links, making experimental and/or clinical validation difficult.

Figure 2 illustrates the three current predominant cardiac source models and the features that can be derived from them: transmembrane voltage-based models, extracellular-potential based models, and activation/recovery-based models. The definition of an appropriate ground truth for comparison among these cardiac source models can be difficult, particularly when using experimental or clinical data sets. Often, investigators need to be satisfied with a derived ground truth data (e.g., activation times) or a ground truth hampered by error due to experimental limitations.

Transmembrane Voltage-Based Model

Taking the transmembrane voltage (TMV, i.e., the potential difference across the cell membrane of a cardiomyocyte, or a continuum approximation of that quantity), as a cardiac source model is the closest approximation to the true cardiac electrical source. Transmural reconstructions of TMV are possible (He et al., 2003; Wang et al., 2010; Potyagaylo et al., 2012), but a reformulation from Geselowitz (assuming equal anisotropy ratios of intracellular and extracellular conductivity tensors) also allows for a reconstruction of TMV on the endo- and epicardial surfaces (Simms and Geselowitz, 1995).

Reconstructions of TMV support identification of depolarized and repolarized regions in the heart and their temporal evolution. They also have the ability to outline areas of reduced amplitude, or completely absent TMV, e.g., ischemic, fibrotic, or border-zone areas. However, TMVs cannot be measured directly in the clinical environment, and thus any validation has to occur indirectly via the extracellular signals that TMV distributions create. Extracellular potentials on the endocardial and epicardial surfaces and activation and recovery times can easily be calculated from TMV distributions and then measured in experiments.

Impressed currents (i.e., the gradient of the TMV multiplied by the intracellular conductivity) can also be seen as sources of electrophysiological signals. In the original formulation, the impressed currents are vector fields, thus increasing the number of unknown properties by a factor of three. Thus, some studies propose to reconstruct only the normal or the tangential component of the impressed currents (Grace et al., 2017). For the case of equal anisotropy ratios of conductivity, the impressed

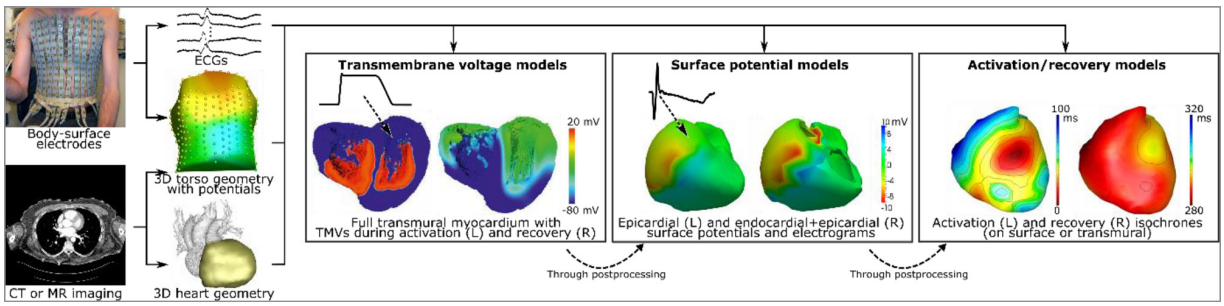

FIGURE 2 | Electrocardiographic imaging requires recording of body-surface potentials and the acquisition of a torso-heart geometry through computed tomography (CT) or magnetic resonance (MR) imaging. The electrical characteristics of the heart can then be computed by employing one of the "source models," i.e., models of cardiac electrical activity that explain the recorded body-surface potentials. Globally, these source models are categorized as: transmembrane voltage (TMV) models, surface-potential models (either epicardial-only or endo-epicardial surface), and activation/recovery-based models. It is possible to compute surface potentials and electrograms from TMVs, and to compute activation and recovery sequences from electrograms, but not the other way around. Image in part reproduced with permission from: Cluitmans (2016); Weiss et al. (2007), and Van Dam et al. (2009).

currents can also be replaced by an equivalent dipole layer with equivalent current density distributions orthogonal to the surface of the heart (Janssen et al., 2017) (also see the EDL model in Section Activation/Recovery-Based Models).

An advantage of TMV or impressed current based solutions is that *a priori* physiological knowledge about the action potential propagation, available through various mathematical models, can be used to constrain the reconstruction. The challenge in terms of validation, on the other hand, is that TMVs or impressed currents are difficult to obtain experimentally or clinically.

Extracellular Potential-Based Model

Potential-based models represent the cardiac source using extracellular potentials on the heart surface. There are several possible definitions of this cardiac surface, typically including only the ventricular or atrial cavities. The most common definition uses the epicardial surface, often artificially closed across the valves and the base. The surface can also be defined as both the endocardium and epicardium, leaving an opening at the valves. Both versions are presented for the ventricles in **Figure 2**. The key requirement for most methods is that the surface encompasses all active electrical sources.

Two key features are directly available from a potential-based model: electrograms and potential maps. Cardiac electrograms are the change in potential over time at a single point on the heart, and potential maps show the potential distribution over the surface at a specific time point. One benefit of potential-based models in terms of validation is that these features are much more easily measurable than TMVs and can be recorded during experimental or catheter-based procedures, even in humans. Moreover, like TMVs, additional information contained within the electrograms, such as activation and recovery processes, can be extracted through post-processing. On the other hand, while potential-based models can provide information on both epicardial and endocardial surfaces (Rudy and Burnes, 1999), direct reconstruction of transmural propagation is currently not possible. Importantly, many potential-based implementations of ECGI only provide epicardial reconstructions, without endocardial or septal potentials. In general, the extracellular approach (formulated either just epicardial or endocardial and epicardial) is the basis of some commercial systems and as such may currently have the highest clinical relevance of all source formulations.

Activation/Recovery-Based Models

The purpose of activation/recovery-time based models is to obtain the local times of activation or recovery directly, without reconstruction of TMVs or extracellular potentials as intermediate. As such they provide a highly stylized, simplified sparse parameterization that captures key aspects of the underlying biophysics. Activation times are described as the time of arrival of the depolarization phase of an action potential. Similarly, recovery times capture the timing of the repolarization phase. Both quantities can be defined either through the 3-dimensional (3D) myocardial wall (Han et al., 2011), or on the heart surface, including both the epicardium and endocardium (Erem et al., 2014). Examples of such methods include the equivalent double layer (EDL) model and the 3D cardiac electrical imaging (3DCEI) model:

- Equivalent Double Layer Model (EDL)
  The macroscopic EDL model (Van Oosterom, 2001) represents the entire electrical activity of the atria or ventricles at any time instant (van Oosterom and Jacquemet, 2005a). This source model stems from the classic bioelectrical double layer as an equivalent source of the currents generated at the boundary between active and resting cells during depolarization, described by Wilson et al. (1933). Initially, this current dipole layer model was used to describe the activity at the front of a depolarization wave propagating through the myocardium. Later, Salu expressed the equivalence between the double layer at the wave front and a uniform double layer at the depolarized part of the surface bounding the myocardium (Salu, 1978), based on solid angle theory (van Oosterom, 2002) (see **Figure 2**). Later, Geselowitz showed, using a bidomain model, that the actual *current* source distribution within

the heart is equivalent to a double layer at the surface of the myocardium with a strength proportional to the local TMV (Geselowitz, 1989, 1992; van Oosterom and Jacquemet, 2005b). The waveform of the TMV at each location on the myocardial surface (both endocardium and epicardium) is described by at least two parameters: the local activation and recovery times. Consequently, the source parameters of the EDL model also consist of the activation and recovery times. More complex versions allow as many as seven parameters (van Oosterom, 2004). One challenge of this model is that the relationship between the source parameters and the source strength is non-linear.

- 3D Cardiac Electrical Imaging (3DCEI)
  While the EDL model allows estimating activation or recovery times over the heart surface (including both epicardium and endocardium), the 3DCEI model aims to reconstruct cardiac activation and recovery process throughout the entire 3D myocardium – including epicardium, endocardium, and intramural tissues (MacLeod et al., 2000; He et al., 2003). While 3DCEI is applicable to both ventricles and atria, its main application is for imaging the ventricular activation sequence (Han et al., 2011) from the inversely reconstructed equivalent current densities (He and Wu, 2001), or imaging the ventricular repolarization process through reconstruction of the activation-repolarization interval at each point within the 3D ventricles (Wang et al., 2013). The relationship between cardiac equivalent current density and local activation time is established based on the "peak criteria" reflecting the fundamental biophysics of cardiac activation (MacLeod et al., 2000). This model has been evaluated extensively in *in vivo* animal models with simultaneous 3D intracardiac mapping in rabbits (Han et al., 2011; Duchateau et al., 2016) and in dogs (Cluitmans et al., 2017), as well in scarred myocardial tissue (Wang et al., 2013).

To solve the inverse problem using these source models usually requires an initial estimate of the activation and recovery times, which is then improved through numerical iteration. An advantage of these approaches is that *a priori* physiological knowledge can be used to obtain very reasonable initial activation and recovery times (Van Dam et al., 2009), thus reducing convergence time and improving accuracy. At the same time, it remains unclear how well the models perform when assumptions of the underlying physiology are violated, e.g., when scar tissue is present but is not incorporated in the model (Erem et al., 2014). For normal healthy subjects and patients with idiopathic PVC, this method has been shown to work well (Van Dam et al., 2009). Current research focuses on developing initial estimate algorithms that deal with inhomogeneous cardiac activation, e.g., when scar tissue is present.

TECHNICAL VALIDATION

Technical validation of ECGI is the most quantitative validation approach, explicitly comparing the ECGI reconstruction to ground truth to determine its absolute accuracy irrespective of the underlying pathology. Technical validation encompasses a broad range of cardiac source models, forward model formulations, inverse methods, and pre- and post-processing techniques. These studies are typically executed using either analytical (Rudy et al., 1979) or simulated potentials (Dubois et al., 2016; Figuera et al., 2016; Svehlikova et al., 2018), *ex vivo* torso tank experiments (Oster et al., 1997; Shome and Macleod, 2007; Bear et al., 2018a) and *in vivo* animal studies (Liu et al., 2012; Oosterhoff et al., 2016; Cluitmans et al., 2017; Bear et al., 2018b), with more limited results from humans (Ghanem et al., 2005; Sapp et al., 2012; Erem et al., 2014; Schulze, 2015; Punshchykova et al., 2016). For simplicity, here we have organized technical validation according to the different features that may be extracted from ECGI, irrespective of source models. These features provide scientists and clinicians with information about cardiac electrical activity and can either be provided directly by the cardiac source model chosen (i.e., electrograms when using a potential-based approach) or extracted through further post-processing of the ECGI-reconstructed signals (i.e., activation or phase mapping from electrograms), as summarized in **Figure 2**.

Transmembrane Voltages

While validation of reconstructed TMVs is possible using simulated data, it is nearly impossible experimentally and clinically as the ground truth data can only be obtained through optical mapping, monophasic action potentials recording, or patch clamping. These are all techniques that are currently difficult to obtain *in vivo* and the latter two are infeasible over more than a very few sites in a whole heart. If these data are available, they serve as the optimal approach for comparing magnitude and shape of different phases, particularly depolarization and repolarization. If these data are not available, the focus of validation shifts to post-processed values of TMPs, such as unipolar electrogram morphology, activation and recovery isochrones, etc.

Electrograms

Electrograms are one of the most common features reconstructed with ECGI, as they provide useful information to clinicians, directly relatable to invasive recordings. Ground truth data is available through simulations (Simms and Geselowitz, 1995; Wang et al., 2010; Figuera et al., 2016; Janssen et al., 2017), recordings obtained with epicardial, endocardial and transmural electrode arrays (with upwards of 200 electrodes) in *ex vivo* (Oster et al., 1997; Shome and Macleod, 2007; Bear et al., 2018b) and *in vivo* (Zhang et al., 2005; Han et al., 2011; Liu et al., 2012; Oosterhoff et al., 2016; Cluitmans et al., 2017; Bear et al., 2018b) experimental models, and invasive mapping clinically (Ghanem et al., 2005; Sapp et al., 2012; Punshchykova et al., 2016). Most validation studies to date use a global evaluation of the QRS, T, or QRS-T waveform reconstruction using correlation and/or error metrics, to demonstrate the accuracy in the overall topology and/or amplitude of electrograms (example in **Figure 3**). Persistent challenges include assessing spatial accuracy (Cluitmans et al., 2017; Bear et al., 2018b)

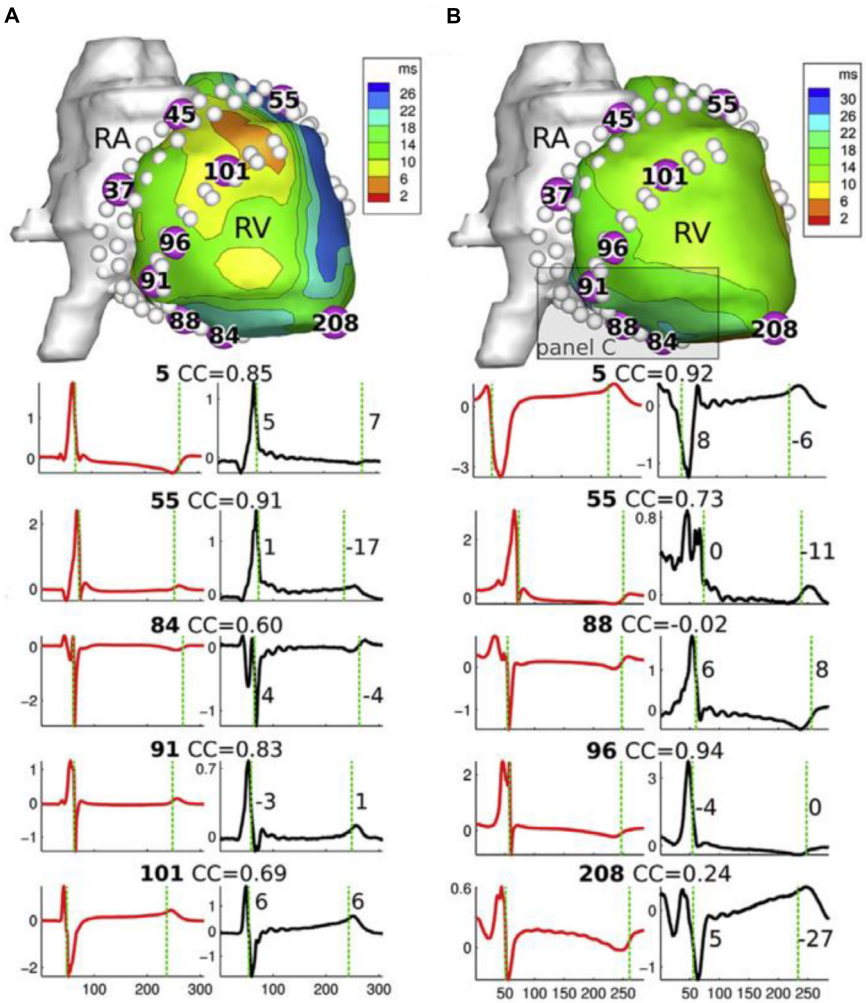

FIGURE 3 | Top: epicardial geometry with reconstructed potentials from a canine *in vivo* study, for a sinus beat **(A)** and a LV-paced beat **(B)**. White dots indicate the position of invasive electrodes used for validation recordings. Bottom: recorded (red) and ECGI-reconstructed (black) electrograms for electrodes numbered in geometry above. CC, correlation coefficient between recorded and reconstructed electrograms. RA, right atrijm; RV, right ventricle. Adapted with permission from Cluitmans et al. (2017).

and the sensitivity of results to different sources of error, i.e., cardiac motion (MacLeod et al., 2000; Cluitmans et al., 2017). To date, while qualitative assessment of reconstructed electrograms is often described, comprehensive quantification of the presence/absence of detailed characteristics in reconstructed electrograms has never been performed, including fractionation, low/high amplitudes, epicardial/endocardial source, ST-segment elevation, etc. The inaccurate reconstruction of these characteristics is often missed using a global evaluation. Metrics to quantify the presence of such local features are needed as this information can be critical to the diagnosis and/or treatment of particular pathologies (see Section Metrics for Validation).

Unipolar electrograms on the cardiac surface are influenced by what are known as "far-field" effects from electrical activity in other parts of the myocardium, this influence varying with electrode size and filtering techniques. Since ECGI electrogram reconstructions may be even more sensitive to such effects given the ill-posedness of the inverse problem, care is required in interpreting validation results, especially if the surface model does not include the endocardium or if validation measurements are only available on either the endo- or the epicardium.

Potential Maps

In addition to electrograms, potentials can be visualized spatially as potential maps that vary in time. Hence, validation is often performed using the same data set as for electrograms through global quantitative comparisons of reconstructed potential maps to the ground truth signals, using correlation and error metrics over time (Oster et al., 1997; Bear et al., 2018b). One limitation of quantitative comparison is that during the early and late phases of activation, only small regions of the heart are activated, leading to distorted values of signal-to-noise and global error metrics (see **Figure 4**). It remains unclear if specific characteristics during

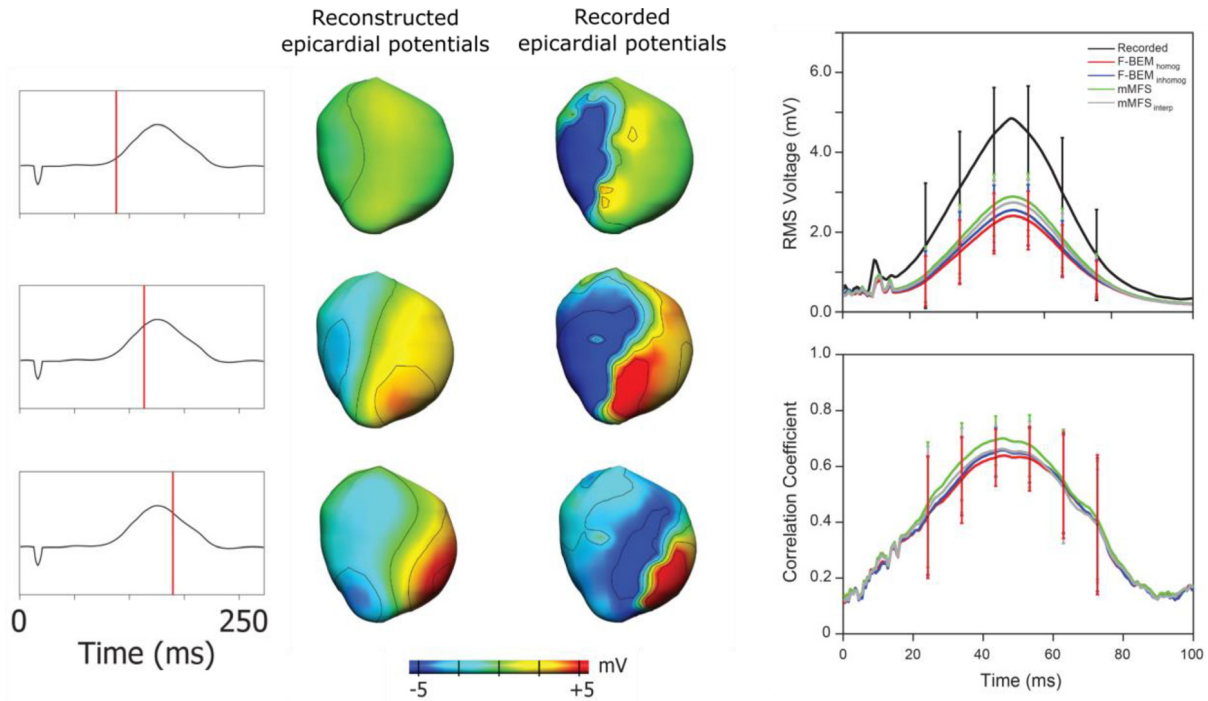

FIGURE 4 | Epicardial potential maps derived from ECGI (left) and recorded (right) epicardial electrograms at three instants during ventricular activation during epicardial pacing from the anterior RV free wall (ECG shown left). During the early and late phases of activation, only small regions of the heart are activated, leading to distorted values of error metrics such as correlation (right, showing different reconstruction approaches in different colors). Adapted with permission from Bear et al. (2018b).

these time periods can be accurately reconstructed, such as the initial site of activation (based on the location of epicardial deepest negative potential) or regions of current sources (similar to ST segment elevation). However, potential maps are only beginning to be used in clinical practice (Jamil-Copley et al., 2015) and assessment of individual electrograms for signal amplitude, activation time or specific characteristics is currently more clinically practical.

Activation/Recovery Maps

Activation and recovery time maps provide very useful static isochrone images of the cardiac electrical depolarization/repolarization sequence. These isochrones may be used clinically to identify several quantities: (a) sites of initiation of activation by focal arrhythmias, e.g., premature ventricular contraction (PVC) origin; (b) delineation of reentry circuits, e.g., macroreentrant atrial flutter (Shah et al., 1997), or (c) abnormalities in propagation, such as areas with delayed activation (Irie et al., 2015), or those with slow or abnormal conduction, e.g., scar-related ventricular tachycardia substrate, or (d) areas with recovery abnormalities, e.g., large recovery gradients (Vijayakumar et al., 2014; Leong et al., 2017). To date, the majority of validation studies have concentrated on the accuracy of activation mapping (Oster et al., 1997; Zhang et al., 2005; Han et al., 2011; Oosterhoff et al., 2016; Bear et al., 2018b), with only a few studies assessing recovery (Van Dam et al., 2009; Cluitmans et al., 2017). The earliest site of activation of paced beats is often reconstructed and compared to the known location of pacing, yielding a localization error. For example, animal validation studies with pacing localization exist for potential-based (Cluitmans et al., 2017; Bear et al., 2018b) and activation/recovery-based approaches (Han et al., 2011; Liu et al., 2012; Oosterhoff et al., 2016).

Apart from beat origins, validation studies of activation- and recovery-time maps tend to assess global accuracy, providing correlation and relative error metrics. This approach may overlook other characteristics/abnormalities, such as steepness of recovery gradients, or the presence/absence of conduction block or localized changes in velocity of activation (conduction). One study (Bear et al., 2018a) has recently demonstrated that in left bundle branch block, ECGI can compress local activation to create an artifactual "line of block," which is not reflected in correlation values (**Figure 5**).

One of the difficulties in activation/recovery map validation is the need to derive the activation/recovery times from electrograms and thus their dependence on the signal processing method used. Most applications use the gold standard method for deriving activation/recovery times from directly recorded signals (defined as the time of minimum and maximum derivatives, respectively, of the unipolar electrogram). However, these gold standard methods are typically imprecise, both for actual recordings and for ECGI-derived electrograms, and alternative methods may be required (Erem et al., 2011; Duchateau et al., 2016; Cluitmans et al., 2017). These methodology-linked

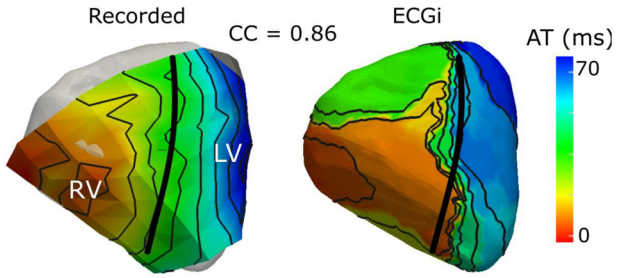

FIGURE 5 | Validation of ECGI derived activation maps using an *ex vivo* torso tank set up has demonstrated that, in electrical dyssynchrony, ECGi (right) produces a "line of activation block" that is not present in recorded signals (left) using an epicardial electrode sock [adapted with permission from Bear et al. (2018a)].

variations in derivations of activation/recovery times may impact overall performance estimate.

Phase Maps

Phase is a feature that was initially designed to decompose action potential signals, the basic concept being to discard amplitude and focus on the temporal sequence (resting state, activation, refractory period, and repolarization). Between two consecutive activations of the tissue, the phase will increase in a monotonic way from $-\pi$ to $+\pi$ (or from 0 to 2 π if preferred). When applied to optical mapping recordings of complex cardiac arrhythmia (atrial and VF), phase is an effective feature in analyzing spatiotemporal organization (Gray et al., 1996). The spatial representation of the instantaneous phase allows one to identify focal activity and/or local reentry using features computed directly from the spatial organization of the phase signal (phase divergence and phase singularities). Such representations have sparked clinical interest in using phase mapping on electrical recordings as a means of detecting organized stable drivers during fibrillation, and potentially target them for ablation therapy (Umapathy et al., 2010; Narayan et al., 2012; Haissaguerre et al., 2013).

An efficient tool commonly used to convert time-varying signals from the voltage domain to the phase domain is the Hilbert Transform. This conversion from voltage to phase does not meet the objective of having a monotonic signal that ranges from $-\pi$ to $+\pi$ (or in general an interval of 2 π) between two consecutive cycles for signals with multiple deflections, such as bipolar or noisy electrograms. For this reason, electrograms are typically smoothed prior to conversion. Depending on the filtering chosen for the preprocessing step, the resulting phase maps may lead to over/under-estimation of the extent of re-entrant cycles (Rodrigo et al., 2017). The lack of methodological consensus on both the preprocessing and the definition of spatially or temporally stable phase singularities has resulted in ongoing debate over phase mapping techniques (Vijayakumar et al., 2016; Kuklik et al., 2017). To minimize such ambiguities, it is advisable to incorporate electrogram characteristics and the time-domain activation sequence into the analysis (as demonstrated in **Figure 6**).

Though applicable to the ventricles (Umapathy et al., 2010), contemporary ECGI applications are most commonly atria based, with validation using some clinical patient data (Metzner et al., 2017) and, more extensively, simulated data (Dubois et al., 2016; Figuera et al., 2016; Pedrón-Torrecilla et al., 2016; Kuklik et al., 2017; Rodrigo et al., 2017). Validation using experimental data is still needed. Phase can be validated in a similar manner to electrograms, using correlation and relative error to assess the global topology of the phase signals. However, phase signals at a particular electrode are themselves not of clinical interest, but rather the spatial distribution and temporal evolution of phase that allows the detection of divergence/singularity points. As such, in addition to correlation and relative error, we support the use of error metrics that assess localization accuracy of the divergence/singularity points or derived maps, such as the weighted under-estimation or the weighted over-estimation indicators (Figuera et al., 2016). Another useful approach entails computing the Phase Locking Value (PLV), which estimates the synchronicity between two signals, without regard to the constant phase shift between them (Dubois et al., 2016).

Dominant Frequency

In addition to phase, frequency is often used in the analysis of atrial and VF, where localized sites of high (or dominant) frequency (DF) serve as target ablation sites to eliminate AF (Sanders et al., 2005) (as seen in **Figure 6**). Because the conventional computation of frequency is done over a time segment, DF produces time-averaged frequency information over space. An absence in stability of the arrhythmia can lead to errors in DF estimation. Metrics to assess stability can be computed, such as the regularity (Everett et al., 2001; Sanders et al., 2005; Sánchez et al., 2017), organization, or coupling indices (Faes and Ravelli, 2007) and they indicate whether the activation is regular/periodic. Sequential analysis can be used to track the movement and determine the stability of DF sites over time (Salinet et al., 2014). In addition, the presence of shape-related and not only rhythm-related DF components can result in incorrect identification of the activation rates in the atria. As with phase, studies have reported controversial results, likely due to the different approaches for signal processing, DF computation, and interpretation. We refer readers to a review by Ng et al. (2007). That explores the technical requirements and limitations of dominant frequency analysis of AF signals.

Like phase mapping, current technical validation of ECGI derived dominant frequency has been limited to the atria and to the use of endocardial mapping measurements (Pedrón-Torrecilla et al., 2016; Zhou et al., 2016) and simulations (Figuera et al., 2016; Rodrigo et al., 2017) to provide ground truth data. Validation of frequency-based estimates can be performed using relative or absolute error, correlation to assess the global map distribution, and, more importantly, error metrics to assess localization of the region of dominant frequency, e.g., direction of DF gradient, either from left atrium to the right atrium, or weighted under/over-estimator indicators (Figuera et al., 2016), as well as other metrics that may be derived such as regularity/organization indexes.

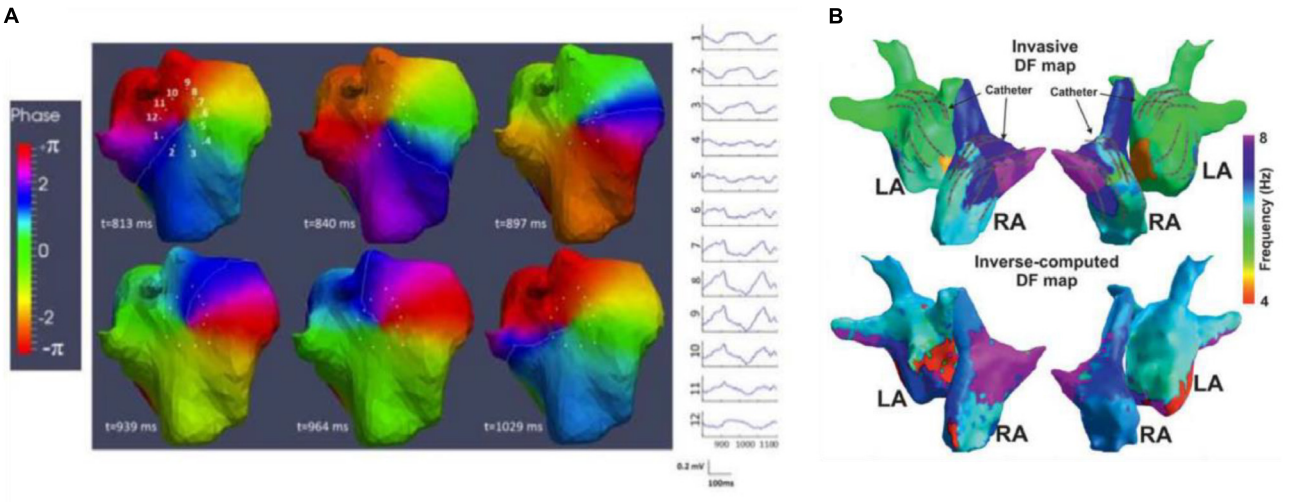

FIGURE 6 | During atrial (AF) or ventricular fibrillation, the mechanism of fibrillation can be assessed using phase and/or frequency mapping. **(A)** [adapted with permission from Haissaguerre et al. (2014)], ECGI derived phase maps of ≥1000-ms-long AF window show reentry events involving the posterior upper right atrium; sites 1–12 show the pre-phase electrograms around its core. By tracking phase singularities (PS) for reentrant activity of at least one full rotation, PS density maps illustrate arrhythmogenic drivers that may be targets for ablation. **(B)** [adapted with permission from Pedrón-Torrecilla et al. (2016)], dominant frequency (DF) using invasive CARTO (top) and non-invasive ECGI (bottom) in AF patients demonstrate good correspondence. Region of high DF (purple) identify arrhythmogenic drivers that may be targets for ablation.

PATHOLOGICAL VALIDATION

The major goal of ECGI is to be useful as a clinical tool to aid in diagnosis and therapy planning of specific pathologies and/or arrhythmias by identifying the mechanisms underlying these electrical disorders and their response to therapy. As such, validation of ECGI to extract the information applicable to a specific pathology/arrhythmia is essential. As mentioned previously, the quantitative accuracy of the reconstructed quantities may not be as important as their ability to separate healthy and diseased states. However, ECGI needs to be accurate enough to ensure that conclusions drawn from specific features are not actually a misinterpretation of artifacts in the solution. Moreover, clinicians typically want insight into the characteristics of a pathology and not just a binary classification. Such depth and detail are particularly important because conclusions drawn from ECGI can lead to the identification and implementation of costly, and potentially life-saving, treatment plans, such as guiding ablation therapy or implanting ICD or CRT devices.

Here we identify some pathologies and/or arrhythmias for which ECGI may be applicable, along with associated features desired for clinical applications. For a summary of the results from previous ECGI studies of arrhythmogenic substrates, we refer the reader to the review by Rudy (2013).

Atrial Arrhythmias

One of the first extensively clinically explored applications of ECGI was to identify the specific mechanisms of arrhythmia onset and/or maintenance for ablation therapy in atrial tachycardia (AT) and fibrillation (AF). ECGI is currently used to determine the specific patterns underlying activation during arrhythmia (i.e., focal vs. re-entrant) through phase mapping (Cuculich et al., 2010; Roten et al., 2012) and to localize the drivers of this activation using either the estimated dominant frequency (Pedrón-Torrecilla et al., 2016), and/or the divergence/singularity points through phase mapping (Haissaguerre et al., 2013, 2014). These drivers have been found to be correlated to the ablated regions in patients with successful outcome (Haissaguerre et al., 2013; Zhou et al., 2016) and are now being targeted directly in clinical validation studies (Haissaguerre et al., 2014; Knecht et al., 2017). While these studies indicate these drivers are targeting the arrhythmogenic substrates, one cannot rule out the possibility of false-positive errors. Technical validation has demonstrated that coarse patterns of DF (seen in **Figure 6**), singularity points, rotor/focal source density, etc., can all be accurately localized with ECGI (Modre et al., 2003; Haissaguerre et al., 2014; Dubois et al., 2016; Figuera et al., 2016; Metzner et al., 2017), but the specific ECGI features that most effectively localize the arrhythmogenic substrate(s) in AT/AF are still under debate. Pathological validation of this kind is nearly impossible as often multiple ablations are performed during a procedure, and it is unclear if all, some, or only the last locations identified the true arrhythmogenic substrate(s). As such, indirect clinical validation studies that show improved patient outcome or reduced procedural times are currently the best option.

Arrhythmogenic Substrate Identification for Ventricular Arrhythmias

As with atrial arrhythmias, one of the primary goals of ECGI is the identification and understanding of arrhythmogenic substrates for the onset and maintenance of ventricular tachycardia (VT) and fibrillation (VF) to aid in treatment planning, e.g., to guide

pharmacologic therapy, ICD implantation, or catheter ablation. Below we outline the major areas ECGI has been used for substrate identification in VT and/or VF.

Premature Ventricular Contraction

Patients with isolated and monomorphic PVCs or focal VT can be treated by ablating the focal source of these arrhythmias, which typically involves long, invasive electrophysiological mapping to localize these ectopic activities. By non-invasively localizing the arrhythmogenic site or at least estimating a region of interest prior to the catheterization procedure, ECGI can provide a useful presurgical guideline for the operator, and substantially improve the planning of the procedure and thus reduce procedure times (Potyagaylo et al., 2013), an example of such guidance is demonstrated in **Figure 7**. Focal idiopathic VTs and PVCs in the absence of structural heart disease are one of the most well validated pathologies for ECGI application, as the arrhythmogenic substrate is clearly defined and one can define accuracy using a simple localization error (Schulze, 2015). For example, a commercial implementation of ECGI (ECVUE, CardioInsight, Cleveland, OH, United States) has been used to localize PVCs (Erkapic and Neumann, 2015). Their ECGI implementation localized the ventricle of origin (LV vs. RV) correctly in 95.2% of the cases, compared to only 76.6% with 12-lead ECG. Sub-localization within the ventricles was accurate in 95.2% of the cases with ECGI, compared to 38.1% with 12-lead ECG. Ablation success was similar in both groups, both acutely and at 3-month follow up. Failure of this ECGI implementation (which uses an epicardial surface source model) to localize PVCs occurred mainly in sites near the septum, especially at the LVOT or RVOT (Erkapic and Neumann, 2015). In a study using NEEES (EP Solutions SA, Yverdon-les-Bains, Switzerland), PVCs were localized in 20 patients; in 86% of the cases, the correct ventricular segment was diagnosed (Wissner et al., 2017). In a preliminary study with nine participants, the Vivo 12-lead ECGI system was able to successfully localize PVCs (defined as location of successful ablation) in 86% of the cases, whereas human-based 12-lead ECG localization of PVC had a 27% accuracy (Gordon et al., 2014).

Future validation would ideally compare old and new methods to these previous works, potentially using a common and broad data set to prevent bias. An international working group called the Consortium for ECG Imaging (CEI[1]) has recently emerged that seeks to enhance progress through collaboration and shared data repositories [EDGAR (Aras et al., 2015)], with first results very recently published (Svehlikova et al., 2018).

Scar Related Ventricular Tachycardia Mapping

Sustained reentrant VT (and VT-induced VF) is often formed by narrow channels of surviving tissue inside a myocardial scar. Catheter ablation is an effective treatment for scar-related VT that modifies the scar substrate, for example by destroying the tissue site at which the VT circuit exits the scar (exit sites) [ESC Guidelines Management Ventr Arrh/AHA 2017 VA/SCD guideline (Reddy et al., 2007; Kuck et al., 2010; Sapp et al., 2016)]. These scar substrates are currently identified by catheter mapping, either during artificially induced VTs (by programmed electrical stimulation), in which the morphology and critical components of the VT circuit can be delineated, or during native rhythm where the region of myocardial scar and potential critical sites can be identified from the characteristics of the measured electrograms (although less specific than VT mapping). However, these procedures can be hindered by a lack of inducible arrhythmia or, more frequently, by the presence of multiple inducible arrhythmias and the patients' hemodynamic intolerance to the induced VTs. Additionally, native-rhythm substrate mapping involves invasive procedures with access often limited to the left endocardium. ECGI, due to its non-invasive nature, has the potential to augment catheter mapping in both enabling instantaneous reconstruction of a single PVC or a brief episode of VT and thus to provide non-invasive identification of scar substrates during native rhythm. For VT mapping, a small number of human studies have investigated the use of ECGI to map the exit sites and activation pattern of reentry circuits, using both epicardial ECGI (Wang et al., 2011; Sapp et al., 2012; Zhang et al., 2012) and more recently using epicardial-endocardial and 3D ECGI (Tsyganov et al., 2017; Wang et al., 2018). For substrate mapping, while the use of ECGI to delineate myocardial scar has been validated using MRI or voltage mapping (Cuculich et al., 2011; Wang et al., 2013; Horáček et al., 2015), studies are just emerging to examine its ability to reveal local abnormal electrograms, such as fractionated electrograms, that are suggestive of potential central pathways forming the VT circuit (Wang et al., 2018). In all of these studies, a significant challenge arises from the difficulty to establish the clinical ground truth for the exit sites and central pathway for VT; as a result, most existing validation studies are limited to qualitative or semi-quantitative evaluations. Validation studies should focus on the ability of ECGI to localize the VT exit site, using a similar metric to validations based on PVCs, as well as other critical sites, such as central pathways within myocardial scar.

Ventricular Fibrillation

Instantaneous whole-ventricle mapping systems such as ECGI open the possibility to also investigate VF mechanisms, by looking at focal centers or anchors of VF activity (similar to AF). Results from this field are only just emerging (Frontera et al., 2018) and could be validated with approaches that are similar to those applied in the AF field, including answering the question of whether these key spots within reentrant loops are really useful targets for ablation.

Wolf-Parkinson White Syndrome

Wolff-Parkinson-White (WPW) syndrome involves a long-standing altered activation sequence, different from normal sinus rhythm, as a result of abnormal conductive cardiac tissue between the atria and the ventricles that provides a pathway for a reentrant tachycardia circuit. Similar to focal VT and PVCs, localization of WPW is a natural application of for ECGI as a means to guide catheter ablation. However, the high rate of success in WPW using conventional approaches (Fitzpatrick et al., 1994) and relatively minor potential for incremental clinical benefit has

[1] http://www.ecg-imaging.org/workgroups/pvc-localization

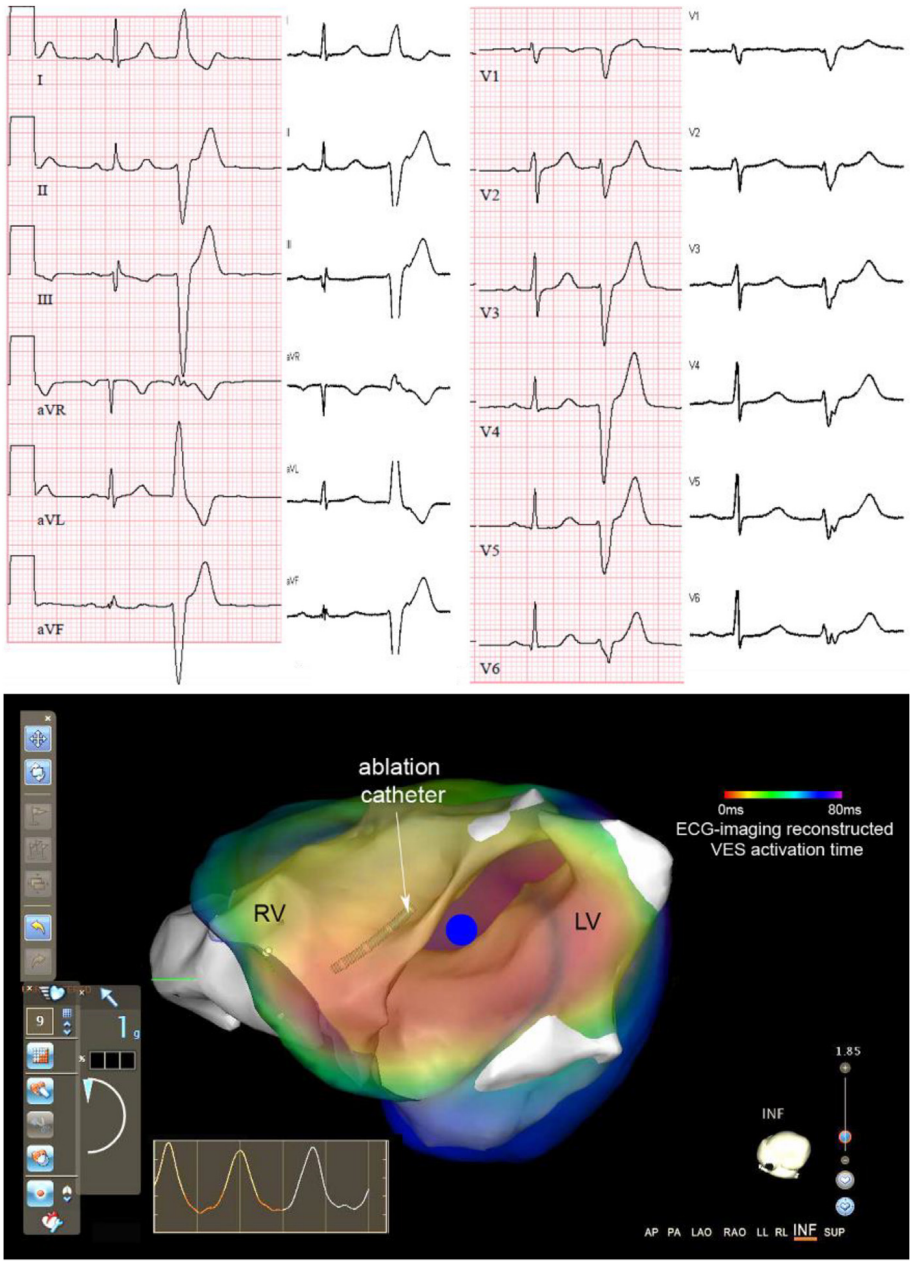

FIGURE 7 | Example of ECGI-guided ablation in a patient. Top: 12-lead ECG recorded during ECGI (white background) and clinical recording during symptoms (pink background), both with a sinus beat and subsequent premature ventricular complex (PVC). Bottom: Live view as visible to the cardiologist-electrophysiologist during the ablation procedure when using the Carto 3 cardiac mapping system. The 3D anatomy as determined by the Carto catheter (white structures) is overlaid with the activation map of the PVC as created pre-procedurally with ECGI (red-to-blue: early-to-late activation time; blue dot: PVC origin). The cardiologist can use this live view during the procedure to navigate the catheter to the area suspected of the PVC origin. Adapted with permission from: Cluitmans et al. (2016).

limited motivation to a few studies (Berger et al., 2006; Ghosh et al., 2008).

Risk Stratification for Ventricular Arrhythmias

In addition to identifying the arrhythmogenic substrate for ventricular arrhythmias, ECGI has more recently been proposed as a tool for risk stratification for arrhythmia, particularly VF and sudden cardiac death. By imaging and quantifying the important substrates for arrhythmia such as conduction and repolarization abnormalities, ECGI may be used for screening of the general public to identify those at risk. Initial studies have begun to identify these potential arrhythmogenic substrates, such as the presence of slow discontinuous conduction and steep dispersion of repolarization in the RVOT of Brugada patients

(Zhang et al., 2015), the presence of repolarization abnormalities in ARVC patients (Andrews et al., 2017), steepness of recovery gradients (Vijayakumar et al., 2014), and recovery substrates in sudden cardiac death survivors (Leong et al., 2017). However, much work is still needed in this area not only to confirm these substrates but also to develop and validate risk stratification markers that identify them and to demonstrate clinical utility.

Heart Failure and Cardiac Resynchronization Therapy

Cardiac Resynchronization Therapy (CRT) through biventricular pacing can improve outcomes in patients with heart failure and with low ejection fraction. However, the effect varies widely with approximately a third of patients failing to respond. To improve CRT response rates, recommendations emphasize attention to low resolution electrical parameters from the 12-lead ECG (i.e., left bundle branch block and QRS duration $\geq$150 ms). However, detailed understanding of the spatiotemporal excitation pattern in the failing human heart and its relationship to a CRT response are lacking. ECGI has been used to fill some of this gap, providing new insights into the electrical substrates specific to responders (Varma et al., 2007; Berger et al., 2011; Ghosh et al., 2011; Ploux et al., 2013), including abnormal activation patterns with slow conduction and/or line of block and electrical dyssynchrony, both within and between the ventricles. With knowledge of these substrates, new ECGI-derived criteria have been developed, demonstrating improved responder selection compared to the current standard metrics (Ploux et al., 2013). Clinical validation of these metrics in the form of large-scale multi-center trials is still required to demonstrate that these metrics are capturing the correct electrical substrates. Technical validation has demonstrated that the presence of functional lines of block seen clinically in these patients may in fact be an artifact of ECGI (Bear et al., 2018a) (see **Figure 4**). Despite this, ECGI has reliably and accurately detected electrical dyssynchrony, resynchronization by biventricular pacing, and the site of latest activation, providing more information than the 12-lead ECG. Further validation of ECGI methods in the presence of heart failure and/or electrical dyssynchrony could improve reconstructions to remove these artifacts and increase the sensitivity and specificity of these markers, and possibly to develop methods for targeted left ventricular lead placement.

CLINICAL (AND SOCIOECONOMIC) VALIDATION

Electrocardiographic imaging validation studies in the past have typically focused on the technical or pathological validation and until recently, large-scale studies using ECGI clinically have not been possible. With the commercialization of ECGI systems, their use on a large scale in hospitals worldwide is now a possibility. As such, this section will deal with the need for studies to address the actual clinical benefit in terms of personalized understanding of disease mechanisms and its potential to open new avenues for therapy, improved patient outcome, and improved workflow. As far as we know, the following systems are currently in development for commercial purposes: the CardioInsight^{TM} Noninvasive 3D Mapping System (Medtronic), the Non-Invasive Electrophysiological Mapping (NIEM) system (EP Solutions SA), and the View Into Ventricular Onset (Vivo) system (Peacs, Catheter Precision).

Clinical Application Domains

The potential applications of ECGI (and their validation) fall into three major categories: (1) Personalized disease understanding and diagnosis; (2) Therapy guidance; and (3) Enabling innovations.

Personalized Disease Understanding

Many of the studies discussed in section "Pathological Validation" have investigated disease mechanisms with ECGI and proposed parameters that carry relevant clinical information. For example, ECGI has been used to uncover repolarization gradients that are more pronounced in symptomatic than asymptomatic LQTS patients (Vijayakumar et al., 2014). Similarly, the more detailed information provided by ECGI has demonstrated the presence of larger ventricular electrical dyssynchrony in CRT responders providing improved CRT patient selection compared to standard 12-lead ECG (Varma et al., 2007; Ploux et al., 2013). These retrospective studies are important to help understand the underlying disease mechanisms and define the parameters or markers that may guide therapy. But to fully demonstrate that this information carries value for an individual patient and could guide therapy or patient selection requires further investigations using large-scale prospective studies.

Therapy Guidance

Most clinical studies have aimed at using ECGI for therapy guidance. To date the focus has been on demonstrating a decrease in radiofrequency ablation and procedural times for atrial arrhythmia substrates or PVC origin ablation therapy, as pathological studies, discussed in sections "Atrial Arrhythmias" and "Premature Ventricular Contraction," have shown that accurate localization of these substrates is feasible. A clinical validation study for AF has reported that using ECGI to identify ablation targets with phase mapping, as seen in **Figure 6**, significantly reduced radio-frequency delivery (28 ± 17 vs. 65 ± 33 min) and thus procedure times for successful outcome, compared to standard methods (Haissaguerre et al., 2014). Likewise, for PVC localization, clinical validation has shown the number of radiofrequency energy applications was significantly lower in the group with CardioInsight-based localization (two applications) in comparison with the control group (four applications) and procedure times were shorter (Erkapic and Neumann, 2015).

In order to be used in other pathologies, it is necessary to overcome technical challenges that currently limit the applicability of ECGI during invasive cardiac procedures (e.g., the need to integrate defibrillation patches and 3-dimensional mapping systems). ECGI might then guide therapy by characterizing electrical substrate(s) in more detail than is possible from the 12-lead ECG. For example, ECGI provides detailed electrical activation patterns of the left (LV) and

right ventricle (RV), which could guide CRT implantation by suggesting the optimal placement of the LV lead (Ploux et al., 2014; Bear et al., 2018a). ECGI may also enable risk stratification and guide ICD implantation for sudden cardiac death by imaging of activation and recovery abnormalities, both important arrhythmogenic substrates (Vijayakumar et al., 2014).

For all of these applications, prospective clinical trials are also needed to validate the clinical benefit. ECGI for AF is leading the way, with one such multi-center trial currently underway (AFACART[2]) aiming to evaluate the effectiveness of ECGI for persistent AF mapping and ablation procedures in comparison to conventional methods. Initial results recently published from this trial have demonstrated a persistent AF termination success of 72% (n = 118), with no significant difference among the 8 European centers in the study (Knecht et al., 2017).

Enabling Innovative Therapies

Electrocardiographic imaging carries the potential to permit new and innovative therapies. A recent study has demonstrated the feasibility of combining ECGI with non-invasive delivery of ablative radiation, suggesting that clinicians may be able to completely non-invasively target VT substrate with radiotherapy (Cuculich et al., 2017). Accurate identification and localization of arrhythmogenic myocardial substrate could facilitate further progress in the development of safe, effective therapeutic interventions.

Furthermore, studies are currently investigating the used of ECGI with tagged MRI/CT or speckle-tracking echocardiography (Dawoud et al., 2016). Combining non-invasive imaging of electrical and mechanical function and their interaction in situ could provide new insights that would be extremely valuable for characterization of disease mechanisms and development of treatment strategies. The wealth of information provided by ECGI, and its non-invasive nature, might open the door to more novel innovations.

Demonstration of Added Clinical Value

Improved Patient Outcome

One obvious goal of clinical validation studies is to show that ECGI can improve patient outcome. This requires long-term, large-scale (thus expensive) clinical trials to validate the findings arising from small scale technical or pathological validation studies; one such example is the AFACART study. These types of studies are needed to prove patient benefit in terms of reduced recurrence rates after such ECGI-guided procedures as PVC ablation (Erkapic and Neumann, 2015) and AF ablation (Haissaguerre et al., 2014) or improved CRT patient selection or lead positioning (Ploux et al., 2013). There are many potential reasons why ECGI may not improve patient outcome including: (1) a lack of understanding of disease mechanisms, making it difficult to specify how ECGI could prove useful (e.g., rotors in AF or lack of response in CRT); (2) the lack of clinical need (PVC ablation can often be performed without expensive or complex mapping systems); and (3) the preliminary nature of many studies seeking to show ECGI results prior to randomized control trials. Large, multi-center studies are currently being designed or are underway to investigate the benefit of ECGI for various diagnostic and therapeutic purposes.

Improved Workflow and Reduced Cost

Another improvement that could be provided by ECGI is in workflow and (socio)economic cost. Such benefits are particularly important if ECGI is to be considered as a tool for risk stratification and general population screening. The associated validation studies should focus on finding the optimal balance between time and financial investment (ECGI is more expensive and more time-consuming than a standard ECG) vs. benefit for society. These benefits could include: lower hospitalization rates with AF and VT ablation, shorter procedural times (or lower variability of procedure results, making hospital planning more reliable), socioeconomic benefit due to improved patient selection for ICD therapy, etc. Commercial implementations of ECGI are essential for this and preferably include regulatory approval and financial reimbursement. To our knowledge, Medtronic's CardioInsight system is the only FDA-approved ECGI implementation, and no ECGI implementation is currently being reimbursed by health care insurers.

Clinical Adoption

Clinical adoption of ECGI depends critically on technical, pathological and clinical validation, but also on practicability, demonstration of cost-effectiveness, and appropriate reimbursement mechanisms. Additionally, if levels of confidence or uncertainty were reported to clinicians for ECGI reconstructions in individual cases (taking into account levels of noise, defective electrodes, regions that are hard to reconstruct, etc.) it might further improve clinical reliance on ECGI results. In general it is not yet clear what is the best context to apply ECGI to improve health care, and it is important to realize that while such benefits might lie in improved diagnosis, therapy guidance, or patient outcome, they may also result from improved workflow (reduction of procedural times, less variability in procedure duration) and reduced cost (shorter or fewer hospitalizations). Whatever the focus, such studies will cost time and money and will benefit from focused clinical applications.

CONSENSUS ON DESIGNING A VALIDATION STUDY

In designing and presenting a validation study, there are many choices that can have a large impact of the validity of the results. In this section, we provide a consensus on the "best" approaches. This consensus is based on discussions among the authors at recent conferences (Computing in Cardiology [CinC] 2015–2017; Frontiers in Computational Electrocardiology [FiCE] 2016; and the International Society for Computerized Electrocardiology [ISCE] conference 2015), and during other meetings.

[2]https://clinicaltrials.gov/ct2/show/NCT02113761

Data Selection

Data sets come in various forms: simulated, experimental (*ex vivo* torso tank or *in vivo* animal model), and clinical as summarized in Macleod and Brooks (2000). The ideal validation would include data in more than one form (i.e., simulated and experimental), and include multiple sources (i.e., multi-institutional clinical and/or experimental data). Depending on a single data set can lead to algorithms becoming biased or tuned to these data and ultimately failing on other independent data. Validation using *in vivo* animal and clinical models are particularly needed to address the technical questions surrounding accuracy, feasibility, and reliability. Using data from multiple sources/forms adds to the rigor, reliability, and reproducibility of the results.

However, obtaining such data sets is often impossible for individual labs due to the large costs and/or lack of available facilities. Collaborative efforts have and will continue to help overcome this problem. To enable such projects, an international consortium has created an open platform for sharing data, which is populated with datasets (14 datasets from 8 different centers as of the submission of this manuscript). This database is called the Experimental Data and Geometric Analysis Repository (EDGAR[3]) and is hosted at the University of Utah, as described in Aras et al. (2015). EDGAR has already supported a number of cross-laboratory validation studies published in both journals and relevant conferences (Chamorro-Servent et al., 2016; Schulze et al., 2017; Cluitmans et al., 2018; Svehlikova et al., 2018).

An essential requirement for the data sets of choice is to define an appropriate ground truth, a goal that as described above is not always easy with experimental or clinical data. We recommend including the error of experimentally determined "ground truth" whenever possible, to give context to validation studies, e.g., the accuracy in localization of an ablation site.

Technical, Pathological or Clinical Validation

Despite the distinction between technical, pathological, and clinical validation in this review, in practice validation should be seen more as existing on a continuum (see **Figure 1**). In the early days, validation studies of a purely technical nature were common, but with time, studies have included pathological aspects; however, there are still only few published purely clinical/socioeconomical validation studies. Given the increased application of ECGI for clinical use, future validation studies should contain aspects of at least two forms of validation, if not all three, by giving a clinically oriented perspective to results. For example, validation of a new formulation for ECGI in a purely technical fashion might report that electrograms are now reconstructed with a correlation slightly better than previously reported methods. However, putting this result into perspective in terms of quantifying, say, improved accuracy to detect arrhythmogenic substrate for ablation targeting, and/or improved patient outcome, would provide for a substantially more powerful contribution.

[3]http://edgar.sci.utah.edu/

Metrics for Validation

To assess ECGI accuracy in technical validation studies, a variety of metrics have been derived and reported. Each metric comes with its own advantages and disadvantages, supporting the use of several different metrics to carry out a useful evaluation. Here, we discuss these metrics, their current uses and their limitations.

Global Comparisons

In general, it is important to quantify accuracy in both time and space in a global sense; to quantify similarity in shape (e.g., temporal waveforms or spatial potential/activation distributions), and amplitude (e.g., voltage). Metrics to quantify global accuracy include:

- Correlation: this metric is often used in ECGI validation as it quantifies the accuracy in shape regardless of any amplitude inaccuracies. However, it may not be clear to clinicians what the different values of correlation correspond to in terms of diagnostic or therapeutic accuracy. For example, electrode 5 in **Figure 3** shows a high correlation coefficient that does not reflect the fact that the reconstructed electrogram misses the (clinically informative) initial positive deflection shown by the ground truth.
- Phase Locking Value (PLV): PLV estimates the average synchronicity between two signals, without regard to the constant phase shift between them (Dubois et al., 2016). This is useful in the evaluation of phase, where the exact synchronicity of the signals is less important.
- Relative or Absolute Error: these metrics are used to quantify the accuracy in amplitude (or timing in the case of activation maps). Relative error has the advantage of defining the accuracy relative to the size of the feature being measured, meaning it can be more clear whether an absolute difference is very significant or not (e.g., an absolute error of 2 mV is not very important when the gold standard is 25 mV, but more substantial when it is 4 mV). However, like correlation, relative error is less meaningful to clinicians. Furthermore, relying on relative error can badly miss critical similarities, e.g., a slight time misalignment of activation could result in a large value of squared error. Conversely, small abnormalities (e.g., a small infarcted region or scar) that are missed in a reconstruction may not significantly affect global relative error.

Local Comparisons

As discussed previously, correlation and/or relative/absolute error correspond to accuracy on a global scale (**Figures 3–5**), but neglect the accuracy of the finer, potentially more important, characteristics. The following metrics have been developed to quantify the accuracy of specific characteristics.

- Localization Error: this metric is used to define the accuracy in localization of specific features (e.g., in space: site of earliest activation; or in time: timing of first breakthrough). While it is easy to interpret, it is not always the most clinically relevant metric. For example, a 5 mm error in PVC localization is more significant than a much larger

error in distance, if the location is incorrectly identified as the LV instead of the RV compared to when both correct and incorrect sites are in the same chamber. Some authors have quantified localization to a predefined segment of the heart [e.g., segmentation according to the AHA classification (Austen et al., 1975)] but these indicators can also be misleading, for example if the correct location lies just on one side of a segment boundary and the reconstructed location is nearby but just on the other (Sapp et al., 2017). Moreover, estimation of activation time and site of first activation from reconstructed electrograms is itself a difficult problem that is currently the topic of active investigation by many groups (Erem et al., 2011; Duchateau et al., 2016), including the CEI workgroup on Activation and Recovery times[4].

- Weighted under/over-estimation indicators (Figuera et al., 2016): are used to assess the localization accuracy of larger features such as the divergence/singularity points maps or ischemic region detection. They define the percentage of misjudged region (either positive or negative), by the ECGI reconstruction. These indicators are highly dependent on the size of the region being assessed, and like relative error can miss critical similarities if the region reconstructed is only slightly misaligned.

While each metric has its merits, the limitations mean it is advisable to use all of these metrics with caution and ideally none should be the only metric used in a technical validation study. That is, for each feature, other clinically relevant, ideally quantitative, comparisons are necessary. These should be based on the characteristics of each feature one wants to reconstruct, e.g., electrogram fractionation, ST-segment elevation, DF or phase singularity points, etc.

Given the sensitivity of inverse reconstructions to noise and model error (which could well be from physiological causes such as respiratory or contractile motion), studies should report the distribution of cumulative results across an ensemble of beats, and not just a single case or a mean reconstruction. For example, box plots showing the median, the quartiles and outliers can be a better choice. More broadly, new metrics will likely need to continue to be developed to achieve these goals.

Reproducibility

A thorough description of all experiments and analyses is essential to allow for reproducibility and reliable comparison to other methods. Such descriptions include the full workflow, from scanner settings to segmentation to therapy application to metric calculation. Clinical study design should be fixed before being executed and registered publicly (e.g., ClinicalTrials.gov). The investigators may also choose to share the data and/or methods used (e.g., via collaboration or the EDGAR database), allowing other research groups to compare approaches and improve accuracy.

[4]http://www.ecg-imaging.org/workgroups/activation-recovery-times-detection

Statistics

The statistical analysis performed for any validation study depends on the form of validation, comparisons made, data set used, and many other factors. The choice of statistical test must be made with care. Unfortunately, many studies use a simple *t*-test, missing potentially important information that may be obtained by taking into account other dependent and independent factors that can influence accuracy (e.g., subject, cardiac sequence, or region of the heart for reconstruction), as well as by including comparisons based on carefully designed metrics of effect size as well as on more comprehensive distributional comparisons. Incorporating these factors into the analysis may help reveal the source of outliers, define regional accuracy, or provide an indication of confidence in the results. In particular, including effect size in addition to the more traditional mean or median-based statistics allows the evaluation of the clinical relevance of statistically significant differences, i.e., outcomes may fall in statistically significantly different groups, based on means or median, but overlap of distribution between those groups may prevent reliable prediction on a per-patient level.

THE FUTURE OF ECGI

Electrocardiographic imaging has a rich history, from the first model development and animal studies in the 1970s, through extensive technical validation studies in computer simulations, *ex vivo* torso tank and *in vivo* animal studies, to its more recent human use to understand pathological mechanisms of diseases and guide clinical procedures in patients. Continued technical, pathological, and especially clinical validation will be essential for full adoption of ECGI as clinical technique. We have highlighted the accomplishments of the last decades, and have given pointers to what remains to be done for specific diseases and applications. Specifically, showing *clinical benefit* is essential for the adoption of this powerful technique. Such benefit may lie in patient outcome improvement, workflow improvement, or cost reduction. Future studies should focus on these aspects to achieve broad adoption of ECGI, but only after the technical challenges have been solved for that specific application/pathology. Importantly, one should realize that ECGI remains a tool used for one half of patient treatment, with the other half being the therapy given. If the therapy itself is inadequate or incomplete, it should be no surprise that the application of ECGI will not directly improve procedure outcome. Similarly, if disease mechanisms are not completely understood, the therapeutic value of ECGI-detected substrate is limited. Continued interaction between engineers, basic scientists and physicians remains essential to find a hybrid between technical achievements, pathological mechanisms insights, and clinical benefit.

AUTHOR CONTRIBUTIONS

MC and LB conceived of the presented idea. All authors discussed and contributed to the writing of the final manuscript.

FUNDING

This study received financial support from the Hein Wellens Fonds, the Cardiovascular Research and Training Institute (CVRTI), the Nora Eccles Treadwell Foundation, the National Institute of General Medical Sciences of the National Institutes of Health (P41GM103545), the National Institutes of Health (NIH HL080093), the French government as part of the Investments of the Future program managed by the National Research Agency (ANR-10-IAHU-04), from the VEGA Grant Agency in Slovakia (2/0071/16), from the Slovak Research and Development Agency (APVV-14-0875), the Fondo Europeo de Desarrollo Regional (FEDER), the Instituto de Salud Carlos III (PI17/01106) and from Conselleria d'Educació, Investigació, Cultura i Esport de la Generalitat Valenciana (AICO/2018/267) and NIH grant (HL125998) and National Science Foundation (ACI-1350374).

REFERENCES

Andrews, C. M., Srinivasan, N. T., Rosmini, S., Bulluck, H., Orini, M., Jenkins, S., et al. (2017). Electrical and structural substrate of arrhythmogenic right ventricular cardiomyopathy determined using noninvasive electrocardiographic imaging and late gadolinium magnetic resonance imaging. *Circ. Arrhythm. Electrophysiol.* 10:e005105. doi: 10.1161/CIRCEP.116.005105

Aras, K., Good, W., Tate, J., Burton, B., Brooks, D., Coll-Font, J., et al. (2015). Experimental data and geometric analysis repository - edgar. *J. Electrocardiol.* 48, 975–981. doi: 10.1016/j.jelectrocard.2015.08.008

Austen, W. G., Edwards, J. E., Frye, R. L., Gensini, G. G., Gott, V. L., Griffith, L. S., et al. (1975). A reporting system on patients evaluated for coronary artery disease. Report of the Ad hoc committee for grading of coronary artery disease, council on cardiovascular surgery. *Circulation* 51, 5–40. doi: 10.1161/01.CIR.51.4.5

Bayley, R. H., and Berry, P. M. (1962). The electrical field produced by the eccentric current dipole in the nonhomogeneous conductor. *Am. Heart J.* 63, 808–820. doi: 10.1016/0002-8703(62)90065-0

Bear, L. R., Huntjens, P. R., Walton, R., Bernus, O., Coronel, R., and Dubois, R. (2018a). Cardiac electrical dyssynchrony is accurately detected by noninvasive electrocardiographic imaging. *Heart Rhythm* 15, 1058–1069. doi: 10.1016/j.hrthm.2018.02.024

Bear, L. R., Legrice, I. J., Sands, G. B., Lever, N. A., Loiselle, D. J., Paterson, D. J. et al. (2018b). How accurate is inverse electrocardiographic mapping? A systematic in vivo evaluation. *Circ. Arrhythm. Electrophysiol.* 11:e006108. doi: 10.1161/CIRCEP.117.006108

Berger, T., Fischer, G., Pfeifer, B., Modre, R., Hanser, F., Trieb, T., et al. (2006). Single-beat noninvasive imaging of cardiac electrophysiology of ventricular pre-excitation. *J. Am. Coll. Cardiol.* 48, 2045–2052. doi: 10.1016/j.jacc.2006.08.019

Berger, T., Pfeifer, B., Hanser, F. F., Hintringer, F., Fischer, G., Netzer, M., et al. (2011). Single-beat noninvasive imaging of ventricular endocardial and epicardial activation in patients undergoing CRT. *PLoS One* 6:e16255. doi: 10.1371/journal.pone.0016255

Chamorro-Servent, J., Bear, L., Duchateau, J., Dallet, C., Coudière, Y., and Dubois, R. (2016). Adaptive placement of the pseudo-boundaries improves the conditioning of the inverse problem. *Comput. Cardiol.* 43, 705–708.

Cluitmans, M. J. M. (2016). *Noninvasive Reconstruction of Cardiac Electrical Activity: Mathematical Innovation, In Vivo Validation and Human Application*. Doctoral Thesis, Maastricht University, Maastricht.

Cluitmans, M. J. M., Bonizzi, P., and Karel, J. M. H. (2017). In-vivo validation of electrocardiographic imaging. *JACC Clin. Electrophysiol.* 3, 232-242. doi: 10.1016/j.jacep.2016.11.012

Cluitmans, M. J. M., Ghimire, S., Dhamala, J., Coll-Font, J., Tate, J. D., Giffard-Roisin, S., et al. (2018). Noninvasive localization of premature ventricular complexes: a research-community-based approach. *Europace* 20(Suppl. 1):i210. doi: 10.1093/europace/euy015.611

Cuculich, P. S., Schill, M. R., Kashani, R., Mutic, S., Lang, A., Cooper, D., et al. (2017). Noninvasive cardiac radiation for ablation of ventricular tachycardia. *N. Engl. J. Med.* 377, 2325–2336. doi: 10.1056/NEJMoa1613773

Cuculich, P. S., Wang, Y., Lindsay, B. D., Faddis, M. N., Schuessler, R. B., Damiano, RJ Jr, et al. (2010). Noninvasive characterization of epicardial activation in humans with diverse atrial fibrillation patterns. *Circ.* 122, 1364–1372. doi: 10.1161/CIRCULATIONAHA.110.945709

Cuculich, P. S., Zhang, J., Wang, Y., Desouza, K. A., Vijayakumar, R., Woodard, P. K., et al. (2011). The electrophysiological cardiac ventricular substrate in patients after myocardial infarction. *J. Am. Coll. Cardiol.* 58, 1893–1902. doi: 10.1016/j.jacc.2011.07.029

Dawoud, F., Schuleri, K. H., Spragg, D. D., Horáček, B. M., and Ronald, D. (2016). Insights from novel non-invasive ct and ecg imaging modalities on electromechanical myocardial activation in a canine model of ischemic dyssynchronous heart failure. *J. Cardiovasc. Electrophysiol.* 27, 1454–1461. doi: 10.1111/jce.13091.This

Dubois, R., Pashaei, A., Duchateau, J., and Vigmond, E. (2016). Evaluation of combined noninvasive electrocardiographic imaging and phase mapping approach for atrial fibrillation: a simulation study. *Comput. Cardiol.* 43, 2–5. doi: 10.22489/CinC.2016.037-540

Duchateau, J., Potse, M., and Dubois, R. (2016). Spatially coherent activation maps for electrocardiographic imaging. *IEEE Trans. Biomed. Eng.* 64, 1149–1156. doi: 10.1109/TBME.2016.2593003

Erem, B., Brooks, D. H., van Dam, P. M., Stinstra, J. G., and MacLeod, R. S. (2011). Spatiotemporal estimation of activation times of fractionated ECGs on complex heart surfaces. *Conf. Proc. Annu. Int. Conf. IEEE Eng. Med. Biol. Soc.* 2011:5884–5887. doi: 10.1109/IEMBS.2011.6091455

Erem, B., Van Dam, P. M., and Brooks, D. H. (2014). Identifying model inaccuracies and solution uncertainties in noninvasive activation-based imaging of cardiac excitation using convex relaxation. *IEEE Trans. Med. Imaging* 33, 902–912. doi: 10.1109/TMI.2014.2297952

Erkapic, D., and Neumann, T. (2015). Ablation of premature ventricular complexes exclusively guided by three-dimensional noninvasive mapping. *Card Electrophysiol. Clin.* 7, 109–115. doi: 10.1016/j.ccep.2014.11.010

Everett, T. H., Kok, L. C., Vaughn, R. H., Moorman, J. R., and Haines, D. E. (2001). Frequency domain algorithm for quantifying atrial fibrillation organization to increase defibrillation efficacy. *IEEE Trans. Biomed. Eng.* 48, 969–978. doi: 10.1109/10.942586

Faes, L., and Ravelli, F. (2007). A morphology-based approach to the evaluation of atrial fibrillation organization. *IEEE Eng. Med. Biol. Magaz.* 26, 59–67. doi: 10.1109/MEMB.2007.384097

Figuera, C., Suárez-Gutiérrez, V., Hernández-Romero, I., Rodrigo, M., Liberos, A., Atienza, F., et al. (2016). Regularization techniques for ECG imaging during atrial fibrillation: a computational study. *Front. Physiol.* 7:466. doi: 10.3389/fphys.2016.00446

Fitzpatrick, A. P., Gonzales, R. P., Lesh, M. D., odin, G. W., Lee, R. J., and Scheinman, M. M. (1994). New algorithm for the localization of accessory atrioventricular connections using a baseline electrocardiogram. *J. Am. Coll. Cardiol.* 23, 107–116. doi: 10.1016/0735-1097(94)90508-8

Frontera, A., Cheniti, G., Martin, C. A., Takigawa, M., Duchateau, J., Puyo, S., et al. (2018). Frontiers in non-invasive cardiac mapping: future implications for arrhythmia treatment. *Minerva Cardioangiol.* 66, 75–82. doi: 10.23736/S0026-4725.17.04463-2

Geselowitz, D. (1989). On the theory of the electrocardiogram. *Proc. IEEE* 77, 857–876. doi: 10.1109/5.29327

Geselowitz, D. (1992). Description of cardiac sources in anisotropic cardiac muscle: application of bidomain model. *J. Electrocardiol.* 25, 65–67. doi: 10.1016/0022-0736(92)90063-6

Ghanem, R. N., Jia, P., Ramanathan, C., Ryu, K., Markowitz, A., and Rudy, Y. (2005). Noninvasive electrocardiographic imaging (ECGI): comparison to intraoperative mapping in patients. *Heart Rhythm* 2, 339–354. doi: 10.1016/j.hrthm.2004.12.022

Ghosh, S., Rhee, E. K., Avari, J. N., Woodard, P. K., and Rudy, Y. (2008). Cardiac memory in patients with Wolff-Parkinson-White syndrome: noninvasive imaging of activation and repolarization before and after catheter ablation. *Circulation.* 118, 907–915. doi: 10.1161/CIRCULATIONAHA.108.781658

Ghosh, S., Silva, J. N., Canham, R. M., Bowman, T. M., Zhang, J., Rhee, E. K., et al. (2011). Electrophysiologic substrate and intraventricular left ventricular dyssynchrony in nonischemic heart failure patients undergoing cardiac resynchronization therapy. *Heart Rhythm* 8, 692–699. doi: 10.1016/j.hrthm.2011.01.017

Gordon, J. P., Laks, M., Boyle, N. G., and van Dam, P. (2014). Advantages of the cardiac isochrone positioning system for localization of PVCs to the endocardium, epicardium, and mid-myocardium from a 12 lead ECG. *Circ Am Heart Assoc* 130, A19734–A19734.

Grace, A., Verma, A., and Willems, S. (2017). Dipole density mapping of atrial fibrillation. *Eur. Heart J.* 38, 5–9. doi: 10.1093/eurheartj/ehw585

Gray, R. A., Pertsov, A. M., and Jalife, J. (1996).). Spatial and temporal organization during cardiac fibrillation. *Nature* 52(Pt 5), 753–769. doi: 10.1107/S0108768196005599

Haissaguerre, M., Hocini, M., Denis, A., Shah, A. J., Komatsu, Y., Yamashita, S., et al. (2014). Driver domains in persistent atrial fibrillation. *Circulation* 130, 530–538. doi: 10.1161/CIRCULATIONAHA.113.005421

Haissaguerre, M., Hocini, M., Shah, A. J., Derval, N., Sacher, F., Jais, P., et al. (2013). Noninvasive panoramic mapping of human atrial fibrillation mechanisms: a feasibility report. *J. Cardiovasc. Electrophysiol.* 24, 711–717. doi: 10.1111/jce.12075

Han, C., Pogwizd, S. M., Killingsworth, C. R., and He, B. (2011). Noninvasive imaging of three-dimensional cardiac activation sequence during pacing and ventricular tachycardia. *Heart Rhythm* 8, 1266–1272. doi: 10.1016/j.hrthm.2011.03.014

He, B., Li, G., and Zhang, X. (2003). Noninvasive imaging of cardiac transmembrane potentials within three-dimensional myocardium by means of a realistic geometry anisotropic heart model. *IEEE Trans. Biomed. Eng.* 50, 1190–1202. doi: 10.1109/TBME.2003.817637

He, B., and Wu, D. (2001). Imaging and visualization of 3-D cardiac electric activity. *IEEE Trans. Inf. Technol. Biomed.* 5, 181–186. doi: 10.1109/4233.945288

Horáček, B. M., Sapp, J. L., Penney, C. J., Warren, J. W., and Wang, J. J. (2011). Comparison of epicardial potential maps derived from the 12-lead electrocardiograms with scintigraphic images during controlled myocardial ischemia. *J. Electrocardiol.* 44, 707–712. doi: 10.1016/j.jelectrocard.2011.08.009

Horáček, B. M., Wang, L., Dawoud, F., Xu, J., and Sapp, J. L. (2015). Noninvasive electrocardiographic imaging of chronic myocardial infarct scar. *J. Electrocardiol.* 48, 952–958. doi: 10.1016/j.jelectrocard.2015.08.035

Irie, T., Yu, R., Bradfield, J. S., Vaseghi, M., Buch, E. F., Ajijola, O., et al. (2015). Relationship between sinus rhythm late activation zones and critical sites for scar-related ventricular tachycardia: systematic analysis of isochronal late activation mapping. *Circ. Arrhythm. Electrophysiol.* 8, 390–399. doi: 10.1161/CIRCEP.114.002637

Jamil-Copley, S., Vergara, P., Carbucicchio, C., Linton, N., Koa-Wing, M., Luther, V., et al. (2015). Application of ripple mapping to visualize slow conduction channels within the infarct-related left ventricular scar. *Circ. Arrhythm. Electrophysiol.* 8, 76–86. doi: 10.1161/CIRCEP.114.001827

Janssen, A. M., Potyagaylo, D., Dössel, O., and Oostendorp, T. F. (2017). Assessment of the equivalent dipole layer source model in the reconstruction of cardiac activation times on the basis of BSPMs produced by an anisotropic model of the heart. *Med. Biol. Eng. Comp.* 56, 1013–1025. doi: 10.1007/s11517-017-1715-x

Knecht, S., Sohal, M., Deisenhofer, I., Albenque, J. P., Arentz, T., Neumann, T., et al. (2017). Multicentre evaluation of non-invasive biatrial mapping for persistent atrial fibrillation ablation: the AFACART study. *Europace* 19, 1302–1309. doi: 10.1093/europace/euw168

Kuck, K. H., Schaumann, A., Eckardt, L., Willems, S., Ventura, R., Delacrétaz, E., et al. (2010). Catheter ablation of stable ventricular tachycardia before defibrillator implantation in patients with coronary heart disease (VTACH): a multicentre randomised controlled trial. *Lancet* 375, 31–40. doi: 10.1016/S0140-6736(09)61755-4

Kuklik, P., Zeemering, S., van, Hunnik A, Maesen, B., Pison, L., Lau, D. H., et al. (2017). Identification of rotors during human atrial fibrillation using contact mapping and phase singularity detection: technical considerations. *IEEE Trans. Biomed. Eng.* 64, 310–318. doi: 10.1109/TBME.2016.2554660

Leong, K. M. W., Ng, F. S., Yao, C., Roney, C., Taraborrelli, P., Linton, N. W. F., et al. (2017). ST-elevation magnitude correlates with right ventricular outflow tract conduction delay in type i brugada ECG. *Circ. Arrhythm. Electrophysiol.* 10, 1–13. doi: 10.1161/CIRCEP.117.005107

Liu, C., Eggen, M. D., Swingen, C. M., Iaizzo, P. A., and He, B. (2012). Noninvasive mapping of transmural potentials during activation in Swine hearts from body surface electrocardiograms. *IEEE Trans. Med. Imaging* 31, 1777–1785. doi: 10.1109/TMI.2012.2202914

Macleod, R., and Brooks, D. H. (2000). "Validation approaches for electrocardiographic inverse problems," in *Advances in Computational Biomedicine*, Vol. 3, ed. P. Johnston (Southampton: WIT Press), 229–268.

MacLeod, R. S., Ni, Q., Punske, B., Ershler, P. R., Yilmaz, B., and Taccardi, B. (2000). Effects of heart position on the body-surface electrocardiogram. *J. Electrocardiol* 33(Suppl.), 229–237. doi: 10.1054/jelc.2000.20357

Metzner, A., Wissner, E., Tsyganov, A., Kalinin, V., Schlüter, M., Lemes, C., et al. (2017). Noninvasive phase mapping of persistent atrial fibrillation in humans: comparison with invasive catheter mapping. *Ann. Noninvasive Electrocardiol.* 23:e12527. doi: 10.1111/anec.12527

Modre, R., Tilg, B., Fischer, G., Hanser, F., Messnarz, B., Seger, M., et al. (2003). Atrial noninvasive activation mapping of paced rhythm data. *J. Cardiovasc. Electrophysiol.* 14, 712–719. doi: 10.1046/j.1540-8167.2003.02558.x

Narayan, S. M., Krummen, D. E., Shivkumar, K., Clopton, P., Rappel, W. J., and Miller, J. M. (2012). Treatment of atrial fibrillation by the ablation of localized sources: CONFIRM (conventional ablation for atrial fibrillation with or without focal impulse and rotor modulation) trial. *J. Am. Coll. Cardiol.* 60, 628–636. doi: 10.1016/j.jacc.2012.05.022

Ng, J., Kadish, A. H., and Goldberger, J. J. (2007). Technical considerations for dominant frequency analysis. *J. Cardiovasc. Electrophysiol.* 18, 757–764. doi: 10.1111/j.1540-8167.2007.00810.x

Oosterhoff, P., Meijborg, V. M., van, Dam PM, van, Dessel PF, Belterman, C. N., Streekstra, G. J., et al. (2016). Experimental validation of noninvasive epicardial and endocardial activation imaging. *Circ. Arrhythm. Electrophysiol.* 9, 1–11. doi: 10.1161/CIRCEP.116.004104

Oster, H. S., Taccardi, B., Lux, R. L., Ershler, P. R., and Rudy, Y. (1997). Noninvasive electrocardiographic imaging reconstruction of epicardial potentials, electrograms, and isochrones and localization of single and multiple electrocardiac events. *Circulation* 96, 1012–1024. doi: 10.1161/01.CIR.96.3.1012

Oster, H. S., Taccardi, B., Lux, R. L., Ershler, P. R., and Rudy, Y. (1998). Electrocardiographic imaging: Noninvasive characterization of intramural myocardial activation from inverse-reconstructed epicardial potentials and electrograms. *Circulation* 97, 1496–1507. doi: 10.1161/01.CIR.97.15.1496

Pedrón-Torrecilla, J., Rodrigo, M., Climent, A. M., Liberos, A., Pérez-David, E., Bermejo, J., et al. (2016). Noninvasive estimation of epicardial dominant high-frequency regions during atrial fibrillation. *J. Cardiovasc. Electrophysiol.* 27, 435–442. doi: 10.1111/jce.12931

Ploux, S., Lumens, J., Whinnett, Z., Montaudon, M., Strom, M., Ramanathan, C., et al. (2013). Noninvasive electrocardiographic mapping to improve patient selection for cardiac resynchronization therapy. *J. Am. Coll. Cardiol.* 61, 2435–2443. doi: 10.1016/j.jacc.2013.01.093

Ploux, S., Strik, M., Van Hunnik, A., Van Middendorp, L., Kuiper, M., and Prinzen, F. W. (2014). Acute electrical and hemodynamic effects of multisite left ventricular pacing for cardiac resynchronization therapy in the dyssynchronous canine heart. *Heart Rhythm* 11, 119–125. doi: 10.1016/j.hrthm.2013.10.018

Potyagaylo, D., Schulze, W. H. W., and Doessel, O. (2012). A new method for choosing the regularization parameter in the transmembrane potential based inverse problem of ECG. *Comput. Cardiol.* 39, 29–32.

Potyagaylo, D., Segel, M., Schulze, W., and Dössel, O. (2013). "Noninvasive localization of ectopic foci: a new optimization approach for simultaneous reconstruction of transmembrane voltages and epicardial potentials," in *Proceedings of the International Conference on Functional Imaging and Modeling of the Heart* (Berlin: Springer), 166–173. doi: 10.1007/978-3-642-38899-6_20

Punshchykova, O., Švehlíková, J., Tyšler, M., Richard, G., Sedova, K., Osmanèík, P., et al. (2016). Influence of torso model complexity on the noninvasive localization of ectopic ventricular activity. *Meas. Sci. Rev.* 16, 96–102. doi: 10.1515/msr-2016-0013

Ramanathan, C., and Rudy, Y. (2001). Electrocardiographic imaging: II. Effect of torso inhomogeneities on noninvasive reconstruction of epicardial potentials, electrograms, and isochrones. *J. Cardiovasc. Electrophysiol.* 12, 241–252. doi: 10.1046/j.1540-8167.2001.00241.x

Reddy, V. Y., Reynolds, M. R., Neuzil, P., and Al, E. (2007). Prophylactic catheter ablation for the prevention of defibrillator therapy. *N. Engl. J. Med.* 357, 2657–2665. doi: 10.1056/NEJMoa065457

Rodrigo, M., Climent, A. M., Liberos, A., Fernández-Avilés, F., Berenfeld, O., Atienza, F., et al. (2017). Technical considerations on phase mapping for identification of atrial reentrant activity in direct-And inverse-computed electrograms. *Circ. Arrhythm. Electrophysiol.* 10:e005008. doi: 10.1161/CIRCEP.117.005008

Roten, L., Pedersen, M., Pascale, P., Shah, A., Eliautou, S., Scherr, D., et al. (2012). Noninvasive electrocardiographic mapping for prediction of tachycardia mechanism and origin of atrial tachycardia following bilateral pulmonary transplantation. *J. Cardiovasc. Electrophysiol.* 23, 553–555. doi: 10.1111/j.1540-8167.2011.02250.x

Rudy, Y. (2013). Noninvasive electrocardiographic imaging of arrhythmogenic substrates in humans. *Circ. Res.* 112, 863–874. doi: 10.1161/CIRCRESAHA.112.279315

Rudy, Y., and Burnes, J. E. (1999). Noninvasive electrocardiographic imaging. *Ann. Noninvasive Electrocardiol.* 4, 340–359. doi: 10.1016/j.hrthm.2008.03.011

Rudy, Y., and Messinger-Rapport, B. J. (1988). The inverse problem in electrocardiography: solutions in terms of epicardial potentials. *Crit. Rev. Biomed. Eng.* 16, 215–268.

Rudy, Y., Plonsey, R., and Liebman, J. (1979). The effects of variations in conductivity and geometrical parameters on the electrocardiogram, using an eccentric spheres model. *Circ. Res.* 44, 104–111. doi: 10.1161/01.RES.44.1.104

Salinet, J. L., Tuan, J. H., Sandilands, A. J., Stafford, P. J., Schlindwein, F. S., and André Ng, G. (2014). Distinctive patterns of dominant frequency trajectory behavior in drug-refractory persistent atrial fibrillation: Preliminary characterization of spatiotemporal instability. *J. Cardiovasc. Electrophysiol.* 25, 371–379. doi: 10.1111/jce.12331

Salu, Y. (1978). Relating the multipole moments of the heart to activated parts of the epicardium and endocardium. *Ann. Biomed. Eng.* 6, 492–505. doi: 10.1007/BF02584552

Sánchez, C., Bueno-Orovio, A., Pueyo, E., and Rodríguez, B. (2017). Atrial fibrillation dynamics and ionic block effects in six heterogeneous human 3D virtual atria with distinct repolarization dynamics. *Front. Bioeng. Biotechnol.* 5:29. doi: 10.3389/fbioe.2017.00029

Sanders, P., Berenfeld, O., Hocini, M., Jaïs, P., Vaidyanathan, R., Hsu, L. F., et al. (2005). Spectral analysis identifies sites of high-frequency activity maintaining atrial fibrillation in humans. *Circulation* 112, 789–797. doi: 10.1161/CIRCULATIONAHA.104.517011

Sapp, J. L., Bar-Tal, M., Howes, A. J., Toma, J. E., El-Damaty, A., Warren, J. W., et al. (2017). Real-time localization of ventricular tachycardia origin From the 12-lead electrocardiogram. *JACC Clin. Electrophysiol.* 3, 687–699. doi: 10.1016/j.jacep.2017.02.024

Sapp, J. L., Dawoud, F., Clements, J. C., and Horáček, B. M. (2012). Inverse solution mapping of epicardial potentials: quantitative comparison with epicardial contact mapping. *Circ. Arrhythm. Electrophysiol.* 5, 1001–1009. doi: 10.1161/CIRCEP.111.970160

Sapp, J. L., Wells, G. A., Parkash, R., Stevenson, W. G., Blier, L., Sarrazin, J. F., et al. (2016). Ventricular tachycardia ablation versus escalation of antiarrhythmic drugs. *N. Engl. J. Med.* 375, 111–121. doi: 10.1056/NEJMoa1513614

Schulze, W. (2015). *ECG Imaging of Ventricular Activity in Clinical Applications*. Karlsruhe: KIT Scientific Publishing.

Schulze, W. H. W., Chen, Z., Relan, J., Potyagaylo, D., Krueger, M. W., Karim, R., et al. (2017). ECG imaging of ventricular tachycardia: evaluation against simultaneous non-contact mapping and CMR-derived grey zone. *Med. Biol. Eng. Comp.* 55, 979–990. doi: 10.1007/s11517-016-1566-x

Shah, D. C., Jaïs, P., Haïssaguerre, M., Chouairi, S., Takahashi, A., Hocini, M., et al. (1997). Three-dimensional mapping of the common atrial flutter circuit in the right atrium. *Circulation* 96, 3904–3912. doi: 10.1161/01.CIR.96.11.3904

Shome, S., and Macleod, R. (2007). "Simultaneous high-resolution electrical imaging of endocardial, epicardial and torso-tank surfaces under varying cardiac metabolic load and coronary flow," in *Proceeding of the International Confrence Functional Imaging and Modeling of the Heart* (Berlin: Springer), 320–329. doi: 10.1007/978-3-540-72907-5_33

Simms, H. D. J., and Geselowitz, D. B. (1995). Computation of heart surface potentials using the surface source model. *J. Cardiovasc. Electrophysiol.* 6, 522–531. doi: 10.1111/j.1540-8167.1995.tb00425.x

Svehlikova, J., Teplan, M., and Tysler, M. (2018). Geometrical constraint of sources in noninvasive localization of premature ventricular contractions. *J. Electrocardiol.* 51, 370–377. doi: 10.1016/j.jelectrocard.2018.02.013

Tsyganov, A., Wissner, E., Metzner, A., Mironovich, S., Chaykovskaya, M., Kalinin, V., et al. (2017). Mapping of ventricular arrhythmias using a novel noninvasive epicardial and endocardial electrophysiology system. *J. Electrocardiol.* 51, 92–98. doi: 10.1016/j.jelectrocard.2017.07.018

Umapathy, K., Nair, K., Masse, S., Krishnan, S., Rogers, J., Nash, M. P., et al. (2010). Phase mapping of cardiac fibrillation. *Circ. Arrhythm. Electrophysiol.* 3, 105–114. doi: 10.1161/CIRCEP.110.853804

Van Dam, P. M., Oostendorp, T. F., Linnenbank, A. C., and Van Oosterom, A. (2009). Non-invasive imaging of cardiac activation and recovery. *Ann. Biomed. Eng.* 37, 1739–1756. doi: 10.1007/s10439-009-9747-5

Van Oosterom, A. (2001). Genesis of the T wave as based on an equivalent surface source model. *J. Electrocardiol.* 34(Suppl.), 217–227. doi: 10.1054/jelc.2001.28896

van Oosterom, A. (2002). Solidifying the solid angle. *J. Electrocardiol.* 35, 181–192. doi: 10.1054/jelc.2002.37176

van Oosterom, A. (2004). ECGSIM: an interactive tool for studying the genesis of QRST waveforms. *Heart* 90, 165–168. doi: 10.1136/hrt.2003.014662

van Oosterom, A., and Jacquemet, V. (2005a). A parameterized description of transmembrane potentials used in forward and inverse procedures. *Int. Conf. Electrocardiol.* 6, 5–8.

van Oosterom, A., and Jacquemet, V. (2005b). Genesis of the P wave: Atrial signals as generated by the equivalent double layer source model. *Europace* 7(Suppl. 2), 21–29. doi: 10.1016/j.eupc.2005.05.001

Varma, N., Jia, P., and Rudy, Y. (2007). Electrocardiographic imaging of patients with heart failure with left bundle branch block and response to cardiac resynchronization therapy. *J. Electrocardiol.* 40(6 Suppl.), S174–S178. doi: 10.1016/j.jelectrocard.2007.06.017

Vijayakumar, R., Silva, J. N. A., Desouza, K. A., Abraham, R. L., Strom, M., and Sacher, F. (2014). Electrophysiologic substrate in congenital long QT syndrome: noninvasive mapping with electrocardiographic imaging (ECGI). *Circulation* 130, 1936–1943. doi: 10.1161/CIRCULATIONAHA.114.011359

Vijayakumar, R., Vasireddi, S. K., Cuculich, P. S., Faddis, M. N., and Rudy, Y. (2016). Methodology considerations in phase mapping of human cardiac arrhythmias. *Circ. Arrhythm. Electrophysiol.* 9:e004409. doi: 10.1161/CIRCEP.116.004409

Wang, L., Dawoud, F., Yeung, S. K., Shi, P., Wong, K. C., Liu, H., et al. (2013). Transmural imaging of ventricular action potentials and post-infarction scars in swine hearts. *IEEE Trans. Med. Imaging* 32, 731–747. doi: 10.1109/TMI.2012.2236567

Wang, L., Gharbia, O. A., Nazarian, S., Horáček, B. M., and Sapp, J. L. (2018). Non-invasive epicardial and endocardial electrocardiographic imaging for scar-related ventricular tachycardia. *Europace* doi: 10.1093/europace/euy082 [Epub ahead of print].

Wang, L., Wong, K. C. L., Zhang, H., Liu, H., Shi, P., and Myocardial, A. (2011). Noninvasive computational imaging of cardiac electrophysiology for 3-D infarct. *IEEE Trans. Biomed. Eng.* 58, 1033–1043. doi: 10.1109/TBME.2010.2099226

Wang, L., Zhang, H., Wong, K., Liu, H., and Shi, P. (2010). Physiological-model-constrained noninvasive reconstruction of volumetric myocardial transmembrane potentials. *IEEE Trans. Biomed. Eng.* 57, 296–315. doi: 10.1109/TBME.2009.2024531

Weiss, D. L., Seemann, G., Keller, D., Farina, D., Sachse, F. B., and Dössel, O. (2007). Modeling of heterogeneous electrophysiology in the human heart with respect to ECG genesis. *Comp. Cardiol.* 34, 49–52. doi: 10.1109/CIC.2007.4745418

Wilson, F. N., Macleod, A. G., and Barker, P. S. (1933). The distribution of the action currents produced by heart muscle and other excitable tissues immersed in extensive media. *J. Gen. Physiol.* 16, 423–456. doi: 10.1085/jgp.16.3.423

Wissner, E., Revishvili, A., Metzner, A., Tsyganov, A., Kalinin, V., Lemes, C., et al. (2017). Noninvasive epicardial and endocardial mapping of premature ventricular contractions. *Europace* 19, 843–849. doi: 10.1093/europace/euw103

Zhang, J., Desouza, K. A., Cuculich, P. S., Cooper, D. H., Chen, J., and Rudy, Y. (2012). Continuous ECGI mapping of spontaneous VT initiation, continuation, and termination with antitachycardia pacing. *Heart Rhythm* 10, 1–2.

Zhang, J., Sacher, F., Hoffmayer, K., O'Hara, T., Strom, M., Cuculich, P., et al. (2015). Cardiac electrophysiological substrate underlying the ECG phenotype and electrogram abnormalities in brugada syndrome patients. *Circulation* 131, 1950–1959. doi: 10.1161/CIRCULATIONAHA.114.013698

Zhang, X., Ramachandra, I., Liu, Z., Muneer, B., Pogwizd, S. M., and He, B. (2005). Noninvasive three-dimensional electrocardiographic imaging of ventricular activation sequence. *Am. J. Physiol. Heart Circ. Physiol.* 289, H2724–H2732. doi: 10.1152/ajpheart.00639.2005

Zhou, Z., Jin, Q., Chen, L. Y., Yu, L., Wu, L., and He, B. (2016). Noninvasive Imaging of High-Frequency Drivers and Reconstruction of Global Dominant Frequency Maps in Patients with Paroxysmal and Persistent Atrial Fibrillation. *IEEE Transactions on Biomedical Engineering* 63, 1333–1340. doi: 10.1109/TBME.2016.2553641

Conflict of Interest Statement: MC is employed by Phillips Research. PvD is the cofounder/owner of Peacs BV. OD is on the scientific advisory board of EP solutions. JS has received research support, consultant reimbursement or honoraria from from Biosense Webster, Medtronic and Abbott.

The remaining authors declare that the research was conducted in the absence of any commercial or financial relationships that could be construed as a potential conflict of interest.

frontiers in Physiology

ORIGINAL RESEARCH
published: 21 September 2018
doi: 10.3389/fphys.2018.01304

Reducing Error in ECG Forward Simulations With Improved Source Sampling

Jess Tate[1,2], Karli Gillette[3], Brett Burton[1,2], Wilson Good[1,2], Brian Zenger[1,2], Jaume Coll-Font[4], Dana Brooks[5] and Rob MacLeod[1,2]*

[1] Department of Bioengineering, University of Utah, Salt Lake City, UT, United States, [2] Scientific Computing and Imaging Institute, University of Utah, Salt Lake City, UT, United States, [3] Institute of Biophysics, Medical University of Graz, Graz, Austria, [4] Computational Radiology Lab, Children's Hospital, Boston, MA, United States, [5] SPIRAL Group, Department of Electrical and Computer Engineering, Northeastern University, Boston, MA, United States

A continuing challenge in validating electrocardiographic imaging (ECGI) is the persistent error in the associated forward problem observed in experimental studies. One possible cause of this error is insufficient representation of the cardiac sources; cardiac source measurements often sample only the ventricular epicardium, ignoring the endocardium and the atria. We hypothesize that measurements that completely cover the pericardial surface are required for accurate forward solutions. In this study, we used simulated and measured cardiac potentials to test the effect of different levels of spatial source sampling on the forward simulation. Not surprisingly, increasing the source sampling over the atria reduced the average error of the forward simulations, but some sampling strategies were more effective than others. Uniform and random distributions of samples across the atrial surface were the most efficient strategies in terms of lowest error with the fewest sampling locations, whereas "single direction" strategies, *i.e.*, adding to the atrioventricular (AV) plane or atrial roof only, were the least efficient. Complete sampling of the atria is needed to eliminate errors from missing cardiac sources, but while high density sampling that covers the entire atria yields the best results, adding as few as 11 electrodes on the atria can significantly reduce these errors. Future validation studies of the ECG forward simulations should use a cardiac source sampling that takes these considerations into account, which will, in turn, improve validation and understanding of ECGI.

Keywords: ECG imaging, ECG forward simulation, cardiac source sampling, epicardial potentials, body-surface potentials

OPEN ACCESS

Edited by:
Carlos Figuera,
Universidad Rey Juan Carlos, Spain

Reviewed by:
Rob Gourdie,
Medical University of South Carolina, United States
Jason D. Bayer,
Université de Bordeaux, France

****Correspondence:***
Jess Tate
jess@sci.utah.edu

Specialty section:
This article was submitted to Cardiac Electrophysiology, a section of the journal Frontiers in Physiology

Received: *12 June 2018*
Accepted: *29 August 2018*
Published: *21 September 2018*

Citation:
Tate J, Gillette K, Burton B, Good W, Zenger B, Coll-Font J, Brooks D and MacLeod R (2018) Reducing Error in ECG Forward Simulations With Improved Source Sampling. Front. Physiol. 9:1304. doi: 10.3389/fphys.2018.01304

1. INTRODUCTION

Electrocardiographic Imaging (ECGI) is a promising technology for diagnosing and treating cardiac arrhythmias (Pullan et al., 2010; Rudy and Lindsay, 2015). Its goal is to compute some formulation of cardiac sources from known patient torso geometry (typically extracted from medical imaging) and body-surface potential mapping (BSPM) recordings (Barr et al., 1977; Plonsey and Barr, 1987; Plonsey and van Oosterom, 1991; Gulrajani, 1998). This computation is possible by first establishing a model of the ECG from knowledge of cardiac sources and geometry, known as a numerical forward simulation (MacLeod and Buist, 2010) and then inverting this process to solve the associated inverse problem (Pullan et al., 2010). Establishing well-validated

ECG forward simulations is, therefore, critical to developing ECGI as a technology.

The purpose of an ECG forward simulation is to predict the electric potential response through a passive volume conductor, i.e., the torso, from cardiac sources (MacLeod and Buist, 2010). Cardiac sources are represented in the literature in several ways, but the most common and most readily measured method is a surface of potentials surrounding the myocardium (Barr et al., 1977; Messinger-Rapport and Rudy, 1986; Plonsey and Barr, 1987; Plonsey and van Oosterom, 1991; Gulrajani, 1998). Predicting the resulting ECGs requires solving a partial differential equation using numerical techniques, such as boundary or finite element methods (BEM and FEM, respectively) (Johnson et al., 1993; Johnson, 1997, 2015; MacLeod and Buist, 2010).

Despite the existence of well-established methods of the ECG forward simulation, previous validation studies have consistently shown differences that were higher than might be expected between simulated and measured body-surface potentials, such as higher overall error and changes in extrema location (Ramsey et al., 1977; Bear et al., 2015). The ECG forward problem is well behaved, and we have sufficient confidence in all aspects of the simulation and measurement protocols to expect errors well below those reported. This disparity between confidence in the simulation approaches and persistent errors in experimental validation, along with the sensitivity of ECGI to model errors due to its ill-posed nature (Pullan et al., 2010), provides powerful motivation to explore possible explanations.

One as yet unexplored source of error in these studies is insufficient cardiac source representation, i.e., either inadequate coverage or spatial density of coverage of the cardiac sources. For example, many experimental validation studies use an epicardial sock electrode array to record cardiac surface potentials from the animal heart (Ramsey et al., 1977; Stanley et al., 1986; Shome and MacLeod, 2007; Bear et al., 2015). A common limitation of these epicardial socks is that they position electrodes on the ventricles only, ignoring the atria. Not only does such a set up exclude measurement of atrial sources, but some ventricular sources, such as locations either on the apex or at the base of the heart, lack either adequate spatial coverage or stable mechanical contact by sock electrodes. Such conditions are problematic as the mathematical formulation of the ECG forward simulation with potential sources assumes a complete and closed representative surface that is adequately sampled; the compromises driven by practical limitations in experiments suggest that missing sources exist and they could have a significant impact on the predicted potential values on the torso surface (Barr et al., 1977). Our goal was to examine some aspects of this dilemma, using a combination of experimental and numerical approaches.

In addition to experimental studies, we can also use computer simulation to help answer questions about the effect of cardiac sampling on the forward simulation. Simulation methods such as pseudo-bidomain (Vigmond et al., 2003, 2008) and cellular automaton (Schulze et al., 2015) can predict full pericardial potentials in a way that cannot be measured experimentally due to regions of the epicardium being inaccessible to measurement. Using simulated potentials together with experimentally recorded values provides a more complete evaluation of the effect of pericardial source sampling.

In this study, we tested the impact of cardiac source representation of the atrial region on ECG forward simulations. We hypothesize that, in the context of forward simulations from epicardial potentials, measurements that completely cover the heart are required for accurate prediction of the body-surface potentials. To test this hypothesis, we used simulated and measured cardiac potentials to determine the effect of different levels of sampling on a typical forward simulation pipeline (Burton et al., 2011). Our results support this hypothesis and encourage us to propose some sampling strategies that may minimize error resulting from incomplete sampling of cardiac sources.

2. METHODS

We analyzed the effect of source representation coverage and density of the atrial region of the heart on ECG forward simulations by sampling the cardiac source with a range of strategies, and then used those sources in our ECG forward simulation pipeline. We tested these sampling strategies on three different geometries and source models: (1) simulated epicardial potentials using the CARP (Vigmond et al., 2003, 2008) cardiac propagation modeling software package, (2) a second set of simulations provided in the EDGAR database (Aras et al., 2015) by the Biomedical Engineering team a the Karlsruhe Institute of Technology, KIT (Schulze et al., 2015), and (3) one experimentally recorded dataset from the CardioVascular Research and Training Institute (CVRTI) at the University of Utah using a unique "cage" electrode (Milanic et al., 2014), also available in the EDGAR database (Aras et al., 2015). We then computed ECG forward simulations from subsampled versions of the original sources, which we compared to FEM simulations from our ground truth cardiac potential sources. We also performed experiments in which we recorded source potentials with a ventricular sock and an electrode plaque placed on the atria and used these recorded potentials in our simulation pipeline to compare the predicted body-surface potentials with and without the additional atrial potential sources.

2.1. Datasets

2.1.0.1. CARP Dataset

The set of cardiac potentials generated using the CARP (Vigmond et al., 2003, 2008) modeling software consisted of simulated extracellular potentials using the pseudo-bidomain method (Bishop and Plank, 2011) in an isolated rabbit ventricle model previously described (Deo et al., 2009). The four pacing profiles were sinus rhythm, left ventricle (LV) free wall pacing, right ventricle (RV) free wall pacing, and apical pacing. The heart geometry was then manually registered and scaled to a human torso geometry of of dimensions $\sim 36 \times 22 \times 40$ cm, 771 nodes, and an internodal distance of 24.6 mm (MacLeod et al., 1995; Shome and MacLeod, 2007; Milanic et al., 2014). An ellipsoidal cap was placed on a mesh of the epicardial surface of the ventricles (to replicate a typical sock array) by fitting a precomputed ellipsoid mesh to the points near the base of

the ventricles and clipping it to cover the open region in the sock. The combination of the sock mesh and the ellipsoid cap formed a pericardial mesh of dimensions $\sim 6 \times 6 \times 7$ cm with 498 nodes with an average internodal spacing of 5.3 mm. To compute the potentials on both the cap of the mesh and the torso surface, we used the previously computed ventricular surface extracellular potentials from both the endocardial and epicardial surfaces and the FEM approach in SCIRun (http://scirun.org, Parker et al., 1997; MacLeod et al., 2004) with the Forward/Inverse Toolkit (Burton et al., 2011). This calculation consisted of generating a tetrahedral mesh for the region between the heart and torso surface, including the vertex locations for the pericardial mesh with the ellipsoid cap. Then for each time step, the endocardial and epicardial potentials were used to set the Dirichlet boundary conditions along the cardiac surface and Neumann boundary conditions on the torso surface to solve for the potentials distribution throughout the homogeneous torso volume. The potentials were extracted at the torso and pericardial surfaces to use in the subsequent sampling tests described below.

2.1.0.2. KIT Dataset

The KIT geometric model of a single heart and torso geometry was generated from a patient scan (Schulze et al., 2015) and is available on the EDGAR database (http://edgar.sci.utah.edu, Aras et al., 2015). The torso surface had the dimensions $\sim 47 \times 30 \times 35$ cm, 2002 nodes, and an internodal distance of 19.0 mm. The cardiac potentials computed from this model, also available from EDGAR, consisted of four activation profiles: septal, RV free wall, LV free wall, and apical pacing. In contrast to the pseudo-bidomain approach using CARP, the KIT investigators computed cardiac potentials using a cellular automaton approach for the activation sequence, and calculated first the transmembrane potentials based on the activation times with a monodomain simulation and the ten Tusscher electrophysiological model (ten Tusscher and Panfilov, 2006; Loewe et al., 2015) and then the extracellular potentials using the bidomain approach (Schulze et al., 2015). As in the CARP dataset, we added an ellipsoidal cap on a mesh of the epicardium to form a pericardial mesh of dimensions $\sim 13 \times 19 \times 10$ cm with 532 nodes with an average spacing of 9.4 mm. We used the ventricular surface extracellular potentials from both the endocardial and epicardial surfaces to simulate the potential values on the ellipsoidal cap and the torso surface using FEM, as described for the CARP dataset.

2.1.0.3. Utah Cage Dataset

The cage dataset available in EDGAR consists of measurements from our group using a perfused, isolated canine heart preparation placed inside a cylindrical cage of dimensions $\sim 10 \times 10 \times 15$ cm (600 electrodes, with average spacing of 10.7 mm) within a human torso-shaped electrolytic tank (dimensions $\sim 36 \times 22 \times 40$ cm) instrumented with 192 surface electrodes (average spacing of 40 mm MacLeod et al., 1995; Shome and MacLeod, 2007; Milanic et al., 2014). For this study, we used recorded signals from three activation profiles: sinus rhythm and left and right ventricular pacing. The geometric model and measured potentials are all available on the EDGAR database. We used the cage electrodes as a pericardial source and compared forward computed and measured torso-tank surface potentials. We also generated simulated ground truth torso potentials from the recorded cage potentials using FEM, just as for the other two datasets.

2.2. Sampling Strategies

The main goal of the study was to evaluate the effect of source representation in the forward solution by varying coverage and sampling density of the signals representing that source. We used five different incremental sampling strategies with each of the datasets to analyze the specific effect of atrial sampling on the simulated ECG, as shown in **Figure 1**. Sampling locations were added to the atria in an increasing fashion: (1) starting near the atrioventricular (AV) plane (closest to the ventricular sock) and moving toward the atrial roof, (2) from the atrial roof to the AV plane, (3) combining sites from the AV plane and atrial roof, (4) adding sites in a uniformly distributed order, and (5) adding sites in a randomly distributed order. The sampling locations were added in nine iterations for the KIT dataset, seven for the CARP dataset, and seven for the cage dataset.

In addition to testing a variable number of added electrodes to the atria, we also tested the effect of adding a cluster of electrodes, similar to a plaque electrode array, in a variety of different locations (**Figure 1**): 22 for the KIT dataset, 34 for the CARP dataset, and 72 for the cage datasets. The simulated plaque was generated by picking the nearest electrodes to each of the central locations. The number of plaque electrodes match the number of electrodes added in each iteration explained above, i.e., 11 for the KIT dataset, 15 for the CARP dataset, and 40 for the cage datasets.

In addition to testing the effect of missing atrial source samples, this study also evaluated the effect of missing ventricular source samples. To test this, source samples were incrementally removed from the basal region of the ventricles (**Figure 1**). Sampling locations were removed in eight iterations for the KIT dataset, six for the CARP dataset, and six for the cage datasets.

2.3. ECG Forward Simulation Pipeline

To simulate the body surface potentials from pericardial surface potentials with various sampling strategies, we first interpolated values from the sampled cardiac surface mesh to the entire cardiac surface and then simulated the torso surface potentials. For the interpolation step, we used Laplacian interpolation (Oostendorp et al., 1989) to estimate the values missing due to undersampling and for the forward simulation we used the BEM, as implemented in SCIRun (Parker et al., 1997; MacLeod et al., 2004) with the Forward/Inverse toolkit (Burton et al., 2011). Similar to the simulations and experiments that provided the ground truth data, the torso was modeled as homogeneous outside the heart.

We compared simulated torso potentials with those from the ground truth data using several standard approaches. We first visually compared potential maps of the results during ventricular activation, identify similarities of the main features of activation. The quantitative comparisons that followed consisted of three standard error metrics, root mean square error ($\bar{E}$),

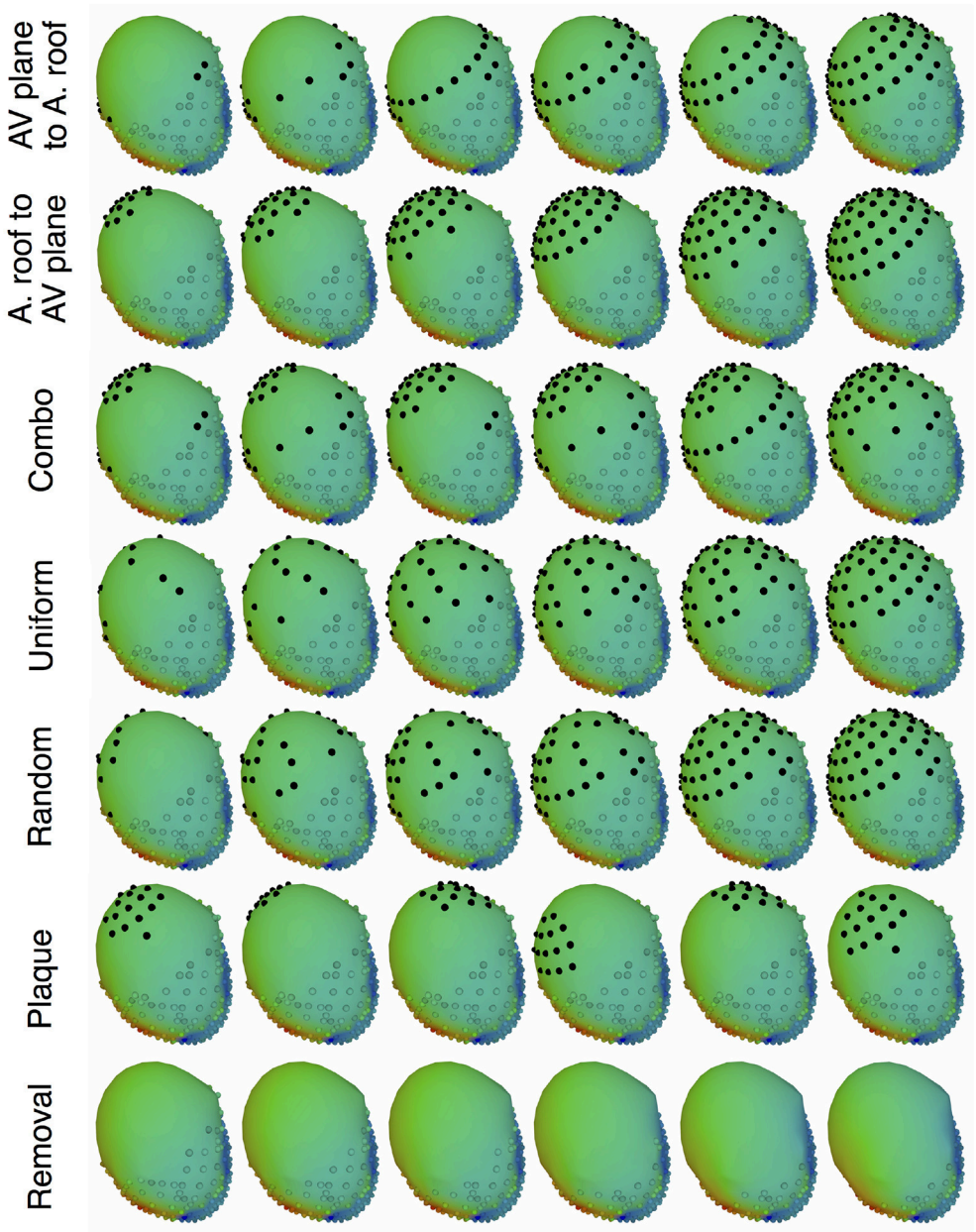

FIGURE 1 | Cardiac source sampling strategies tested. Recording locations were added from the AV plane of the heart to the atrial roof, from the roof to the AV plane, a combination of the first two, uniform sampling, and random sampling of the atria. Black spheres indicate added atrial sampling locations.

relative root mean squared error (*rRMSE*), and correlation (ρ), defined as follows:

$$\bar{E} = \frac{||\Phi_{gt} - \Phi_s||}{\sqrt{n}} \tag{1}$$

$$rRMSE = \frac{||\Phi_{gt} - \Phi_s||}{||\Phi_{gt}||} \tag{2}$$

$$\rho = \frac{\Phi_{gt}^T \Phi_s}{||\Phi_{gt}||||\Phi_s||}, \tag{3}$$

where Φ_{gt} is a vector of the ground truth BSPM values, Φ_s is a vector of the associated simulated BSPMs, and n is the number of body surface electrodes.

2.4. Validation Experiments

With data acquired in experiments, we tested the sampling strategy of placing a regularly spaced array of electrodes on the atria to validate the prediction of our hypothesis. In an *in situ* open-chest preparation (Aras, 2015; Aras et al., 2016), we placed a cardiac sock with 247 electrodes

around the ventricles and a plaque electrode array with 24 electrodes fixed to the atria on an accessible anterior epicardial region near the AV plane. With the electrodes in place, we recorded electrograms in sinus rhythm and as the heart developed ventricular tachycardia through the duration of the experiments.

Generating datasets for validation required the electrograms from the experiments be placed inside a complete geometric model of the torso. At the end of the experiments, we used a manual digitizer (Microscribe, Solution Technologies, Inc.) to capture the locations of anatomically distinct landmarks. We identified correspondance points from a previously generated geometric model of a human thorax, resulting in two meshes of the heart surfaces with a set of corresponding spatial reference points. These meshes were then registered using a combination of the RANSAC (Fischler and Bolles, 1981), Iterative closest point (ICP) (Besl and McKay, 1992), and thin plate spline techniques, followed by any necessary manual adjustments, implemented in MATLAB and SCIRun. To process the electrogram recordings, we isolated representative beats and performed baseline correction and filtering with the default settings in PFEIFER (https://www.sci.utah.edu/software/pfeifer.html; Rodenhauser et al., 2018).

The resulting registered meshes and processed cardiac surface recordings served as the input for our ECG forward simulation pipeline. The forward computations of body surface potentials also required closed surfaces, so we integrated the cardiac sock and atrial plaque meshes into an ellipsoidal cap similar to those described in section 2.1. Laplacian interpolation was then used to estimate the missing potential values on the cap. The resulting complete set of cardiac potentials was used in the ECG forward simulation pipeline, as explained in section 2.3. Torso potentials were simulated from cardiac potentials, with and without the additional plaque recordings, and compared using the metrics explained in section 2.3. We compared the resulting metrics to those from the simulated cardiac potentials described above (**Figure 1**).

2.5. Ethics

All experiments were performed with approval from the Institutional Animal Care and Use Committee at the University of Utah and conform to the Guide for the Care and Use of Laboratory Animals (National Institutes of Health publication No. 85-23).

2.6. Data Availability

Some of the data used in this study (KIT and cage datasests) are available in the EDGAR database (http://edgar.sci.utah.edu), as previously noted. The rabbit model used in the CARP dataset was obtained from a third party, and requests for that data should be directed to the CARP software team (Deo et al., 2009). The raw data collected or generated for this study will be made available by the authors, without undue reservation, to any qualified researcher.

3. RESULTS

Removing potentials from the atrial region of the cardiac surface had a significant impact on the computed forward simulations. For all pacing profiles and data sets, the errors in computed body-surface potentials increased when atrial samples were omitted. Furthermore, the errors grew monotonically with reduced numbers of atrial sample sites. Our experimentally recorded data also produced similar effects on the torso surface to those observed with the simulated data.

Figures 2, **3** show representative tracings of the various metrics over the course of ventricular activation with and without atrial sampling. As shown, the *rRMSE* tracings of the forward simulation using full pericardial sampling more closely match those of the ground truth. The values of ρ computed from pericardial potentials both with and without atrial sampling were high during most of the time signals, but the minima were reduced or eliminated when we included atrial sampling. The mean ρ without atrial sampling was 0.94 compared to 0.99 with atrial sampling. The *rRMSE* values showed a similar trend when comparing the forward solution with and without full atrial sampling; the maxima were reduced or eliminated when atrial samples were included. In a few time steps, adding atrial sampling produced a slight increase in *rRMSE* error, as seen in the KIT (**Figure 2**) and cage experiment datasets (**Figure 3**). However, the mean *rRMSE* was always reduced, with the total mean *rRMSE* reduced from 0.54 to 0.08. The peak $\bar{E}$ with only ventricular sampling ranged from 0.05 to 0.77 mV, while the peak $\bar{E}$ with full sampling dropped substantially, ranging from 0.01 to 0.19 mV and the peak $\bar{E}$ was reduced for each simulation by a mean of 0.40 mV.

Figure 4 shows the representative cases of the general effect of excluding the potential sources in the atrial region. Comparing the potential maps simulated from only ventricular sources to the ground truth demonstrates qualitative differences, especially in the right anterior region in the CARP and KIT datasets, and over the entire anterior region with the cage datasets. However, there were no qualitative differences in the location of the extrema. The observed differences in the potential maps were reduced when we used full sampling of the atrial surface. The areas with the greatest differences were consistent across all activation profiles, as were the improvements whenever we included atrial sampling.

Increasing the number of recording locations on the atrial surface systematically resulted in reduced error in the forward simulations. Every dataset and activation profile showed a progressive decrease in the peak *rRMSE*, except the apical stimulation of the KIT dataset, which showed an increase in the peak *rRMSE* from the previous iteration when adding 22 electrodes (from 11) near the AV plane (2.85 from 1.84). The mean peak *rRMSE* over all datasets and activation profiles decreased from 2.40 to 0.06. The mean *rRMSE* also progressively decreased as atrial sampling increased in all datasets, with the same exception of the apical stimulation of the KIT dataset, which showed an increase in mean the *rRMSE* from the previous iteration (0.30 from 0.27) when adding 22 electrodes (from 11). The mean *rRMSE* decreased from 0.54 to 0.08.

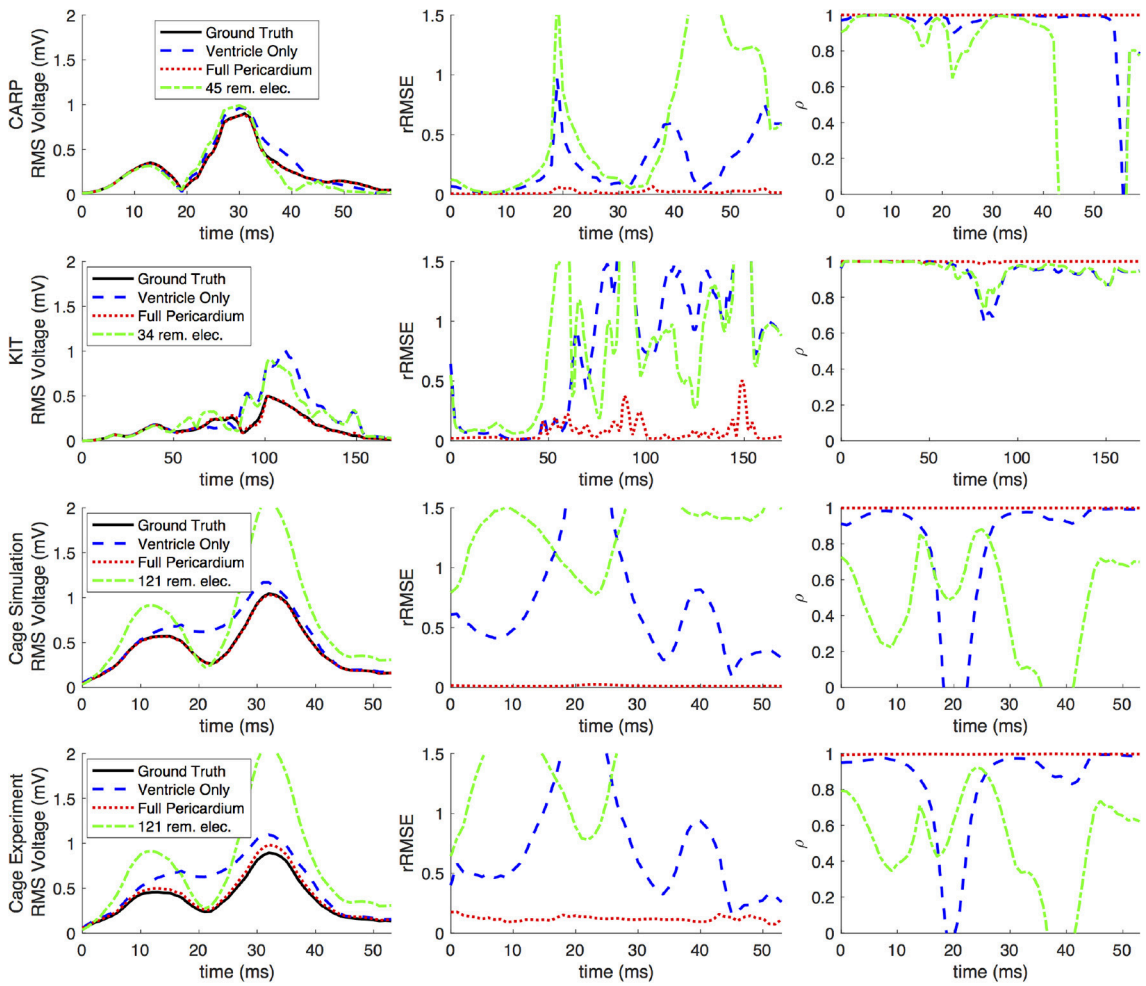

FIGURE 2 | Effects of removing atrial and some ventricular sampling over time on the sinus or septal activation profile for each dataset. Each row presents the error for each dataset. Each column corresponds to a metric, RMS voltage, relative RMS error (*rRMSE*), and correlation (ρ). Each plot shows a tracing of the error over the ventricular activation in four case: ground truth (RMS voltage only), using ventricle-only sources, full pericardial sources, and when some ventricular sources are removed from the basal region.

Figure 5 shows the mean peak *rRMSE* for each dataset. An increase in the number of samples resulted in a near asymptotic reduction in error, so that adding even a few recording locations to the atrial surface provided a significant reduction in error. Every sampling strategy we employed reduced the mean peak *rRMSE* in a similarly asymptotic relationship, but some strategies approached the minimum error with fewer added electrodes. In general, the single-direction strategies, i.e., applying electrodes only to the atrial roof or the AV plane, were less efficient than the more distributed approaches, i.e., the uniform and random distributions. The approach that combined adding electrodes to both the atrial roof and the AV plane was usually more efficient in reducing the mean peak *rRMSE* than the single-direction strategies. However, for the CARP dataset, the combined approach was only more efficient than adding electrodes to the atrial roof first. The specific order of most efficient strategies varied based on the dataset and activation profile. For example, the random distribution showed the greatest reduction of mean peak *rRMSE* after one iteration for all but the CARP dataset.

Figures 6,**7** show how the peak *rRMSE* and the mean *rRMSE*, respectively, were affected by the different activation profiles when adding a limited number of recording electrodes to the atria with various sampling strategies. In general, the uniform, random, and combined distributions produced lower error for each of the activation profiles than the remaining two strategies. The uniform distribution produced the lowest error of any of the strategies for most of the tested activation profiles. The random distribution had the second lowest error for most activation profiles and the combined approach was third lowest for most activation profiles. Adding recording electrodes to the atrial roof first generally had the highest error of any of sampling strategy, both in terms of the mean and peak *rRMSE*. Though there are some overall trends, there are noticeable anomalies in the

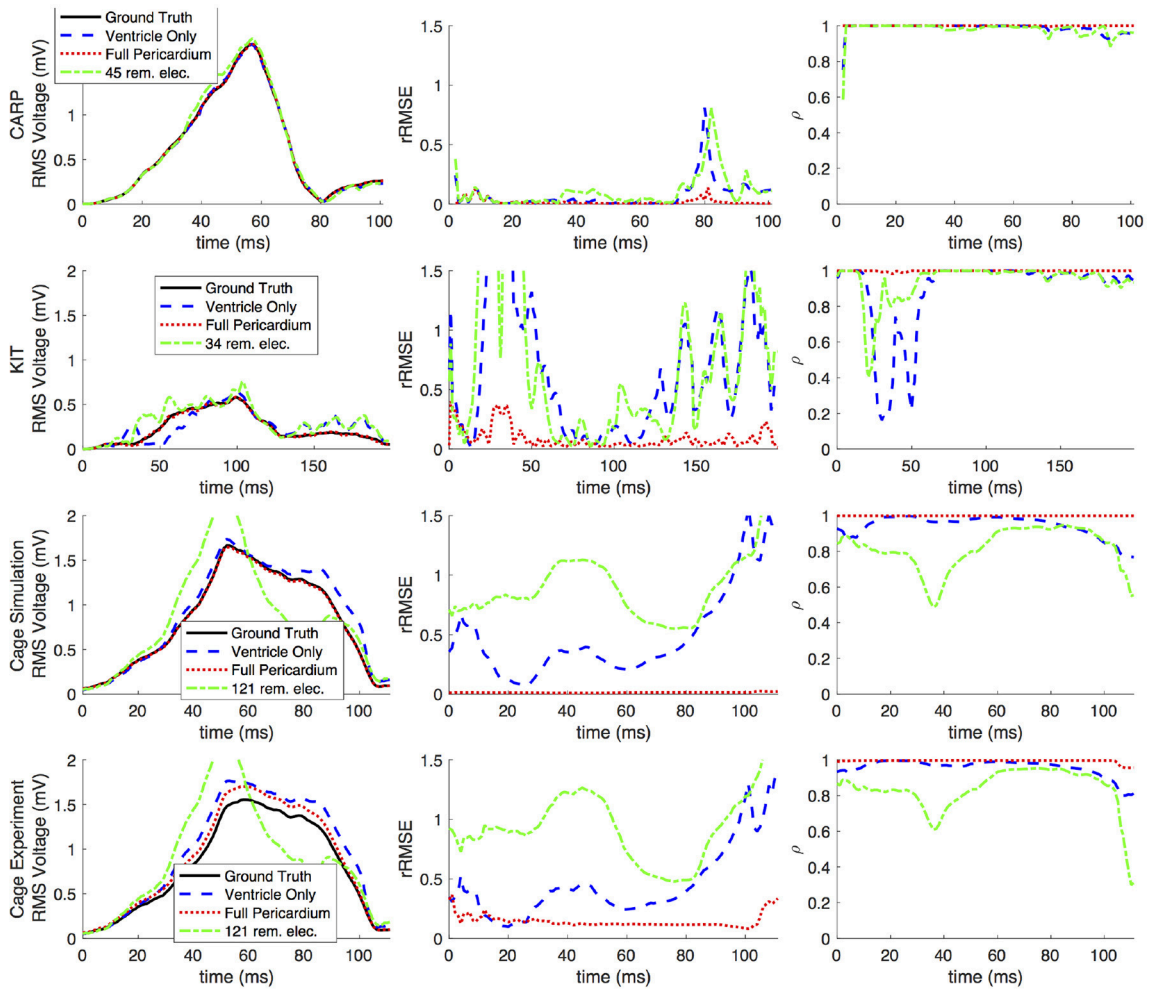

FIGURE 3 | Effects of removing atrial and some ventricular sampling over time on the left ventricle simtulation activation profile for each dataset. Each row presents the error for each dataset. Each column corresponds to a metric, RMS voltage, relative RMS error (*rRMSE*), and correlation (ρ). Each plot shows a tracing of the error over the ventricular activation in four case: ground truth (RMS voltage only), using ventricle-only sources, full pericardial sources, and when some ventricular sources are removed from the basal region.

responses to sampling. For instance, the apical stimulation of the CARP dataset had a noticeably higher mean and peak *rRMSE* for all sampling strategies than the other activation profiles in the same dataset. There are also cases with the CARP dataset in which the AV plane or atrial roof strategies produced lower or similar errors compared to the distributed strategies.

Simulated BSPM results from ventricular epicardial sources with potentials from an additional simulated plaque array placed in various locations showed a consistent reduction in error when compared to the simulations with ventricle-only sources. The mean *rRMSE* from all the plaque placements was 0.28 and the mean ρ was 0.97, compared to 0.40 and 0.95 with the ventricle-only sampling. The peak $\bar{E}$ was reduced by a mean of 0.45 mV. The placement that resulted in the lowest error was at the roof of the atria, yet there was no other trend to predict the plaque location with lower error.

When source samples were removed from the ventricular sock, there was a general increase in error for most of the QRS complex, as shown in **Figure 2**. By reducing the number of ventricular leads by approximately 45% of the total added on the atria (45, 34, and 121 for the CARP, KIT, and cage datasets, respectively), the mean ρ dropped from 0.94 to 0.84, the mean *rRMSE* increased from 0.16 to 0.28, and the peak $\bar{E}$ increased by a mean of 0.40 mV.

Progressively reducing the number of ventricular samples also generally increased the error, but not consistently. As shown in **Figure 8**, using the KIT dataset, the mean peak *rRSME* decreased initially, but then increased continuously as samples were removed. The CARP dataset showed a increased continuously as samples were removed, with the exception of the final step. Results from the cage datasets showed a similar trend: an increase in mean peak *rRMSE* with the first set of removed sources, a reduction with the second, and then a fairly consistent mean

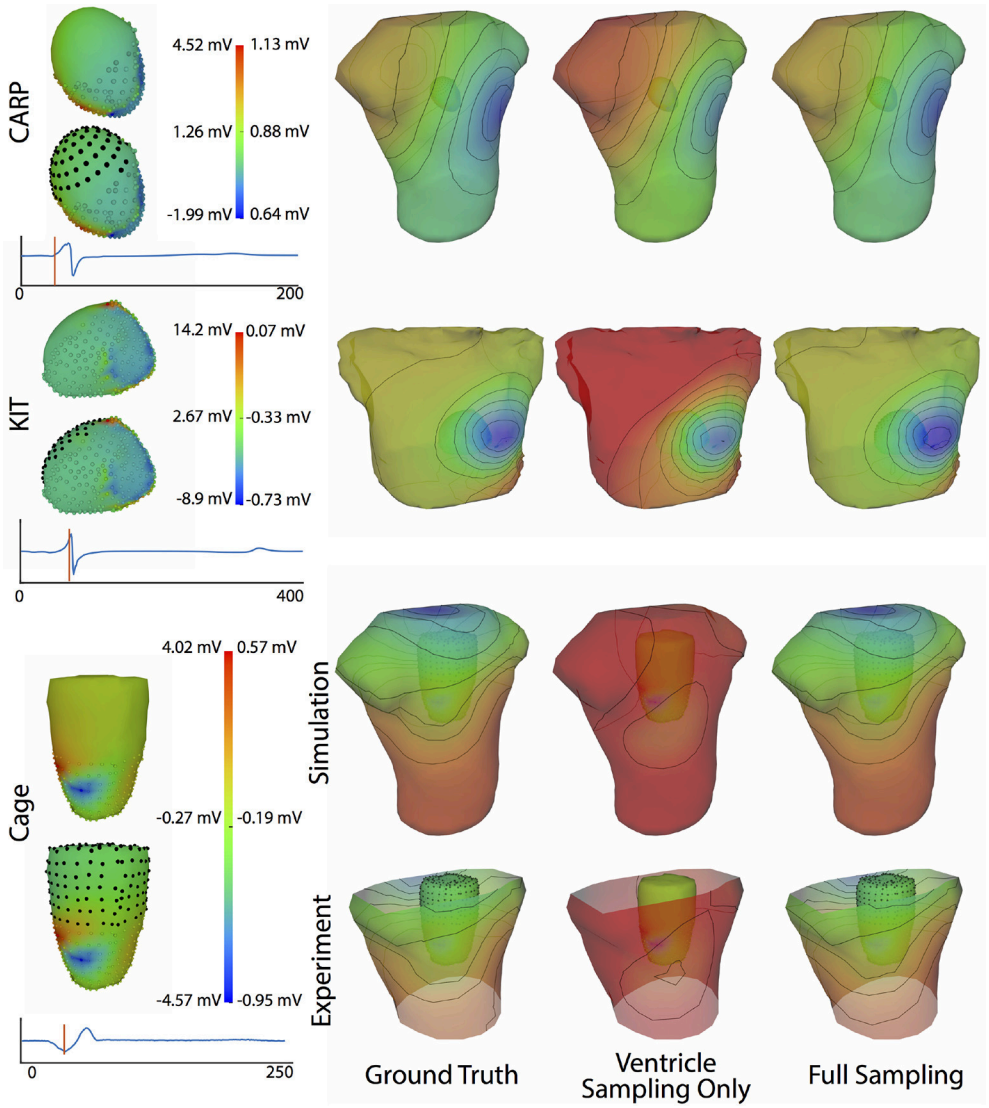

FIGURE 4 | Effect of atrial region sampling on simulated BSPMs. Shown is the ground truth potential map and the forward simulation with sampling of the ventricles only and with full coverage of the ventricles and atria. The cardiac/cage surface potentials with the two sampling methods are also shown. Results are from the same representative beats shown in **Figure 2** and at the time sample 25 ms into the QRS complex for the CARP dataset, 78 ms for the KIT dataset, and 18 ms for the cage datasets.

peak *rRMSE* for the remaining steps. The plateau mean peak *rRMSE* remained higher than for the full ventricular sampling for the cage experiment dataset, yet it was slightly lower for the cage simulation dataset. The mean *rRMSE* gradually increased for the CARP and cage datasets as ventricle samples were remove. However, for the KIT dataset, the mean *rRMSE* decreased slightly for the first four iterations before dramatically increase for the final stages. The mean ρ consistently dropped as samples were removed for the CARP dataset and for all but one step in the cage datasets. For the KIT dataset, the mean ρ increase slightly for three iterations, then decrease for the remaining steps.

Figure 9 illustrates representative cases of changes in the predicted BSPMs as ventricle samples were reduced. Most notably, removing ventricular sources produced greater qualitative differences than could be generated by removing the atrial sources (**Figure 4**). In each dataset, removing the ventricular sources produced changes in the apparent location of the extrema on the BSPM, or, as in the case of the simulated cage dataset, removed an extremum. Interestingly, although an extremum remained missing from the BSPMs, reducing the sampling further actually otherwise improved the qualitative and quantitative accuracy of the BSPM (**Figures 8**, **9**). This result was likely due to removing a more balanced distribution of potentials in the more extreme sampling reduction.

Comparing forward simulations using experimentally recorded cardiac sock potentials, with and without additional

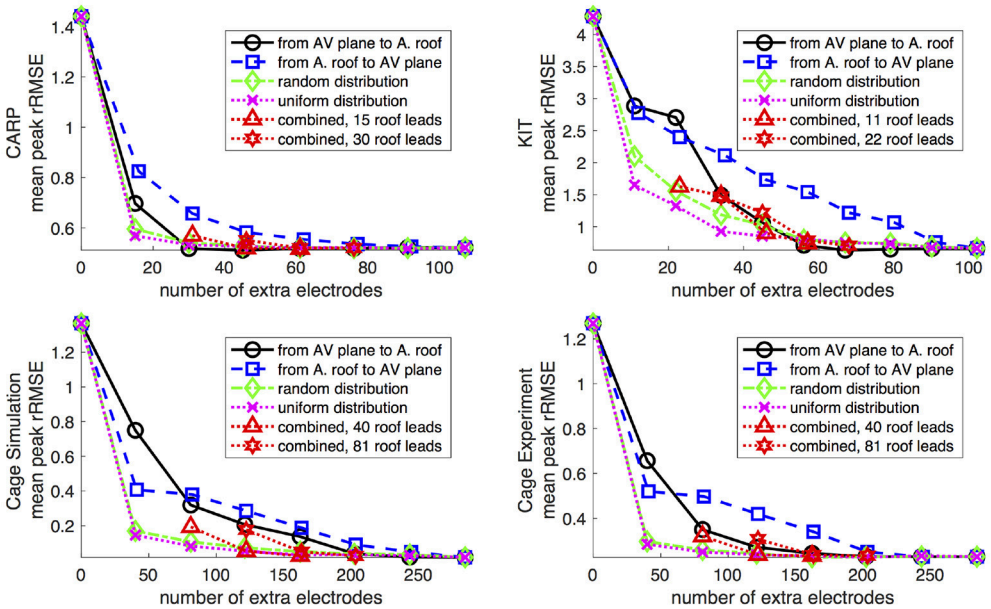

FIGURE 5 | Peak *rRMSE* of the forward simulation using different sampling strategies with increasing number of electrodes. The plots are the CARP, KIT, simulated cage, and recorded cage datasets.

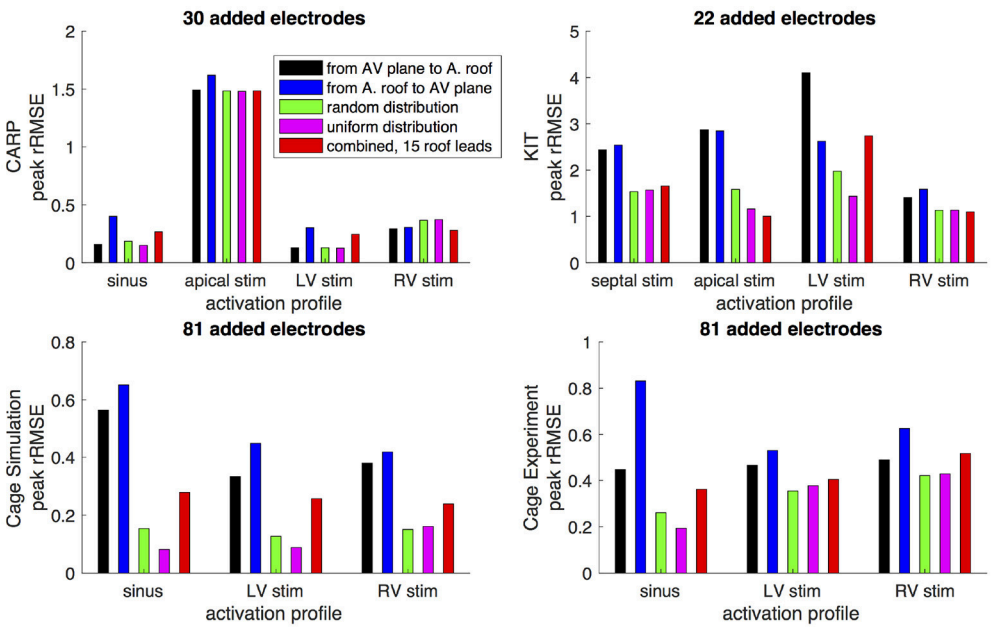

FIGURE 6 | Peak *rRMSE* of the forward simulation from different activation profiles using different sampling strategies. The plots are the CARP, KIT, simulated cage, and recorded cage datasets.

atrial plaque recordings, showed that the using a plaque electrode could alter the accuracy of the forward simulation. The comparison showed a mean *rRMSE* of 0.21 and a mean ρ of 0.98 across all experiments. **Figure 10** shows a representative comparison over time for each of the experiments. The RMS values of the potential maps showed only minor variations, and the *rRMSE* showed some time frames with high error, most notably near the beginning of the QRS complex. The ρ remained high throughout ventricular activation, except at the beginning time instants (**Figure 10**, panels 1 & 2) Repeating the same experiment with simulated results yielded similar results.

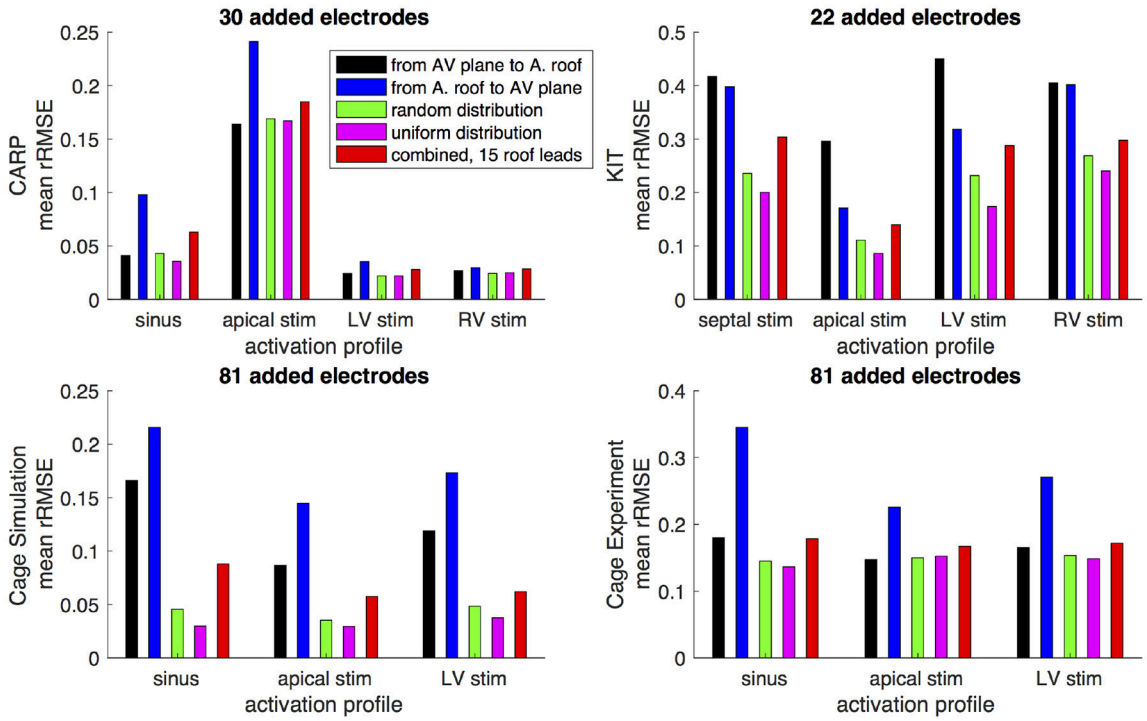

FIGURE 7 | Mean *rRMSE* of the forward simulation from different activation profiles using different sampling strategies. The plots are the CARP, KIT, simulated cage, and recorded cage datasets.

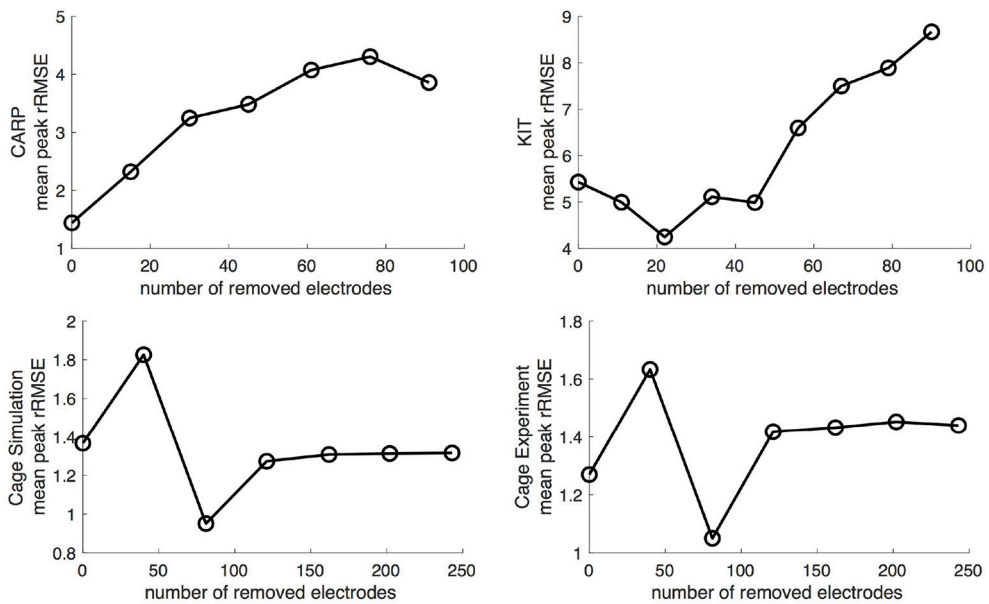

FIGURE 8 | Peak *rRMSE* of the forward simulation in response to reduced ventricular sampling.

Repeating the same experiment with simulated data, i.e., comparing forward simulation using cardiac sock potentials with and without an additional plaque, yielded similar results (**Figure 10**). The mean *rRMSE* and ρ were 0.26 and 0.98, respectively. The comparison of the BSPM over the time showed different *rRMSE* and ρ profiles compared to the experimental data, in that there peaks or dips near the middle of ventricular activation in addition to near the beginning or the end

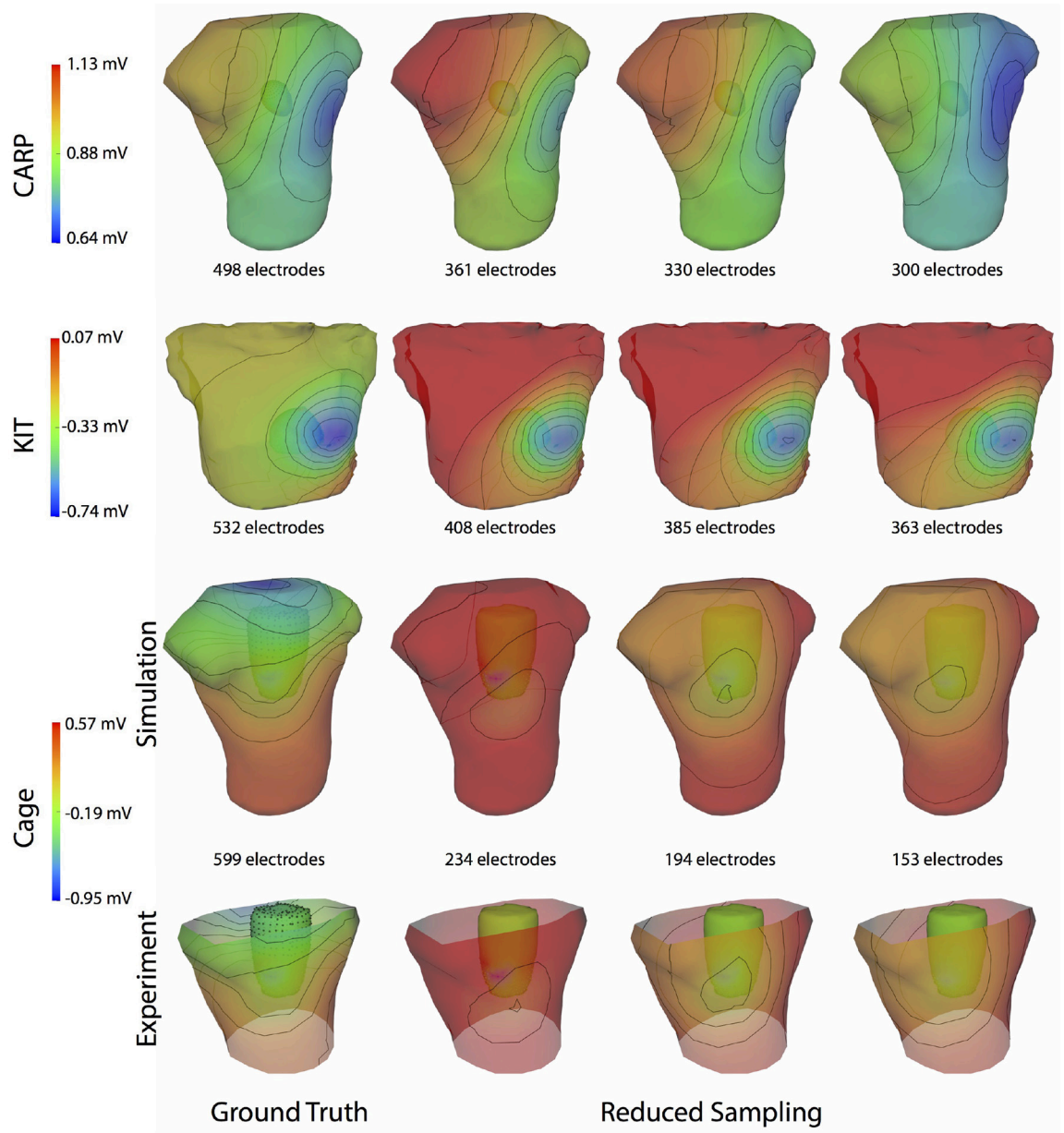

FIGURE 9 | Effect of removing ventricular source sampling on simulated BSPMs. Shown is the ground truth potential map and the forward simulation with progressively reduced sampling of the ventricles. The same representative beats and time samples are shown as in **Figure 4**.

(**Figure 10**). However, these profiles were similar, yet with a lower amplitude, to the corresponding profiles in **Figure 2** comparing the ventricle-only recordings to the ground truth data.

Figure 11 shows the potential maps generated with and without additional recorded electrograms from a plaque based over the roof of the atria. The difference between BSPMs was relatively minor overall, but the region of greatest difference was in the right anterior region. The right posterior region also showed observable differences.

4. DISCUSSION

The goal of this study was to evaluate the hypothesis that complete sampling of the cardiac surface is needed to accurately perform forward simulations of body surface potentials based on pericardial potentials, a hypothesis our results support. Moreover, our findings indicate that the accuracy of the forward simulation depends in subtle ways on the specific atrial sampling strategies. Surprisingly, some strategies are more effective than others even though they contain fewer points, indicating that sampling *location* is as important as sampling *number*. The

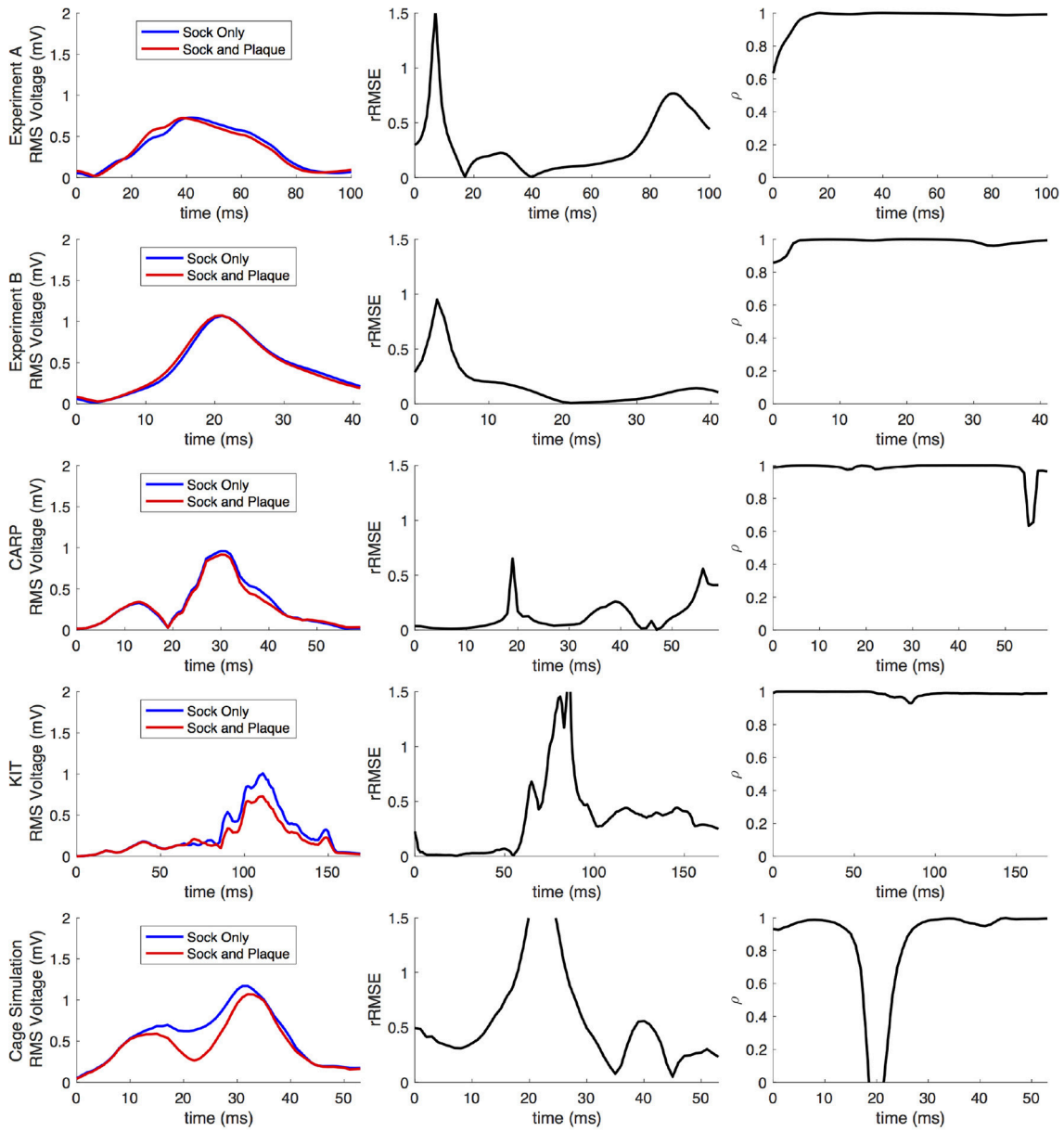

FIGURE 10 | Comparison of forward simulations with cardiac sock recordings to those with additional plaque electrode recordings over time on a representative beat. Metrics from the experimental simulations and a similar comparison with simulated datasets are shown. Each row presents the error for each dataset. Each column corresponds to a metric, RMS voltage, relative RMS error (*rRMSE*), and correlation (ρ).

results of this study could serve as guidance when carrying out simulations or animal and human experiments to validate electrocardiographic imaging approaches and may even impact the ECGI strategy for dealing with missing samples.

The motivation for the study came from reports and our own observations that forward simulations with ventricular pericardial sources often produced errors that exceed anticipated levels based on the relatively well-posed nature of the electrocardiographic forward problem (Ramsey et al., 1977; Bear et al., 2015). Previous, unreported results from our group based on studies with torso-tank phantoms (Shome and MacLeod, 2007) also produced a similar level of error.

The results of this study indicate that, in general, any source sampling added to the atrial region will reduce the error between the measured potentials and computed forward simulation. Even a relatively small number, *e.g.*, 11–40, of additional source samples produced a reduction in the overall error (**Figures 5**–**7**) across every dataset and with every sampling strategy. Similarly, simulations that included measurements from atrial plaque

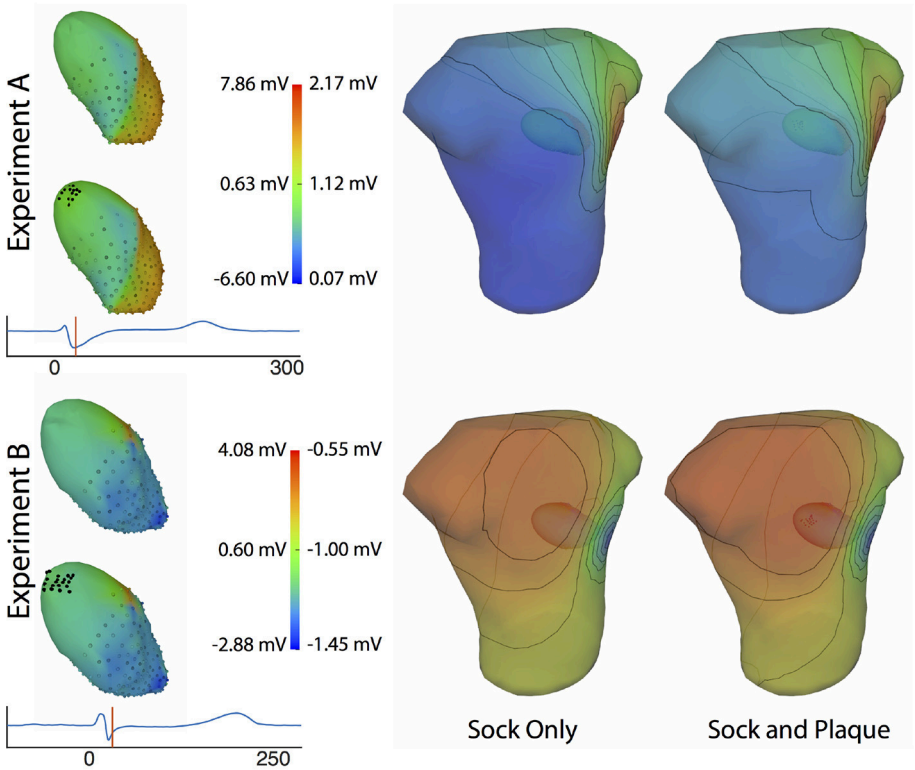

FIGURE 11 | Effect of additional atrial sampling from a plaque electrode array on the forward simulation. Time frame shown is from the same representative beats shown in **Figure 10** and is 30 ms into the QRS complex for Experiment A and 25 ms for the Experiment B.

electrodes also improved the agreement between ground truth torso potentials and simulations.

Although all strategies for additional atrial sampling improved the errors, we also sought specific strategies for picking the sample locations in future validation experiments. Analysis of the approaches we tested reveals that selecting evenly distributed points, such as the random and uniform strategies, are likely to produce greater accuracy with fewer added samples than other strategies (**Figure 5**). The combined strategy (i.e., basal plus atrial roof locations) also performed well, although not with the CARP dataset. The distributed nature of these strategies is likely a reason for their efficiency, because they reduce the need for interpolation over large distances that is an either explicit or implicit component of solving the forward problem.

Our analysis of the effect of various atrial plaque configurations on the simulated torso potentials revealed that the most valuable location may be at the roof of the atria, but placements even slightly away from the roof had lower accuracy. Therefore, it is difficult to identify and achieve the best location of additional measurement sites, typically in the form of a plaque electrode, in an experimental setting. Nevertheless, every plaque placement reduced the overall error of the simulated BSPMs, so it is likely that any plaque electrode placed on the atria will improve the overall accuracy of the forward simulation.

In comparing our results to similar studies, we found that eliminating the atrial sampling produced *rRMSE* and $\bar{E}$ values in the simulated torso potentials similar to those reported as early as the mid 1970s by Ramsey et al. (1977) and as recently as by Bear et al. (2015). We eliminated or dramatically reduced these errors by including sampling over the atria, which suggests that the absence of atrial sampling contributed to the errors in their studies. However, both these studies showed higher qualitative differences in simulated BSPMs, *e.g.*, differences in extrema location, than we could account for by removing atrial sampling locations, which suggests additional causes of error, possibly from registration, segmentation, or addition missing sampling.

One potentially significant additional source of error is in missing ventricular sampling locations. Such undersampling of the ventricle is possible even when using a ventricular sock because parts of the epicardium may not be sufficiently sampled, for example, because of poor electrode contact around the base of the heart or a lack of electrode density in regions of high spatial complexity of the potentials. Our results indicate that eliminating sampling locations from the ventricle can produce shifts in extrema locations, or remove them entirely, (**Figure 9**), and, in general, will decrease the overall accuracy of the forward simulations (**Figures 2**, **8**). Removing ventricular samples can increase the *rRMSE* even beyond that reported by Bear et al. (2015). All these results suggest that adequate sampling of both ventricles and atria is required to achieve the expected match between measured and predicted torso potentials.

The strategy of using more distributed sampling over the atria did not always produce the lowest error in the forward simulations (**Figures 6**, **7**). The spatial variability of cardiac potentials means that there are likely sampling configurations that could reduce error more efficiently for specific geometries and activation profiles, for example, those that combined AV plane and atrial roof strategy produced the lowest error for apical stimulation in the KIT dataset, but in no other example (**Figures 6**, **7**). Moreover, reducing error during different times of the cardiac cycle could also motivate different sampling strategies. There can be dramatic changes in the error and correlation through the cardiac cycle, as seen in the late stages of the CARP dataset sinus beat and cage datasets following left ventricular stimulation (**Figures 2**, **3**). In a similar vein, the dramatic shift in error and correlation when the atria and basal region of the ventricles were undersampled could be attributed to incorrectly interpolating late activity near the AV plane over the atrial surface. The reduction in sampling either removes local potential extrema in this region, or could possibly remove transition regions to cause the extrema to become larger with the interpolation. In both these examples, we found that adding samples near the AV plane of the atria reduced error more than adding samples to the atrial roof (**Figures 6**, **7**), which indicates that strategies that sample the AV plane would be important for late sinus activation or left ventricular activation. Therefore, with some *a priori* knowledge about activation profile and the regions of interest within the cardiac cycle, researchers could design specific strategies to correctly record them.

Implementing many of the strategies we tested in an experimental setting has many practical and logistical obstacles. For example, placing uniformly distributed recording electrodes on the epicardial surfaces of the atria is virtually impossible, due to limited access to the active myocardium. A combined approach including sampling near the atrial roof and near the AV plane would be feasible using multiple plaque electrodes and/or and a ventricle sock that extended over the base to the atrial surface. Such sampling would likely be feasible in an *in situ* animal preparations, although placement of the plaque would remain a challenge due to the many vessels attached to the atria. The isolated, perfused heart suspended in a torso-shaped tank phantom (MacLeod et al., 1995; Shome and MacLeod, 2007; Milanic et al., 2014), similar to the one used to acquire the cage dataset, could provide the best option for recording full coverage cardiac source potentials because the vessels supplying the heart are gathered and fed through a small opening, and the rest of the surrounding surface can be instrumented with electrodes. A limitation of this approach is that the atria are not filled with blood and so collapse to lie on the base of the ventricles and lack both realistic shape and a stable surface for attaching electrodes.

Limitations to the study generally involved compromises in capturing cardiac sources and the associated torso potentials. By using fully simulated potentials, we could achieve levels of coverage and resolution not possible with experiments but with the caveat that these are simulations and reflect certain assumptions and conditions. For example, we ignored any electrical activation of the atria, assumed that the conductivity of the atria was the same as for the torso, and greatly simplified the atrial epicardial surface by replacing it with a parameterized and smooth epicardial cap. Additionally, we did not account for possible scar or fibrosis formation which would occur in many disease states, possibly affecting any attempt to use these strategies in patients. Another source of validation data was a set of potentials from an isolated, perfused heart, captured with an instrumented rigid cage surrounding the heart. This arrangement provides full coverage of the heart and thus a complete source model, but the distance between heart and cage electrodes causes the signals to be smoother than on the epicardium and does not reflect perfectly the ECGI application. Finally, we assumed in this study that the only error would be due to insufficient source sampling of the atrial region, and thus we ignored other possible causes of error in source sampling, such as sampling density, uncertainty in individual electrode locations, or any other possible errors in capturing and representing the geometric model. These additional sources of error may compound those due to incomplete sampling over the atria.

This study focused specifically on the sampling of the atrial region and how it generally affected the forward simulation, but there are several additional, related questions that could be addressed in future studies. For example, of great interest would be a more direct spatial sensitivity analysis of the relationship between the potentials on the cardiac surface and the torso, or from the endocardial surface to the atria. Such results could suggest sampling strategies that would be specialized for specific regions of tissue, or types of activation. Other questions that could be similarly explored relate to the shape, location, and orientation of the heart, and how they might influence the forward simulation. Inclusion of torso heterogeneity due to other organs would affect the flow of current through the torso and may therefore affect the sampling strategies needed to more accurately predict BSPM. These questions and others could be the focus of future studies to help fully understand the effect of discretizing the cardiac electrical source with potential recordings.

This study illustrates the need to acquire adequate cardiac source sampling in ECG forward simulations, as well as the challenges in doing so. These findings also have implications for solving and validating the inverse solutions required for ECGI. Most mathematical formulations of ECGI solve for a subset of the cardiac sources without any cost to accuracy, but they are based on the assumption of a robust forward solution, i.e., that the relationship between the cardiac sources and the torso potentials is represented accurately (Barr et al., 1977; Plonsey and Barr, 1987; Plonsey and van Oosterom, 1991; Gulrajani, 1998). Our results suggest that coverage of the atrial surface with at least a schematic multielectrode cap could improve the resulting ECGI solutions. Additionally, our results have implications for how researchers validate ECGI methods using forward simulated BSPM data (Erem et al., 2011; Wang et al., 2011). Our findings suggest that the computed BSPMs used as inputs in these ECGI pipelines may contain errors due to inadequate cardiac sampling. Using BSPMs with such errors may bias the tuning of the constraints in the ECGI inverse problem and even alter the levels of accuracy achieved.

We conclude that complete sampling of the cardiac surface potentials is required to create realistic source descriptions for

validation experiments and simulations of ECGI. Ignoring or crudely interpolating over sources on the atrial surfaces or even parts of the ventricular surface will also reduce the accuracy of simulations. Researchers can mitigate these effects by ensuring that both the full ventricular epicardium and at least some locations on the atria are sampled. Even modest coverage of the atria can increase the accuracy of the resulting simulations dramatically. Distributed sampling over the atrial will likely produce the lowest error, yet may be a challenge to implement experimentally. These efforts to improve source sampling will also improve the accuracy of the ECG forward simulations, which will further clarify the aspects of ECGI that need more research and development.

AUTHOR CONTRIBUTIONS

JT and RM originated the study idea and developed the hypothesis. JT, KG, BB, WG, BZ, JC-F, DB, and RM contributed to the study design. JT, KG, BB, WG, and BZ contributed to data collection, organization, and processing. JT, KG, and JC-F contributed to developing the simulation pipelines used in the study. JT wrote the first draft of the manuscript. JT, KG, BB, WG, BZ, JC-F, DB, and RM contributed to manuscript revision and approved the submission of the manuscript.

ACKNOWLEDGMENTS

The research presented in this paper was made possible with help from the Cardiovascular Research and Training Institute (CVRTI) and the Nora Eccles Treadwell Foundation. This project was also supported by the National Institute of General Medical Sciences of the National Institutes of Health under grant number P41 GM103545-18. Some data used in this study was made available by a joint research project between the First Department of Medicine (Cardiology), University Medical Centre Mannheim, and the Karlsruhe Institute of Technology (KIT).

REFERENCES

Aras, K. (2015). *Bioelectric Source Characterization of Acute Myocardial Ischemia*. Ph.D. thesis, University of Utah.

Aras, K., Burton, B., Swenson, D., and MacLeod, R. (2016). Spatial organization of acute myocardial ischemia. *J. Electrocardiol.* 49, 689–692. doi: 10.1016/j.jelectrocard.2016.02.014

Aras, K., Good, W., Tate, J., Burton, B., Brooks, D., Coll-Font, J., et al. (2015). Experimental data and geometric analysis repository: EDGAR. *J. Electrocardiol.* 48, 975–981. doi: 10.1016/j.jelectrocard.2015.08.008

Barr, R., Ramsey, M., and Spach, M. (1977). Relating epicardial to body surface potential distributions by means of transfer coefficients based on geometry measurements. *IEEE Trans. Biomed. Eng.* 24, 1–11. doi: 10.1109/TBME.1977.326201

Bear, L. R., Cheng, L. K., LeGrice, I. J., Sands, G. B., Lever, N. A., Paterson, D. J., et al. (2015). The forward problem of electrocardiography: is it solved? *Circ. Arrhythm. Electrophysiol.* 8, 677–684. doi: 10.1161/CIRCEP.114.001573

Besl, P., and McKay, N. (1992). A method for registration of 3-D shapes. *IEEE Trans. Pat. Anal. Mach. Intell.* 14, 239–256. doi: 10.1109/34.121791

Bishop, M. J., and Plank, G. (2011). Representing cardiac bidomain bath-loading effects by an augmented monodomain approach: application to complex ventricular models. *IEEE Trans. Biomed. Eng.* 58, 1066–1075. doi: 10.1109/TBME.2010.2096425

Burton, B., Tate, J., Erem, B., Swenson, D., Wang, D., Brooks, D., et al. (2011). "A toolkit for forward/inverse problems in electrocardiography within the scirun problem solving environment," in *Proceedings of the IEEE Engineering in Medicine and Biology Society 33rd Annual International Conference* . Boston, MA: IEEE, 1–4.

Deo, M., Boyle, P., Plank, G., and Vigmond, E. (2009). Arrhythmogenic mechanisms of the purkinje system during electric shocks: a modeling study. *Heart Rhythm. J.* 6, 1782–1789. doi: 10.1016/j.hrthm.2009.08.023

Erem, B., Ghodrati, A., Tadmor, G., MacLeod, R., and Brooks, D. (2011). Combining initialization and solution inverse methods for inverse electrocardiography. *J. Electrocardiol.* 44:e21. doi: 10.1016/j.jelectrocard.2010.12.059

Fischler, M. A. and Bolles, R. C. (1981). Random sample consensus: a paradigm for model fitting with applications to image analysis and automated cartography. *Commun. ACM* 24, 381–395. doi: 10.1145/358669.358692

Gulrajani, R. (1998). The forward and inverse problems of electrocardiography. *EMBS Mag.* 17, 84–101. doi: 10.1109/51.715491

Johnson, C. (1997). Computational and numerical methods for bioelectric field problems. *Crit. Rev. Biomed. Eng.* 25, 1–81. doi: 10.1615/CritRevBiomedEng.v25.i1.10

Johnson, C. (2015). *Chapter 43: Computational Methods and Software for Bioelectric Field Problems, Vol. 1, 4th Edn*. Boca Raton, FL: CRC Press, 1–28.

Johnson, C., MacLeod, R., and Matheson, M. (1993). Computational medicine: Bioelectric field problems. *IEEE Comput.* 26, 59–67. doi: 10.1109/2.237454

Loewe, A., Schulze, W. H. W., Jiang, Y., Wilhelms, M., Luik, A., Dössel, O., et al. (2015). ECG-based detection of early myocardial ischemia in a computational model: impact of additional electrodes, optimal placement, and a new feature for ST deviation. *BioMed Res. Int.* 2015:530352. doi: 10.1155/2015/530352

MacLeod, R., and Buist, M. (2010). "The forward problem of electrocardiography," in *Comprehensive Electrocardiology*, eds P. Macfarlane, A. van Oosterom, O. Pahlm, P. Kligfield, M. Janse, and J. Camm (London, UK: Springer Verlag), 247–298.

MacLeod, R., Taccardi, B., and Lux, R. (1995). "Electrocardiographic mapping in a realistic torso tank preparation," in *Proceedings of the IEEE Engineering in Medicine and Biology Society 17th Annual International Conference* (Montreal, QC: IEEE Press), 245–246.

MacLeod, R., Weinstein, D., de St. Germain, J. D., Brooks, D., Johnson, C., and Parker, S. (2004). "SCIRun/BioPSE: integrated problem solving environment for bioelectric field problems and visualization," in *IEEE International Symposium on Biomedical Imaging (ISBI)*, Arlington, VA: IEEE Press, 1–3.

Messinger-Rapport, B., and Rudy, Y. (1986). The inverse problem in electrocardiography: a model study of the effects of geometry and conductivity parameters on the reconstruction of epicardial potentials. *IEEE Trans. Biomed. Eng.* 33, 667–676. doi: 10.1109/TBME.1986.325756

Milanic, M., Jazbinsek, V., Macleod, R., Brooks, D., and Hren, R. (2014). Assessment of regularization techniques for electrocardiographic imaging. *J. Electrocardiol.* 47, 20–28. doi: 10.1016/j.jelectrocard.2013.10.004

Oostendorp, T., van Oosterom, A., and Huiskamp, G. (1989). Interpolation on a triangulated 3D surface. *J. Comp. Phys.* 80, 331–343. doi: 10.1016/0021-9991(89)90103-4

Parker, S., Weinstein, D., and Johnson, C. (1997). "The SCIRun computational steering software system," in *Modern Software Tools in Scientific Computing*, eds E. Arge, A. Bruaset, and H. Langtangen, Boston, MA : Birkhauser Press, 1–40.

Plonsey, R., and Barr, R. (1987). Mathematical modeling of electrical activity of the heart. *J. Electrocardiol.* 20, 219–226. doi: 10.1016/S0022-0736(87)80019-5

Plonsey, R., and van Oosterom, A. (1991). Implications of macroscopic source strength on cardiac cellular activation models. *J. Electrocardiol.* 24, 99–112. doi: 10.1016/0022-0736(91)90001-3

Pullan, A., Cheng, L. K., Nash, M., Brooks, D., Ghodrati, A., and MacLeod, R. (2010). "The inverse problem of electrocardiography," in *Comprehensive*

Electrocardiology, eds P. Macfarlane, A. van Oosterom, O. Pahlm, P. Kligfield, M. Janse, and J. Camm (London, UK: Springer Verlag), 299–344.

Ramsey, M., Barr, R. C., and Spach, M. S. (1977). Comparison of measured torso potentials with those simulated from epicardial potentials for ventricular depolarization and repolarization in the intact dog. *Circulation* 41, 660–672. doi: 10.1161/01.RES.41.5.660

Rodenhauser, A., Good, W., Zenger, B., Tate, J., Aras, K., Burton, B., et al. (2018). Pfeifer: Preprocessing framework for electrograms intermittently fiducialized from experimental recordings. *J. Open Source Softw.* 3, 472. doi: 10.21105/joss.00472

Rudy, Y., and Lindsay, B. (2015). Electrocardiographic imaging of heart rhythm disorders: from bench to bedside. *Card Electrophysiol. Clin.* 7, 17–35. doi: 10.1016/j.ccep.2014.11.013

Schulze, W. H. W., Potyagaylo, D., Schimpf, R., Papavassiliu, T., Tülümen, E., Rudic, B., et al. (2015). "A simulation dataset for ECG imaging of paced beats with models for transmural, endo-and epicardial and pericardial source imaging," in *First Meeting of the Consortium for EGI Imaging* (Bad Herrenalp), 1.

Shome, S., and MacLeod, R. (2007). "Simultaneous high-resolution electrical imaging of endocardial, epicardial and torso-tank surfaces under varying cardiac metabolic load and coronary flow," in *Functional Imaging and Modeling of the Heart*, Lecture Notes in Computer Science 4466 (Berlin: Springer-Verlag), 320–329.

Stanley, P., Pilkington, T., and Morrow, M. (1986). The effects of thoracic inhomogeneities on the relationship between epicardial and torso potentials. *IEEE Trans. Biomed. Eng.* 33, 273–284. doi: 10.1109/TBME.1986.325711

ten Tusscher, K. H. W. J., and Panfilov, A. V. (2006). Alternans and spiral breakup in a human ventricular tissue model. *Am. J. Physiol. Heart Circ. Physiol.* 291, H1088–H100. doi: 10.1152/ajpheart.00109.2006

Vigmond, E., Hughes, M., Plank, G., and Leon, L. (2003). Computational tools for modeling electrical activity in cardiac tissue. *J. Electrocardiol.* 36(Suppl.), 69–74. doi: 10.1016/j.jelectrocard.2003.09.017

Vigmond, E. J., Weber dos Santos, R., Prassl, A. J., Deo, M., and Plank, G. (2008). Solvers for the cardiac bidomain equations. *Prog. Biophys. Mol. Biol.* 96, 3–18. doi: 10.1016/j.pbiomolbio.2007.07.012

Wang, D., Kirby, R., and Johnson, C. (2011). Finite-element-based discretization and regularization strategies for 3-D inverse electrocardiography. *IEEE Trans. Biomed. Eng.* 58, 1827–1838. doi: 10.1109/TBME.2011.2122305

Conflict of Interest Statement: The authors declare that the research was conducted in the absence of any commercial or financial relationships that could be construed as a potential conflict of interest.

frontiers in Physiology

ORIGINAL RESEARCH
published: 29 November 2018
doi: 10.3389/fphys.2018.01708

Evaluation of Fifteen Algorithms for the Resolution of the Electrocardiography Imaging Inverse Problem Using *ex-vivo* and *in-silico* Data

Amel Karoui[1,2,3]*, *Laura Bear*[3], *Pauline Migerditichan*[2,3] *and Nejib Zemzemi*[1,2,3]*

[1] Institute of Mathematics, University of Bordeaux, Bordeaux, France, [2] INRIA Bordeaux Sud-Ouest, Bordeaux, France, [3] IHU Lyric, Bordeaux, France

The electrocardiographic imaging inverse problem is ill-posed. Regularization has to be applied to stabilize the problem and solve for a realistic solution. Here, we assess different regularization methods for solving the inverse problem. In this study, we assess (i) zero order Tikhonov regularization (ZOT) in conjunction with the Method of Fundamental Solutions (MFS), (ii) ZOT regularization using the Finite Element Method (FEM), and (iii) the L1-Norm regularization of the current density on the heart surface combined with FEM. Moreover, we apply different approaches for computing the optimal regularization parameter, all based on the Generalized Singular Value Decomposition (GSVD). These methods include Generalized Cross Validation (GCV), Robust Generalized Cross Validation (RGCV), ADPC, U-Curve and Composite REsidual and Smoothing Operator (CRESO) methods. Both simulated and experimental data are used for this evaluation. Results show that the RGCV approach provides the best results to determine the optimal regularization parameter using both the FEM-ZOT and the FEM-L1-Norm. However for the MFS-ZOT, the GCV outperformed all the other regularization parameter choice methods in terms of relative error and correlation coefficient. Regarding the epicardial potential reconstruction, FEM-L1-Norm clearly outperforms the other methods using the simulated data but, using the experimental data, FEM based methods perform as well as MFS. Finally, the use of FEM-L1-Norm combined with RGCV provides robust results in the pacing site localization.

Keywords: inverse problem, Tikhonov regularization, L1-norm regularization, regularization parameter, method of fundamental solutions, finite element method, generalized singular value decomposition, pacing site localization

OPEN ACCESS

Edited by:
Carlos Figuera, Universidad Rey Juan Carlos, Spain

Reviewed by:
Andreu Climent, Fundación Hospital Gregorio Marañon, Spain
Olaf Doessel, Karlsruher Institut für Technologie (KIT), Germany

***Correspondence:**
Amel Karoui
amel.karoui@inria.fr
Nejib Zemzemi
nejib.zemzemi@inria.fr

Specialty section:
This article was submitted to Cardiac Electrophysiology, a section of the journal Frontiers in Physiology

Received: *21 May 2018*
Accepted: *13 November 2018*
Published: *29 November 2018*

Citation:
Karoui A, Bear L, Migerditichan P and Zemzemi N (2018) Evaluation of Fifteen Algorithms for the Resolution of the Electrocardiography Imaging Inverse Problem Using ex-vivo and in-silico Data. Front. Physiol. 9:1708. doi: 10.3389/fphys.2018.01708

1. INTRODUCTION

The non-invasive electrocardiographic imaging (ECGI) is an imaging technique that allows one to non-invasively reconstruct the electrical activity of the heart using electrocardiograms and a patient specific heart-torso geometry. This clinical tool is used by electrophysiologists to understand the mechanisms underlying arrhythmias and to localize targets for ablation therapy, such as for atrial fibrillation (Haissaguerre et al., 2013; Rudy, 2013). This technology is based on a mathematical relationship defining the propagation of the electrical activity between the heart and the torso

surface Γ_{ext}. Given the extracellular electrical potential u_{H} on the epicardial heart boundary Γ_H, the distribution of the electrical potential u_{T} in the torso domain Ω_T and specifically at electrodes distributed on the body surface Γ_{ext}, could be obtained by solving the following Laplace equation:

$$\begin{cases} \nabla \cdot (\sigma_T \nabla u_{\mathrm{T}}) = 0, & \text{in} \quad \Omega_T, \\ \sigma_T \nabla u_{\mathrm{T}} \cdot n_{\mathrm{T}} = 0, & \text{on} \quad \Gamma_{ext}, \\ u_{\mathrm{T}} = u_{\mathrm{H}}, & \text{on} \quad \Gamma_H. \end{cases} \tag{1}$$

where σ_T stands for the torso conductivity tensor and n_{T} is the outward unit normal to the torso external boundary Γ_{ext}. This is what we call a forward problem. Now, given a body surface potential distribution and knowing that the flux of potential over the body surface is zero, could we obtain the right distribution of the electrical potential on the heart surface? This is what we call an inverse problem in electrocardiography. In almost all of the works reported in the literature, the mathematical approach used for solving the inverse problem is based on a transfer matrix which has been first formulated by Barr et al. (1977). The transfer matrix can be computed using different approaches such as the finite element method (FEM) (Wang et al., 2010; Zemzemi et al., 2015) or the boundary elements method like in Stenroos and Haueisen (2008); Stenroos (2009); Schuler et al. (2017); Ghosh and Rudy (2009); Chamorro-Servent et al. (2017); Barr et al. (1977), the method of fundamental solutions (MFS) (Wang and Rudy, 2006) or mixed methods like the factorization of boundary value method (Bouyssier et al., 2015) or finite element with mixed element types (Wang et al., 2010). In this study, we are only interested in FEM and MFS. Using any of these numerical approaches, the governing Equation (1) can be reduced to a matrix-vector system:

$$Ax = b, \tag{2}$$

where **A** is the transfer matrix, its form depends on the numerical method used. The vector **x** is either the unknown epicardial potentials on the surface of the heart in the case of the FEM or a vector of weighting coefficients from which it's possible to reconstruct the epicardial potential in the case of MFS. Finally, **b** represents either the body surface potentials (BSPs) for the first case or a concatenation of the BSPs and a null vector representing the non flux boundary condition for the second case.

Generally, the inverse problem of electrocardiography is known to be ill-posed in the sense of Hadamard Hadamard (1923) which means that a small perturbation of the Cauchy data may lead to a high variation in the inverse solution. This could be explained at the discrete level by the ill-conditioning of the transfer matrix **A** and the measurement noise that we have in the vector **b**. To overcome this, a regularization approach is often used to solve Equation (2). However, this has led to a large variety of different inverse algorithms being developed. To date, few studies have attempted to compare the different methods available. Cheng et al. (2003) looked at different regularization methods and methods to compute the regularization parameter. Since this work, many new methods have been developed.

A recent work by Barnes and Johnston (2016) compares several regularization techniques but without changing either the regularization operator or the numerical method defining the transfer matrix. Finally, both of these studies were based purely on simulated data, and their applicability to experimental or clinical work is unknown.

In this work we compare not only different methods for computing the transfer matrix, but also different regularization operators and different methods for optimizing the regularization parameter to assess how they perform on two sets of data: simulated and experimental.

2. METHODS

To date, the regularization approach most commonly used to solve the electrocardiographic imaging inverse problem is the Tikhonov regularization defined by the following objective function:

$$\min_x \left\{ \|Ax - b\|^2 + \lambda^2 \|Lx\|^2 \right\}, \tag{3}$$

where **L** is the regularization operator, λ is the regularization parameter and $\|.\|$ is the L2-norm. Here, **L** can be the identity matrix (zero-order) or an approximation operator of a potential's derivative form (first or second order). Independent of the numerical method used to compute the transfer matrix, the best way to analyze the different methods to computing the optimal regularization parameter is to use the GSVD of the couple $\{\mathbf{A}, L\}$ for first or second order Tikhonov regularization and the singular value decomposition of **A** for zero-order.

2.1. Generalized Singular Value Decomposition

In the case where $\boldsymbol{L} = \boldsymbol{I}$, we use the Singular Value Decomposition of the $\boldsymbol{m} \times \boldsymbol{n}$ transfer matrix **A**, where $\boldsymbol{m} \geq \boldsymbol{n}$, $\boldsymbol{m}$ is the number of torso nodes and $\boldsymbol{n}$ is the number of heart nodes. Following Hansen (1998), we decompose $\boldsymbol{A}$ as follows

$$\boldsymbol{A = U \Sigma V^T = \sum_{i=1}^{n} u_i \sigma_i v_i^T}, \tag{4}$$

where **U** is a $\boldsymbol{m} \times \boldsymbol{n}$ orthonormal matrix containing the left singular vectors of **A**,**V** is a $\boldsymbol{n} \times \boldsymbol{n}$ orthonormal matrix containing the right singular vectors of **A** and $\boldsymbol{\Sigma}$ is a $\boldsymbol{n} \times \boldsymbol{n}$ diagonal matrix with the singular values of **A** on its diagonal. Note that $\boldsymbol{u_i}$, $\boldsymbol{v_i}$ and $\boldsymbol{\sigma_i}$ are, respectively, the columns of **U**, **V** and the singular values of **A** arranged in a decreasing order. In terms of the singular value decomposition, the solution of the regularized problem expressed by:

$$\boldsymbol{\min_x \left\{ \|Ax - b\|^2 + \lambda^2 \|x\|^2 \right\}}, \tag{5}$$

can be written as (Hansen, 1998):

$$\boldsymbol{x = A^{\dagger} b = (A^T A + \lambda^2 I)^{-1} A^T b = \sum_{i=1}^{n} \frac{\sigma_i^2}{\sigma_i^2 + \lambda^2} \frac{u_i^T b}{\sigma_i} v_i}. \tag{6}$$

It can be shown that the two terms of (5) can be written as (Johnston and Gulrajani, 1997):

$$\rho_1(\lambda) = \|Ax - b\|^2 = \sum_{i=1}^{n} \frac{\lambda^4 \mu_i^2}{(\lambda^2 + \sigma_i^2)^2} + \|r_\perp\|^2 \qquad (7)$$

and

$$\eta_1(\lambda) = \|x\|^2 = \sum_{i=1}^{n} \frac{\sigma_i^2 \mu_i^2}{(\lambda^2 + \sigma_i^2)^2}, \qquad (8)$$

where $\|r_\perp\|^2 = \|Ax_{LSS} - b\|^2$ is the residual of the least squares solution x_{LSS} and $\mu_i = u_i^T b$.

In the case where $L \neq I$, the Generalized Singular Value Decomposition of the pair $\{A, L\}$ is defined by (Hansen, 2010):

$$A = PCZ^{-1}, \qquad L = QSZ^{-1}, \qquad (9)$$

where **P** and **Q** are, respectively, $m \times n$ and $n \times n$ orthogonal matrices. **C** and **S** are $m \times n$ and $n \times n$ diagonal matrices satisfying $C^T C + S^T S = I$ where $diag(C) = \{\sigma_1 ... \sigma_n\}$ and $diag(S) = \{v_1 ... v_n\}$. Diagonal elements of **C** and **S** satisfy $0 \leq \sigma_1 \leq ... \leq \sigma_n \leq 1$ and $1 \geq v_1 \geq ... \geq v_n \geq 0$. The matrix **Z** is non singular. We define $\bar{\lambda}_i = \frac{\sigma_i}{v_i}$ as the generalized singular values of the pair $\{A, L\}$.

Using the generalized singular value decomposition, the solution of the problem expressed by Equation (3) can be written as (Chung et al., 2014):

$$x^* = A^{\#} b = (A^T A + \lambda^2 L^T L)^{-1} A^T b = \sum_{i=1}^{n} \phi_i \frac{p_i^T b}{\sigma_i} z_i, \qquad (10)$$

where Φ is a $n \times n$ diagonal matrix containing the **filter factors** defined by:

$$\phi_i = \frac{\bar{\lambda}_i^2}{\bar{\lambda}_i^2 + \lambda^2}, \qquad \text{for } i = 1...n. \qquad (11)$$

It can be shown that the two terms of (3) can be written in terms of generalized singular values as (Chung et al., 2014):

$$\rho_2(\lambda) = \|Ax^* - b\|^2 = \sum_{i=1}^{n} \left(\frac{\lambda^2}{\bar{\lambda}_i^2 + \lambda^2} \right)^2 \left(p_i^T b \right)^2 + \sum_{i=n+1}^{m} \left(p_i^T b \right)^2, \qquad (12)$$

and (Ghista, 2012)

$$\eta_2(\lambda) = \|Lx^*\|^2 = \sum_{i=1}^{n} \left(\frac{\bar{\lambda}_i}{\bar{\lambda}_i^2 + \lambda^2} \right)^2 \left(p_i^T b \right)^2. \qquad (13)$$

2.2. Regularization Techniques

Several regularization techniques can be applied to the ill-posed inverse problem of electrocardiography. In this study, we focus on two methods.

2.2.1. Zero Order Tikhonov Regularization

Using the zero order Tikhonov regularization, the objective function can be expressed by (5). This type of regularization places a constraint on the magnitude of the reconstructed epicardial potentials which is known to provide a smooth solution but may lead to the loss of meaningful information.

2.2.2. L1-Norm Regularization of the Current Density Over the Heart Surface

Previous studies have shown that using the L1-Norm can provide a better reconstruction when applied in different fields (Wolters et al., 2004; Bai et al., 2007; Ding and Hei, 2008). In this paper, we choose to apply the regularization scheme used in Ghosh and Rudy (2009). Here, we penalized the L1-Norm of the normal derivative of the solution. The potential normal derivative represents the distribution of electrical flux over the epicardial surface.

This will yield less smoothed potentials than zero-order Tikhonov. The use of current density in the regularization of the inverse problem in electrocardiography was first introduced by Khoury (1994) and proved to provide significant improvement in the inverse problem.

The objective function using L1-Norm based regularization is given by:

$$\min_x \|Ax - b\| + \lambda^2 \|\nabla x . \mathbf{n}_H\|_1, \qquad (14)$$

where $\mathbf{n}_H$ is the outward unit normal to the epicardium surface.

Using the Finite Element Method, and thanks to the linearity of the solution of problem (1) to its boundary conditions, we can define the Dirichlet-To-Neumann operator D satisfying:

$$\begin{pmatrix} \frac{\partial u_T}{\partial n}(p_1) \\ \vdots \\ \frac{\partial u_T}{\partial n}(p_n) \end{pmatrix} = D \begin{pmatrix} x_1 \\ \vdots \\ x_n \end{pmatrix}, \qquad (15)$$

where D is an n-by-n matrix and the points $(p_1, p_2, ..., p_n)$ are the coordinate tuples of the heart mesh vertices. Note that the operator D is different from the gradient over the surface used for the total variation regularization. In fact the gradient of x over the heart surface ($\nabla_{\Gamma_H} x$) is the tangential component of electrical potential gradient (∇u_T), whereas Dx is its normal component. Thus one could write the 3D gradient of the potential on the epicardial boundary as the sum of both components ($\nabla u_T = (\nabla_{\Gamma_H} x + Dx)$. The operator ∇_{Γ_H} depends only on the epicardial surface Γ_H, whereas, D depends on the whole torso domain Ω. The objective function (14) can be expressed as follows:

$$\min_x \|Ax - b\| + \lambda^2 \|Dx\|_1. \qquad (16)$$

The L1-Norm regularization of the current density leads to a non-linear problem. Following Karl (2005), we can smoothly approximate the L1-Norm of the derivative by:

$$\|Dx\|_1 = \sum_{i=1}^{n} |\lfloor Dx \rfloor_i| \approx \sum_{i=1}^{n} \sqrt{|\lfloor Dx \rfloor_i|^2 + \beta}, \qquad (17)$$

with β a small constant satisfying $\beta > 0$ and $\lfloor Dx \rfloor_i$ the i^{th} component of the vector Dx.
This approximation leads to an interesting formulation of the L1-Norm regularization problem in the form of a set of equations whose resolution as $\beta \longrightarrow 0$ gives an estimate of the solution of (16). The linear problem to be solved is then:

$$\left[A^T A + \lambda^2 D^T W_\beta(x) D\right] x = A^T b, \tag{18}$$

where $W_\beta(x)$ is a diagonal matrix called **weight matrix**, expressed by:

$$W_\beta(x) = \frac{1}{2}\, diag\left[\frac{1}{\sqrt{|\lfloor Dx \rfloor_i|^2 + \beta}}\right]. \tag{19}$$

We notice that (19) has an effect on the variation of the normal derivative penalty. In fact, when the local normal derivative is too small, the weight goes to larger values imposing greater smoothness on the solution. When the local normal derivative is large, the weight goes to small values allowing larger gradients in the solution in these regions.
The above formulation can be further simplified in a way that it can be seen as a first-order Tikhonov regularization. In fact, thanks to the diagonality of $W_\beta(x)$, (18) can be written such that:

$$\left[A^T A + \lambda^2 D^T \left(\sqrt{W_\beta(x)}\right)^T \left(\sqrt{W_\beta(x)}\right) D\right] x = A^T b, \tag{20}$$

which leads to:

$$\left[A^T A + \lambda^2 \tilde{D}^T(x)\tilde{D}(x)\right] x = A^T b, \tag{21}$$

where $\tilde{D}(x) = \sqrt{W_\beta(x)} D$.
Computationally, the Equation (21) is still non-linear since the weighting matrix $W_\beta(x)$ depends on the solution x. To overcome this constraint, we suggest to use the zero-order Tikhonov solution instead of the solution itself. Thus, the problem that we solve is

$$\left[A^T A + \lambda^2 \tilde{D}^T(x_0)\tilde{D}(x_0)\right] x = A^T b, \tag{22}$$

where x_0 is the zero-order Tikhonov solution determined by the Finite Element Method.

2.3. Methods for Choosing Regularization Parameter

In this section, we detail the formulation of several methods used for choosing the optimal regularization parameter in terms of, both, the singular value decomposition in the case of the zero-order Tikhonov regularization and the generalized singular value decomposition in the case of L1-Norm regularization of the current density treated as a first-order Tikhonov regularization. It's fundamental for a good regularization parameter λ to satisfy the **Discrete Picard Condition** (DPC) (Hansen, 1990). In other words, this means that the singular values σ_i and the generalized singular values $\bar{\lambda}$ that are greater than λ must decay to zero slower than the corresponding $|u_i^T b|$ and $|p_i^T b|$, respectively.

2.3.1. U-Curve

The U-Curve is a plot of the sum of the inverse of $\eta_1(\lambda)$ (respectively, $\eta_2(\lambda)$) and the inverse of the corresponding residual $\rho_1(\lambda)$ (respectively, $\rho_2(\lambda)$) in the case where $L = I$ (respectively, $L \neq I$), in terms of λ on a log-log scale:

$$\begin{cases} Ucurve(\lambda) = \dfrac{1}{\rho_1(\lambda)} + \dfrac{1}{\eta_1(\lambda)}, & \text{if } L = I, \\ Ucurve(\lambda) = \dfrac{1}{\rho_2(\lambda)} + \dfrac{1}{\eta_2(\lambda)}, & \text{if } L \neq I. \end{cases} \tag{23}$$

The U-Curve method was proposed by Krawczyk-Stańdo and Rudnicki (2007) and Krawczyk-Stańdo and Rudnicki (2008) and tested by Krawczyk-Stańdo and Rudnicki (2007), Krawczyk-Stańdo and Rudnicki (2008), and Yuan et al. (2010) for the selection of the regularization parameter in the inverse problem. These works presented the method as a tool to determine the interval to which the regularization parameter belongs, providing a better computing efficiency.
According to Krawczyk-Stańdo and Rudnicki (2007) results, $Ucurve(\lambda)$ is strictly decreasing on the interval $\left[0, {\delta_n}^{2/3}\right]$ and strictly increasing on the interval $\left[\delta_1^{2/3}, \infty\right]$ where δ_1 and δ_n are, respectively, the biggest and the smallest singular values (generalized singular value in the case where $L \neq I$). Thus, $Ucurve(\lambda)$ reaches a local minimum in the interval $\left[\delta_n^{2/3}, \delta_1^{2/3}\right]$. If we have at least one non-zero singular value, we can ensure the uniqueness of the $Ucurve(\lambda)$ minimizer, λ_u, the optimum value of λ.

2.3.2. ADPC

As mentioned above, the optimal regularization parameter should satisfy the DPC. Therefore, ADPC is a regularization parameter choice method based on this condition. The idea is to look for the last index i before the DPC is no longer satisfied (Chamorro-Servent et al., 2017). This means before σ_i becomes smaller than $|u_i^T b_t|$ in a **log-log** scale where t is time. For the sake of simplification, $\log(|u_i^T b_t|)$ is fitted by a polynomial $p_t(i, \log(|u_i^T b_t|))$ of degree 5 to 7. Then, for each p_t, we seek for $\alpha_t = \sigma_{maxi}$ such that $\log(\sigma_i) \geq p_t$. The ADPC regularization parameter is then $\lambda = median(\alpha_t)$.

2.3.3. CRESO

The Composite REsidual and Smoothing Operator (CRESO) method was introduced by Colli-Franzone et al. (1985). It chooses the parameter that corresponds to the first local maximum of the derivative of the difference between the constraint term and the residual term with respect to λ^2.

$$\begin{cases} C(\lambda) = \frac{d}{d(\lambda^2)}(\lambda^2 \eta_1(\lambda) - \rho_1(\lambda)), & \text{if } L = I, \\ C(\lambda) = \frac{d}{d(\lambda^2)}(\lambda^2 \eta_2(\lambda) - \rho_2(\lambda)), & \text{if } L \neq I. \end{cases} \tag{24}$$

In terms of the singular value decomposition, this can be written as (Johnston and Gulrajani, 1997; Ghista, 2012):

$$\begin{cases} C(\lambda) = \sum_{i=1}^{n} \dfrac{\sigma_i^2 \mu_i^2 (\sigma_i^2 - 3\lambda^2)}{(\sigma_i^2 + \lambda^2)^3}, & \text{if } L = I, \\ C(\lambda) = \sum_{i=1}^{n} \dfrac{\bar{\lambda}_i^2 \alpha_i^2 (\bar{\lambda}_i^2 - 3\lambda^2)}{(\bar{\lambda}_i^2 + \lambda^2)^3}, & \text{if } L \neq I. \end{cases} \tag{25}$$

where $\alpha_i = p_i^T b, \quad i = 1...n$.

2.3.4. GCV

The Generalized-Cross Validation (GCV) (Wahba, 1977) is also a well-known method to choose the regularization parameter. It provides the optimal value of λ by minimizing the function:

$$\begin{cases} G(\lambda) = \dfrac{\rho_1(\lambda)}{\left[Trace(I - AA^{\dagger})\right]^2}, & \text{if } L = I, \\ G(\lambda) = \dfrac{\rho_2(\lambda)}{\left[Trace(I - AA^{\#})\right]^2}, & \text{if } L \neq I. \end{cases} \tag{26}$$

The function $G(\lambda)$ is, according to ***Wahba*** (Wahba, 1977), equal to the weighted linear combination of the m prediction errors by leaving out, in each time, the k^{th} data point, $k = 1..m$ and resolving the inverse problem by the use of the $m - 1$ remaining data points. The idea is that the optimum of the regularization parameter provides the best prediction of a measurement as a function of the others. In terms of singular value decomposition, $G(\lambda)$ is expressed by (Wahba, 1977; Chung et al., 2014):

$$\begin{cases} G(\lambda) = \dfrac{\sum_{i=1}^{n} \dfrac{\lambda^4 \mu_i^2}{(\sigma_i^2 + \lambda^2)^2} + \|r_{\perp}\|^2}{\left(m - \sum_{i=1}^{n} \dfrac{\sigma_i^2}{\sigma_i^2 + \lambda^2}\right)^2}, & \text{if } L = I, \\ G(\lambda) = \dfrac{\sum_{i=1}^{n} \dfrac{\lambda^4 \alpha_i^2}{(\bar{\lambda}_i^2 + \lambda^2)^2} + \sum_{i=n+1}^{m} \alpha_i^2}{\left(m - \sum_{i=1}^{n} \dfrac{\bar{\lambda}_i^2}{\bar{\lambda}_i^2 + \lambda^2}\right)^2}, & \text{if } L \neq I. \end{cases} \tag{27}$$

It's known that the GCV method has good asymptotic properties as $n \longrightarrow \infty$ (Craven and Wahba, 1978; Golub et al., 1979; Lukas, 1993). However, it may not be reliable for small or medium values of n and can give values of λ that are too small resulting in a very noisy regularized solution.

2.3.5. RGCV

In Lukas (2006), a new method called Robust GCV (RGCV) is proposed and proved to be more reliable than GCV for small values of n and generally more accurate. The RGCV estimate is defined by the minimizer of the following function:

$$R(\lambda) = \left[\gamma + (1 - \gamma)\xi(\lambda)\right] G(\lambda), \tag{28}$$

where $G(\lambda)$ is given by (26) and $\xi(\lambda)$ is defined as:

$$\begin{cases} \xi(\lambda) = Trace\left[(AA^{\dagger})^2\right] = \sum_{i=1}^{n} \dfrac{\sigma_i^4}{\left(\lambda^2 + \sigma_i^2\right)^2}, & \text{if } L = I, \\ \xi(\lambda) = Trace\left[(AA^{\#})^2\right] = \sum_{i=1}^{n} \dfrac{\bar{\lambda}_i^4}{\left(\lambda^2 + \bar{\lambda}_i^2\right)^2}, & \text{if } L \neq I. \end{cases} \tag{29}$$

Here, γ is called a robustness parameter, $\gamma \in [0, 1]$.

The RGCV method is based on the average influence $\frac{1}{m} \sum_{i=1}^{m} \|Ax_{\lambda} - Ax_{\lambda}^{[i]}\|^2$, where $\|Ax_{\lambda} - Ax_{\lambda}^{[i]}\|^2$ is a measure of the influence of the i^{th} data point on the regularized solution. It's trivial that, when $\gamma = 1$, $R(\lambda)$ is reduced to $G(\lambda)$. It can be shown that the term $(1 - \gamma)\xi(\lambda)$ penalizes the too small values of λ. In fact, when $\lambda \to \infty$, $\xi(\lambda) \to 0$, so $\frac{1}{\gamma} R(\lambda)$ becomes equivalent to $G(\lambda)$. Otherwise, if $\lambda \to 0$, $\xi(0) = n$, so $\frac{1}{\gamma} R(\lambda) \gg G(\lambda)$ for small values of γ which means that the smaller γ, the more robust is the RGCV method (Lukas, 2006).

3. EXPERIMENTAL METHODS AND SIMULATION PROTOCOLS

3.1. Data Sets

ECGI reconstructions were performed on two different sets of data:

I Simulated data obtained by considering a realistic 3D heart-torso geometry segmented from CT-Scan images as illustrated in **Figure 1** (see Zemzemi et al., 2014 for more details). The propagation of the electrical wave was computed using the monodomain reaction-diffusion model. The transmembrane currents used to compute the extracellular potential distribution throughout the torso were computed by solving a static bidomain problem in an homogeneous, isotropic torso model (Boulakia et al., 2010). Synchronized electrical potential on the epicardium and on the body surface were extracted in order to test the inverse methods. The torso mesh contained 2,873 nodes and the heart mesh 519 nodes.

II Experimental data were obtained using an *ex-vivo* pig heart perfused in Langendorff mode suspended into a human-shaped torso tank. The heart was paced by 2 ms pulses at 2 Hz, with constant current amplitudes 2x the diastolic threshold, on the left and right ventricular epicardial surface, mimicking ectopic activity. Epicardial ventricular electrograms were recorded using a 108-electrode sock (of which 93 were used) simultaneously with torso potentials from 128 electrodes embedded in the tank surface as it appears in **Figure 2**.

Tank and sock unipolar electrograms were recorded at 2 kHz (BioSemi, the Netherlands) and referenced to a Wilson's central terminal defined using tank electrodes. A multi-lead signal averaging algorithm was used to remove noise and non-synchronized p-waves on recordings. In most cases, retrograde VA conduction was present with P-waves only present during the non-analyzed ST-segment. The tank mesh contains 1,177 nodes and the epicardium 761 nodes. For the application

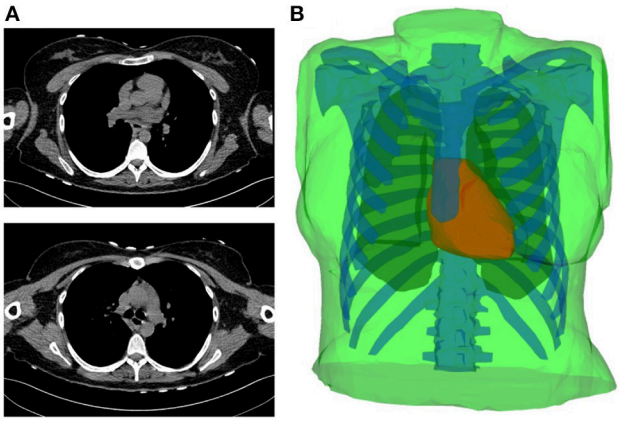

FIGURE 1 | (A) Two slices of the CT-scan images. **(B)** Torso geometry showing the epicardium (heart-torso interface Σ) (red), lungs (yellow), bones (blue) and torso external boundary Γ_{ext} (green).

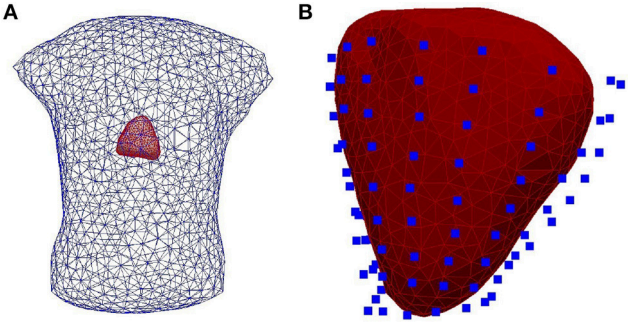

FIGURE 2 | (A) The heart-human-shaped torso tank model used for the experimental data simulations. The heart consists of 761 nodes and 1,518 elements and the tank contains 1,177 nodes and 2,350 elements. **(B)** The heart geometry covered by the sock consisting of 108 electrodes (blue points).

of described inverse methods, potential recordings need to be available for all the mesh nodes. To do so, a linear interpolation was applied to the *ex-vivo* recordings. More details about the *ex-vivo* experimental protocol can be found in Bear et al. (2018).

For all the carried out tests using the L1-Norm regularization, $\boldsymbol{\beta}$ is kept fixed and equal to $\mathbf{10^{-5}}$.

3.2. Choice of the Robustness Parameter

The choice of $\boldsymbol{\gamma}$ for the RGCV tests is based on the study made by Barnes and Johnston (2016). In fact, they proved that applying RGCV with $\boldsymbol{\gamma = 0}$ gives a good approximation of the optimal regularization parameter, especially when using realistic geometries and potential measures. To justify this choice, **Figure 3** represents a plot of the RGCV criterion in terms of the parameters $\boldsymbol{\lambda}$ and $\boldsymbol{\gamma}$ where the color map defines the value of the RGCV function and the red marks correspond to the local minima . We observe that the local minima are almost reached at the same $\boldsymbol{\lambda}$ value except the case where $\boldsymbol{\gamma = 1}$ corresponding to

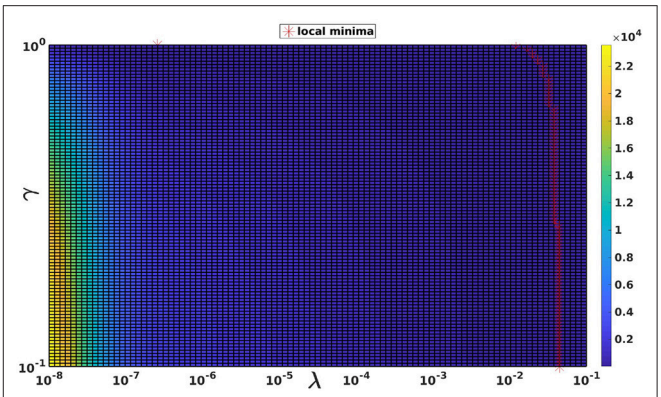

FIGURE 3 | The RGCV criterion plotted in terms of λ and γ. The red markers are the grid points where RGCV(λ,γ) is minimum when γ is fixed.

the GCV. For organization reasons, we present here only a graph realized using experimental data at a specific time step, but we observe the same behavior for all the other cases. This confirms the fact that for the inverse problem of electrocardiography, RGCV is not sensitive to $\boldsymbol{\gamma}$ when $\boldsymbol{\gamma \in [0, 0.5]}$.

3.3. Evaluation Criteria

To assess the accuracy of the results obtained by the different approaches, we define the relative error (**RE**) and the correlation coefficient (**CC**):

$$RE = \sqrt{\frac{\sum_{i=1}^{n}(x_i^c - x_i^e)^2}{\sum_{i=1}^{n}(x_i^e)^2}} \tag{30}$$

$$CC = \frac{\sum_{i=1}^{n}\left[x_i^c - \bar{x^c}\right]\left[x_i^e - \bar{x^e}\right]}{\sqrt{\sum_{i=1}^{n}(x_i^c - \bar{x^c})^2 \sum_{i=1}^{n}(x_i^e - \bar{x^e})^2}} \tag{31}$$

where $\boldsymbol{x^c}$ and $\boldsymbol{x^e}$ denote, respectively, the computed epicardial potential and the known one. $\boldsymbol{n}$ is either the number of epicardial nodes or the total number of time steps. In the first case, $\bar{x^c}$ and $\bar{x^e}$ are the spatial mean values of $\boldsymbol{x^c}$ and $\boldsymbol{x^e}$ over the $\boldsymbol{n}$ epicardial nodes. Otherwise, $\bar{x^c}$ and $\bar{x^e}$ are the temporal mean values of $\boldsymbol{x^c}$ and $\boldsymbol{x^e}$ over the $\boldsymbol{n}$ time steps. The means and the standard deviations of RE and CC are then computed and represented as bar graphs. The accuracy of pacing sites localization is measured by the geodesic distance between real and estimated pacing sites.

4. RESULTS

4.1. Epicardial Potential Reconstruction

4.1.1. Simulated Data

First, we assessed regularization techniques and numerical methods using simulated data. The five regularization parameter choice criteria described above were assessed using all the suggested numerical methods: MFS, FEM-ZOT, and FEM-L1 which make 15 different algorithms.

Figure 4 presents the mean and the standard deviation of the spatial REs and CCs of the reconstructed potentials by the

different numerical tests. For MFS, GCV gives the best estimation of the optimal regularization parameter in terms of relative error (**0.24 ± 0.15**) and correlation coefficient (**0.98 ± 0.04**). we notice an improvement by **10%** comparing to RGCV and CRESO methods. These 3 techniques outperform with different grades ADPC and U-Curve which seem to be unsuitable for MFS resolution.

For all the runned simulations using FEM, GCV and ADPC fail to compute the optimal regularization parameter. In fact, GCV tends to be flat for small values of λ which make it difficult to pick a minimum. RGCV is suggested to help with this difficulty. We observe here that it outperforms U-Curve by nearly **30%** using the zero order Tikhonov and **20%** using the L1-norm regularization of the current density while it gives similar results to CRESO in terms of both spatial RE and CC.

Figure 4 shows also the accuracy of L1-norm regularization in the reconstruction of epicardial potential maps. We observe that it provides the minimum of mean relative error (**0.21 ± 0.2**) and the maximum of spatial correlation coefficient (**0.99 ± 0.04**).

Figures 5, **6** show simulated epicardial potential maps (A) and reconstructed ones using FEM-ZOT (B) and FEM-L1-Norm (C) at the stimulation sample time and at 212 ms, after the electrical pacing leading to a reentry arrythmia, respectively. It can be seen that L1-Norm regularization provides a better reconstruction compared to the zero-order Tikhonov regularization especially on the regions where we have a potential leap. This fits exactly

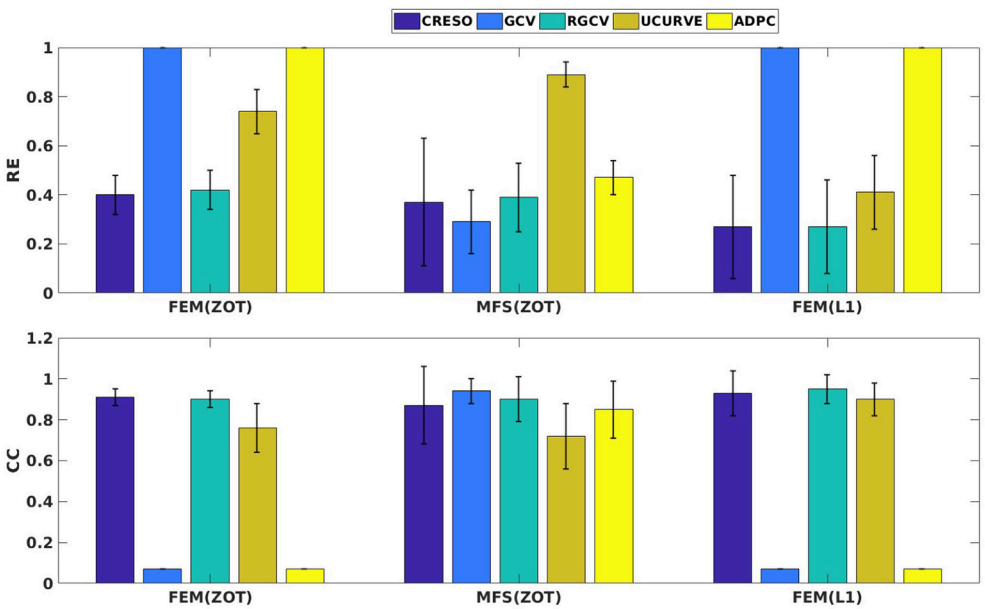

FIGURE 4 | Bar graphs of means of relative errors and correlation coefficients with the standard deviations for simulated data.

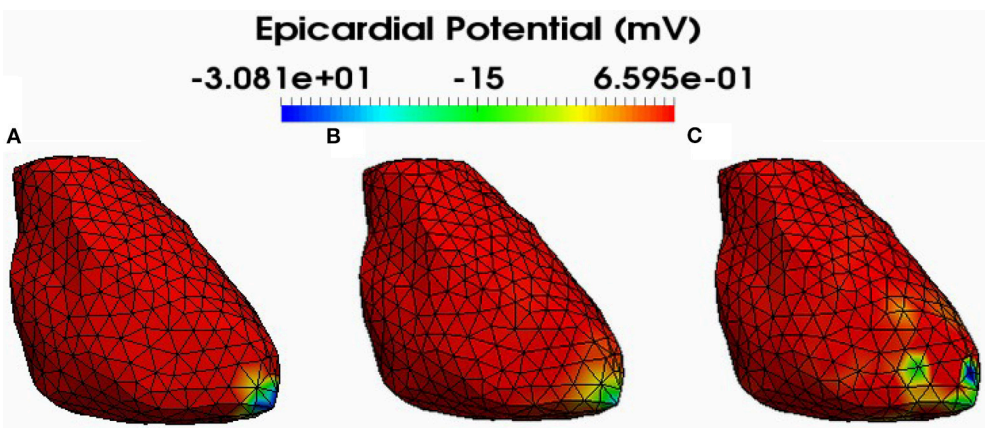

FIGURE 5 | Simulated **(A)** and reconstructed epicardial potential distributions on the epicardium at the stimulation sample time using FEM-ZOT **(B)** with the optimal regularization parameter (RGCV), L1-Norm **(C)** with the optimal regularization parameter (RGCV).

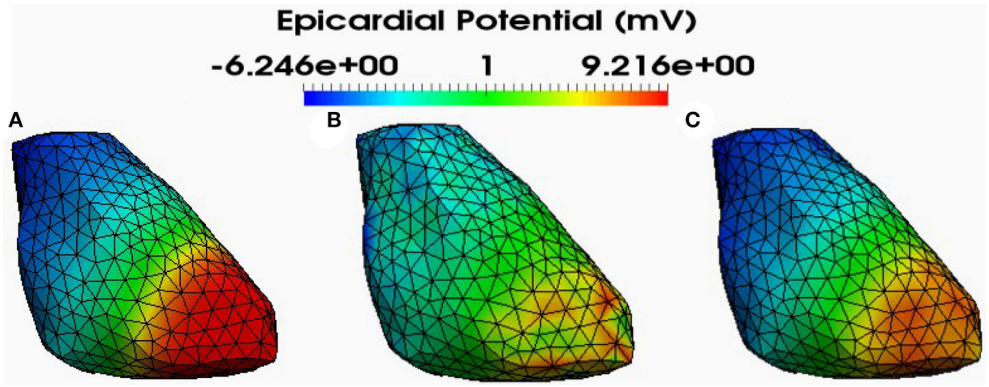

FIGURE 6 | Simulated **(A)** and reconstructed epicardial potential distributions on the epicardium at 212ms after stimulation using FEM-ZOT **(B)** with the optimal regularization parameter (RGCV) and L1-Norm **(C)** with the optimal regularization parameter (RGCV).

with the role of the L1-Norm regularization which is a better way to detect the gradient changes compared to Zero order Tikhonov.

4.1.2. Experimental Data

Preprocessing of the experimental data revealed the existence of a few localized sites of ischemia produced due to electrode pressure on the epicardium. This produced monophasic action potential-like signals. These electrodes were identified when the potential was greater than a fixed threshold equal to **50%** of the maximum signal magnitude in the plateau phase, 250 ms after pacing. This choice is based on observations of the QT interval in order to eliminate the ischemic signals. This leads us to run two sets of comparisons, with all the working electrodes and after removing the above threshold electrodes. We observe that results after thresholding are better than those obtained with ischemic signals. For the sake of clarity, we present here only results after thresholding. **Figure 7** shows the mean and standard deviation of spatial RE and CC. We observe a degradation of the metrics for the three models of experimental data (RV, LV, and BiV). This can be explained by different factors, the subject of section **4.4**. In **Figure 7**, we observe that using MFS, all the methods demonstrated similar trends in RE mean values. It shows also that GCV outperforms the other methods in terms of spatial correlation coefficient. For FEM, GCV and ADPC have always difficulties in computing the optimal value of the regularization parameter while RGCV, CRESO and U-Curve perform the same with a mean relative error near to **0.95** for all the three paced rhythms. Regarding the performance, there is not a clear difference among all the methods.

For the sake of completeness, statistical detailed results of RE and CC in time and space on the reconstructed potential for all cases are reported in the **Supplementary Material**.

4.2. Localization of Pacing Sites

For the localization of pacing sites, we used three different experiments, two of them provide LV, RV, and BiV pacing data sets and the other one has only RV and LV models. In summary, we have 3 cases of LV pacing, 3 cases of RV pacing and 2 cases of BiV pacing. In **Figure 8** (respectively, **Figure 9**) (top), we show measured and reconstructed potential maps right at the pacing sample time in an LV-pacing (respectively, RV-pacing) case. The detected pacing sites are marked by bigger red crosses than the actual pacing site and the length of the green segment between them represents the geodesic distance. For the sake of comparison, only the simulation using the regularization parameter technique providing the better localization is selected for the figures. The case where the reconstructed epicardial potential do not allow us to extract the pacing sites are reported in **Table 1** as non applicable (N.A) cases.

For the LV-pacing (respectively, RV-pacing) case , we observe that L1-norm regularization of the current density combined with RGCV provides the best localization with an error of $\mathbf{0.45}\,\boldsymbol{cm}$ (respectively, $\mathbf{2.15}\,\boldsymbol{cm}$). It outperforms FEM-ZOT $\mathbf{2.55}\,\boldsymbol{cm}$ (respectively, $\mathbf{2.16}\,\boldsymbol{cm}$) and MFS $\mathbf{0.83}\,\boldsymbol{cm}$ (respectively, $\mathbf{3.15}\,\boldsymbol{cm}$) that give similar approximations. We also plot in the bottom of the figure the time course of the electrical potential at the actual pacing site position detected from the measured data. For LV-pacing case, MFS, (respectively FEM-ZOT and FEM-L1) present temporal relative error and correlation coefficient equal to $\mathbf{(0.83, 0.72)}$ (respectively $\mathbf{(0.86, 0.75)}$, $\mathbf{(0.8, 0.72)}$). For the RV-pacing case, MFS, (respectively FEM-ZOT and FEM-L1) present temporal relative error and correlation coefficient equal to $\mathbf{(1.05, 0.3)}$ (respectively $\mathbf{(1.12, 0.40)}$, $\mathbf{(1.01, 0.33)}$).

For both LV and RV-pacing we observe that none of the methods is clear-cut.

In the case of a bi-ventricular pacing (BiV), not all the methods were able to locate both pacing sites. Only MFS-ZOT combined with GCV, FEM-ZOT and FEM-L1 with RGCV succeed to detect the two pacing sites with more-less good accuracy. **Figure 10** presents the real and estimated pacing sites and their electrograms for a BiV pacing rhythm for which all the methods work. The **Figures 10B–D** show the results for the BiV pacing sites. Errors of localization of the LV pacing site are $\mathbf{1.3}\,\boldsymbol{cm}$ for FEM-L1, $\mathbf{1.8}\,\boldsymbol{cm}$ for FEM-ZOT and $\mathbf{2.3}\,\boldsymbol{cm}$ for MFS. The bottom row of each panel represents the reconstructed electrograms in the real pacing sites using the specified method. The temporal relative errors and correlation coefficients for LV

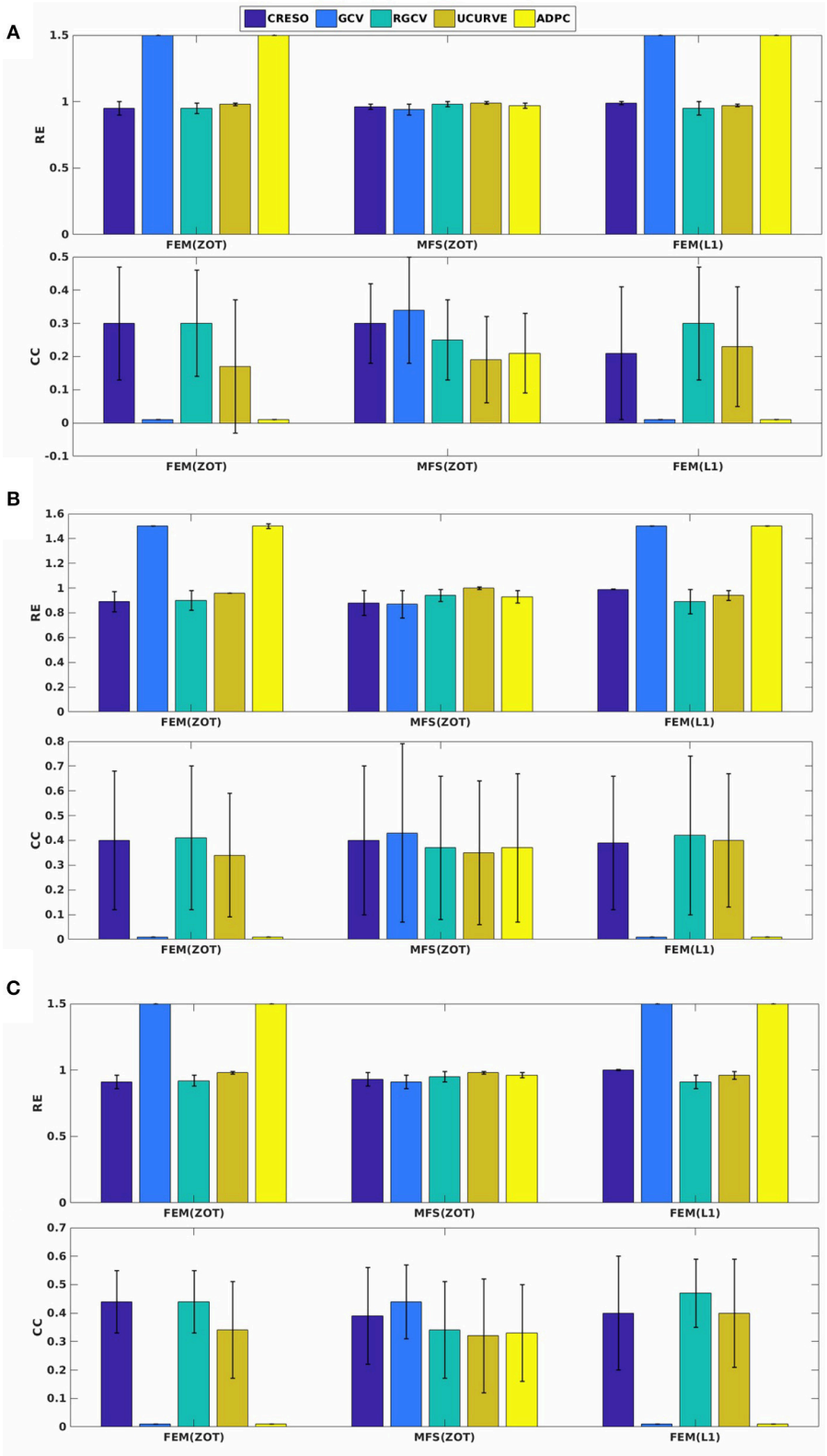

FIGURE 7 | Spatial mean relative errors and correlation coefficients and their standard deviations for reconstructed epicardial potentials with all the algorithms for three paced rhythms: **(A)** Biv, **(B)** RV, and **(C)** LV.

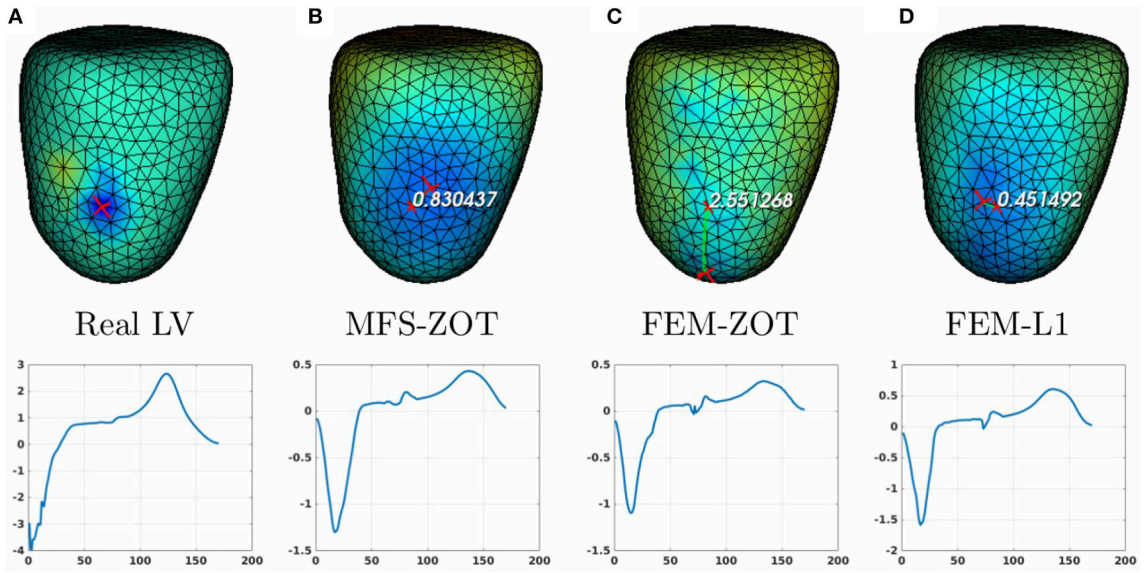

FIGURE 8 | Real **(A)** and the estimated LV pacing sites (top) and its electrograms (bottom) using MFS-ZOT (B), FEM-ZOT **(C)**, and FEM-L1 **(D)**, respectively.

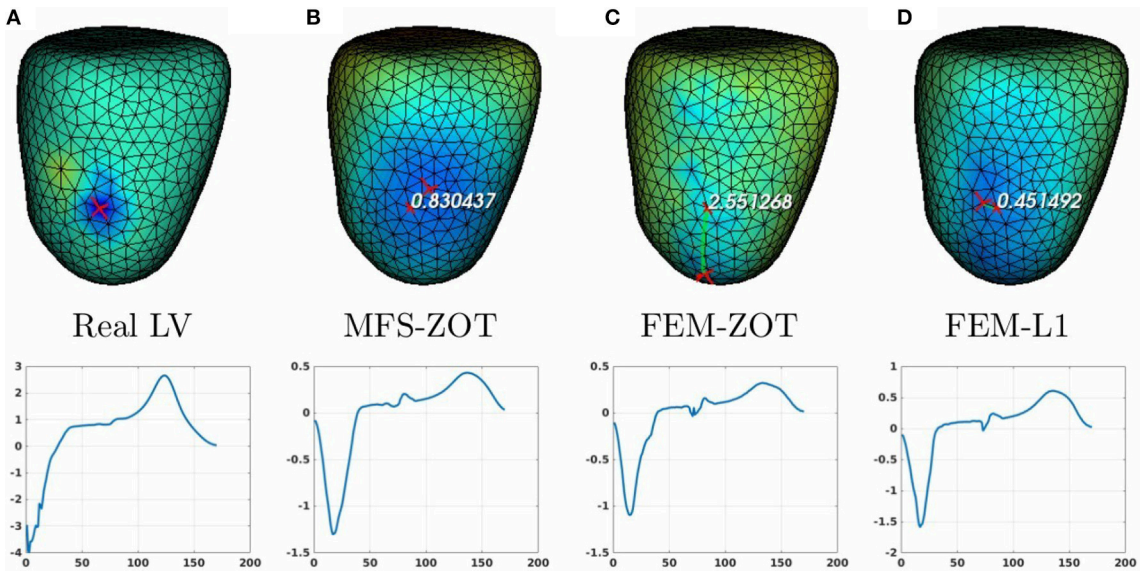

FIGURE 9 | Real **(A)** and the estimated RV pacing sites (top) and its electrograms (bottom) using MFS-ZOT **(B)**, FEM-ZOT **(C)**, and FEM-L1 **(D)**, respectively.

are (**0.80, 0.71**) using FEM-L1, (**0.86, 0.75**) with FEM-ZOT and (**0.83, 0.72**) using MFS. As shown in **Figure 10B**, MFS nearly fails to detect the left ventricular pacing site. The epicardial potential in the whole left ventricle is almost in the same range. For the RV pacing site, results are nearly the same as for the LV pacing site.

The performance in terms of pacing site localization of the 15 algorithms on the set of the experimental data are reported in **Table 1** where we provide the mean values and standard deviations of pacing sites localization errors for the three cases, LV, RV, and BiV. We remark that, L1-norm regularization of the current density combined with RGCV parameter choice method outperforms all the other methods with minimum errors and more stable standard deviations.

4.3. Limitations

4.3.1. The Imperfect Knowledge of the Transfer Matrix

It's important to mention that in this work, the use of simulated data provides an optimal knowledge of the transfer matrix $\boldsymbol{A}$, which is not the case of experimental data. It explains somehow the degradation of the results using the experimental data. To assess the impact of the transfer matrix, we computed a relative

TABLE 1 | Mean errors and standard deviations of localization of pacing sites for the 2 paced rhythms RV, LV using the 3 numerical methods MFS-ZOT, FEM-ZOT, and FEM-L1 combined with the regularization parameter choice methods.

		CRESO	GCV	RGCV	UCurve	ADPC
RV	MFS-ZOT	2.8 ± 1.2	2.4 ± 1.1	1.9 ± 0.9	2.4 ± 0.8	2.5 ± 0.8
	FEM-ZOT	2.7 ± 0.8	N.A	2.7 ± 0.9	2.0 ± 0.1	N.A
	FEM-L1	1.9 ± 0.5	N.A	1.8 ± 0.3	1.8 ± 0.4	N. A
LV	MFS-ZOT	1.7 ± 0.7	2.1 ± 0.3	2.0 ± 1.1	1.3 ± 0.6	2.1 ± 0.2
	FEM-ZOT	2.1 ± 0.4	N.A	2.8 ± 1.0	3.0 ± 0.2	N.A
	FEM-L1	1.3 ± 0.5	N.A	1.2 ± 0.6	1.3 ± 0.6	N.A
	MFS-ZOT	2.5/*N.A*	2.3/1.5	0/*N.A*	2.3/*N.A*	2.7/2.0
BiV	FEM-ZOT	1.8/*N.A*	N.A	1.8/2.1	2.5/N.A	N.A
	FEM-L1	2.5/N.A	N.A	1.3/1.4	1.4/N.A	N.A

For BiV, values are the geodesic distances (LV/RV). N.A means that one could not extract the pacing site from the reconstructed signals. Highlighted values are the best localization errors.

error defined by:

$$RE_d = \frac{\|Ax_{ex} - b\|}{\|b\|} \tag{32}$$

where x_{ex} is the exact solution whether it's the simulated epicardial potential or the measured one.

The RE_d is almost equal to zero using the simulated transfer matrix. However, it increases for the experimental data to reach, for some time steps, $RE_d \approx 0.9$. Although this issue is out of the scope of this paper, the degradation can be due to different factors like the measurement errors and geometrie's inaccuracy due to the fact that the heart is moving during the experiment, but also to the mathematical modeling of the physical phenomenon which is reduced to the Laplace equation. These hypotheses make the issue subject to further analyzes.

4.3.2. Experimental Protocols

Obviously, the experimental conditions have a very important impact on the quality of the data that we obtain from experiments. One of the limitations of this study is the dataset of epicardial signals. In fact, the experimental protocol described in Bear et al. (2018) indicates that the epicardial surface is not totally covered with electrodes which provides less information and biased results. Further studies should be done in this context. The protocols we have set until now do not include endocardial stimulation, this is one of the limitation of our work. Of course, if we have to evaluate the methods against endocardial and septal stimulations we have to make use of a W-shape geometry of the ventricles including endocardial, epicardial and septal surfaces instead of a nut-shape geometry that only represents the epicardial surface.

5. DISCUSSION AND CONCLUSION

In this paper, we numerically assessed 15 different algorithms for the resolution of the inverse problem of electrocardiography based on the Generalized Singular Value Decomposition of the pair {Transfer matrix, Regularization matrix} combined with different regularization parameter choice methods. Although the L1-Norm of the normal derivative regularization method has been presented before (Khoury, 1994; Ghosh and Rudy, 2009) to solve the ECGI inverse problem, there are two novelties in this paper: First, the non quadratic scheme was solved using the generalized singular values decomposition, whereas, in Ghosh and Rudy (2009) authors use an iterative method. Second, the regularization method was combined with five regularization parameter choice methods to assess its performance on simulated and experimental data. In Barnes and Johnston (2016), authors used only ZOT regularization and compared results only on simulated data. In this paper and in the majority of the studies looking for the ECGI inverse solution, the problem is formulated in terms of electrical potential. There are other approaches, where the problem is formulated in terms of propagating wave front (Cuppen and Van Oosterom, 1984; Huiskamp and Greensite, 1997). In Van Dam et al. (2009), the activation and recovery times and the transmembrane potentials are constructed. Other approaches are interested in constructing directly dominant frequencies on the heart surface and torso surfaces (Pedrón-Torrecilla et al., 2016; Beltrán-Molina et al., 2017).

The evaluation of the different approaches studied in this paper is based on the reconstruction of the epicardial potential maps and the localization of pacing sites. For that, we used 3 different cardiac paced rhythms: left-ventricular, right-ventricular and bi-ventricular pacing.

Unlike the work presented by Barnes and Johnston (2016), this study considered two types of transfer matrices: MFS and FEM and two different approaches of regularization: zero-order Tikhonov and L1-Norm. This study demonstrated that, when using the MFS discretization approach, the GCV method is more appropriate and optimal than RGCV and the other parameter choice methods. Otherwise, for the FEM approach, the RGCV gives the best results using simulated data. But also, GCV and ADPC provide very weak results with FEM, this is mainly due to the fact that the minimization criteria in both cases chooses the regularization parameter λ at the lower bound of the provided interval.

However, for the experimental data, all the methods perform nearly the same with a slight difference in terms of both spatial and temporal relative error and correlation coefficient when comparing the epicardial potential distribution. We think that this is mainly due to the magnitude of the recorded potentials but also to the noise and other experimental uncertainties. Results show, also, that L1-Norm regularization of the potential normal derivative yields generally the best solution. For the purpose of benchmarking, the represented algorithms were evaluated against the data set used in the paper (Figuera et al., 2016). Results are reported in the **Supplementary Material**. They show similar performance for the sinus rhythm model using the L1-norm regularization of the current density. This last regularization has a better performance for the atrial fibrillation models compared to all the ZOT based methods but weaker results than the Bayesian approach (Serinagaoglu et al., 2005; Figuera et al., 2016). This should be subject of several further studies.

Regarding the pacing site localization, **Table 1** show clearly that the estimation of pacing sites is more accurate using L1-norm regularization than other methods with minimum errors and less variance despite the fact that it depends of the epicardial potential reconstruction. This is due to the use of L1-Norm

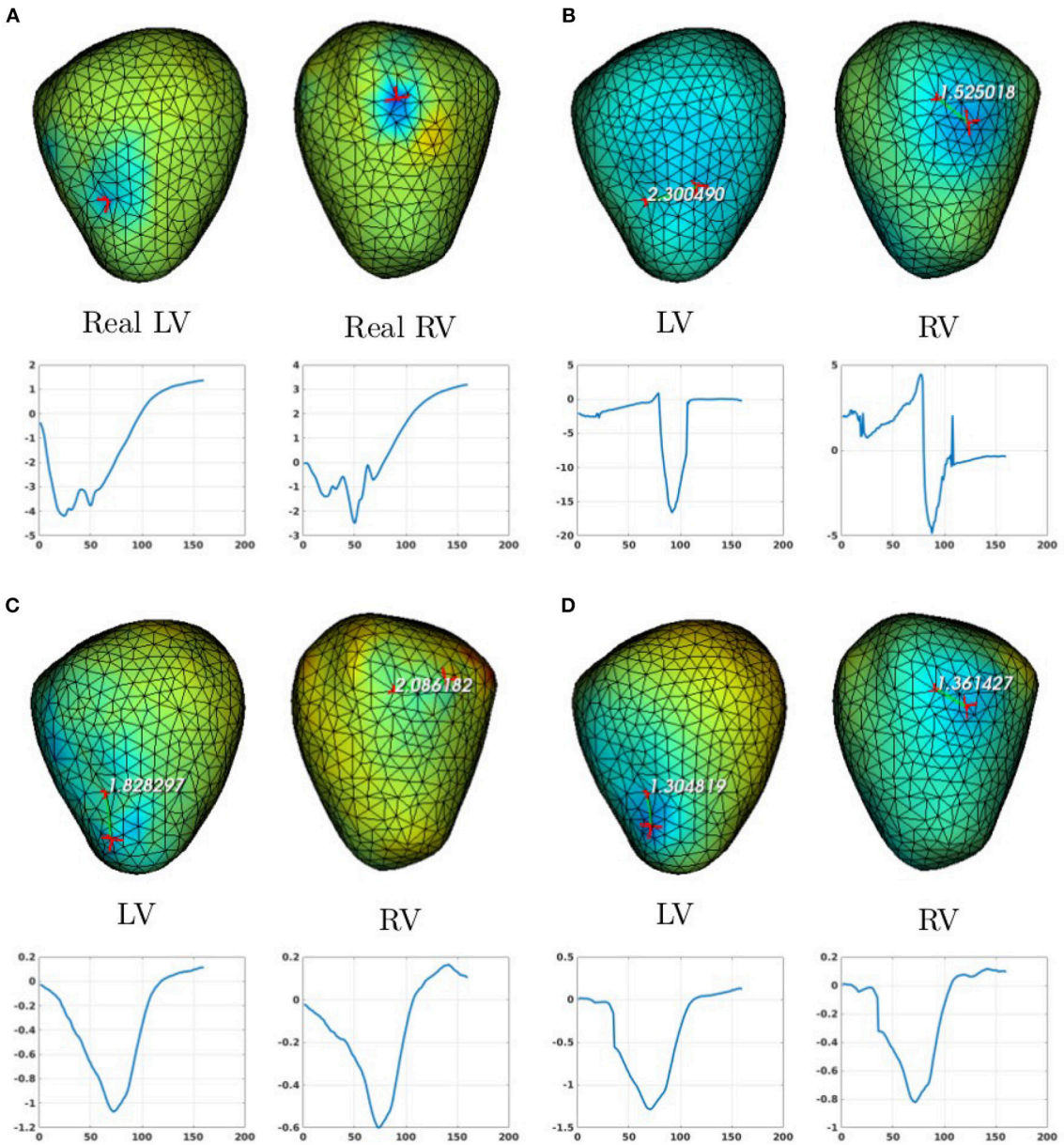

FIGURE 10 | Real **(A)** and the estimated BiV pacing sites with its electrograms using the numerical methods **(B)** MFS-ZOT, **(C)** FEM-ZOT, and **(D)** FEM-L1. In each panel, LV and RV pacing sites (top) with their electrograms (bottom) are represented using the mentioned numerical method.

regularization that preserves the spatial gradient changes in the solution which is not the case for the L2-Norm regularization that tends to give smoother solutions. Despite the good performance of the methods in the case of LV and RV, they have faced difficulties in localizing two pacing sites for the BiV pacing and localize in some cases only one pacing site nearly equidistant to the two real ones. Some limitations of this study have been explored such as the imperfect knowledge of the transfer matrix and the noise in the ground truth data that could lead to biased results. This explains the degradation of the RE and CC metrics in terms of electrical potential for the experimental data compared to the simulated model.

AUTHOR CONTRIBUTIONS

AK is the main author of the paper. She participated in the implementation of the methods. She participated in the analysis of the results. PM participated in the implementation of the different methods. She participated in the analysis of the results. LB performed the *ex-vivo* experiment. She participated in the writing of the paper. She participated in the analysis of the results. NZ is the supervisor of AK and PM. He performed the *in silico* simulations, participated in the design of the software implementing all of the methods used here. He participated in the

analysis of the results. He participated in the writing of the paper.

FUNDING

This study received financial support from the French Government as part of the Investments of the future program managed by the National Research Agency (ANR), Grant reference ANR-10-IAHU-04-LIRYC.

SUPPLEMENTARY MATERIAL

The Supplementary Material for this article can be found online at: https://www.frontiersin.org/articles/10.3389/fphys.2018.01708/full#supplementary-material

REFERENCES

Bai, X., Towle, V. L., He, E. J., and He, B. (2007). Evaluation of cortical current density imaging methods using intracranial electrocorticograms and functional MRI. *NeuroImage* 35, 598–608. doi: 10.1016/j.neuroimage.2006.12.026

Barnes, J. P., and Johnston, P. R. (2016). Application of robust generalised cross-validation to the inverse problem of electrocardiology. *Comput. Biol. Med.* 69, 213–225. doi: 10.1016/j.compbiomed.2015.12.011

Barr, R. C., Ramsey, M., and Spach, M. S. (1977). Relating epicardial to body surface potential distributions by means of transfer coefficients based on geometry measurements. *IEEE Trans. Biomed. Eng.* 24, 1–11. doi: 10.1109/TBME.1977.326201

Bear, L. R., Huntjens, P. R., Walton, R., Bernus, O., Coronel, R., and Dubois, R. (2018). Cardiac electrical dyssynchrony is accurately detected by noninvasive electrocardiographic imaging. *Heart Rhythm* 15, 1058–1069. doi: 10.1016/j.hrthm.2018.02.024

Beltrán-Molina, F. A., Requena-Carrión, J., Alonso-Atienza, F., and Zemzemi, N. (2017). An analytical model for the effects of the spatial resolution of electrode systems on the spectrum of cardiac signals. *IEEE Access* 5, 18488–18497. doi: 10.1109/ACCESS.2017.2747632

Boulakia, M., Cazeau, S., Fernández, M., Gerbeau, J., and Zemzemi, N. (2010). Mathematical modeling of electrocardiograms: a numerical study. *Ann. Biomed. Eng.* 38, 1071–1097. doi: 10.1007/s10439-009-9873-0

Bouyssier, J., Zemzemi, N., and Henry, J. (2015). "Inverse problem in electrocardography via the factorization method of boundary value problems," in *2015 IEEE 12th International Symposium on Biomedical Imaging (ISBI)* (Brooklyn, NY: IEEE), 743–746.

Chamorro-Servent, J., Dubois, R., Potse, M., and Coudière, Y. (2017). "Improving the spatial solution of electrocardiographic imaging: a new regularization parameter choice technique for the tikhonov method," in *Functional Imaging and Modelling of the Heart*, eds M. Pop and G. A. Wright (Cham: Springer International Publishing), 289–300.

Cheng, L. K., Bodley, J. M., and Pullan, A. J. (2003). Comparison of potential- and activation-based formulations for the inverse problem of electrocardiology. *IEEE Trans. Biomed. Eng.* 50, 11–22. doi: 10.1109/TBME.2002.807326

Chung, J., Español, M. I., and Nguyen, T. (2014). Optimal regularization parameters for general-form Tikhonov regularization. *arXiv:1407.1911* [preprint].

Colli-Franzone, P., Guerri, L., Tentoni, S., Viganotti, C., Baruffi, S., Spaggiari, S., et al. (1985). A mathematical procedure for solving the inverse potential problem of electrocardiography. Analysis of the time-space accuracy from *in vitro* experimental data. *Math. Biosci.* 77, 353–396. doi: 10.1016/0025-5564(85)90106-3

Craven, P., and Wahba, G. (1978). Smoothing noisy data with spline functions. *Numerische Mathematik* 31, 377–403. doi: 10.1007/BF01404567

Cuppen, J. J., and Van Oosterom, A. (1984). Model studies with the inversely calculated lsochrones of ventricular depolarization. *IEEE Trans. Biomed. Eng.* 31, 652–659. doi: 10.1109/TBME.1984.325315

Ding, L., and Hei, B. (2008). Sparse source imaging in EEG with accurate field modeling. *Hum. Brain Mapp.* 29, 1053–1067. doi: 10.1002/hbm.20448

Figuera, C., Suárez-Gutiérrez, V., Hernández-Romero, I., Rodrigo, M., Liberos, A., Atienza, F., et al. (2016). Regularization techniques for ECG imaging during atrial fibrillation: a computational study. *Front. Physiol.* 7:466. doi: 10.3389/fphys.2016.00466

Ghista, D. (2012). *Biomedical and Life Physics: Proceedings of the Second Gauss Symposium, 2–8th August 1993*. Munich: Vieweg, Teubner Verlag.

Ghosh, S., and Rudy, Y. (2009). Application of l1-norm regularization to epicardial potential solution of the inverse electrocardiography problem. *Ann. Biomed. Eng.* 37, 902–912. doi: 10.1007/s10439-009-9665-6

Golub, G. H., Heath, M., and Wahba, G. (1979). Generalized cross-validation as a method for choosing a good ridge parameter. *Technometrics* 21, 215–223. doi: 10.1080/00401706.1979.10489751

Hadamard, J. (1923). *Lectures on Cauchy's Problem in Linear Partial Differential Equations*. New Haven, CT: Yale University Press.

Haissaguerre, M., Hocini, M., Shah, A. J., Derval, N., Sacher, F., Jais, P., et al. (2013). Noninvasive panoramic mapping of human atrial fibrillation mechanisms: a feasibility report. *J. Cardiovasc. Electrophysiol.* 24, 711–717. doi: 10.1111/jce.12075

Hansen, P. C. (1990). Truncated singular value decomposition solutions to discrete ill-posed problems with ill-determined numerical rank. *SIAM J. Sci. Stat. Comput.* 11, 503–518. doi: 10.1137/0911028

Hansen, P. C. (1998). *Rank-Deficient and Discrete Ill-Posed Problems*. Philadelphia, PA: SIAM.

Hansen, P. C. (2010). *Discrete Inverse Problems : Insight and Algorithms*, Vol. 7 of *Fundamentals of Algithms*. Philadelphia, PA: SIAM.

Huiskamp, G., and Greensite, F. (1997). A new method for myocardial activation imaging. *IEEE Trans. Biomed. Eng.* 44, 433–446. doi: 10.1109/10.581930

Johnston, P., and Gulrajani, R. (1997). A new method for regularization parameter determination in the inverse problem of electrocardiography. *IEEE Trans. Biomed. Eng.* 44, 19–39. doi: 10.1109/10.553710

Karl, W. C. (2005). "Regularization in image restoration and reconstruction," in *Handbook of Image and Video Processing (2nd Edn.), Communications, Networking and Multimedia*, ed A. Bovik (Burlington, VT: Academic Press), 183.

Khoury, D. (1994). "Use of current density an the regularization of the inverse problem of electrocardiography," in *Engineering in Medicine and Biology Society, 1994. Engineering Advances: New Opportunities for Biomedical Engineers. Proceedings of the 16th Annual International Conference of the IEEE*, Vol. 1 (Baltimore, MD: IEEE), 133–134.

Krawczyk-Stańdo, D., and Rudnicki, M. (2007). Regularization parameter selection in discrete ill-posed problems - the use of the u-curve. *Int. J. Appl. Math. Comput. Sci.* 17, 157–164. doi: 10.2478/v10006-007-0014-3

Krawczyk-Stańdo, D., and Rudnicki, M. (2008). "The use of l-curve and u-curve in inverse electromagnetic modelling," in *Intelligent Computer Techniques in Applied Electromagnetics*, Vol. 119, eds S. Wiak, A. Krawczyk, and I. Dolezel (Berlin; Heidelberg: Springer), 73–82.

Lukas, M. A. (1993). Asymptotic optimality of generalized cross-validation for choosing the regularization parameter. *Numerische Mathematik* 66, 41–66. doi: 10.1007/BF01385687

Lukas, M. A. (2006). Robust generalized cross-validation for choosing the regularization parameter. *Inverse Prob.* 22:1883. doi: 10.1088/0266-5611/22/5/021

Pedrón-Torrecilla, J., Rodrigo, M., Climent, A. M., Liberos, A., Pérez-David, E., Bermejo, J., et al. (2016). Noninvasive estimation of epicardial dominant high-frequency regions during atrial fibrillation. *J. Cardiovasc. Electrophysiol.* 27, 435–442. doi: 10.1111/jce.12931

Rudy, Y. (2013). Noninvasive electrocardiographic imaging of arrhythmogenic substrates in humans. *Circul. Res.* 112, 863–874. doi: 10.1161/CIRCRESAHA.112.279315

Schuler, S., Potyagaylo, D., and Dössel, O. (2017). ECG imaging of simulated atrial fibrillation: imposing epi-endocardial similarity facilitates the reconstruction of transmembrane voltages. *Computing* 44:1.

Serinagaoglu, Y., Brooks, D. H., and MacLeod, R. S. (2005). Bayesian solutions and performance analysis in bioelectric inverse problems. *IEEE Trans. Biomed. Eng.* 52, 1009–1020. doi: 10.1109/TBME.2005.846725

Stenroos, M. (2009). The transfer matrix for epicardial potential in a piece-wise homogeneous thorax model: the boundary element formulation. *Phys. Med. Biol.* 54:5443. doi: 10.1088/0031-9155/54/18/006

Stenroos, M., and Haueisen, J. (2008). Boundary element computations in the forward and inverse problems of electrocardiography: comparison of collocation and galerkin weightings. *IEEE Trans. Biomed. Eng.* 55:2124. doi: 10.1109/TBME.2008.923913

Van Dam, P. M., Oostendorp, T. F., Linnenbank, A. C., and Van Oosterom, A. (2009). Non-invasive imaging of cardiac activation and recovery. *Ann. Biomed. Eng.* 37, 1739–1756. doi: 10.1007/s10439-009-9747-5

Wahba, G. (1977). Practical approximate solutions to linear operator equations when the data are noisy. *SIAM J. Numer. Anal.* 14, 651–667. doi: 10.1137/0714044

Wang, D., Kirby, R. M., and Johnson, C. R. (2010). Resolution strategies for the finite-element-based solution of the ecg inverse problem. *IEEE Trans. Biomed. Eng.* 57, 220–237. doi: 10.1109/TBME.2009.2024928

Wang, Y., and Rudy, Y. (2006). Application of the method of fundamental solutions to potential-based inverse electrocardiography. *Ann. Biomed. Eng.* 34, 1272–1288. doi: 10.1007/s10439-006-9131-7

Wolters, C., Anwander, A., Maess, B., MacLeod, R., and Friederici, A. (2004). "The influence of volume conduction effects on the EEG/MEG reconstruction of the sources of the early left anterior negativity," in *The 26th Annual International Conference of the IEEE Engineering in Medicine and Biology Society* (IEEE), 3569–3572.

Yuan, Q., Zhang, L., Shen, H., and Li, P. (2010). Adaptive multiple-frame image super-resolution based on u-curve. *IEEE Trans. Image Process.* 19, 3157–3170. doi: 10.1109/TIP.2010.2055571

Zemzemi, N., Bourenane, H., and Cochet, H. (2014). "An iterative method for solving the inverse problem in electrocardiography imaging: from body surface to heart potential," in *Computing in Cardiology Conference (CinC), 2014* (Cambridge, MA: IEEE), 717–720.

Zemzemi, N., Dobrzynski, C., Bear, L., Potse, M., Dallet, C., Coudière, Y., et al. (2015). "Effect of the torso conductivity heterogeneities on the ecgi inverse problem solution," in *Computing in Cardiology Conference (CinC), 2015* (Nice: IEEE), 233–236.

Conflict of Interest Statement: The authors declare that the research was conducted in the absence of any commercial or financial relationships that could be construed as a potential conflict of interest.

frontiers in Physiology

ORIGINAL RESEARCH
published: 03 December 2018
doi: 10.3389/fphys.2018.01727

Tracking the Position of the Heart From Body Surface Potential Maps and Electrograms

Jaume Coll-Font[1,2]* *and Dana H. Brooks*[3]

[1] Computational Radiology Laboratory, Children's Hospital, Boston, MA, United States, [2] Harvard Medical School, Boston, MA, United States, [3] Signal Processing, Imaging, Reasoning, and Learning (SPIRAL) Group, Electrical and Computer Engineering Department, Northeastern University, Boston, MA, United States

The accurate generation of forward models is an important element in general research in electrocardiography, and in particular for the techniques for ElectroCardioGraphic Imaging (ECGI). Recent research efforts have been devoted to the reliable and fast generation of forward models. However, these model can suffer from several sources of inaccuracy, which in turn can lead to considerable error in both the forward simulation of body surface potentials and even more so for ECGI solutions. In particular, the accurate localization of the heart within the torso is sensitive to movements due to respiration and changes in position of the subject, a problem that cannot be resolved with better imaging and segmentation alone. Here, we propose an algorithm to localize the position of the heart using electrocardiographic recordings on both the heart and torso surface over a sequence of cardiac cycles. We leverage the dependency of electrocardiographic forward models on the underlying geometry to parameterize the forward model with respect to the position (translation) and orientation of the heart, and then estimate these parameters from heart and body surface potentials in a numerical inverse problem. We show that this approach is capable of localizing the position of the heart in synthetic experiments and that it reduces the modeling error in the forward models and resulting inverse solutions in canine experiments. Our results show a consistent decrease in error of both simulated body surface potentials and inverse reconstructed heart surface potentials after re-localizing the heart based on our estimated geometric correction. These results suggest that this method is capable of improving electrocardiographic models used in research settings and suggest the basis for the extension of the model presented here to its application in a purely inverse setting, where the heart potentials are unknown.

Keywords: electrocardiographic imaging, inverse problems, respiration, ECGI, forward problem, electrocardiography, heart tracking

OPEN ACCESS

Edited by:
Mark Potse,
Inria Bordeaux-Sud-Ouest Research Centre, France

Reviewed by:
Henggui Zhang,
University of Manchester, United Kingdom
Yves Coudière,
Université de Bordeaux, France

***Correspondence:**
Jaume Coll-Font
jaume.coll-font@childrens.harvard.edu

Specialty section:
This article was submitted to Cardiac Electrophysiology, a section of the journal Frontiers in Physiology

Received: *21 May 2018*
Accepted: *16 November 2018*
Published: *03 December 2018*

Citation:
Coll-Font J and Brooks DH (2018) Tracking the Position of the Heart From Body Surface Potential Maps and Electrograms. Front. Physiol. 9:1727. doi: 10.3389/fphys.2018.01727

1. INTRODUCTION

Subject-specific solutions to the forward problem of electrocardiography, that is, producing a mathematical model that can estimate body surface potential maps (BSPMs) from knowledge of cardiac electrical activity and an individualized thoracic volume conductor model, is important in a number of settings. These include tools for understanding and pedagogy about the

ECG (van Oosterom and Oostendorp, 2004), methods to guide interventions such as ablation through simulation (Trayanova, 2011), and solutions to the corresponding inverse problem of characterizing cardiac electrical activity from body surface measurements (commonly known as ElectroCardioGraphic Imaging, ECGI) (Pullan et al., 2010). The forward solution is known, from electrostatic theory, to be quasistatic and to depend only on the geometry of the torso and of the organs inside of it and their respective conductivities. Moreover, under specific assumptions about the electrical source models on the heart this relationship can be accurately modeled as linear. However, forward solutions depend on the underlying geometry, since it specifies the boundary conditions for the underlying partial differential equation, and even though this sensitivity is well-behaved, it is particularly critical when solving the ECGI inverse problem, since that inverse problem is ill-posed and very sensitive to errors in the forward model. Thus methods to improve forward modeling have received considerable attention in the ECGI community (Coll-Font et al., 2016a) and there is open discussion about, for example, what is the "best" forward model to use, which source models better characterize the electrical activity of the heart, how many, and which, organs should be included in the geometry, and how their respective conductivities should be estimated (Ferguson and Stroink, 1997; Ramanathan and Rudy, 2001a,b; Weber et al., 2011; Jones et al., 2013; Bear et al., 2015; Dehaghani, 2015; Potyagaylo et al., 2016; Punshchykova et al., 2016).

However, there is an additional challenge that is often ignored in this discussion: the positions of the organs within the torso, including the heart, are not static; rather they vary due to respiration and to changes in position of the subject. The sensitivity of forward solutions to these variations have been studied (Geneser et al., 2008; Swenson et al., 2011) but overcoming it remains challenging. It cannot be resolved a priori with better segmentation and it is not always possible to address by procedural mechanisms such as requiring the patient to retain breath-hold position. This challenge also appears in many phantom and animal experiments, such as validation of ECGI (MacLeod et al., 2000; Erem et al., 2014; Bear et al., 2015; Cluitmans and Volders, 2017), where the true position of the heart is not only unknown but subject to several experimental uncertainties and might change from beat to beat.

Here we address this limitation by attempting to use the changes in ECG due to changes in heart position—in other words, the manifestation of the problem itself—as the source of a solution. Specifically, since changes in position of the heart produce changes in the distribution of body surface potentials, we investigate whether that very variation can be used to track these positional changes and thus "correct" the forward model. In this paper we describe a method to estimate and correct for the translation and rotation of the heart for each heartbeat. We evaluate our accuracy in doing so by examining geometric accuracy in a controlled simulation and to what extent estimating these geometry changes leads to decreased errors in accuracy of both forward model body surface potential calculations and of associated inverse solutions. We report results for both synthetic experiments and in the context of three different physical experiments carried out with canine hearts suspended in a human torso-shaped tank phantom.

Our work builds on previous reports relating changes in geometry—and thus changes in forward models—to changes in the ECG. The classical studies described the changes in ECGs from patients as a function of the respiratory cycle. These studies showed that the changes can be characterized as a continuous displacement of the maxima and minima of the body surface potential maps (BSPM) (Amoore et al., 1988), have different effects along the PQRST sequence (Adams and Drew, 1997; Madias, 2006), and are subject specific (Nelwan et al., 2001). More systematic experiments on animal models and synthetic data provided methods to estimate the average BSPM and the variance that can occur due to movement of the heart in a subject (MacLeod et al., 2000; Swenson et al., 2011). More recently, cardiac magnetic resonance imaging allowed characterization of the relationship between standard clinical metrics of the ECG and changes in the heart geometry (Lyon et al., 2017) and, specific to ECGI, Cluitmans et al. explored the effects of these geometry errors on inverse solutions (Cluitmans and Volders, 2017).

Closer to our work, there have been a few reports attempting to track the changes in position of the heart using BSPM. Shvelikhova et al. estimated the vertical position of the heart by characterizing its electrical activity with a moving dipole whose position was tracked from the ECG (Svehlikova et al., 2011). Recently, Rodrigo et al. proposed to pre-compute a set of candidate forward models and then used a metric derived from the L-curve in Tikhonov regularization to select the "best" candidate forward model (Rodrigo et al., 2017, 2018). These approaches produce an optimization problem to be solved that is computationally tractable, but require pre-computation of a set of forward models from which to choose, or have very strong assumptions about the form of the source and geometry models, which may limit their generalization. In any case they are complementary to the method described here.

In this paper we describe the formulation and experimental validation of our approach. Specifically we reverse the role of geometric assumptions and cardiac surface potentials with respect to the traditional inverse problem of electrocardiography; instead of estimating the electrical sources of the heart from the ECG measurements and the geometry, we correct the geometric model (e.g., translations and rotations of the heart) assuming knowledge of the electrical measurements on both the heart and the body surface (Coll-Font, 2016; Coll-Font et al., 2016b, 2017). Direct application of this approach is relevant to a variety of phantom and animal studies where measurements can be made on both surfaces. A future extension might allow use of only a limited set of heart surface potentials such as those acquired during catheter procedures. Future application to ECGI would require estimating both heart surface potentials as well as geometry correction parameters and, while preliminary results are positive, success clearly depends on establishing the validity and limitations of the geometry correction approach in its own right, which we attempt to do in the current paper.

In the following we describe in section 2 how our method is applied to this type of data, we present the experiments we used for validation and the corresponding results obtained sections 3 and 4, respectively, discuss their implications in section 5, and summarize our conclusions in section 6.

2. METHODS

The work presented here assumes the availability of a nominal discretized surface model for the heart and torso geometries; however we do not assume that the position of the heart within the torso is accurately known. The torso is treated as homogeneous in the experiments reported here but this is not required by the method as long as the geometry of any other organs included in the model is known. The electrical activity of the heart is modeled as a time series of potentials on a surface that surrounds the ventricles. (Again, extension to alternative source models would be straightforward). We further assume that we have available potentials measured on the heart and torso surfaces at multiple time instances, denoted $x_b(t)$ and $y_b(t)$, respectively, where we index time within a beat by t and heartbeats by b. Under these assumptions, the electrical forward model is represented in the form of a forward matrix (denoted A) with the heart at some reasonable position in the torso volume. We refer to the matrix A that corresponds to this nominal position in the sequel as the "nominal" forward solution. We note that this nominal position will be used as a starting point in our iterative algorithm but that there is no requirement that it be particularly accurate; we assume that a nominal model computed from imaging scans will provide a reasonable "initial guess." With these assumptions, we have the following putative nominal relationship between heart and body surface potentials (MacLeod and Buist, 2010):

$$y_b(t) = Ax_b(t). \tag{1}$$

Our work assumes that the heart can change position at every heartbeat b; thus Equation (1) must be extended to reflect the corresponding changes in the forward model. We postulate an equivalent sequence of forward models, $A(p_b)$, parameterized by a joint position and orientation parameter vector p_b, that relates the position of the heart to the measured body and heart surface potentials.

$$y_b(t) = A(p_b)x_b(t). \tag{2}$$

We chose a specific parameterization that effectively characterizes the expected translation and rotation of the heart due to respiration. In particular, although the respiratory movement of the heart is subject specific, there are common features that can be leveraged to describe it: the heart translates vertically and undergoes rotation around a tethering point on the left atrium (Netter, 2006; Coll-Font et al., 2011; Aras et al., 2015). Based on this description, we defined translation parameters using a standard coordinate system (from the EDGAR database formulation; Aras et al., 2015), and defined rotations with respect to two anatomical references: one is an anchor point placed at the centroid of the atria and the other a septal axis that crosses the heart through the septum from that atrial anchor point to the apex (see **Figure 1** for illustration). Based on these references the rotation angles are defined as:

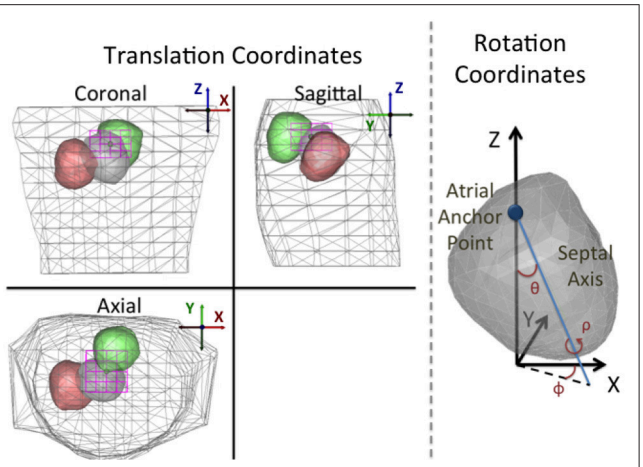

FIGURE 1 | Depiction of the parameterization of the translation and rotation coordinates. **Left**: Standard orthogonal projection views of the torso and heart for three different position/angle combinations. Translation coordinate axes are defined following the convention presented in the EDGAR repository (Aras et al., 2015). The magenta box shows the translation bounding box for the assumed anchor point. As described in the text, the translation and angle constraints are defined such that the heart geometry can never intersect the torso surface. **Right**: Rotation angles defined on the heart. Pitch (θ): the angle formed between the Z axis and the septal axis. Yaw (ϕ): the angle that the septal axis projected on the X/Y plane forms with the X coordinate. Roll (ρ): the rotation of the heart around the septal axis.

- Pitch (θ): the angle formed between the Z axis and the septal axis.
- Yaw (ϕ): the angle formed between the septal axis projected on the axial plane and the X axis.
- Roll (ρ): the rotation of the heart around the septal axis.

Once this parameterization is defined, the generation of forward matrices requires moving the heart to the position and rotation described by the parameters p_b and then computing the corresponding forward matrix with an appropriate forward solver.

The implicit function $A(p_b)$ defined in this formulation is a manifold in the space of matrices. It is a non-linear, continuous and smooth function—i.e., small variations in the position of the heart will lead to small changes in the forward matrix—and hence it can be used in an optimization framework. Specifically, we need to solve an optimization problem that searches for the translation and rotation parameters of the heart—within some reasonable bounds—that minimize the error between ECG potentials synthesized using Equation (2) and the potential measurements on both surfaces. The main assumption in this optimization problem is that the dominant error observed in the synthesized potentials is caused by errors in the position and orientation of the heart and that other sources of error can be modeled as additive white Gaussian noise or are negligible. This results in a non-linear least-squares problem over the

six-dimensional vector p_b, restricted in each dimension to a hyper-rectangle as in Equation (3).

$$\min_{p_b} \sum_t \|y_b(t) - A(p_b)x_b(t)\|_2^2 \quad st. p_b \in \Xi \tag{3}$$

were the norm is taken over both time and space. The hyper-rectangle constraint, illustrated in **Figure 1** and denoted as Ξ, was defined a priori to prevent any intersection between the heart geometry and the torso surface.

This constrained non-linear optimization problem can be solved with any off-the-shelf solver. In the particular case of these experiments, we used MATLAB's default iterative solver of the fmincon function[1], which implements an Interior-Point method with numerically approximated gradients and Hessians..

We note that in this problem the solution is constrained to lie on a non-linear manifold induced by the parameterization in a high-dimensional subset of matrices restricted to be approximations to the underlying PDE. Thus the problem is difficult to analyze mathematically and, in particular, we have no guarantee that it is well-posed[2]. However these restrictions imposed on the solution are highly constraining. Thus we believe it is reasonable to hypothesize that solutions are stable. Our experimental results, as reported below, support this hypothesis.

3. EXPERIMENTS

The immediate purpose of the work presented here is to determine if in fact the translation and rotation of the heart estimated by our proposed algorithm can reduce the effects of model errors present in the numerical and physical experiments we studied. To that purpose, we both created synthetic data to model respiratory movement and employed data recorded during three different torso-tank canine experiments conducted at the Cardiovascular Research and Training Institute (CVRTI), University of Utah.

Synthetic Data:

We generated synthetic respiratory motion influenced data using the **sock2** heart and body surface geometry described below and the potentials from a single beat on the epicardial surface recorded with an electrode mesh, also as described below. Starting from a nominal position inside the homogeneous torso model, we moved the heart to 10 different positions and orientations following a respiratory-like trajectory described in (Coll-Font et al., 2011).[3] For each of these positions/orientations, we synthesized one heartbeat of BSPM using a forward model computed from that geometry using the Boundary Element Method (BEM) provided with the SCIRun software system (SCI-Institute, 2014)[4] and added independent Gaussian noise to achieve an SNR = 30 dB. We then fed the epicardial and body surface data and the (incorrect) nominal forward model into our algorithm and attempted to estimate the corrected position and orientation of the heart for each of the 10 beats. We repeated this procedure 10 times for different realizations of the pseudorandom noise.

Experimental Data:

Data was generously provided to us from canine experiments that had been carried out for previous studies with applicable IACUC approval. These experiments consisted of unipolar recordings of potentials on or near the epicardial surface of an explanted canine heart measured simultaneously with similar recordings on the surface of a torso-shaped tank in which the heart was suspended (MacLeod et al., 1995a,b). The tank was filled with conductive medium. The homogeneous conducting medium and the availability of unipolar recordings on both surfaces match the assumptions described in section 2. During the experiment, the suspended heart was kept alive through retrograde perfusion with blood from a "support" animal that provided circulation through the left anterior descending (LAD) artery. This setting allowed the experimenters to both pace the heart at different locations, through electrodes placed intramurally or on the heart surface, and to induce ischemia by either accelerating the pacing rate or by occluding the LAD. At the end of the experiment, the heart was vertically raised from its position during the experiment and the 3D coordinates of several electrodes were digitized and used to register the heart geometry to its estimated position within the tank. This registration procedure includes the measured vertical displacement of the heart, thus assuming that it was raised and lowered into the tank with no inclination with respect to the tank geometry. Note that buoyancy effects and tension from electrical cables and blood supply tubing might introduce error in the geometry that is not corrected by the registration.

We used this measured geometry to construct our nominal forward model, again computed with the SCIRun BEM solver, and then used the recorded potentials on both surfaces over multiple beats in the method described above to estimate the position and orientation of the heart on a beat-by-beat basis.

Two different experimental methods were used to record the heart surface potentials. In one experiment, the heart was enclosed in a small wire cage with electrodes on the cage itself. In the other two, a mesh, or "sock," that had been wired with a large number of electrodes was stretched around the heart surface and tightly tied around the ventricles. **Figure 2** shows visual examples of the apparatus during an experiment. These two heart surface potential measurement approaches have respective benefits and drawbacks. The cage electrodes are placed at some distance

[1]Beyond the default configuration, we set the function and objective tolerance at 10^{-6} and extended the function evaluations to 10^{10}

[2]In theory rotational symmetries of the heart geometry could produce non-uniqueness of the parameterization itself, but this is not a practical concern with a realistic heart shape, and in addition in the setting under study here we have access to the potentials on both surfaces, so that even rotational symmetries are removed modulo a highly improbable symmetry in the heart surface potentials as well as its geometry.

[3]The respiratory-like trajectory was interpolated from a time series of sagittal MRI scans of the torso at different phases of the respiratory cycle

[4]The SCIRun BEM solver is a standard BEM implementation for potential sources on an interior closed (epicardial) surface and measurements on an bounding closed (torso) surface, based on the classical "solid angle" integrations. Boundary conditions are the known epicardial potentials and an insulating boundary on the body surface; electrodes are treated as point electrodes with infinite impedance.

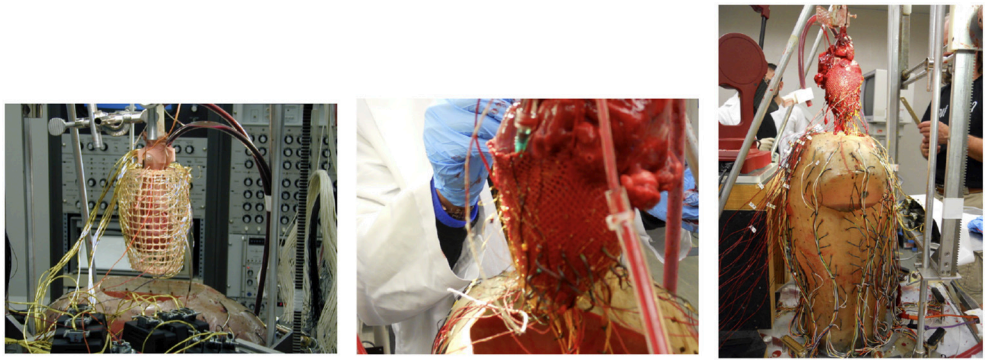

FIGURE 2 | Pictures of the recording devices on the heart using a cage geometry **(Left)**, a sock geometry **(Middle)**, and the entire experimental apparatus **(Right)**.

from the heart and thus measure its electrical activity over a rather broad area, resulting in considerable spatial smoothing of potential distributions compared to measuring them directly on the heart surface. In contrast, the sock electrodes measure more local, spatially resolved, electrical activity. However, the sock is flexible and hard to fix in place on the heart surface, and its geometry is sensitive to contraction, swelling of the heart, and any other changes in heart shape, and in addition may be displaced during any interventions. Moreover the sock moves as the heart moves, and the heart was not securely fixed in a consistent, repeatable, and accurately measurable location during the entire experiment. In contrast the position of the cage is easier to both measure and maintain throughout the experiment. Thus sock recordings are more prone to error in the geometric model, including time-varying errors, than are cage recordings. Another technical limitation of the sock is that the electrodes only cover the ventricles, leaving an opening around the atria. In order to use BEM forward solvers, the heart geometry must form a closed surface, thus requiring the generation of "extra" nodes closing the geometry for which there are no actual measurements available. By contrast the cage has electrodes that completely surround the heart surface.

Two views of the nominal geometries are shown for the three experiments are shown in green (torso) and black (heart) in **Figure 8**.

3.1. Additional Details for the Experimental Datasets

We note that these three experiments were carried out at different times on three different animals, one using the cage and two using socks; for clarity we label these experiments in what follows as **cage**, **sock1**, and **sock2**. We describe further details about each of these experiments next.

cage: In this experiment the electrical activity of the heart was measured with a cage geometry containing 599 electrodes surrounding the heart and with 192 electrodes on the tank surface. The experimental procedure consisted of recordings during a series of ventricular pacings at four different sites followed by three series of ischemic episodes, as described above, all during sinoatrial pacing.

sock1: The sock used was outfitted with 247 electrodes and again there were 192 electrodes on the tank surface. Extra nodes, with no corresponding measurements, were added to the sock geometry to close the surface above the base of the ventricles, leading to a total of 337 nodes in the epicardial geometry mesh model. Ischemic interventions were interleaved with control periods; in this experiment there were 4 such ischemic episodes. All heartbeats during the experiment were paced at the sinoatrial node.

sock2: The sock, epicardial mesh model, and tank had the same dimensions as in **sock1**. The interventions consisted of an ischemic experiments with sinoatrial pacing followed by a series of ventricular pacings at five different locations. The specific sequence of interventions was: two initial series of sinoatrial paced control recordings, a series of ventricular pacings at various locations, and then a sequence of two ischemic interventions interleaved with control recordings, all under sinoatrial pacing. One important difference between this experiment and the others is that, after the first of the two initial series of control recordings, the heart was raised above the top of the tank and needle electrodes were inserted into the myocaridal wall (to be used for the ventricular pacing), and then the heart was lowered to the original nominal position. This difference plays a significant role in the results reported below.

Preprocessing: Before using the experimental data in both synthetic and experimental settings, we extracted the QRS complex from each heartbeat of both heart and torso surface recordings and applied a moving average filter of length 20 ms to both sets of signals to reduce noise. In the synthetic setting, only the heart surface recordings from one beat were used, while in the experimental setting all the data from both surfaces were used.

3.2. Computational Procedure and Validation Details

We applied our geometry correction method to estimate the rotation and translation of the heart for each synthesized or recorded heartbeat. Given those estimated parameters we computed a corrected forward matrix for each heartbeat, synthesized the corresponding corrected BSP using the measured

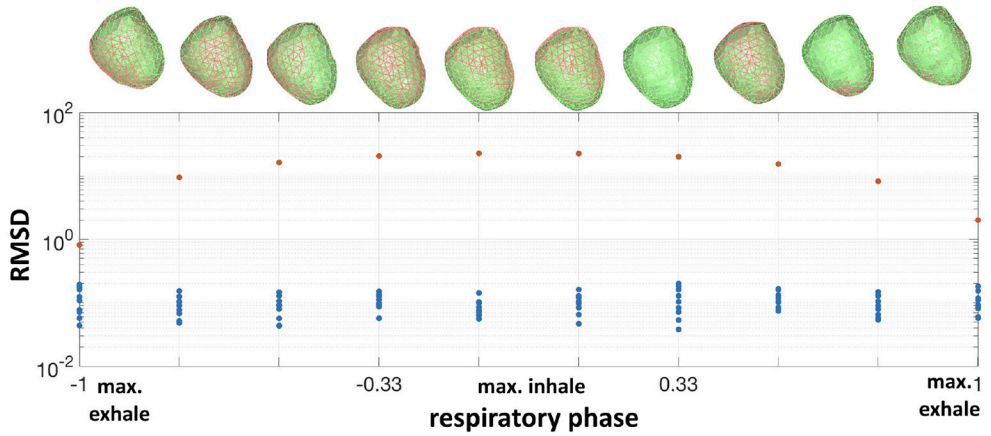

FIGURE 3 | Bottom: RMSD of the nominal heart (red dots) vs. corrected (blue dots) for all respiratory phases. **Top**: corresponding true heart geometry (green) and corrected (red) for one repetition.The horizontal axis is normalized respiratory phase on a scale from −1 to 1.

heart potentials as described in Equation (2), and computed two sets of inverse solutions using the synthesized / measured BSP and both the nominal and corrected forward matrices. We calculated inverse solutions using a zero'th order Tikhonov regularization solver (Equation 4).

$$\min_{x_b(t)} \|y_b(t) - A_b x_b(t)\|_2^2 + \lambda^2 \|x_b(t)\|_2^2 \tag{4}$$

where the norm was taken over both space and time within a single QRS. We used the L-curve method with 100 lambdas equally spaced between 10^{-6} to 1 on a logarithmic scale. We computed each point of the L-curve using all time instances within a beat to determine a single regularization parameter (λ) (Hansen, 2007) per beat.

Given these results, we calculated the relative error for beat b as the sum squared differences across all electrodes (l) and time instances (t) between measured BSP ($y_b(l,t)$) and BSP synthesized using the corrected geometry ($\hat{y}_b(l,t)$) divided by the sum-of-squares of the measured BSP (Equation 5).

$$relErr_b = \frac{\sum_l \sum_t (y_b(l,t) - \hat{y}_b(l,t))^2}{\sum_l \sum_t y_b(l,t)^2} \tag{5}$$

To show the degree of improvement, we also computed the BSP relative error using the nominal geometry in the same fashion. Similarly, we computed the relative errors for the estimated cage/sock potentials for both corrected and nominal geometries. In the case of the synthetic experiment, where the true heart geometry was available, we also computed the root-mean-squared error (RMSD) between the true and corrected geometries as the square root of the average sum-of-squares of per-node errors (thus combining translation and rotation errors) across all nodes on the heart.

4. RESULTS

In the **synthetic** experiments, as described above, we calculated the misplacement after correction at each time instant. The average RMSD after correction was 0.1 ± 0.04mm, compared to an average error of 13.7 ± 8mm before correction. To illustrate this result we plot the evolution of the RMSD and true and corrected heart geometries as a function of respiratory phase in **Figure 3**. As expected, the error of the nominal heart increased when approaching maximum inhale position, reaching 22.7 mm. This increase in error corresponds to the vertical displacement and slight rotation of the heart geometry. On the other hand, the RMSD for the corrected geometries was close to 0mm for most beats with a maximum RMSD of 0.19mm. This small RMSD can be observed in the almost indistinguishable true and corrected geometries shown in the figure.

We obviously cannot calculate actual misplacement for the three canine experiments, but we can study the differences between measured and synthesized signals both before and after correction. We plot these results in terms of relative error, as described above, in the form of histograms in **Figure 4**. To make comparisons easier, we used color to allow us to report all results for a single experiment on one plot. We report errors for both nominal geometries (top row of panels) and corrected geometries (bottom row) and for both errors in body surface potentials (left panels) and reconstructed EGMs (right). Color designates the specific experiment as shown in the legend. Each bar in the histogram shows the number of beats with relative error in the bin designated by the value on the horizontal axis at the position of the bar. So, for example, the red bars in the top left panel show that relative errors in the body surface potentials for the nominal geometry were distributed between 0 and 0.25, while after correction, in the bottom left panel, they were concentrated very close to zero, indicating the improvement after the correction.

From the top-left panel, we see that for the **synthetic** experiment the relative error between nominal and uncorrected forward-computed BSPM is rather evenly distributed between 0.0 and 0.17. For the **cage** experiment the relative error is in the same range and very stable across heartbeats—the average ± standard deviation BSPM relative error was 0.1 ± 0.01. For

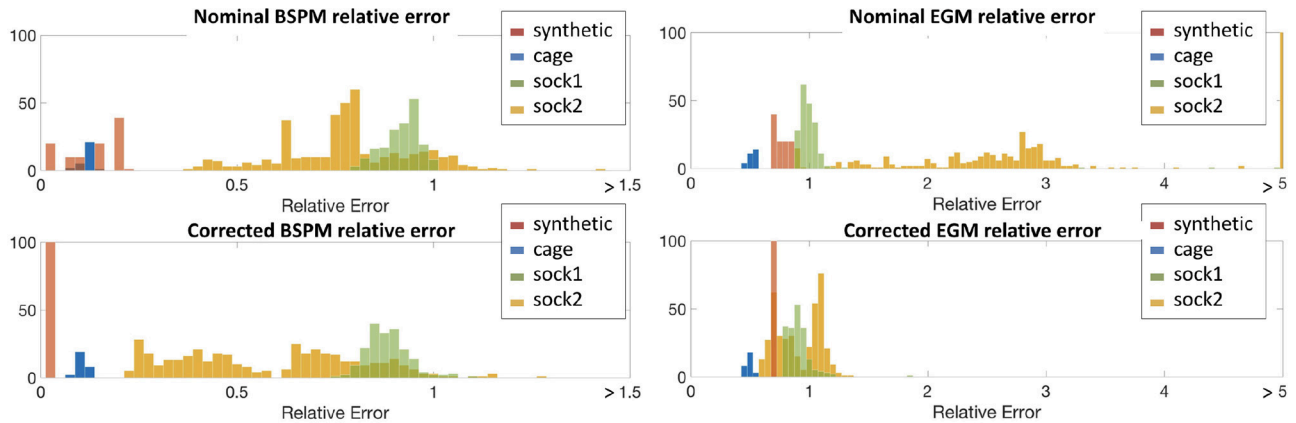

FIGURE 4 | Histograms of relative errors for forward-computed BSPM (**Left**) and inverse-computed cardiac electrograms (EGM) (**Right**) potentials for all four experiments. Top row shows the relative error computed using the nominal geometry, bottom row using the corrected geometry. Data is shown from all four experiments in each panel: **synthetic** (red), **cage** (blue), **sock1** (green), and **sock2** (yellow).

sock1 the relative error was again stable across all the recorded heartbeats but larger in magnitude (0.79 ± 0.06). In contrast for **sock2** although the mean relative error was similar to **sock1**, the variability was considerably larger (0.8 ± 0.25).

In the case of the inverse-computed EGM solutions, shown in the right column of the same row, the first notable observation about results from the nominal geometry is that the range of relative errors is, as might be expected due to ill-posedness, much higher than for the BSP. However within this range we note similar differences among results for the four experiments: a uniform distribution for **synthetic** data (0.76 ± 0.06), lower mean error and small variability for the **cage** data (0.5 ± 0.03), higher mean error but again small variability for the **sock1** data (1.3 ± 0.39), and much higher variability for the **sock2** data (3.8 ± 6.8). We also can observe that here the mean error for **sock2** was also higher than for **sock1**, in contrast to the results for the BSP's.

The bottom panels indicate a clear reduction in the relative error when geometry correction is applied. Numerically, the improvement in BSP relative error—measured as the difference between corrected and nominal relative error— was 0.07 ± 0.04 for **synthetic**, 0.02 ± 0.005 for **cage**, 0.1 ± 0.02 for **sock1**, and 0.3 ± 0.11 for **sock2**. The corresponding improvement in inverse-computed heart potential relative error was 0.067 ± 0.06, 0.02 ± 0.01, 0.4 ± 0.4, and 3 ± 6.4, respectively. Thus we see that the improvement is more pronounced for the inverse solutions than for the synthesized BSP, and greater in **sock2**. We also note that in general the improvement in inverse solutions, on average, accounted for much of the error we found using the nominal models.

We show some illustrative potential maps taken as a snapshot at the QRS peak to give more insight into these summary results in **Figure 5**, which shows isopotential maps on the body and heart surfaces for representative beats. Maps of measured potentials are shown in the top row, maps of the nominal potentials in the middle, and maps of the corrected potentials in the bottom. The columns correspond to different example cases. The left column shows the heartbeat whose improvement in BSP relative error is closest to the median relative error of 0.18 across all three canine experiments, while the middle column shows the heartbeat with smallest relative error improvement, 0.006, and the right column shows the heartbeat with the biggest improvement, 0.56, again across all beats in all experiments. The median beat was sinoatrially paced and from **sock2**, the beat with biggest improvement is a ventricularly paced beat, also from **sock2**, and the smallest improvement beat comes from the **cage** experiment. Visually, the geometry correction provides a noticeable improvement for the "biggest" example beat, moderate improvement for the median example, and no obvious change for the "smallest" example.

Since the results for **sock2** were significantly more dramatic than those for **sock1** we examined the results from that experiment more carefully, as reported in **Figure 6**. We divided this experiment into into 11 consecutive stages that correspond to different control, pacing, and intervention epochs, briefly described in the table at the bottom of **Figure 6**. The errors summarized in the whisker plots at the top of the figure have considerable variability across all beats and interventions and decrease when using the corrected geometry. This decrease is more pronounced in the EGM inverse solutions, which appear to be very sensitive to the variations in the geometry. One noticeable result is that the first sequence of sinoatrial pacings—before the insertion of the needles—shows smaller relative error using the nominal geometries and correcting the geometry does not yield much improvement.

In **Figure 7**, we show heart potential maps at peak QRS of a representative beat for each of the above stages of this experiment, as indicated by the headers using the codes from the table in **Figure 6**[5]. We note that in all stages after the

[5]In each case the illustrated beat was selected as the beat with BSP relative error closest to the median of each group

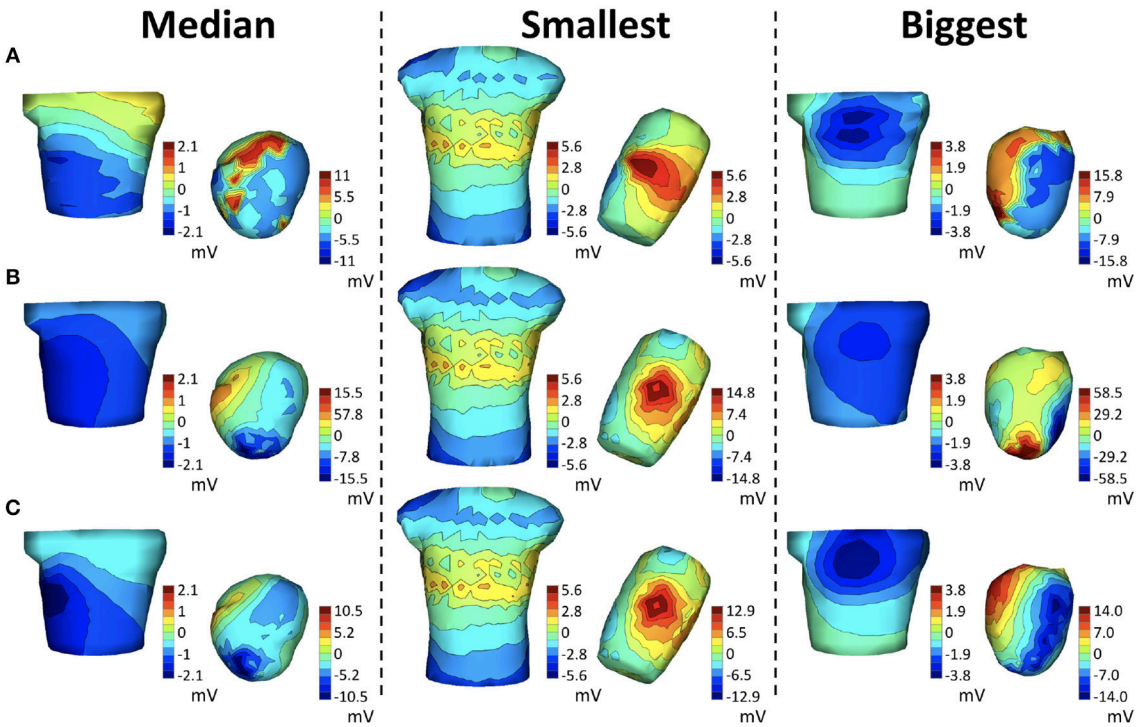

FIGURE 5 | Potential maps of representative examples across all real experiments at QRS peak. The left column corresponds to the beat closest to the median BSP across all three canine experiments of the relative error improvement (0.18 in **sock2**), the middle column to the smallest improvement (0.006 in **cage**) and the right column to the biggest improvement (0.56 in **sock2**) across all experiments. Each row shows the BSP and EGM maps of the measured potentials **(A)**, maps synthesized with the nominal geometries **(B)** and maps synthesized with the corrected geometry **(C)**.

insertion of the needles the inverse maps are more similar to the originals when the corrected geometry is used, and that the ventricularly paced beats show the most noticeable improvement.

Looking at the reconstructed geometries themselves, in **Figure 8** we illustrate the torso-tank geometries (in green), the nodes of the nominal heart geometry (in black) and the nodes of all corrected heart geometries (all other colors), from the three canine tank experiments. The behavior of the solutions varies depending on the experiment, although they cluster around a central location in each. As expected, the cage experiment does not show much change from the nominal geometry. The root mean square distance (RMSD) between the nodes of the nominal and corrected geometries is 4.5 ± 0.8 mm. On the other hand, the sock experiments show considerable variability across heartbeats. Specifically, **sock1** has an RMSD of 22.6 ± 4.8 mm and **sock2** 51.3 ± 4.8 mm. The average translation and rotation of the θ angle—pitch of the heart—of the corrected hearts with respect to the nominal position are 20.3 mm and 19.1° for **sock1** and 37.2 mm and $\theta = 51.8^\circ$ for **sock2**. Importantly, the heart in **sock2** has an estimated pitch rotation of $\sim 50^\circ$ after the insertion of the needles with respect to before the needles were inserted. To illustrate this change, **Figure 8** shows the median estimated position and orientation of the heart before and after insertion of the needles in this experiment.

5. DISCUSSION

The results presented above support the hypothesis that our method does improve the quality of the forward models. The method reliably corrected the heart geometry for the **synthetic** experiment, where ground truth was known, and provided considerable improvement in relative error of the inverse solutions. Moreover, although there is still unexplained error after applying our geometry correction to the real experiments, the estimated translations and rotations of the heart provide considerable improvement in both the synthesized BSP and all inverse solutions, in terms of both relative error and visual features of potential maps. In addition we note that inverse solutions improved notably even in some cases when the reduction in BSP error was small. The improvement was particularly strong for the **sock2** experiment, in which the broad spread of the error distribution of the inverse solutions with the nominal geometry was reduced to a much more concentrated one, similar to what was seen with **sock1**, after the correction.

We also observe that the positions of the heart estimated by this method are not randomly distributed throughout the torso, but rather show a physically meaningful structure: in particular, the largest correction factor is rotation near the anchor point above the atria. Moreover, the large rotation in **sock2** appears only after the insertion of the needles, suggesting that the needle cables could have been pulling the apex in an upwards direction.

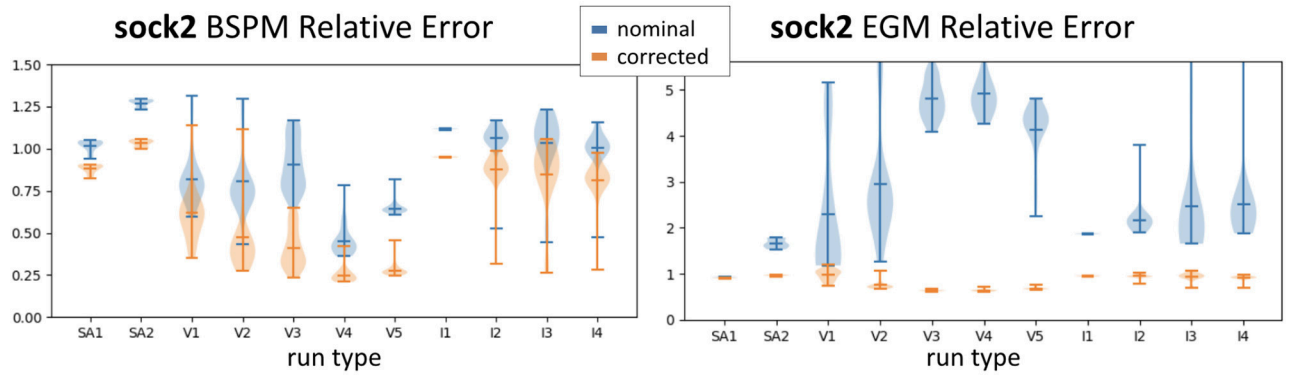

Code	Description	BSPM nominal	BSPM corrected	EGM nominal	EGM corrected
SA1	Atrial pacing before insertion of needles	1.02 +/-0.04	0.88 +/-0.03	0.93 +/-0.01	0.91 +/-0.01
SA2	Atrial pacing after insertion of needles	1.27 +/-0.03	1.03 +/-0.02	1.66 +/-0.10	0.97 +/-0.01
V1	Ventricular pacing from the LV-base	0.82 +/-0.16	0.62 +/-0.17	2.29 +/-1.38	0.97 +/-0.12
V2	Ventricular pacing from the LV-apex	0.81 +/-0.18	0.47 +/-0.22	2.94 +/-1.22	0.75+/-0.10
V3	Ventricular pacing from the LV-septum	0.91 +/-0.15	0.41 +/-0.12	4.80 +/-0.43	0.64 +/-0.01
V4	Ventricular pacing from the LV-freewall	0.45 +/-0.09	0.25 +/-0.04	4.91 +/-0.73	0.64 +/-0.02
V5	Ventricular pacing from the RV-wall	0.64 +/-0.03	0.28 +/-0.03	4.14 +/-0.60	0.68 +/-0.02
I1	Atrial pacing, normal perfusion, control 1	1.12 +/-0.00	0.95 +/-0.00	1.87 +/-0.01	0.95 +/-0.01
I2	Atrial pacing, ischemia intervention I-1	1.06 +/-0.10	0.88 +/-0.11	2.16 +/-0.29	0.95 +/-0.04
I3	Atrial pacing, normal perfusion, control 2	1.03 +/-0.20	0.85 +/-0.22	2.47 +/-1.34	0.93 +/-0.09
I4	Atrial pacing, ischemia intervention I-2	1.00 +/-0.12	0.81 +/-0.13	2.51 +/-1.06	0.92 +/-0.05

FIGURE 6 | Summary of results for **sock2**. **Top**: whisker plots show relative error of BSPM **(Left)** and EGM **(Right)**. Blue whiskers correspond to relative error computed using the nominal geometry and orange using the corrected geometry. **Bottom**: the table contains a brief description of the type of intervention and summary statistics of the results.

By contrast, the small change in the cage geometry experiment confirms the stability of the algorithm when the geometry is already accurate.These results suggest that the algorithm is detecting meaningful changes in position and orientation and not just overfitting to the noise.

On the other hand, there are some characteristics of the solutions in the sock experiments that are not consistent with the experimental setup. In particular there is a beat-to-beat variability around the central position that exceeds what might be expected, and the heart appears to be translated toward the edge of the bounding box of the optimization, well beyond what the experimental apparatus would permit. We believe that these errors are introduced by unmodeled sources of noise such as error in the shape of the heart and the lack of measurements around the atrial surface.[6] Perhaps future developments, including estimating shape deformations as well as translation and rotation, as well as better characterization of the missing measurements (as was done in the cage experiment) could reduce these effects.

We also observe that although **sock2** showed considerable variability in the relative error of inverse solutions, the variability of the estimated position of the heart was relatively small (standard deviation of RMSD is 5.7 mm after the insertion of the needles). In fact, **sock1** showed much less variability in inverse solution relative error despite a similar standard deviation in RMSD (5.8 mm). The main difference between these two experiments was, however, in rotation correction, which was much larger for **sock2**, suggesting that rotation accuracy is a rather important factor in geometry model errors for ECGI.

In order to avoid constraining this approach to a specific forward solver, we used a black-box optimization method to solve Equation (3). For specific forward solvers and definitions of the geometry transformation, it should be possible to derive the corresponding gradients and Hessians for $A(p_b)$ such as in (Babaeizadeh and Brooks, 2007; Babaeizadeh et al., 2007) where we previously described how to compute Jacobians of both BEM and FEM models with respect to translation; Jacobians for rotation should also be possible to compute based on this work via the chain rule and appropriate rotation matrices.These

[6]The sensitivity of the solutions to the lack of measured data on the atria can be taken as another indication that solutions are indeed sensitive to the measurements, that is, that the problem is reasonably well-posed.

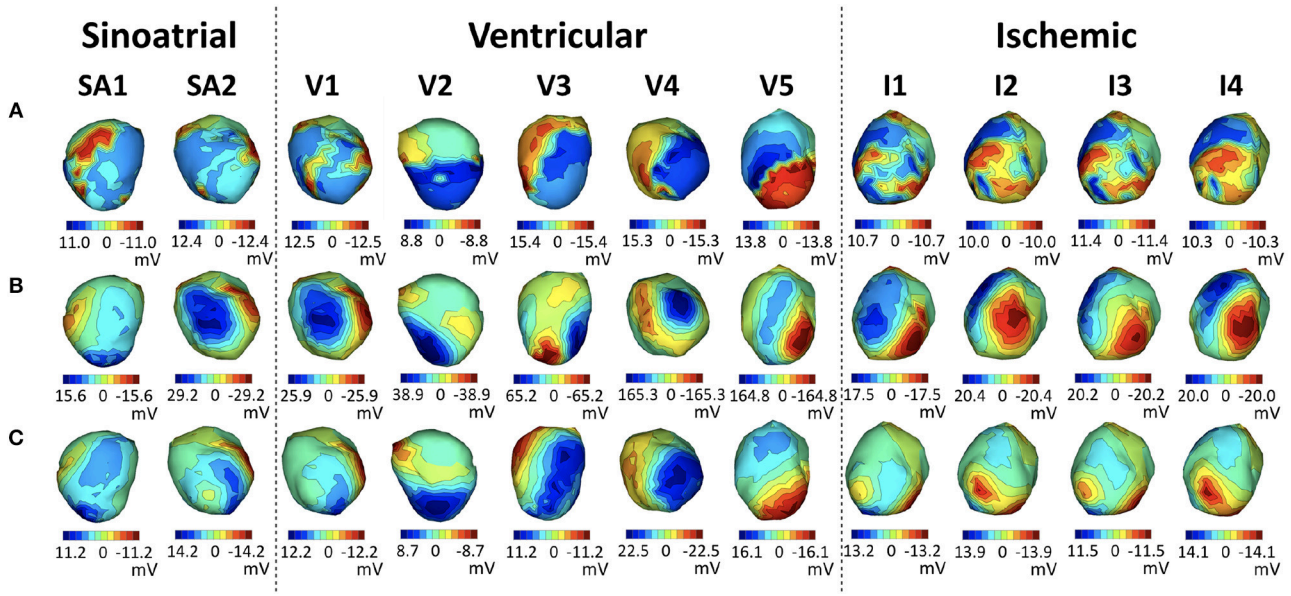

FIGURE 7 | Representative examples of each stage of the **sock2** experiment. Each row shows EGM maps at QRS peak of the measured potentials **(A)**, synthesized with the nominal geometries **(B)** and synthesized with the corrected geometry **(C)**. Each column corresponds to a representative solution from each stage of the experiment, as described in the table in **Figure 6**.

analytical derivations should speed up the optimization and reduce the current computational demands of the method. However in the current work, since the computational demands were modest and easily within the scope of the Matlab solver we employed, and since as noted we preferred to be as general as possible in our presentation, we leave working out the details of such an approach to future work. However in cases with more densely sampled geometries, inclusion of more organs, or more complex source models, it might be necessary to explore alternative optimization approaches that are computationally less demanding. For example, in addition to analytically-based derivative computation, it may be useful to approximate the geometry with a smaller mesh or interpolate the manifold of forward matrices $A(p_b)$ with a continuous function that provides simpler analytic gradients and faster computation (Coll-Font, 2016). A second algorithmic consideration is that we are solving a non-linear optimization problem, which can have local minima. We have observed in our experiments to date that the nominal position of the heart is a good initial guess for global convergence using convex optimization solvers. However, this might not be applicable to all geometries and heartbeats and could be addressed, for example, by restarting the algorithm with different initial guesses or using global optimization techniques. An example of the latter that also addresses computational efficiency challenges is the class of Bayesian Optimization methods (Coll-Font et al., 2017), which carry out smart sampling of the unknown objective function based on a probabilistic representation that approximates it.

We want to point out that we used the zero-th order Tikhonov inverse method because it is so widely used for ECGI and its behavior is well-understood. However, this method tends to produce overly smooth inverse solutions with high relative error, even for ideal geometries, which may impact numerical results. Future work using other inverse methods might provide a better understanding of the interplay between regularization methods and geometry errors. Moreover, in settings where our simplified geometry assumptions—homogeneous torso and epicardial surface model—do not hold, we speculate that inverse solutions might show greater sensitivity to the accuracy of the position of the heart and thus benefit even more from the methods presented here.

A significant challenge for validation of our methodology is the lack of datasets with a reliable measurement of the real time-varying (e.g., from respiration) position of the heart. All existing ECGI datasets that we are aware of assume a static heart geometry and only provide a measure of its position at the beginning or the end of the experiment. Thus, existing datasets either have a highly accurate nominal geometry—which is not generally representative of clinical practice—or have geometry errors that pose a challenge to most ECGI methods. To better validate the method presented here, it would be helpful in the future to generate datasets with a continuous measure of the position of the heart using an external measurement modality such as with ultrasound.

Finally, an important follow-up to this work will be to incorporate estimation of the heart potentials along with the geometric changes, thus allowing extension of the scope of this method to clinical ECGI settings. Our initial work on this approach indicates that such an extension is possible and may provide useful results (Coll-Font, 2016; Coll-Font et al., 2017); a more extensive evaluation is currently underway.

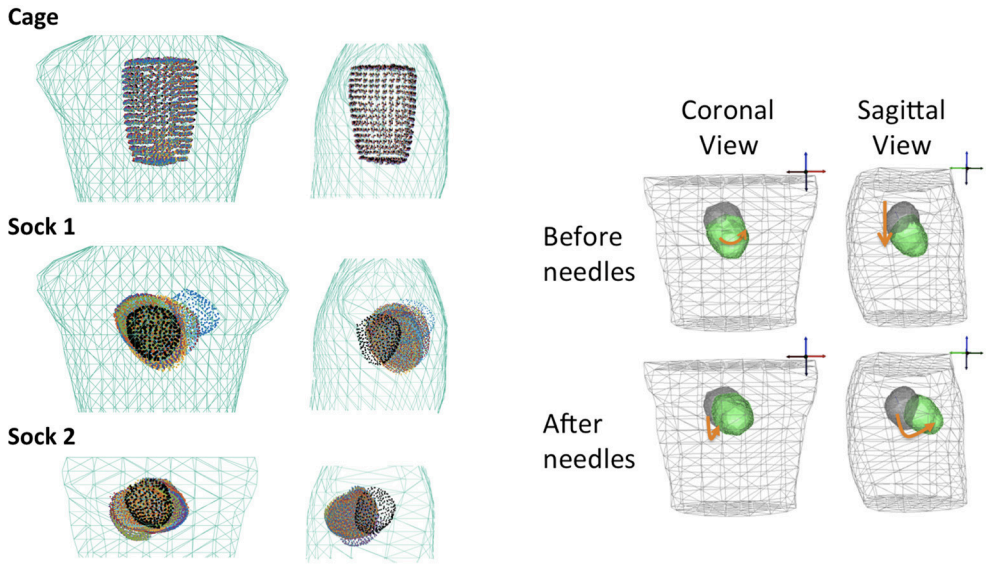

FIGURE 8 | Left: Close-up of the nominal torso (green) and heart (black) geometries. The hearts corrected with the algorithm are overlaid in a different color per heartbeat. Top geometry is **cage**, middle is **sock1** and bottom is **sock2**. **Right:** Median position of the heart in **sock2** before the insertion of the needles (top) and after the insertion of the needles (bottom).

6. CONCLUSIONS

In this work, we have introduced an approach to correct for the position and orientation of the heart inside the torso based purely on changes in electrocardiographic recordings along with an initial, nominal, geometry. We have shown that this approach can improve the forward models for both forward and inverse estimation of potentials and that it can provide useful insight for current experimental procedures used to validate ECGI methods. Moreover, the algorithm may be a first step toward solving the problem of joint estimation of the potential distribution on the heart and the heart's position and orientation within the torso.

We also add that our method may have implications beyond improving forward models in ECGI since the ability to non-invasively track the position of the heart might impact a number of other clinical problems, for example, improving catheter registration in ablation procedures.

ETHICS STATEMENT

This study was carried out in accordance with the animal treatment and ethical research recommendations of the IACUC at the University of Utah. The protocol was approved by the IACUC at the University of Utah.

AUTHOR CONTRIBUTIONS

Both authors have made a substantial, direct and intellectual contribution to the work, and approved it for publication.

FUNDING

Support for both authors came from the Center for Integrative Biomedical Computing under grant number P41 GM103545-18 from the National Institute of General Medical Sciences of the National Institutes of Health.

ACKNOWLEDGMENTS

We would like to thank the experimenters at the CardioVascular Research and Training Institute at the University of Utah for providing the canine data used in this work.

REFERENCES

Adams, M. G., and Drew, B. J. (1997). Body position effects on the ECG:implication for ischemia monitoring. *J. Electrocardiol.* 30, 285–291.

Amoore, J. N., Rudy, Y., and Liebman, J. (1988). Respiration and the ECG: a study using body surface potential maps. *J. Electrocardiol.* 21, 263–271.

Aras, K., Good, W., Tate, J., Burton, B., Brooks, D., Coll-font, J., et al. (2015). Experimental data and geometric analysis repository - EDGAR. *J. Electrocardiol.* 48, 975–981. doi: 10.1016/j.jelectrocard.2015.08.008

Babaeizadeh, S., and Brooks, D. H. (2007). Electrical impedance tomography for piecewise constant domains using boundary element shape-based inverse solutions. *IEEE Trans. Med. Imaging* 26, 637–647. doi: 10.1109/TMI.2006.887367

Babaeizadeh, S., Brooks, D. H., and Isaacson, D. (2007). 3-D electrical impedance tomography for piecewise constant domains with known internal boundaries. *IEEE Trans. Biomed. Eng.* 54, 2–10. doi: 10.1109/TBME.2006.886839

Bear, L. R., Cheng, L. K., LeGrice, I. J., Sands, G. B., Lever, N. A., Paterson, D. J., et al. (2015). Forward problem of electrocardiography: is it solved? *Circ. Arrhythm. Electrophysiol.* 8, 677–684. doi: 10.1161/CIRCEP.114.001573

Cluitmans, M. J. M. and Volders, P. G. A. (2017). "Influence of body-surface geometry accuracy on non-invasive reconstruction of electrical activation and recovery in electrocardiographic imaging," in *2017 Computing in Cardiology (CinC)* (Rennes), 1–4.

Coll-Font, J. (2016). *Model Based Approaches to Incorporate Recordings of Multiple Heartbeats into the Inverse Problem of Electrocardiography*. Ph.D. thesis, Northeastern University.

Coll-Font, J., Ariafar, S., and Brooks, D. H. (2017). ECG-based reconstruction of heart position and orientation with bayesian optimization. *Comput. Cardiol.* 44, 1–4. doi: 10.22489/CinC.2017.054-387

Coll-Font, J., Brooks, D. H., and Tadmor, G. (2011). *Comparison of Low-Order 4D Dynamical Models for Cardiac Respiratory Motion Using MRI*. Ph.D. thesis, Universitat Politècnica de Catalunya, Barcelona.

Coll-Font, J., Dhamala, J., Potyagaylo, D., Schulze, W. H., Tate, J. D., Guillem, M. S., et al. (2016a). "The consortium for electrocardiographic imaging," in *2016 Computing in Cardiology Conference (CinC)* (Vancouver, BC), 325–328.

Coll-Font, J., Roig-Solvas, B., van Dam, P., MacLeod, R. S., and Brooks, D. H. (2016b). Can we track respiratory movement of the heart from the ECG itself and improve inverse solutions too? *J. Electrocardiol.* 49:927. doi: 10.1016/j.jelectrocard.2016.09.016

Dehaghani, A. R. (2015). *Uncertainty Quantification and Reduction in Cardiac Electrophysiological Imaging Uncertainty Quantification and Reduction in Cardiac Electrophysiological Imaging*. Ph.D. thesis, Rochester Insitute of Technology.

Erem, B., Coll-Font, J., Orellana, R. M., Stovicek, P., and Brooks, D. H. (2014). Using transmural regularization and dynamic modeling for non-invasive cardiac potential imaging of endocardial pacing with imprecise thoracic geometry. *IEEE Trans. Med. Imaging* 33, 726–738. doi: 10.1109/TMI.2013.2295220

Ferguson, A. S., and Stroink, G. (1997). Factors affecting the accuracy of the boundary element method in the forward problem-I: calculating surface potentials. *IEEE Trans. Biomed. Eng.* 44, 1139–1155. doi: 10.1109/10.641342

Geneser, S. E., Kirby, R. M., and MacLeod, R. S. (2008). Application of stochastic finite element methods to study the sensitivity of ECG forward modeling to organ conductivity. *IEEE Trans. Biomed. Eng.* 55, 31–40. doi: 10.1109/TBME.2007.900563

Hansen, P. C. (2007). Regularization tools version 4.0 for Matlab 7.3. *Numer. Algor.* 46, 189–194. doi: 10.1007/s11075-007-9136-9

Jones, R., Schulze, W. H. W., Potyagaylo, D., Dössel, O., and Weber, F. M. (2013). Computing lead-field matrices for a body tissue conductivity range. *Biomed. Tech.* 58, 24–25. doi: 10.1515/bmt-2013-4157

Lyon, A., Minchol, A., Passini, E., and Rodriguez, B. (2017). "Investigation of the presence and mechanisms of action potential alternans in hypertrophic cardiomyopathy," in *2017 Computing in Cardiology (CinC)* (Rennes), 1–4. doi: 10.22489/CinC.2017.251-262

MacLeod, R., and Buist, M. (2010). "The forward problem of electrocardiography," in *Comprehensive Electrocardiology*, eds P. W. Macfarlane, A. van Oosterom, O. Pahlm, P. Kligfield, M. Janse, and J. Camm (London: Springer).

MacLeod, R., Miller, R., Gardner, M., and Horáček, B. (1995a). Application of an electrocardiographic inverse solution to localize myocardial ischemia during percutaneous transluminal coronary angioplasty. *J. Cardiovasc. Electrophysiol.* 6, 2–18. doi: 10.1111/j.1540-8167.1995.tb00752.x

MacLeod, R., Taccardi, B., and Lux, R. (1995b). "Electrocardiographic mapping in a realistic torso tank preparation," in *c-EMBS95* (Montreal, QC: IEEE Press), 245–246. doi: 10.1109/IEMBS.1995.575092

MacLeod, R. S., Ni, Q., Punske, B., Ershler, P. R., Yilmaz, B., and Taccardi, B. (2000). Effects of heart position on the body-surface electrocardiogram. PG-229-37. *J. Electrocardiol.* 33, 229–237. doi: 10.1054/jelc.2000.20357

Madias, J. E. (2006). Comparability of the standing and supine standard electrocardiograms and standing sitting and supine stress electrocardiograms. *J. Electrocardiol.* 39, 142–149. doi: 10.1016/j.jelectrocard.2005.07.006

Nelwan, S. P., Meij, S. H., van Dam, T. B., and Kors, J. A. (2001). Correction of ECG variations caused by body position changes and electrode placement during ST-T monitoring. *J. Electrocardiol.* 34(Suppl.), 213–216. doi: 10.1054/jelc.2001.28895

Netter, F. (2006). *Atlas of Human Anatomy, 4th Edn.* Philadelphia, PA: Saunders/Elsevier.

Potyagaylo, D., Doessel, O., and Van Dam, P. (2016). Influence of modeling errors on the initial estimate for non-linear myocardial activation times imaging calculated with fastest route algorithm. *IEEE Trans. Biomed. Eng.* 63, 2576–2584. doi: 10.1109/TBME.2016.2561973

Pullan, A., Cheng, L., Nash, M., Ghodrati, A., MacLeod, R., and Brooks, D. (2010). "The inverse problem of electrocardiographym," in *Comprehensive Electrocardiology,* eds P. W. MacFarlane, A. van Oosterom, O. Pahlm, P. Kligfield, M. Janse, and J. Camm (London: Springer), 299–344.

Punshchykova, O., Švehlíková, J., Tyšler, M., Grünes, R., Sedova, K., Osmančík, P., et al. (2016). Influence of Torso model complexity on the noninvasive localization of ectopic ventricular activity. *Meas. Sci. Rev.* 16, 96–102. doi: 10.1515/msr-2016-0013

Ramanathan, C., and Rudy, Y. (2001a). Electrocardiographic imaging: I. Effect of torso inhomogeneities onbody surface electrocardiographic potentials. *J. Cardiovasc. Electrophysiol.* 12, 229–240. doi: 10.1046/j.1540-8167.2001.00229.x

Ramanathan, C., and Rudy, Y. (2001b). Electrocardiographic imaging: II. Effect of torso inhomogeneities on noninvasive reconstruction of epicardial potentials, electrograms, and isochrones. *J. Cardiovasc. Electrophysiol.* 12, 241–252. doi: 10.1046/j.1540-8167.2001.00241.x

Rodrigo, M., Climent, A., Liberos, A., Hernández-Romero, I., Arenal, A., Bermejo, J., et al. (2017). Solving inaccuracies in the heart position and orientation for inverse solution by using electric information. *Comput. Cardiol.* 44, 3–6. doi: 10.22489/CinC.2017.226-202

Rodrigo, M., Climent, A. M., Liberos, A., Hernandez-Romero, I., Arenal, A., Bermejo, J., et al. (2018). Solving inaccuracies in anatomical models for electrocardiographic inverse problem resolution by maximizing reconstruction quality. *IEEE Trans. Med. Imaging* 37, 733–740. doi: 10.1109/TMI.2017.2707413

SCI-Institute (2014). *SCIRun: A Scientific Computing Problem Solving Environment*. Scientific Computing and Imaging Institute (SCI), Available online at: http://www.scirun.org

Svehlikova, J., Lenkova, J., Drkosova, A., Foltin, M., and Tysler, M. (2011). ECG based assessment of the heart position in standard Torso model. *IFMBE Proc.* 37, 474–477. doi: 10.1007/978-3-642-23508-5_123

Swenson, D. J., Geneser, S. E., Stinstra, J. G., Kirby, R. M., and MacLeod, R. S. (2011). Cardiac position sensitivity study in the electrocardiographic forward problem using stochastic collocation and boundary element methods. *Ann. Biomed. Eng.* 39, 2900–2910. doi: 10.1007/s10439-011-0391-5

Trayanova, N. A. (2011). Whole-heart modeling : applications to cardiac electrophysiology and electromechanics. *Circ. Res.* 108, 113–128. doi: 10.1161/CIRCRESAHA.110.223610

van Oosterom, A., and Oostendorp, T. (2004). ECGSIM: an interactive tool for studying the genesis of QRST waveforms. *Heart* 90, 165–168. doi: 10.1136/hrt.2003.014662

Weber, F. M., Keller, D. U., Bauer, S., Seemann, G., Lorenz, C., and Dossel, O. (2011). Predicting tissue conductivity influences on body surface potentials-an efficient approach based on principal component analysis. *IEEE Trans. Biomed. Eng.* 58, 265–273. doi: 10.1109/TBME.2010.2090151

Conflict of Interest Statement: The authors declare that the research was conducted in the absence of any commercial or financial relationships that could be construed as a potential conflict of interest.

frontiers in Physiology

ORIGINAL RESEARCH
published: 22 January 2019
doi: 10.3389/fphys.2018.01946

Impact of the Endocardium in a Parameter Optimization to Solve the Inverse Problem of Electrocardiography

Gwladys Ravon[1,2,3]*, *Yves Coudière*[1,4,5], *Mark Potse*[1,4,5] *and Rémi Dubois*[1,2,3]

[1] IHU Liryc, Electrophysiology and Heart Modeling Institute, Pessac, France, [2] Univ Bordeaux, CRCTB, U1045, Bordeaux, France, [3] INSERM, CRCTB, U1045, Bordeaux, France, [4] Carmen Research Team, Inria, Bordeaux, France, [5] Univ Bordeaux, IMB UMR 5251, Talence, France

Electrocardiographic imaging aims at reconstructing cardiac electrical events from electrical signals measured on the body surface. The most common approach relies on the inverse solution of the Laplace equation in the torso to reconstruct epicardial potential maps from body surface potential maps. Here we apply a method based on a parameter identification problem to reconstruct both activation and repolarization times. From an ansatz of action potential, based on the Mitchell-Schaeffer ionic model, we compute body surface potential signals. The inverse problem is reduced to the identification of the parameters of the Mitchell-Schaeffer model. We investigate whether solving the inverse problem with the endocardium improves the results or not. We solved the parameter identification problem on two different meshes: one with only the epicardium, and one with both the epicardium and the endocardium. We compared the results on both the heart (activation and repolarization times) and the torso. The comparison was done on validation data of sinus rhythm and ventricular pacing. We found similar results with both meshes in 6 cases out of 7: the presence of the endocardium slightly improved the activation times. This was the most visible on a sinus beat, leading to the conclusion that inclusion of the endocardium would be useful in situations where endo-epicardial gradients in activation or repolarization times play an important role.

Keywords: ECGI, endocardium, parameter optimization, gradient descent method, Mitchell-Schaeffer, endo-epicardial gradients

OPEN ACCESS

Edited by:
Maria S. Guillem, Universitat Politècnica de València, Spain

Reviewed by:
Dana H. Brooks, Northeastern University, United States
Linwei Wang, Rochester Institute of Technology, United States

***Correspondence:**
Gwladys Ravon
gwladys.ravon@ihu-liryc.fr

Specialty section:
This article was submitted to Cardiac Electrophysiology, a section of the journal Frontiers in Physiology

Received: *21 May 2018*
Accepted: *22 December 2018*
Published: *22 January 2019*

Citation:
Ravon G, Coudière Y, Potse M and Dubois R (2019) Impact of the Endocardium in a Parameter Optimization to Solve the Inverse Problem of Electrocardiography. Front. Physiol. 9:1946. doi: 10.3389/fphys.2018.01946

1. INTRODUCTION

Electrocardiographic imaging aims at reconstructing cardiac electrical events from electrical signals measured on the body surface. The most common approach relies on the inverse solution of the Laplace equation in the torso to reconstruct epicardial potential maps from the body surface electrical potential maps (BSPM) (Wang and Rudy, 2006). This technique requires a regularization strategy to deal with the ill-posedness of the problem, for example Tikhonov regularization. However, as this regularization is applied to potential patterns, it suppresses the steep voltage gradients that characterize activation wavefronts. This leads to prominent errors such as artefactual block lines in the reconstructed activation map (Duchateau et al., 2017; Ravon et al., 2017).

Other methods have been designed to reconstruct directly the activation times (van Oosterom and Oostendorp, 1992; Liu et al., 2006). While Liu et al. (2006) look for the three-dimensional activation sequence in the ventricular muscle, van Oosterom and Oostendorp (1992) reconstruct activation on both the epicardium and the endocardium. van Dam et al. (2009) proposed a method that solved both the activation and the repolarization. Based on an equivalent double layer model, it updates activation and repolarization times alternatingly. Ghodrati et al. (2006) developed two methods to reconstruct epicardial information. One optimizes the position of the depolarization front at each time. The second reconstructs epicardial potentials with a regularization term based on the estimation of the wavefront behavior. These approaches still rely on a Tikhonov-like regularization technique. Recently, studies that reconstruct both the activation and the recovery, with a novel regularization technique, have been published (Cluitmans et al., 2017, 2018). The regularization is done through an electrophysiological input and the potentials on the torso are sparsely represented to deal with the ill-posedness of the problem. Others used a probabilistic approach to find parameters (Rahimi et al., 2016; Dhamala et al., 2018). The former used the two-variable Aliev-Panfilov model (Aliev and Panfilov, 1996) to model the AP. Their aim was to probabilistically personalize a model parameter using machine learning methods. The estimation was made on a whole-heart 3D model, from BSPMs or extracellular potentials. In the latter the parameters of the model are assumed and the behavior of the wavefront is optimized. The same group worked on regularizing both the spatial and the temporal propagation of action potential (Wang et al., 2010). The method relies on a two-variable propagation model with fixed parameters in a volumetric myocardium. It was then improved in Ghimire et al. (2017). Note that in these studies constraints in the spatial distribution are considered.

In a previous study (Ravon et al., 2017) we introduced a new technique that aims at recovering directly both the activation and repolarization maps on the epicardium. The general idea consists in looking for an ansatz of an action potential (AP) under the form of a function $v(P; t)$ parameterized by a small number of parameters P, e.g., less than three. The upstroke of this AP is supposed to be at $t = 0$. From the knowledge of the activation times $\tau(x)$ on the heart, we can map the AP to a space- and time-dependent function $V_m(t, x) = v(P; t - \tau)$. In addition, the parameters P may have space-dependent values distributed on the surface, which enriches the model, but increases the number of unknown parameters. Then this transmembrane voltage function $V_m(t, x)$ is projected to body surface potential signals. The method searches for the parameters P and activation map τ that realize the best fit to the target body surface signals on a given time interval. It amounts to solving a nonlinear least squares parameter identification problem with a small number of (possibly distributed) parameters. We previously represented the action potential as the product of two logistic functions, as proposed by Van Oosterom and Jacquemet (2005). The final parameter identification problem (Ravon et al., 2017) consisted of identifying three distributed parameters, given the BSPM of a complete ventricular activation and repolarization sequence (i.e., a QRST waveform). This method was demonstrated to give a better range of activation times (ATs) and a smoother AT distribution than a solution based on the Laplace equation with Tikhonov regularization of order zero. However, it only reconstructed APs on the epicardium. In general, large and physiologically very relevant differences in AT and repolarization time (RT) can exist across the wall. Therefore, in this study we investigated whether including the endocardium improves the results.

To this aim, we tested our method on *in silico* data with and without important transmural gradients. The parameter identification problem was solved either on the epicardium only, or on both the epicardium and endocardium. We found that the quality of the reconstructed activation and repolarization maps (in terms of correlation coefficients) was similar when transmural gradients were small, but that inclusion of the endocardium improved the solution in a case where these gradients were important.

As compared to Ravon et al. (2017), we also changed the representation of the AP from the product of two logistic functions to the solution of the two-variable ionic model of Mitchell and Schaeffer (2003), to have a more relevant AP shape without increasing the number of parameters.

We resorted to a discretize-then-optimize strategy: we first set the direct problem that maps the parameters P and activation map τ to the voltage $V_m(t, x)$, and then to the BSPM ϕ_T. This problem was discretized using triangulated surfaces. The parameters were identified in the discrete problem using a gradient descent method on a discrete least squares cost function.

2. MATERIALS AND METHODS

2.1. Mapping the Parameters to the Transmembrane Voltage

The parameterization was based on the two-current model proposed by Mitchell and Schaeffer (2003). This model describes the dynamics of two functions: the voltage v and an auxiliary variable h. Both quantities are dimensionless and scaled between 0 and 1, and solve the following ordinary differential equations:

$$v' = \frac{hv^2(1-v)}{\tau_{in}} - \frac{v}{\tau_{out}}, \tag{1}$$

$$h' = \frac{1-h}{\tau_{open}} \quad \text{if } v < v_{gate}, \quad \text{and} \quad h' = \frac{-h}{\tau_{close}} \quad \text{if } v > v_{gate}. \tag{2}$$

The five parameters were originally chosen as (Mitchell and Schaeffer, 2003): $\tau_{in} = 0.3$ ms, $\tau_{out} = 6$ ms, $\tau_{open} = 120$ ms, $\tau_{close} = 150$ ms, and $v_{gate} = 0.13$. The steady state for this model is $(v, h) = (0, 1)$. The voltage v takes the shape of an AP if we set the initial condition as $\big(v(0), h(0)\big) = (0.15, 1)$, see the red curve in **Figure 1**.

The function $v(t)$ defined for $t \geq 0$ as the solution of the initial value problem (1)-(2) with $\big(v(0), h(0)\big) = (0.15, 1)$ was completed by 0 for $t < 0$. It was our ansatz of an AP, denoted by $v(P; t)$

for $t \in \mathbb{R}$, and in general $P = \{\tau_{in}, \tau_{out}, \tau_{open}, \tau_{close}, v_{gate}\}$. For instance, the blue curve in **Figure 1** is the graph of $v(P, t-\tau)$ for an activation time $\tau = 50$ ms and the default values for P stated above.

In practice, the parameters τ_{in} and τ_{open} define the upstroke of the AP, and were fixed with their default values $\tau_{in} = 0.3$ ms and $\tau_{open} = 120$ ms. Similarly, the parameter v_{gate} defines the excitability threshold and was fixed at $v_{gate} = 0.13$. Hence, only the parameters τ_{out} and τ_{close} were searched as unknown parameters, because they are directly related to the AP duration. τ_{close} can be seen as the plateau phase duration whereas τ_{out} is linked to the speed of the repolarization. τ_{out} also has a small impact on the amplitude of the voltage v.

In addition, we rescaled the voltage v by a factor $\mathcal{A}$, so as to fit the scaling of the measured BSPM. Hence, we considered the mapping

$$\mathcal{P} := (\mathcal{A}, \underbrace{\tau_{out}, \tau_{close}}_{P}, \tau) \in \mathbb{R}^4 \mapsto V_m(x,t) = \mathcal{A}v(P, t-\tau). \quad (3)$$

The parameter τ was distributed on the heart surface by the design of the method. Meanwhile, the parameters $\mathcal{A}$, τ_{out}, and τ_{close} may be constant or distributed. Since AP duration varies across the heart surface, we would rather consider varying distributed parameters τ_{out} and τ_{close}.

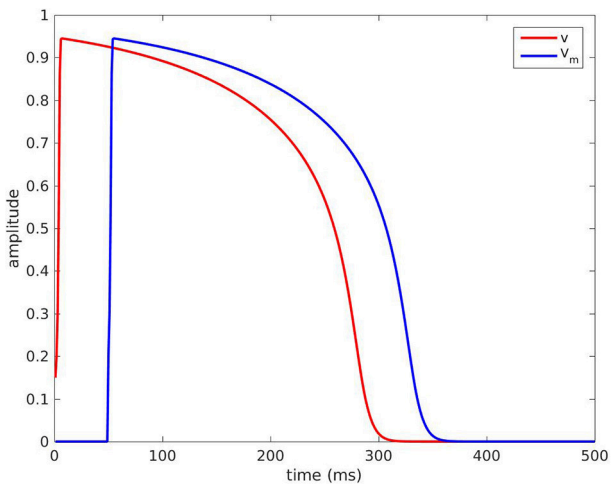

FIGURE 1 | Red curve: voltage $v(P, t)$ with the default parameters P. Blue curve: TMP $V_m(t) = v(P; t-\tau)$ with $\tau = 50$ ms.

2.2. Projecting the Transmembrane Voltage to the Body Surface Potential Map

Afterwards, we mapped the transmembrane voltage $V_m(x,t)$ to extracellular potentials $\phi_e(x,t)$ as in Potse et al. (2009):

$$V_m(x,t) \mapsto \phi_e(x,t) = \overline{V_m}(t) - V_m(x,t), \quad (4)$$

where $\overline{V_m}(t)$ was a fixed spatial average of $V_m(x,t)$, $\overline{V_m}(t) = \frac{1}{|S|}\int_S V_m(x,t)ds(x)$ where S is the heart surface (epicardium only, or epicardium and endocardium). The rationale of the formula is a rewriting of the bidomain model coupled with the hypothesis that conductivity tensor fields in both extra- and intra-cellular domains are homogeneous and isotropic. Here the ratio of conductivities was hidden in the factor $\mathcal{A}$. Finally, we projected the extracellular potentials $\phi_e(x,t)$ to the body surface potentials $\phi_T(y,t)$ for any point y on the torso surface as follows:

$$\phi_e(x,t) \mapsto \phi_T(y,t) = \int_S \frac{1}{4\pi \|x-y\|}\phi_e(x,t)ds(x), \quad (5)$$

This amounted to approximating the solution of the Laplace equation outside the heart domain, assuming it is an infinite homogeneous medium (Malmivuo and Plonsey, 1995; Macfarlane et al., 2010).

2.3. Discrete Surfaces and Approximations

In practice, the endocardial and epicardial surfaces were discretized by two separate triangular meshes (**Figure 2**) with

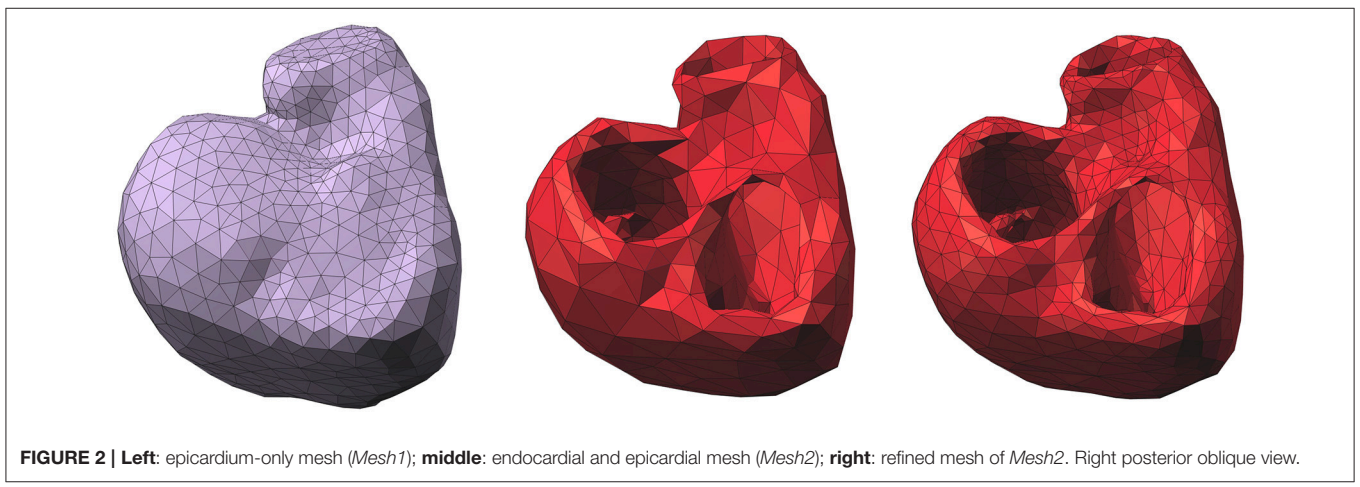

FIGURE 2 | Left: epicardium-only mesh (*Mesh1*); **middle**: endocardial and epicardial mesh (*Mesh2*); **right**: refined mesh of *Mesh2*. Right posterior oblique view.

vertices denoted by $(x_i)_{i=1\ldots N_H}$. The endocardial surface included the surface of the free wall and the septum (**Figure 2**, middle).

For the sake of computational simplicity, the mappings (4) and (5) were replaced by their discrete counterparts:

$$\phi_e(x_i,t) = \frac{1}{N_H}\sum_{k=1}^{N_H} V_m(x_k,t) - V_m(x_i,t),$$
$$\phi_T(y,t) = \sum_{i=1}^{N_H} \frac{1}{4\pi\|x_i - y\|}\phi_e(x_i,t), \quad (6)$$

where $V_m(x_i,t)$ was given by the mapping (3) for given parameters $\mathcal{A} \in \mathbb{R}$, $\left(\tau_{out}(x_i)\right)_i \in \mathbb{R}^{N_H}$, $\left(\tau_{close}(x_i)\right)_i \in \mathbb{R}^{N_H}$ and $\left(\tau(x_i)\right)_i \in \mathbb{R}^{N_H}$. Hence there are $1 + 3N_H$ parameters to be identified.

2.4. The Parameter Identification Problem

We looked for the parameter set $\mathcal{P} = (\mathcal{A}, \tau_{out}, \tau_{close}, \tau) \in \mathbb{R}^{1+3N_H}$ that minimized the least squares error

$$J(\mathcal{P}) = \frac{1}{2}\sum_{k=1}^{T_{max}}\sum_{j=1}^{N_T}\left|\left(\phi_T(y_j,t_k) - \overline{\phi_T(t_k)}\right) - \left(\phi^\star(y_j,t_k) - \overline{\phi^\star(t_k)}\right)\right|^2, \quad (7)$$

where $(y_j)_{j=1\ldots N_T}$ were the N_T electrode locations on the body surface, $(t_k)_{k=1\ldots T_{max}}$ was the time sequence of interest, $(\phi^\star(y_j,t_k))$ were the measured BSPMs, and $(\phi_T(y_j,t_k))$ were the BSPMs computed according to equations (6). For each time t_k, the spatial averages $\overline{\phi_T(t_k)}$ and $\overline{\phi^\star(t_k)}$ were defined by $\overline{\phi_T(t_k)} = \frac{1}{N_T}\sum_{j=1}^{N_T}\phi_T(y_j,t_k)$ and $\overline{\phi^\star(t_k)} = \frac{1}{N_T}\sum_{j=1}^{N_T}\phi^\star(y_j,t_k)$. Potentials are given up to a constant. This constant can be a reference electrode on the torso, the WCT or the mean of all the electrodes. We chose the mean. As Wilson's Central Terminal it was also a way to reduce noise. Moreover, it rescaled the data around their mean value.

The total number of data elements is finally $T_{max}N_T$, which may be compared to the number of unknown parameters $1 + 3N_H$. This nonlinear least squares problem was solved by the gradient descent method with the RMSprop update (Tieleman and Hinton, 2012). This is an adaptive learning rate method: at each iteration, the update reads:

$$\kappa := \gamma\kappa + (1-\gamma)\nabla_{\mathcal{P}}J \otimes \nabla_{\mathcal{P}}J \quad \text{in } \mathbb{R}^{1+3N_H}, \quad (8)$$
$$\mathcal{P} := \mathcal{P} - \eta\nabla_{\mathcal{P}}J \oslash (\kappa^{\circ 1/2} + 10^{-7}) \quad \text{in } \mathbb{R}^{1+3N_H}, \quad (9)$$

with $\kappa \in \mathbb{R}^{1+3N_H}$ an intermediate variable, $\eta \in \mathbb{R}$ the learning rate and $\gamma = 0.9$. The learning rate was not fixed, an optimal value for η was chosen at each iteration in the range $\left[10^{-5}, 10^2\right]$. In equations 8 and 9 the operators $\otimes$, $\oslash$, and $^\circ$ denote the Hadamard product, division, and power, respectively. The gradient of the cost function J with respect to the unknown parameters $\mathcal{P}$ was calculated analytically.

For the gradient descent method, an initial guess was required. We arbitrarily chose $\mathcal{A} = 10$, the default values $\tau_{out,i} = 6$ ms and $\tau_{close,i} = 150$ ms for all i, and τ_i constant $\tau_i = \tau_0 \in \mathbb{R}$. Since the initialization was the same for all the nodes, the initial torso potentials were zero. The optimization ended when the cost function J and its gradient remained constant. The code was in Matlab and not parallel. Computational time was quite long and similar for all the cases, namely about one day. A more flexible stopping criterion and parallelism would reduce computational time.

2.5. Validation Data

In order to create testing data, simulations were run on an anatomically realistic 3D geometry of the torso, including heart, blood vessels, lungs, and skeletal muscle (**Figure 3**). Each organ had its own conductivity. Propagating AP were generated using a monodomain reaction-diffusion model with a TNNP membrane model (Ten Tusscher et al., 2004) on an anisotropic heart model at 0.2 mm resolution. To compute ϕ_T the computed transmembrane current density in the myocardium was projected on an inhomogeneous heart-torso model with anisotropic skeletal muscle layer at 1 mm resolution and the potential field ϕ_T was found by solving an anisotropic Laplace problem using a finite-difference method (Potse, 2018). Boundary conditions did not match between the monodomain model and the Laplace equation. This approach leads to slightly different extracellular potentials within a few hundred

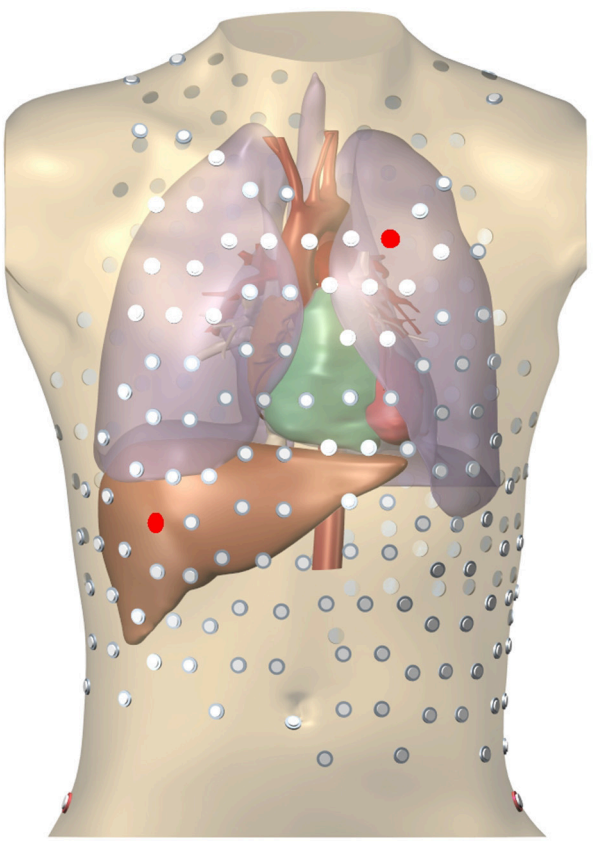

FIGURE 3 | Heart-torso mesh used for the computation of validation data. The 252-electrode body surface mapping set is shown. Red electrodes mark two locations used in **Figure 8**.

micrometers from the surface only (Potse et al., 2006). All simulations were performed with a recent version of the Propag-5 software (Krause et al., 2012) on a BullX cluster machine.

We had access to the activation times on the epicardium and the endocardium (named reference ATs in the following). Repolarization times were computed from extra-cellular potentials as the time with highest positive slope during the repolarization phase.

3. RESULTS

On the same model anatomy, seven different simulations were run: one sinus rhythm (SR) and six different pacing cases. The description of the cases can be found in **Table 1**. For all the cases, we solved the parameter identification problem on the epicardium-only mesh (*Mesh1*) and on the epicardium and endocardium mesh (*Mesh2*). *Mesh1* and *Mesh2* had 641 and 534 vertices respectively. We will describe the results in detail for two cases: right-ventricular pacing and sinus rhythm.

3.1. Epicardial Ventricular Pacing

The reconstructed activation maps in case of right-ventricular pacing were of the same quality on both meshes. In particular the late ATs were not well reconstructed in both cases (first row, dark blue part in **Figure 4**). The correlation coefficient (CC) and relative error (RE) between ATs were close for both meshes, about 0.7 and 0.3 respectively. However, **Figure 5** shows that a part of the reference ATs between 120 and 160 ms was less well reconstructed with *Mesh1* than with *Mesh2*. For both meshes some reference ATs between 100 and 150 ms were not well reconstructed (**Figure 5**, left, black box). These points were located between the two valves, where the reconstruction is more difficult. The pacing site was better localized with *Mesh1* (11.4 mm from the actual position, geodesic distance) than with *Mesh2* (16 mm), as shown in **Figure 12**. For *Mesh2* we also calculated CC for the points on the epicardium (CC = 0.72) and on the endocardium (CC = 0.77). With the endocardium we did not improve the accuracy on the epicardium compared to the results with the epicardium only.

The benefit of considering the endocardium was to look for gradients of depolarization between the endocardium and epicardium. For each point on the epicardium, we selected the closest point on the endocardium and computed the delay in the activation. **Figure 6** presents box plot of these delays for the 7 cases. Delays existed in the reference ATs (first box) and the delays we obtained were smaller on average. We also obtained large delays (more than 20 ms and up to 135) that were not consistent with the actual ones.

On both meshes, the quality of repolarization maps was less good than the activation maps (**Figure 4**, second row). The CC was slightly better with *Mesh1* (0.55 vs. 0.51). It was highlighted on the scatter plot, especially for the earlier RTs (**Figure 5**, right).

Figure 7 shows the evolution in time of the CC between the measured BSPM and the reconstructed ones. Reconstructed torso potentials were computed from equation (3), (4), and (5) with the optimized parameters and the corresponding mesh *Mesh1* or *Mesh2*. On both meshes, the behavior was similar: at the beginning and the end of the simulation the reconstruction was less accurate. As shown by **Figure 8**, after 400 ms, measured and reconstructed BSPMs are close to zero, which explained that the CC dropped. On average, the CC was 0.88 with *Mesh1*, and 0.9 with *Mesh2*. On both electrodes, depolarization, and repolarization phases were quite well fitted for the two meshes. There were just slight differences between the reconstructed BSPMs. We also calculated the root mean square error (RMSE) between the measured BSPMs and the reconstructed ones (**Figure 9**). Two peaks can be seen: one corresponding to the depolarization phase and the second to the repolarization phase. They were mainly due to the amplitude: the optimized amplitude did not allow to fit the signals on all the electrodes (**Figure 8**). RMSE was similar for the 2 meshes.

TABLE 1 | Description of the 7 cases.

Case	Description
1	Epicardial ventricular pacing
2	Sinus rhythm
3	Endocardial ventricular pacing
4	Epicardial ventricular pacing (near apex)
5	Endocardial ventricular pacing (near apex)
6	Pacing on the basis of the pulmonary vein
7	Pacing on the septum, halfway up to the right ventricle

3.2. Sinus Rhythm

It is well known that the QRS duration is shorter in sinus beat than in a paced beat. Moreover, there were multiple breakthroughs in the myocardium. For these reasons it was harder to obtain a satisfying reconstruction than in the pacing cases. For both meshes the reconstructed total activation time was longer than the actual. The CC and RE were better with the endocardium than without, but still not as good as in the pacing cases (**Figure 10**, left). For *Mesh2* we also calculated CC for the points on the epicardium (CC = 0.64) and on the endocardium (CC = 0.57). With the endocardium we improved the accuracy on the epicardium (CC = 0.64) compared to the results with *Mesh1* (CC = 0.49).

We also looked at the delays between endocardium and epicardium (**Figure 6**). These were similar on the reference ATs for the SR and RV pacing case (first and third boxes). Since the total activation time (TAT) is smaller in a sinus beat, the relative values of these gradients to the TAT were more important than in RV pacing. We reconstructed different delays for this two cases. The delays were not reconstructed as well for the SR as for the pacing cases. Indeed as shown in **Figure 11**, there was a gradient of activation on the left ventricular free wall that we did not recover. Similarly there were delays in the activation of the septum that we did not reconstruct.

CC and RE for the repolarization times were better with *Mesh1*: 0.51 and 0.18 respectively with the endocardium and 0.68 and 0.1 without (**Figure 10**, right). Indeed with the endocardium

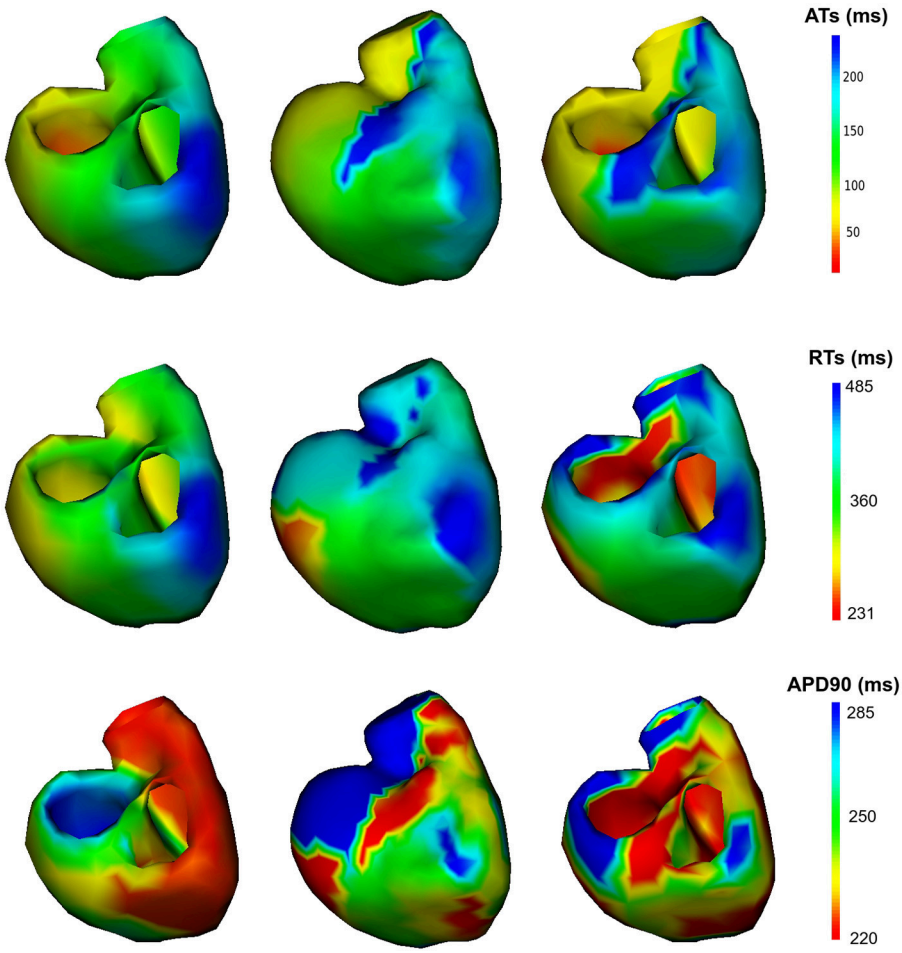

FIGURE 4 | Activation, repolarization and APD90 maps of the RV pacing case. **Left**: reference ATs; **middle**: optimized ATs from *Mesh1*; **right**: optimized ATs from *Mesh2*. Right posterior oblique view.

the range of RTs was much larger, from $t = 108$ ms to $t = 628$ ms, whereas the actual range was from $t = 259$ ms to $t = 393$ ms.

Finally we compared the signals on the torso. As in the pacing case, CC and RMSE evolved in the same way for both meshes, with close values over time. In both cases the CC dropped after 350 ms because reconstructed T waves sometimes ended later than the real ones. In the simulation the heart was almost at rest after 350 ms, which was not the case with our optimized parameters. On average, the CC was 0.83 with *Mesh1*, and 0.87 with *Mesh2*.

3.2.1. Sensitivity to the Initialization

In order to test if the method was sensitive to the initialization, we solved the inverse problem with two other triplets. The results we previously presented were obtained from the triplet $(\tau_i, \tau_{\text{out},i}, \tau_{\text{close},i}) = (60, 6, 150)$. The second and third triplets were $(75, 5, 130)$ and $(75, 6, 15)$ respectively. The results are presented in **Table 2**. The three initializations ended with very close results: CC for ATs and RTs were in the same range, as well as for the BSPM. Moreover, for the three triplets, the method gave a better accuracy of the ATs with *Mesh2*, while RTs were better reconstructed with *Mesh1*. Changing the initial ATs did not improve the accuracy on the reconstructed ATs. Finally, the reconstructed torso potentials were very close to each other for the three initializations (CC between 0.83 and 0.9). Especially, the QRS complex and the T wave were fitted in the same way.

3.3. All the Cases

We present the results for all the cases in **Table 3**. A box plot representation can be found on **Supplementary Material**, as well as activation, repolarization, and APD90 maps for all the cases. In cases 4 and 6 CC of ATs were better with *Mesh2*. In all others cases, CC were similar for both meshes. In all cases, solving the inverse problem with *Mesh2* gave at least as accurate ATs on the epicardium as with *Mesh1*. Optimized RTs were better with *Mesh2* in only 2 cases: pacing on the basis of the pulmonary vein (case 6) and pacing on the septum (case 7). **Figure 6** shows the delays in activation. On average we reconstructed smaller delays in all cases.

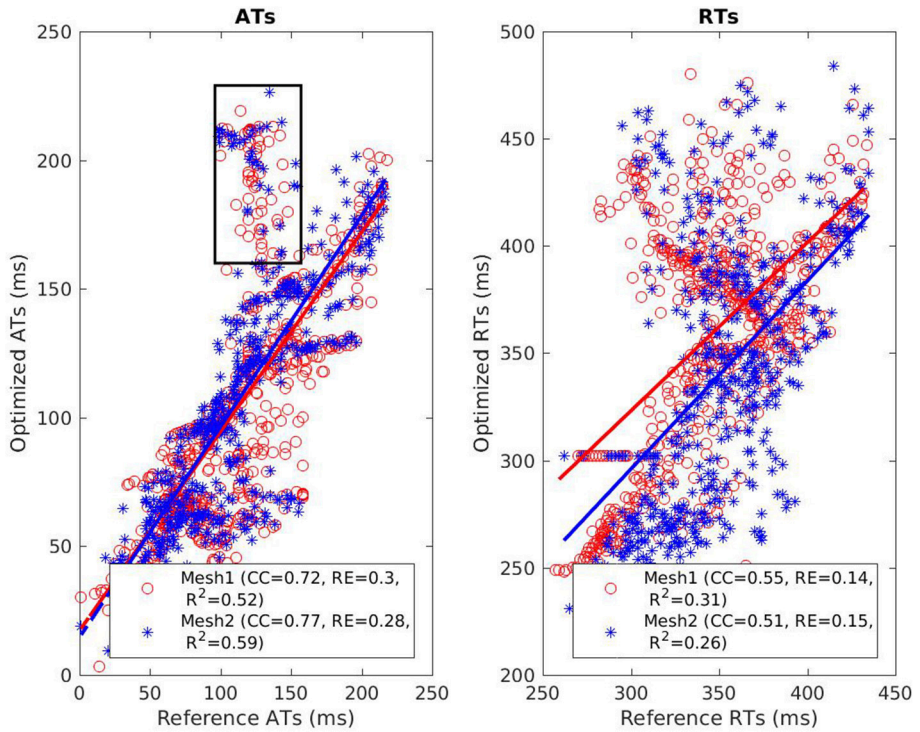

FIGURE 5 | Scatter plot of the ATs **(left)** and RTs **(right)** for the RV pacing case. For each point, the *x* coordinate is the reference AT (resp. RT) and the *y* coordinate is the corresponding reconstructed AT (resp. RT). The dashed lines represent the linear fitting. The black box on the left exhibits ATs that were badly reconstructed with both meshes.

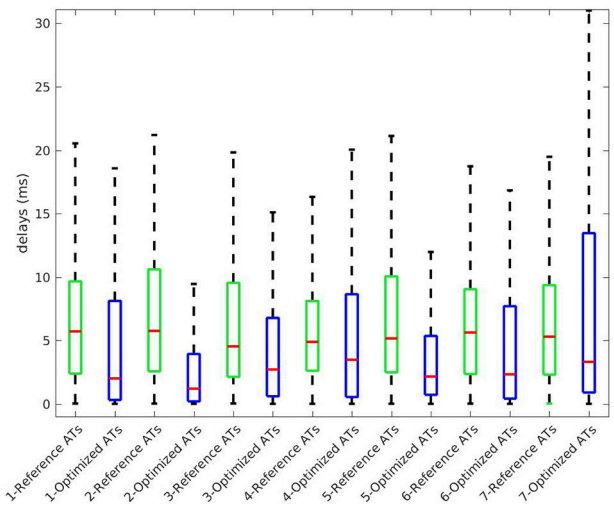

FIGURE 6 | Delays in ATs between endocardium and epicardium for the 7 cases. Box plot represent the median and the first and third quartiles. Whiskers represent the extreme values. Optimized ATs are AT given by the inverse method with *Mesh2*.

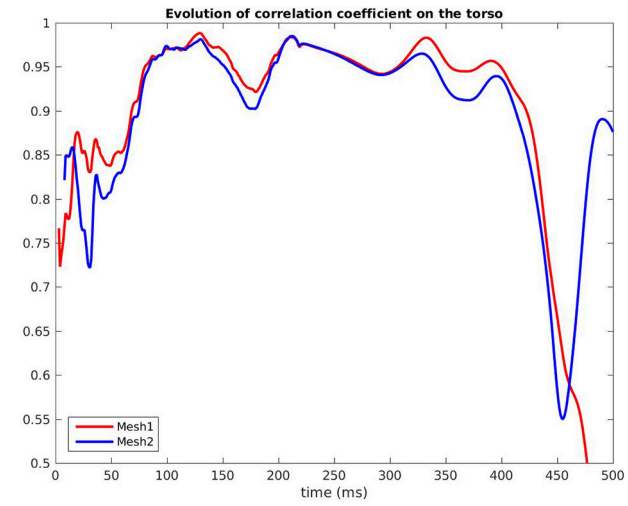

FIGURE 7 | Correlation coefficient of the BSPM, RV pacing case.

Concerning the reconstructed BSPMs, averaged CC and RMSE are given in **Table 3**. Except in case 7, the averaged CC were very similar for both meshes. They kept very close values over time. We observed the same behavior for the RMSE in all the cases. The lower averaged CC in case 7 with *Mesh2* was due to a shorter total activation time: late ATs were not well reconstructed.

A statistical *T*-test was performed on the CC for ATs, RTs, and BSPM. The resulting *p*-values were 0.5, 0.41, and 0.28

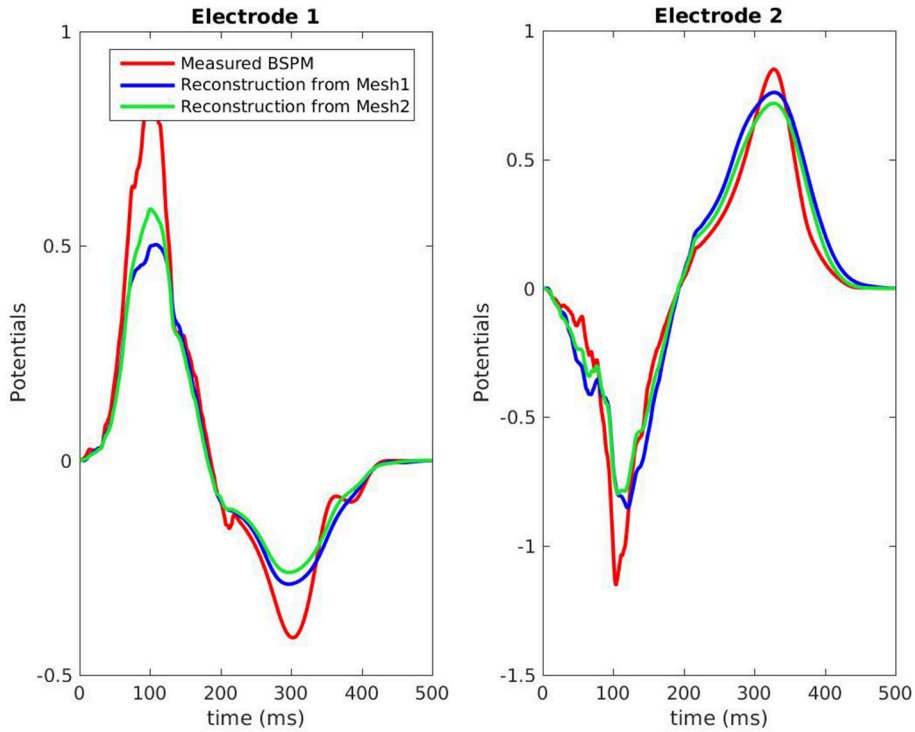

FIGURE 8 | Potentials on the torso, RV pacing case. The locations of the 2 electrodes are marked in red in **Figure 3**.

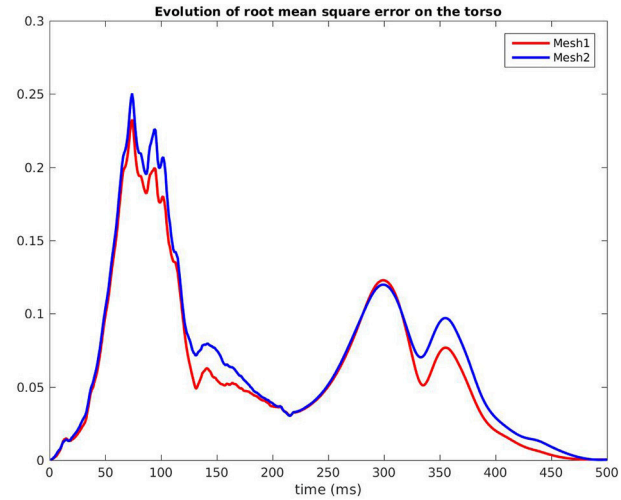

FIGURE 9 | Root mean square error of the BSPM, RV pacing case.

respectively, showing no significant differences between the two meshes.

We computed the geodesic distance between the actual pacing site locations and the one given by the inverse solution for cases 1, 4, and 6 (epicardial pacing). For endocardial pacing (cases 3, 5, and 7) we computed the distance between actual and reconstructed breakthrough on the epicardium. From the optimization, the pacing site (or breakthrough) was identified as the mesh node with the earliest AT (resp. on the epicardium). We added a visual validation to exclude irrelevant, isolated, early ATs. Results can be found in **Figure 12**. In most of the cases, the distance was smaller with *Mesh1* than *Mesh2*. However, except for case 6, the identified site with *Mesh2* was a neighbor of the actual site. So the differences in the mesh density could explain the smaller distances with *Mesh1*.

We looked at the AP duration. For the 7 cases the reference APD90 varied between 225 and 285 ms. A difference was clearly visible between the endocardium and the epicardium. We were not able to reproduce this difference with *Mesh2*. However, APD90 were similar on the epicardium for both meshes. Our method tended to reconstruct maximal APD90s much higher than 285 ms, especially in cases 1, 2, and 7.

4. DISCUSSION

We presented a new ECGI method designed to recover both the depolarization and the repolarization sequence, by solving a parameter identification problem. We hypothesized that this method would work better when both the endocardium and epicardium are included in the model, since important and physiologically relevant differences in both depolarization and repolarization timing exist between these surfaces. Therefore, we tested the method on two different heart meshes: the one a

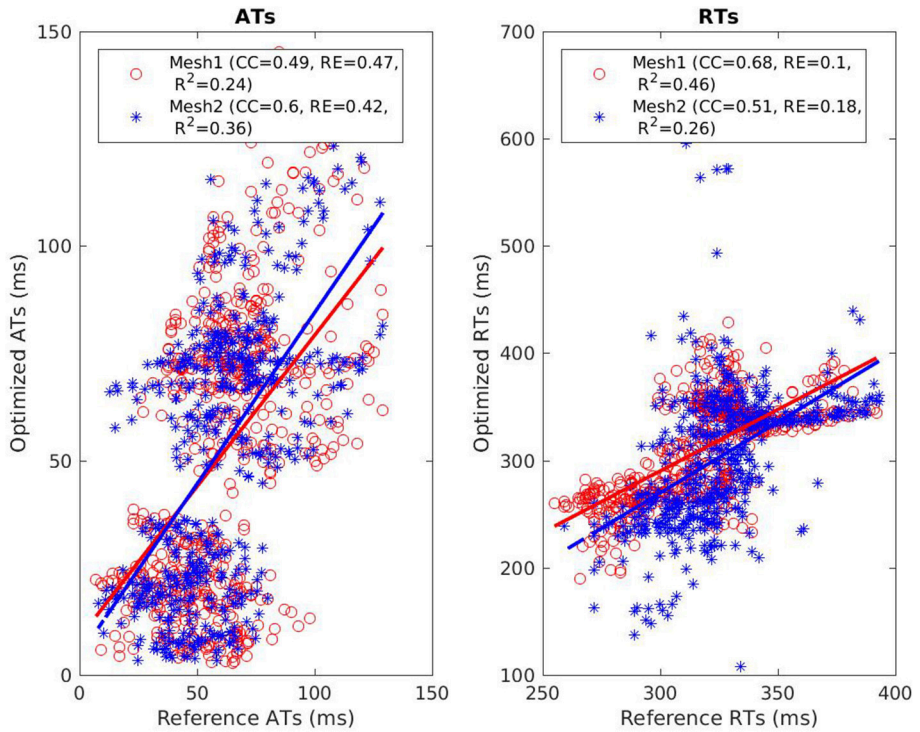

FIGURE 10 | Scatter plot of the ATs **(left)** and RTs **(right)** for the SR case. For each point, the *x* coordinate is the reference AT (resp. RT) and the *y* coordinate is the corresponding reconstructed AT (resp. RT). The dashed lines represent the linear fitting.

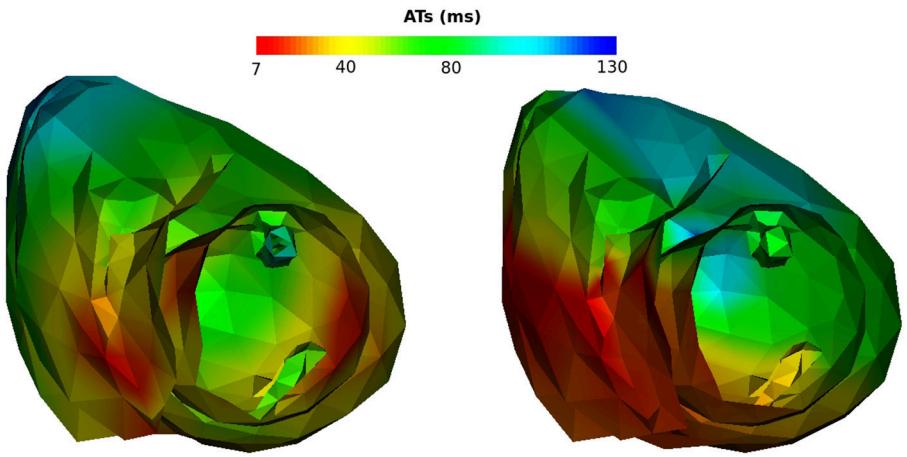

FIGURE 11 | Activation maps on *Mesh2*, SR case. **Left**: reference activation map, **right**: reconstructed activation map.

closed surface of the epicardium alone, and the other including both epicardium and endocardium. Tests were performed using *in silico* data for a sinus beat and six different ventricularly paced beats. Results were very similar for both meshes in 6 cases: all the characteristics we looked at were of the same good quality. The presence of the endocardium slightly improved the ATs on the epicardium. In contrast, for the RTs the effect of including the endocardium was variable. In two other cases (sinus rhythm, case 2, and septal pacing case 7), the reconstruction of AT with *Mesh1* was poor. In the sinus rhythm case, inclusion of the endocardium (*Mesh2*) improved the reconstruction substantially. This was the only case where endo-epicardial gradients, with respect to the total activation time, were significant. In all cases, the repolarization times were better reconstructed with the epicardium only.

We showed that our method was not sensitive to the initialization. Especially the choice for τ_{out} and τ_{close} did not impact the reconstruction of ATs, since these two parameters play a role only during the repolarization. Similarly, imposing global instead of distributed parameters will not worsen ATs reconstruction. The quality of the estimation of the Mitchell-Schaeffer parameters can only be seen through RTs and APD90 reconstructions. CC for RTs were smaller than the ones for ATs which may suggest that the reconstruction of τ_{out} and τ_{close} was less precise than ATs reconstruction. APD90 maps confirmed that, on a same case, we can overestimate as well as underestimate APD90 on large areas.

In general, our method underestimated AT delays between endocardium and epicardium (**Figure 6**). A possible explanation is that from the torso surface the two heart surfaces are too close to be seen separately. The endocardial activity is masked by the epicardial one, even in the case of endocardial pacing. The problems we solved, with *Mesh1* or *Mesh2*, were actually the same; we ended with similar results. It may also explain why we did not reconstruct APD differences between the epicardium and the endocardium.

Another possible explanation is the difference in density between the two meshes. We chose to have about the same number of nodes in each mesh, so that the difference in the number of parameters to identify could not alone explain the results. However, it implied that *Mesh2* was coarser than *Mesh1*. A test was made on a refined mesh of *Mesh2* (**Figure 2**, right). This third mesh had 1328 nodes and a density similar to the one of *Mesh1*. We solved the inverse problem on this mesh for the ventricular pacing case 1. The results we obtained were very similar to those with *Mesh2*: the CC for ATs was 0.79 (0.77 for *Mesh2*) and the average CC for the BSPM was 0.86 (0.9 for *Mesh2*). This test may suggest that the density of the mesh does not have an impact on the results.

We solved the inverse problem with a constant factor $\mathcal{A}$ over the whole heart. However, this factor (proportional to the amplitude of the AP) may not be constant, e.g., in the case of ischemia. We attempted to consider a distributed factor, more relevant from a physiological point of view. In that case the method was not converging, or converged to both positive and negative amplitudes.

So far we did not add noise to the testing data. Even if the models to create the data and to solve the inverse problem are different, it would be helpful to assess the robustness of the method.

Validation data were created from a volumetric heart mesh with a much higher density than *Mesh1* and *Mesh2*. The reference

TABLE 2 | Comparison of different initializations for the sinus rhythm case. Each triplet is of the form (τ_i, $\tau_{out,i}$, $\tau_{close,i}$).

		Heart		Torso	
		ATs	RTs	BSPM	Reduction of *J* (%)
Initialization	**Mesh**	**CC**	**CC**	**CC**	
(60, 6, 150)	*Mesh1*	0.49	0.68	0.83 ± 0.25	87
	Mesh2	0.6	0.51	0.87 ± 0.17	83
(75, 5, 130)	*Mesh1*	0.44	0.65	0.9 ± 0.12	83
	Mesh2	0.51	0.54	0.87 ± 0.16	81
(75, 6, 150)	*Mesh1*	0.48	0.65	0.84 ± 0.26	86
	Mesh2	0.59	0.57	0.89 ± 0.12	82

TABLE 3 | Results for the 7 cases.

		Heart						Torso		
		ATs			RTs			BSPM		
Case	**Mesh**	**CC**	**RE**	**CC epi**	**CC**	**RE**	**CC epi**	**CC**	**RMSE**	**Reduction of *J* (%)**
1	*Mesh1*	0.72	0.3		0.55	0.14		0.88 ± 0.19	0.06 ± 0.05	90
	Mesh2	0.77	0.28	0.72	0.51	0.15	0.5	0.9 ± 0.1	0.07 ± 0.06	86
2	*Mesh1*	0.49	0.47		0.68	0.1		0.83 ± 0.25	0.04 ± 0.04	87
	Mesh2	0.6	0.42	0.64	0.51	0.18	0.5	0.87 ± 0.17	0.05 ± 0.05	83
3	*Mesh1*	0.86	0.22		0.7	0.16		0.89 ± 0.17	0.15 ± 0.09	88
	Mesh2	0.85	0.23	0.89	0.61	0.19	0.69	0.86 ± 0.26	0.15 ± 0.1	87
4	*Mesh1*	0.67	0.32		0.75	0.14		0.84 ± 0.23	0.16 ± 0.13	78
	Mesh2	0.74	0.31	0.67	0.54	0.19	0.44	0.81 ± 0.24	0.16 ± 0.13	79
5	*Mesh1*	0.73	0.28		0.76	0.13		0.84 ± 0.26	0.12 ± 0.1	87
	Mesh2	0.72	0.29	0.72	0.7	0.14	0.75	0.85 ± 0.24	0.12 ± 0.1	87
6	*Mesh1*	0.66	0.35		0.67	0.17		0.74 ± 0.44	0.15 ± 0.14	74
	Mesh2	0.77	0.23	0.74	0.7	0.15	0.7	0.75 ± 0.47	0.14 ± 0.13	77
7	*Mesh1*	0.4	0.42		0.38	0.17		0.88 ± 0.13	0.05 ± 0.05	87
	Mesh2	0.45	0.41	0.43	0.57	0.13	0.48	0.58 ± 0.47	0.08 ± 0.06	89

Case 1: epicardial ventricular pacing. Case 2: sinus rhythm. Case 3: endocardial ventricular pacing. Case 4: epicardial ventricular pacing (near apex). Case 5: endocardial ventricular pacing (near apex). Case 6: pacing on the basis of the pulmonary vein. Case 7: pacing on the septum.

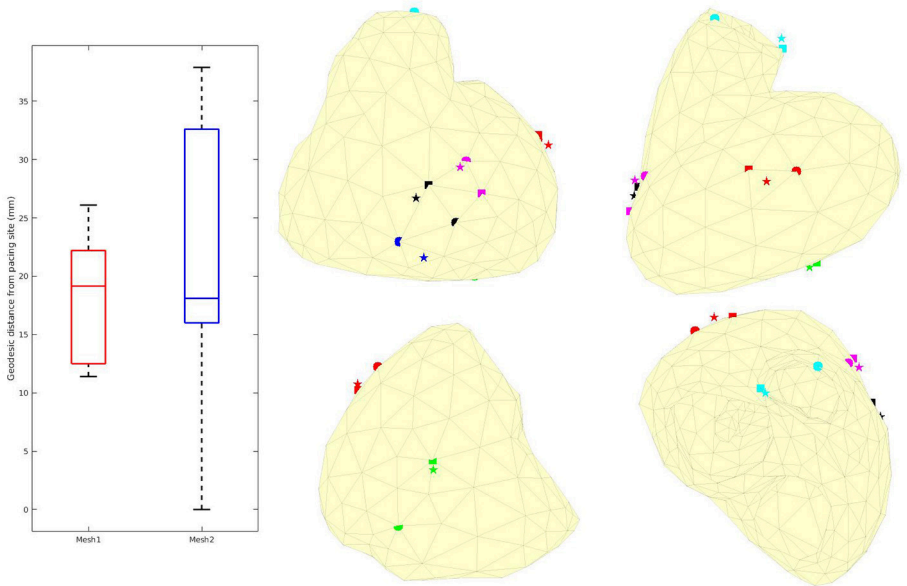

FIGURE 12 | Left: Box plots of the geodesic distances between actual and identified pacing sites. **Middle and right**: actual (sphere), identified with *Mesh1* (pentagram) and *Mesh2* (square) pacing locations. Red: case 1, blue: case 3, green: case 4, black: case 5, cyan: case 6, magenta: case 7. We obtained a *p*-value of 0.74.

values (AT, RT) were the values on the mesh nodes. In contrast, the inverse problem on a surface leads to values that contain information averaged over a considerable volume. This may explain why the delays between reconstructed ATs were smaller than the delays between the reference ATs.

4.1. Comparison With Other Methods

Currently, most ECGI methods are based on a Laplace problem for the potential in the torso. Using the MFS (Wang and Rudy, 2006) or boundary-element models (Sapp et al., 2012; Bear et al., 2018) these methods reconstruct instantaneous potential patterns on the surface of the heart. These methods use Tikhonov or similar forms of regularization to counter the ill-posedness of this problem. This form of regularization leads to smooth solutions for the potential distribution, while the actual pattern, especially in case of an activation wavefront, is characterized by steep gradients. This leads to unrealistic solutions for the activation pattern, featuring large areas that appear to be activated nearly simultaneously, separated by artefactual lines of conduction block (Duchateau et al., 2017; Ravon et al., 2017). Various methods have been proposed to counter this effect, e.g., by reconstructing AT maps from local delays estimated from the whole signal morphology (Duchateau et al., 2017) or by simply smoothing the activation map (Bear et al., 2018). The latter method claims that it does not wipe out true block lines, as well as the artefactual ones, without any validation yet. The method that we proposed here does not require such postprocessing. It imposes a predefined action potential waveform, parameterized in terms of AT and parameters of the Mitchell-Schaeffer model, and does not require further regularization. We have previously shown that our method leads to more realistic activation maps than the MFS (Ravon et al., 2017). In the larger sample of this study we also did not observe the clustering of AT that is typical for MFS methods.

A similar parameter optimization approach, also in terms of endocardial and epicardial AT and RT, was used by van Dam et al. (2009). In contrast to our method it still relied on a (Laplacian) regularization of the AT field, and ahead of the parameter estimation phase it performed an initial estimate based on an exhaustive search. On the other hand, it used a more realistic volume conductor model that took the boundedness and inhomogeneity of the torso into account. Unlike our method they showed that the choice of the initial estimates had an impact on the quality of the inverse procedure. This importance had also been reported by Potyagaylo et al. (2016) and Erem et al. (2014).

Others have worked on the impact of the endocardium in the case of atrial fibrillation Schuler et al. (2017). Considering that atria are very thin, they imposed similar TMP values on the epicardium and the endocardium. Due to the greater thickness of the ventricles, this hypothesis would not be suitable in our study. In a previous study (Potyagaylo et al., 2014) the same group proposed a local regularization of the two surfaces to localize ectopic beats. The regularization parameter can differ between the endocardium and the epicardium. It was a way to better distinguish endocardial events from epicardial events. This approach might be applicable in our case with two different factors $\mathcal{A}$.

4.2. Conclusion

Our parameter optimization method reconstructs accurate activation times and, to a lesser extent, repolarization times. In

some cases inclusion of the endocardium in the solution helps to improve the reconstruction of activation times, while in general it does not improve the reconstruction of repolarization times.

AUTHOR CONTRIBUTIONS

All authors have made substantial contributions to this study. GR designed the study, implemented the algorithms, analyzed, and interpreted the results, and drafted the manuscript. YC and RD helped conceive the study, provided feedback about the implementation of the methods and the interpretation of the results, and revised the manuscript. MP provided the validation data and feedback about the results, and revised the manuscript.

FUNDING

This study received financial support from the French Government as part of the Investments for the Future program managed by the National Research Agency (ANR), Grant reference ANR-10-IAHU-04. This work was granted access to the HPC resources of TGCC under the allocation x2016037379 made by GENCI.

SUPPLEMENTARY MATERIAL

The Supplementary Material for this article can be found online at: https://www.frontiersin.org/articles/10.3389/fphys.2018.01946/full#supplementary-material

REFERENCES

Aliev, R. R., and Panfilov, A. V. (1996). A simple two-variable model of cardiac excitation. *Chaos Solit. Fract.* 7, 293–301. doi: 10.1016/0960-0779(95)00089-5

Bear, L. R., LeGrice, I. J., Sands, G. B., Lever, N. A., Loiselle, D. S., Paterson, D. J., et al. (2018). How accurate is inverse electrocardiographic mapping?: A systematic *in vivo* evaluation. *Circ. Arrhythm. Electrophysiol.* 11:e006108. doi: 10.1161/CIRCEP.117.006108

Cluitmans, M., Karel, J., Bonizzi, P., Volders, P., Westra, R., and Peeters, R. (2018). Wavelet-promoted sparsity for non-invasive reconstruction of electrical activity of the heart. *Med. Biol. Eng. Comput.* 56, 2039–2050. doi: 10.1007/s11517-018-1831-2

Cluitmans, M. J., Clerx, M., Vandersickel, N., Peeters, R. L., Volders, P. G., and Westra, R. L. (2017). Physiology-based regularization of the electrocardiographic inverse problem. *Med. Biol. Eng. Comput.* 55, 1353–1365. doi: 10.1007/s11517-016-1595-5

Dhamala, J., Arevalo, H. J., Sapp, J., Horácek, B. M., Wu, K. C., Trayanova, N. A., et al. (2018). Quantifying the uncertainty in model parameters using gaussian process-based markov chain monte carlo in cardiac electrophysiology. *Med. Imag. Anal.* 48, 43–57. doi: 10.1016/j.media.2018.05.007

Duchateau, J., Potse, M., and Dubois, R. (2017). Spatially coherent activation maps for electrocardiographic imaging. *IEEE Trans. Biomed. Eng.* 64, 1149–1156. doi: 10.1109/TBME.2016.2593003

Erem, B., van Dam, P. M., and Brooks, D. H. (2014). Identifying model inaccuracies and solution uncertainties in non-invasive activation-based imaging of cardiac excitation using convex relaxation. *IEEE Trans. Med. Imaging* 33:902. doi: 10.1109/TMI.2014.2297952

Ghimire, S., Sapp, J. L., Horacek, M., and Wang, L. (2017). "A variational approach to sparse model error estimation in cardiac electrophysiological imaging," in *International Conference on Medical Image Computing and Computer-Assisted Intervention* (Quebec City).

Ghodrati, A., Brooks, D. H., Tadmor, G., and MacLeod, R. S. (2006). Wavefront-based models for inverse electrocardiography. *IEEE Trans. Biomed. Eng.* 53, 1821–1831. doi: 10.1109/TBME.2006.878117

Krause, D., Potse, M., Dickopf, T., Krause, R., Auricchio, A., and Prinzen, F. W. (2012). "Hybrid parallelization of a large-scale heart model," in *Facing the Multicore-Challenge II*, Vol 7174 of *Lecture Notes in Computer Science*, eds, R. Keller, D. Kramer, and J.-P. Weiss, (Berlin:Springer), 120–132

Liu, Z., Liu, C., and He, B. (2006). Noninvasive reconstruction of three-dimensional ventricular activation sequence from the inverse solution of distributed equivalent current density. *IEEE Trans. Med. Imag.* 25, 1307–1318. doi: 10.1109/TMI.2006.882140

Macfarlane, P. W., Van Oosterom, A., Pahlm, O., Kligfield, P., Janse, M., and Camm, J. (2010). *Comprehensive Electrocardiology*. Springer Science & Business Media.

Malmivuo, J., and Plonsey, R. (1995). *Bioelectromagnetism: Principles and Applications of Bioelectric and Biomagnetic Fields*. Oxford University Press.

Mitchell, C. C., and Schaeffer, D. G. (2003). A two-current model for the dynamics of cardiac membrane. *Bull. Math. Biol.* 65, 767–793. doi: 10.1016/S0092-8240(03)00041-7

Potse, M. (2018). Scalable and accurate ECG simulation for reaction-diffusion models of the human heart. *Front. Physiol.* 9:370. doi: 10.3389/fphys.2018.00370

Potse, M., Dubé, B., Richer, J., Vinet, A., and Gulrajani, R. M. (2006). A comparison of monodomain and bidomain reaction-diffusion models for action potential propagation in the human heart. *IEEE Trans. Biomed. Eng.* 53, 2425–2435. doi: 10.1109/TBME.2006.880875

Potse, M., Vinet, A., Opthof, T., and Coronel, R. (2009). Validation of a simple model for the morphology of the T wave in unipolar electrograms. *Am. J. Physiol. Heart Circ. Physiol.* 297, H792–H801. doi: 10.1152/ajpheart.00064.2009

Potyagaylo, D., Dössel, O., and van Dam, P. (2016). Influence of modeling errors on the initial estimate for nonlinear myocardial activation times imaging calculated with fastest route algorithm. *IEEE Trans. Biomed. Eng.* 63, 2576–2584. doi: 10.1109/TBME.2016.2561973

Potyagaylo, D., Schulze, W. H., and Dóssel, O. (2014). "Local regularization of endocardial and epicardial surfaces for better localization of ectopic beats in the inverse problem of ecg," in *Computing*. (IEEE), 837–840.

Rahimi, A., Sapp, J., Xu, J., Bajorski, P., Horacek, M., and Wang, L. (2016). Examining the impact of prior models in transmural electrophysiological imaging: a hierarchical multiple-model bayesian approach. *IEEE Trans. Med. Imaging* 35, 229–243. doi: 10.1109/TMI.2015.2464315

Ravon, G., Dubois, R., Coudière, Y., and Potse, M. (2017). "A parameter optimization to solve the inverse problem in electrocardiography," in *Functional Imaging and Modelling of the Heart* (Toronto, ON), 219–229.

Sapp, J. L., Dawoud, F., Clements, J. C., and Horáček, B. M. (2012). Inverse solution mapping of epicardial potentials; quantitative comparison with epicardial contact mapping. *Circ. Arrhythm. Electrophysiol.* 5, 1001–1009. doi: 10.1161/CIRCEP.111.970160

Schuler, S., Potyagaylo, D., and Dössel, O. (2017). Ecg imaging of simulated atrial fibrillation: imposing epi-endocardial similarity facilitates the reconstruction of transmembrane voltages. *Computing* 44:1.

Ten Tusscher, K. H. W. J., Noble, D., Noble, P. J., and Panfilov, A. V. (2004). A model for human ventricular tissue. *Am. J. Physiol. Heart Circ. Physiol.* 286, H1573–H1589. doi: 10.1152/ajpheart.00794.2003

Tieleman, T., and Hinton, G. (2012). Lecture 6.5-rmsprop: divide the gradient by a running average of its recent magnitude. *COURSERA* 4, 26–31.

van Dam, P. M., Oostendorp, T. F., Linnenbank, A. C., and Van Oosterom, A. (2009). Non-invasive imaging of cardiac activation and recovery. *Ann. Biomed. Eng.* 37, 1739–1756. doi: 10.1007/s10439-009-9747-5

Van Oosterom, A., and Jacquemet, V. (2005). A parameterized description of transmembrane potentials used in forward and inverse procedures. *Folia Cardiol.* 12(Suppl D):111.

van Oosterom, A., and Oostendorp, T. F. (1992). On computing pericardial potentials and current densities in inverse electrocardiography. *J. Electrocardiol.* 25, 102–106. doi: 10.1016/0022-0736(92)90070-G

Wang, L., Zhang, H., Wong, K. C., Liu, H., and Shi, P. (2010). Physiological-model-constrained noninvasive reconstruction of volumetric myocardial transmembrane potentials. *IEEE Trans. Biomed. Eng.* 57, 296–315. doi: 10.1109/TBME.2009.2024531

Wang, Y., and Rudy, Y. (2006). Application of the method of fundamental solutions to potential-based inverse electrocardiography. *Ann. Biomed. Eng.* 34, 1272–1288. doi: 10.1007/s10439-006-9131-7

Conflict of Interest Statement: The authors declare that the research was conducted in the absence of any commercial or financial relationships that could be construed as a potential conflict of interest.

The handling editor and reviewer LW declared their involvement as co-editors in the Research Topic, and confirm the absence of any other collaboration.

frontiers in Physiology

ORIGINAL RESEARCH
published: 05 February 2019
doi: 10.3389/fphys.2019.00058

Solving the Inverse Problem of Electrocardiography on the Endocardium Using a Single Layer Source

Alexander Kalinin, Danila Potyagaylo and Vitaly Kalinin*

EP Solutions SA, Yverdon-les-Bains, Switzerland

The inverse problem of electrocardiography consists in reconstructing cardiac electrical activity from given body surface electrocardiographic measurements. Despite tremendous progress in the field over the last decades, the solution of this problem in terms of electrical potentials on both epi- and the endocardial heart surfaces with acceptable accuracy remains challenging. This paper presents a novel numerical approach aimed at improving the solution quality on the endocardium. Our method exploits the solution representation in the form of electrical single layer densities on the myocardial surface. We demonstrate that this representation brings twofold benefits: first, the inverse problem can be solved for the physiologically meaningful single layer densities. Secondly, a conventional transfer matrix for electrical potentials can be split into two parts, one of which turned out to posess regularizing properties leading to improved endocardial reconstructions. The method was tested *in-silico* for ventricular pacings utilizing realistic CT-based heart and torso geometries. The proposed approach provided more accurate solution on the ventricular endocardium compared to the conventional potential-based solutions with Tikhonov regularization of the 0th, 1st, and 2nd orders. Furthermore, we show a uniform spatio-temporal behavior of the single layer densities over the heart surface, which could be conveniently employed in the regularization procedure.

Keywords: inverse ECG problem, transfer matrix, Tikhonov regularization, single layer potential, endocardial surface

OPEN ACCESS

Edited by:
Ruben Coronel,
University of Amsterdam, Netherlands

Reviewed by:
Matthijs Cluitmans,
Maastricht University, Netherlands
Peter Van Dam,
Radboud University Nijmegen, Netherlands

****Correspondence:***
Alexander Kalinin
alec.kalinin@gmail.com

Specialty section:
This article was submitted to Cardiac Electrophysiology, a section of the journal Frontiers in Physiology

Received: *28 August 2018*
Accepted: *18 January 2019*
Published: *05 February 2019*

Citation:
Kalinin A, Potyagaylo D and Kalinin V (2019) Solving the Inverse Problem of Electrocardiography on the Endocardium Using a Single Layer Source. Front. Physiol. 10:58. doi: 10.3389/fphys.2019.00058

1. INTRODUCTION

Non-invasive electrocardiographic imaging (ECGI) is a novel imaging modality which is based on numerical reconstruction of cardiac electrical activity using the so-called body surface potential maps (BSPM) and patient-specific heart and torso geometries (Ramanathan et al., 2004). The ultimate goal of the ECGI is to allow non-invasive panoramic cardiac mapping in a beat-to-beat mode, thus facilitating diagnostics and treatment planning for non-sustained, aperiodic or non-tolerable cardiac arrhythmia.

A mathematical problem underlaying ECGI is known as the inverse problem of ECG. This problem can be formulated in several ways with respect to the unknown physical values that are sought after. Its early formulation concerned pericardial (also called epicardial) potentials, which

by definition neglect electrophysiological processes ongoing on the inner heart walls (Franzone et al., 1978; Rudy and Messinger-Rapport, 1988). Mathematically, this is a Cauchy problem for the Laplace equation, a classical example of ill-posed problem: even small amount of noise in the Cauchy boundary data can lead to arbitrary high errors in the solution (Kubo, 1994; Takeuchi and Yamamoto, 2008). Therefore, special regularizing algorithms must be used in order to obtain a stable solution approximation.

With this respect, significant progress has been recently made in the development of numerical algorithms for solving the inverse problem of ECG in terms of epicardial potentials, which is reflected in a constantly increasing number of clinical applications of the ECGI. This methodology was successfully used for optimizing cardiac resynchronization therapy, guiding catheter ablation of origins of focal atrial and ventricular tachycardia, detecting macro-reentrant circuits and electrical rotors in patients with reentrant ventricular tachycardia, atrial flutter and atrial fibrillation (Guillem et al., 2013; Erkapic et al., 2014; Shah et al., 2014; Dubois et al., 2015; Varma, 2015; Rodrigo et al., 2017). Moreover, Cuculich et al. demonstrated the way ECGI can provide a support for guiding non-invasive ablation of cardiac arrhythmia (Cuculich et al., 2017).

Unfortunately, epicardial imaging bears one significant limitation of potentially losing electrophysiologically relevant information about cardiac electrical activity on the cardiac endocardium and, especially, on the interventricular and interatrial septum. To overcome this drawback, one can consider reconstructing electrical potentials on both epicardial and endocardial heart surfaces. Formally, this statement results in the same Cauchy problem for the Laplace equation. Due to a more complex non-convex geometry of the epi-endocardial heart surface compared to its relatively simple "convex hull" (epicardium/pericardium), the inverse problem for endo-epicardial reconstruction becomes even worse conditioned.

Nevertheless, solution of the endo-epicadial inverse problem was employed for detection of origins of focal ventricular tachycardia (Revishvili et al., 2015; Wissner et al., 2016), determination of electrical rotors in atrial fibrillation (Metzner et al., 2017), exploring morphology of unipolar epicardial and endocardial electrograms in the right ventricular outflow tract in patients with Brugada syndrome (Rudic et al., 2016), analysis of excitation patterns in reentrant ventricular tachycardia (Tsyganov et al., 2017) and atrial flutter (Wissner et al., 2018). In these studies, a numerical algorithm based on a combination of Tikhonov and iterative regularization was used (Bokeriya et al., 2008; Kalinin, 2011).

Alternative to the potential-based statement, the problem can also be formulated in terms of surface electrical layer source models. The most prominent example of such statement is the equivalent double layer (EDL) defined on both epi- and endocardial surfaces of the heart (van Oosterom, 2014). According to the bidomain model (Tung, 1978), the EDL is proportional to the transmembrane potential when the body electrical conductivity as well as the extracellular and intracellular myocardial conductivities are considered to be isotropic and the sum of the extracellular and intracellular conductivities is equal to those of the body (Geselowitz, 1989; Kalinin et al., 2017). This electrophysiological meaning was shown to be highly beneficial for construction of ECGI-specific regularization techniques (Berger et al., 2006, 2011; van Dam et al., 2009).

In contrast to the surface EDL source model, the electrical sources inside the myocardium cannot be reconstructed unambiguously (Geselowitz, 1989; Kalinin et al., 2017). However, employement of proper regularization schemes targeting intramural transmembrane potentials or current densities was reported to overcome this rather theoretical limitation delivering promising results (see for example He et al., 2003; Skipa, 2004; Schulze et al., 2013; Wang et al., 2013; Xu et al., 2014; Zhou et al., 2016).

Overall, despite the efforts and progress made in the ECGI field, non-invasive reconstruction of the local cardiac activity on both epi- and endocardium of the heart remains a challenging task for clinical, mathematical and engineering research. Furthermore, it is evident that, irrespectively of the source model under consideration, effectiveness of Tikhonov regularization method strongly depends on the choice of a regularization operator R. In addition to the simplest option, i.e., using an identity matrix, the surface Laplacian L as well as an operator D mapping the electrical potential on the cardiac surface to its normal derivative or the transmural gradient were used for the ECGI applications (Horácek and Clements, 1997; Erem et al., 2014; Wang et al., 2016). However, the problem of an optimal choice of the regularization operator in Tikhonov regularization is still open.

In this article, we describe a novel numerical approach for treating the epi-endocardial reconstruction problem by introducing an alternative source model formulation, the single layer density. We consider this problem from three interrelated perspectives. From the numerical algebraic point of view, we introduce the involved transfer matrices associated to the boundary elements method. Furthermore, we investigate regularizing properties of the inverse single layer operator for Tikhonov regularization. Finally, we investigate spatio-temporal behavior of the single layer density source model, which can be employed in the regularization procedures.

2. METHODS

In this paper we use the geometry notation reported in **Figure 1**. Let Γ_0 be a body surface and Γ_1 be a surface of ventricles (or atria) circumpassing both epi- and endocardial parts. Let $\Omega \subset \mathbb{R}^3$ be a body domain bounded from the outside by the surface Γ_0 and from the inside by surface Γ_1, with outward unit normal vectors. Let $\Omega_M \subset \Omega$ represent the myocardial domain bounded by Γ_1 with inward unit normal vectors. Surfaces Γ_0 and Γ_1 are supposed to be sufficiently smooth.

In the physical model considered here, the electrical field is originated by the electrical sources situated in the myocardium domain Ω_M only. We neglect electrical sources in the human body domain Ω and consider the body domain as a passive volume conductor. This body domain Ω includes extracardiac

organs as well as the cardiac chambers filled with the blood. Moreover, for those time moments when the ventricles/atria are in the resting state the atrial/ventricular myocardium can be also considered as a passive volume conductor.

The commonly used approach for the mathematical description of myocardial electrical activity is based on so the called bidomain model. Within this model, myocardial tissue is considered to consist of homogenized intracellular and extracellular spaces. The set of accompanying differential equations establishes the relationship between the intra- and extracellular potentials taking into account cell membrane properties and ionic concentrations (see e.g., Tung, 1978; Bourgault et al., 2009). The electrical conductivity in the intra- and extracellular media are provided in tensor form reflecting faster excitation propagation along the myocardial fibers than across them. In this work, we employed the bidomain model with isotropic cardiac electrical conductivity values and a homogeneous torso model to simulate the electrical potentials throughout the geometry volume for ectopic ventricular stimuli. The potentials obtained on the body surface, the body surface potential maps (BSPM), were then used as the input for validating the proposed approach of non-invasive reconstruction of cardiac electrical activity. This, so-called forward problem of ECG, was solved with the CHASTE software (Mirams et al., 2013), which provided the reference transmembrane potentials in the heart and electrical potentials in the whole geometry volume.

For biological tissues frequencies under the conventional assumptions the Maxwell equations, describing propagation of electromagnetic fields in the body volume conductor, can be simplified to the quasi-static form (Gulrajani, 1998). It allows temporal separation of the cardiac sources, meaning that one can solve the inverse problem of ECG for distinct time instants $t_0, t_1, \ldots, t_M$ independently from each other.

Furthermore, the inverse problem of ECG can be treated using direct and indirect regularization approaches. The direct way is the computation of the harmonic function value on Γ_1 without considering myocardial electrical sources. The indirect way consists of presenting the electrical potential on Γ_1 as a potential of the myocardial sources. It is well known that an endless number of the sources distributions in the myocardium domain can generate the same potential in the passive volume conductor domain. Therefore, they use an "effective" unique representation of the electrical sources in form of sources on the myocardial surface. In this article we consider the direct and the indirect ways for numerical solving the inverse electrocardiography problem.

2.1. Computational Method for the Inverse Potential Problem: A Conventional Approach

The inverse problem of ECG in terms of electrical potentials for the geometry depicted in **Figure 2** reads to find a function $u(x)$ in $\overline{\Omega}$ such that

$$\Delta u(x) = 0, \quad x \in \Omega, \tag{1}$$

$$u(x) = \varphi(x), \quad x \in \Gamma_0, \tag{2}$$

$$\frac{\partial u(x)}{\partial n} = 0, \quad x \in \Gamma_0, \tag{3}$$

where $\varphi(x)$ is the measured BSPM. Problem (1)–(3) is known as the Cauchy problem for the Laplace equation. Its solution is unique, however, the problem is ill-posed: even a small amount of noise in the boundary conditions can lead to an arbitrary high error in the solution.

To solve the problem a direct boundary element method (BEM) can be used. Accordingly, the problem (1)–(3) is

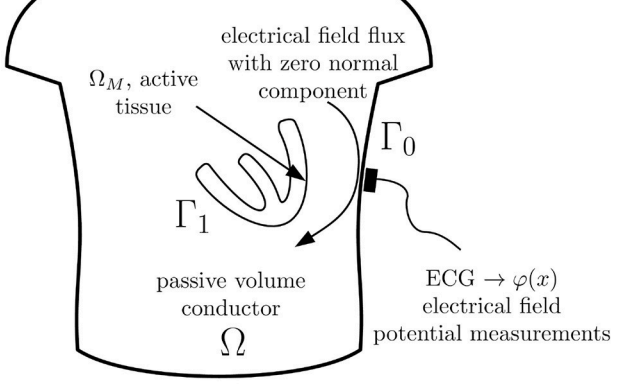

FIGURE 1 | Physical model underlying the inverse ECG problem.

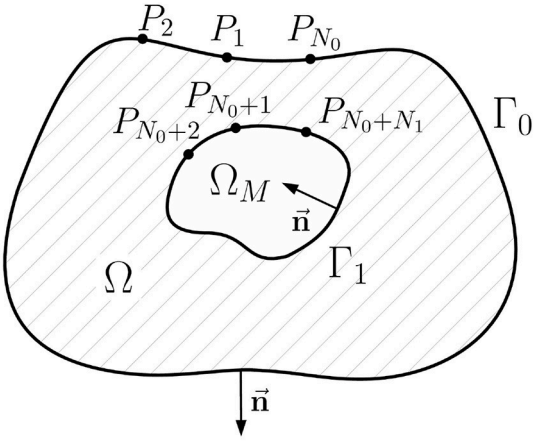

FIGURE 2 | Schematic geometric relationships of the inverse potential problem in the internal statement. Ω is the passive volume conductor domain, Ω_M is the myocardial domain, Γ_0 is the body surface, Γ_1 is the myocardial surface (endo- and epicardial surface), $\vec{\mathbf{n}}$ its unit normal vector directed inward, P_i, $i = 1..N_0 + N_1$ are collocation points used in direct boundary element method, N_0 is the number of collocation points on the Γ_0, N_1 is the number of collocation points on Γ_1.

reformulated as a boundary integral equation based on the third Green's identity: for any given point $P \in \Gamma_0 \cup \Gamma_1$ and harmonic function u in domain Ω

$$c(P)u(P) + \int\limits_{\Gamma_0 \cup \Gamma_1} u(Q) \frac{\partial G(P,Q)}{\partial n}\, d\Gamma = \int\limits_{\Gamma_0 \cup \Gamma_1} \frac{\partial u(Q)}{\partial n} G(P,Q)\, d\Gamma, \quad (4)$$

where $Q \in d\Gamma$ is the integration variable and

$$G(P,Q) = \frac{1}{|P-Q|} \quad (5)$$

is the inverse Euclidean distance between P and Q, $c(P)$ is the solid angle at the point P.

Next step is to establish a system of linear algebra equations suitable for numerical calculations from the continues statement (4). This step is called discretization. We use the following discretization scheme: (a) approximation of the surfaces Γ_0 and Γ_1 by the triangular meshes, (b) approximation of the functions $u(x)$ and $\frac{\partial u(x)}{\partial n}$ by series of linear basis functions, and (c) computation of the single and double layer type integrals over basis functions. Computation of such integrals over basis function is most important step. Fortunately, it is well studied, see e.g., Dunavant (1985), Davey and Hinduja (1989), and van Oosterom (2012). Full details of the discretization process are described in the **Appendix A**.

After the discretization we get the following system of linear equations:

$$\begin{aligned} H_{00}u_0 + H_{01}u_1 &= G_{01}q_1 \\ H_{10}u_0 + H_{11}u_1 &= G_{11}q_1 \end{aligned} \quad (6)$$

where u_0, u_1 are electrical potentials on the surfaces Γ_0 and Γ_1 respectively, q_1 is the normal derivative of the electrical potential on the surface Γ_1, matrices G_{ij} arise from the discretization of the surface integrals corresponding to the single layer

$$\int\limits_{\Gamma_j} \frac{\partial u(Q)}{\partial n} G(P_{\Gamma_i}, Q)\, d\Gamma_Q, \quad (7)$$

while matrices H_{ij} arise from the discretization of the surface integrals corresponding to the double layer

$$\int\limits_{\Gamma_j} u(Q) \frac{\partial G(P_{\Gamma_i}, Q)}{\partial n}\, d\Gamma_Q, \quad (8)$$

Finally, i is the index of the surface containing the point P, j is that of the surface containing Q.

In **Figure 3** we provide the plots of the singular values' decay of the matrices above. In agreement with the boundary element theory, matrices G_{11}, H_{00} and H_{11} are well-conditioned and can be inverted without regularization.

From the system (6) we can get the transfer matrix $u_1 \rightarrow u_0$ (relating EP to BSPM, EP stands for endo- and epicardial potentials):

$$\left(-H_{01} + G_{01}G_{11}^{-1}H_{11}\right) u_1 = \left(H_{00} - G_{01}G_{11}^{-1}H_{10}\right) u_0, \quad (9)$$

in short form

$$Au_1 = f_0, \quad (10)$$

where f_0 is known right-hand side of Equation (9). In the following, we call the inverse ECG problem statement (1)–(3) the *internal* statement and Equation (9) the *internal* equation.

In order to find the normal derivative of the potential on Γ_1 let us introduce the Dirichlet-Neumann mapping matrix $u_1 \rightarrow q_1$ relating EP to its normal derivative on the heart. This matrix can be derived from the system (6) in the form

$$\left(G_{11} - H_{10}H_{00}^{-1}G_{01}\right)^{-1} \left(H_{11} - H_{10}H_{00}^{-1}H_{01}\right) u_1 = q_1, \quad (11)$$

or

$$Du_1 = q_1 \quad (12)$$

Note that representations (9) and (11) require inversion of well-conditioned matrices only. Matrices A and D are well known in the literature (e.g., see Yun et al., 1997; Gulrajani, 1998).

Matrix A is ill-conditioned, therefore the numerical solution of Equation (10) requires suitable regularization techniques. The commonly used approach is the Tikhonov regularization method:

$$u_1^{\lambda} = \arg\min(\|Au_1 - f_0\|_2^2 + \lambda^2 \|Ru_1\|_2^2), \quad (13)$$

where u_1^{λ} is the regularized solution, λ^2 is the regularization parameter and R is the regularization operator. Minimization problem (13) has the closed-form solution:

$$u_1^{\lambda} = (A^T A + \lambda^2 R^T R)^{-1} A^T f_0. \quad (14)$$

Regularization operator R can be taken, for example, as $R = I_{11}$ (identity matrix) for 0 order, $R = D$ for 1th order and as a Laplace-Beltrami ("surface Laplacian") operator $Lu_1 = \Delta_{\Gamma_1} u_1$ (see for example Huiskamp, 1991) for the 2nd order Tikhonov regularization.

2.2. Computational Method for the Inverse Potential Problem: A Single Layer Approach

In this section we will formulate an alternative representation of the $u_1 \rightarrow u_0$ transfer matrix and propose a new statement of the inverse problem in terms of the equivalent single layer (ESL). Geometry notations for this statement are depicted on **Figure 4**.

Although the cardiac electrical potential $u(x)$ is not a harmonic function in the domain Ω_M, we can define another function $\hat{u}$ harmonic in Ω_M whose boundary values on Γ_1 are equal to those of $u(x)$, the solution of problem (1)–(3). The function $\hat{u}$ can be defined as the unique solution of the following Dirichlet problem for the Laplace equation:

$$\Delta \hat{u}(x) = 0, \quad x \in \Omega_M, \quad (15)$$

$$\hat{u}(x) = u(x), \quad x \in \Gamma_1. \quad (16)$$

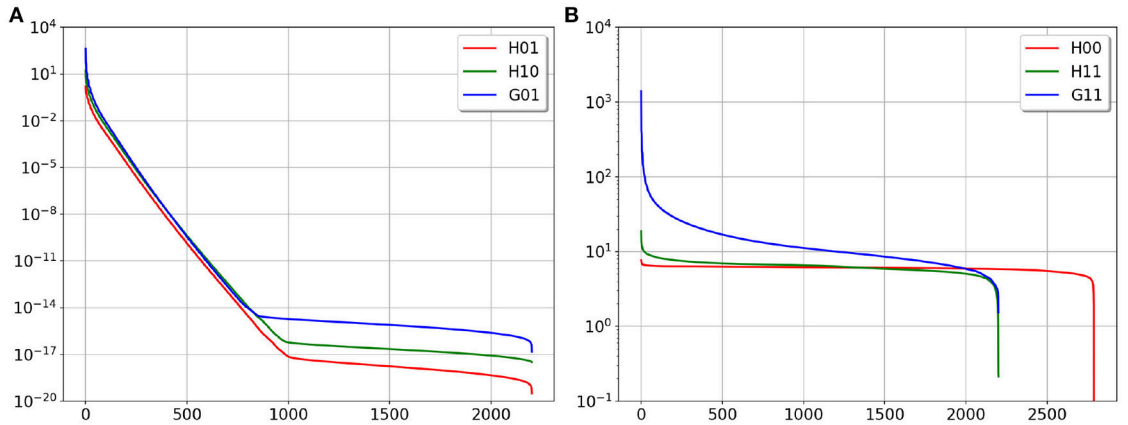

FIGURE 3 | SVD plot of the considered matrices, **(A)** is ill-conditioned matrices, **(B)** is well-conditioned matrices.

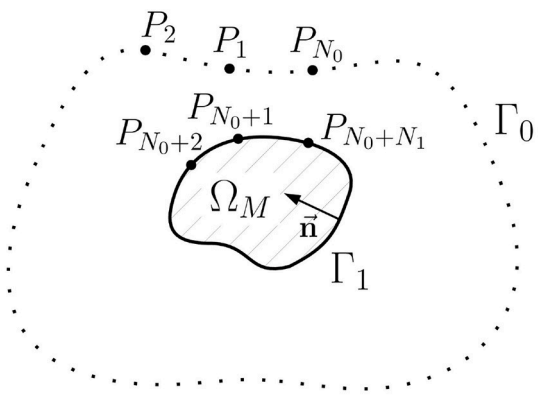

FIGURE 4 | Schematic geometric relationships of the inverse potential problem in the external statement. Ω_M is the myocardial domain, Γ_0 is the body surface, Γ_1 is the myocardial surface (endo- and epicardial surface), $\vec{\mathbf{n}}$ is unit normal vector, P_i, $i = 1..N_0 + N_1$ are collocation points used in direct boundary element method, N_0 is the number of collocation points on the Γ_0, N_1 is the number of collocation points on Γ_1.

The idea under this definition is following. With the function $\hat{u}(x)$ harmonic in the domain Ω_M we force the electric sources to be only on the endo- and epicardial surface. And with the condition $\hat{u}(x) = u(x)$ on Γ_1 we can link such sources densities with the actual electrical potential $u(x)$. To derive such relationships we use boundary element method.

For any given point $P \in \Gamma_1$ and harmonic function $\hat{u}$ in domain Ω_M the third Green's identity gives us the following boundary integral equation

$$\hat{c}(P)\hat{u}(P) + \int_{\Gamma_1} \hat{u}(Q)\frac{\partial G(P,Q)}{\partial n}\,d\Gamma_Q = \int_{\Gamma_1} \frac{\partial \hat{u}(Q)}{\partial n} G(P,Q)\,d\Gamma_Q, \quad P \in \Gamma_1. \tag{17}$$

Moreover, for any point $P \in \Gamma_0$ and harmonic function $\hat{u}$ in domain Ω_M the third Green's identity give us the following boundary integral equation

$$\int_{\Gamma_1} \hat{u}(Q)\frac{\partial G(P,Q)}{\partial n}\,d\Gamma_Q = \int_{\Gamma_1} \frac{\partial \hat{u}(Q)}{\partial n} G(P,Q)\,d\Gamma_Q, \quad P \in \Gamma_0, \tag{18}$$

Applying the same discretization as in section 2.1 we get the following algebraic system:

$$\begin{aligned} \hat{H}_{11}\hat{u}_1 &= \hat{G}_{11}\hat{q}_1 \\ \hat{H}_{01}\hat{u}_1 &= \hat{G}_{01}\hat{q}_1. \end{aligned} \tag{19}$$

where $\hat{u}_1$ is a vector containing values of function $\hat{u}(x)$ at the points on the surface Γ_1, $\hat{q}_1$ is a vector containing values of function $\frac{\partial \hat{u}(x)}{\partial n}$ on Γ_1, matrices $\hat{G}_{ij}$ arise from the discretization of the surface integrals corresponding to the single layer

$$\int_{\Gamma_j} \frac{\partial \hat{u}(Q)}{\partial n} G(P_{\Gamma_i}, Q)\,d\Gamma_Q, \tag{20}$$

matrices $\hat{H}_{ij}$ arise from the discretization of the surface integrals corresponding to the double layer

$$\int_{\Gamma_j} \hat{u}(Q)\frac{\partial G(P_{\Gamma_i}, Q)}{\partial n}\,d\Gamma_Q, \tag{21}$$

i is the index of the surface with the fixed point P, j is the index of the surface with points of integration Q.

We can express the unknown variable $\hat{q}_1$ from the first equation and obtain a new matrix-vector identity for the variable $\hat{u}_1$

$$\hat{H}_{01}\hat{u}_1 = \hat{G}_{01}\hat{G}_{11}^{-1}\hat{H}_{11}\hat{u}_1 \tag{22}$$

Using (16) we can write (22) as

$$\hat{H}_{01}u_1 = \hat{G}_{01}\hat{G}_{11}^{-1}\hat{H}_{11}u_1. \tag{23}$$

Let us compare matrices $\hat{G}_{01}$, $\hat{G}_{11}$, $\hat{H}_{01}$, and $\hat{H}_{11}$ with matrices G_{01}, G_{11}, H_{01}, and H_{11} defined in section 2.1. All matrices are determined only by the same surfaces Γ_0 and Γ_1. However, normal vectors to the surface Γ_1 were directed outwards related to the domain Ω and inwards related to the domain Ω_M. Taking into account these facts it is easy to demonstrate that

$$\hat{G}_{01} = G_{01}, \tag{24}$$

$$\hat{G}_{11} = G_{11}, \tag{25}$$

$$\hat{H}_{01} = H_{01}, \tag{26}$$

$$\hat{H}_{11} = H_{11} - 4\pi I_{11}, \tag{27}$$

where I_{11} is the identity matrix.

Now we can rewrite (23) using the matrix defined in section 2.1:

$$H_{01}u_1 = G_{01}G_{11}^{-1}(H_{11} - 4\pi I_{11})u_1 \tag{28}$$

or

$$4\pi G_{01}G_{11}^{-1}u_1 = \left(-H_{01} + G_{01}G_{11}^{-1}H_{11}\right)u_1 \tag{29}$$

Comparing (29) with (9) we can see that the right hand side of the Equation (29) is the same as the left hand side of the Equation (9). Therefore

$$4\pi G_{01}G_{11}^{-1}u_1 = \left(H_{00} - G_{01}G_{11}^{-1}H_{10}\right)u_0 \tag{30}$$

or in short form

$$4\pi G_{01}G_{11}^{-1}u_1 = f_0. \tag{31}$$

Equation (31) is a new representation of the $u_1 \rightarrow u_0$ transfer matrix. In this article we call this approach the *external* statement of the inverse problem and transfer matrix (30) the *external* form of the transfer matrix.

Matrix G_{11} is well-conditioned (see **Figure 3**), so we can define a new function

$$w_1 \equiv G_{11}^{-1}u_1 \tag{32}$$

and new equation for the function w_1

$$4\pi G_{01}w_1 = f_0. \tag{33}$$

Matrices G_{11} and G_{01} are discretizations of the single layer integral operators. Therefore, the function w_1 has a physical meaning of electrical sources in form of single layer on the myocardial surface. In this paper we call function w_1 the equivalent single layer (ESL) density. Equation (33) allows us to solve the inverse ECG problem in terms of the ESL.

Furthermore, we propose two methods for regularizing the inverse potential problem. The first method consists of the ESL computation by solving the Equation (33) and reconstruction of the potential u_1 from the obtained ESL by formula $u_1 = G_{11}w_1$.

Matrix G_{01} is ill-conditioned, therefore the numerical solution of Equation (33) requires suitable regularization algorithms. The Tikhonov regularization method of 0th order consists in solving

$$w_1^{\lambda} = \arg\min(4\pi\|G_{01}w_1 - f_0\|_2^2 + \lambda^2\|w_1\|_2^2), \tag{34}$$

whose solution reads

$$w_1^{\lambda} = (G_{01}^T G_{01} + \lambda^2 I_{11})^{-1}G_{01}^T f_0, \tag{35}$$

and next we compute

$$u_1^{\lambda} = G_{11}w_1^{\lambda}, \tag{36}$$

where w_1^{λ}, u_1^{λ} are the regularized solutions in terms of the ESL and potentials respectively, λ^2 is the regularization parameter.

The second method relies on solving the transfer Equation (10) using Tikhonov regularization method with constraints on the ESL, i.e., using inverse ESL matrix G_{11}^{-1} as regularization operator:

$$u_1^{\lambda} = \arg\min(\|Au_1 - f_0\|_2^2 + \lambda^2\|w_1\|_2^2), \tag{37}$$

or

$$u_1^{\lambda} = \arg\min(\|Au_1 - f_0\|_2^2 + \lambda^2\|G_{11}^{-1}u_1\|_2^2), \tag{38}$$

with solution:

$$u_1^{\lambda} = (A^T A + \lambda^2 {G_{11}^{-1}}^T G_{11}^{-1})^{-1}A^T f_0. \tag{39}$$

2.3. Experimental Methods and Evaluation Protocols

Accuracy of the numerical algorithms for solving the inverse problem of ECG was tested on realistic *in-silico* data of cardiac electrical activity. Computer tomography (CT) scans of three patients were used for obtaining the personalized anatomy of the torso and heart surfaces.

These patients were examined in Bakulev National Medical Research Center of Cardiovascular Surgery (Moscow, Russia) in 2017 year. The study was performed in accordance with principles of the Declaration of Helsinki. The protocol of the study was approved by local ethics committee of Bakulev Research Center. All patients provided written informed consent to the CT scanning procedures and agreed to data retrieval, analysis and publication.

A patient-specific anatomical model was comprised of a biventricular cardiac model and a homogeneous torso model. Data processing steps included segmentation of the torso and the ventricles CT volume models, generation of the polygonal surface meshes ("Amycard 01 C" software, EP Solutions SA) and creation of tetrahedral final element meshes ("Gmsh" software Geuzaine and Remacle, 2009).

The bidomain model with the strong heart-torso coupling and TNNP cellular model (ten Tusscher et al., 2004) were used for simulation of a myocardium electrical activity. Transmural and apico-basal cellular heterogeneities were simulated using the approaches proposed in Keller et al. (2012) and ten Tusscher

and Panfilov (2006), respectively. Simulations of cardiac electrical activity were performed with the methodology described in Ushenin et al. (2017) using the Cardiac CHASTE software (Mirams et al., 2013). In each anatomical patient model, these finite-element calculations resulted in the transmembrane potentials in the myocardial volume, while the electrical potentials were simulated at each node of the tetrahedral meshes. The torso surface potentials were used as the input for testing the proposed inverse routines.

We simulated three focal type electrical activation patterns. The focal origins were in the lateral wall of the left ventricle (LV) for the patient heart 1, in the right ventricular apex (RVA) for the patient heart 2 and in the right ventricular outflow tract (RVOT) for the patient heart 3. A "virtual" rectangular current pulse of $-50\mu A$ with a duration of 3 ms applied to an area of 6 mm was used for initiation of a cardiac excitation. "Virtual" action potential signals and local unipolar electrograms on the ventricular surface as well as the body surface ECG were obtained as a result of the simulation.

The first part of the evaluation protocol included computation of the ESL (function w_1) from the simulated electrical potential u_1 on the myocardial surface according to the formula (32) and comparison of this function's morphology in space and time with the transmembrane action potentials.

The second part of the evaluation protocol included an actual testing of the proposed algorithms for the solution of the inverse problem. For this, the BSPM were distorted by an additive Gaussian noise of 50 dB SNR and used for reconstruction of the electrical potential on the endocardial and epicardial surface of the ventricles. The reconstructed local unipolar electrograms on the myocardial surface were compared to the references electrograms obtained from the simulations.

We used the following metrics to estimate solution quality:

$$re_x = \frac{1}{M}\sum_{i=1}^{M}\frac{\sqrt{\sum_{j=1}^{N_1}(u_1(x_j,t_i)-u_1^{num}(x_j,t_i))^2}}{\sqrt{\sum_{j=1}^{N_1}u_1(x_j,t_i)^2}} \qquad (40)$$

$$cc_t = \frac{1}{N_1}\sum_{i=1}^{N_1} cc(u_1(x_i,t),u_1^{num}(x_i,t)), \qquad (41)$$

where $u_1(x,t)$ is the given solution, $u_1^{num}(x,t)$ is the inverse reconstruction, $cc(\cdot,\cdot)$ – is the correlation coefficient, M is the number of time instances, N_1 number of nodes in the heart triangular mesh.

The quantity re_x provides the spatial error of the solution for each instant t_i, whereas cc_t shows the accuracy of the reconstructed electrogram at each node on the heart mesh. These errors are calculated separately for epicardial and endocardial surfaces of the heart ventricles.

We tested the following inverse numerical scheme:

1. Tikhonov solution of the equation $Au_1 = f_0$ with the conventional EP transfer matrix A and three types of constraints: 0th order $\|u_1\|_2^2 \equiv \|I_{11}u_1\|_2^2$, 1st order $\|\frac{\partial u_1}{\partial n}\|_2^2 \equiv \|Du_1\|_{L_2}$ and 2nd order $\|\Delta_{\Gamma_1}u_1\|_2^2 \equiv \|Lu_1\|_2^2$.
2. Tikhonov solution of the equation $4\pi G_{01}w_1 = f_0, u_1 = G_{11}w_1$ with the ESL transfer matrix G_{01} and the constraint $\|w_1\|_2^2 \equiv \|I_{11}w_1\|_2^2$, see Equation (34).
3. Combination of these two approaches, i.e., Tikhonov solution of the equation $Au_1 = f_0$ with conventional EP matrix A but with the new type of constraint $\|w_1\|_2^2 \equiv \|G_{11}^{-1}u_1\|_2^2$ for the ESL, see Equations (37), (38).

We found the value of the regularization parameter λ thanks to the L-Curve method (Hansen, 2000).

3. RESULTS

3.1. Properties of the ESL (Function w_1)

Figure 5 shows the distribution of the ESL (function $w_1(x,t)$) on the heart surface for several time instants of the cardiocycle. **Figure 6** shows ESL as time signals at several points of the ventricular surface. The ESL in space as well as in time domains looks like a sparsed function and well reflects the fronts of myocardial depolarization and repolarization.

The ESL signals shape has a form of bipolar spike associated with time moments of myocardial depolarization and low-amplitude wave associated with myocardium repolarization. Depolarization part of the signal has similar morphology at all points of the myocardial surface with the first peak being positive and the second one negative (see **Figure 6B**). Duration of depolarization spike varied from 12 to 22 ms, its magnitude varied from 0.5 to 1.2 mC/m^2.

The repolarization waves were positive in 91% of ESL signals and negative in 2% of the signals. In 7% of the signals the repolarization waves were biphasic with the first negative half-wave. Duration of the repolarization waves varied from 18 to 27 ms, their magnitude varied from 0.05 to 0.2 mC/m^2.

The zero-crossing value between positive and negative peaks of the signals matched with depolarization time moment (see **Figure 6C**). The mean difference between that zero point of the single layer density signal and maximal slope of transmembrane action potential (TMP) up-stroke was 1.3 ± 2.4 ms.

The time moment of maximum positive monophasic repolarization waves in ESL signals corresponded to 91 ± 4% level of TMP repolarization (see **Figure 6C**). Biphasic and negative repolarization waves were also associated with repolarization phase of TMP, but reliable identification of connections between the moment of their appearance and the level of myocardial repolarization requires more data and further analysis. Therefore, ESL signals can be potentially used for detection of depolarization and repolarization of the myocardium. However, development of this method requires further investigations.

3.2. Accuracy of the Inverse Solutions

Table 1 shows results of the numerical experiments. The first column in the table shows the type of equation used, the second column shows the regularization constraint and the last columns show the re_x and cc_t metric values (see (40), (41)) separately

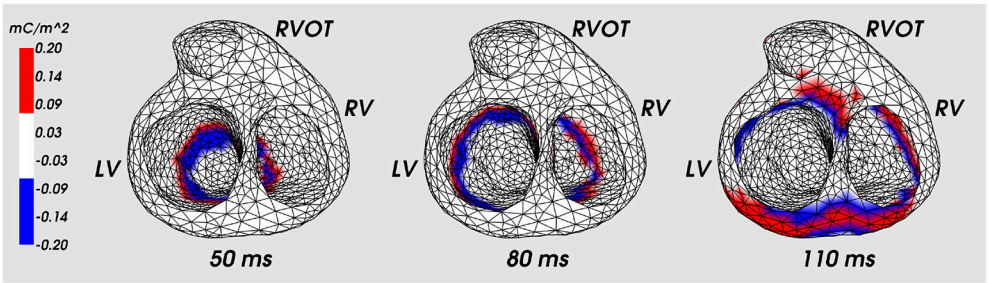

FIGURE 5 | Distribution of the ESL density (function w_1) on the heart surface for the fixed time moments of cardiocycle. Cardiac excitation was initiated in the apical area. LV, left ventricle; RV, right ventricle; RVOT, right ventricle outflow tract.

for the LV, RVA and RVOT simulations and epicardial and endocardial surfaces.

Electrical signals from the several epicardial and endocardial sites of the ventricles were selected as representative examples in order to provide visual evaluation of their morphology (see **Figure 7**). The center of LV lateral wall (Epi LV lateral), the apical region (Epi LV apex), anterior-lateral zone of the RVOT (Epi RVOT) and the center of RV lateral wall (Epi RV lateral) were taken on the epicardial surface. The center of LV lateral wall (Endo LV lateral), the central zones of the left (Septum LV) and the right sides (Septum RV) of the ventrical septum and the center of RV lateral wall (Endo RV lateral) were taken on the endocardial surface.

In **Figure 7** we present the results of the inverse reconstruction of the electrograms in the defined above points on the heart surface. **Figure 7A** shows results of reconstruction with the conventional EP transfer matrix A and Tikhonov regularization of the 2nd order. **Figure 7B** shows results of reconstruction with the ESL transfer matrix G_{01} and Tikhonov regularization of 0th order.

All algorithms demonstrated similar accuracy on the epicardial surface, but their accuracy on the endocardial surface was significantly different.

On the endocardial surface algorithm in terms of EP with conventional transfer matrix A and 0th order regularization demonstrated poor accuracy. The reconstructed electrograms have near-zero magnitude and poor correlation with the references electrograms. Algorithms with the 1st order regularization provided poor accuracy in terms of relative error, but the reconstructed electrograms correlated better with the reference signals (see **Table 1**). Algorithm with the 2nd order regularization showed slightly better results in comparison to 1st order. However, this algorithm did not allow to reconstruct the electrograms morphology with acceptable quality. In particular, reconstructed electrograms at the Endo LV lateral, RV lateral and Septum RV sites has opposite polarity at QRS part and at the Endo LV lateral site has opposite polarity at ST part than the reference electrograms (see **Figure 7A**). Detailed metrics values are given in the **Table 1**.

Both algorithms in terms of ESL significantly improved the accuracy on the endocardial surface. These algorithms showed low relative error and high correlation coefficient. The morphology of endocardial electrograms on the LV and RV lateral walls of the ventricles as well as at RVOT were reconstructed with enough accuracy. The electrograms on the LV and RV ventricular septum were more smoothed, but the basic elements of their morphology (polarities of the electrogram waves) were reconstructed correctly.

Activation and recovery times are commonly used in the clinical practice as one of the important outputs of non-invasive cardiac imaging. Some numerical results in detection of activation and repolarization times from electrograms reconstructed by the proposed ESL algorithm are given in the **Supplementary Material 1**.

4. DISCUSSION

Non-invasive cardiac electrical mapping on both epi- and edocardial surfaces of the heart can provide more detailed information about cardiac electrical activity. However, this methodology is more challenging compared to the non-invasive epicardial mapping. In previous works the problem of endo-epicardial mapping was attacked in two directions. The former was to extend the inverse electrocardiography problem in terms of epicardial potentials to a problem in terms of epicardial and endocardial potentials. The second one was to reconstruct cardiac electrical activity on the epicardium and endocardium in terms of the EDL or in terms of intramural "equivalent" electrical sources related to cardiac transmembrane potentials.

In this article, we introduced a novel representation of cardiac sources in terms of the ESL potential. This approach, in a sense, combines these two directions. Utilizing EDL for representation of cardiac electrical activity was motivated by the following reasons. First, it is well known that the electrical potential on the cardiac surface can be understood as a sum of two components: so-called "near field," reflecting local myocardial electrical activity and so-called "far field," which is generated by electrical sources at remote segments of the heart. This fact leads to certain difficulties in interpretation of local unipolar electrograms with respect to depolarization and repolarization times. In contrast, EDL allows detecting the local electrical activity of the myocardium with greater

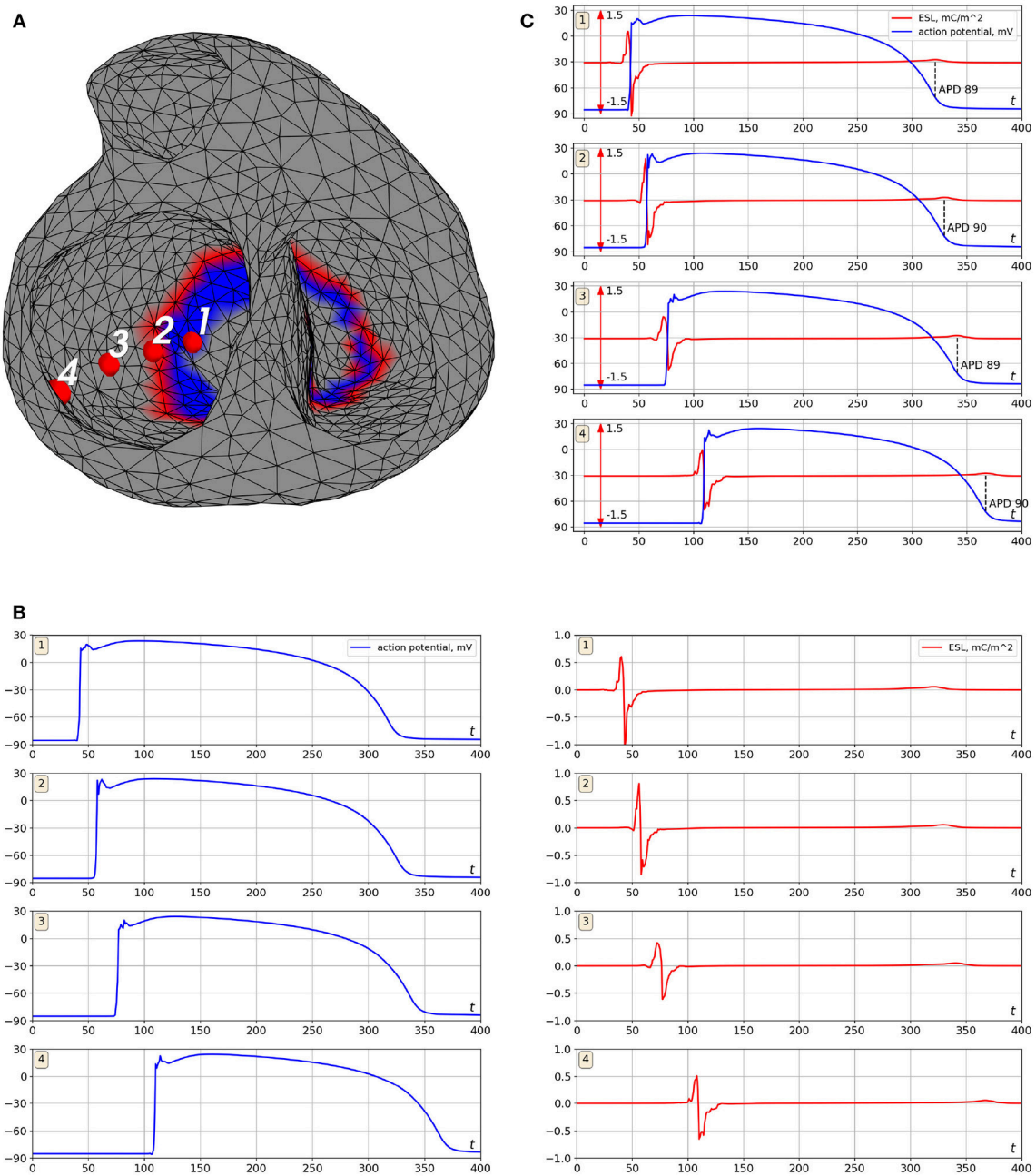

FIGURE 6 | Example of ESL and transmembrane action potential signals (simulation data). Cardiac excitation was initiated in the apical area. **(A)** is locations of the points where the signal was computed, **(B)** is transmembrane action potentials (left panel) and the ESL signals (right panel), **(C)** is merged transmembrane action potentials and ESL signals. Notation mC/m^2 is the millicoulomb per square meter, the unit for an electrical charge density.

precision. Secondly, EDL signals have higher level of regularity in comparison to local unipolar electrograms. This trait of EDL may provide additional opportunities for regularization of the inverse problem.

Our results of the presented *in-silico* experiments showed that the ESL representation of cardiac electrical activity has also some attractive properties. ESL density correlated well with the local electrical activity of the myocardium. ESL density as time signals can be used for detection of activation and recovery times, calculating activation and recovery intervals and reconstruction of activation and recovery sequences. Note that detection of repolarization sequences by local electrograms meets some methodological difficulties (Cluitmans et al., 2017). However, repolarization abnormalities can be an important substrate of reentrant atrial and ventricular arrhythmias. Therefore, possible application of

TABLE 1 | Results of the inverse reconstruction.

Equation	Reg	LV lateral				RV apex				RVOT			
		Epi		Endo		Epi		Endo		Epi		Endo	
		re_x	cc_t	re_x	cc_t	re_x	cc_t	re_x	cc_t	re_x	cc_t	re_x	cc_t
INTERNAL STATEMENT IN TERMS OF EP													
$Au_1 = f_0$	$\|u_1\|_2^2$	6.7e−1	0.89	9.6e−1	0.19	9.0e−1	0.85	9.7e−1	0.12	6.8e−1	0.85	9.5e−1	0.33
$Au_1 = f_0$	$\|\frac{\partial u_1}{\partial n}\|_2^2$	6.3e−1	0.91	17.8e−1	0.45	13.8e−1	0.86	27.2e−1	0.24	7.6e−1	0.87	15.9e−1	0.40
$Au_1 = f_0$	$\|Lu_1\|_2^2$	6.2e−1	0.91	14.6e−1	0.52	7.8e−1	0.84	19.7e−1	0.32	8.0e−1	0.87	15.7e−1	0.46
EXTERNAL STATEMENT IN TERMS OF ESL													
$G_{01}w_1 = f_0$	$\|w_1\|_2^2$	6.2e−1	0.91	4.3e−1	0.83	6.0e−1	0.84	7.6e−1	0.69	7.6e−1	0.87	7.7e−1	0.75
COMBINED STATEMENT IN TERMS OF EP AND CONSTRAINT ON ESL													
$Au_1 = f_0$	$\|w_1\|_2^2$	6.2e−1	0.91	4.4e−1	0.83	6.1e−1	0.84	7.6e−1	0.69	7.6e−1	0.87	7.8e−1	0.75

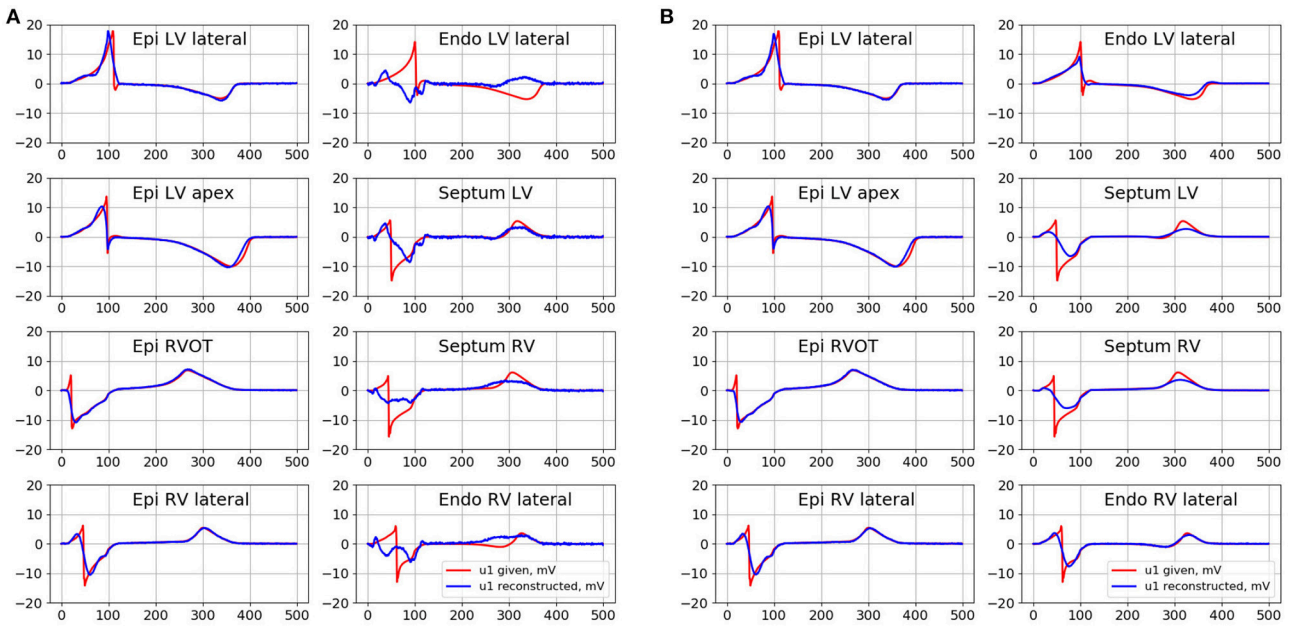

FIGURE 7 | Given (red curves) and inverse reconstructed electrograms (blue curves) in different point of epicardial and endocardial surface for the simulation of the pacing from the RVOT. **(A)** Is the reconstruction with the conventional EP transfer matrix A and Tikhonov regularization of 2nd order, **(B)** is the reconstruction with the ESL transfer matrix G_{01} and Tikhonov regularization of 0 order.

ESL for detection of repolarization abnormalities seems to be promising.

Moreover, ESL density is a temporally localized function exhibiting very similar morphology for all ventricular sites. These ESL features can be potentially used for narrowing down the set of admissible solutions in construction of regularization methods.

Note, these results were obtained for the myocardial model with isotropic electrical conductivities. The proposed approach for ESL computation does not require assumptions of myocardium anisotropy. Therefore, it can be translated directly to the more realistic anisotropic model of the myocardium. However, ESL been computed this way may slightly differ from the "physical" single layer density in case of the media with anisotropic electrical conductivity. To emphasize this fact, we used the term "equivalent" single layer density (ESL). However, we suppose that investigation of electrophysiological meaning of representation of cardiac electrical activity in form of electrical single layer for the more realistic anisotropic model requires more precise mathematical definition of electrical single layer and more complex algorithm for its computation. We address this task to further research.

The most common discretization method for the inverse potential problem, i.e., for reducing the boundary value problem for Laplace equation to a system of linear algebraic equations is BEM (Yun et al., 1997; Gulrajani, 1998 and description in section 2.1). It this work we proposed an alternative BEM scheme for assembling the transfer matrix, which is closely related to the ESL representation of the cardiac electrical field. Though we

considered this method in the context of the endo-epicardial potential inverse problem, this approach can be used for the reconstruction of electrical potentials on the epicardial surface only, in contrast to the EDL.

Moreover, the presented derivation of the ESL transfer matrix allowed to identify the intrinsic structure of the conventional one, that can be split into two matrices: a well-conditioned G_{11} and ill-conditioned G_{01}, whereby their elements are the inverse euclidean distances not depending on the solid angles involved by EDL computations.

A technical benefit of the splitting lies in this simple structure allowing greater numerical precision of the two matrices. In particular, the novel way for construction of the transfer matrix does not require calculation of normal vectors, thus eliminating possible mesh-related artifacts. Furthermore, a simple structure of ill-conditioned matrix G_{01} provides an alternative basis for regularization approaches.

The above results were obtained for the simplified torso model with homogeneous electrical conductivities. We suppose that the translation of the reconstruction algorithm to the clinical practice requires more realistic human torso model with different electrical conductivities of the internal organs. In that cases the structure of the transfer matrix for the inverse problem in terms of ESL will be more complex. Identification of its structure is a task for further research.

We also presented a two-step method for solving the inverse potential problem including computation of the ESL density as an intermediate step. This method has some formal similarities with the method of fundamental solutions (MFS). The MFS was proposed for solving the inverse problem in the epicardial statement and showed promising results (Wang and Rudy, 2006). Briefly, MFS is based on computation of values of "virtual" point electrical sources placed outside of the domain of interest and subsequent computation of the cardiac electrical potential as a linear combination of these electrical sources. The MFS also allows usage of meshless construction of the transfer matrix. However, in contrast to the ESL on the myocardial surface, the electrical sources do not have a physiological meaning, i.e., they cannot be used for evaluating the local electrical activity of the myocardium. Next, in contrast to the ESL matrix G_{11}, the MFS matrix mapping electrical source values to the electrical potential on the cardiac surface is ill-conditioned. Thus, this matrix cannot be used as a regularization operator.

The most interesting and unexpected result was, in our opinion, obtained in the investigation of regularization effects of the ESL density on the heart. We first tested the 0th order Tikhonov regularization for the inverse problem in the ESL statement. Then, we used G_{11}^{-1} as a regularization operator for the conventional EP statement of the inverse problem. We found that both schemes provided significantly more accurate solutions compared to the other Tikhonov regularizations.

Still, the regularizing properties of the inverse single layer operator require further investigation and theoretical explanation. It is worth noting that the ESL regularization increased the accuracy predominately on the endocardial surface of the heart. We can hypothesize that independence of the ESL from solid angles contributed to the accuracy increase for the complex "w-shape" geometry of the endocardial surface. Nevertheless, a detailed mathematical interpretation of the obtained results as well as a more general challenge of developing an optimal regularization operator for the inverse ECG problem is a subject for further investigations.

As our conceptual approach targeted an improved reconstruction of the electrogram itself, further efforts should be undertaken to quantify ESL advantages in estimation of derived parameters, such as activation times, frequency maps etc. The presented work focused solely on a mathematical description of the novel ESL formulation and its simulation-based proof-of-concept, making thorough *in silico* and clinical evaluation needed in order to translate our findings into practical benefits.

5. CONCLUSIONS

In this article, we proposed a novel statement of the inverse problem of ECG which is based on a representation of the electrical potential on the cardiac surface as ESL on the same surface. The results of *in-silico* experiments using personalized cardiac models demonstrated that the introduced ESL density well correlates with local electrical activity of the myocardium.

The reconstruction method was considered in two basic versions. The first version included assembling of a transfer matrix mapping the ESL density to the body surface potentials using the BEM and solving the matrix equation with Tikhonov regularization of 0th order. The second version used the conventional transfer matrix mapping EP on the cardiac surface to the BSPM and then applied Tikhonov regularization imposing constraints based on the single layer operator on the heart. The results demonstrated that both versions provided more accurate solution on the ventricular endocardial surface compared to the classical approach with Tikhonov regularization of 0th, 1st, and 2nd orders.

The proposed modifications in the solution scheme may improve non-invasive reconstruction of cardiac electrical activities on the endocardial part of the heart.

6. LIMITATIONS

We used only limited numerical simulations cases for testing feasibility of the proposed method. In our future work, we intend to extensively study performance of the presented approach in both *in silico* and clinical setups. Forward and inverse simulations were performed for a homogeneous torso model with an isotropic heart. While heart anisotropy affects both heart and torso surface potentials, it does not influence the relationship between the ESL source model and EP on the heart surface. The ESL variable obtained this way may slightly differ from the "physical" single layer density in case of the media with anisotropic electrical conductivity. To emphasize this fact, we used the term "equivalent" single layer density.

Only ventricular focal activation patterns were considered in the present work. Further studies should include more complex excitation propagation patterns as well as a comparative analysis between the derived (e.g., activation times) clinically relevant parameters.

AUTHOR CONTRIBUTIONS

All authors contributed equally to this manuscript including development of algorithms, data processing and manuscript writing.

ACKNOWLEDGMENTS

The authors would like to thank Prof. Quarteroni for the thorough reading and his constructive comments and suggestions, Dr. Sopov, MD, PhD and Dr. Magomedova, MD for the help in patient's examinations.

SUPPLEMENTARY MATERIAL

The Supplementary Material for this article can be found online at: https://www.frontiersin.org/articles/10.3389/fphys.2019.00058/full#supplementary-material

REFERENCES

Berger, T., Fischer, G., Pfeifer, B., Modre, R., Hanser, F., Trieb, T., et al. (2006). Single-beat noninvasive imaging of cardiac electrophysiology of ventricular pre-excitation. *J. Am. Coll. Cardiol.* 48, 2045–2052. doi: 10.1016/j.jacc.2006.08.019

Berger, T., Pfeifer, B., Hanser, F. F., Hintringer, F., Fischer, G., Netzer, M., et al. (2011). Single-beat noninvasive imaging of ventricular endocardial and epicardial activation in patients undergoing crt. *PLoS ONE* 6:e16255. doi: 10.1371/journal.pone.0016255

Bokeriya, L., Revishvili, A., Kalinin, A., Kalinin, V., Lyadzhina, O., and Fetisova, E. (2008). Hardware–software system for noninvasive electrocardiographic heart examination based on inverse problem of electrocardiography. *Biomed. Eng.* 42, 273–279. doi: 10.1007/s10527-009-9065-0

Bourgault, Y., Coudiere, Y., and Pierre, C. (2009). Existence and uniqueness of the solution for the bidomain model used in cardiac electrophysiology. *Nonlin. Anal.* 10, 458–482. doi: 10.1016/j.nonrwa.2007.10.007

Cluitmans, M. J. M., Bonizzi, P., Karel, J. M. H., Das, M., Kietselaer, B. L. J. H., de Jong, M. M. J., et al. (2017). *In vivo* validation of electrocardiographic imaging. *JACC* 3, 232–242. doi: 10.1016/j.jacep.2016.11.012

Cuculich, P. S., Schill, M. R., Kashani, R., Mutic, S., Lang, A., Cooper, D., et al. (2017). Noninvasive cardiac radiation for ablation of ventricular tachycardia. *N. Engl. J. Med.* 377, 2325–2336. doi: 10.1056/NEJMoa1613773

Davey, K., and Hinduja, S. (1989). Analytical integration of linear three-dimensional triangular elements in bem. *Appl. Math. Model.* 13, 450–461. doi: 10.1016/0307-904X(89)90093-0

Dubois, R., Shah, A. J., Hocini, M., Denis, A., Derval, N., Cochet, H., et al. (2015). Non-invasive cardiac mapping in clinical practice: application to the ablation of cardiac arrhythmias. *J. Electrocardiol.* 48, 966–974. doi: 10.1016/j.jelectrocard.2015.08.028

Dunavant, D. (1985). High degree efficient symmetrical gaussian quadrature rules for the triangle. *Int. J. Numer. Methods Eng.* 21, 1129–1148. doi: 10.1002/nme.1620210612

Erem, B., Coll-Font, J., Orellana, R. M., Stovícek, P., and Brooks, D. H. (2014). Using transmural regularization and dynamic modeling for noninvasive cardiac potential imaging of endocardial pacing with imprecise thoracic geometry. *IEEE Trans. Med. imaging* 33, 726–738. doi: 10.1109/TMI.2013.2295220

Erkapic, D., Greiss, H., Pajitnev, D., Zaltsberg, S., Deubner, N., Berkowitsch, A., et al. (2014). Clinical impact of a novel three-dimensional electrocardiographic imaging for non-invasive mapping of ventricular arrhythmias—a prospective randomized trial. *EP Europace* 17, 591–597. doi: 10.1093/europace/euu282

Franzone, P. C., Taccardi, B., and Viganotti, C. (1978). "An approach to inverse calculation of epicardial potentials from body surface maps," in *Electrocardiology III/Vectorcardiography. 3rd International Congress / 17th International Symposium on Vectorcardiography* Vol. 21. ed F. Kornreich (Brussels: Karger Publishers), 50–54. doi: 10.1159/000400421

Geselowitz, D. B. (1989). On the theory of the electrocardiogram. *Proc. IEEE* 77, 857–876. doi: 10.1109/5.29327

Geuzaine, C., and Remacle, J.-F. (2009). Gmsh: a 3-d finite element mesh generator with built-in pre-and post-processing facilities. *Int. J. Numer. Methods Eng.* 79, 1309–1331. doi: 10.1002/nme.2579

Guillem, M. S., Climent, A. M., Millet, J., Arenal, Á., Fernández-Avilés, F., Jalife, J., et al. (2013). Non-invasive localization of maximal frequency sites of atrial fibrillation by body surface potential mapping. *Circ. Arrhythm. Electrophysiol.* 6, 294–301. doi: 10.1161/CIRCEP.112.000167

Gulrajani, R. M. (1998). The forward and inverse problems of electrocardiography. *IEEE Eng. Med. Biol. Mag.* 17, 84–122. doi: 10.1109/51.715491

Hansen, P. C. (2000). "The l-curve and its use in the numerical treatment of inverse problems," in *in Computational Inverse Problems in Electrocardiology, Advances in Computational Bioengineering*, ed P. Johnston (Southampton: WIT Press), 119–142.

He, B., Li, G., and Zhang, X. (2003). Noninvasive imaging of cardiac transmembrane potentials within three-dimensional myocardium by means of a realistic geometry anisotropic heart model. *IEEE Trans. Biomed. Eng.* 50, 1190–1202. doi: 10.1109/TBME.2003.817637

Horácek, B. M., and Clements, J. C. (1997). The inverse problem of electrocardiography: a solution in terms of single- and double-layer sources on the epicardial surface. *Math. Biosci.* 144, 119–154. doi: 10.1016/S0025-5564(97)00024-2

Huiskamp, G. (1991). Difference formulas for the surface laplacian on a triangulated surface. *J. Comput. Phys.* 95, 477–496. doi: 10.1016/0021-9991(91)90286-T

Kalinin, A. (2011). Iterative algorithm for the inverse problem of electrocardiography in a medium with piecewise-constant electrical conductivity. *Comput. Math. Model.* 22, 30–34. doi: 10.1007/s10598-011-9086-x

Kalinin, V., Kalinin, A., Schulze, W., Potyagaylo, D., and Shlapunov, A. (2017). On the correctness of the transmembrane potential based inverse problem of ECG. *Comput. Cardiol.* 44, 1–4. doi: 10.22489/CinC.2017.077-438

Keller, D. U., Weiss, D. L., Dossel, O., and Seemann, G. (2012). Influence of I_{Ks} heterogeneities on the genesis of the t-wave: a computational evaluation. *IEEE Trans. Biomed. Eng.* 59, 311–322. doi: 10.1109/TBME.2011.2168397

Kubo, M. (1994). L2-conditional stability estimate for the cauchy problem for the laplace equation. *J. Inverse Ill-Posed Prob.* 2, 253–262. doi: 10.1515/jiip.1994.2.3.253

Metzner, A., Wissner, E., Tsyganov, A., Kalinin, V., Schlüter, M., Lemes, C., et al. (2017). Noninvasive phase mapping of persistent atrial fibrillation in humans: comparison with invasive catheter mapping. *Ann. Noninvasive Electrocardiol.* 23:e12527. doi: 10.1111/anec.12527

Mirams, G. R., Arthurs, C. J., Bernabeu, M. O., Bordas, R., Cooper, J., Corrias, A., et al. (2013). Chaste: an open source c++ library for computational physiology and biology. *PLoS Comput. Biol.* 9:e1002970. doi: 10.1371/journal.pcbi.1002970

Ramanathan, C., Ghanem, R. N., Jia, P., Ryu, K., and Rudy, Y. (2004). Noninvasive electrocardiographic imaging for cardiac electrophysiology and arrhythmia. *Nat. Med.* 10, 422–428. doi: 10.1038/nm1011

Revishvili, A. S., Wissner, E., Lebedev, D. S., Lemes, C., Deiss, S., Metzner, A., et al. (2015). Validation of the mapping accuracy of a novel non-invasive epicardial and endocardial electrophysiology system. *EP Europace* 17, 1282–1288. doi: 10.1093/europace/euu339

Rodrigo, M., Climent, A. M., Liberos, A., Fernández-Avilés, F., Berenfeld, O., Atienza, F., et al. (2017). Technical considerations on phase mapping

for identification of atrial reentrant activity in direct-and inverse-computed electrograms. *Circ. Arrhythm. Electrophysiol.* 10:e005008. doi: 10.1161/CIRCEP.117.005008

Rudic, B., Chaykovskaya, M., Tsyganov, A., Kalinin, V., Tülümen, E., Papavassiliu, T., et al. (2016). Simultaneous non-invasive epicardial and endocardial mapping in patients with brugada syndrome: new insights into arrhythmia mechanisms. *J. Am. Heart Assoc.* 5:e004095. doi: 10.1161/JAHA.116.004095

Rudy, Y., and Messinger-Rapport, B. J. (1988). The inverse problem in electrocardiography: solutions in terms of epicardial potentials. *Crit. Rev. Biomed. Eng.* 16, 215–268.

Schulze, W. H., Henar, F. E., Potyagaylo, D., Loewe, A., Stenroos, M., and Dössel, O. (2013). "Kalman filter with augmented measurement model: an ECG imaging simulation study," in *Functional Imaging and Modeling of the Heart. FIMH 2013. Lecture Notes in Computer Science* Vol. 7945, eds S. Ourselin, D. Rueckert, and N. Smith (Berlin; Heidelberg: Springer), 200–207. doi: 10.1007/978-3-642-38899-6_24

Shah, A. J., Lim, H. S., Yamashita, S., Zellerhoff, S., Berte, B., Mahida, S., et al. (2014). Non invasive ECG mapping to guide catheter ablation. *J. Atrial Fibrill.* 7:1139. doi: 10.4022/jafib.1139

Skipa, O. (2004). *Linear Inverse Problem of Electrocardiography: Epicardial Potentials and Transmembrane Voltages*. Karlsruhe: Helmesverl.

Takeuchi, T., and Yamamoto, M. (2008). Tikhonov regularization by a reproducing kernel hilbert space for the cauchy problem for an elliptic equation. *SIAM J. Sci. Comput.* 31, 112–142. doi: 10.1137/070684793

ten Tusscher, K., Noble, D., Noble, P. J., and Panfilov, A. V. (2004). A model for human ventricular tissue. *Am. J. Physiol. Heart Circul. Physiol.* 286, H1573–H1589. doi: 10.1152/ajpheart.00794.2003

ten Tusscher, K. H., and Panfilov, A. V. (2006). Alternans and spiral breakup in a human ventricular tissue model. *Am. J. Physiol. Heart Circul. Physiol.* 291, H1088–H1100. doi: 10.1152/ajpheart.00109.2006

Tsyganov, A., Wissner, E., Metzner, A., Mironovich, S., Chaykovskaya, M., Kalinin, V., et al. (2017). Mapping of ventricular arrhythmias using a novel noninvasive epicardial and endocardial electrophysiology system. *J. Electrocardiol.* 51, 92–98. doi: 10.1016/j.jelectrocard.2017.07.018

Tung, L. (1978). *A Bi-domain Model for Describing Ischemic Myocardial d-c Potentials*. PhD thesis, MIT, Cambridge, MA.

Ushenin, K. S., Dokuchaev, A., Magomedova, S., Sopov, O. V., Kalinin, V. V., and Solovyova, O. (2017). "Role of myocardial properties and pacing lead location on ECG in personalized paced heart models," in *Computing in Cardiology Conference (CinC)* (Rennes: IEEE), 56. Available online at: https://ieeexplore.ieee.org/document/8331631

van Dam, P. M., Oostendorp, T. F., Linnenbank, A. C., and Van Oosterom, A. (2009). Non-invasive imaging of cardiac activation and recovery. *Ann. Biomed. Eng.* 37, 1739–1756. doi: 10.1007/s10439-009-9747-5

van Oosterom, A. (2012). Closed-form analytical expressions for the potential fields generated by triangular monolayers with linearly distributed source strength. *Med. Biol. Eng. Comput.* 50, 1–9. doi: 10.1007/s11517-011-0837-9

van Oosterom, A. (2014). A comparison of electrocardiographic imaging based on two source types. *Europace* 16, iv120–iv128. doi: 10.1093/europace/euu268

Varma, N. (2015). Left ventricular electrical activation during right ventricular pacing in heart failure patients with lbbb: visualization by electrocardiographic imaging and implications for cardiac resynchronization therapy. *J. Electrocardiol.* 48, 53–61. doi: 10.1016/j.jelectrocard.2014.09.002

Wang, L., Dawoud, F., Yeung, S. K., Shi, P., Wong, K. C., Liu, H., et al. (2013). Transmural imaging of ventricular action potentials and post-infarction scars in swine hearts. *IEEE Trans. Med. Imaging* 32, 731–747. doi: 10.1109/TMI.2012.2236567

Wang, L., Gharbia, O. A., Horáček, B. M., and Sapp, J. L. (2016). Noninvasive epicardial and endocardial electrocardiographic imaging of scar-related ventricular tachycardia. *J. Electrocardiol.* 49, 887–893. doi: 10.1016/j.jelectrocard.2016.07.026

Wang, Y., and Rudy, Y. (2006). Application of the method of fundamental solutions to potential-based inverse electrocardiography. *Ann. Biomed. Eng.* 34, 1272–1288. doi: 10.1007/s10439-006-9131-7

Wissner, E., Kalinin, V., Kalinin, A., Sopov, O., Chmelevsky, M., Metzner, A., et al. (2018). Noninvasive phase mapping of atrial flutter in humans – comparison with invasive mapping. *Eur. J. Arrhythm. Electrophysiol.* 4, 15–20. doi: 10.17925/EJAE.2018.04.01.15

Wissner, E., Revishvili, A., Metzner, A., Tsyganov, A., Kalinin, V., Lemes, C., et al. (2016). Noninvasive epicardial and endocardial mapping of premature ventricular contractions. *Europace* 19, 843–849. doi: 10.1093/europace/euw103

Xu, J., Dehaghani, A. R., Gao, F., and Wang, L. (2014). Noninvasive transmural electrophysiological imaging based on minimization of total-variation functional. *IEEE Trans. Med. Imaging* 33, 1860–1874. doi: 10.1109/TMI.2014.2324900

Yun, Z. Q., Tan, B. D., and Huang, J. (1997). A comparison of different transfer matrices for the calculation of an inverse problem using bem. *IEEE Trans. Magn.* 33, 1189–1191. doi: 10.1109/20.582465

Zhou, Z., Jin, Q., Yu, L., Wu, L., and He, B. (2016). Noninvasive imaging of human atrial activation during atrial flutter and normal rhythm from body surface potential maps. *PLoS ONE* 11:e0163445. doi: 10.1371/journal.pone.0163445

Conflict of Interest Statement: The authors declare that the research was conducted in the absence of any commercial or financial relationships that could be construed as a potential conflict of interest.

frontiers in Physiology

ORIGINAL RESEARCH
published: 11 February 2019
doi: 10.3389/fphys.2019.00050

ECG Imaging to Detect the Site of Ventricular Ischemia Using Torso Electrodes: A Computational Study

Vinay Kara[1], *Haibo Ni*[1,2], *Erick Andres Perez Alday*[3] *and Henggui Zhang*[1,4,5*]

[1] Biological Physics Group, School of Physics and Astronomy, The University of Manchester, Manchester, United Kingdom, [2] Department of Pharmacology, The University of California, Davis, Davis, CA, United States, [3] Division of Cardiovascular Medicine, Oregon Health and Science University, Portland, OR, United States, [4] School of Computer Science and Technology, Harbin Institute of Technology, Harbin, China, [5] China Space Institute of Southern China, Shenzhen, China

Electrocardiography provides some information useful for ischemic diagnosis. However, more recently there has been substantial growth in the area of ECG imaging, which by solving the inverse problem of electrocardiography aims to produce high-resolution mapping of the electrical and magnetic dynamics of the heart. Most inverse studies use the full resolution of the body surface potential (BSP) to reconstruct the epicardial potentials, however using a limited number of torso electrodes to interpolate the BSP is more clinically relevant and has an important effect on the reconstruction which must be quantified. A circular ischemic lesion on the right ventricle lateral wall 27 mm in radius is reconstructed using three Tikhonov methods along with 6 different electrode configurations ranging from 32 leads to 1,024 leads. The 2nd order Tikhonov solution performed the most accurately (∼80% lesion identified) followed by the 1st (∼50% lesion identified) and then the 0 order Tikhonov solution performed the worst with a maximum of ∼30% lesion identified regardless of how many leads were used. With an increasing number of leads the solution produces less error, and the error becomes more localised around the lesion for all three regularisation methods. In noisy conditions, the relative performance gap of the 1st and 2nd order Tikhonov solutions was reduced, and determining an accurate regularisation parameter became relatively more difficult. Lesions located on the left ventricle walls were also able to be identified but comparatively to the right ventricle lateral wall performed marginally worse with lesions located on the interventricular septum being able to be indicated by the reconstructions but not successfully identified against the error. The quality of reconstruction was found to decrease as the lesion radius decreased, with a lesion radius of <20 mm becoming difficult to correctly identify against the error even when using >512 torso electrodes.

Keywords: ECGI, ventricle, torso electrodes, inverse problem, ventricular ischemia, regularisation methods

OPEN ACCESS

Edited by:
Carlos Figuera,
Universidad Rey Juan Carlos, Spain

Reviewed by:
Martin Bishop,
King's College London,
United Kingdom
Edward Joseph Vigmond,
Université de Bordeaux, France

***Correspondence:**
Henggui Zhang
henggui.zhang@manchester.ac.uk

Specialty section:
This article was submitted to Cardiac Electrophysiology, a section of the journal Frontiers in Physiology

Received: *02 September 2018*
Accepted: *17 January 2019*
Published: *11 February 2019*

Citation:
Kara V, Ni H, Perez Alday EA and Zhang H (2019) ECG Imaging to Detect the Site of Ventricular Ischemia Using Torso Electrodes: A Computational Study. Front. Physiol. 10:50. doi: 10.3389/fphys.2019.00050

INTRODUCTION

Cardiovascular disease is the most common cause of morbidity and mortality in developed countries. Although atrial arrhythmias are more common, ventricular arrhythmias are the more lethal arrhythmias accounting for around 50% of all sudden cardiac deaths (Huikuri et al., 2001). It is well known that myocardial ischemia predisposes to ventricular tachyarrhythmias and fibrillation

(Ghuran and Camm, 2001), and early and effective diagnosis of myocardial ischemia is most essential for proper treatment of patients with cardiac ischemia in order to save their lives.

Electrocardiography (ECG) provides some information useful for ischemic diagnosis. Conventionally, a standard 12-lead ECG is widely used to detect abnormalities in the heart electrical activity, therefore, provides a convenient way for detection of myocardial ischemia (Sejersten et al., 2007). However, due to a low-level reflection of spatial-temporal electrophysiological dynamics of the heart of the 12-lead ECG, there are some limitations in its use for ischemic diagnosis, especially in the detection of the ischemic lesion in the heart (Alday et al., 2016).

The newly developed ECG imaging (ECGI) modality provides a promising technology for high-resolution mapping of the electrical and magnetic dynamics of the heart in normal and pathological conditions (Ramanathan et al., 2003; Intini et al., 2005; Rudy, 2017). This approach uses an array of networked electrodes to directly reconstruct the electrophysiological activity of the heart by using the full body surface potential (BSP) and solving the inverse problem in electrocardiography. The inverse problem in electrocardiography is generally ill-posed, this leads to having to use regularisation methods in order to try and constrain the solution (Brooks and Macleod, 1997; Gulrajani, 1998). These regularisation methods have been found to perform differently depending on the heart electrical excitation activity being reconstructed (Figuera et al., 2016; Alday, 2016). Each regularisation method as well as assessing the reconstruction performance has an associated computational cost that requires to be extensively evaluated.

In this work we aim to evaluate the use of ECGI imaging to detect ischemic lesion using a virtual ventricle-torso model. While ECGI may not provide an alternative to conventional imaging techniques (Daly and Kwong, 2013; Carrascosa and Capunay, 2017; Carvalho et al., 2017), it is important to fully evaluate the ECGI technique to assess its strengths and weaknesses and assess how much information could be potentially recovered.

Previous works in to localising ischemia using ECGI has shown the relative performance of two types of Tikhonov regularisation, however the possible effects of using a limited number of electrodes have not been investigated (Messnarz et al., 2004; Ruud et al., 2009). For more clinical relevance in computational ECGI studies, a limited number of recording electrodes should be used, which will have a substantial effect on the overall reconstructed heart surface potential (HSP). As well as HSP's, transmembrane potentials (TMP) have also been explored using a number of methods and frameworks to localise ischemia (Messnarz et al., 2004; Jiang et al., 2009; Wang et al., 2013). A study using a limited number of electrodes developed an optimised 64 electrode layout (Jiang et al., 2009). In this work for simplicity, a grid like structure was used for the each of the electrode layouts (see **Figure 2**).

The focus of this paper is to evaluate the strengths and weaknesses in the performance of the variant regularisation in localising ischemia in combination with different numbers of recording electrodes. Specifically, it aims to evaluate the ECGI ability to reconstruct the ischemic lesion on a ventricle, in order to (i) provide an assessment on the relative performance in regularisation techniques in reconstructing the ischemic lesion; (ii) to compare to how changing the number of electrodes mapping the BSP will affect the accuracy of ischemic lesion reconstruction; (iii) compare the performance of the ECGI varying the size and location of the ischemic lesion; (iv) quantify effects of signal noise on the performance of the regularisation techniques. Further to this, a particular focus has been put on how the error in the detection results manifests itself when using a limited number of electrodes.

This paper is organised as follows. Methods describes the mathematical models used in the computational experiments, the setup and the performance metrics used. Results are split into 3 sections; General Epicardial Potential Reconstructions, Location, Noise and Sensitivity and Lesion Size. These results are then discussed in the following Discussion along with the Limitations and Conclusion.

METHODS

Forward Problem

The biophysically detailed human ventricular and torso model developed in our previous study (Ni, 2016) was used in this study to simulate the electrical excitation waves in the heart. Full in depth details about the cellular model for the electrical action potentials of the endocardial, midcardial and epicardial ventricular cells, and anatomical structure of the ventricles and torso model can be found in previous studies (Adeniran et al., 2011; Alday et al., 2016; Ni, 2016) which was well validated by the simulated 12-leads ECGs which matched to experimental data. In simulations, the 3D ventricular model was paced at the empirically determined activation sites, mimicking the coupling between the Purkinje fibre network and the ventricles across the endo-surface of ventricular walls (Adeniran et al., 2013; Ni, 2016). The timing of excitation stimulus to the individual activation sites was predetermined, with which the generated ventricular excitation sequence matched to experimental observations and was validated by the simulated 12-lead ECG (Keller et al., 2010; Adeniran et al., 2011; Ni, 2016).

Figure 1 shows the formulation of the forward problem used in this study, including the anatomical geometry of the ventricle and torso meshes used. The ventricle mesh contains 2,499 nodes (5,000 triangular elements) and a male torso mesh contains of 6,923 nodes (13,842 triangular elements), both meshes were down sampled from more detailed geometries used in previous studies (Adeniran et al., 2011, 2013) to reduce the computational time involved in this study. A homogenous torso (isotropic conductivity, i.e., no heterogeneous conductivity introduced by organs such as liver, lungs, ribs, kidneys) is used to create the transfer matrix A in this study considering non-significant effects of these tissues on the ECG (Ramanathan and Rudy, 2001). This also reduces the potential sources of noise to allow comparison of the different regularisation methods. In clinical practice it has been shown that the noise level hides

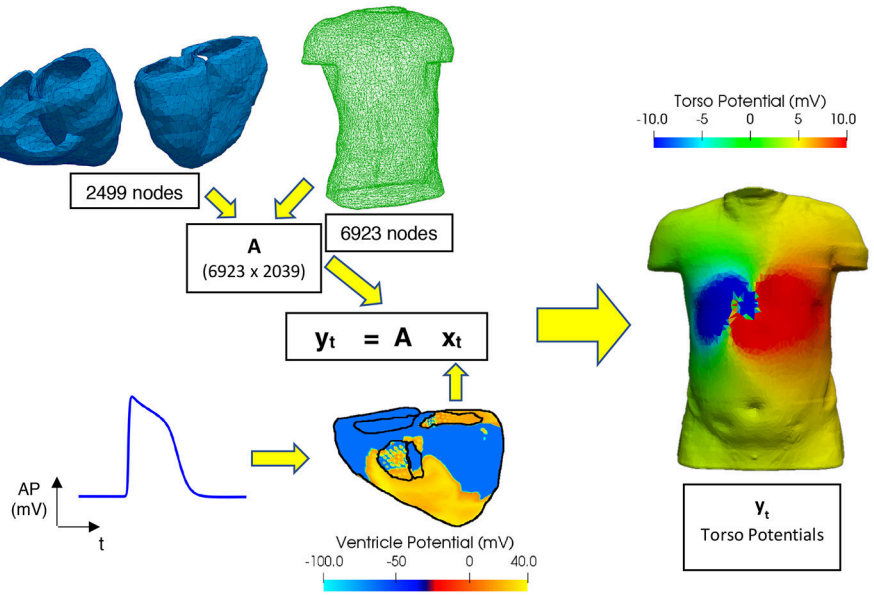

FIGURE 1 | Workflow for performing the forward problem. Transfer matrix **(A)** constructed using a 6,923-node male torso geometry and 2,499-node ventricle geometry, $\mathbf{x}_t$ and $\mathbf{y}_t$ are matrices filled with the epicardial ventricular potentials and torso potentials at each time t, respectively. Ventricular electrical excitations were simulated using a biophysically accurate 3D computer model of the human ventricles (Ni, 2016). The electrical action potentials on the epicardial surface are extracted and mapped onto the ventricular mesh representing the epicardial surface. Body surface potentials on the torso are then computed using the boundary element method (Stenroos and Haueisen, 2008).

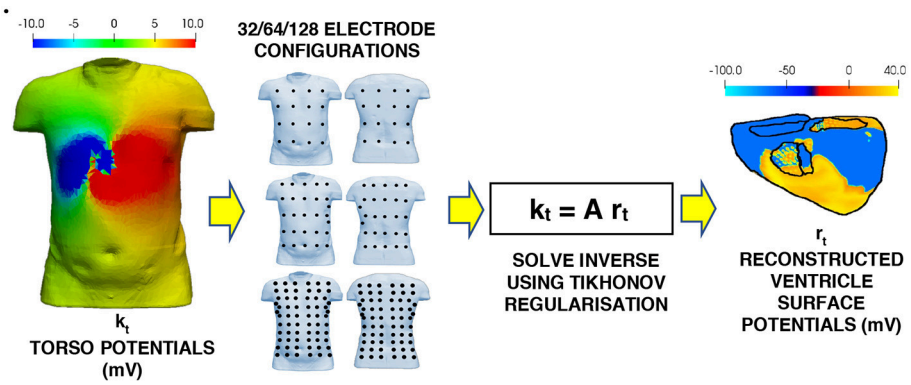

FIGURE 2 | Workflow for the inverse problem. Multi-lead ECG's using the various electrode configurations to the torso potential results from the forward problem. The BSP for the torso is then interpolated from the multi-lead ECG's. This interpolated BSP is then used as the torso potentials in the inverse solution to produce the epicardial potentials on the ventricle.

the effect of the torso heterogeneity on the inverse solution (Zemzemi et al., 2015).

In simulations, the ischemic lesion model was idealised as a fully transmural circular zone with a 27 mm radius, unless otherwise stated in the section Location, Noise, and Sensitivity where the size of the ischemic lesion is varied. Similar to previous studies (Jie et al., 2010; Jie and Trayanova, 2011) these lesions consisted of two zones: a central zone and a boundary zone. The central zone consisted of 80% of the radius of the lesion from the centre and the boundary zone the remaining 20%. In the central and boundary zones, cellular electrical remodelling in ion channels and intercellular electrical coupling due to myocardial ischemia were simulated in the same way as in the study of Wang et al. (2013). The parameters associated with the ion channel alteration describing the ischemic zone decrease linearly from central zone to the edge of the boundary zone. As compared to the normal ventricular AP, the ischemic-induced remodelling in ion channel properties resulted in substantial abbreviation in the APD of the ventricular cells (the normal, boundary ischemic zone and central ischemic zone on the right ventricle epicardial myocytes, were 274, 228, and 150 ms, respectively), a markedly depolarised resting potential (by 10 and 18 mV in the border and

central ischaemic zone, respectively), and a dramatic reduction in the upstroke velocity of the AP as seen in our previous study (Ni, 2016).

For this study the main lesion placement is on the right ventricle lateral wall (RV LAT). The electrical action potentials on the epicardial surface are extracted and mapped onto the triangulated ventricular mesh representing the epicardial surface. This is done to limit the sources of noise to the sources we can control and quantify and to reduce the computational time. Body surface potentials on the torso are then computed using the boundary element method (Stenroos and Haueisen, 2008) and are used to solve the matrix equation shown in **Figure 1**.

Inverse Problem

The complete inverse workflow is shown in **Figure 2**. The electrode configurations on the torso body surface evaluated in this study are 32, 64, 128, 512, and 1,024 electrodes. The multi-lead ECG's produced by using different electrode configurations, and a linear interpolation algorithm were used to reconstruct the BSP (Oostendorp et al., 1989). The interpolated BSP is then used in the in inverse solution to produce the epicardial potentials from which the ischemic lesion zone can be computed from.

The inverse problem in this study can be represented by the following linear model

$$\boldsymbol{k}_t = \boldsymbol{A}\boldsymbol{r}_t, \tag{1}$$

where $\boldsymbol{k}_t$ is the torso potential at time t (6,923 × 1 matrix) after reconstruction via interpolation from the torso electrodes, A is the transfer matrix formulated entirely from the geometry of the two meshes (Barr et al., 1977) and $\boldsymbol{r}_t$ is the reconstructed epicardial potential at time t (6,923 × 1 matrix). As mentioned previously, this is generally an ill-posed problem which means that simply solving it without any regularisation using an ordinary least squares linear regression will likely lead to a solution dominated by errors. Thus, regularisation techniques are needed to constrain the solution. In this work three regularisation methods were evaluated: 0 order Tikhonov, 1st order Tikhonov and 2nd order Tikhonov.

Tikhonov regularisation

The ordinary least squares solution which seeks to minimise the sum of the squared residuals can be written compactly as

$$\|\boldsymbol{A}\mathbf{r}_t - \boldsymbol{k}_t\|_2^2 , \tag{2}$$

where $\|.\|_2^2$ is the Euclidean norm. In order to penalise undesirable solutions and give preference to desirable solutions a regularisation term is added to the minimisation to form the Tikhonov regularisation (Benning and Burger, 2018).

$$\|\boldsymbol{A}\boldsymbol{r}_t - \boldsymbol{k}_t\|_2^2 + {\lambda_t}^2 \|\boldsymbol{L}\boldsymbol{r}_t\|_2^2 , \tag{3}$$

Where λ_t is the regularisation parameter at time t and the matrix **L** is the regularisation operator. For each Tikhonov method the Matrix **L** takes a different form

$$\text{zero order } \boldsymbol{L} = \boldsymbol{I},$$

$$\text{first order } \boldsymbol{L} = \nabla,$$

$$\text{second order } \boldsymbol{L} = \nabla^{\mathbf{2}} ,$$

where **I** is the identity matrix, ∇ is the gradient operator, and $\nabla^{\mathbf{2}}$ is the Laplacian. Each method favours and penalises the solution in different ways with the gradient operator favouring relatively flat solutions and the laplacian penalising rough solutions in a second derivative sense. The solution to the inverse problem at each time step can then be written as

$$\hat{\boldsymbol{r}}_t = \left(\boldsymbol{A}^T\boldsymbol{A} + {\lambda_t}^2\boldsymbol{L}^T\boldsymbol{L}\right)^{-1}\boldsymbol{A}^T\boldsymbol{k}_t, \tag{4}$$

where $\hat{\boldsymbol{r}}_t$ is the newly reconstructed epicardial potential. By plotting the log of magnitude term ($\|\mathbf{L}\mathbf{r}_t\|_2^2$) vs. the error term ($\|\mathbf{A}\mathbf{r}_t - \mathbf{k}_t\|_2^2$) yields in most cases an L shaped trade off graph which can be used to identify the most optimal choice for the variable lambda (Hansen, 1992). This optimal λ_t is found by locating the corner of the L curve, this corner varies in sharpness depending solution and in this study an iterative method (Castellanos et al., 2002; Cultrera and Callegaro, 2016) was used to locate it. In Equation (4), λ_t would need to be worked out for each time step, requiring an L curve at every time step and thus is quite computationally expensive. In this work the time instants were stacked together into a single matrix **R** and **K.** This allows the computation of just a single λ globally that is independent of time giving the following solution:

$$\hat{\boldsymbol{R}} = \left(\boldsymbol{A}^T\boldsymbol{A} + \lambda^2\boldsymbol{L}^T\boldsymbol{L}\right)^{-1}\boldsymbol{A}^T\boldsymbol{K}, \tag{5}$$

This approach means that the λ_t value is not fully optimised for each individual time instant. Testing of using both the single λ_t for each time instant against the global method for λ determination resulted in the a very small improvement (<0.1) in the average relative difference mean star (RDMS) score (Equation 6) along with a substantial increase in computational time and so the global method was chosen.

Performance Metrics

Two performance metrics are used in this study, firstly to quantify the overall quality of the epicardial reconstruction and secondly to quantify the quality of the ischemic lesion detection.

Relative Difference Mean Star

In this study the relative difference mean star (RDMS) quantifies the amount of error between the reconstructed potentials, $\hat{\mathbf{x}}$, and the real potentials, **x**, as in previous inverse studies (Figuera et al., 2016; Gharbalchi et al., 2016):

$$RDMS = \sqrt{\sum_n \left(\left(\frac{x_n}{\|\boldsymbol{x}^2\|}\right) - \left(\frac{\hat{x}_n}{\|\hat{\boldsymbol{x}}^2\|}\right)\right)^2}. \tag{6}$$

This produces a more representative error score then a standard percentage error produces, allowing for better comparison of performance between solutions. There are two ways of

calculating this score spatially, in which case you sum over the geometry for each time step, or temporally, in which case you sum over the timesteps for each element in the mesh. Both methods were tested however, the spatial method is the one used throughout this study. This was chosen as it produced more stable error and the average RDMS over all time steps produced a value that represented the data more accurately when visually assessing the epicardial solutions. When comparing RDMS values for different solutions, a lower RDMS value will indicate a better solution.

Ischemic Lesion Detection

To detect the ischemic lesion, a threshold approach was implemented in a similar way as previous studies (Wang et al., 2013). Due to the changes in action potential discussed earlier, leads to a lower potential in the central and boundary regions when compared to the surrounding tissue was produced. Thus, if the potential of an element was below a threshold $w_{threshold}$, then that element was classified as ischemic, else, the element was classified as healthy. To calculate the threshold value the following formula was used

$$w_{threshold} = \overline{w} - Q\,(\overline{w} - w_{\min})\,, \tag{7}$$

where $\overline{w}$ is the average epicardial potential and $w_{\min}$ is the minimum epicardial potential and Q is a threshold factor which unless stated otherwise is equal to 0.4. Brief sensitivity analysis on the factor Q is shown in section titled Location, Noise and Sensitivity. Three more metrics can be calculated using this threshold which can help evaluate the performance of the ischemic lesion detection.

(i) Percentage of ischemic lesion correctly identified as ischemic (CI).
(ii) Percentage of ischemic lesion incorrectly identified as healthy (IH).
(iii) To allow meaningful comparison against (i) and (ii), the area of the ventricle geometry incorrectly identified as ischemic is also displayed as a percentage the total ischemic lesion area (II).

In this study there are 6 variables are considered in total:

(i) The order of the Tikhonov regularisation (0, 1st 2nd).
(ii) The number of leads used to reconstruct the BSP (32, 64, 128, 256, 512, 1,024).
(iii) The location of the lesion (Right ventricle lateral wall, left ventricle anterior, lateral and posterior wall and interventricular septum).
(iv) The level of gaussian added noise measured as a signal to noise ratio (SNR) in decibels (dB) to the BSP before interpolation (10, 20, 30, and 40 dB).
(v) The sensitivity of Equation (7), to the factor Q, which will affect the choice of threshold potential used to classify an area as ischemic or healthy (0.3, 0.4, and 0.5 which unless stated otherwise $Q = 0.4$).
(vi) The size of the ischemic lesion (14, 20, and 27 mm).

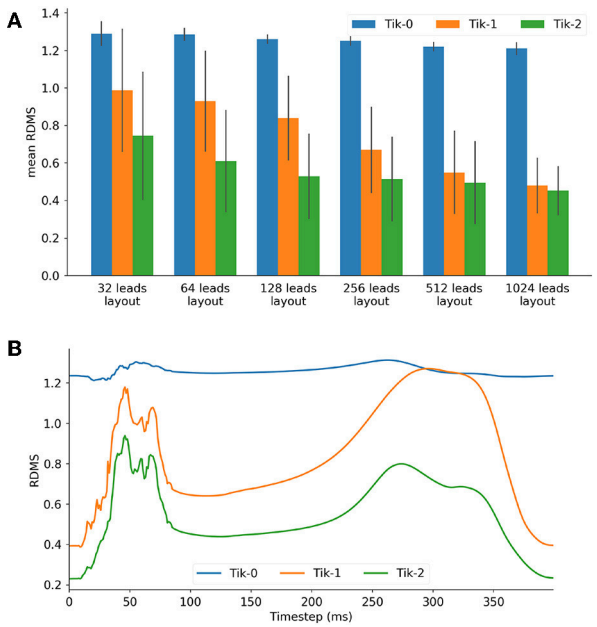

FIGURE 3 | (A) Mean RDMS against lead layout, **(B)** 128 lead layout RDMS vs. timestep for the 3 Tikhonov solutions.

RESULTS

General Epicardial Potential Reconstruction

Figure 3A shows the mean RDMS (which was calculated spatially and then averaged over all timesteps) for different lead layouts using an increasing number of leads up to 1,024 leads. It can be seen here that all three solutions as expected perform better as the number of leads increases. Both the 1st and 2nd order Tikhonov solutions outperformed the 0 order regardless of how many leads were used. When lead numbers are smaller (less <256) the 2nd order Tikhonov solution clearly outperforms the 1st order solution, however as the lead number increases the difference in mean RDMS between solutions would seem to decrease. At 128 leads the RDMS of the overall 2nd order solution seems to stabilise and not improve greatly as the number of leads increases. Error bars plotted show ± 1 standard deviation in the mean RDMS.

For the 128 lead solutions the RDMS is plotted against timestep in **Figure 3B**. The RDMS for the 0 order Tikhonov solution is fairly constant but displays the same characteristics as both the 1st and 2nd order solutions. All solutions show an increasing RDMS as the ventricle depolarises and repolarises while stabilising at a lower RDMS during the plateau phase of the action potentials (AP). These characteristics are present more prominently in the 1st and 2nd order results. If we compare these characteristics with the timesteps shown in **Figure 4** there is a correlation between the spatial complexity of the epicardial potential and the RDMS. It can be seen that the 2nd order solution outperforms the 1st order solution which would indicate that the ischemic lesion detection algorithm will perform more accurately.

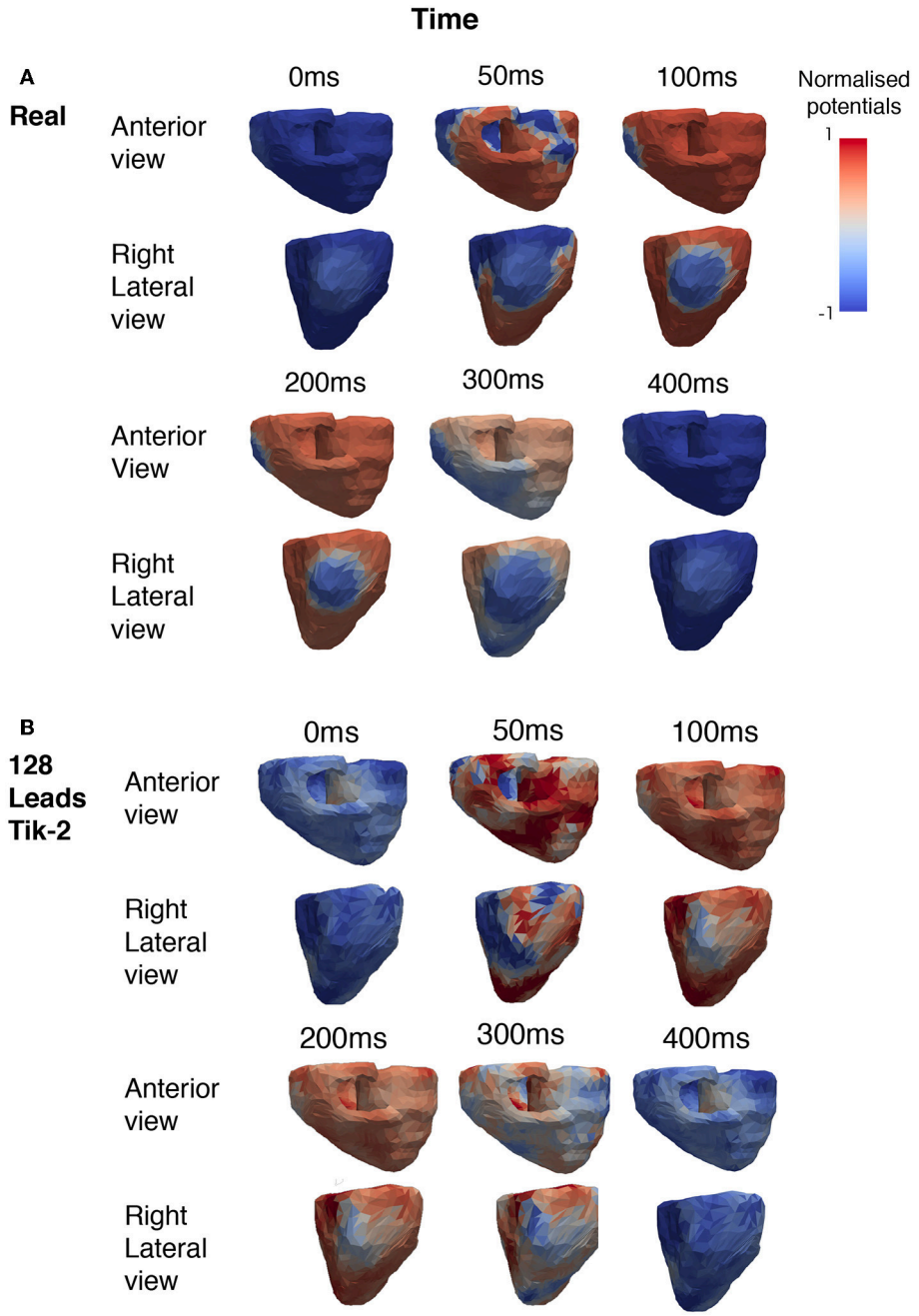

FIGURE 4 | Snapshots showing the comparison between real and reconstructed epicardial excitation pattern. Both anterior and right lateral view of the ventricle were shown for over a period of 400 ms. **(A)** Real epicardial potential patterns at different timings. **(B)** Reconstructed epicardial potential pattern at different timings by using 128 leads and the 2nd order Tikhonov regularisation method.

Figure 4A shows the how the real solution varies over time from two different viewpoints. The first is the anterior view and the second the right lateral view which faces the lesion head on. The full ischemic lesion is clearly visible in the timesteps between 100 and 250 ms, with the maximum range of potential between the ischemic area and the rest of the ventricle occurring at 100 ms. **Figure 4B** shows the timesteps for the reconstructed solution solved using a 2nd order Tikhonov regularisation. This was chosen as in **Figure 3A** it was shown to have performed well comparatively and as 128 lead has greater clinical relevance then a larger number (>128) of lead layouts. At 50 ms when the spatial complexity of the real solution is high, we can see how the increased error leads to a pattern that is similar but not very accurate. However, at 100 ms we can clearly make out

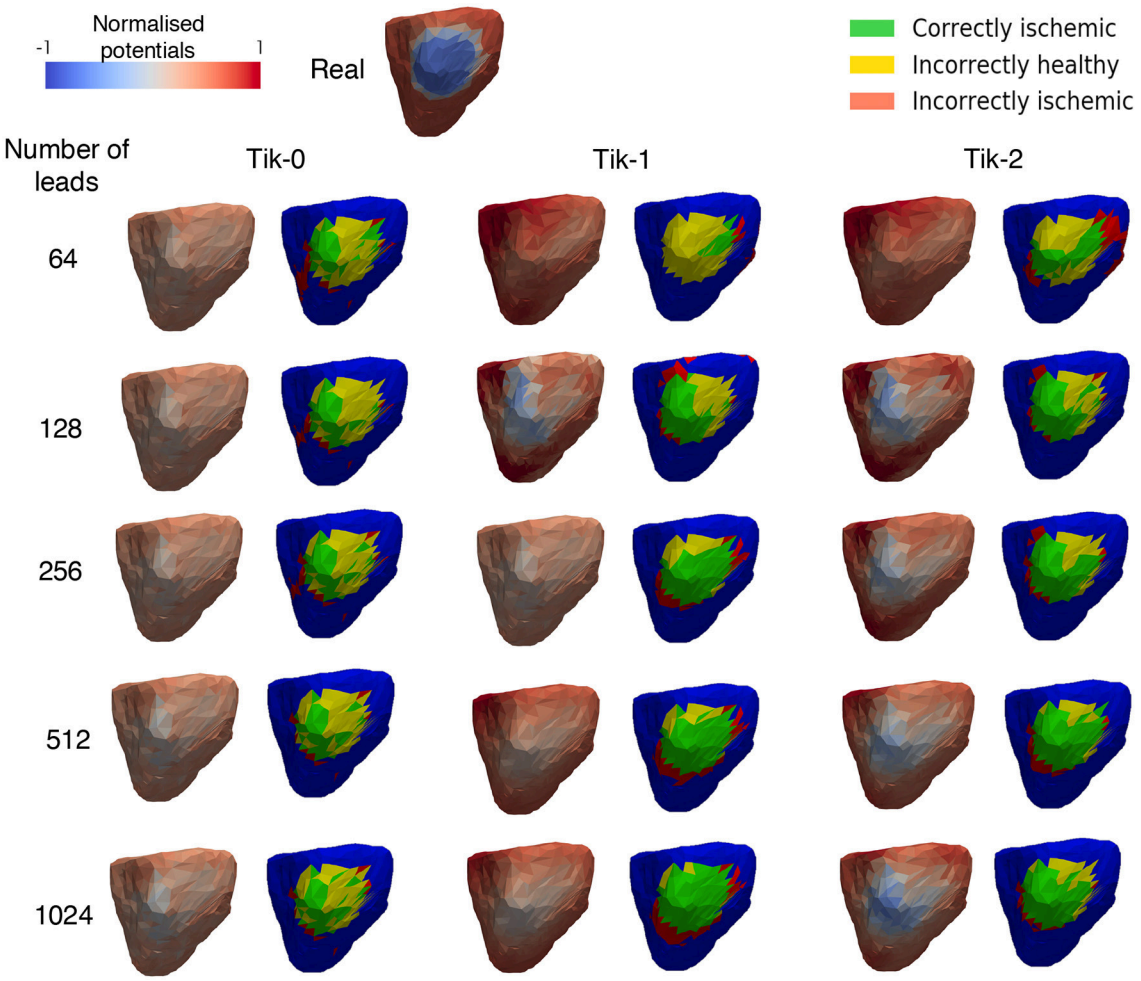

FIGURE 5 | Reconstructed epicardial excitation pattern from the right lateral view of the ventricle at 100 ms. Each regularisation column has two sub columns, **(Left)** is the reconstructed epicardial potential and **(Right)** is a "traffic light" diagram coloured according the ischemia detection results. Green areas represent the successful identification of the ischemic lesion, yellow areas are ischemic which were not identified, and red areas indicate areas incorrectly identified as ischemic.

the presence of an ischemic lesion and general location, but definition is lost in the shape.

Ischemic Lesion Reconstruction

Figure 5 shows the exemplar results at 100 ms and applying the formula for the threshold ischemic detection described in section Ischemic lesion Detection for all possible combinations of regularisation method and number of leads reconstructing the BSP. This diagram should be viewed in conjunction with **Figure 6**. It can be seen that the positioning of the correctly identified ischemic lesion in green is generally toward the bottom left of the ischemic lesion. Taking both the green and yellow areas together will show the real ischemic lesion, taking the green and red areas together will show the reconstructed ischemic lesion and taking the red and yellow areas together shows the error in the detection.

Much like the results in **Figure 3**, further confirmation that the increase in leads brings about an increase in the correctly identified ischemic area. It is important to note that the "traffic light" diagrams shown in **Figure 5** only shows the right lateral view of the ventricle as that is view most pertinent to this study. However, by looking at the other angles of the ventricle a varying amount of red misidentified ischemic lesions on other parts on the ventricle will be seen depending on the configuration being evaluated. This data is represented in **Figures 6–8** as best as possible, however the full ventricle animations are included in the **Supplementary Material**.

Using **Figures 5**, **6A** together it can be seen that for the 0 order Tikhonov solution regardless of the number of leads the CI (green) never goes above 30%. However, as number of leads increase the II (red) decreases. The lead layouts from 32 to 256 leads show that even though around 30% of the lesion is detected the II area dominates the overall solution and so even reliably learning the position of the lesion is not possible. The 512 and 1024 lead layouts show much reduced II at 17% and 13%, respectively, this means that by using this configuration it

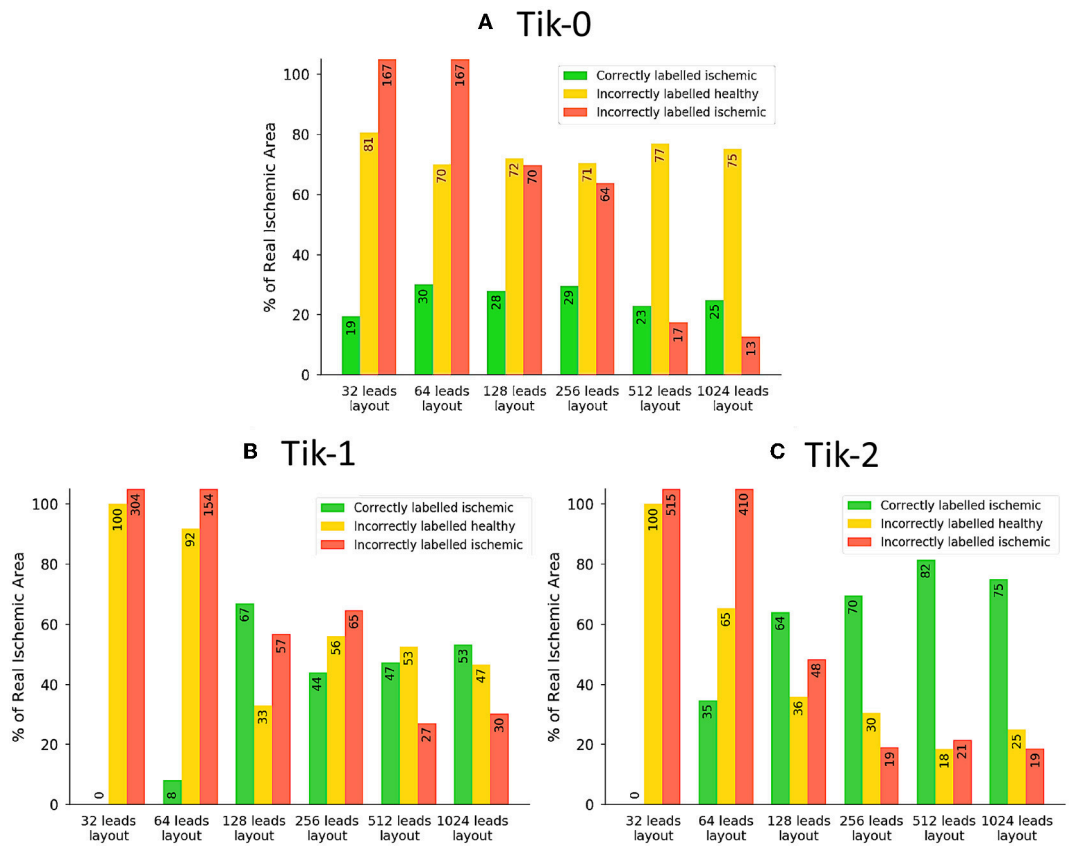

FIGURE 6 | The traffic light data from the ischemic lesion detection visualised as a bar chart. **(A)** 0 order Tikhonov, **(B)** 1st order Tikhonov, and **(C)** 2nd order Tikhonov. Green bars represent the successful identification of the ischemic lesion (correctly ischemic—CI), yellow bars are ischemic which were not identified and shown as healthy (incorrectly healthy—IH) and red bars indicate areas incorrectly identified as ischemic (incorrectly ischemic—II). All area values are represented as a percentage of the real circular lesion. Please note that some bars go above the height of the y axis, bar numbers are present on each bar to aid with this fact.

is possible to learn the rough position of the lesion, but nothing about the size and/or shape of the lesion.

Figures 6B,C show at below 128 leads there are not enough leads to accurately map the torso BSP, leading to results that show little CI (green) and very large II (red). Above 128 leads, the results show that increasing the number of leads generally reduces the amount of II. The best ratio of CI:II occur in the 1,024 lead layout solutions for all the regularisation methods. Using **Figure 7** it can be seen that as the II decreases as the number of leads increases, the remaining II is more localised around the real lesion. At leads configuration <512 leads it can be seen that a lesion on the inside wall of the left ventricle is erroneously detected in addition to the correct lesion.

Although **Figure 5** shows similar results between the 1st and 2nd order Tikhonov solutions in detecting the ischemic lesion, it can be seen that the 2nd order solution outperform the 1st order solutions when considering the full ventricle. This is due the presence of the ischemic lesion on the inside wall of the right ventricle. **Figure 8** shows that the 1st order solution struggles to detect any of the inner wall lesion even at 1,024 leads thus leading to a CI of approximately 50%. The 2nd order solution does however perform better in identifying the inner wall lesion, which allows it to reach a CI of around 80% of the total real lesion.

Location, Noise, and Sensitivity

Location

In addition to the right ventricle lateral wall location used so far, 4 more locations were also tested. The locations tested in this study are the left ventricle anterior wall (LV ANT), left ventricle lateral wall (LV LAT), left ventricle posterior wall (LV POS), and the interventricular septum (IV SEP). The lesion size was kept constant at 27 mm while only the location and the number of leads were changed. **Figure 9** shows the results of 12 lead ECG taken under healthy conditions, and the different ischemic lesion locations. All lesion locations are represented in the first column in **Figure 10A**, the following columns show the ischemic detection result in each case. As **Figure 10A** only shows one single view of the three-dimensional ventricle, and due to the limited space available for figures, **Figure 10B** shows the results of the detection as a bar graph using the data taken from the full geometry.

Using **Figure 9** we can see the changes to the ECG profiles for different lesion locations on a 12 lead ECG. The black line

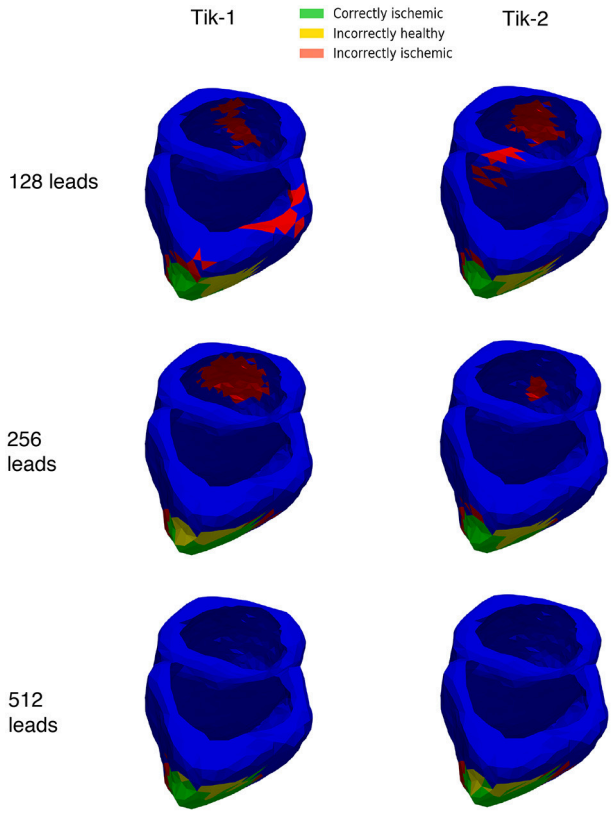

FIGURE 7 | 3D ventricle detection results for 1st and 2nd order Tikhonov solutions for 128, 256, and 512 leads. Green areas represent the successful identification of the ischemic lesion, yellow areas are ischemic which were not identified, and red areas indicate areas incorrectly identified as ischemic.

is the control case with no lesion present and the coloured lines represent different lesion location over the ventricle. The most prominent change in the profile comes in either an elevated or depressed ST segment, along with both an increase or decrease in the T wave amplitude and then to a lesser degree increases to the amplitudes of the R and S peaks. These changes are consistent with those seen in previous studies (Jie et al., 2010; Hampton, 2013; Perez Alday et al., 2016; Roffi et al., 2016).

Figure 10 shows the equivalent results using the ECGI method, the LV ANT location shows less II error for equivalent number of lead results comparatively with both LV LAT and LV POS. Using the 256 leads LV ANT results we can see that although only 16% was CI, the II error is comparatively low, from the diagram this can be seen as the reconstructed lesion being placed too high on the left ventricle, and thus a high number of leads were then needed to correctly position the lesion further. For the LV LAT and LV POS cases only by using 1,024 leads would lead to successful identification of the lesion position without misidentifying the lesion elsewhere on the ventricle due to error. Similar results were achieved in comparison to the location used with **Figures 5**, **6** identifying ∼80% of the lesion and high lead values. Reconstructions involving the lesion located on the IV SEP performed the worst comparatively having extremely high II error even when using 1,024 leads. Ninety-one percent of the lesion was CI, however this result becomes less useful when viewed along with the II error (240%) which is located on a large percentage of the inside walls of both the left and right ventricle.

Electrograms can be used to indicate and localise ischemia practically through identifying ST elevations. However, whilst ST elevations present in anatomical contiguous leads may strongly suggest ischemia ST elevations are not unique to ischemia and can be caused by a number of other conditions. Localisation of the ischemia can be inferred to regions such as anterior, lateral, apical and septum by observing which leads display the elevations. Using the ECGI technique with more electrodes we are able to learn additional information such as indication of the size, the shape, and location of the lesion.

Noise and Sensitivity

The effects of both noise and our chosen threshold factor Q in Equation (7) were evaluated. The results of 4 different signal to noise ratios measured in decibels and 3 choices for the factor Q are shown in **Figure 11A** using a lesion on the LV ANT location and 512 leads to interpolate the BSP. As in previous studies, the results show that noise does have a detrimental effect on the performance of the regularised solutions particularly at low SNR (10 dB) leading to low CI and high II. However, over 50% CI is achievable when noise levels reduce as shown by the 20–40 dB columns in **Figure 11A**. At 10 dB, the II error increase in the case of lesion on the LV ANT location tended to manifest itself increasingly around the top of the left ventricle, thus no real assessment of shape could be made. This same trend occurs to a lesser extent for the detection results using 20–40 dB as the SNR increases.

Figure 11B shows the results with the addition including 20 dB of noise on the relative performance of the 3 regularisation methods using the 256-electrode layout. The order in performance is the same as when not including noise, with the 2nd order Tikhonov performing best, followed by the 1st and 0 orders, respectively. The 2nd order Tikhonov again outperforms the 1st order in terms of identifying the lesion on the inside wall which leads to the two results CI. However, as can be seen in **Figure 11B**, conversely the 1st order performs better at detecting the lesion on the epicardial wall displaying a more accurate shape and detecting more CI area. At low electrode numbers (<256) with noise included made finding the optimal lambda value using the L curve method more difficult, with the corner of the curve becoming less pronounced and harder to locate. The 2nd order Tikhonov in particular produced L curves which were comparatively more difficult to determine the optimal lambda value compared to the 0 and 1st order Tikhonov solutions.

The Q factor sensitivity is shown in both the rows of **Figure 11A** and represented as error bars in **Figure 11B**. As expected using a higher Q factor (0.5) leads to using a lower threshold and thus a smaller area is identified as ischemic, this lead to lower a CI and II in all cases by around 10%. Conversely, using a lower Q factor of 0.3 leads to a higher threshold and thus a larger area is identified as ischemic, this lead to a small increase in the CI however in most cases the II error increased

by more thus leading to a poorer overall detection result. The change in Q factor resulted in an either an increased/decreased area detected, this effect was distributed evenly across the both the correct region and the erroneous regions.

Lesion Size

Four different sized lesions (labelled A-D) were centred in the same location on the right ventricular lateral wall as in the previous. The radii of the lesions are 27, 20, 14, and 8 mm. **Figures 12A–C** shows the results of the reconstruction of different sized lesions using the 2nd order Tikhonov regularisation, after the previous sections results showed that most accurate. The 512 lead configuration was chosen to display as this configuration as in the previous analysis it showed the similar results to the 1,024 lead configuration but with fewer leads. The 8 mm radius lesion however could not be reconstructed to any degree even with the highest lead configuration.

The II error increased as the size of the lesion decreased. Thus, there is an increase in the overestimate in ischemic area as the lesion size decreases. Comparison using the charts shown in **Figure 6** is not worthwhile in this case as the size of the individual triangular elements of the mesh start to have a large effect on the analysis as the lesion size becomes smaller. However, a limited comparison can made in much the same way as in **Figure 6**, using only the incorrectly ischemic (II) measurement as shown in **Figure 12D**. The percentages were calculated in all cases using the 27 mm lesion area as a reference, this allows results between the solutions to be plotted on the same axis. **Figure 12D** shows the results of incorrectly ischemic error, for all 3 lesion sizes taken from over the whole ventricle geometry. It can be seen that there is an increase in the II error as the lesion size decreases.

DISCUSSION

In this study, we implemented a ventricle-torso model developed in our previous study to investigate ischemic lesion detection on the ventricle. We quantified the quality of lesion identification while changing the number of leads used to reconstruct the BSP. Effects of 3 different regularisation methods on the lesion detection were also investigated. Smaller investigations into the effect of lesion location and size were also quantified.

Main Findings

The main findings of this study are that regardless of regularisation technique at least 128 leads are required to reconstruct the ischemic lesion to a level where a location could be established although to reduce the erroneous identification to only localised around the real lesion >256 leads are needed. Using a 0 order Tikhonov solution did not perform well regardless of the number of leads. Using a low number of electrodes (<256), the misidentified ischemic area around the ventricle is large (>70% of the real lesion size), thus this would not produce a solution accurate enough to even identify a rough location for the lesion. At high lead numbers (>256) the misidentified ischemic lesion area reduces in size and are more localised as seen in **Figure 7** to the lesion and so a successful accurate location could be identified using these configurations. Further optimisation of the lead positioning could allow for more accurate reconstructions at lower leads numbers (Jiang et al., 2009).

Using the 1st order Tikhonov solution gives a good solution for the outer lesion area, even outperforming the 2nd order, but fails to identify the lesion on the inner wall, thus leading to solutions which at maximum identify about 53% of the total lesion area. With increasing number of leads the solution produce less error, and the error becomes more localised around the lesion in contrast to lower leads solutions. The 2nd order Tikhonov solution proved to be the best of the three regularisation methods, both in terms of error and amount of correctly identified ischemic lesion. It also outperformed the 1st order solution identifying more successfully the inner wall ischemic lesion leading to around 80% lesion area identification. This agrees with previous work to localise ischemia which show results in which the 2nd order Tikhonov performs better (Messnarz et al., 2004; Ruud et al., 2009) and this still stands when using a limited number of recording electrodes with no noise.

Varying the location of the lesion showed that ischemic lesion detection performs more accurately for LV ANT location and LV POS then LV LAT, with solutions achieving lower comparative II error using the same number of leads. This follows along with what was expected as the distance between the ventricle and torso is smaller here along with being more aligned with the layout of the leads which are heavily skewed mainly towards the front and back of the torso. Finally, the lesion located on the IV SEP showed comparatively less accurate results, this is expected as the outer walls of the ventricle shield and mask the effect of the lesion on the BSP to a certain degree. Although results indicated that a lesion on the inner walls of the geometry was present, it would not be accurate enough to successfully identify the lesion size and location. A more accurate BSP measurement is needed to improve the solution to a successful level, requiring either more leads or a more accurate interpolation method.

The addition of noise causes the solutions to reduce in detection accuracy. The 2nd order solution proves to be more accurate when looking at both the inner and outer walls of the ventricle, however if the criteria was changed to only recognise the outer epicardial layer the 1st order solution proved to be better. The addition of noise caused noticeable change in the sharpness of the L curve used to optimise the selection of the regularisation parameter lambda in combination with a limited number of electrodes. The 2nd order solution in particular was most affected by this. As the choice of lambda value has such a pivotal role in the ECGI workflow, determining the optimal value needs to be accurate and clear, perhaps another method (Golub et al., 1979; Pei et al., 2015; Barnes and Johnston, 2016; Chung and Español, 2017) would prove to be more useful in high noise low recording electrode configurations. Taking ST-integral of the BSP electrograms instead of just one timestep as used in this study could also help reduce the effect of measurement noise as employed in a previous study (Jiang et al., 2009).

As expected the smaller the lesion size the less accurate the lesion reconstruction becomes. Using this current setup accurate

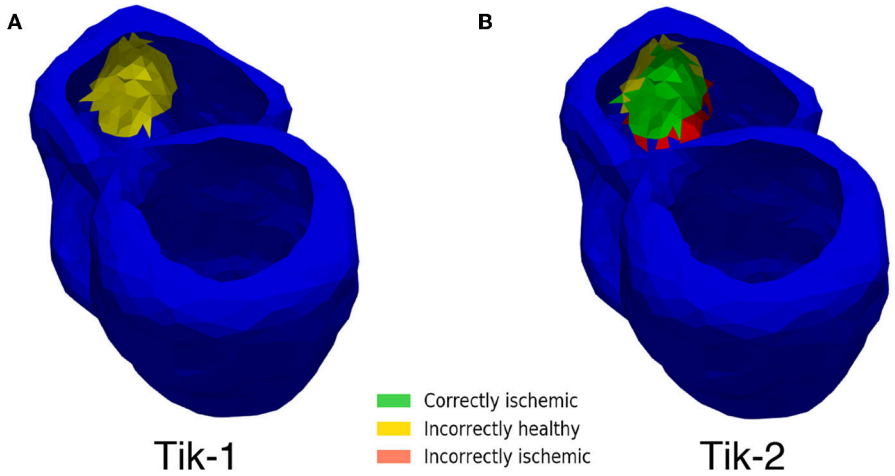

FIGURE 8 | Inner wall lesion detection. **(A)** 1st order Tikhonov 1,024 leads **(B)** 2nd order Tikhonov 1,024 leads.

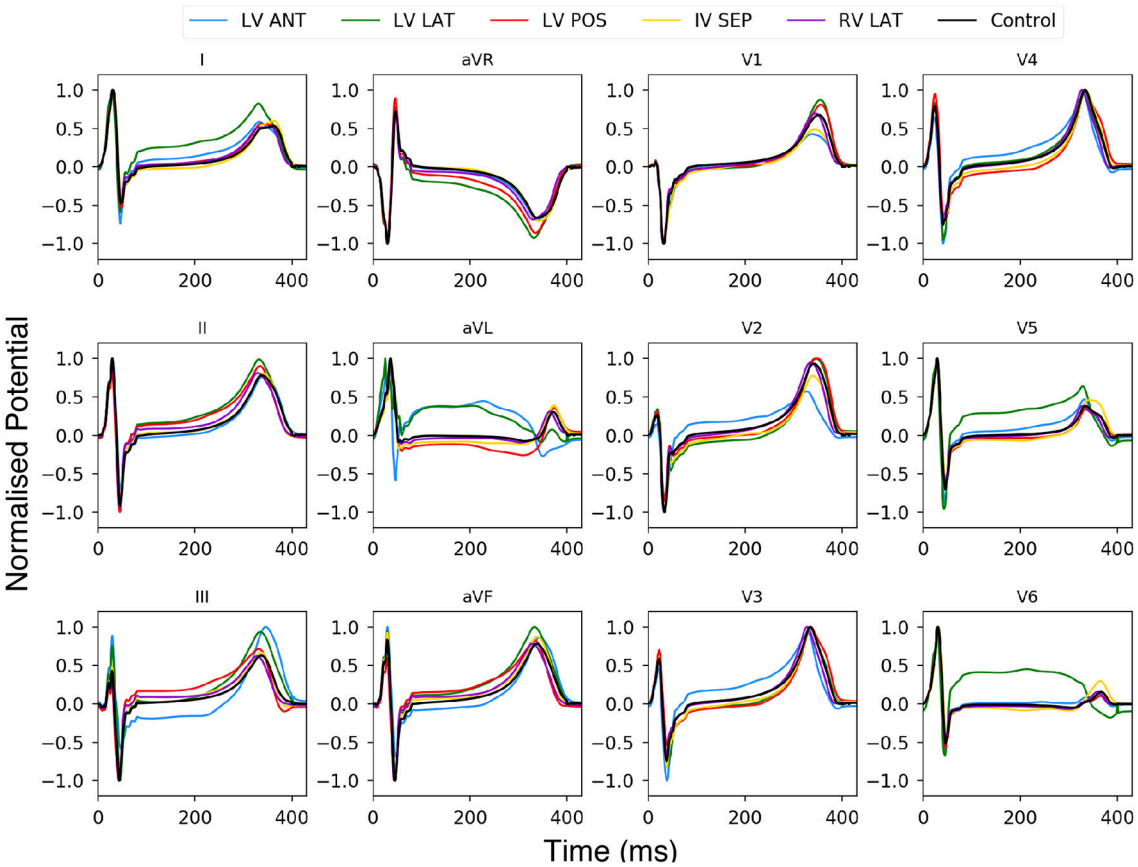

FIGURE 9 | Twelve lead ECG using BSP produced with the human ventricle-torso model. Simulation using healthy control conditions (black) and 5 ischemic lesion locations (5 colours). The y axis has been normalised between 1 and −1.

lesion detection was achieved at a lesion size of 20 mm and above using 512 leads. Decreasing lesion size also caused an increase in the overestimate of the lesion size when reconstructed. However, the 14 mm lesion was detected but along with a substantial area of incorrect regions that should have been detected as healthy areas of the ventricle as seen in **Figure 12C**. Therefore, this

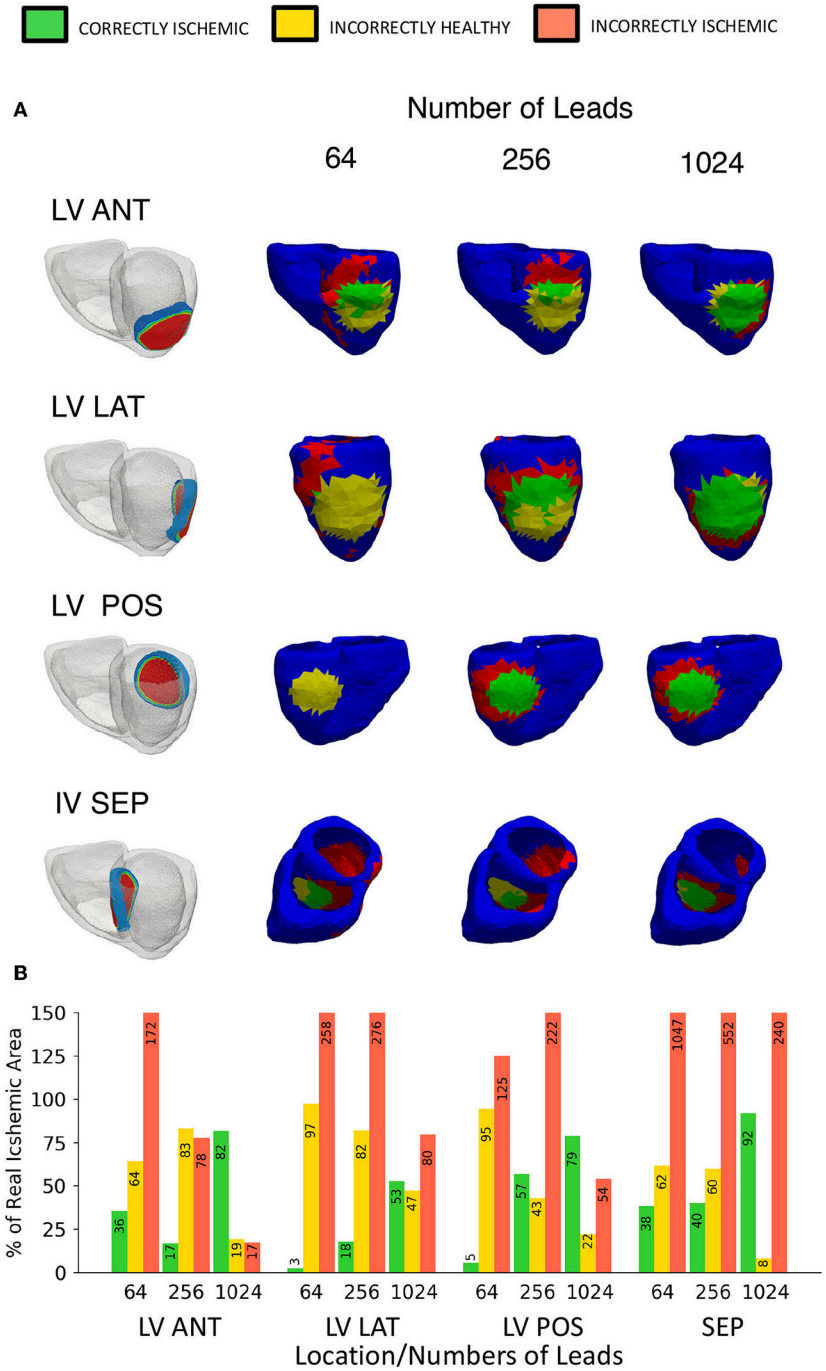

FIGURE 10 | Variable location ischemic lesion detection results using traffic light representation. **(A)** Location vs. number of leads diagram showing the "traffic light" representation of the ischemic lesion detection results, a head on lesion view is shown for each location. First column shows the location of the ischemic lesion on the ventricle, remaining columns show a head on lesion view of the results **(B)** A bar chart visualizing the "traffic light" data taken from the whole geometry as views in **(A)** only show a single view. Please note that some bars go above the height of the y axis, bar numbers are present on each bar to aid with this fact.

setup is not well suited for detecting lesions of that size or smaller. As a benchmark the 14 mm lesion was reconstructed without the use of recording electrodes and thus no interpolation and similar results were achieved but with slightly less error (∼6% using the same scale as **Figure 12D**) and so even with a perfect BSP reconstruction 14 mm lesions cannot be detected accurately using this workflow. Further study is needed to see if using a more detailed mesh (>5,000 triangles) would allow for a more accurate reconstruction of the smaller lesion. Using a more detailed mesh increases the complexity of the problem,

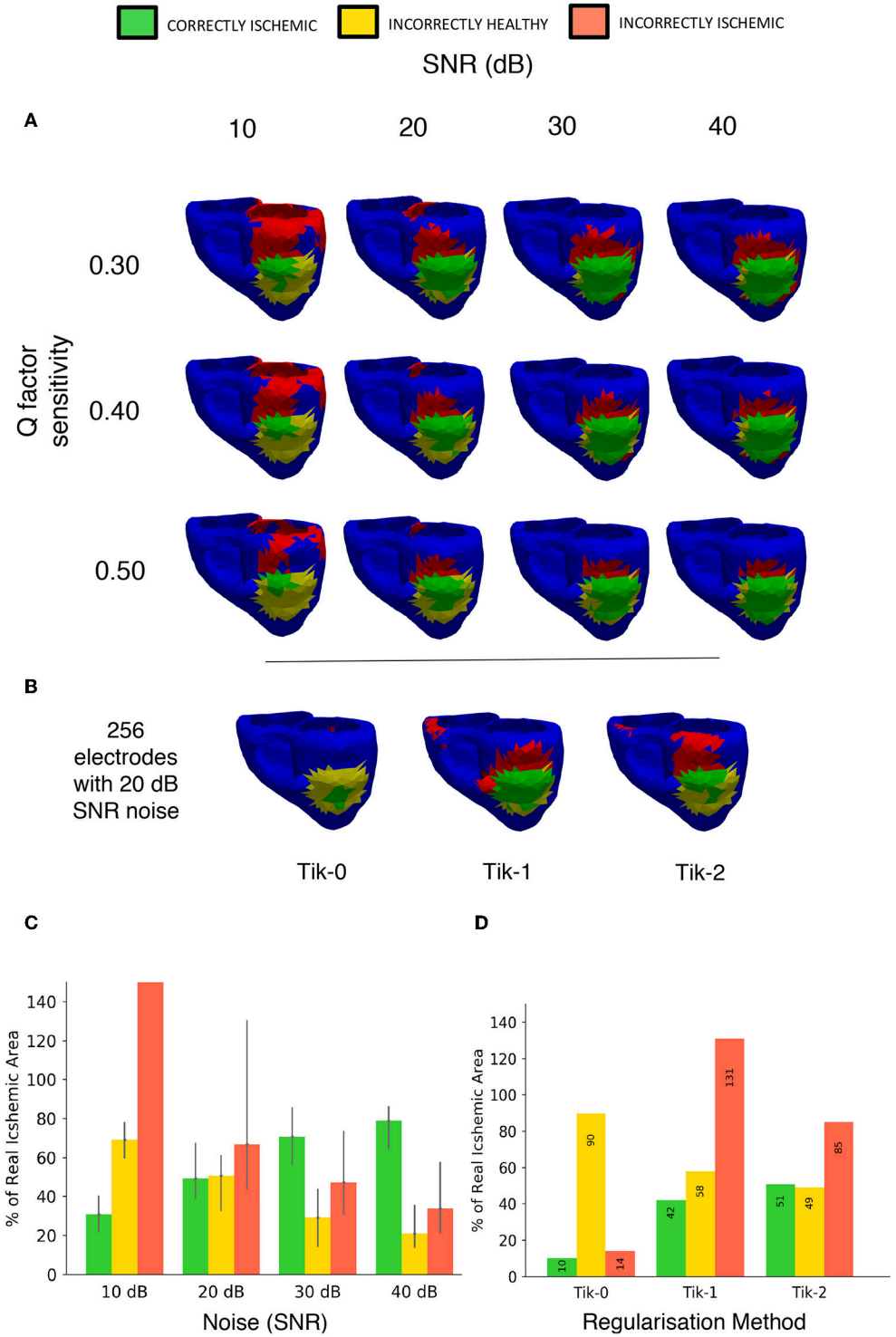

FIGURE 11 | Noise and sensitivity analysis on the lesion detection results and Tikhonov regularisation performance results including 20 dB SNR. **(A)** Signal to Noise ratio (10, 20, 30, 40 dB) vs. lesion threshold algorithm sensitivity with the lesion located on the left ventricle anterior wall. **(B)** Detection results using the 3 different regularisation techniques constructed from BSP's containing noise at 20 dB SNR using 256 electrodes layout. **(C)** Bar chart visualizing the "traffic light" data taken from **(A)** over the whole geometry. Bar height represents data taken from the $Q = 0.4$ in Equation (7) with error bars on the bar showing results of setting Q from 0.3 to 0.5. **(D)** Bar chart visualizing the "traffic light" data taken from **(B)** over the whole geometry.

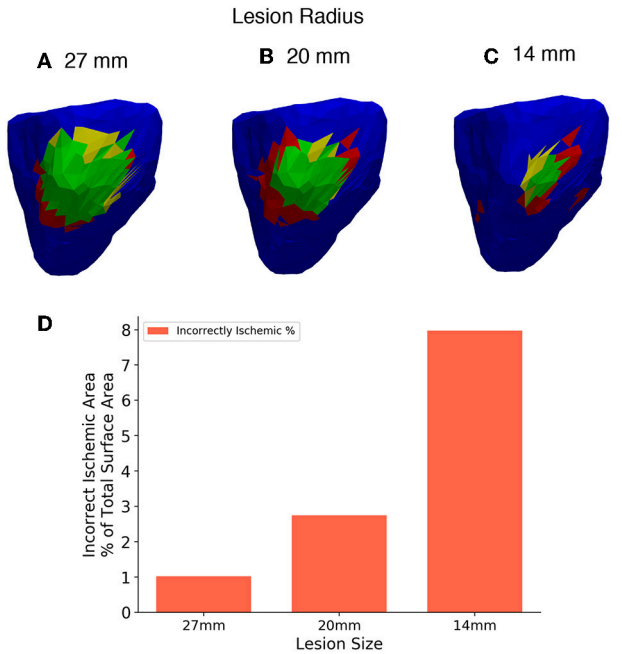

FIGURE 12 | (A–C) Three different lesion sizes reconstructed with the 2nd order Tikhonov solution and 512 leads. **(D)** Bar chart showing the areas incorrectly identified as ischemic in each solution as a percentage of the 27mm lesion area for comparison. Right lateral wall view and lesions have radius **(A)** 27 mm, **(B)** 20 mm, **(C)** 14 mm.

as well as its "ill-posedness" and so more accurate results are not guaranteed.

LIMITATIONS

There are a number of limitations with this study which should be considered when interpreting the results. Firstly, a global method was used to produce a single lambda value for the regularisation across all timesteps to generate the RDMS values shown in **Figure 4**. An individual timestep approach was implemented but the results provided only a marginal improvement whilst also requiring substantially more computing time. There are other regularisation methods (Figuera et al., 2016; Benning and Burger, 2018) which may or may not improve the solution however these have not been tested in this study. The shape of the lesion is idealised to be circular for computational/modelling simplicity, it is not yet clear how more complex/multiple lesions will perform. The smoothing properties of inverse regularisation methods may impact these complex shapes differently and will have to be further investigated. This study has not been tested and validated in a clinical setting, however computer modelling provides a direct comparison between results computed from solving the forward and inverse problem which can then be used as a basis for clinical studies. Finally, clinically electroanatomic mapping (EAM) studies have shown that using general unipolar electrogram thresholds can be unreliable in detecting scar, as unipolar voltages show large variations even in non-scar locations and are effected by tissue fat (Nguyên et al., 2017). Bipolar electrograms have been shown to be more reliable (Codreanu et al., 2008) and so further study is warranted to test and evaluate the use of different metrics to evaluate ECGI reconstructions.

CONCLUSION

A ventricle-torso model was used to investigate the use of ECGI as a tool to detect ischemic lesions. We quantified the quality of lesion identification while changing the number of leads used to reconstruct the BSP. The results show that the 2nd order Tikhonov is the best of the three regularisation methods tested in this study, showing and detecting a circular ischemic lesion of 27 mm with lead numbers >256. At >256 leads the 2nd order Tikhonov showed not only a higher % of lesion detected but a reduced and more localised error around the lesion itself. Further to this, the 2nd order Tikhonov proved to be more accurate identifying the lesion on the inner wall of the ventricle. This superior inner wall detection still proved to be the case when noise was added into the workflow, however the relative performance gap between then 1st and 2nd order Tikhonov is reduced. The combination of both noise and a limited number of recording electrodes produced "L curves" with a less pronounced corner when viewed comparatively against their no noise counterparts. Lesions on the left ventricle walls were also able to be identified but comparatively to the right ventricle lateral wall performed marginally worse, with lesions located on the interventricular septum being able to be indicated by the reconstructions but not successfully identified against the error.

AUTHOR CONTRIBUTIONS

VK and HZ conceived the experiments. VK performed the code implementation, development, testing, and analysis. HN and EP contributed computing resources. VK, HN, and HZ contributed to the manuscript.

FUNDING

This work was supported by the EPSRC (EP/J00958X/1; EP/I029826/1).

SUPPLEMENTARY MATERIAL

The Supplementary Material for this article can be found online at: https://www.frontiersin.org/articles/10.3389/fphys.2019.00050/full#supplementary-material

Video S1 | Ventricle reconstruction using 0 order Tikhonov and 1024 leads.

Video S2 | Ventricle reconstruction using 1 order Tikhonov and 1024 leads.

Video S3 | Ventricle reconstruction using 2 order Tikhonov and 1024 leads.

Video S4 | Ventricle detection result using 0 order and 1024 leads.

Video S5 | Ventricle detection result using 1 order and 128 leads.

Video S6 | Ventricle detection result using 1 order and 1024 leads.

Video S7 | Ventricle detection result using 2 order and 128 leads.

Video S8 | Ventricle detection result using 2 order and 1024 leads.

REFERENCES

Adeniran, I., Hancox, J. C., and Zhang, H. (2013). Effect of cardiac ventricular mechanical contraction on the characteristics of the ECG : a simulation study. *J. Biomed. Sci. Eng.* 2013, 47–60. doi: 10.4236/jbise.2013.612A007

Adeniran, I., McPate, M. J., Witchel, H. J., Hancox, J. C., and Zhang, H. (2011). Increased vulnerability of human ventricle to re-entrant excitation in HERG-linked variant 1 short QT syndrome. *PLoS Comput. Biol.* 7:e1002313. doi: 10.1371/journal.pcbi.1002313

Alday, E. A. (2016). *Theoretical Investigation of Non-Invasive Methods to Identify Origins of Cardiac Arrhythmias.* PhD Thesis, University of Manchester. Available online at: https://www.library.manchester.ac.uk/search-resources/theses/

Alday, E. A., Ni, H., Zhang, C., Colman, M. A., Gan, Z., and Zhang, H. (2016). Comparison of electric- and magnetic- cardiograms produced by myocardial ischemia in models of the human ventricle and torso. *Comput. Cardiol.* 11:e0160999. doi: 10.1371/journal.pone.0160999

Barnes, J. P., and Johnston, P. R. (2016). Application of robust generalised cross-validation to the inverse problem of electrocardiology. *Comput. Biol. Med.* 69, 213–25. doi: 10.1016/j.compbiomed.2015.12.011

Barr, R. C., Ramsey, M., and Spach, M. S. (1977). Relating epicardial to body surface potential distributions by means of transfer coefficients based on geometry measurements. *IEEE Trans. Biomed. Eng.* 2, 1–11 . doi: 10.1109/TBME.1977.326201

Benning, M., and Burger, M. (2018). Modern regularization methods for inverse problems. *arXiv:1801.0992.* doi: 10.1017/S0962492918000016

Brooks, D. H., and Macleod, R. (1997). "Electrical imaging of the heart : electrophysical underpinnings and signal processing opportunities introduction," in *Proceedings of the Conference 32nd Asilomar Conference on Signals, Systems, and Computers*, 24–42.

Carrascosa, P., and Capunay, C. (2017). Myocardial CT perfusion imaging for ischemia *Detection* 7, 112–128. doi: 10.21037/cdt.2017.04.07

Carvalho, F. S., Mukai, K., Clayton, J., and Ordovas, G. K. (2017). Cardiac MRI : a preferred method for assessing myocardial ischemia and infarct burden. *Appl. Radiol.* 46, 21–29.

Castellanos, J. L., Gómez, S., and Guerra, V. (2002). The triangle method for finding the corner of the L-curve. *Appl. Numer. Math.* 43, 359–373. doi: 10.1016/S0168-9274(01)00179-9

Chung, J., and Español, M. I. (2017). Learning regularization parameters for general-form Tikhonov. *Inverse Prob.* 33, 1–21. doi: 10.1088/1361-6420/33/7/074004

Codreanu, A., Odille, F., Aliot, E., Marie, P. Y., Magnin-Poull, I., Andronache, M., et al. (2008). Electroanatomic characterization of post-infarct scars. comparison with 3-dimensional myocardial scar reconstruction based on magnetic resonance imaging. *J. Am. Col. Cardiol.* 52, 839–842. doi: 10.1016/j.jacc.2008.05.038

Cultrera, A., and Callegaro, L. (2016). A simple algorithm to find the L-curve corner in the regularization of inverse problems. *CoRR* abs/1608.04571.

Daly, C., and Kwong, R. Y. (2013). Cardiac MRI for myocardial ischemia. 9, 123–131. doi: 10.14797/mdcj-9-3-123

Figuera, C., Suárez, G. V., Hernández, R. I., Rodrigo, M., Liberos, A., Atienza, F., et al. (2016). Regularization techniques for ECG imaging during atrial fibrillation: a computational study. *Front. Physiol.* 7:466. doi: 10.3389/fphys.2016.00466

Gharbalchi, F., Dogrusoz, Y. S., and Weber, G. W. (2016). Lanczos bidiagonalization-based inverse solution methods applied to electrical imaging of the heart by using reduced lead-sets: a simulation study. *Cogent. Math.* 3, 1–13. doi: 10.1080/23311835.2016.1256461

Ghuran, A. V., and Camm, A. J. (2001). Ischaemic heart disease presenting as arrhythmias. *Br. Med. Bull.* 59, 193–210. doi: 10.1093/bmb/59.1.193

Golub, G. H., Heath, M. T., and Wahba, G. (1979). Generalized cross-validation as a method for choosing a good ridge parameter. *Technometrics* 21, 215–223. doi: 10.1080/00401706.1979.10489751

Gulrajani, R. M. (1998). The forward and inverse problems of electrocardiography. *IEEE Eng. Med. Biol.* 17, 84–122. doi: 10.1109/51.715491

Hampton, J. (2013). *The ECG Made Easy*. London: Elsevier Health Sciences.

Hansen, P. (1992). Analysis of discrete ILL-posed problems by means of the L-curve. *SIAM Rev.* 34, 561–580.

Huikuri, H. V., Castellanos, A., and Myerburg, R. J. (2001). Sudden death due to cardiac arrhythmias. *N. Engl. J. Med.* 345, 1473–182. doi: 10.1056/NEJMra000650

Intini, A., Goldstein, R. N., Jia, P., Ramanathan, C., Ryu, K., Giannattasio, B., et al. (2005). Electrocardiographic Imaging (ECGI), a novel diagnostic modality used for mapping of focal left ventricular tachycardia in a young athlete. *Heart Rhythm* 2, 1250–1252. doi: 10.1016/j.hrthm.2005.08.019

Jiang, Y., Qian, C., Hanna, R., Farina, D., and Dössel, O. (2009). Optimization of the electrode positions of multichannel ECG for the reconstruction of ischemic areas by solving the inverse electrocardiographic problem. *Int. J. Bioelectr.* 11, 27–37.

Jie, X., Gurev, V., and Trayanova, N. (2010). Mechanisms of mechanically induced spontaneous arrhythmias in acute regional ischemia. *Circ. Res.* 106, 185–192. doi: 10.1161/CIRCRESAHA.109.210864

Jie, X., and Trayanova, N. A. (2011). Mechanisms for initiation of reentry in acute regional ischemia phase 1B. 40, 1301–1315. doi: 10.1016/j.hrthm.2009.11.014

Keller, D. U. J., Kalayciyan, R., Dössel, O., and Seemann, G. (2010). "Fast creation of endocardial stimulation profiles for the realistic simulation of body surface ECGs," in *World Congress on Medical Physics and Bioal Engineering, September 7-12, 2009, Munich, Germany,* eds O. Dössel and W. C. Schlegel (Berlin; Heidelberg: Springer), 145–148.

Messnarz, B., Tilg, B., Modre, R., Fischer, G., and Hanser, F. (2004). A new spatiotemporal regularization approach for reconstruction of cardiac transmembrane potential patterns. *IEEE Trans. Biomed. Eng.* 51, 273–281. doi: 10.1109/TBME.2003.820394

Nguyên, U. C., Maffessanti, F., Mafi-Rad, M., Conte, G., Zeemering, S., Regoli, F., et al. (2017). Evaluation of the use of unipolar voltage amplitudes for detection of myocardial scar assessed by cardiac magnetic resonance imaging in heart failure patients. *PLoS ONE* 12:e0180637. doi: 10.1371/journal.pone.0180637

Ni, H. (2016) *Biophysical Modelling of Functional Impacts of Potassium Channel Mutations on Human Atrial and Ventricular Dynamics.* PhD Thesis, University of Manchester. Available online at: https://www.library.manchester.ac.uk/search-resources/theses/

Oostendorp, T. F., Oosterom, A. V., and Huiskamp, G. (1989). Interpolation on a triangulated 3D surface. *J. Comp. Phys.* 80, 331–343. doi: 10.1016/0021-9991(89)90103-4

Pei, Y., Yanbin, X., and Feng, D. (2015). "A modified L-curve method for choosing regularization parameter in electrical resistance tomography," in *Proceedings of IEEE International Conference on Imaging Systems and Techniques* (Tianjin). doi: 10.1109/IST.2015.7294469

Ramanathan, C., Jia, P., Ghanem, R., Calvetti, D., and Rudy, Y. (2003). Noninvasive electrocardiographic imaging (ECGI): application of the Generalized Minimal Residual (GMRes) method. *Ann. Biomed. Eng.* 31, 981–994. doi: 10.1114/1.1588655

Ramanathan, C., and Rudy, Y. (2001). Electrocardiographic imaging: II. Effect of torso inhomogeneities on noninvasive reconstruction of epicardial potentials, electrograms, and isochrones. *J. Cardiovasc. Electr.* 12, 241–52. doi: 10.1046/j.1540-8167.2001.00241.x

Roffi, M., Patrono, C., Collet, J. P., Mueller, C., Valgimigli, M., Andreotti, F., et al. (2016). 2015 ESC guidelines for the management of acute coronary syndromes in patients presenting without persistent St-segment elevation: task force for the management of acute coronary syndromes in patients presenting without persistent ST-segment elevation of the European Society of Cardiology (ESC). *Eur. Heart J.* 37, 267–315. doi: 10.1093/eurheartj/ehv320

Rudy, Y. (2017). Noninvasive ECG imaging (ECGI): mapping the arrhythmic substrate of the human heart. *Int. J. Cardiol.* 237:13–14. doi: 10.1016/j.ijcard.2017.02.104

Ruud, T. S., Nielsen, B. F., Lysaker, M., and Sundnes, J. (2009). A computationally efficient method for determining the size and location of myocardial ischemia. *IEEE Trans. Biomed. Eng.* 56, 263–272. doi: 10.1109/TBME.2008.2009068

Sejersten, M., Wagner, G. S., Pahlm, O., Warren, J. W., Feldman, C. L., and Horácek, B. M. (2007). Detection of acute ischemia from the EASI-derived 12-lead electrocardiogram and from the 12-lead electrocardiogram acquired in clinical practice. *J. Electrocardiol.* 40, 120–126. doi: 10.1016/j.jelectrocard.2006.08.099

Stenroos, M., and Haueisen, J. (2008). Boundary element computations in the forward and inverse problems of electrocardiography: comparison of collocation and galerkin weightings. *IEEE Trans. Biomed. Eng.* 55, 2124–2133. doi: 10.1109/TBME.2008.923913

Wang, D., Kirby, R. M., Macleod, R. S., and Johnson, C. R. (2013). Inverse electrocardiographic source localization of ischemia: an optimization framework and finite element solution. *J. Comp. Phys.* 250, 403–424. doi: 10.1016/j.jcp.2013.05.027

Zemzemi, N., Dobrzynski, C., Bear, L., Potse, M., Dallet, C., Coudiere, Y., et al. (2015). Effect of the torso conductivity heterogeneities on the ECGI inverse problem solution. *Comp. Cardiol.* 42, 233–236. doi: 10.1109/CIC.2015.7408629

Conflict of Interest Statement: The authors declare that the research was conducted in the absence of any commercial or financial relationships that could be construed as a potential conflict of interest.

frontiers in Physiology

CORRECTION
published: 29 May 2019
doi: 10.3389/fphys.2019.00692

Corrigendum: ECG Imaging to Detect the Site of Ventricular Ischemia Using Torso Electrodes: A Computational Study

Vinay Kara[1], *Haibo Ni*[1,2], *Erick Andres Perez Alday*[3] *and Henggui Zhang*[1,4,5*]

[1] Biological Physics Group, School of Physics and Astronomy, The University of Manchester, Manchester, United Kingdom, [2] Department of Pharmacology, The University of California, Davis, Davis, CA, United States, [3] Division of Cardiovascular Medicine, Oregon Health and Science University, Portland, OR, United States, [4] School of Computer Science and Technology, Harbin Institute of Technology, Harbin, China, [5] China Space Institute of Southern China, Shenzhen, China

Keywords: ECGI, ventricle, torso electrodes, inverse problem, ventricular ischemia, regularisation methods

OPEN ACCESS

Approved by:
Frontiers Editorial Office, Frontiers Media SA, Switzerland

***Correspondence:**
Henggui Zhang
henggui.zhang@manchester.ac.uk

Specialty section:
This article was submitted to Cardiac Electrophysiology, a section of the journal Frontiers in Physiology

Received: *10 May 2019*
Accepted: *16 May 2019*
Published: *29 May 2019*

Citation:
Kara V, Ni H, Alday EAP and Zhang H (2019) Corrigendum: ECG Imaging to Detect the Site of Ventricular Ischemia Using Torso Electrodes: A Computational Study. Front. Physiol. 10:692. doi: 10.3389/fphys.2019.00692

A Corrigendum on

ECG Imaging to Detect the Site of Ventricular Ischemia Using Torso Electrodes: A Computational Study

by Kara, V., Ni, H., Perez Alday, E. A., and Zhang, H. (2019). Front. Physiol. 10:50. doi: 10.3389/fphys.2019.00050

There is an error in the **Funding** statement. The correct number for "EPSRC" is "(EP/J00958X/1; EP/I029826/1)."

The authors apologize for this error and state that this does not change the scientific conclusions of the article in any way. The original article has been updated.

frontiers in Physiology

ORIGINAL RESEARCH
published: 26 February 2019
doi: 10.3389/fphys.2019.00146

Optical Imaging of Ventricular Action Potentials in a Torso Tank: A New Platform for Non-Invasive Electrocardiographic Imaging Validation

Laura R. Bear[1,2,3], Richard D. Walton[1,2,3], Emma Abell[1,2,3], Yves Coudière[1,2,4,5], Michel Haissaguerre[1,2,3,6], Olivier Bernus[1,2,3] and Rémi Dubois[1,2,3]*

[1] IHU Liryc, Electrophysiology and Heart Modeling Institute, Fondation Bordeaux Université, Bordeaux, France, [2] Univ. Bordeaux, Centre de Recherche Cardio-Thoracique de Bordeaux, U1045, Bordeaux, France, [3] INSERM, Centre de Recherche Cardio-Thoracique de Bordeaux, U1045, Bordeaux, France, [4] CARMEN Research Team, INRIA, Talence, France, [5] CNRS, IMB, UMR 5251, Talence, France, [6] Bordeaux University Hospital (CHU), Electrophysiology and Ablation Unit, Pessac, France

Background: Non-invasive electrocardiographic imaging (ECGI) is a promising tool to provide high-resolution panoramic imaging of cardiac electrical activity noninvasively from body surface potential measurements. Current experimental methods for ECGI validation are limited to comparison with unipolar electrograms and the relatively low spatial resolution of cardiac mapping arrays. We aim to develop a novel experimental set up combining a human shaped torso tank with high-resolution optical mapping allowing the validation of ECGI reconstructions.

Methods: Langendorff-perfused pig hearts (n = 3) were suspended in a human torso-shaped tank, with the left anterior descending artery (LAD) cannulated on a separate perfusion. Electrical signals were recorded from an 108-electrode epicardial sock and 128 electrodes embedded in the tank surface. Simultaneously, optical mapping of the heart was performed through the anterior surface of the tank. Recordings were made in sinus rhythm and ventricular pacing (n = 55), with activation and repolarization heterogeneities induced by perfusion of hot and cold solutions as well as Sotalol through the LAD. Fluoroscopy provided 3D cardiac and electrode geometries in the tank that were transformed to the 2D optical mapping window using an optimization algorithm. Epicardial unipolar electrograms were reconstructed from torso potentials using ECGI and validated using optical activation and repolarization maps.

Results: The transformation and alignment of the 3D geometries onto the 2D optical mapping window was good with an average correlation of 0.87 ± 0.10 and error of 7.7 ± 3.1 ms with activation derived from the sock. The difference in repolarization times were more substantial (error = 17.4 ± 3.7 ms) although the sock and optical repolarization patterns themselves were very similar (correlation = 0.83 ± 0.13). Validation of ECGI reconstructions revealed ECGI accurately captures the pattern of activation (correlation = 0.79 ± 0.11) and identified regions of late and/or early repolarization during different perfusions through LAD. ECGI also correctly demonstrated gradients in both activation and repolarization, although in some cases these were under or over-estimated or shifted slightly in space.

OPEN ACCESS

Edited by:
Carlos Figuera, Universidad Rey Juan Carlos, Spain

Reviewed by:
Rachel C. Myles, University of Glasgow, United Kingdom
Gernot Plank, Medical University of Graz, Austria

****Correspondence:***
Laura R. Bear
laura.bear@ihu-liryc.fr

Specialty section:
This article was submitted to Cardiac Electrophysiology, a section of the journal Frontiers in Physiology

Received: *14 September 2018*
Accepted: *07 February 2019*
Published: *26 February 2019*

Citation:
Bear LR, Walton RD, Abell E, Coudière Y, Haissaguerre M, Bernus O and Dubois R (2019) Optical Imaging of Ventricular Action Potentials in a Torso Tank: A New Platform for Non-Invasive Electrocardiographic Imaging Validation. Front. Physiol. 10:146. doi: 10.3389/fphys.2019.00146

Conclusion: A novel experimental setup has been developed, combining a human-shaped torso tank with optical mapping, which can be effectively used in the validation of ECGI techniques; including the reconstruction of activation and repolarization patterns and gradients.

Keywords: ECGI, validation, optical mapping, torso tank, inverse problem

INTRODUCTION

Non-invasive electrocardiographic imaging (ECGI) is a promising tool to provide high-resolution panoramic imaging of cardiac electrical activity noninvasively from body surface potential measurements (Rudy, 2013). While ECGI has seen considerable development over the past four decades, the inverse problem is ill-posed, highly sensitive to noise, and can have many (both physiological and non-physiological) solutions. As such, a multitude of methods have been, and are still being developed to overcome this (such as regularization) (Tikhonov and Arsenin, 1977; Colli-Franzone et al., 1985a; Wang and Rudy, 2006). Given this ill-posed nature, robust validation is essential for the complete adoption of this powerful technique clinically. Such validation needs to be as close as possible to the conditions of clinical applications, and for applications to arrhythmia, due to their dynamic nature, simultaneous body surface potential mapping (BSPM) and intracardiac recordings is needed.

One of the advantages often cited of ECGI is the ability to map the ventricular surface at a high-resolution, theoretically only limited by the epicardial mesh created. The majority of validation studies to date have evaluated ECGI methods using an *ex vivo* torso tank (Oster et al., 1998; Bear et al., 2018a), *in vivo* large animal models (Oosterhoff et al., 2016; Cluitmans et al., 2017; Bear et al., 2018b), or in patients (Ghanem et al., 2005; Sapp et al., 2012). While there are often several hundred electrodes in the arrays used to provide ground truth data, the spatial resolution (number of electrodes per unit area) is typically lower than that of the cardiac mesh used for ECGI reconstructions. While this means the gross abilities of ECGI to reconstruct cardiac activity can be evaluated, they may not be reliable to assess the accuracy of high-resolution spatial and temporal features such as slow conduction, line of block and/or repolarization gradients. For example, the ability to accurately depict repolarization gradients may be clinically relevant as these have been linked to patients susceptible to ventricular fibrillation (Vijayakumar et al., 2014). No previous study has attempted to validate the accuracy of ECGI to capture gradients in either activation or recovery, possibly because the resolution of ground truth recordings are not high enough.

Currently the only means to validate ECGI at high-resolution is through the use of computational models. This approach has the obvious, significant strength of not requiring the expense and extensive infrastructure of experimental studies, meaning modifying conditions or changing parameters is substantially easier. However, like all data sources, computational models have their limitations including the ability to accurately reflect cardiac pathologies when the ionic mechanisms are unknown and the fact that this approach often commits an "inverse crime" by neglecting the effect of any errors in the problem formulation and using the same problem formulation for both the forward and inverse solutions (Macleod and Brooks, 2000). Validation for ECGI is most ideally performed using an integrative approach with multiple forms of data, and having an experimental or clinical source of high resolution ground truth data would enable this (Cluitmans et al., 2018). The validation of ECGI also depends on its formulation and chosen underlying cardiac source to be reconstructed. The most common formulations use the epicardial extracellular potentials as the cardiac source model (Sapp et al., 2012; Cluitmans et al., 2017; Bear et al., 2018b) which can be compared directly to the signals measured using epicardial mapping techniques. Alternative formulations using transmembrane potential based models, however, require post-processing of the inverse solutions in order to validate against the extracellular potentials measured by an electrode array. The post-processing method chosen may affect the perceived accuracy of the inverse methods used and to date direct validation of reconstructed transmembrane potentials cannot be performed using experimental data.

Optical mapping overcomes the limitations of current ECGI experimental validation setups, enabling high spatial resolution mapping (in the order of 0.5 mm) of cardiac action potentials (Efimov et al., 2004). To date, optical mapping has never been used in the validation of ECGI reconstructions, possibly because the optical mapping window is defined by a 2D surface, and comparing this to ECGI reconstructions based on a 3D cardiac model is a technical challenge. Furthermore, this technique is limited to *ex vivo* models and requires a transparent medium between the camera and cardiac surface.

The aim of this study was to develop a novel experimental set up combining a human shaped torso tank with optical mapping allowing the validation of ECGI reconstructions. The preliminary results presented in this paper aim to demonstrate the application of this setup to validate ECGI reconstructions of activation and repolarization abnormalities and gradients.

MATERIALS AND METHODS

This study was carried out in accordance with the recommendations of the Directive 2010/63/EU of the European Parliament on the protection of animals used for scientific purposes and approved by the local ethical committee of Bordeaux CEEA50.

Experimental Setup

Pigs (n = 3; 30–40 kg) were pre-medicated with acepromazine (0.1 mg/kg) and ketamine (20 mg/kg), anaesthetized with propofol (1 mg/kg) and maintained under isofluorane, 2%, in air/O_2 (50/50) after intratracheal intubation. The thorax was opened and heparin (2 ml) infused intravenously. 1.5 L of blood was collected during intravenous infusion of Voluven. Cardiac arrest was induced with cold cardioplegia introduced into the aortic root. The heart was rapidly excised and immersed in ice-cold Tyrode's solution. The aorta was cannulated and the heart perfused in Langendorff mode with blood oxygenated with 95/5% O_2/CO_2, pH 7.4, temperature 37°C.

An epicardial electrode sock (108 electrodes) was attached to the heart (**Figure 1A**) and bipolar pacing leads were fixed to the right atria (RA) and ventricles with hooks (∼2 mm between electrodes tips). The left anterior descending artery (LAD) was freed above the first diagonal branch for a distance of 5 mm. A cannula was introduced through a small incision, and held in place with a ligature. The cannula was connected to the main perfusion system via a miniature heat exchanger. After instrumentation, perfusion was changed to 100% Tyrode's solution containing (mM) NaCl, 128; $NaHCO_3$, 28; NaH_2PO_4, 0.5; $MgCl_2$, 0.7; glucose, 11; KCl, 4.7; $CaCl_2$, 1.5. The solution was oxygenated with 95/5% O_2/CO_2 and kept at pH 7.4, temperature 37°C. The heart was transferred to a human-shaped torso tank made from clear plastic with 256 electrodes embedded in the surface (**Figure 1B**).

The anterior epicardial surface was imaged using optical mapping through the chest of the torso tank (**Figure 1C**). Prior to imaging, the heart was mechanically-uncoupled using blebbistatin (15 μM), and stained with the voltage-sensitive dye, Di-4-ANBDQBS (10 μM). The epicardial surface was illuminated with monochromatic LEDs at 627 nm (Cairn Research Ltd., Kent, United Kingdom). Optical images (100 × 100 pixels) of signals passed through a 715 nm long-pass filter were acquired using a Micam Ultima CMOS camera (SciMedia USA Ltd., Costa Mesa, CA, United States) with a spatial resolution of 700 μm/pixel.

Electrophysiological Recordings

The heart was paced by 2 ms pulses at 2 Hz, with constant current amplitudes 2× the diastolic threshold, on either the left (LV) or right (RV) ventricular epicardial surface, mimicking ectopic activity, and during RA pacing representing normal sinus rhythm. Regional activation and repolarization heterogeneities were introduced through cooling then heating of the LAD perfusate to various temperature (min 21°C; max 40°C), as well as through local perfusion of Sotalol (10 mg/mL) from Sigma-Aldrich (Zwijndrecht, Netherlands). Recordings were taken in these different states during sinus rhythm and ventricular pacing. In total 55 different sequences were obtained across the three hearts.

Electrical and optical signals were measured simultaneously for each sequence. Tank and sock unipolar electrograms were recorded at 2 kHz (BioSemi, Netherlands) and referenced to a Wilson's central terminal defined using tank electrodes. Optical mapping signals were acquired simultaneously at a frame rate of 1 kHz

Geometric and Optical Alignment

3D angiographic fluoroscopy (Artis, Siemens) was used at the end of each experiment to obtain the exact location and orientation of the epicardium (mean edge length 4 ± 1 mm), perfusion beds and electrodes with respect to the tank (**Figure 2A**). To align the electrical and optical maps, a perspective projection based on a 3D camera position X_{COP} and a 3D focal center point X_{FOC} (**Figure 2C**) was used to project the torso and sock 3D electrode locations (E_{3D}) onto the 2D optical mapping frames ($\hat{E}_{2D}$) (**Figure 2B**)

$$\hat{E}_{2D} = E_{3D}\ P\left(X_{COP}, X_{FOP}\right)$$

Where P is the projection matrix. The camera and focal points were first optimized by minimizing the mean Euclidean distance between projected electrodes positions ($\hat{E}_{2D}$) and their true 2D locations (E_{2D}) visible in optical images (**Figures 2C,D**).

$$min_{X_{COP},X_{FOP}}\ J = \ min_{X_{COP},X_{FOP}} \frac{\sum \parallel \hat{E}_{2D} - \ E_{2D} \parallel^2}{n}$$

Where J is the cost function and n the number of electrodes used in the optimization. This proved to be insufficient due to error in identifying electrodes points in 2D and 3D, therefore a second optimization step was performed minimizing the mean absolute difference in activation times (AT) derived from sock electrodes and optical maps for a single activation sequence:

$$min_{X_{COP},X_{FOP}}\ J = \ \frac{\sum \left|AT_{sock} - AT_{optical}\right|^2}{n}$$

To validate the final projection, activation maps (that were not used in the optimization process) derived from sock electrograms and optical mapping signals were compared across all sinus rhythm and pacing sequences (methods described below). The same projection matrix was then applied on the epicardial and LAD geometries, to define their 2D locations in optical mapping window. As the posterior sock electrodes and epicardial surface were not visible in this window, they were removed for all comparisons.

Signal Processing

Tank and sock channels in which signals were absent as a result of lead fracture or poor electrode contact were immediately evident on visual inspection and were discarded. Electrical signals were temporally aligned to optical maps by a square wave output generated by the optical mapping setup during camera operation that was recorded directly by the BioSemi system. Optical signals were filtered using spatial averaging (kernel 2.1 mm) and temporal averaging (kernel 1.5 ms). A data mask was defined by removing optical signals with an amplitude less than 20% of the maximum signal, removing unconnected components and using a dilation erosion technique to smooth the edges (Laughner et al., 2012). A multi-lead signal averaging algorithm was used to remove remaining noise in both electrical and optical recordings (Aström et al., 2000).

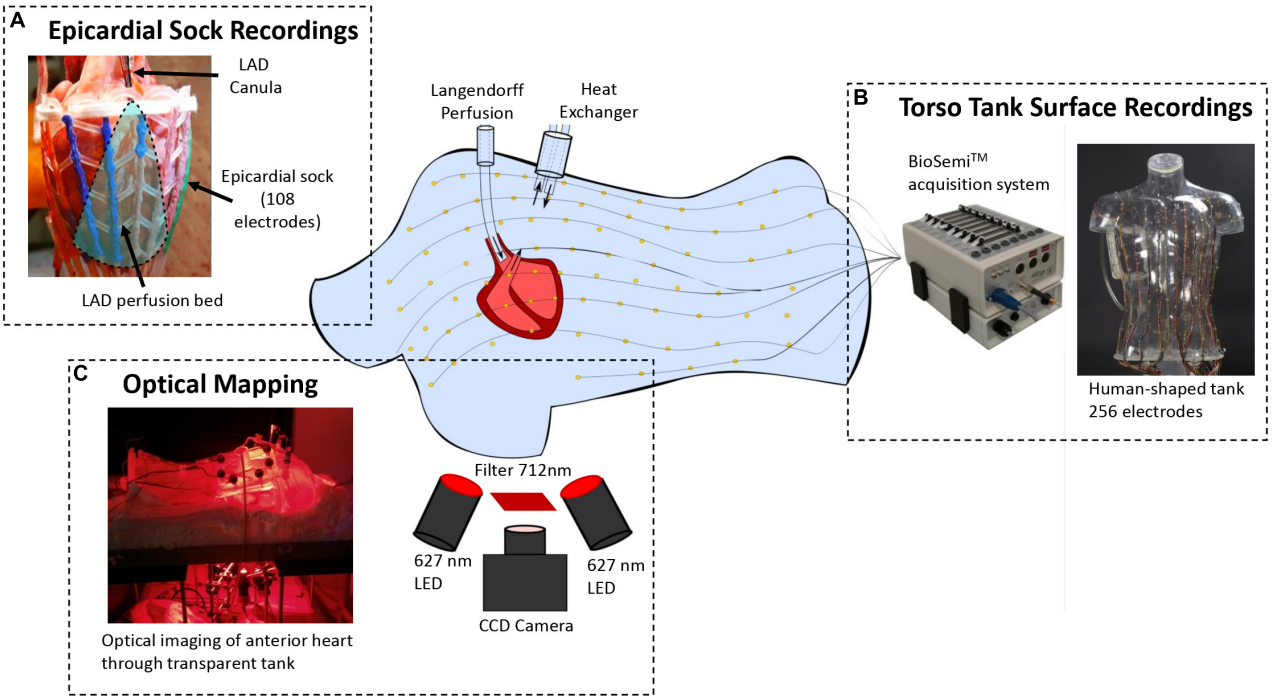

FIGURE 1 | Experimental setup demonstrating **(A)** the pig heart perfused in Langendorff mode with an 108-electrode sock placed over the ventricles and the LAD cannulated on a separate perfusion, **(B)** the human shaped torso tank with 256 electrodes embedded in the surface that the heart is suspended within, and **(C)** the optical mapping that is performed through the anterior surface of the torso.

Electrocardiographic imaging electrograms were reconstructed from tank potentials to experiment-specific epicardial surfaces derived from fluoroscopy scans using the method of fundamental solutions (Wang and Rudy, 2006) with Tikhonov regularization (Tikhonov and Arsenin, 1977) and the CRESO method (Colli-Franzone et al., 1985b) to define the regularization parameter.

Activation/depolarization times (AT) were defined from recorded sock electrograms as the time of minimum derivative (dV/dT) of the intrinsic deflection, for optical action potentials as the maximum dF/dT during the action potential upstroke and for ECGI signals by fitting a global activation field to electrogram delays between electrograms (Duchateau et al., 2016). Recovery/repolarization times (RT) were defined from recorded sock and ECGI-derived electrograms as the time of maximum dV/dT of the *T*-wave, a widely used for experimental and clinical electrophysiological studies using unipolar electrograms (Coronel et al., 2009; Lux and Gettes, 2011). For optical signals, repolarization was defined as the time of minimum dF/dT, an index shown to closely match the maximum dV/dT of electrograms (Potse et al., 2009).

Data Analysis

The minimum dV/dT of recorded electrograms has been shown to very closely match the maximum dV/dT of the action potential upstroke as measured from a floating micro electrode within 1 mm of the small unipolar electrode (Millar et al., 1985; Haws and Lux, 1990). Therefore, transformation and alignment of the 3D geometries into the 2D optical mapping frame were first validated by comparing recorded sock and optical activation maps during sinus rhythm and pacing. As with ATs, a relationship exists between RTs derived from unipolar electrograms and action potentials. RT recorded by sock electrodes were also compared their optical equivalents. Optical activation and repolarization maps were then used to validate ECGI reconstructions. Quantitative comparison of marker timings was performed by defining the nearest optical pixel to each sock electrode and heart mesh node using the Euclidean distance. Activation and RT at these locations directly compared using a root mean square error (RMSE) and Pearson's correlation coefficient (CC).

Statistical analysis was conducted using GraphPad Prism 7.04. For each metric, the significance of differences was tested using paired *t*-tests with $p < 0.05$ defined as significant. Data are expressed as mean ± SD unless otherwise stated.

RESULTS

Sock and Optical Electrical Alignment

Activation Maps

Figure 3 (left) presents an example of an aligned optical and sock activation map during a sinus rhythm sequence with cold perfusion through the LAD marked in black. Sock ATs are represented as spheres with the optical mapping activation underneath. Below, three representative electrograms (top) and

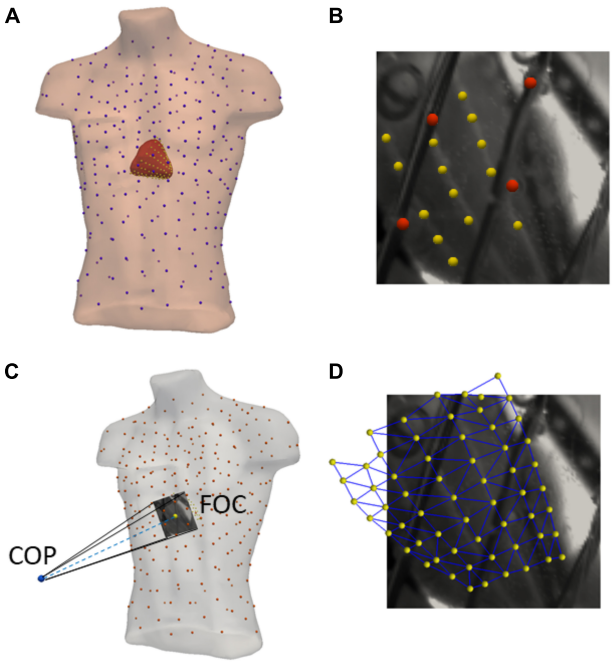

FIGURE 2 | Model creation and optical alignment: **(A)** Meshes are created from 3D angiographic fluoroscopy scans of the epicardial surface (red), sock electrodes (yellow), torso surface (peach), and tank electrodes (blue). **(B)** Example of sock (yellow) and torso (red) electrode identification using the optical mapping field of view. **(C)** Optimization of the camera position (COP) and focal point (FOC) for the perspective projection of the 3D geometries into 2D using the identified sock/torso electrodes. **(D)** Example of the final projection of 3D sock electrodes (yellow) and mesh (blue) onto the 2D optical mapping field of view.

action potentials (bottom) are presented with sock (blue) and optical (red) derived AT markers over the QRS.

The pattern of activation derived from sock and optical signals were very similar, as quantified by a correlation of 0.96 and RMSE of 6.1 ms. The larger differences (>5 ms) in ATs were seen when electrograms, action potentials or both had fractionated or shallow intrinsic deflections. This indicates poor electrode contact or fluorescence and naturally making AT calculation more prone to error. The examples in **Figure 3** show that despite a 4–7 ms difference in marker placement, the upstroke of the action potential is well aligned with the sock electrograms downslope.

For all experiments, the transformation and alignment of the 3D sock onto the 2D optical mapping window was good as presented in **Figure 4**, with an average correlation of 0.87 ± 0.10 and RMSE of 7.7 ± 3.1 ms across all activation sequences. There was no significant difference between pacing and sinus rhythm signals for correlation or RMSE ($p > 0.99$).

Repolarization Maps

Sock and optical derived repolarization maps were then compared. In **Figure 3** (right), the sock and optical repolarization maps are shown for the same sinus rhythm sequence as the activation map (left) described previously. Like activation, the repolarization pattern derived by each technique was the same with late repolarization seen in the LAD perfusion bed. However, the difference in individual RT marker placement were substantially more diverse than with ATs, with differences up to 20 ms. This is seen in the three example electrogram and action potentials presented in **Figure 3**. The first demonstrates that the negative dF/dT peak in the optical action potentials corresponds very well with the *T*-wave upstrokes in the equivalent electrogram. In second two electrodes, though the *T*-wave upstroke and action potential repolarization curves align temporally, external factors such as poor contact/fluorescence, noise or movement may have substantially shifted marker placement in either or both electrograms and action potentials.

Qualitative comparison of RTs across all sequences demonstrated that sock and optical repolarization patterns were similar, as quantified by high correlation values (0.83 ± 0.13), not significantly different than for ATs ($p = 0.27$). However, the alignment of markers was significantly less accurate than for ATs ($p < 0.05$), with RMSE of 17.4 ± 3.7 (**Figure 4**). There was no significant difference between experiments ($p > 0.05$), nor between pacing and sinus rhythm signals for correlation or RMSE ($p > 0.99$).

Optical Mapping for ECGI Validation

Activation Times and Conduction Block

ECGI-derived AT were compared to those derived from the optical action potentials. **Figure 5** presents two cases during RV pacing with (1) normal perfusion and (2) cold perfusion through the LAD marked in black. In both cases, ECGI captured the general pattern of activation. However, the timing of the earliest activated region was approximately 15–20 ms after the true onset of activation in both cases as measured with optical mapping. This resulted in a large region of tissue with nearly the same activation time, making it less clear how to define the earliest activation site from ECGI reconstructions.

The advantage of the high-resolution optical mapping is demonstrated by looking at the gradient across the border of the LAD perfusion bed (black box). In the plots on the right we present the ECGI (red) and optical (black) AT within this box against their distance from the black star. In case 2, the cold perfusion creates a line of conduction block across the border of the LAD perfusion bed. ECGI accurately reconstructed the AT on either side of this border, but the conduction block is now seen as a smooth activation wavefront.

Quantitative comparison of optical and ECGI activation maps were performed across the entire data set. Using correlation and RMSE, as presented in **Figure 6**. The majority of cases produced very high correlation (median = 0.83) and low RMSE (1median = 9.6 ms). Qualitative analysis of the three cases with a correlation near 0.5 demonstrated similar activation patterns but shifted slightly in space.

Repolarization Times and Gradients

Overall, ECGI did not reconstruct repolarization maps as accurately as ATs, with significantly lower correlation and higher RMSE values (**Figure 6**). Qualitative comparison of repolarization maps showed that despite this, ECGI accurately identifies regions of late and/or early repolarization during

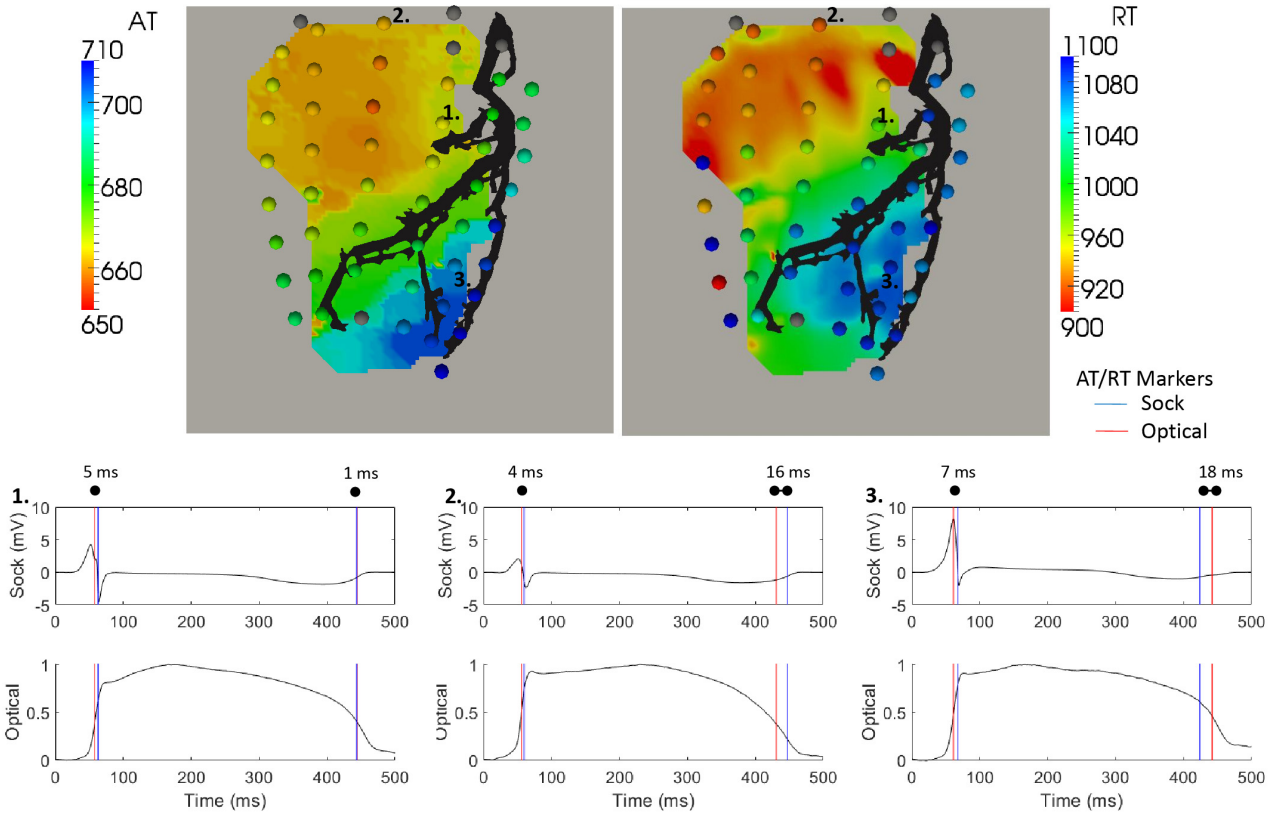

FIGURE 3 | Optical activation (left) and repolarization (right) map with equivalent sock (spheres) timings overlaid during a sinus rhythm sequence with cold perfusion through the LAD (black). Sock electrograms and optical action potentials (normalized) are shown at three electrode locations demonstrating the range in differences between AT and RT markers.

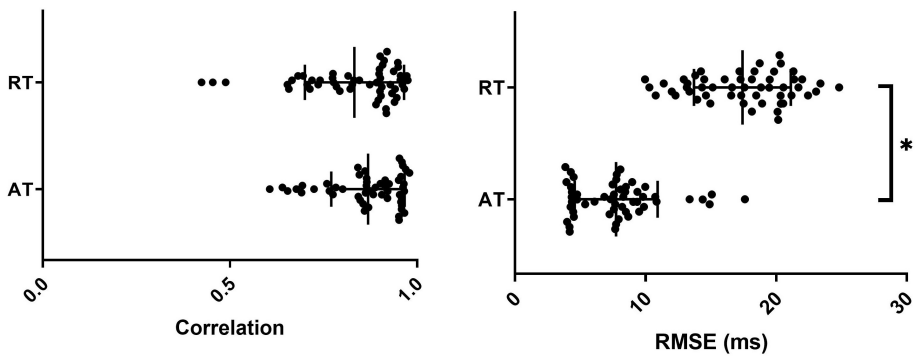

FIGURE 4 | Correlation and RMSE between optical and sock derived activation (AT) and repolarization (RT) times for all sequences with mean and SD overlain. *represents a significant difference between AT and RT results ($p < 0.05$).

perfusion of hot and cold solution and Sotalol into the LAD. **Figure 7** presents three representative examples of optical (left) and ECGI (right) repolarization maps during (1) sinus rhythm, (2) in sinus rhythm with cold perfusion through the LAD (black) to create a gradient in repolarization, and (3) during LV pacing with cold Tyrode's with Sotalol perfusion through the LAD to augment the gradient. In each example, ECGI clearly distinguishes the regions of early and late repolarization, although the timings are smoothed compared to the optical maps.

The reconstruction of the repolarization gradient across the LAD perfusion bed was assessed by plotting the RTs within the black box against distance from the yellow star (right). In the first case, ECGI accurately shows there is no repolarization gradient. In the second and third cases ECGI captures the existing repolarization gradients though in both cases the gradient is

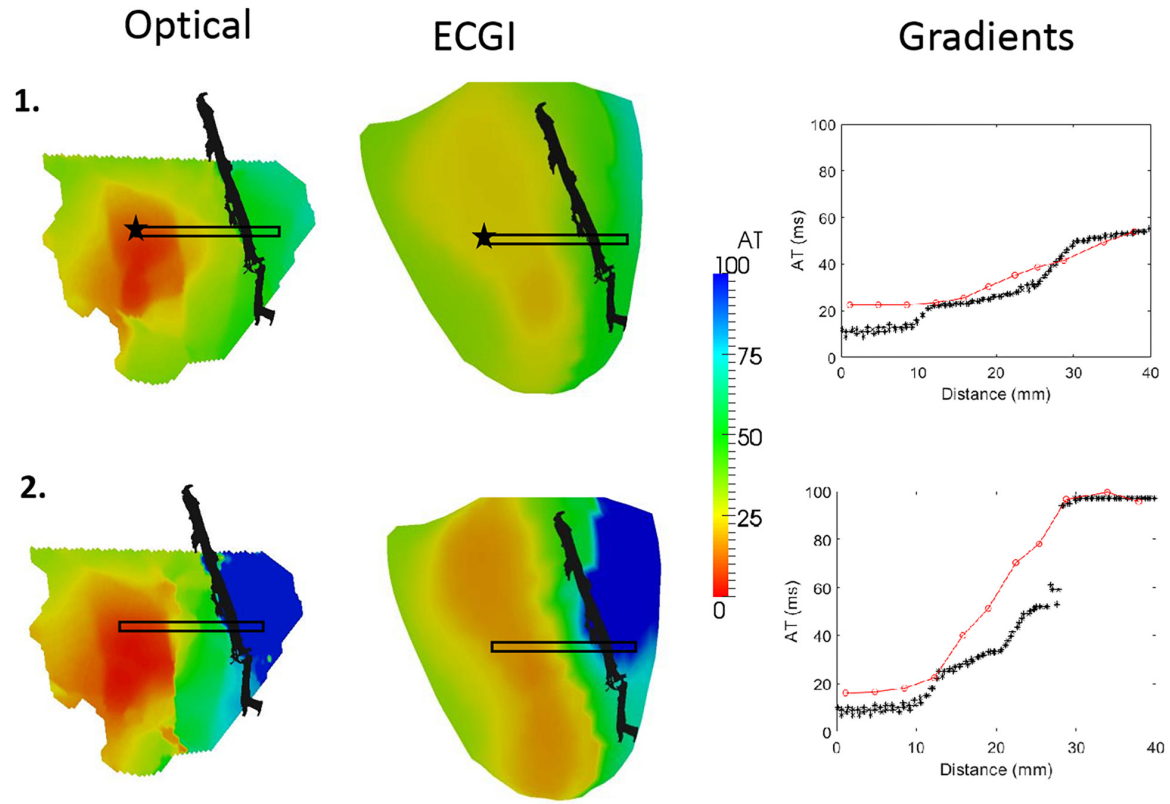

FIGURE 5 | Optical (left) and ECGI (middle) derived activation maps during RV pacing with (1) normal and (2) cold perfusion through the LAD (black). Plots of ATs inside the black box against distance from the star are presented (right) for each sequence derived from optical (black; *) and ECGI (red; o) signals.

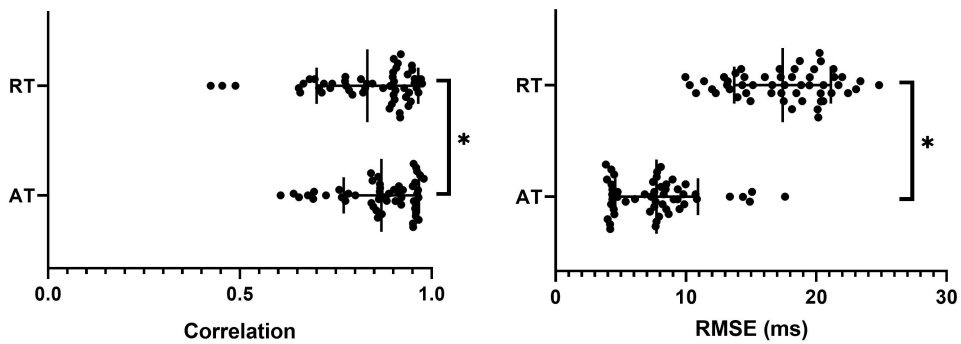

FIGURE 6 | Correlation and RMSE between optical and ECGI derived activation (AT) and repolarization (RT) times with mean and SD overlain. *Represents a significant difference between AT and RT results ($p < 0.05$).

shifted by approximately 10 mm toward the base and is steeper than the ground truth.

DISCUSSION

This study presents a novel experimental setup combining body surface mapping from a human shaped torso tank with optical mapping of large animal hearts suspended inside. The results of this study have validated the methods for accurately transforming and aligning the 3D epicardial surface onto the 2D optical mapping window. Furthermore, we have demonstrated the setup can be used effectively in the validation of ECGI reconstructed activation and repolarization patterns and gradients.

Accuracy of Optical Alignment

In order to use the developed experimental setup for ECGI validation, alignment of the 2D optical mapping window

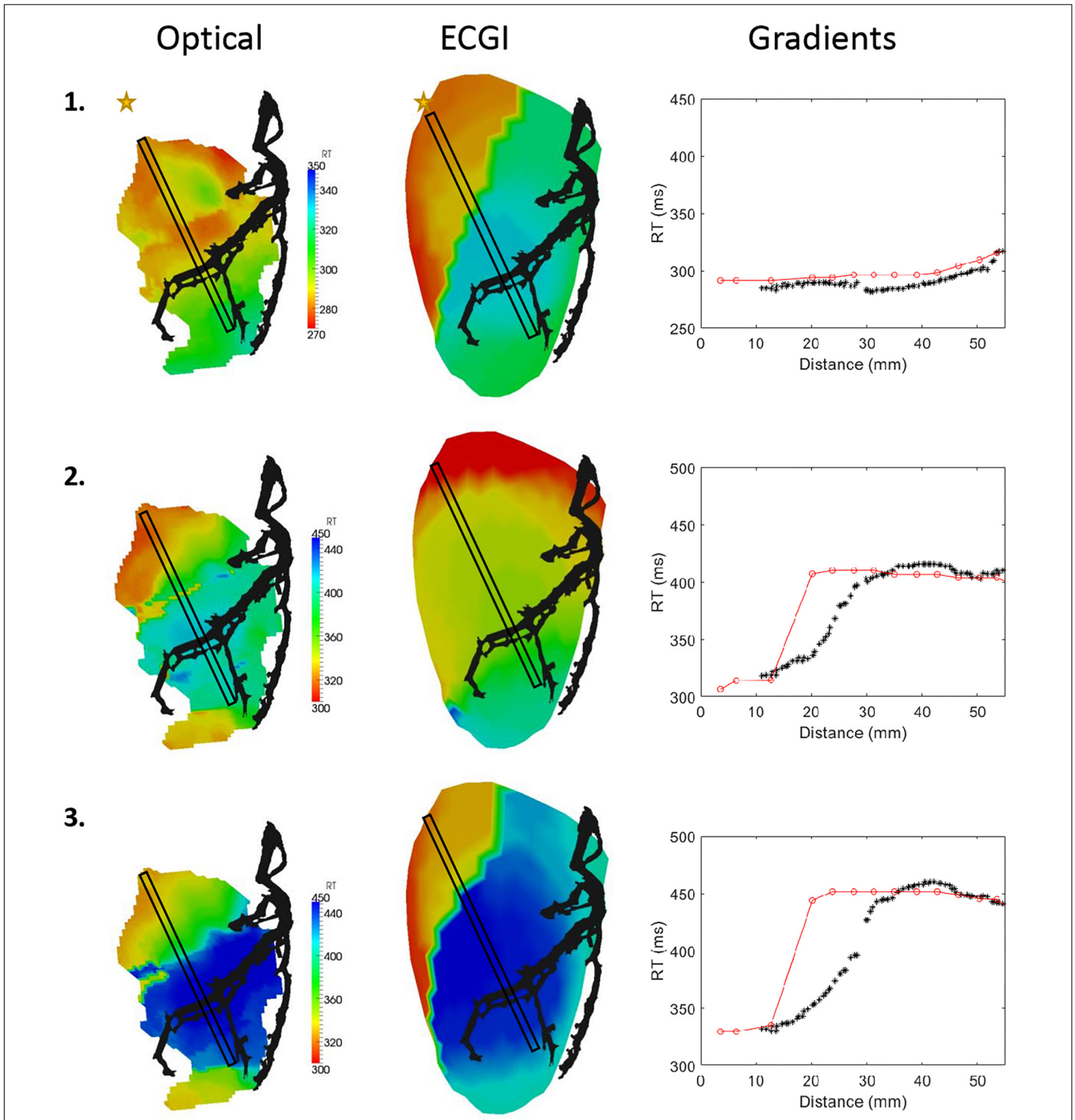

FIGURE 7 | Optical (left) and ECGI (middle) derived repolarizations maps derived from (1) sinus rhythm with normal and (2) cold perfusion through the LAD (black) and (3) LV pacing with cold Tyrode's and Sotalol perfusion through the LAD. Plots of RTs inside the black box against distance from the star are presented (right) for each sequence derived from optical (black; *) and ECGI (red; o) signals.

with the 3D epicardial mesh derived from fluoroscopy is critical. Many metrics used for ECGI validation are distance-based measurements, where error in the alignment of the "ground truth" would impact the result e.g., localization error of VT exit sites (Wang et al., 2016), premature ventricular contractions (Van Dam et al., 2009), focal discharges and rotor cores (Figuera et al., 2016). In addition, quantitative comparisons of action potentials or activation maps using correlation and RMSE could be dramatically affected by spatial inaccuracies.

In this study, we have developed and validated an optimization method to define the transformation and alignment of the 3D epicardial mesh into the 2D optical window based on markers visible in the both dimensions and one activation pattern derived from recorded sock electrograms and optical mapping (**Figure 2**).

Comparison of all optical and sock activation maps for each experiment demonstrated that this provides a reliable and robust transformation (**Figure 3**). On the other hand, repolarization maps showed a larger discrepancy in marker placement between optical and sock signals. As with activation markers, a relationship exists between RT derived from unipolar electrograms and action potentials. However, unlike with ATs this relationship is very sensitive to conditions (Steinhaus, 1989) and has experimentally shown differences in RTs with a standard error from 11 to 26 ms (Wyatt et al., 1981). One explanation for the difference seen here is the fact that the optical signals at the wavelengths used in this study represents an average over a significant depth (up to 4 mm) and lateral distance. Likewise, unipolar electrograms represent the integration of activity through the heart, and particularly the myocardial wall. Although the dF/dt max gives the "true" epicardial activation time [ADD REF to Walton et al. Biophys J 2012], there will still be some blurring, which could play a role in RT marker placement. It is unknown what effects transmural gradients in repolarization play on marker placement for these signals. The large differences seen might also simply be due to the increased inaccuracy in computation of repolarization compared to activation where small movement, ischemia, and signal noise affects the smoothness/duration of the *T*-wave resulting in larger errors in marker placement using automated algorithms. Futhermore, there exists several methods to compute RT from both optical action potentials and unipolar electrograms. While we have chosen indices that have been shown to correlate well from simulation studies (Potse et al., 2009) alternative indices, such as the max d^2V/dT^2 typically used for optical mapping signals (Laughner et al., 2012), may result in a closer match.

Optical Mapping for ECGI Validation

Once the transformation and alignment were defined, ECGI reconstructed activation and repolarization patterns were validated using the optical maps. This is the first study to use optical mapping for the validation of ECGI reconstructions. Several previous studies have evaluated similar ECGI methods using epicardial sock recordings of various resolution to define the ground truth (Bear et al., 2018a,b). In a recent study using the same torso tank model presented here, ECGI was shown to reconstruct activation maps with a correlation of 0.68 ± 0.25 and RMSE = 13.4 ± 5.3 ms in LBBB (Bear et al., 2018a), comparable to the results seen using optical mapping as the reference. The only other studies to report quantitative accuracy of activation maps derived using potential-based ECGI methods have used *in vivo* experimental models. The first in dogs using a 103 non-uniformly spaced electrodes reported a mean correlation values of 0.82 (Cluitmans et al., 2017). The second in pigs using a 239-electrode sock array a mean correlation of 0.78 (Bear et al., 2018b). Despite the differences between these studies in spatial resolution for the ground truth recordings, the results are remarkably similar. This corroboration with previous ECGI validation studies provides further validation of the accurate alignment of the 2D and 3D mapping domains.

Very few studies have evaluated the reconstruction of RT using ECGI, and the only previous experimental study directly comparable to ours in terms of methodology was the study recently performed by Cluitmans et al. (2017) using the *in vivo* dog model. Like activation, despite validation being based on lower resolution ground truth data, the correlation values reported between measured and reconstructed repolarization maps match almost exactly to those seen in this study.

Rather than in the simple comparison of activation and recovery maps, the real benefit of high-resolution optical mapping for ECGI validation is seen in the ability to compare high-resolutions features. Here we have demonstrated one such application in the comparison of activation and repolarization gradients, which has never been previously attempted. It was demonstrated that ECGI reveals the gradients present in both activation and repolarization, although these could be under- and over-estimated, and in some cases shifted slightly in space. For activation maps, underestimation of the gradient may be a reflection of the algorithm used on ECGI signals for marker placement which spatially smooths the activation map. While this typically improves ECGI activation map reconstruction in normal hearts (Duchateau et al., 2016; Bear et al., 2018b), it may also smooth a line of conduction block into a region of slow conduction as seen in **Figure 5**. In contrast, the over-estimation of recovery gradients seen in **Figure 7** is likely due to that same problem that produces artefactual jumps in AT that has previously been noted in ECGI validation studies (Duchateau et al., 2016, 2018). This data and experimental setup will help us to further develop new algorithms to improve activation and repolarization marker detection in the presence of heterogeneities.

In addition to repolarization gradients, this set up will be useful in the validation of ECGI for fibrillation, where an adequate spatial resolution is paramount to the accurate detection of focal sources and rotor cores (Roney et al., 2017); the optimization of parameter selection for ECGI algorithms, such as the choice of regularization parameter; and to evaluate ECGI formulations using transmembrane potentials as the cardiac source, which previously could not be achieved with post-processing of the signals.

Limitations

The results presented should be considered in light of limitations inherent in the study. First, the field of view of the optical mapping window was limited to approximately 10 cm × 10 cm, only capturing the anterior surface of the heart. While validation of any ECGI algorithm would ideally compare the reconstructions for the entire cardiac surface used, typically the region of interest for high resolution would fit inside this window (e.g., regions of myocardial infarction), and lower resolution mapping of the rest of the heart can be achieved using a traditional electrode sock as has been used in this study.

Another limitation of optical mapping is the necessity of electro-mechanical uncoupling. This removes a condition that

is present in clinical applications, and that might impact ECGI reconstruction accuracy particularly during repolarization. However, removing contraction is also an advantage as it enables one to assess the efficacy of ECGI reconstructions without motion artefact. Furthermore, methods are currently being developed to enable optical mapping to counteract motion artefacts, and these methods could be integrated into the system in the future. The use of optical mapping for ECGI validation is limited to using an *ex vivo* model and thus a torso tank with uniform isotropic electrical properties. This is not the case *in vivo* and can result in validation studies reporting better results than are seen using an *in vivo* model. However, like with removing contraction from the heart, torso tank models also allow us to assess the efficacy of a different ECGI formulation when the forward problem is accurately formulated.

Finally, the n number for this study is low, and does not allow insight into inter-heart variability.

CONCLUSION

We have demonstrated a novel experimental setup combining BSPM from a human shaped torso tank with optical mapping of large animal hearts suspended inside that can be used in the validation of ECGI reconstructed activation and repolarization patterns and gradients.

AUTHOR CONTRIBUTIONS

All the authors contributed to the conception and design of the study, contributed to manuscript revision, read, and approved the submitted version. LB, RW, and EA performed the experimental studies. LB organized the database, performed the statistical analysis, and wrote the first draft of the manuscript.

FUNDING

This work was supported by the French National Research Agency (ANR-10-IAHU04-LIRYC), La Fondation Coeur et Artères (FCA14T2), the European Research Council under the European Union's Seventh Framework Programme (FP/2007-2013), and the Leducq Foundation transatlantic network of excellence RHYTHM transatlantic network (16CVD02).

REFERENCES

Aström, M., Santos, E. C., Sörnmo, L. Laguna, P., and Wohlfart, B. (2000). Vectorcardiographic loop alignment and the measurement of morphologic beat-to-beat variability in noisy signals. *IEEE Trans. Biomed. Eng.* 47, 497–506. doi: 10.1109/10.828149

Bear, L. R., Huntjens, P. R., Walton, R., Bernus, O., Coronel, R., and Dubois, R. (2018a). Cardiac electrical dyssynchrony is accurately detected by noninvasive electrocardiographic imaging. *Heart Rhythm* 15, 1058–1069. doi: 10.1016/j.hrthm.2018.02.024

Bear, L. R., Legrice, I. J., Sands, G. B., Lever, N. A., Loiselle, D., Paterson, D. J., et al. (2018b). How accurate is inverse electrocardiographic mapping?: A systematic in vivo evaluation. *Circ. Arrhythm. Electrophysiol.* 11:e006108. doi: 10.1161/CIRCEP.117.006108

Cluitmans, M., Brooks, D. H., MacLeod, R., Dössel, O., Guillem, M. S., van Dam, P. M., et al. (2018). Validation and opportunities of electrocardiographic imaging: from technical achievements to clinical applications. *Front. Physiol.* 9:1035. doi: 10.3389/fphys.2018.01305

Cluitmans, M. J. M., Bonizzi, P., Karel, J. M. H., Das, M., Kietselaer, B. L. J. H., de Jong, M., et al. (2017). in vivo validation of electrocardiographic imaging. *JACC Clin. Electrophysiol.* 3, 1–11. doi: 10.1016/j.jacep.2016.11.012

Colli-Franzone, P. C., Guerri, L., Taccardi, B., and Viganotti, C. (1985a). Finite element approximation of regularized solutions of the inverse potential problem of electrocardiography and applications to experimental data. *Calcolo* 22, 91–186. doi: 10.1007/BF02576202

Colli-Franzone, P. C., Guerri, L., Tentoni, S., Viganotti, C., Baruffi, S., Spaggiari, S., et al. (1985b). A mathematical procedure for solving the inverse potential problem of electrocardiography. analysis of the time-space accuracy from in vitro experimental data? *Mathemat. Biosci.* 77, 353–396. doi: 10.1016/0025-5564(85)90106-3

Coronel, R., Wilms-Schopman, F. J. Opthof, T., and Janse, M. J. (2009). Dispersion of repolarization and arrhythmogenesis. *Heart Rhythm* 6, 537–543. doi: 10.1016/j.hrthm.2009.01.013

Duchateau, J., Potse, M., and Dubois, R. (2016). Spatially coherent activation maps for electrocardiographic imaging. *IEEE Trans. Biomed. Eng.* 64, 1–8.

Duchateau, J., Sacher, F., Pambrun, T., Derval, N., Chamorro-Servent, J. Denis, A., Ploux, S., et al. (2018). Performance and limitations of noninvasive cardiac activation mapping. *Heart Rhythm* [Epub ahead of print]. doi: 10.1016/j.hrthm.2018.10.010

Efimov, I. R., Nikolski, V. P., and Salama, G. (2004). Optical imaging of the heart. *Circ. Res.* 95, 21–33. doi: 10.1161/01.RES.0000130529.18016.35

Figuera, C., Suárez-Gutiérrez, V., Hern.ández-Romero, I., Rodrigo, M., Liberos, A., Atienza, F., et al. (2016). Regularization techniques for ECG imaging during atrial fibrillation: a computational study. *Front. Physiol.* 7:556. doi: 10.3389/fphys.2016.00556

Ghanem, R. N., Jia, P., Ramanathan, C., Ryu, K., Markowitz, A., and Rudy, Y. (2005). Noninvasive electrocardiographic imaging (ECGI): comparison to intraoperative mapping in patients. *Heart Rhythm* 2, 339–354. doi: 10.1016/j.hrthm.2004.12.022

Haws, C., and Lux, R. (1990). Correlation between in vivo transmembrane action potential durations and activation-recovery intervals from electrograms. Effects of interventions that alter repolarization time. *Circulation* 81, 281–288. doi: 10.1161/01.CIR.81.1.281

Laughner, J. I., Ng, F. S., Sulkin, M. S., Arthur, R. M., and Efimov, I. R. (2012). Processing and analysis of cardiac optical mapping data obtained with potentiometric dyes. *Am. J. Physiol. Heart Circ. Physiol.* 303, H753–H765. doi: 10.1152/ajpheart.00404.2012

Lux, R., and Gettes, L. (2011). Repolarization heterogeneity and rate dependency in a canine rapid pacing model of heart failure. *J. Electrocardiol.* 44, 730–735. doi: 10.1016/j.jelectrocard.2011.08.001

Macleod, R., and Brooks, D. H. (2000). "Validation approaches for electrocardiographic inverse problems," in *Advances in Computational Biomedicine 3*, 3rd Edn, Vol. 3, ed. P. Johnston (Billerica, MA: WIT Press), 229–268.

Millar, C., Kralios, F., and Lux, R. (1985). Correlation between refractory periods and ARIs from electrograms: effects of rate and adrenergic interventions. *Circulation* 72:1372. doi: 10.1161/01.CIR.72.6.1372

Oosterhoff, P., Meijborg, V. M. F., Van Dam, P. M., Van Dessel, P. F. H. M., Belterman, C. N. W., et al. (2016). Experimental validation of noninvasive epicardial and endocardial activation imaging. *Circ. Arrhythmia Electrophysiol.* 9, 1–11. doi: 10.1161/CIRCEP.116.004104

Oster, H. S., Taccardi, B., Lux, R. L., Ershler, P. R., and Rudy, Y. (1998). Electrocardiographic imaging: noninvasive characterization of intramural myocardial activation from inverse-reconstructed epicardial potentials and electrograms. *Circulation* 97, 1496–1507. doi: 10.1161/01.CIR.97.15.1496

Potse, M., Vinet, A., Opthof, T., and Coronel, R. (2009). Validation of a simple model for the morphology of the T wave in unipolar electrograms. *Am. J. Physiol. Heart Circ. Physiol.* 297, H792–H801. doi: 10.1152/ajpheart.00064.2009

Roney, C. H., Cantwell, C. D., Bayer, J. D., Qureshi, N. A., Lim, P. B., Tweedy, J. H., et al. (2017). Spatial resolution requirements for accurate identification of drivers of atrial fibrillation. *Circ. Arrhythmia Electrophysiol.* 10:e004899. doi: 10.1161/CIRCEP.116.004899

Rudy, Y. (2013). Noninvasive electrocardiographic imaging of arrhythmogenic substrates in humans. *Circ. Res.* 112, 863–874. doi: 10.1161/CIRCRESAHA.112.279315

Sapp, J. L., Dawoud, F., Clements, J. C., and Horácek, B. M. (2012). Inverse solution mapping of epicardial potentials: quantitative comparison with epicardial contact mapping. *Circ. Arrhythm Electrophysiol.* 5, 1001–1009. doi: 10.1161/CIRCEP.111.970160

Steinhaus, B. M. (1989). Estimating cardiac transmembrane activation and recovery times from unipolar and bipolar extracellular electrograms: a simulation study. *Circ. Res.* 64, 449–462. doi: 10.1161/01.RES.64.3.449

Tikhonov, A., and Arsenin, V. (1977). *Solution of Ill-Posed Problems*. Washington, D.C: John Wiley & Sons.

Van Dam, P. M., Oostendorp, T. F., Linnenbank, A. C., and Van Oosterom, A. (2009). Non-invasive imaging of cardiac activation and recovery. *Ann. Biomed. Eng.* 37, 1739–1756. doi: 10.1007/s10439-009-9747-5

Vijayakumar, R., Silva, J. N. A., Desouza, K. A., Abraham, R. L., Strom, M., Sacher, F., et al. (2014). Electrophysiologic substrate in congenital Long QT syndrome: noninvasive mapping with electrocardiographic imaging (ECGI). *Circulation* 130, 1936–1943. doi: 10.1161/CIRCULATIONAHA.114.011359

Wang, L., Gharbia, O. A., Horáček, M. B., and Sapp, J. L. (2016). Noninvasive epicardial and endocardial electrocardiographic imaging of scar-related ventricular tachycardia. *J. Electrocardiol.* 49, 887–893. doi: 10.1016/j.jelectrocard.2016.07.026

Wang, Y., and Rudy, Y. (2006). Application of the method of fundamental solutions to potential-based inverse electrocardiography. *Ann. Biomed. Eng.* 34, 1272–1288. doi: 10.1007/s10439-006-9131-7

Wyatt, R., Burgess, M., Evans, A., Lux, R., Abildskov, J., and Tsutsumi, T. (1981). Estimation of ventricular transmembrane action potential durations and repolarization times from unipolar electrograms. *Am. J. Cardiol.* 47:488. doi: 10.1016/0002-9149(81)91028-6

Conflict of Interest Statement: The authors declare that the research was conducted in the absence of any commercial or financial relationships that could be construed as a potential conflict of interest.

frontiers in Physiology

ORIGINAL RESEARCH
published: 11 March 2019
doi: 10.3389/fphys.2019.00183

ECG Adapted Fastest Route Algorithm to Localize the Ectopic Excitation Origin in CRT Patients

Danila Potyagaylo[1†], Mikhail Chmelevsky[1,2†], Peter van Dam[3], Margarita Budanova[2], Stepan Zubarev[2], Tatjana Treshkur[2] and Dmitry Lebedev[2]*

[1] EP Solutions SA, Yverdon-les-Bains, Switzerland, [2] Almazov National Medical Research Center, Saint Petersburg, Russia, [3] Cardiology Department, University Medical Center Utrecht, Utrecht, Netherlands

OPEN ACCESS

Edited by:
Linwei Wang, Rochester Institute of Technology, United States

Reviewed by:
Andreu Climent, Fundación Hospital Gregorio Marañon, Spain
Shijie Zhou, Johns Hopkins University, United States

***Correspondence:**
Danila Potyagaylo
danila.potyagaylo@ep-solutions.ch

[†] *These authors have contributed equally to this work*

Specialty section:
This article was submitted to Cardiac Electrophysiology, a section of the journal Frontiers in Physiology

Received: *08 October 2018*
Accepted: *14 February 2019*
Published: *11 March 2019*

Citation:
Potyagaylo D, Chmelevsky M, van Dam P, Budanova M, Zubarev S, Treshkur T and Lebedev D (2019) ECG Adapted Fastest Route Algorithm to Localize the Ectopic Excitation Origin in CRT Patients. Front. Physiol. 10:183. doi: 10.3389/fphys.2019.00183

Although model-based solution strategies for the ECGI were reported to deliver promising clinical results, they strongly rely on some a priori assumptions, which do not hold true for many pathological cases. The fastest route algorithm (FRA) is a well-established method for noninvasive imaging of ectopic activities. It generates test activation sequences on the heart and compares the corresponding test body surface potential maps (BSPMs) to the measured ones. The test excitation propagation patterns are constructed under the assumption of a global conduction velocity in the heart, which is violated in the cardiac resynchronization (CRT) patients suffering from conduction disturbances. In the present work, we propose to apply dynamic time warping (DTW) to the test and measured ECGs before measuring their similarity. The warping step is a non-linear pattern matching that compensates for local delays in the temporal sequences, thus accounting for the inhomogeneous excitation propagation, while aligning them in an optimal way with respect to a distance function. To evaluate benefits of the temporal warping for FRA-based BSPMs, we considered three scenarios. In the first setting, a simplified simulation example was constructed to illustrate the temporal warping and display the resulting distance map. Then, we applied the proposed method to eight BSPMs produced by realistic ectopic activation sequences and compared its performance to FRA. Finally, we assessed localization accuracy of both techniques in ten CRT patients. For each patient, we noninvasively imaged two paced ECGs: from left and right ventricular implanted leads. In all scenarios, FRA-DTW outperformed FRA in terms of LEs. For the clinical cases, the median (25–75% range) distance errors were reduced from 16 (8–23)mm to 5 (2–10)mm for all pacings, from 15 (11–25)mm to 8 (3–13)mm in the left, and from 19 (6–23)mm to 4 (2–8)mm in the right ventricle, respectively. The obtained results suggest the ability of temporal ECG warping to compensate for an inhomogeneous conduction profile, while retaining computational efficiency intrinsic to FRA.

Keywords: ECG imaging, fastest route algorithm, FRA, dynamic time warping, inverse problem of ECG, CRT, inhomogeneous excitation propagation

1. INTRODUCTION

Due to the aging population, increase in unhealthy lifestyle and advances in acute management of myocardial infarction, heart failure is becoming the world leading cause of death. Thereby congenital and acquired ventricular dysfunction result in poor short- and mid-term prognosis, making cardiac resynchronization therapy (CRT) the first choice of care to decrease hospitalization and improve the quality of life for heart failure patients. However, around 30% of CRT candidates fail to respond to this treatment, which leads to increasing morbidity and involved medical insurance costs (Daubert et al., 2016). In general, patient-specific optimization of CRT treatment and selection, being essential for improved success rates, can be accomplished only upon knowledge of underlying cardiac substrate and electrophysiological properties.

Invasive acquisition of individual heart model parameters is laborious, associated with risks and, therefore, prohibitive for many CRT candidates. For these candidates, the ECG imaging (ECGI) technique represents a noninvasive alternative (Gulrajani, 1998; Pullan et al., 2001). Based on a patient-specific geometry, ECGI maps measured body surface potentials to activation times on the cardiac anatomy. Although there has recently been a distinct interest raise from both engineering and clinical communities, this technology has not yet found its niche in the clinical work-flow (Cluitmans et al., 2018). For this, known technical issues have to be solved and clear clinical benefits have to be defined in cooperation with physicians. Furthermore, the validation of ECGI is extremely challenging, which is mostly due to the lack of invasively obtained high quality data.

In a nutshell, ECG imaging consists in solving an ill-posed problem of finding cardiac sources configurations causing the observed body surface potential maps (BSPMs) (Cluitmans et al., 2018). Different approaches to ECGI, or inverse problem of ECG, could deliver information on the earliest activation site (Erem et al., 2014a; van Dam et al., 2016; Giffard-Roisin et al., 2017; Yu et al., 2018), isochronal, isopotential, or phase maps (van Dam et al., 2009a; Revishvili et al., 2015; Wang et al., 2016; Rodrigo et al., 2017), and substrate characterization (Rudy, 2013; Sohns et al., 2018). One way to tackle the inverse problem is the classical regularization by imposing appropriate regularization constraints (Brooks et al., 1999). Another, model-based, approach consists in employing a realistic excitation propagation model and fitting the model parameters to match the measured BSPMs. In van Dam et al. (2009a) the nonlinear inverse problem was solved based on the action potential wave forms specified by two parameters at each cardiac node, activation and recovery times. The initial estimation for this task was provided by a physiologically inspired fastest route algorithm. Wang et al. developed a Bayesian framework for coupling personal data with the prior model based on the unscented Kalman filter for integration of the nonlinear action potential's dynamics (Wang et al., 2011). Performance of an artificial network optimizing cellular-automaton excitation parameters in a 3-D heart was presented in Li and He (2001) and Liu et al. (2008). Parameter tuning in a more complex bidomain model was evaluated in terms of simulated ECG similarities with the measured 12-lead signals in heart-failure patients (Potse et al., 2014). Dhamala et al. (2017) introduced a computational framework featuring spatially adaptive coarse-to-fine optimization of cardiac excitation properties to match the measured ECGs. The work by Giffard-Roisin et al. (2017) aimed at noninvasive estimation of the global conduction velocity and activation onset by regressing the measured BSPMs from a simulated database.

Despite being one of the most straightforward among the existing model-based inverse strategies, the fastest route algorithm (FRA) has demonstrated a number of encouraging simulation as well as clinical results in imaging of ectopic and normal activation sequences (van Dam et al., 2009a; van Dam et al., 2016; Oosterhoff et al., 2016; Janssen et al., 2018). For a patient-specific cardiac geometry, FRA simulates excitation patterns starting from every node of the discretized heart mesh. The obtained activation sequences are converted to the BSPMs by solving a linear forward problem of ECG for the corresponding volume conductor model. This is followed by a full-search step resulting in the activation sequence associated to the BSPMs with the highest correlation compared to the measured electrocardiograms. Depending on the clinical application, the best sequence can be either used independently, e.g., for estimation of the excitation origin (Potyagaylo, 2016; Potyagaylo et al., 2016a,b), or followed by an iterative nonlinear least-squares (NLLS) procedure (van Dam et al., 2009a; Erem et al., 2014b). The NLLS itself is a severely ill-posed optimization problem with multiple local minima, which makes it extremely sensitive to the initial estimate (Modre et al., 2002; Janssen et al., 2018).

For a global conduction velocity (CV), an initialization provided by FRA was shown to be robust with respect to the forward modeling errors in an *in silico* study in Potyagaylo et al. (2016a). For the calculation of the FRA activation sequences, transmural cardiac connections are assigned with half the value for propagation speed in the direction tangential to the heart surface (van Dam et al., 2009a). While this model aims at taking into account a slower transmural wave propagation, it can neither fully compensate for anisotropic excitation nor tackle differences in the local CVs due, for instance, to scar. Furthermore, the NLLS optimization step was demonstrated to be highly sensitive with respect to the assumed propagation velocity used within FRA (Erem et al., 2014b).

To overcome the above-mentioned limitations of the standard FRA approach, we propose to apply dynamic time warping (DTW) to the BSPMs. The simulated BSPMs are adjusted and aligned with the measured signals. After the alignment, euclidean "distances" between warped simulated test potentials and recorded BSPMs are calculated. The cardiac mesh node associated with the excitation pattern corresponding to the smallest error is considered the sought-after activation origin. In the sequel, we denote this method as FRA-DTW.

2. MATERIALS AND METHODS

To demonstrate superior performance of the proposed strategy, we first consider a simplified focal excitation scenario with an artificially introduced region of slow CV and provide an ECG

signal warping example. Then, we compare performance of FRA-DTW against the standard correlation-based FRA for eight realistic simulation cases of ectopic excitation used in Janssen et al. (2018). We analyze localization errors (LEs) and visualize both correlation and DTW-based distance maps for studying possible reconstruction ambiguities.

Finally, we performed clinical evaluation and comparison of both techniques using isolated univentricular left and right ventricular (RV and LV, respectively) pacing in 10 patients (n = 10) with previously implanted CRT devices. For the first time, we quantitatively estimate performance of FRA and time warping applied to FRA-generated BSPMs on the CRT patients.

2.1. Source Model and Fastest Route Algorithm (FRA)

In this study equivalent dipole layer (EDL) is used. For equal anisotropy ratios in intra- and extracellular electrical conductivity tensors the cardiac current sources were shown to behave like an EDL (Geselowitz and Miller, 1983; Yamashita and Geselowitz, 1985; Geselowitz, 1989). The EDL has an orientation normal to the heart surface, encompassing both endo- and epicardium, and is proportional to the surface transmembrane potentials (TMP) (van Oosterom and Jacquemet, 2005; van Dam et al., 2009a,b).

Furthermore, this source model allows a linear relationship between the TMP and BSPMs given by a transfer (also known as forward, or lead-field) matrix A, which depends solely on the volume conductor model. For the depolarization phase, when the cardiac cells can be assumed to be either at rest or activated, electrical activity of the heart is fully described by the activation times $\tau(\vec{x})$. Then, the expression for body surface potentials at time t reads as follows (Huiskamp and Van Oosterom, 1988; Janssen et al., 2018):

$$y(t) = \int_{S_h} H(t - \tau(\vec{x}))A(\vec{x})\, d\vec{x} \tag{1}$$

where $A(\vec{x})$ is the lead-field for $\vec{x}$, i.e., the potentials generated by an infinitesimal source at location $\vec{x}$ on the heart surface dS_h, and $H(t)$ is the Heaviside step function characterizing "on" and "off" states of the cellular activity. For the present work, the transfer matrix A was calculated by means of the boundary element method (BEM).

The inverse problem of ECG associated with (1) consists in finding the depolarization (activation) times $\tau(\vec{x})$ on the heart surface. Due to its intrinsic ill-posedness, this nonlinear optimization problem has multiple local minima and is, therefore, highly sensitive to the initial estimate (Modre et al., 2002; Erem et al., 2014b). With this respect, the fastest route algorithm (FRA) was reported to provide a physiologically meaningful initialization for (1) (van Dam et al., 2009a). In essence, FRA is a, possibly multi-foci, search, where each cardiac node is considered as an initial focus. For computation of the corresponding test activation sequences, a times matrix T based on the adjacency graph of the triangulated heart mesh is used. Although a global conduction velocity is assumed for calculation of T, the transmural wavefront speed is set to be twice less than those along the heart surface, which mimics cardiac transmural anisotropy. For each cardiac node, the respective BSPMs are compared to the measured signals on the basis of correlation coefficient (CC), providing a correlation map on the heart surface. The sequence resulting in the highest correlation is taken as the initialization for (1). However, the best activation pattern can be effectively used together with the accompanying correlation map in order to estimate the solution uncertainty and illustrate reconstruction ambiguities (Potyagaylo et al., 2016a; Janssen et al., 2018).

Despite its simplicity, FRA has proven to be a robust method delivering a physiologically meaningful solution approximation for (multi-foci) excitation patterns (Oosterhoff et al., 2016; Potyagaylo et al., 2016a; van Dam et al., 2016). Nonetheless, FRA gets computational very expensive when it accounts for regions with a local different CV. Consequently information on their anatomical location needs to be incorporated explicitly into the activation model given by the matrix T. In these cases, FRA scales the global CV (0.8 m/s for this work) in order to match the QRS complex duration, which can apparently result in a distorted CC distribution and a misleading solution. To alleviate this FRA drawback, we propose to apply temporal warping to the test and measured BSPMs before calculating their mismatch.

2.2. Dynamic Time Warping (DTW)

Dynamic time warping (DTW) is an algorithm for measuring similarity between time series that may vary in velocity, even if there were acceleration or deceleration phases in one of the signals. We hypothesized that local CV differences reduces the accuracy of FRA performance, which can at least be partially compensated by the nonlinear time warping of the simulated BSPMs in the FRA-DTW method.

Within the FRA formulation all test activation sequences are linearly temporally scaled to match the reference BSPMs duration. This results in a particular case for the dynamic time warping, where both reference Y and test $\widetilde{Y}$ ECG sequences have the same length of T ms, i.e., $\widetilde{Y}, Y \in \mathbb{R}^{P\times T}$ with P being the number of electrodes. Outlining the general approach, a local distance measure $c(\widetilde{y}, y)$ between their elements is introduced first. Each element represents body surface potentials for one time instance recorded at P positions. In this way, we align the whole temporal BSPMs matrices simultaneously for all electrodes positions. Then, a cost matrix $C \in \mathbb{R}^{T\times T}$ is constructed by local costs for all element pairs from $\widetilde{Y}$ and Y. Provided C, the goal of the DTW algorithm is to find an optimal temporal alignment between $\widetilde{Y}$ and Y, i.e., such an alignment that runs through the two-dimensional matrix C along the path of the lowest total cost. In other words, DTW minimizes the body surface potentials mismatch by a proper reordering of the temporal indices.

More formally, a warping path $p = (p_1, \ldots, p_L)$ with $p_l = (n_l, m_l) \in [1, T] \times [1, T]$ and $l \in [1, L]$ is defined by assigning the elements $\widetilde{y}_{n_l}$ in $\widetilde{Y}$ to the elements y_{m_l} in Y. While n_l and m_l take the values of temporal indices, L denotes the number of path elements which is in general greater than the sequences' length T. This is the case when at least one element in one sequence is matched to multiple elements in the other sequence (Müller, 2007).

Furthermore, a feasible warping path is specified to satisfy some common sense observations: boundary, monotonicity and step size conditions have to be met. The boundary condition means that the first index from the first sequence must be aligned with the first index of the second sequence (and possibly following indices), i.e., $p_1 = (1, 1)$. Furthermore, the last index of the first sequence must be aligned with the last index of the second one (and possibly previous indices), i.e., $p_L = (T, T)$. The monotonicity condition applies to both positional arguments of p: $n_1 \leq n_2 \leq \ldots \leq n_L$ and $m_1 \leq m_2 \leq \ldots \leq m_L$ and reflects the requirement of a proper time progression. The third condition restricts the step size in each index: $p_{l+1} - p_l \in (1, 0), (0, 1), (1, 1)$ for $l \in [1, L-1]$, meaning that every index in both arrays must get a pair from the other sequence.

Under these conditions, the total cost function $c_p(\widetilde{Y}, Y)$ is formed by a sum of distances between elements from $\widetilde{Y}$ and Y with the path indices (n_l, m_l):

$$c_p(\widetilde{Y}, Y) = \sum_{l=1}^{L} c(\widetilde{y}_{n_l}, y_{m_l}) = \sum_{l=1}^{L} c(\widetilde{Y}(:, n_l), Y(:, m_l)) \tag{2}$$

and the DTW algorithm minimizes the total cost among all feasible paths (Müller, 2007):

$$c_{p^*}(\widetilde{Y}, Y) = \min \left\{ c_p(\widetilde{Y}, Y) \mid p \text{ is a warping path} \right\} \tag{3}$$

Obviously, the number of all possible paths c_p through a two-dimensional grid C is very large. In order to reduce the computational complexity, we used a dynamic programming algorithm for calculating the optimal path p^*. For this purpose, the accumulated cost matrix $D \in \mathbb{R}^{T \times T}$ is introduced as follows:

$$D(n, m) = c_{p^*}(\widetilde{Y}(:, 1:n), Y(:, 1:m)) \tag{4}$$

The matrix D contains optimal costs for all temporal subsequences in $\widetilde{Y}$ and Y and its element $D(T, T)$ is equal to the optimal cost function value $c_{p^*}(\widetilde{Y}, Y)$. Furthermore, it can be shown that the matrix elements satisfy the following identity (Müller, 2007):

$$\begin{aligned} D(n, m) \;=\; & \min \left\{ D(n-1, m-1),\, D(n-1, m),\, D(n, m-1) \right\} \\ & +\; c(\widetilde{y}_n, y_m) \end{aligned} \tag{5}$$

Extending the matrix by an additional row and column and setting $D(0, :) = D(:, 0) = \infty$ and $D(0, 0) = 0$ facilitates recursive calculation of D.

Provided the accumulated cost matrix D, an optimal warping path $p^* = (p_1, \ldots, p_L)$ is computed in the reverse manner by starting from the index $p_L = (T, T)$:

$$p_{l-1} = \begin{cases} (1, m-1), & \text{if } n = 1 \\ (n-1, 1), & \text{if } m = 1 \\ \arg\min \left\{ D(n-1, m-1), \right. & \\ \qquad \left. D(n-1, m),\, D(n, m-1) \right\} & \text{otherwise} \end{cases} \tag{6}$$

Apparently, the optimal warping path depends on the choice of a cost function $c(\widetilde{y}_{n_l}, y_{m_l})$ being the only algorithm's parameter. For this study, we used the euclidean norm as the distance function, i.e., $c(\widetilde{y}_{n_l}, y_{m_l}) = \|\widetilde{y}_{n_l} - \widetilde{y}_{m_l}\|_{L_2}$. Similar to Giffard-Roisin et al. (2018), both test and measured BSPMs signals were normalized beforehand in order to reduce the influence of torso inhomogeneities on the ECG amplitude. To this end, we scaled all BSPMs signals column-wise by subtracting the mean and component-wise scaling to unit variance (preprocessing scale function from sciki-learn (Pedregosa et al., 2011) was used). For a pseudo-code of the employed inverse pipeline the reader is referred to the **Appendix A**.

Same as within standard FRA methodology, for each cardiac node we computed the corresponding test activation sequence and the associated test BSPMs. Then, each test BSPMs sequence in pair with the reference BSPMs were temporally warped by computing the optimal path cost (3). As minimizing the cost function c_p in (3) is equivalent to maximization of $1/c_p$, for the sake of consistency with the standard FRA approach searching for the maximum correlation, we used the reciprocal (or inverse) distance function $1/c_p$ for visualization. Calculated for test BSPMs relating to each cardiac node, the obtained reciprocal distances $1/c_p$ can be displayed on the heart surface. By analogy with the FRA-based correlation maps, the resulting inverse distance maps can be employed as an uncertainty quantification tool.

2.2.1. Simplified Simulation Case of Slow CV Area

First, we provide a simulation example based on a realistic human geometry. For the considered heart mesh, the activation times matrix T was computed as utilized by FRA. Next, a node on the lateral LV wall was selected to be the ectopic focus, the one to be noninvasively localized . Additionally, a region with 20 mm radius about 60 mm from the selected focus in which the CV was reduced by a factor of three. According to this modification in CV, the activation times were created, see **Figure 1A**. The corresponding BSPMs from this activation sequence was computed. For both FRA and FRA-DTW the unaltered times matrix T was used. For FRA the correlation map was used to estimate the focus, for FRA-DTW the reciprocal distance as similarity measure was used. In **Figure 1B**, the FRA-based correlation map is visualized together with the true and localized origins shifted by 31 mm in the direction opposite to the location of the slow CV area relative to the reference focus. In contrast to that, the nonlinear temporal warping was able to account for this modeling error, which is reflected in the exact onset reconstruction provided by the inverse cost map shown in **Figure 1C**.

To illustrate temporal warping of the ECG signals, the ECG channel with the lowest correlation (88 %) is shown. **Figure 2A** depicts both reference and test signals together with their nonlinear alignment, whilst **Figure 2B** visualizes the optimally warped signals. As mentioned previously, the duration of an optimal warping path c_{p^*} is generally larger than the signals' length due to the fact that multiple elements of one sequence can be aligned with the same element of the other one. Obviously, no temporal shifts can compensate for amplitudes mismatch due

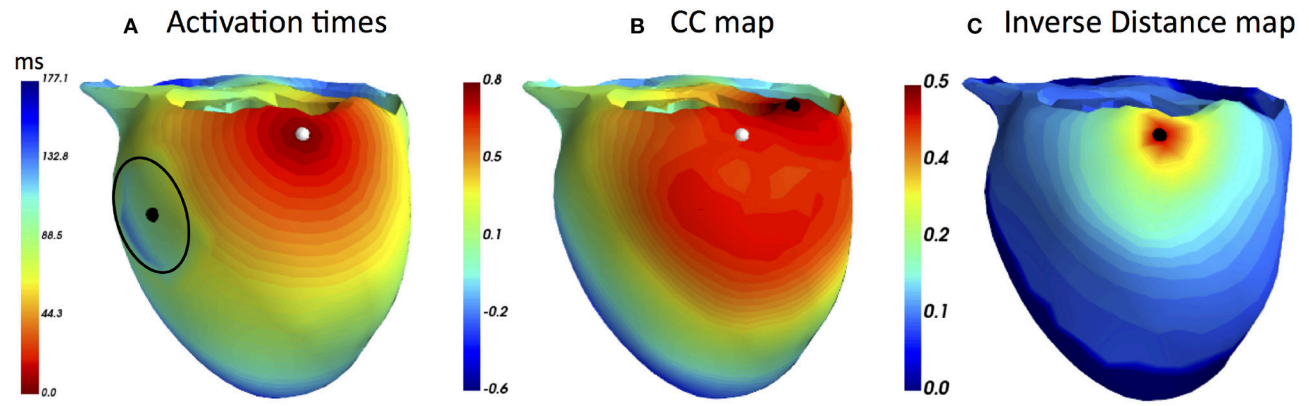

FIGURE 1 | (A) Modified ectopic excitation sequence starting from the node marked by the white marker with the reduced CV in the area centered at the black dot and enclosed by the black line. **(B)** Correlation map generated by the standard FRA with the reconstructed onset marked by the black point. It is worth noting that a relatively large area exhibits upper percentile of the high correlation coefficient values, implying higher solution ambiguity and, thereby, weakening the prediction **(C)** Distribution of the DTW-based inverse distance function (dimensionless due to the ECG scaling). The black point overlaps the reference origin, meaning that the temporal warping could account for the excitation delay and resulted in the exact inverse localization. Notably, only a few heart nodes corresponded to the upper percentile of the inverse distance.

to a complex nonlinear relationship (1) connecting activation times on the heart to the body surface potentials. However, the difference in a local conduction speed was accounted for by the warping function.

2.3. Realistic Simulations of Ectopic Excitation

After the proof-of-concept provided by the manually constructed and, certainly, oversimplified simulation case, we conducted a comparison between FRA and FRA-DTW and evaluated performance of the latter for realistic excitation patterns. For this study eight ectopic activation sequences presented in Janssen et al. (2018) were used.

In short, the excitation propagation patterns were simulated with the monodomain model and the BSPMs were then generated for a realistic finite-element volume conductor with an anisotropic heart model. In Janssen et al. (2018), the authors investigated the influence of bidomain conductivity tensors in the forward modeling on the quality of inverse reconstructions obtained with the EDL model. In the present work, only the most realistic case is considered, the model with unequal anisotropy ratio in the intra- and extracellular spaces.

In Janssen et al. (2018) FRA was used to compute an initial estimate for solving the subsequent NLLS (1). As the final solution was shown to heavily depend on the initialization, the goal of this study was to determine, whether the FRA with incorporated temporal warping is able to provide an improved estimate compared to its standard version. The focus locations considered for this study listed: "two foci on both sides of the septal wall, two left ventricular free wall foci, two foci on the right ventricular free wall, and two beats originating from a basal part of the ventricles close to the septal wall" (Janssen et al., 2018).

2.4. Clinical Data

The implanted biventricular pacemaker leads position are exactly known from CT scans, providing ideal ECGI validation data for single paced activation sequences from the LV and RV for each patient. Therefore, we enrolled in this study 10 patients (n = 10) from 54 to 70 years (median 65; 25–75% range 59–64; 8 male) with previously implanted CRT devices. Among them nine patients had a left bundle branch block (LBBB) QRS morphology of the intrinsic rhythm, and seven of them had a LV scar with low conduction velocity zones after myocardial infarction. These LV zones were not taken into account in the inverse procedure.

The study was reviewed and approved by the Ethical Committee of Almazov National Medical Research Center in Saint Petersburg, Russia. Written informed consent was obtained from each patient after detailed description and explanation of the study before the procedures. This single-center cross-sectional study was performed in accordance with the Good Clinical Practice guidelines and Helsinki declaration for biomedical research.

2.4.1. ECG and CT Data

A total maximum number of 240 body surface electrodes were applied on the patient's torso and connected to the multichannel Amycard 01C EP system ECG amplifier (EP Solutions SA, Switzerland). CRT device in each patient was programmed and continuous ECGs of isolated RV/LV pacing from implanted leads at rate not more than 90 bpm were recorded during 10 sec. The pacing amplitude and duration were selected individually based on the originally established parameters of the CRT device. The original parameters were set up 2–3 months prior to the procedure during a regular check-up based on standard criteria in the clinical practice. According to the results of an automatic threshold test in the CRT device, the minimal spike amplitude and duration have been selected to have stable effective capture during RV and LV pacing. All measurements were performed during breath hold. Immediately after recording of the multichannel ECG, all patients underwent cardiac CT imaging with applied

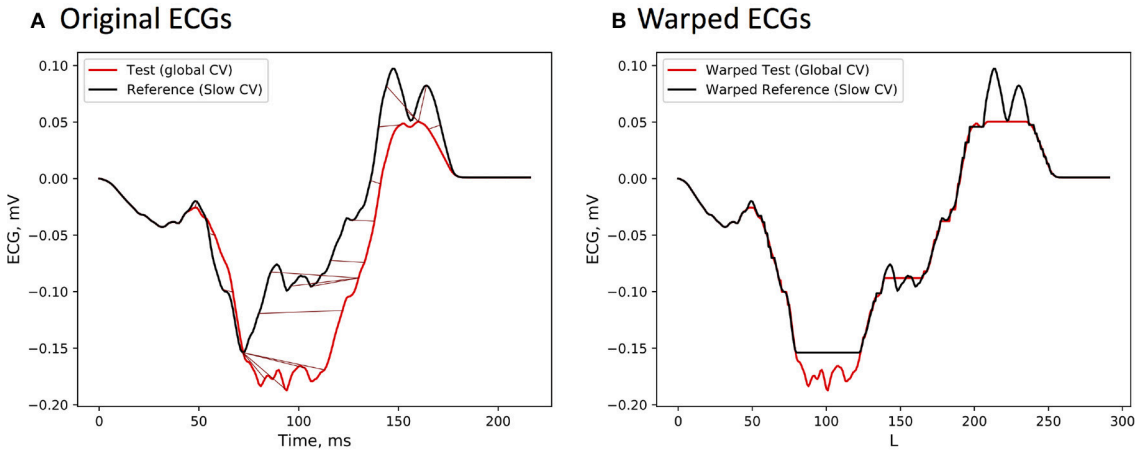

FIGURE 2 | (A) ECG signals from the reference BSPMs, which was computed from the activation sequence with locally modified CV value, and the test BSPMs generated by the standard FRA under the assumption of a global CV. The signals differ only on the time interval corresponding to the wavefront passing through the low CV region. **(B)** Temporally warped ECG sequences with the path length *L*.

body surface electrodes. The obtained CT data was imported into Amycard 01C EP system software in DICOM format to reconstruct polygonal meshes of the torso, lungs and detailed epi-endocardial ventricular heart models based on the semi-automatic segmentation.

2.4.2. Anatomical Models

For our inverse calculations, a piece-wise heterogeneous volume conductor model was used with thorax, lungs and ventricular blood masses as regions with an electrical conductivity deviating from that of the torso. Following the guidelines commonly accepted in the ECGI community, the assigned electrical conductivity values were 0.6, 0.04 and 0.2 Sm/m for blood masses, lungs and ventricles, respectively (see e.g., Modre et al., 2002; van Dam et al., 2009a).

2.4.3. Quality Metrics

In order to estimate the inverse routine performance, the distances were computed between the known pacemaker locations and noninvasively identified earliest excitation sites. All estimated LV and RV pacemaker lead positions were localized for the epi- or endocardial heart surfaces, respectively. The geodesic distance was considered as a more reliable quality measure for curved surfaces, and for endocardial solutions separated from a pacemaker by the septal wall. As a supplementary metric targeting the misclassified ectopic origins, we analyzed whether the overall earliest activation site was found on the same (endo- or epicardial) cardiac surface as the corresponding pacemaker lead.

In addition, we performed a bias-corrected and accelerated bootstrap analysis (in accordance to Efron and Tibshiran correction) in order to check the stability, variability, and robustness of the estimated ECGI accuracy and provide more confidence to the results of this study. We used 2.5 and 97.5 percentile interval for the calculation of the 95% confidence intervals for reference limits in all continuous variables. Bootstrap was performed with 1,000 replications for each variable with a Mersenne twister as a random number generator.

TABLE 1 | Localization error for the realistic ectopic simulations.

Activation pattern	Localization error FRA, mm	Localization error FRA-DTW, mm
Left side of septum (1)	0	0
Right side of septum (2)	11	7
Base LV near septum (3)	15	0
Base RV near septum (4)	18	4
LV epicardial free wall (5)	20	14
LV endocardial free wall (6)	12	19
RV endocardial free wall (7)	6	6
RV epicardial free wall (8)	14	7

3. RESULTS

3.1. ECGI for Realistic Simulations of Ectopic Excitation

A summary of LEs delivered by both FRA and FRA-DTW for the considered eight excitation patterns is shown in **Table 1**. The order of appearance is the same as in the original work (Janssen et al., 2018). As seen from the table, temporal alignment of the FRA-simulated test BSPMs resulted in lower LEs in seven cases. In **Figure 3** shows the correlation maps obtained with FRA and inverse distance maps yielded from subsequent time warping for the excitation patterns 3 and 6. Although for pattern 6 the localization error from FRA-DTW is slightly higher than that of FRA, the focus was still correctly classified to originate from the endocardial wall.

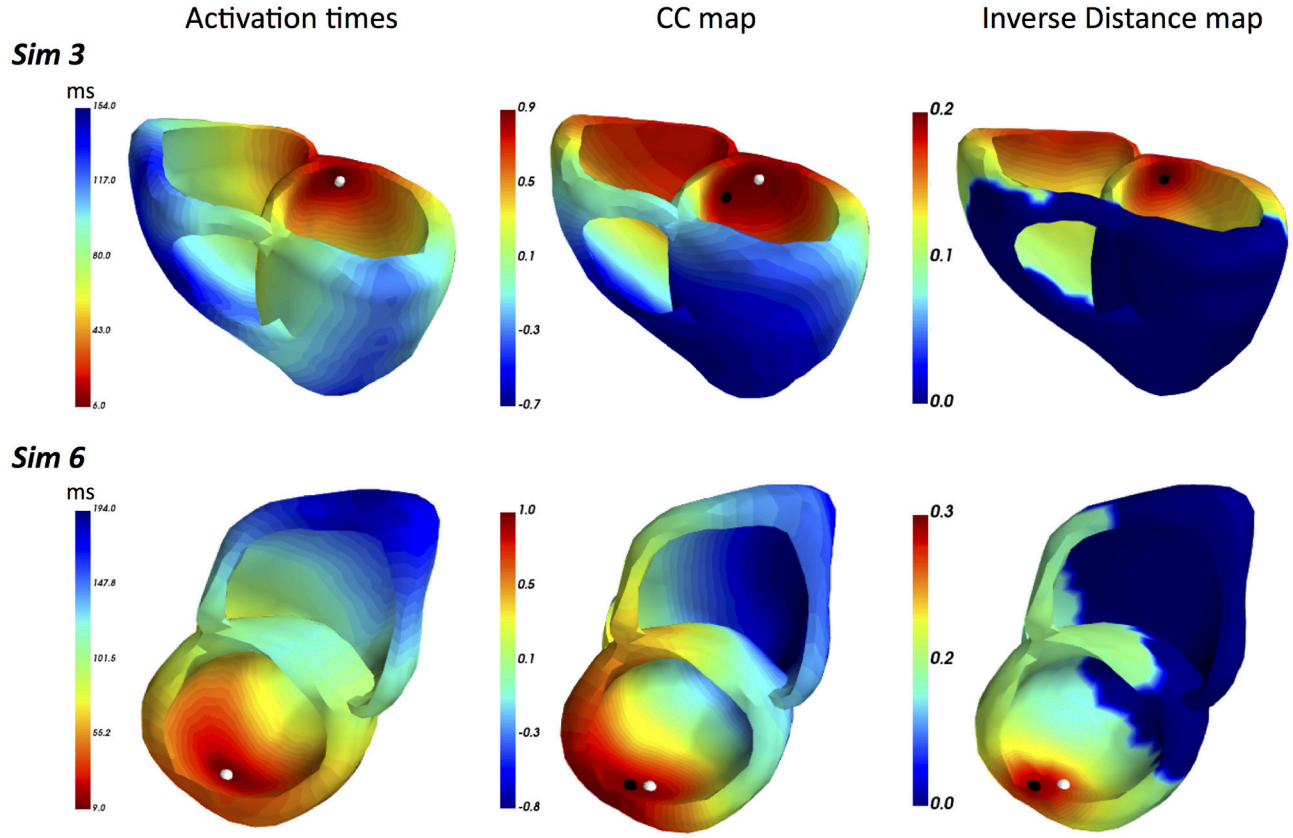

FIGURE 3 | ECGI results for realistic simulated patterns 3 and 6. For pattern 3, the combination of FRA with subsequent time warping exhibited the highest error decrease from 15 to 0 mm. For this activation sequence, the onset reconstructed by FRA-DTW and marked by the black point coincides with the true focus. Pattern 6 was the only case among the considered eight, where the localization error provided by FRA-DTW was higher than that from the standard FRA.

3.2. ECGI of Single Pacings in CRT Patients

The main accuracy characteristics are provided in **Table 2**. For all 10 patients, median (25–75% range) accuracy for FRA was 16 (8–23) mm and 5 (2–10) mm for FRA-DTW algorithm. The median accuracy for FRA in the LV was 15 (11–25) mm and 8 (3–13) mm for FRA-DTW algorithm, while in the RV the values were 19 (6–23) mm for FRA and 4 (2–8) mm for FRA-DTW. There was a significant difference in accuracy values calculated with FRA and FRA-DTW algorithms for LV, RV, and both LV and RV, which is shown in **Figures 4A–C**. It can also be seen from **Figures 5A,B** displaying the histograms that represent overall accuracy distributions for both algorithms. 95% bootstrap confidence intervals were also more narrow for LEs based on FRA-DTW compared to FRA algorithm. Furthermore, FRA-DTW was able to detect the correct (epi / endo) surface of an early activation for all LV pacings and one RV, whereas FRA detected the correct surface in four LV cases and wrongly associated all RV paced sequences to the epicaridal part of the heart surface (**Figure 6**). However, there was no significant difference in this accuracy feature between the RV and LV in every algorithm. For two patients, FRA-DTW resulted in a lower localization error in the RV septum compared to FRA. The LEs were reduced from 20–8 mm to 9–3 mm, respectively. Exemplarily, performance results from both methods for the cases featuring maximal and minimal LEs in the RV and LV are displayed in **Figure 7**.

4. DISCUSSION

In the presented work, the fastest route algorithm (FRA) was modified to account for local differences in conduction velocities. The dynamic time warping for matching simulated and measured BSPMs proved to increase robustness and accuracy of FRA. The improvements were shown both in simulation data as well as in a small CRT patient population with known inhomogeneous conduction velocity within the ventricular myocardium.

As within the standard FRA-based inverse procedure (van Dam et al., 2009b), for each cardiac mesh node activation sequences are generated with FRA, and the corresponding simulated test BSPMs are computed for a patient specific volume conductor model. Then, instead of correlation-based comparison between simulated and measured ECGs, the signals are temporally warped on the basis of an associated cost, or distance, function. To evaluate possible benefits of the warping step, we benchmarked this strategy against the CC-based FRA routine in three scenarios.

TABLE 2 | Main characteristics of ECGI accuracy for FRA and FRA-DTW algorithms. m, mean; SD, standard deviation; M, median; LQ, lower quartile; UQ, upper quartile; min, minimum; max, maximum, ratio of correctly detected early activation site's surface-R (in percents). For the localization error characteristics, 95% bootstrap confidence interval (CI) is provided in parentheses.

Accuracy features, mm (95% bootstrap CI)	LV		RV		LV + RV	
	FRA	FRA-DTW	FRA	FRA-DTW	FRA	FRA-DTW
m	17 (12–22)	8 (5–12)	16 (10–22)	4 (3–6)	17 (13–21)	6 (5–9)
SD	9 (3–11)	6 (4–8)	10 (6–12)	3 (2–4)	9 (7–11)	5 (3–7)
M	15 (12–23)	8 (3–13)	19 (6–24)	4 (2–8)	16 (10–22)	5 (3–9)
LQ (25%)	11 (7–15)	3 (1–9)	6 (3–20)	2 (1–4)	8 (2–14)	2 (1–4)
UQ (75%)	25 (14–33)	13 (7–20)	23 (18–31)	8 (4–9)	23 (18–31)	10 (6–14)
min	7	1	3	1	3	1
max	33	20	31	9	33	20
R	40	100	0	10	20	55

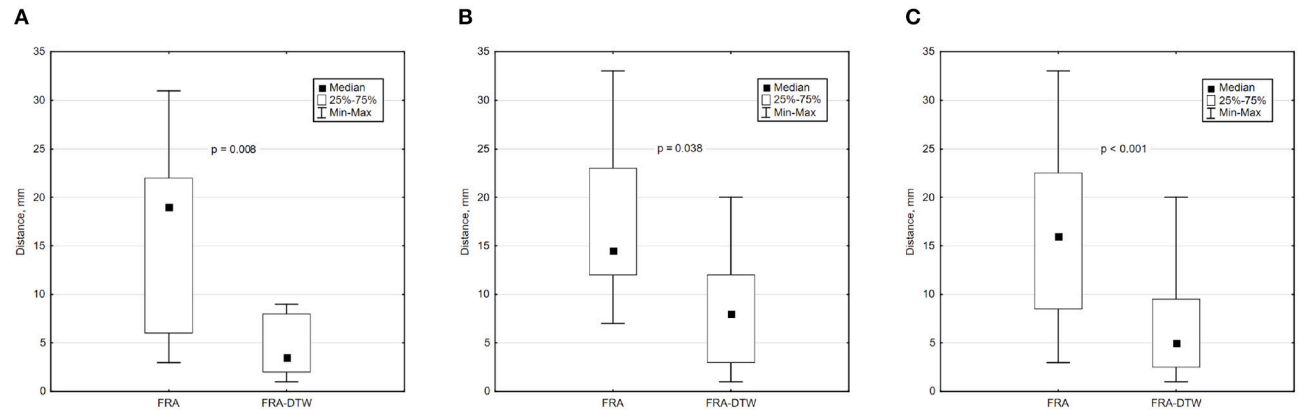

FIGURE 4 | Box and whisker plots of LEs for FRA and FRA-DTW for the LV **(A)**, RV **(B)**, and all considered pacings **(C)**. The Wilcoxon signed-rank test was performed to compare localization accuracy provided by the two ECGI algorithms. A $p < 0.05$ was considered as statistically significant due to the relatively small sample size.

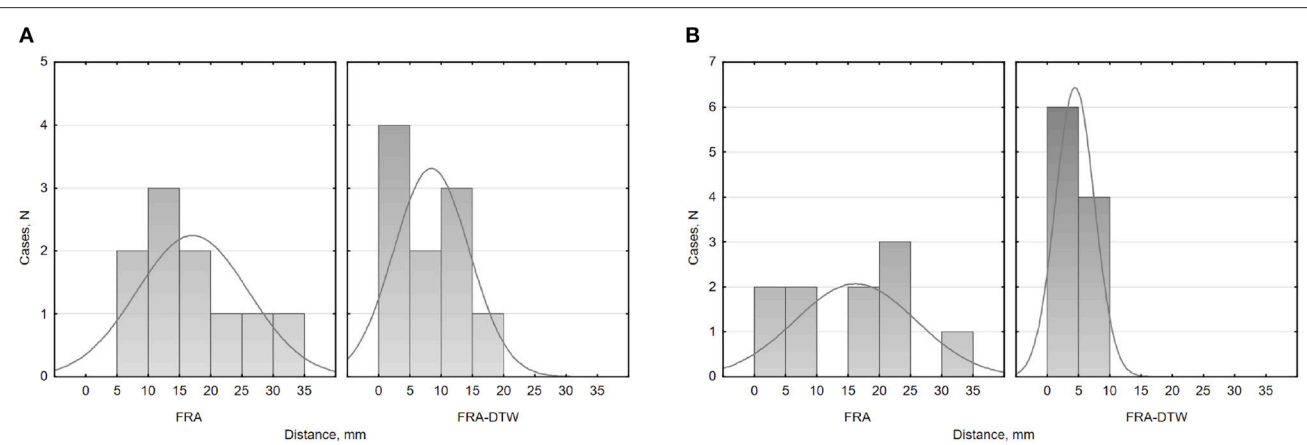

FIGURE 5 | Histograms of LEs for the LV **(A)**, and RV **(B)** pacings. The curves represent fitted normal distributions.

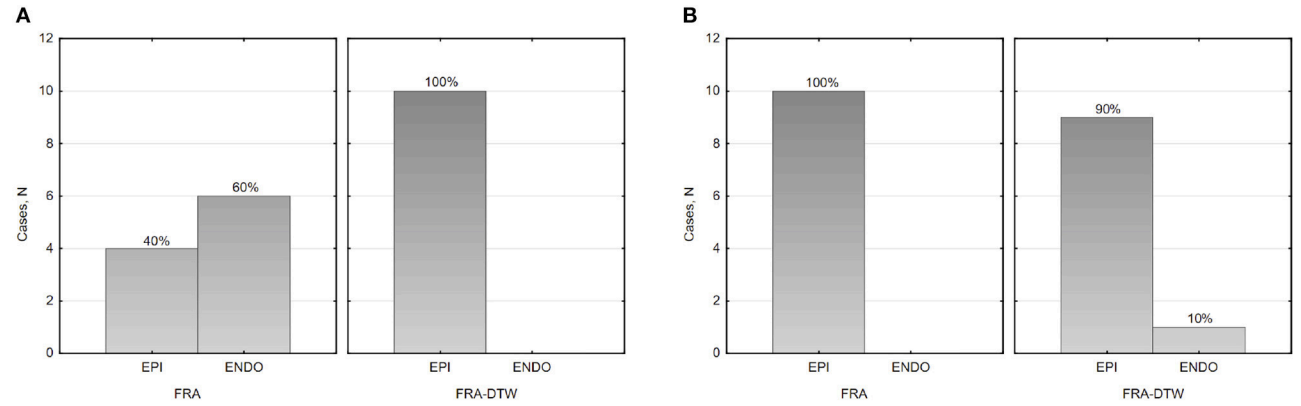

FIGURE 6 | Histograms of the epi-endocardial early activation site's surface identification in the LV **(A)** and RV **(B)**.

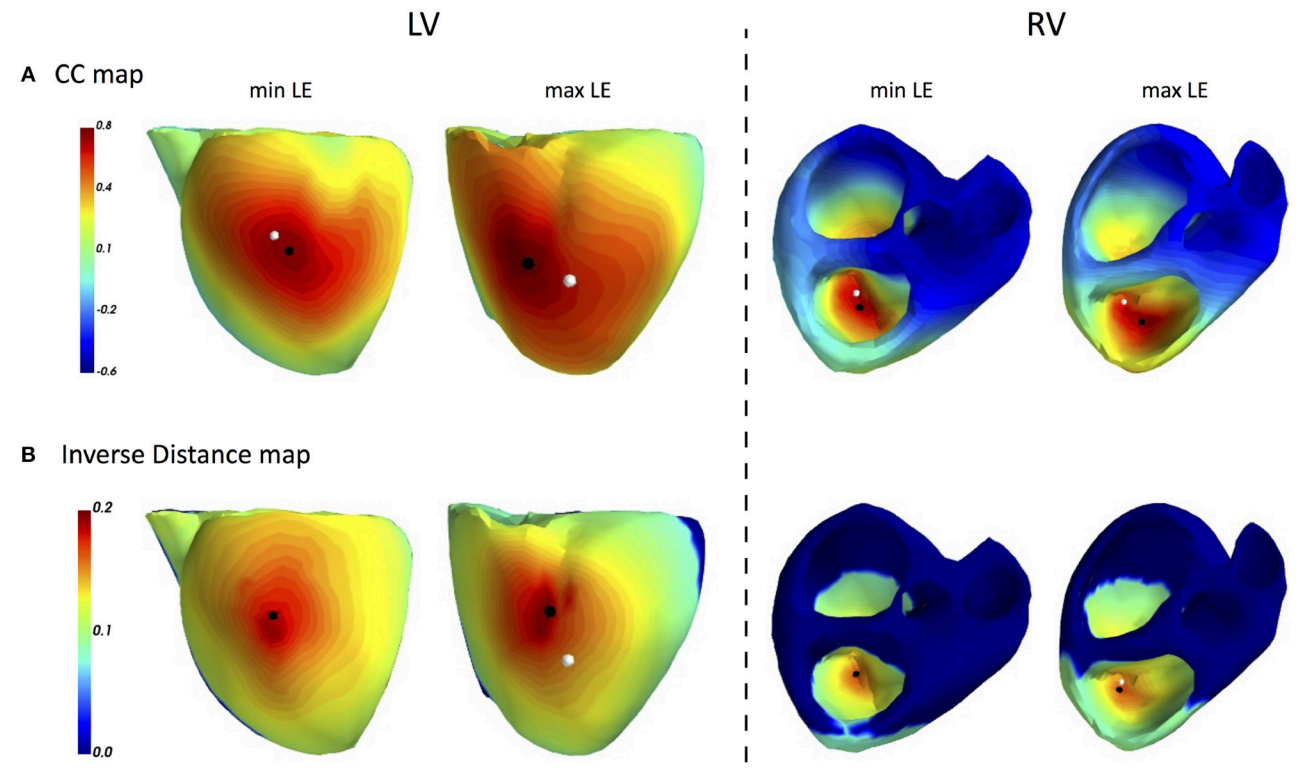

FIGURE 7 | ECGI results for single pacings in CRT patients: FRA based CC maps **(A)** and FRA-DTW based inverse distance maps **(B)**. The white dot marks a pacemaker lead position projected on the cardiac surface, while the black point labels the reconstructed excitation origin. In the cases of minimal LEs for both LV and RV (first and third columns), the FRA-DTW method localized the onset at the same mesh node as the pacemaker lead. The accuracy of FRA was 8 and 16 mm, respectively. The cases, featuring maximal LEs for FRA-DTW, resulted in 16 and 16 mm for FRA.

First, FRA-DTW was able to correct the localization error due to slower CV in a small heart region for a simple simulation case. Though this construct was purely artificial and did not represent a physiologically meaningful simulation, it served as a proof-of-concept that the excitation delays can be accounted for by BSPMs warping in the temporal domain.

In the next model-to-model comparison, the LEs were on average reduced by 5 mm when using the DTW-FRA algorithm vs. the standard FRA algorithm (**Table 1**). Previously, the authors examined three setups with respect to cardiac anisotropy used in the forward modeling: isotropic model, anisotropic model with equal anisotropy ratios in the extra- and intracellular

spaces and an unequal anisotropy ratios case. For our purpose, we compared FRA to its warping modification only for the most realistic case of BSPMs produced by an anisotropic heart with unequal anisotropy ratios in the extra- and intracellualr domains. For seven cases, FRA-DTW performed similar or better than the original FRA. For a focus on the endocardial LV wall, FRA-DTW correctly identified endocardium as the onset origin, but resulted in a higher localization error compared to FRA. However, the ambiguity area, which can be taken as a region exhibiting the upper percentile of a similarity measure, was generally smaller for the reciprocal distance maps delivered by FRA-DTW method compared to the FRA-based CC maps.

Finally, we applied both methodologies to twenty paced activation sequences in ten CRT patients. The Wilcoxon non-parametric test suggested superior performance of FRA-DTW, yielding $p = 0.0076$ and 0.038 for LV and RV pacings, respectively. Importantly, the warping step improved localization accuracy for two cases with RV leads implanted in a septal area. An interesting aspect of all FRA related methods is the automatic detection of an early activation zone, which usually requires an additional sophisticated post-processing step for potential-based ECGI solutions (Duchateau et al., 2017). At the same time, both methods suffered from a low classification rate with respect to the correct cardiac surface for the RV pacings. We believe this issue to be due to the limited thickness of the RV wall, as no significant association was found between clinical characteristics, pacing modalities, number of body surface electrodes on one side and ECGI localization accuracy on the other. This fact can be considered as an indirect representativity evidence of the original clinical data set. We performed a bootstrap analysis for a robuster estimation of the obtained LEs because of a relatively small original sample size with the unknown distribution parameters in accordance to recommendations from Adèr (2008). In addition, bootstrap allowed us to use a resampling approach to mimic the process of obtaining new data sets, so that we can evaluate the variability of our assessment without generating additional samples. The bootstrap analysis showed that LE variability was significantly lower for the FRA-DTW algorithm, indicating its greater robustness against outliers. The bootstrap also helps to estimate LEs in the population, making results more predictable for clinical work. Furthermore, univentricular LV and RV pacings are the optimal ECGI validation data for single ectopic activation sequences. Thus, obtained results show the potential of the proposed methodology to significantly improve noninvasive detection of focal arrhythmia sources in clinical practice (Duchateau et al., 2018).

However, despite these promising results, it remains unclear how to relate an optimal warping path to the actual excitation in the heart. With this respect, we intend to perform further research by adding the optimization step in solving the NNLS problem using both initializations. FRA procedure in combination with time warping could compensate for the uniform excitation assumption of FRA. An example of explicit scar removal from the heart geometry for the EDL inverse model was presented by Oostendorp et al. (2002). Sapp et al. showed that the quality of potential-based ECG imaging of epicardial pacing sites in ventricular tachycardia patients deteriorates over myocardial scar or slowly conducting tissue (Sapp et al., 2012). Interestingly, the data from this study was recently reused by Zhou et al. investigating performance of a data-driven Bayesian method (Zhou et al., 2018). Though overall LEs were reduced by this novel approach, its accuracy was still suffering in cases when a pacing was performed in the scar region. These observations suggest potential improvements from combining ECGI in general, and FRA or other model-based approaches in particular, with anatomical substrate information.

Nonetheless, even in the absense of the underlying substrate data, ECGI was reported to provide important insights on the electrical excitation in CRT patients with varied LV pathology (Jia et al., 2006). A recent study by Bear *et al.* further demonstrated the ability of ECGI to accurately detect electrical dyssynchrony and identify the latest activation site with 9.1 ± 0.6 mm in Langendorff-perfused pig hearts (Bear et al., 2018). As a representative of model-based approaches, an offline created database of realistic forward simulations with different EP setups was shown to facilitate estimation of clinically relevant parameters, such as pacing configuration and CV profile (Giffard-Roisin et al., 2018). Such an offline strategy aiming at the real-time performance is computationally efficient, whilst enjoying an essential extensibility with every suitable clinical case. Our future efforts will be focused on deploying imaging modalities together with personalized biophysical computer models and ECG imaging.

5. CONCLUSIONS

In this work, we quantitatively assessed FRA performance on CRT patients. An important enhancement of the FRA method, a temporal warping of FRA-generated BSPMs sequences, was introduced. Using FRA-DTRW reduced the LE by approximately a factor of two, demonstrating a significant accuracy improvement for clinical data of CRT patients with a complex etiology.

6. LIMITATIONS

Evaluation of ECGI accuracy using CRT devices is intrinsically limited to the LV lateral wall, RV apex and septum, while other anatomical regions cannot be tested in the same manner. For drawing clinically relevant conclusions, another study with a larger sample size should be considered for a detailed representativity evaluation of the data used. The presented bootstrap analysis models potential outcomes of such a study and, therefore, serves as a reference point for future investigations.

The lack of late gadolinium enhancement MRI data in patients with previous myocardial infarction did not allow us to quantify the influence of this factor on the tested algorithms.

DATA AVAILABILITY

The datasets for this study will not be made publicly available because the clinical datasets belong to the Almazov National Medical Research Center, Saint-Petersburg, Russia. Therefore, the corresponding author is not authorised to provide them upon request. However, the respective co-authors can be asked for it.

AUTHOR CONTRIBUTIONS

DP conceived the presented warping extension of FRA, designed the simulation setups and conducted the numerical part of the clinical study. MC performed statistical analysis of the clinical results. PvD provided technical expertise and revised the methodology. DP, MC, and PvD discussed the main findings and results, and wrote the manuscript. MC, SZ, and MB conducted the clinical data acquisition and post-processing. TT and DL provided medical expertise and contributed to the clinical study design.

ACKNOWLEDGMENTS

First, we would like to thank the Institute of Biomedical Engineering at Karlsruhe Institute of Technology (KIT) for sharing the simulation data used in this work. We also greatly appreciate all efforts and help from the Department of Radiology in Almazov National Medical Research Center, Saint Petersburg. Our further sincere thanks go to Dr. Andrey Kozlenok, the head of Department for Cardiovascular Physiology for his great support in organizing and hosting this study.

REFERENCES

Adèr, H. J. (2008). *Advising on Research Methods: A Consultant's Companion*. Huizen: Johannes van Kessel Publishing.

Bear, L. R., Huntjens, P. R., Walton, R. D., Bernus, O., Coronel, R., and Dubois, R. (2018). Cardiac electrical dyssynchrony is accurately detected by noninvasive electrocardiographic imaging. *Heart Rhythm* 15, 1058–1069. doi: 10.1016/j.hrthm.2018.02.024

Brooks, D. H., Ahmad, G. F., MacLeod, R. S., and Maratos, G. M. (1999). Inverse electrocardiography by simultaneous imposition of multiple constraints. *IEEE Trans. Biomed. Eng.* 46, 3–18. doi: 10.1109/10.736746

Cluitmans, M., Brooks, D. H., MacLeod, R., Dössel, O., Guillem, M. S., van Dam, P. M., et al. (2018). Validation and opportunities of electrocardiographic imaging: from technical achievements to clinical applications. *Front. Physiol.* 9:1305. doi: 10.3389/fphys.2018.01305

Daubert, C., Behar, N., Martins, R. P., Mabo, P., and Leclercq, C. (2016). Avoiding non-responders to cardiac resynchronization therapy: a practical guide. *Eur. Heart J.* 38, 1463–1472. doi: 10.1093/eurheartj/ehw270

Dhamala, J., Arevalo, H. J., Sapp, J., Horacek, M., Wu, K. C., Trayanova, N. A., et al. (2017). Spatially adaptive multi-scale optimization for local parameter estimation in cardiac electrophysiology. *IEEE Trans. Med. Imaging* 36, 1966–1978. doi: 10.1109/TMI.2017.2697820

Duchateau, J., Potse, M., and Dubois, R. (2017). Spatially coherent activation maps for electrocardiographic imaging. *IEEE Trans. Biomed. Eng.* 64, 1149–1156. doi: 10.1109/TBME.2016.2593003

Duchateau, J., Sacher, F., Pambrun, T., Derval, N., Chamorro-Servent, J., Denis, A., et al. (2018). Performance and limitations of noninvasive cardiac activation mapping. *Heart Rhythm*. doi: 10.1016/j.hrthm.2018.10.010

Erem, B., Coll-Font, J., Orellana, R. M., St'ovicek, P., and Brooks, D. H. (2014a). Using transmural regularization and dynamic modeling for noninvasive cardiac potential imaging of endocardial pacing with imprecise thoracic geometry. *IEEE Trans. Med. Imaging* 33, 726–738. doi: 10.1109/TMI.2013.2295220

Erem, B., van Dam, P. M., and Brooks, D. H. (2014b). Identifying model inaccuracies and solution uncertainties in non-invasive activation-based imaging of cardiac excitation using convex relaxation. *IEEE Trans. Med. Imaging* 33, 902–912. doi: 10.1109/TMI.2014.2297952

Geselowitz, D. B. (1989). On the theory of the electrocardiogram. *IEEE Proc.* 77, 857–876. doi: 10.1109/5.29327

Geselowitz, D. B., and Miller, W. (1983). A bidomain model for anisotropic cardiac muscle. *Ann. Biomed. Eng.* 11, 191–206. doi: 10.1007/BF02363286

Giffard-Roisin, S., Delingette, H., Jackson, T., Webb, J., Fovargue, L., Lee, J., et al. (2018). Transfer learning from simulations on a reference anatomy for ecgi in personalised cardiac resynchronization therapy. *IEEE Trans. Biomed. Eng.* 66, 343–353. doi: 10.1109/TBME.2018.2839713

Giffard-Roisin, S., Jackson, T., Fovargue, L., Lee, J., Delingette, H., Razavi, R., et al. (2017). Noninvasive personalization of a cardiac electrophysiology model from body surface potential mapping. *IEEE Trans. Biomed. Eng.* 64, 2206–2218. doi: 10.1109/TBME.2016.2629849

Gulrajani, R. M. (1998). The forward and inverse problems of electrocardiography. *IEEE Eng. Med. Biol. Mag.* 17, 84–122. doi: 10.1109/51.715491

Huiskamp, G., and Van Oosterom, A. (1988). The depolarization sequence of the human heart surface computed from measured body surface potentials. *IEEE Trans. Biomed. Eng.* 35, 1047–1058. doi: 10.1109/10.8689

Janssen, A. M., Potyagaylo, D., Dössel, O., and Oostendorp, T. F. (2018). Assessment of the equivalent dipole layer source model in the reconstruction of cardiac activation times on the basis of bspms produced by an anisotropic model of the heart. *Med. Biol. Eng. Comput.* 56, 1013–1025. doi: 10.1007/s11517-017-1715-x

Jia, P., Ramanathan, C., Ghanem, R. N., Ryu, K., Varma, N., and Rudy, Y. (2006). Electrocardiographic imaging of cardiac resynchronization therapy in heart failure: observation of variable electrophysiologic responses. *Heart Rhythm* 3, 296–310. doi: 10.1016/j.hrthm.2005.11.025

Li, G., and He, B. (2001). Localization of the site of origin of cardiac activation by means of a heart-model-based electrocardiographic imaging approach. *IEEE Trans. Biomed. Eng.* 48, 660–669. doi: 10.1109/10.923784

Liu, C., Skadsberg, N. D., Ahlberg, S. E., Swingen, C. M., Iaizzo, P. A., and He, B. (2008). Estimation of global ventricular activation sequences by noninvasive three-dimensional electrical imaging: Validation studies in a swine model during pacing. *J. Cardiovasc. Electrophysiol.* 19, 535–540. doi: 10.1111/j.1540-8167.2007.01066.x

Modre, R., Tilg, B., Fischer, G., and Wach, P. (2002). Noninvasive myocardial activation time imaging: a novel inverse algorithm applied to clinical ecg mapping data. *IEEE Trans. Biomed. Eng.* 49, 1153–1161. doi: 10.1109/TBME.2002.803519

Müller, M. (2007). *Information Retrieval for Music and Motion*, Vol. 2. Heidelberg: Springer.

Oostendorp, T., Nenonen, J., and Korhonen, P. (2002). Noninvasive determination of the activation sequence of the heart: application to patients with previous myocardial infarctions. *J. Electrocardiol.* 35, 75–80. doi: 10.1054/jelc.2002.37158

Oosterhoff, P., Meijborg, V. M., van Dam, P. M., van Dessel, P. F., Belterman, C. N., Streekstra, G. J., et al. (2016). Experimental validation of noninvasive epicardial and endocardial activation imaging. *Circ. Arrhythm. Electrophysiol.* 9:e004104. doi: 10.1161/CIRCEP.116.004104

Pedregosa, F., Varoquaux, G., Gramfort, A., Michel, V., Thirion, B., Grisel, O., et al. (2011). Scikit-learn: machine learning in Python. *J. Mach. Learn. Res.* 12, 2825–2830. Available online at: http://dl.acm.org/citation.cfm?id=1953048.2078195

Potse, M., Krause, D., Kroon, W., Murzilli, R., Muzzarelli, S., Regoli, F., et al. (2014). Patient-specific modelling of cardiac electrophysiology in heart-failure patients. *Europace* 16(Suppl. 4):iv56–iv61. doi: 10.1093/europace/euu257

Potyagaylo, D. (2016). *Non-Invasive Electrocardiographic Imaging of Ventricular Activities: Data-Driven and Model-Based Approaches*. Ph.D. thesis, Karlsruher Institut für Technologie (KIT).

Potyagaylo, D., Dössel, O., and Van Dam, P. (2016a). Influence of modeling errors on the initial estimate for nonlinear myocardial activation times imaging calculated with fastest route algorithm. *IEEE Trans. Biomed. Eng.* 63, 2576–2584. doi: 10.1109/TBME.2016.2561973

Potyagaylo, D., Loewe, A., van Dam, P., and Dössel, O. (2016b). Ecg imaging of focal atrial excitation: evaluation in a realistic simulation setup. in *Computing in Cardiology Conference* (Vancouver, BC), 113–116.

Pullan, A., Cheng, L., Nash, M., Bradley, C., and Paterson, D. (2001). Noninvasive electrical imaging of the heart: theory and model development. *Ann. Biomed. Eng.* 29, 817–836. doi: 10.1114/1.1408921

Revishvili, A. S., Wissner, E., Lebedev, D. S., Lemes, C., Deiss, S., Metzner, A., et al. (2015). Validation of the mapping accuracy of a novel non-invasive epicardial and endocardial electrophysiology system. *EP Europace* 17, 1282–1288. doi: 10.1093/europace/euu339

Rodrigo, M., Climent, A. M., Liberos, A., Fernández-Avilés, F., Berenfeld, O., et al. (2017). Technical considerations on phase mapping for identification of atrial reentrant activity in direct-and inverse-computed electrograms. *Circ. Arrhythm. Electrophysiol.* 10:e005008. doi: 10.1161/CIRCEP.117.005008

Rudy, Y. (2013). Noninvasive electrocardiographic imaging of arrhythmogenic substrates in humans. *Circ. Res.* 112, 863–874. doi: 10.1161/CIRCRESAHA.112.279315

Sapp, J. L., Dawoud, F., Clements, J. C., and Horáček, B. M. (2012). Inverse solution mapping of epicardial potentials: quantitative comparison with epicardial contact mapping. *Circ. Arrhythm. Electrophysiol.* 5, 1001–1009. doi: 10.1161/CIRCEP.111.970160

Sohns, C., Metzner, A., Chmelevsky, M., and Kuck, K.-H. (2018). A new algorithm to visualize the individual relationship between electrical rotors from non-invasive panoramic mapping and atrial fibrosis to guide ablation of persistent atrial fibrillation. *Clin. Res. Cardiol.* 107, 444–446. doi: 10.1007/s00392-017-1196-9

van Dam, P. M., Boyle, N. G., Laks, M. M., and Tung, R. (2016). Localization of premature ventricular contractions from the papillary muscles using the standard 12-lead electrocardiogram: a feasibility study using a novel cardiac isochrone positioning system. *Europace* 18(Suppl. 4):iv16–iv22. doi: 10.1093/europace/euw347

Van Dam, P. M., Oostendorp, T. F., Linnenbank, A. C., and Van Oosterom, A. (2009a). Non-invasive imaging of cardiac activation and recovery. *Ann. Biomed. Eng.* 37, 1739–1756. doi: 10.1007/s10439-009-9747-5

van Dam, P. M., Oostendorp, T. F., and van Oosterom, A. (2009b). Application of the fastest route algorithm in the interactive simulation of the effect of local ischemia on the ecg. *Med. Biol. Eng. Comput.* 47, 11–20. doi: 10.1007/s11517-008-0391-2

van Oosterom, A., and Jacquemet, V. (2005). Genesis of the p wave: atrial signals as generated by the equivalent double layer source model. *Europace* 7, S21–S29. doi: 10.1016/j.eupc.2005.05.001

Wang, L., Gharbia, O. A., Horáček, B. M., and Sapp, J. L. (2016). Noninvasive epicardial and endocardial electrocardiographic imaging of scar-related ventricular tachycardia. *J. Electrocardiol.* 49, 887–893. doi: 10.1016/j.jelectrocard.2016.07.026

Wang, L., Wong, K. C. L., Zhang, H., Liu, H., and Shi, P. (2011). Noninvasive computational imaging of cardiac electrophysiology for 3-d infarct. *IEEE Trans. Biomed. Eng.* 58, 1033–1043. doi: 10.1109/TBME.2010.2099226

Yamashita, Y., and Geselowitz, D. B. (1985). Source-field relationships for cardiac generators on the heart surface based on their transfer coefficients. *IEEE Trans. Biomed. Eng.* 32, 964–970. doi: 10.1109/TBME.1985.325647

Yu, L., Jin, Q., Zhou, Z., Wu, L., and He, B. (2018). Three-dimensional noninvasive imaging of ventricular arrhythmias in patients with premature ventricular contractions. *IEEE Trans. Biomed. Eng.* 65, 1495–1503. doi: 10.1109/TBME.2017.2758369

Zhou, S., Sapp, J. L., Dawoud, F., and Horáč, B. M. (2018). Localization of activation origin on patient-specific epicardial surface by empirical bayesian method. *IEEE Trans. Biomed. Eng.* doi: 10.1109/TBME.2018.2872983. [Epub ahead of print].

Conflict of Interest Statement: DP and MC are employed by EP Solutions SA, Switzerland (EPS). SZ and MB are providing clinical support for EPS. PvD is an owner of Peacs BV, Netherlands.

The remaining authors declare that the research was conducted in the absence of any commercial or financial relationships that could be construed as a potential conflict of interest.

A. APPENDIX: PSEUDO-CODE FOR EMPLOYED PIPELINE

Some datasets of ventricular ectopic excitation, though simulated with a cellular automaton, could be found on the open ECGI validation platform EDGAR. For dynamic time warping, the authors used a *Python* implementation available under https://github.com/pierre-rouanet/dtw. The fastest route algorithm is based on Dijkstra's shortest path routine, for which multiple numeric realizations are freely available.

To systematize the inverse processing flow applied, we provide its pseudo-code in the following:

Algorithm 1 *

Inverse distance map $1/c_p$ calculation

Input: BSPMs matrix Y, transfer matrix A, functions *FRA* and *DTW*

$[m, n] = size(A)$

$c_p = zeros(n,)$

$\bar{Y} = (Y - mean(Y, axis = 0))/std(Y, axis = 0)$ z-normalization of each BSPMs column

for $i = 1, \ldots, n$ **do**

$\tau_i \leftarrow FRA(i)$ FRA-based activation times due to the onset at the cardiac node i

$\widetilde{Y} = A * TMP(\tau_i)$ test BSPMs due to cardiac node i using formula (1)

$\widetilde{Y} = (\widetilde{Y} - mean(\widetilde{Y}, axis = 0))/std(\widetilde{Y}, axis = 0)$

$dist_i$, $p_i \leftarrow DTW(\widetilde{Y}, Y)$

the optimal path p_i itself is not further used

$c_p(i) = dist_i$

end for

return $1/c_p$

frontiers in Physiology

METHODS
published: 27 March 2019
doi: 10.3389/fphys.2019.00273

Considering New Regularization Parameter-Choice Techniques for the Tikhonov Method to Improve the Accuracy of Electrocardiographic Imaging

Judit Chamorro-Servent [1,2,3,4*], *Rémi Dubois* [1,5,6] *and Yves Coudière* [1,2,3]

[1] *IHU-Liryc, Electrophysiology and Heart Modeling Institute, Foundation Bordeaux Université, Bordeaux, France,* [2] *CARMEN Research Team, INRIA, Bordeaux, France,* [3] *Univ. Bordeaux, IMB UMR 5251, CNRS, Talence, France,* [4] *Univ. Pompeu Fabra, PhySense Group, DTIC and BCN-Medtech, Barcelona, Spain,* [5] *Univ. Bordeaux, Centre de Recherche Cardio-Thoracique de Bordeaux, U1045, Bordeaux, France,* [6] *INSERM, Centre de Recherche Cardio-Thoracique de Bordeaux, U1045, Bordeaux, France*

The electrocardiographic imaging (ECGI) inverse problem highly relies on adding constraints, a process called regularization, as the problem is ill-posed. When there are no prior information provided about the unknown epicardial potentials, the Tikhonov regularization method seems to be the most commonly used technique. In the Tikhonov approach the weight of the constraints is determined by the regularization parameter. However, the regularization parameter is problem and data dependent, meaning that different numerical models or different clinical data may require different regularization parameters. Then, we need to have as many regularization parameter-choice methods as techniques to validate them. In this work, we addressed this issue by showing that the Discrete Picard Condition (DPC) can guide a good regularization parameter choice for the two-norm Tikhonov method. We also studied the feasibility of two techniques: The U-curve method (not yet used in the cardiac field) and a novel automatic method, called ADPC due its basis on the DPC. Both techniques were tested with simulated and experimental data when using the method of fundamental solutions as a numerical model. Their efficacy was compared with the efficacy of two widely used techniques in the literature, the L-curve and the CRESO methods. These solutions showed the feasibility of the new techniques in the cardiac setting, an improvement of the morphology of the reconstructed epicardial potentials, and in most of the cases of their amplitude.

Keywords: inverse problem, Tikhonov, regularization, electrocardiography, MFS, ill-posed, ECG, body surface potentials

OPEN ACCESS

Edited by:
Maria S. Guillem, Universitat Politècnica de València, Spain

Reviewed by:
Michael Alan Colman, University of Leeds, United Kingdom
Óscar Barquero-Pérez, Universidad Rey Juan Carlos, Spain

***Correspondence:**
Judit Chamorro-Servent
judit.chamorro@upf.edu

Specialty section:
This article was submitted to Cardiac Electrophysiology, a section of the journal Frontiers in Physiology

Received: *15 September 2018*
Accepted: *28 February 2019*
Published: *27 March 2019*

Citation:
Chamorro-Servent J, Dubois R and Coudière Y (2019) Considering New Regularization Parameter-Choice Techniques for the Tikhonov Method to Improve the Accuracy of Electrocardiographic Imaging. Front. Physiol. 10:273. doi: 10.3389/fphys.2019.00273

INTRODUCTION

Cardiovascular diseases causes 17.9 million deaths every year, accounting for 31% of all global deaths. Electrocardiographic imaging (ECGI) is a non-invasive technique that reconstructs epicardial potentials and epicardial activation maps by combining body surface measurements with respective epicardial and body geometries. In a recent manuscript comparing the non-invasive ECGI with prior invasive techniques (Duchateau et al., 2018), the authors summarized the use of

ECGI in different pre-clinical and clinical settings. While (Duchateau et al., 2018) highlights the favorable outcome of ECGI for treatment response prediction of cardiac resynchronization and ablation guidance for atrial fibrillation and ventricular tachycardia; it also states the need of further work on the ECGI inverse problem to improve its accuracy.

The ECGI inverse problem of computing epicardial potentials, Φ_E, from the body surface measured potentials, Φ_T, (MacLeod and Brooks, 1998; Ramanathan et al., 2004; Oostendorp et al., 2011; Wang et al., 2011; Oosterom van, 2012; Haissaguerre et al., 2013; Rudy, 2013; Cochet et al., 2014; Dubois et al., 2015; Shah, 2015) is an ill-posed problem (MacLeod and Brooks, 1998; Milanič et al., 2014; Cluitmans et al., 2015; Shah, 2015; Figuera et al., 2016). By introducing additional information, by using regularization techniques, we can overcome this ill-posedness (MacLeod and Brooks, 1998; Milanič et al., 2014; Cluitmans et al., 2015; Shah, 2015; Figuera et al., 2016).

Two recent manuscripts (Milanič et al., 2014; Figuera et al., 2016) studied the performance of different regularization techniques and concluded that due to the little differences among the more than 13 techniques used in each study, the most likely method to solve the ECGI problem in absence of prior information about the epicardial potentials was the two-norm Tikhonov regularization technique.

The two-norm Tikhonov regularization method (from now on referred to as Tikhonov) constrains the solution to be smooth or to have a small signal energy resolution. The Tikhonov regularization parameter weights the residual norm against the solution norm. Its role is to find a balance between solutions based on the body surface potential measurements and solutions that are constrained too much. Parameter-choice methods therefore became very data dependent (Hansen, 2010). Finally, regularization parameters that may perform well for a determined numerical model, may perform poorly when changing key factors of the model, such as the discretization or the boundary conditions (Hansen, 2010; Chamorro-Servent et al., 2016a,b). Then, for solving different clinical problems (different data) and different numerical models, it is preferable to have several automatic parameter-choice algorithms available (Hansen, 2010; Chamorro-Servent et al., 2016a,b).

In many cases, the regularization parameter, α, from the Tikhonov method is selected manually. This is done by subjectively choosing the value that provides the best results from a sequence of regularization parameters. The procedure becomes user dependent and time consuming and less likely reproducible. Several automatic methods have been suggested to overcome this problem. These include: (i) Strategies requiring prior knowledge of the noise (such as unbiased predictive risk estimator method, the discrepancy principle method, or the normalized cumulative periodogram), and (ii) strategies that do not need *a priori* information (such as zero-crossing method, Composite Residual and Smoothing Operator, L-curve, generalized cross-validation) (Hansen, 2010). For the ECGI, we will focus on the latter. In addition, from this latter group, we will focus on regularization parameter-choice methods that can easily be extended to the new goals (i.e., methods that not only consider information about the residual norm but also about the solution norm). This choice is due to the recent interest in improving the ECGI inverse solution by introducing physiological-based prior information on the regularization term (Figuera et al., 2016; Duchateau et al., 2018).

The automatic regularization parameter-choice method previously used in the ECGI literature, when using the method of fundamental solution (MFS) (Rudy, 2004; Wang and Rudy, 2006), without prior information, is the Composite Residual and Smoothing Operator (CRESO) technique (Colli-Franzone et al., 1985). The CRESO method has been found to provide the minimum root-mean-square error (RMSE) between the computed epicardial potentials (Φ_E) and the measured ones (Rudy, 2004). When other numerical models were used to solve the ECGI problem (such as the Boundary Element method), the community has commonly used the L-curve method to find the regularization parameter (Milanič et al., 2014; Cluitmans et al., 2015; Figuera et al., 2016).

Both the CRESO and the L-curve methods have shown efficacy in the wide inverse problems' bibliography (Ruan et al., 1999; Rudy, 2004; Wang and Rudy, 2006; Hansen, 2010; Milanič et al., 2014; Cluitmans et al., 2015; Figuera et al., 2016). However, it becomes challenging to find an automatic regularization parameter-choice method for Tikhonov regularization that is suitable for all ill-posed inverse problems (Hansen, 2010). The CRESO and the L-curve techniques may require *a priori* information and/or manual adjustment (Rudy et al., 2006), due to an over-regularization of the solution. In addition, the convergence of the L-curve has failed in some cases, when the generalized Fourier coefficients of the data decayed at the same rate or a lower rate than the singular values (SVs) of the operator (Vogel, 1996).

PC Hansen showed that a necessary mathematical condition for the existence of a meaningful solution for Tikhonov regularization is the Discrete Picard Condition (DPC) (Hansen, 1990, 2010). DPC says exactly that "a good regularization parameter avoids SVs decaying to zero faster than the respective Fourier coefficients of the data." The DPC has been used as a visual verification tool when studying the suitability of a regularization parameter for Tikhonov in several fields (Hansen, 1990, 2010; Chamorro-Servent et al., 2011), including ECG (Greensite et al., 1998). However, to the best of our knowledge an automatic DPC-based method does not exist yet.

Finally, the U-curve method has been introduced to overcome some drawbacks caused by the L-curve method in other fields (Krawzyck-Stando and Rudnicki, 2007; Chamorro-Servent et al., 2011; Chen et al., 2016), such as: (i) its non-convergence, (ii) the over smoothing of its solution, (iii) its lack of computational robustness when dealing with large scale problems. The L-curve computational cost has already been questioned in the ECGI setting (Figuera et al., 2016).

The target of this paper is to show the feasibility of the U-curve method, never used in the cardiac inverse problem setting, and to develop a new automatic DPC-based method, named ADPC. Both techniques are validated

when using the MFS with simulated and experimental data. Their efficacy (in terms of amplitude and morphology preservation of the reconstructed potentials and dV/dT patterns) is compared with the existent L-curve and CRESO methods.

As a first step, we present the MFS and the Tikhonov regularization method, we summarize the role of the DPC in the Tikhonov regularization, and we introduce the different regularization parameter-choice methods. Afterwards, we describe the *in-silico* and experimental data, as well as the statistical analysis performed to compare the results. Later, we summarize the main results obtained. Finally, we draw conclusions and discuss the issues and the limitations raised.

METHODS

The Method of Fundamental Solution (MFS) and l2-Norm Tikhonov Regularization

In the MFS (Wang and Rudy, 2006), the potential expression is defined as a linear combination of the Laplace fundamental solutions over a discrete set of virtual source points. The necessary virtual source points are located outside of Ω, where Ω is the domain of interest, specifically the volume conductor enclosed by the body surface (Γ_T) and the epicardial surface (Γ_E) . The potential Φ for xϵΩ is stated as $\Phi(\boldsymbol{x}) = \boldsymbol{a_0} + \sum_{j=1}^{N_S} \boldsymbol{f}\left(|\boldsymbol{x}-\boldsymbol{y_j}|\right)\boldsymbol{a_j}$, where the $\left(\boldsymbol{y_j}\right)_{j=1..N_S}$ are the N_S fixed locations of the virtual sources points $\left(\boldsymbol{y_j} \notin \Omega\right)$, and the $\left(\boldsymbol{a_j}\right)_{j=1..N_S}$ are their respective coefficients. Here, $\boldsymbol{f}$ stands for the Laplace fundamental solution, $f\left(\boldsymbol{x},\boldsymbol{y_j}\right) = \frac{1}{4\pi r}$, where $\boldsymbol{r} = \left|\boldsymbol{x}-\boldsymbol{y_j}\right|$ is the 3D Euclidean distance. The $N_S = N_T + N_E$ virtual sources locations are fixed by deflating the $\left(\boldsymbol{x_i^E}\right)_{i=1,2,\cdots,N_E}$ locations at Γ_E (by a numerical factor 0.8) and inflating the $\left(\boldsymbol{x_i^T}\right)_{i=1,2,\cdots,N_T}$ electrodes locations at Γ_T (by a factor 1.2), relatively to the geometrical center of the heart. This deflation and inflation schemes are based on (Wang and Rudy, 2006).

The potentials on Γ_E , $\Phi_E = \left(\Phi\left(x_i^E\right)\right)_{i=1,\cdots,N_E}$, can be also expressed by the equation above as $\Phi\left(x_i^E\right) = a_0 + \sum_{j=1}^{N_S} f\left(\left|x_i^E - y_j\right|\right)a_j$, where the only unknowns are the coefficients of the virtual sources $\left(a_0, a_1, \cdots, a_{N_S}\right)$. Such coefficients are found in (Wang and Rudy, 2006) by imposing on Γ_T the Dirichlet ($\Phi = \Phi_T$) and the zero-flux or homogeneous Neumann ($\partial_n\Phi = 0$) boundary conditions in an equivalent weight. This is done by using potential definition and the values of its normal derivatives, and it yields to solve the linear system

$$\Phi\left(x_i^T\right) = a_0 + \sum_{j=1}^{N_S} f\left(\left|x_i^T - y_j\right|\right)a_j = \Phi_T,$$
$$\partial_n\Phi\left(x_i^T\right) = a_0 + \sum_{j=1}^{N_S} \partial_{n_i} f\left(\left|x_i^T - y_j\right|\right)a_j = 0$$

where $\Phi_T = (\Phi_i)_{i=1,\cdots,N_T}$ are the potentials recorded on the $\left(x_i^T\right)_{i=1,2,\cdots,N_T}$ torso electrodes locations.

This system can be written in a matrix notation as $Ma = b$, being

$$M = \begin{pmatrix} 1 & f\left(|x_1^T - y_1|\right) & \cdots & f\left(|x_1^T - y_{N_S}|\right) \\ \vdots & & \ddots & \vdots \\ 1 & f\left(|x_{N_T}^T - y_1|\right) & \cdots & f\left(|x_{N_T}^T - y_{N_S}|\right) \\ 0 & \partial_{n_1} f\left(|x_1^T - y_1|\right) & \cdots & \partial_{n_1} f\left(|x_1^T - y_{N_S}|\right) \\ \vdots & & \ddots & \vdots \\ 0 & \partial_{n_{N_T}} f\left(|x_{N_T}^T - y_1|\right) & \cdots & \partial_{n_{N_T}} f\left(|x_{N_T}^T - y_{N_S}|\right) \end{pmatrix},$$

$$a = \left(a_0, a_1, \cdots, a_{N_S}\right)^T \epsilon \mathbb{R}^{1+N_s} \text{ and } b = \begin{pmatrix} \Phi_T \\ 0 \end{pmatrix} \epsilon \mathbb{R}^{2N_T}.$$

Then, finding the sources coefficients ($a\epsilon\mathbb{R}^{1+N_s}$) results in solving a quadratic minimization problem

$$J(a,\alpha) = \frac{1}{2}\left\|Ma - b\right\|^2 + \frac{\alpha^2}{2}\|a\|^2,$$

where $\alpha > 0$ is the Tikhonov regularization parameter.

The Tikhonov solution can be defined in terms of singular values (SV) decomposition of M ($M = USV^T$), by equaling the gradient of $J(a,\alpha)$ to zero and writing $I = VV^T$

$$\nabla J_a(a,\alpha) = \frac{1}{2}\nabla\left(\left(Ma-b\right)^T\left(Ma-b\right) + \alpha^2 Ia^T a\right)$$
$$= \left(M^T M\right)a - M^T b + \alpha^2 Ia = 0,$$
$$a_\alpha = \left(M^T M + \alpha^2 I\right)^{-1} M^T b = \sum_{i=1}^{\min\left(2^* N_{T,} N_S+1\right)} \frac{\sigma_i^2}{\sigma_i^2+\alpha^2} u_i^T b v_i = \sum_{i=1}^{\min\left(2^* N_{T,} N_S+1\right)} \frac{\sigma_i^2}{\sigma_i^2+\alpha^2}\frac{u_i^T b}{\sigma_i} v_i,$$

where σ_i are the SVs (the elements of the diagonal matrix S) in descending order, $\sigma_1 \geq \cdots \geq \sigma_{\min\left(2^* N_{T,} N_S+1\right)}$.

Once the Tikhonov regularization problem has been solved, we can calculate the epicardial potentials, $\Phi\left(x_i^E\right)$.

Discrete Picard Condition (DPC)

The DPC is satisfied "if the so-called Fourier coefficients of the right-hand side (when expressed in terms of the generalized SV decomposition coefficients), $\left|u_i^T b\right|$, decay to zero faster than the respective generalized SVs, σ_i's." In other words, the regularization parameter must be used to control the undesired high-frequency oscillations that contaminate the solution.

The Picard plot (Hansen, 1990, 2010), depicts the $\left|u_i^T b\right|$ and σ_i-values against their respective quotient in a same logarithmic scale plot.

In ill-posed problems the solution coefficients $\frac{\left|u_i^T b\right|}{\sigma_i}$ increase for larger values of the index i. Hence, the computed solutions ($a_\alpha = \sum_{i=1}^{\min\left(2^* N_{T,} N_S+1\right)} \frac{\sigma_i^2}{\sigma_i^2+\alpha^2}\frac{u_i^T b}{\sigma_i} v_i$ above) are completely dominated by the smallest SVs. In these cases, if we want

to calculate a satisfactory solution by means of Tikhonov regularization, the DPC must be fulfilled (Vogel, 1996; Hansen, 2010). The DPC allows to balance how well the regularized solution approaches the unknown (i.e., the exact solution). The σ_i above the regularization parameter α (useful SVs) must decay to zero less quickly than the corresponding right-hand side coefficients, $\left| u_i^T b \right|$. In other words, the DPC says that an ill-conditioned system must be regularized if a suitable solution is to be obtained and a solution based on a vector $\frac{|u_i^T b|}{\sigma_i}$ that only increases is generally not useful.

Automatic Regularization Techniques

Composite Residual and Smoothing Operator (CRESO)

The CRESO method (Colli-Franzone et al., 1985) was presented as a practical method but has turned out to be extensively accepted as the preferred parameter choice-method in widely ill-posed bioelectric inverse problems (Ruan et al., 1999). It chooses the parameter value which produces the first local maximum of the difference between the derivative of the regularization term and the derivative of the residual term

$$C(\alpha) = \left\{ \frac{d}{d(\alpha^2)} \left(\alpha^2 \left\| a(\alpha) \right\|^2 \right) - \frac{d}{d(\alpha^2)} \left\| Ma(\alpha) - b \right\|^2, \alpha > 0 \right\}$$

L-Curve

The L-curve has become the best-known method for assessing a regularization parameter-value in widely ill-posed problems fields (Hansen, 1990; Hansen and O'Leary, 1993; Ruan et al., 1999). It is defined in terms of

$$L(\alpha) = \left\{ \left(\left\| Ma(\alpha) - b \right\|, \left\| a(\alpha) \right\| \right), \alpha > 0 \right\}$$

If we plot the L-curve, it has a L-shape and we can choose the regularization parameter value by using Hansen and O'Leary's criterion (Hansen, 1990; Hansen and O'Leary, 1993). This criterion chooses the α-value corresponding to the point of maximum curvature on the log-log plot of the L-curve.

U-Curve

The U-curve (Krawzyck-Stando and Rudnicki, 2007) is defined as the log-log scale plot of the sum of the inverse of the regularized solution norm $\left\| a(\alpha) \right\|$ and the respective residual error norm $\left\| Ma(\alpha) - b \right\|$, for $\alpha > 0$

$$U(\alpha) = \frac{1}{\left\| Ma(\alpha) - b \right\|^2} + \frac{1}{\left\| a(\alpha) \right\|^2}$$

The U-curve plot has a U-shape. The optimum regularization parameter is the value for which the U-curve achieves its minimum. And the sides of the U-curve correspond to the regularization values for which either the solution norm or the residual norm dominates. When dealing with large scale problems, the U-curve is computationally efficient. This is due to its a priori interval definition where the appropriate regularization parameter is located (Krawzyck-Stando and Rudnicki, 2007; Chamorro-Servent et al., 2011; Chen et al., 2016).

ADPC: A New Regularization Parameter Choice Method

As mentioned previously, an optimal regularization value, α, for Tikhonov method, when dealing with l2-norm constraints, must fulfill the DPC (Hansen, 1990, 2010). This means that the σ_i above the suitable α must not decay to zero faster than the corresponding $\left| u_i^T b \right|$, to avoid the computed Tikhonov solutions (a_α) from being entirely dominated by the smallest SVs.

Based on the DPC, we performed an automatic regularization parameter-choice algorithm (**Figure 1**):

1. We computed the SV decomposition of the MFS matrix, M, to find the SVs (σ_i) and the left singular vectors (u_i).
2. For each time step, t_k (ms), we calculated the $\log(\left| u_i^T b_{t_k} \right|)$ and $\log(\left| u_i^T b_{t_k} \right| / \sigma_i)$ and we fit both of them by two polynomials $p\left(i, \log\left(\left| u_i^T b_{t_k} \right|\right)\right)_{t_k}$ and $q\left(i, \log\left| u_i^T b_{t_k} \right| / \sigma_i\right)_{t_k}$ of degree from 5 to 7, where $k = 1, \cdots, N_t$ are the time instants. Hence, we obtained: $p_{t_1,\cdots}, p_{t_{N_t}}$ and $q_{t_1,\cdots}, q_{t_{N_t}}$, two polynomials set for each time step t_k.
3. For each pair of polynomials at each time step, t_k, we found: $\alpha_{t_k} = \sigma_{\max\{i\}} (\sigma_0 \geq \sigma_1 \geq \cdots \geq \sigma_r > 0)$, such that DPC was fulfilled.
4. The suitable ADPC regularization parameter was defined as: $\alpha = \text{median}\left(\alpha_{t_k}\right)$.

Steps two and three of this algorithm consists in the lower limit that any suitable Tikhonov regularization value can attain to still fulfill the DPC. Step three consists of looking for the index i, which corresponds to the last SV, before the small SVs coefficients start to dominate the solution. That means, previously $\log(\sigma_i)$ starts to decrease faster than $\log(\left| u_i^T b_{t_k} \right|)$. The fitting of the $\log(\left| u_i^T b_{t_k} \right|)$ and $\log(\left| u_i^T b_{t_k} \right| / \sigma_i)$ by two polynomials in step two is done to simplify the automatic achievement of the optimal index i (in step three).

In-silico and Experimental Data

A total of sixteen datasets were used to test our algorithms, eight *in-silico* data and eight experimental data. In both cases, body surface potentials and epicardial potentials were provided.

In-silico Data

To test the effect of the new approaches described and to compare them with previous ones, eight *in-silico* different activation patterns were used (Duchateau et al., 2017). This included, one single site pacing in the right ventricular free wall, three single sites pacing in the left ventricular (lateral endocardial wall, mid wall, and lateral epi) and four single spiral waves. A monodomain reaction-diffusion model was simulated in a realistic 3D model of the human ventricles to mimic the propagating activation (Duchateau et al., 2017). The Ten Tusscher et al. model for the human ventricular myocyte (Ten Tusscher et al., 2004) was used to compute the transmembrane ionic currents. These currents were used to calculate the extracellular potential distribution all over the torso, by solving a static bidomain problem in a torso mode at 1 mm resolution (Potse et al., 2009). The torso model had heterogeneous conductivity, with anisotropic skeletal muscle,

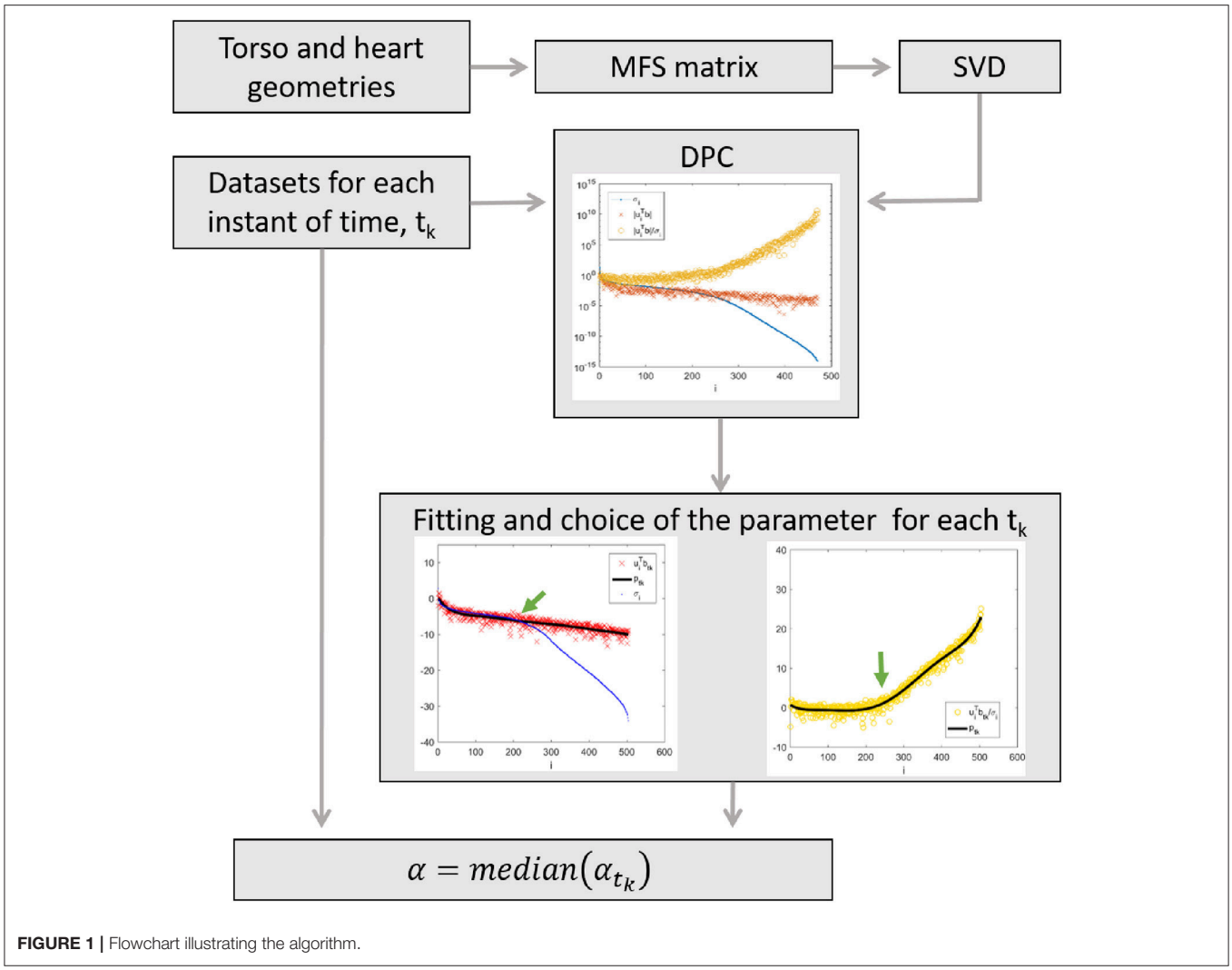

FIGURE 1 | Flowchart illustrating the algorithm.

lungs, and intracavitary blood. The heart model comprised of right and left ventricles at 0.2 mm spatial resolution. From the rule-based fiber orientation derived an anisotropic conduction in the heart model. Both, heart and thoracic anatomies were based on MRI data (**Figure 2**). *In-silico* Φ_T and Φ_E every 1 ms were provided by these simulations.

Experimental Data

To test how much the regularization parameter-choice depended on the datasets chosen and to facilitate later comparison with other possible algorithms, we decided to use, in addition to the simulated data, eight datasets from the Experimental Data and Geometric Analysis Repository (EDGAR) (Aras et al., 2015) hosted by the SCI Institute at the University of Utah and freely distributed. The purpose of EDGAR is to share and collate electrocardiological data, specifically for the validation and advancement of ECGI problems among a worldwide consortium of academic institutions.

In the EDGAR data used, both potentials from the body surface and epicardial were simultaneously measured. The data selected for this study was: Sinus rhythm and paced beats from (i) a canine experiment (paced from the epicardial left ventricular apex) (Aras et al., 2015; Cluitmans et al., 2017) and (ii) from a pig experiment (Aras et al., 2015; Bear et al., 2015). And a control and three myocardial ischemia from a canine experiment, where the high right atrium was paced while an occlusion to the LAD induced ischemia (Aras et al., 2015).

In (Cluitmans et al., 2017), a computed tomography scan was first performed to localize the electrodes and epicardial surface, second, the body-surface potentials were recorded with 192 electrodes simultaneously to 67 electrodes implanted around the epicardium via a thoracotomy. In Bear et al. (2015) epicardial electrodes were placed with a custom-made elastic sock containing 239 unipolar silver-wire electrodes (5-to 10-mm spacing) drawn over the ventricles, after which the thorax was closed, and air expelled. Flexible strips (BioSemi, Amsterdam, The Netherlands) containing 184 electrodes (30- to 45-mm spacing) were attached to the body surface. Epicardial and body surface potentials were bandlimited (0.05–1,000 Hz) and

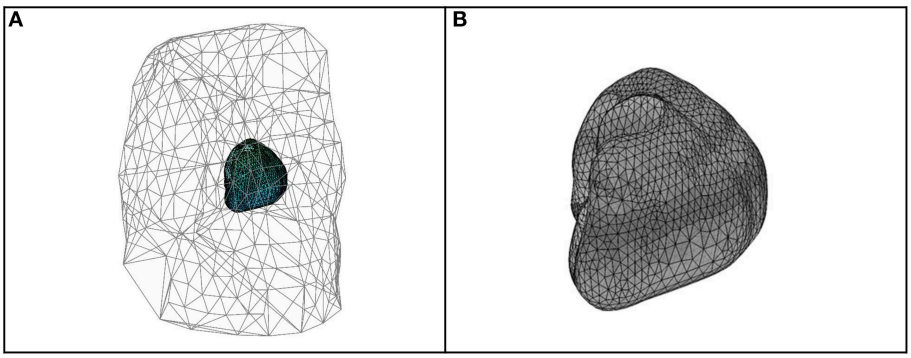

FIGURE 2 | Geometries and meshes of the *in-silico* used data. **(A)** Body surface and heart geometries, and body surface mesh. **(B)** Heart geometry and mesh.

recorded simultaneously at 2 kHz using separate acquisition systems (UnEmap, Auckland Uniservices Ltd, Auckland, New Zealand and ActiveTwo, BioSemi, respectively). Magnetic resonance imaging from the heart and thorax were acquired by placing contrast markers on the sock and body surface strips to localize the electrodes. Finally, the signals were temporally aligned by identifying the onset of a short burst of square 2 ms pulses recorded simultaneously on a single channel in both the systems.

Statistical Analysis

We computed the potentials on the epicardium for the diverse regularization parameters choices.

Afterwards, correlation coefficients (CCs) and relative root-mean squared errors (rRMSEs) were computed over the time steps as specified below.

$$CC = \frac{\sum_{i=1}^{N_{L^*}} \left(\Phi_{TE_i} - \overline{\Phi_{TE_i}}\right)\left(\Phi_{CE_i} - \overline{\Phi_{CE_i}}\right)}{\sqrt{\sum_{i=1}^{N_{L^*}} \left(\Phi_{TE_i} - \overline{\Phi_{TE_i}}\right)^2}\sqrt{\sum_{i=1}^{N_{L^*}} \left(\Phi_{ME_i} - \overline{\Phi_{ME_i}}\right)^2}}$$

$$rRMSE = \sqrt{\frac{\sum_{i=1}^{N_{L^*}} \left(\Phi_{CE_i} - \Phi_{TE_i}\right)^2}{\sum_{i=1}^{N_{L^*}} \left(\Phi_{TE_i}\right)^2}}$$

where Φ_{TE} were the target potentials and Φ_{CE} the computed ones. For the *in-silico* data, the Φ_{TE} were the simulated epicardial potentials and the Φ_{CE} the reconstructed ones at the same $N_{L^*} = N_{LE}$ locations. In the case of the experimental data, the Φ_{TE} were the potentials measured on the heart, and Φ_{CE} the reconstructed at the $N_{L^*} = N_{LS}$ closest epicardial locations.

Lastly, we showed the respective boxplots to allow their comparison. For the *in-silico* data, we also computed the dV/dT patterns and the correspondent correlation coefficients and the relative root-mean squared errors. We showed them in a table in the format [Median, (min, max)]. The highest correlation coefficients (CC) represents the best morphology and the lowest relative root mean-square error (rRMSE) represents the best amplitude of the reconstructed potentials.

RESULTS

In-silico Data

Some of the effects related to the regularization parameter choice methods for a single site pacing in the midwall left ventricle *in-silico* dataset are depicted in **Figures 3**, **4** below. The reconstructed potentials by the different regularization parameter-choice methods are plotted against the *in-silico* heart potentials in **Figures 3A–E**. Next to each subplot an arrow marks, on the heart geometry, the location where the potentials are shown. In addition, **Figures 3F** shows the DPC plot depicting the resulting regularization parameter values on horizontal lines.

The activation time (AT) maps for the single site pacing in the midwall left ventricle *in-silico* dataset are shown in **Figure 4**.

Similarly, **Figures 5**, **6** depict the same results for a single spiral wave with increased transverse conductivity. In addition, in the **Supplementary Material**, we included the dV/dT maps of the six additional *in-silico* datasets.

We can see on both DPC plots (**Figures 3F**, **5F**) that the ADPC regularization parameter was chosen just before the SVs (σ_i) start to decay faster than the respective $\left|u_i^T b_{t_k}\right|$. That moment corresponds to the moment just before $\left|u_i^T b_{t_k}\right| / \sigma_i$ starts to increase fast. If we look at the values of the solution vectors, $\left|u_i^T b_{t_k}\right| / \sigma_i$, and we try to find a minimum, followed by a significant growth in the moving average; the point where the average grows above the minimum by a certain factor, locate the points were the high frequencies starts dominating. It is well-known than when high frequencies dominate, any error, artifact, or noise will start to dominate the solution. Our regularization parameter must therefore be chosen just before this starts to happen.

The statistics for the eight simulations datasets are shown on **Figure 7** and **Table 1**. They compile the effect of the choice of the regularization parameter, on the reconstructed potentials (boxplots **Figure 7**) and on the dV/dT maps (**Table 1**). The relative root-mean squared errors give an estimate of the amplitude difference and the correlation coefficients give an estimate of the similarity of potential patterns or electrogram morphologies between measured and reconstructed data. We are interested in the highest correlation coefficients (best

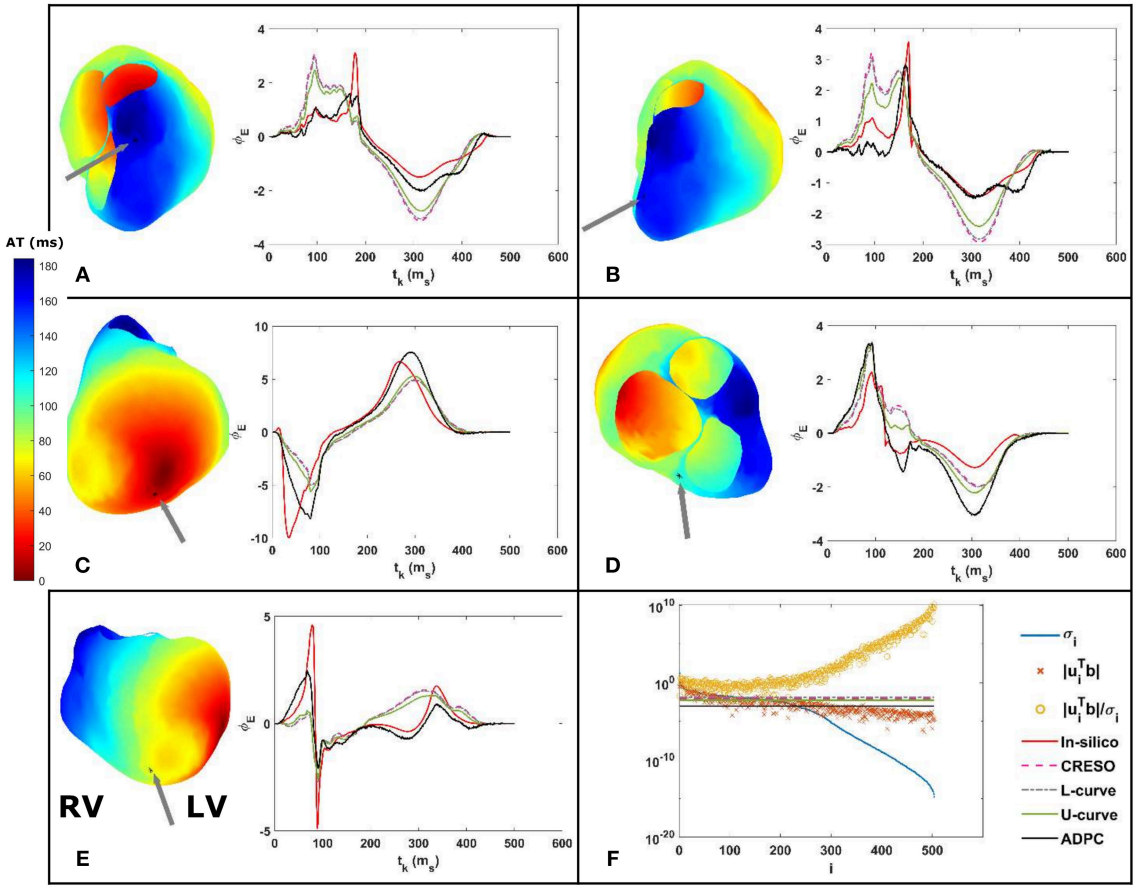

FIGURE 3 | (A–E) On the right: reconstructed potentials provided by the different regularization parameters against the *in-silico* heart potentials. On the left: arrows on the 3D *in-silico*/reference AT map correspond to the spatial heart locations where each respective potential is shown. The arrow on the 3D map of figure **(C)** shows the single site pacing in the left ventricle lateral midwall. **(F)** DPC plot for $t_K = 100$ ms with the different computed regularization parameter values drawn as horizontal lines. The legend included in **(F)** serves the respective DPC plot, as well as the **(A–E)** potential plots discussed in this figure.

morphology) and the lowest relative root-mean squared errors (best amplitude). With the boxplots, we included statistics referring to all the 501-time steps where the heart potentials were simulated (**Figures 7A,C**) and the ones referring only to the 200-time steps where the dV/dT maps were reconstructed (**Figures 7B,D**). Finally, in the **Supplementary Material**, we included the boxplots of the reconstructed potentials for each individual dataset.

The L-curve provided a clearly over-regularized solution for the singular single pacing in the right ventricle and for three of the single spiral waves inhibiting the computation of some of the dV/dT maps.

EXPERIMENTAL DATA

Like **Figures 3, 5**, the **Figure 8** shows the reconstructed potentials for the paced pig experiment referred to in section Experimental data against the measured potentials, and the DPC with the different regularization values chosen.

For the geometries of **Figure 9A** from the paced dog described in section Experimental data, the **Figures 9B–E** show: (B) the reconstructed heart potentials against the measured ones in a marked heart point, (C) the statistics boxplots of the correlation coefficients (CC), (D) the statistics boxplots relative root-mean square errors (rRMSE) and (E) the DPC plot holding the different chosen regularization values.

The statistics boxplots for the different reconstructions of each paced heart and sinus rhythm datasets described in section Experimental data can be found all separately depicted in the **Supplementary Material**. **Figure 10** also includes the separated statistic boxplots for the control and the three myocardial ischemia from a canine experiment described also in section Experimental data.

Finally, **Figure 11** compiles the statistic boxplots for the different reconstructions of all the paced and sinus rhythm datasets together (A,B) and the control and myocardial ischemia together (C,D).

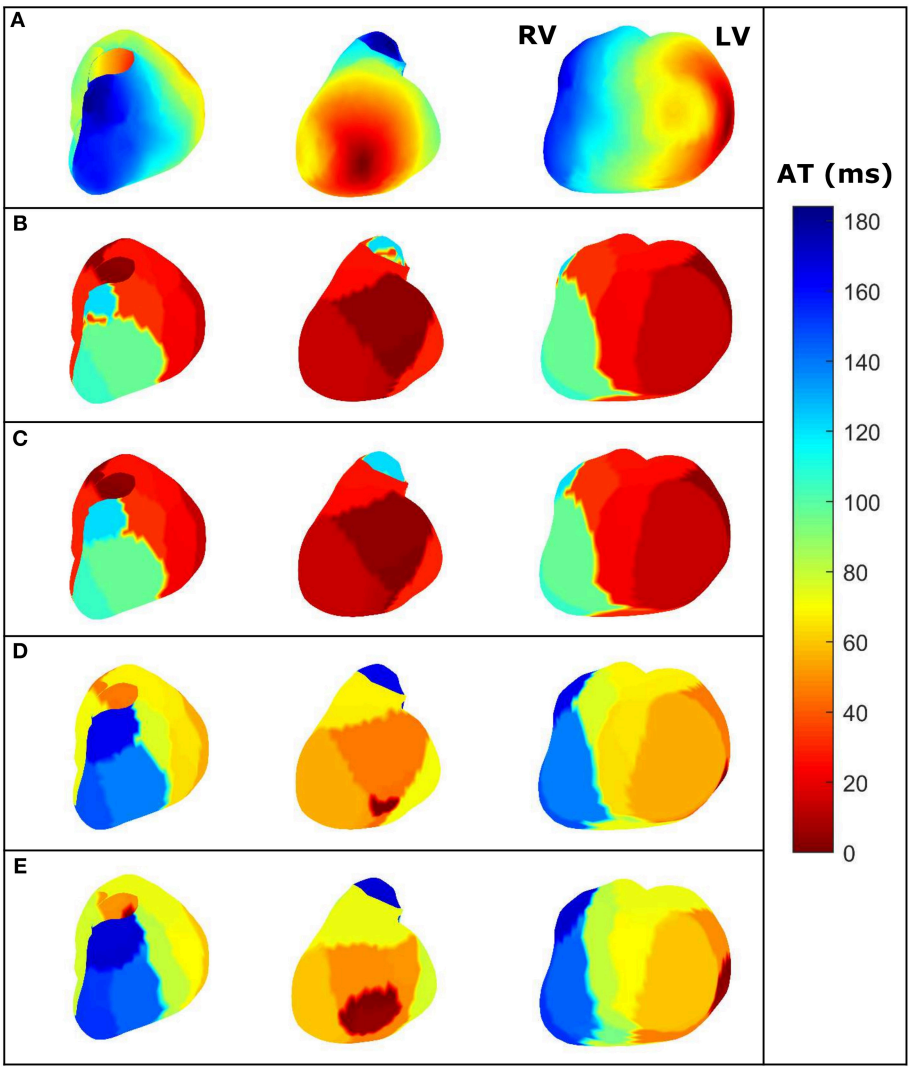

FIGURE 4 | For the same dataset employed in **Figure 3**—three different views of the AT maps reconstructed from the heart potentials from: **(A)** *In-silico* reference data, **(B)** CRESO solution, **(C)** L-curve solution, **(D)** U-curve solution, and **(E)** ADPC solution. RV and LV are denoted in the *in-silico* AT map for reference.

DISCUSSION

Two new methods were introduced to calculate the regularization parameter of the two-norm Tikhonov regularization method (referred in the manuscript as Tikhonov regularization method) when using the MFS for ECGI: The U-curve (a method never used before in cardiac applications) and the ADPC (a new automatic developed method based on DPC).

The reason for this study came about from the limitations found when using the most common parameter-choice methods (the L-Curve and the CRESO) for the ECGI MFS setting.

We focused on the introduction and validation of new automatic regularization parameter-choice methods, combining information not only about the residual norm but also about the solution norm. This choice is based on the idea of later introducing the physiologically-based prior information on the regularization term in order to improve the ECGI inverse problem, as shown in recent manuscripts (Figuera et al., 2016; Cluitmans et al., 2017; Duchateau et al., 2018; Schuler et al., 2018). To introduce the physiologically-based prior information, regularization techniques need to adjust its solution norm constraint on this information. We did not compare methods that only considered the information of the residual norm (ignoring the solution norm information), such as the cited generalized cross validation, which also did not compute a suitable regularization parameter when dealing with highly correlated errors (Hansen, 1992).

The ADPC algorithm presented here provides a suitable regularization parameter due to the behavior of the SVs of the ECGI MFS problem (decaying slower for the higher SVs and faster for the lower ones such as in **Figures 3**, **5**, **8**, **9**). The fact that the ADPC parameter choice is based on the necessary DPC

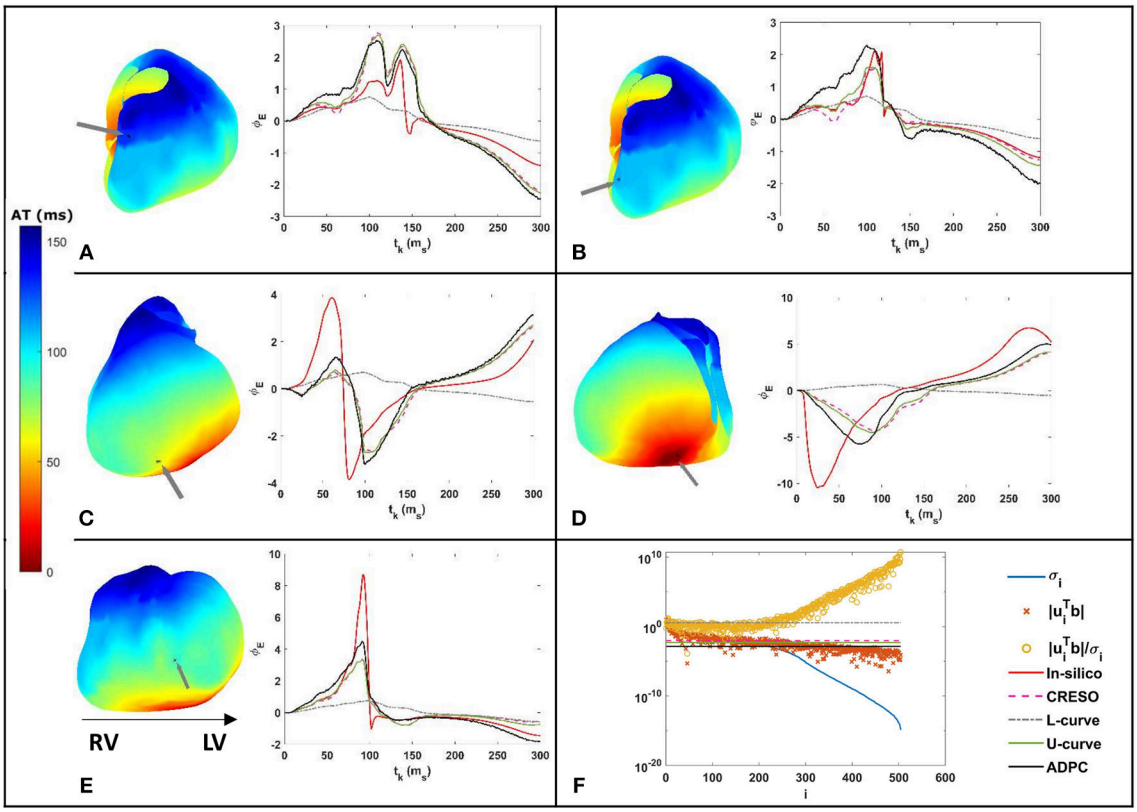

FIGURE 5 | (A–E) On the right: reconstructed potentials provided by the different regularization parameters against the *in-silico* heart potentials. On the left: arrows on the 3D *in-silico*/reference AT map correspond to the spatial heart locations where each respective potential is shown. **(F)** DPC plot for $t_K = 100$ ms with the different computed regularization parameters values drawn as horizontal lines. The legend included in **(F)** serves the respective DPC plot, as well as the **(A–E)** potential plots discussed in this figure.

fulfillment for any regularization parameter for the Tikhonov regularization method (Hansen and O'Leary, 1993; Hansen, 2010) ensures an optimal solution for highly ill-posed problems. In addition, the DPC plot gives us a valuable indication of the over-regularization level of a solution. This is perfectly shown by the location of the regularization parameters in the DPC chart and the relationship of this location with their respective reconstructed potentials and the dV/dT patterns (**Figures 3–6**). In the first DPC plot (**Figure 3F**) the CRESO, the L-curve and U-curve parameters are located fairly above the moment the SVs start to decay faster, and this results in a wider QRS (losing also the S-wave in most of cases) on the respective potentials along the time plot (**Figures 3A–E**). The U-curve method and notably the ADPC method seem to better localize the pacing on the LV lateral midwall (**Figure 4**). In the *in-silico* examples included in this manuscript and the **Supplementary Material**, the L-curve method provided the most over-regularized solution. In the cases of the single spiral wave (**Figure 5**), the L-curve parameter is located even higher on the DPC plot, and it results in an extremely over-regularized reconstruction of the potentials along time (losing both, the morphology, and the amplitude of the reconstructed potentials). This therefore causes the inhibition of the computation of the corresponding dV/dT map (data not shown in **Figure 6** or highlighted in **Table 1** as NA*). Finally, regarding the dV/dT maps in **Figure 6** we can clearly see the improvement of the ADPC solution against the CRESO solution. The dV/dT maps of each singular simulation dataset, reconstructed by the different methods, are included in the **Supplementary Material** of this manuscript.

Regarding the single site pacing simulations statistics (**Figures 7A,B**): (i) The correlation coefficients (CC) best center tendency is achieved by the ADPC method followed by the U-curve method. In addition, the correlation coefficients of these two methods and specially of the ADPC, have a larger upper spread out. While the ADPC has the smallest variability, it has some lower outlayers in the same range where the resulting interquartile values of other methods vary (being the interquartile the height of the boxes, 1st−3rd quartile). The outlayers indicate values greater than the 1.5 interquartile ranges away from the 25th percentiles. The L-curve solution has the worst correlation coefficients center tendency and the CRESO solution has a center tendency similar to the U-curve, but with higher variability. (ii) The relative root-mean squared errors (rRMSE) best center tendency is also achieved by the ADPC method followed by the U-curve and the CRESO method, but again the CRESO method shows a higher variability error. The L-curve solution

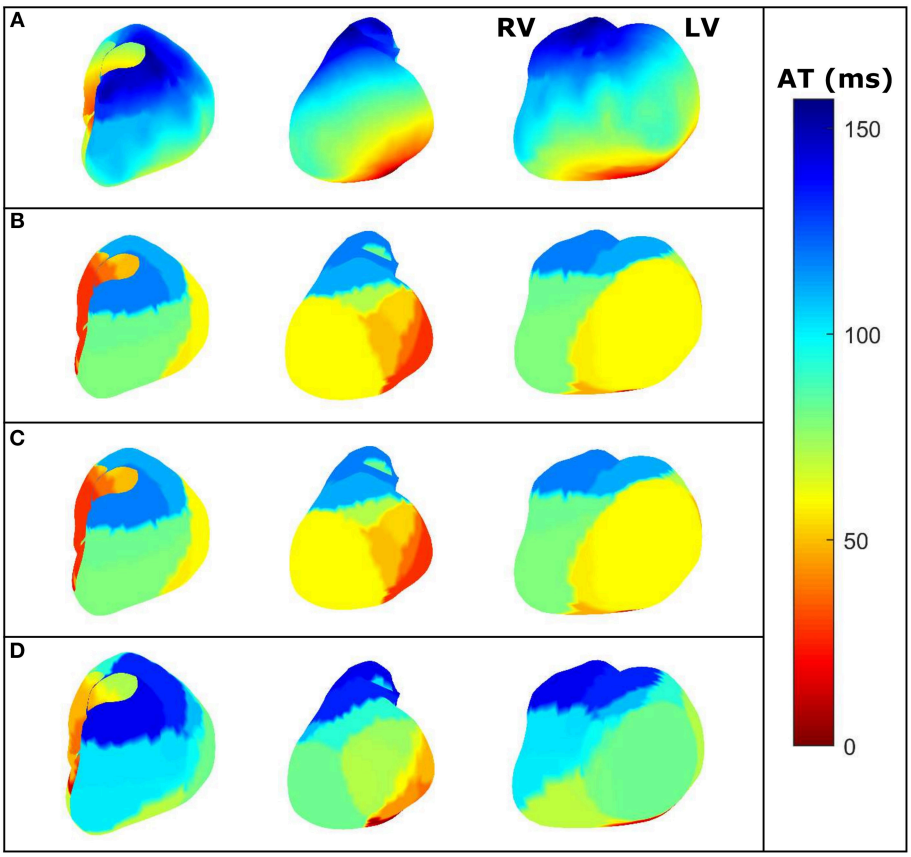

FIGURE 6 | For the same dataset employed in **Figure 5**—three different views of the dV/dT maps reconstructed from the heart potentials from: **(A)** *in-silico* reference data, **(B)** CRESO solution, **(C)** U-curve solution and **(D)** ADPC solution. The L-curve inhibited the dV/dT map computation. RV and LV are denoted in the *in-silico* AT map for reference.

also shows the worst performance in terms of relative root-mean squared error (lowest center tendency and highest variability). Finally, the upper outlayers from the ADPC resulting relative root-mean squared errors are located out of the other methods interquartile values. However, all these outlayers come from the *in-silico* LV lateral endocardial data as can be observed in the single simulations' boxplots of the **Supplementary Material**.

In the case of the single spiral simulations' statistics (**Figures 7C,D**): (i) The correlation coefficients (CC) best center tendency is achieved through the ADPC method. In addition, its distribution is also more focused in the upper values. However, the U-curve and the CRESO methods provide close results for correlation coefficients for the spirals than for the single site pacing simulations. Again, the ADPC has some outlayers inside the other methods' value ranges. The L-curve solution has the worst correlation coefficient center tendency and the highest variability, meaning that its performance (compared with the other methods solutions) is even worse than for the single site pacing simulations. (ii) The relative root-mean squared errors' (rRMSE) better center tendency is also achieved by the ADPC method followed by the U-curve and the CRESO methods. Here, the L-curve method has less upper outlayers but its center tendency (around 1) continues being the worst, and its correlation coefficients are higher distributed and are worse than the other methods.

In terms of the *in-silico* data dV/dT patterns statistics (**Table 1**): (i) In the single site pacing *in-silico* datasets, the highest correlation coefficients (CC) and lowest relative root-mean squared errors (rRMSE) are achieved by the ADPC, followed by the U-curve. The L-curve over-regularized some of the solutions that inhibit the computation of the respective activation time maps. (ii) In the case of the spirals *in-silico* datasets, the ADPC also provided the highest correlation coefficients and the lowest relative root-mean squared errors, followed by the U-curve. However, differences between the ADPC, the U-curve and the CRESO methods here are more significant in terms of correlation coefficients (morphology) than in terms of relative root-mean squared errors (amplitude), where the results are closer. Finally, the L-curve also inhibited some dV/dT map computations for the spirals *in-silico* data.

In the case of the EDGAR datasets, we found fewer differences between the different regularization parameter choice methods for the paced and sinus rhythm datasets (**Figures 8**, **9**, **11A,B** and

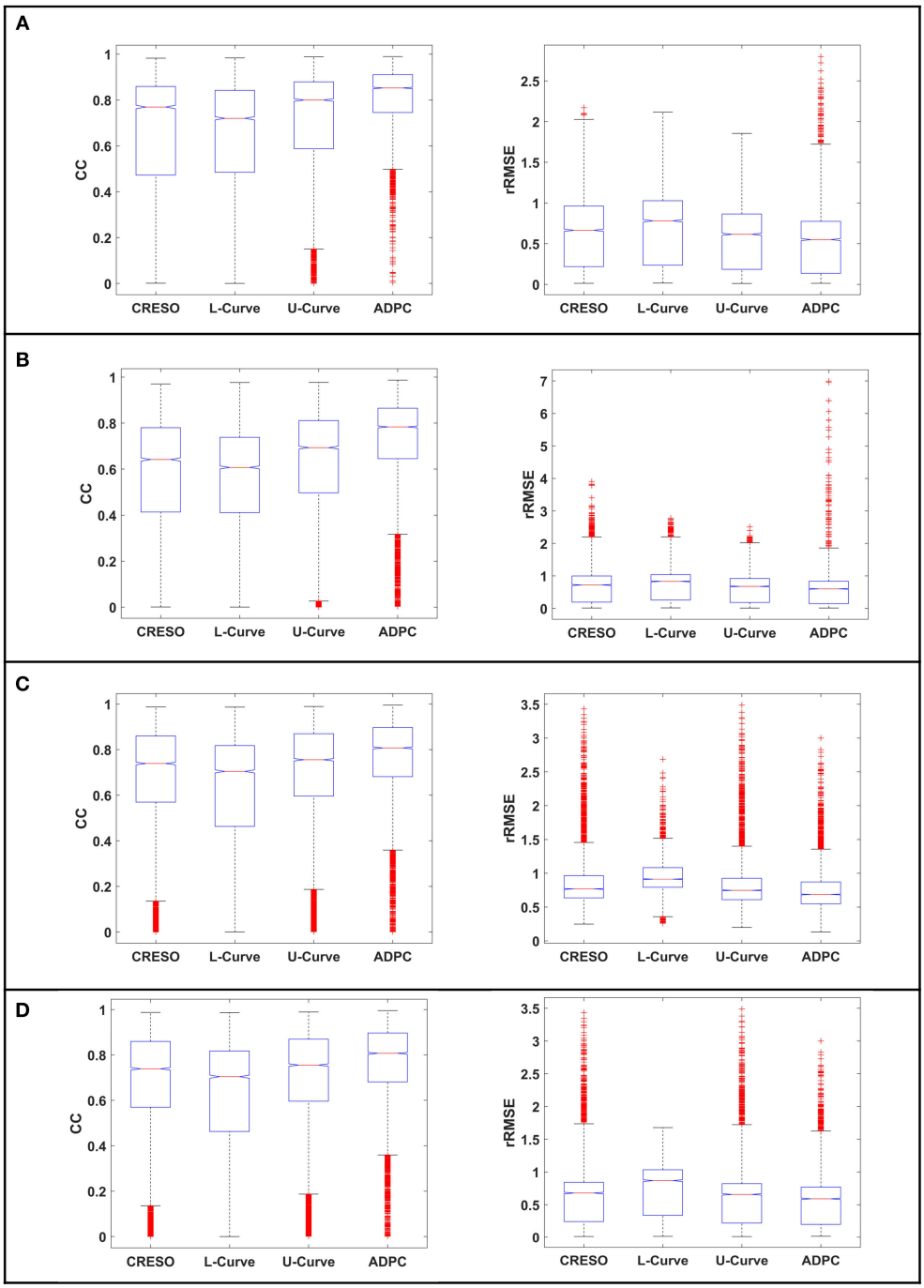

FIGURE 7 | Boxplots of the correlation coefficients (CC) and the relative root-mean squared errors (rRMSE) between the reconstructed potentials and the respective *in-silico* heart potentials: **(A,B)** for the single site pacing simulations, **(C,D)** for the spiral simulations. **(A,C)** for all the 501-time steps where the heart data was simulated. **(B,D)** for the 200-time steps where we calculate the dV/dT maps. The red crosses denote the outlayers.

respective separated boxplots in the **Supplementary Material**). However, in the case of the pig experiment described in section Experimental data (**Figure 9**) we could not impose compliance with the zero-flux or homogeneous Neumann conditions on the MFS solutions [such as in Wang and Rudy (2006) and the rest of the datasets of this manuscript]. This was due to some problems encountered when computing the normal directions for the geometries provided. In **Figure 8D**, we can see that singular values start to decay faster to zero quite late (meaning that the problem is less ill-posed than for other

TABLE 1 | Median [min, max]% differences of **(A–C)** the correlation coefficients and **(B–D)** the relative root-mean squared errors between each reconstructed dV/dT patterns and the dV/dT pattern resulting from the *in-silico* heart potentials.

(A)				(B)			
CORRELATION COEFFICIENTS (CC)				**RELATIVE ROOT-MEAN-SQUARED ERROR (rRMSE)**			
CRESO	**L-Curve**	**U-curve**	**ADPC**	**CRESO**	**L-Curve**	**U-curve**	**ADPC**
0.7735	NA*	**0.8343**	0.7948	0.5006	1	0.4272	**0.3780**
0.7691	NA*	0.8307	**0.9039**	0.5801	1	**0.5274**	**0.4395**
0.7817	0.8215	0.8498	**0.8961**	0.6063	0.5803	0.2419	**0.2009**
0.8224	0.8387	0.8702	**0.9091**	0.3248	0.3107	0.2915	**0.2665**
(C)				**(D)**			
CORRELATION COEFFICIENTS (CC)				**RELATIVE ROOT-MEAN-SQUARED ERROR (rRMSE)**			
CRESO	**L-Curve**	**U-curve**	**ADPC**	**CRESO**	**L-Curve**	**U-curve**	**ADPC**
0.8505	0.8317	0.8733	**0.9053**	0.3062	0.3187	0.2904	**0.2683**
0.8535	NA*	0.8704	**0.8902**	0.2019	1	**0.1977**	0.2134
0.8320	NA*	0.8531	**0.8971**	0.2717	1	0.1985	**0.1683**
0.8371	NA*	**0.8386**	0.8266	0.44	1	0.4654	**0.321**

(A,B) For the single site pacing. (C,D) From the in-silico heart potentials for the spirals. NA, Not applicable because the computation of the dV/dT patterns is inhibited due to the over-regularized solution provided by L-curve. The best results are highlighted in bold.*

examples). This agrees with our previous work (Chamorro-Servent et al., 2016b) where we showed that not applying the zero flux or Neumann conditions resulted in a less ill-posed problem, less dependent on the regularization choice. Therefore, minor differences between applying different regularization parameter-choices methods were found as expected in terms of the solutions for the pig datasets. The results for these datasets are not fully comparable with the rest of the manuscript due to this change on the numerical MFS problem solved. Instead, the results of **Figure 9**, fully comparable in terms of correlation coefficients (CC), continues to show an improvement on the U-curve and the ADPC solutions against the CRESO and the L-curve. Nevertheless, the authors of these datasets specified in their readme file that they had a un-solved issue with the amplitude of the recorded potentials. We therefore prefer not to draw conclusions on the resulting amplitudes (relative root-mean squared error or rRMSE) for the canine paced and sinus rhythm datasets. But in terms of the morphology of potentials, the ADPC continues to be the most stable method. For the four datasets, the ADPC keeps the potentials morphology (correlation coefficients) comparable or better than the CRESO method (the gold standard) does.

Finally, referring to the control and the three myocardial ischemia datasets from the canine EDGAR experiments, the data recorded was quite noisy, as shown in the recorded potentials snapshot of the **Supplementary Figure 10**. This resulted in poor (very high) relative root mean square errors (rRMSE). However, this is not due to an amplitude problem of the reconstructed potentials (see the **Supplementary Material**) but due to the existent noise. Nevertheless, we can see an upper and better central tendency from the U-curve and the ADPC correlation coefficients (CC) compared to the other methods, when reconstructing the ischemia datasets (**Figures 10B–D** from manuscript). This is less appreciated in the summary of the statistics, when the control case in **Figure 11C** is included.

In conclusion, this study shows the feasibility of the U-curve and the ADPC techniques in the ECGI inverse problem setting, when using the MFS as a numerical method. The new techniques result in an improvement of the morphology of the reconstructed epicardial potentials and in the *in-silico* cases of their amplitude. The ADPC seems to be the most stable method to keep the morphology of potentials.

LIMITATIONS

This study provides results for the ECGI MFS problem, such as described in Wang and Rudy (2006). The empirical lower threshold of the ADPC and the median choice works well due to the behavior of the decay of the singular values of the MFS matrix (see **Figures 3F**, **5F**, **8D**, **9E**). However, it is well-known that parameter-choice methods are problem dependent (Hansen, 2010). Note for example that the authors in Milanič et al. (2014), Cluitmans et al. (2015), Figuera et al. (2016) found suitable results through the L-curve method when using the BEM as a numerical model, which is not always the case when using the MFS instead.

As explained in the discussion, we focused on automatic methods that can be extended to include physiologically-based prior information. Nevertheless, for the cases where physiologically-based prior information of the solution could not be provided, it can be interesting to compare our methods with the generalized cross validation method.

A finer discretization of the AT for visualization, would be more sensible and provide more continuous data. In addition

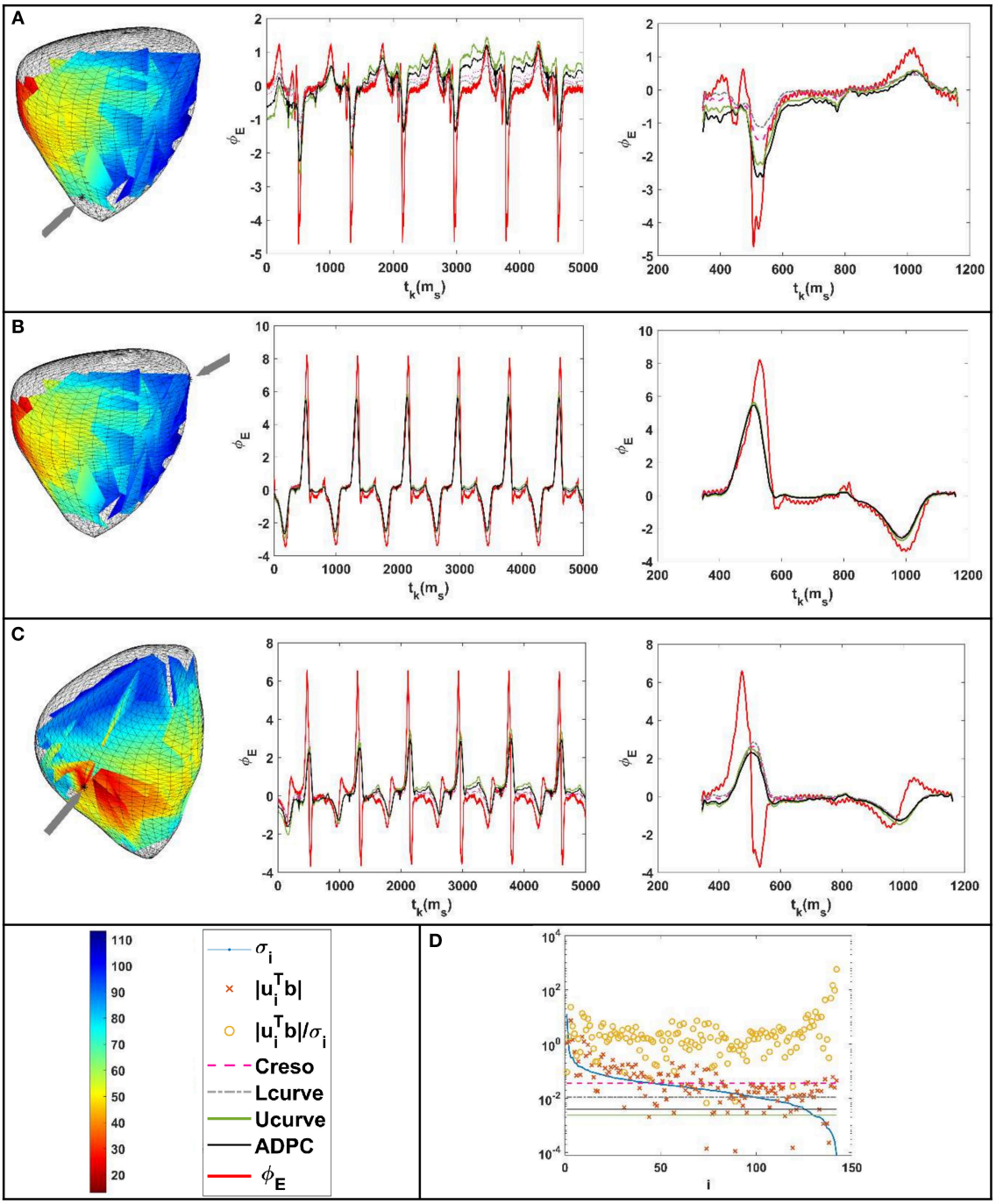

FIGURE 8 | Results for the paced beat of the pig experiment (Bear et al., 2015). **(A–C)** From the left to the right: location of the epicardium where the potentials were compared (marked with an arrow above the recorded activation pattern). Reconstructed potentials against the measured ones for all the time steps and all the parameter-choice methods such as indicated in the legend below. Respective zoom (of the reconstructed potentials against the measured ones) at the t_k interval comprised between 343 and 1,161 ms. **(D)** DPC plot at $t_k = 472$ ms with the different regularization parameters values holding on horizontal lines following the legend.

to improving the AT maps accuracy, methods such the one described in Duchateau et al. (2017) can be used.

While we anticipate in section U-curve that the U-curve method is computationally cheaper than the L-curve (due to its prior interval) (Krawzyck-Stando and Rudnicki, 2007; Chamorro-Servent et al., 2011; Chen et al., 2016), we need further studies, in terms of the computational burden of the whole parameter choice method.

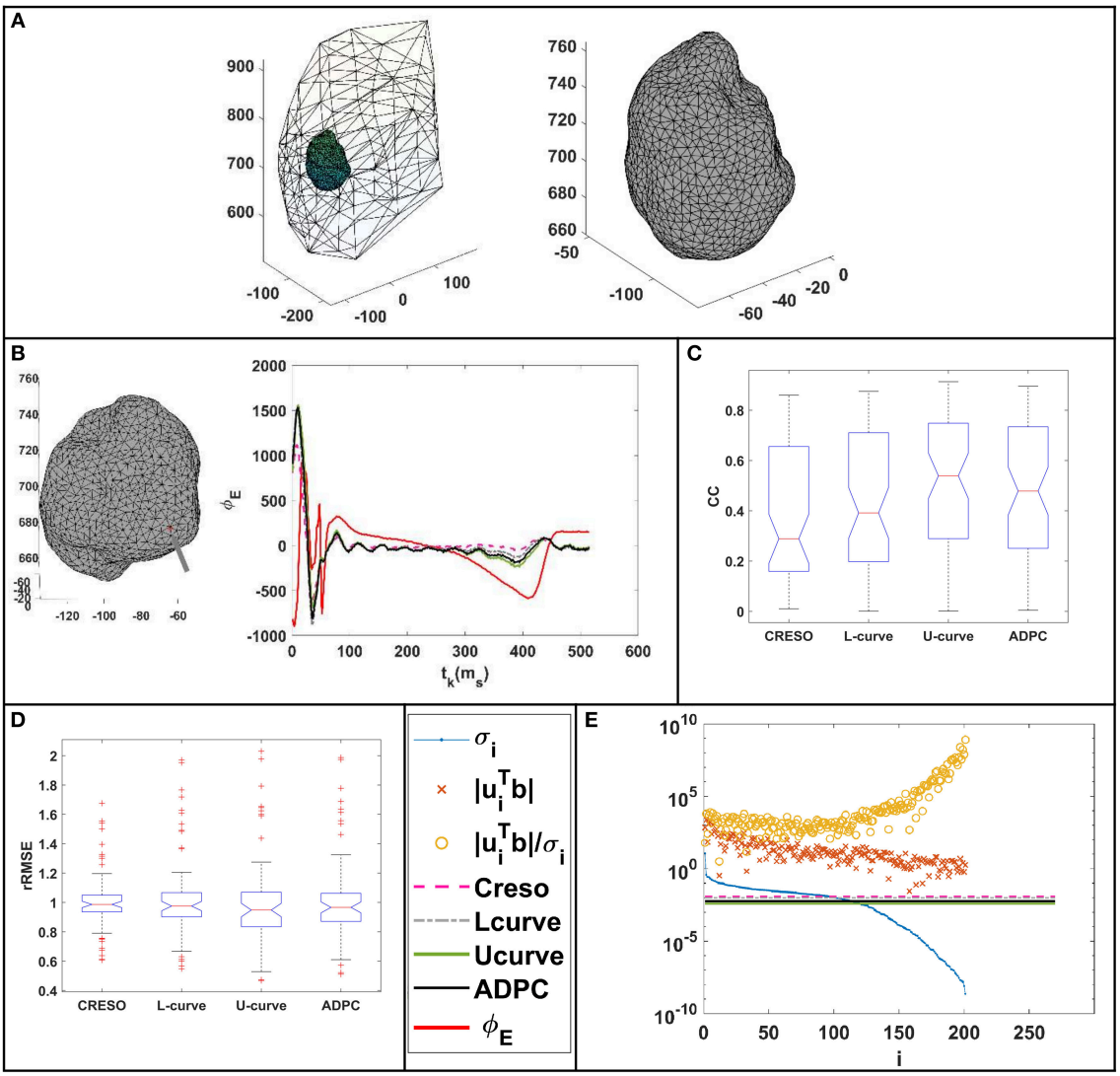

FIGURE 9 | (A) Geometries of the canine paced heart EDGAR datasets (Cluitmans et al., 2017). **(B)** Reconstructed potentials for the different regularization parameter-choice methods against the measured ones for a point of the epicardium marked with an arrow on its geometry. **(C)** Correlation coefficients (CC) between the reconstructed potentials and the respective measured heart potentials. **(D)** Relative root-mean squared errors (rRMSE) between the reconstructed potentials and the respective measured heart potentials. **(E)** DPC plot at $t_k = 35$ ms with the different regularization parameters values holding on horizontal lines following the legend.

If anyone wanted to use the new ADPC or the U-curve method, with other numerical problems such as the BEM, the FEM or even the MFS with different placement of the virtual source points such as (Chamorro-Servent et al., 2016a), or different boundary conditions such as (Chamorro-Servent et al., 2016b), we recommend repeating this study before drawing further conclusions. A clear example of this is shown with the results from the pig experiments (**Figures 8**, **11A,B**), where we did not impose to the solution compliance with the zero-flux or homogeneous boundary conditions, and we found fewer differences between the methods, in agreement with (Chamorro-Servent et al., 2016b).

Finally, the ADPC method and the L-curve based on the mathematical solution of a problem with l2-norm constraints (Hansen, 2010) such as the one presented here, and may not perform as well when using constraints based on another norm (for example the l1-regularization norm) (Hansen, 2010). If l1-norm prior-information needs to be added, then the ADPC method will not work because it is based on the DPC. PC Hansen, the author of DPC (Hansen, 1990, 2010) has explained this issue well in his work. The poor performance of ADPC or L-curve in l1-regularization approaches is not due to a lack of robustness of the DPC or the method, but due to a misusage. The mathematical basis of both, the condition and the method, is the l2-norm Tikhonov solution definition. The DPC is a condition that must fulfill any regularization parameter for the l2-norm Tikhonov approach. In the latter, i.e., cases involving other regularization norm terms, the U-curve method may provide better results.

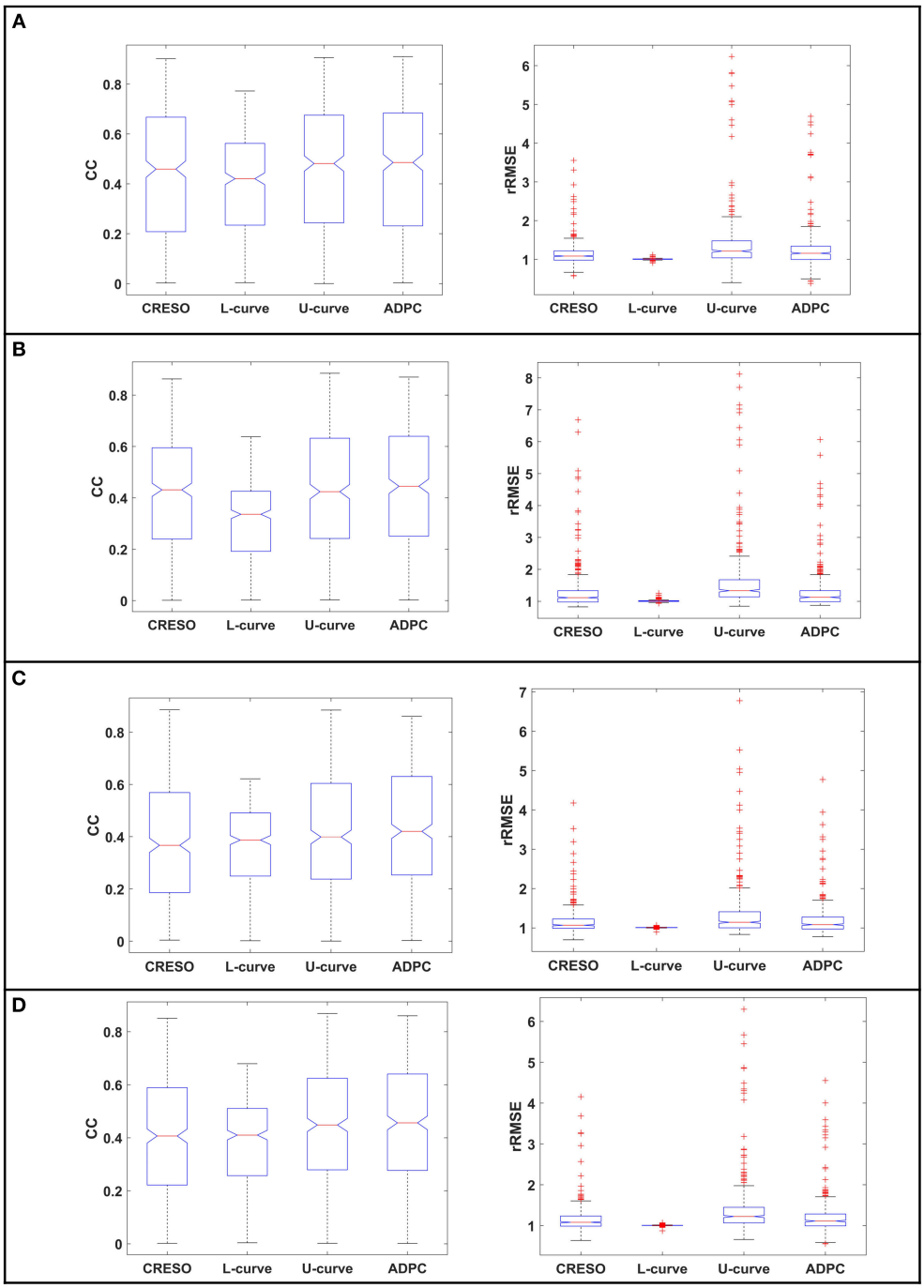

FIGURE 10 | The statistics boxplot show the correlation coefficients (CC) and relative root mean-square errors (rRMSE) for the reconstructions with the different regularization parameter-choice algorithm against the respective *in-silico* heart potentials. EDGAR canine experiments: **(A)** control, **(B–D)** myocardial ischemia's (datasets number 16, 39, and 54 from the referred EDGAR experiments). The red crosses denote the outlayers.

OUTLOOK

This study assumed that no *a priori* physiologically information about the epicardial potentials were available, while studying regularization parameter-choice methods that can be adjusted to problems introducing different l2-norm constraints. Due to the increasing number of work that proposes the incorporation electrophysiological knowledge (Figuera et al., 2016; Cluitmans et al., 2017; Duchateau et al., 2018; Schuler et al., 2018), it would be interesting to see how the U-curve and ADPC adapted

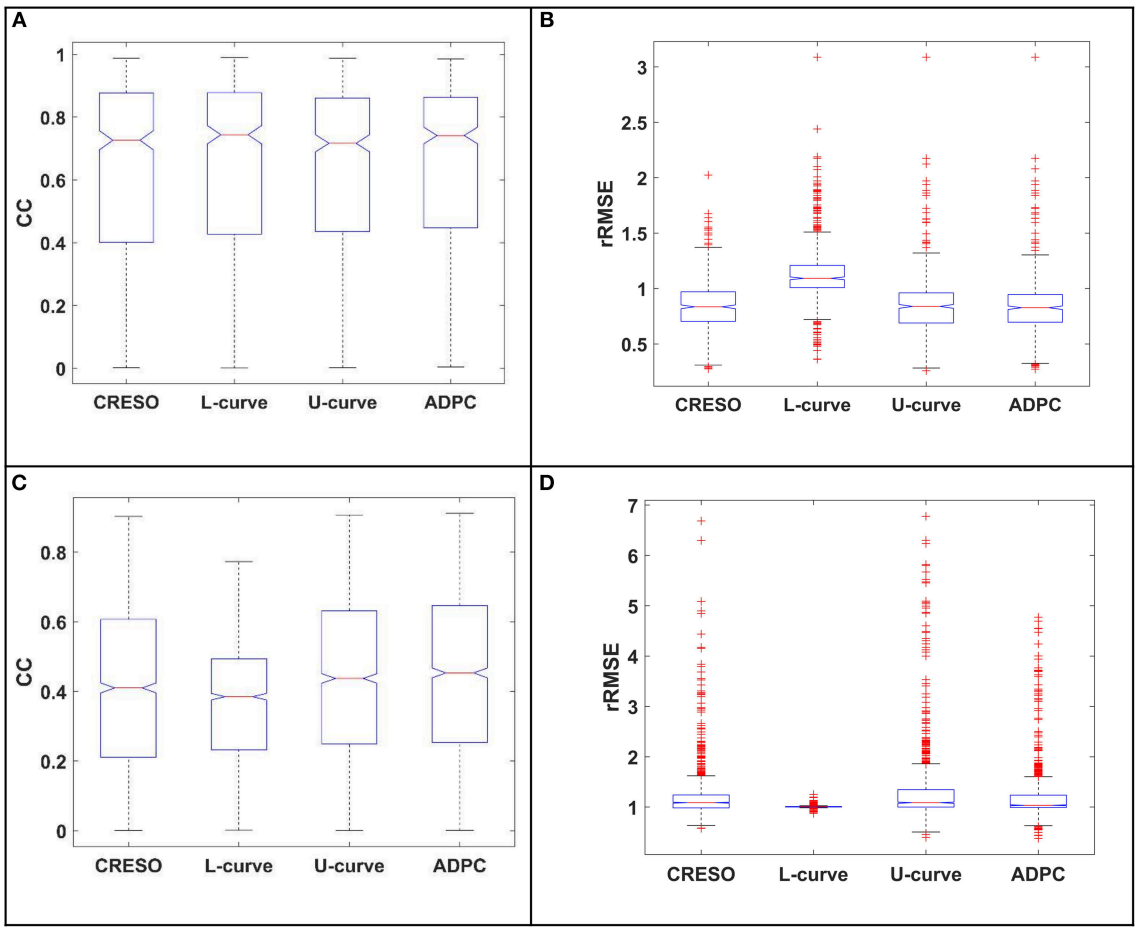

FIGURE 11 | The statistics boxplots show: **(A,C)** the correlation coefficients (CC) and **(B,D)** the relative root mean-square errors (rRMSE) for the reconstructions with the different regularization parameter-choice algorithm against the respective *in-silico* heart potentials. EDGAR experiments: **(A,B)** paced and sinus rhythm dog and pig experiments together, **(C,D)** Control and myocardial ischemia datasets canine experiments from Utah together (ischemia datasets number 16, 39, and 54 from the referred EDGAR experiments) The red crosses denote the outlayers.

methods perform when including electrophysiological prior knowledge into a l2-norm constraint.

The reader may observe that the ADPC and the U-curve continued to preserve the morphology for experimental data and specifically for high noisy data, such as the control and the three myocardial ischemia datasets from the canine EDGAR experiments (**Figure 10** and **Supplementary Figure 10**). However, it will be interesting to develop a noise robustness study for the *in-silico* data, both including noise on the measured datasets and on the geometric locations of the electrodes.

ETHICS STATEMENT

The experimental data used is from EDGAR.

AUTHOR CONTRIBUTIONS

JC-S designed and developed the ADPC method, and developed the regularization criteria techniques and the MFS, designed and conducted the study and wrote the manuscript. RD and YC provided technical expertise and contributed during manuscript preparation.

FUNDING

This study received financial support from the French Government under the Investments of the Future program managed by the National Research Agency (ANR), Grant reference ANR-10-IAHU-04 and from the Conseil Régional Aquitaine as part of the project Assimilation de données en cancérologie et cardiologie.

ACKNOWLEDGMENTS

We would like to thank Dr. Mark Potse for providing us with the *in-silico* data (Potse et al., 2009; Duchateau et al., 2017), the availably of the EDGAR data (Aras et al., 2015; Bear et al., 2015; Cluitmans et al., 2017), as well as the experiments performed

by the Cardiovascular Research and Training Institute (CVRTI) and the Scientific Computing and Imaging (SCI) Institute at the University of Utah with funding from the Nora Eccles Treadwell foundation and the NIH/NIGMS Center of Integrative Biomedical Computing under grant P41 GM103545-17).

SUPPLEMENTARY MATERIAL

The Supplementary Material for this article can be found online at: https://www.frontiersin.org/articles/10.3389/fphys.2019.00273/full#supplementary-material

REFERENCES

Aras, K., Good, W., Tate, J., Burton, B., Brooks, D., Coll-Font, J., et al. (2015). Experimental data and geometric analysis repository—EDGAR. *J. Electrocardiol.* 48, 975–981. doi: 10.1016/j.jelectrocard.2015.08.008

Bear, L. R., Cheng, L. K., LeGrice, I. J., Sands, G. B., Lever, N. A., Paterson, D. J., et al. (2015). Forward problem of electrocardiography. *Circulation* 8, 677–684. doi: 10.1161/CIRCEP.114.001573

Chamorro-Servent, J., Aguirre, J., Ripoll, J., Vaquero, J. J., and Desco, M. (2011). Feasibility of U-curve method to select the regularization parameter for fluorescence diffuse optical tomography in phantom and small animal studies. *Opt. Express* 19, 11490–11506. doi: 10.1364/OE.19.011490

Chamorro-Servent, J., Bear, L., Duchateau, J., Dallet, C., Coudière, Y., Dubois, R., et al. (2016a). Adaptive placement of the pseudo-boundaries improves the conditioning of the inverse problem. *Comput. Cardiol. Conf.* 43, 425–428. doi: 10.23919/CIC.2016.7868840

Chamorro-Servent, J., Bear, L., Duchateau, J., Potse, M., Dubois, R., Coudière, Y., et al. (2016b). Do we need to enforce the homogeneous Neumann condition on the Torso for solving the inverse electrocardiographic problem? *Comput. Cardiol. Conf.* 43, 705–708. doi: 10.22489/CinC.2016.123-290

Chen, M., Su, H., Zhou, Y., Cai, C., Zhang, D., Luo, J., et al. (2016). Automatic selection of regularization parameters for dynamic fluorescence molecular tomography: a comparison of L-curve and U-curve methods. *Biomed. Opt. Express* 7, 5021–5041. doi: 10.1364/BOE.7.005021

Cluitmans, M. J., Clerx, M., Vandersickel, N., Peeters, R. L., Volders, P. G., and Westra, R. L. (2017). Physiology-based regularization of the electrocardiographic inverse problem. *Med. Biol. Eng. Comput.* 55, 1353–1365. doi: 10.1007/s11517-016-1595-5

Cluitmans, M. J., Peeters, R. L., Westra, R. L., and Volders, P. G. (2015). Noninvasive reconstruction of cardiac electrical activity: update on current methods, applications and challenges. *Neth. Heart J.* 23, 301–311. doi: 10.1007/s12471-015-0690-9

Cochet, H., Dubois, R., Sacher, F., Derval, N., Sermesant, M., Hocini, M., et al. (2014). Cardiac arrythmias: multimodal assessment integrating body surface ECG mapping into cardiac imaging. *Radiology* 271, 239–247. doi: 10.1148/radiol.13131331

Colli-Franzone, P., Guerri, L., Tentoni, S., Viganotti, C., Baruffi, S., Spaggiari, S., et al. (1985). A mathematical procedure for solving the inverse potential problem of electrocardiography. Analysis of the time-space accuracy from *in vitro* experimental data. *Math. Biosci.* 77 , 353–396. doi: 10.1016/0025-5564(85)90106-3

Dubois, R., Shah, A. J., Hocini, M., Denis, A., Derval, N., Cochet, H., et al. (2015). Non-invasive cardiac mapping in clinical practice: application to the ablation of cardiac arrhythmias. *J. Electrocardiol.* 48, 966–974. doi: 10.1016/j.jelectrocard.2015.08.028

Duchateau, J., Potse, M., and Dubois, R. (2017). Spatially coherent activation maps for electrocardiographic imaging. *IEEE Trans. Biomed. Eng.* 64, 1149–1156. doi: 10.1109/TBME.2016.2593003

Duchateau, J., Sacher, F., Pambrun, T., Derval, N., Chamorro-Servent, J., Denis, A., et al. (2018). Performance and limitations of non-invasive cardiac activation mapping. *Heart Rhythm.* 16, 435–442. doi: 10.1016/j.hrthm.2018.10.010

Figuera, C., Suárez-Gutiérrez, V., Hernández-Romero, I., Rodrigo, M., Liberos, A., Atienza, F., et al. (2016). Regularization techniques for ECG imaging during atrial fibrillation: a computational study. *Front. Physiol.* 7:466. doi: 10.3389/fphys.2016.00466

Greensite, F., and Huiskamp, G.,Greensite, F., and Huiskamp, G. (1998). An improved method for estimating epicardial potentials from the body surface. *IEEE Trans. Biomed. Eng.* 45, 98–104. doi: 10.1109/10.650360

Haissaguerre, M., Hocini, M., Shah, A. J., Derval, N., Sacher, F., Jais, P., et al. (2013). Noninvasive panoramic mapping of human atrial fibrillation mechanisms: a feasibility report. *J. Cardiovasc. Electrophysiol.* 24, 711–717. doi: 10.1111/jce.12075

Hansen, P. C. (1990). The discrete Picard condition for discrete ill-posed problems. *BIT Num. Math.* 30, 658–672. doi: 10.1007/BF01933214

Hansen, P. C. (1992). Analysis of discrete ill-posed problems by means of the L-curve. *SIAM Rev.* 34, 561–580. doi: 10.1137/1034115

Hansen, P. C. (2010). *Discrete Inverse Problems: Insight and Algorithms*. Vol. 7. Philadelphia, PA: SIAM. doi: 10.1137/1.9780898718836

Hansen, P. C., and O'Leary, D. P. (1993). The use of the L-curve in the regularization of discrete ill-posed problems. *SIAM J. Sci. Comput.* 14, 1487–1503. doi: 10.1137/0914086

Krawzyck-Stando, D., and Rudnicki, M. (2007). Regularization parameter selection in discrete ill-posed problems - the use of the U-curve. *Int. J. Appl. Math. Comput. Sci.* 17, 157–164. doi: 10.2478/v10006-007-0014-3

MacLeod, R. S., and Brooks, D. H. (1998). Recent progress in inverse problems in electrocardiology. *IEEE Eng. Med. Biol. Mag.* 17, 73–78. doi: 10.1109/51.646224

Milanič, M., Jazbinšek, V., Macleod, R. S., Brooks, D. H., and Hren, R. (2014). Assessment of regularization techniques for electrocardiographic imaging. *J. Electrocardiol.* 47, 20–28. doi: 10.1016/j.jelectrocard.2013.10.004

Oostendorp, T. F., van Dessel, P. F., Coronel, R., Belterman, C., Linnenbank, A. C., van Schie, I. H., et al. (2011). Noninvasive detection of epicardial and endocardial activity of the heart. *Neth. Heart J.* 19, 488–491. doi: 10.1007/s12471-011-0206-1

Oosterom van, A. (2012). The inverse problem of bioelectricity: an evaluation. *Med. Biol. Eng. Comput.* 502, 891–902. doi: 10.1007/s11517-012-0941-5

Potse, M., Dubé, B., and Vinet, A. (2009). Cardiac anisotropy in boundary-element models for the electrocardiogram. *Med. Biol. Eng. Comput.* 47, 719–729. doi: 10.1007/s11517-009-0472-x

Ramanathan, C., Ghanem, R. N., Jia, P., Ryu, K., and Rudy, Y. (2004). Noninvasive electrocardiographic imaging for cardiac electrophysiology and arrhythmia. *Nat. Med.* 10, 422–428. doi: 10.1038/nm1011

Ruan, S., Wolkowicz, G. S. K., and Wu, J. (1999). *Differential Equations with Applications to Biology, Vol. 21*. Providence, RI: American Mathematical Society.

Rudy, Y. (2004). *System and Method for Non-invasive Electrocardiographic Imaging*. U.S. Patent No. 6772004. Washington, DC: U.S. Patent and Trademark Office.

Rudy, Y. (2013). Noninvasive electrocardiographic imaging of arrhytmogenic substrates in humans. *Circ. Res.* 112, 849–862. doi: 10.1161/CIRCRESAHA.112.279315

Rudy, Y., Ramanathan, C., Ghanem, R., and Jia, P. (2006). U.S. Patent No. 7016719. Washington, DC: U.S. Patent and Trademark Office.

Schuler, S., Wachter, A., and Dössel, O. (2018). Electrocardiographic imaging using a spatio-temporal basis of body surface potentials–application to atrial ectopic activity. *Front. Physiol.* 9:1126. doi: 10.3389/fphys.2018.01126

Shah, A. (2015). Frontiers in noninvasive cardiac mapping, an issue of cardiac electrophysiology clinics. *Elsevier Health Sci.* 7, 1–164. doi: 10.1016/S1877-9182(15)00004-0

Ten Tusscher, K. H., Noble, D., Noble, P. J., and Panfilov, A. V. (2004). A model for human ventricular tissue. *Am. J. Physiol.Heart Circ. Physiol.* 286, H1573–H1589. doi: 10.1152/ajpheart.00794.2003

Vogel, C. R. (1996). Non-convergence of the L-curve regularization parameter selection method. *Inverse Probl.* 12:535. doi: 10.1088/0266-5611/12/4/013

Wang, Y., Cuculich, P. S., Zhang, J., Desouza, K. A., Vijayakumar, R., Chen, J., et al. (2011). Noninvasive electro anatomic mapping of human ventricular arrhythmias with electrocardiographic imaging. *Science Transl. Med.* 3:98ra84. doi: 10.1126/scitranslmed.3002152

Wang, Y., and Rudy, Y. (2006). Application of the method of fundamental solutions to potential-based inverse electrocardiography. *Ann. Biomed. Eng.* 34, 1272–1288. doi: 10.1007/s10439-006-9131-7

Conflict of Interest Statement: The authors declare that the research was conducted in the absence of any commercial or financial relationships that could be construed as a potential conflict of interest.

frontiers in Physiology

ORIGINAL RESEARCH
published: 05 April 2019
doi: 10.3389/fphys.2019.00308

Effects of Heart Rate and Ventricular Wall Thickness on Non-invasive Mapping: An *in silico* Study

Erick Andres Perez Alday[1]*, *Dominic G. Whittaker*[2], *Alan P. Benson*[2] and *Michael A. Colman*[2]*

[1] Knight Cardiovascular Institute, Oregon Health & Science University, Portland, OR, United States, [2] School of Biomedical Science and Multidisciplinary Cardiovascular Research Centre, University of Leeds, Leeds, United Kingdom

OPEN ACCESS

Edited by:
Maria S. Guillem,
Universitat Politècnica de València, Spain

Reviewed by:
Matthijs Cluitmans,
Maastricht University, Netherlands
Crystal M. Ripplinger,
University of California, Davis, United States
Jess D. Tate,
University of Utah, United States

***Correspondence:**
Erick Andres Perez Alday
perezald@ohsu.edu
Michael A. Colman
m.a.colman@leeds.ac.uk

Specialty section:
This article was submitted to Cardiac Electrophysiology, a section of the journal Frontiers in Physiology

Received: 13 September 2018
Accepted: 07 March 2019
Published: 05 April 2019

Citation:
Perez Alday EA, Whittaker DG, Benson AP and Colman MA (2019) Effects of Heart Rate and Ventricular Wall Thickness on Non-invasive Mapping: An in silico Study. Front. Physiol. 10:308. doi: 10.3389/fphys.2019.00308

Background: Non-invasive cardiac mapping—also known as Electrocardiographic imaging (ECGi)—is a novel, painless and relatively economic method to map the electrical activation and repolarization patterns of the heart, providing a valuable tool for early identification and diagnosis of conduction abnormalities and arrhythmias. Moreover, the ability to obtain information on cardiac electrical activity non-invasively using ECGi provides the potential for *a priori* information to guide invasive surgical procedures, improving success rates, and reducing procedure time.

Previous studies have shown the influence of clinical variables, such as heart rate, heart size, endocardial wall, and body composition on surface electrocardiogram (ECG) measurements. The influence of clinical variables on the ECG variability has provided information on cardiovascular control and its abnormalities in various pathologies. However, the effects of such clinical variables on the Body Surface Potential (BSP) and ECGi maps have yet to be systematically investigated.

Methods: In this study we investigated the effects of heart size, intracardiac thickness, and heart rate on BSP and ECGi maps using a previously-developed 3D electrophysiologically-detailed ventricles-torso model. The inverse solution was solved using the three different Tikhonov regularization methods.

Results: Through comparison of multiple measures of error/accuracy on the ECGi reconstructions, our results showed that using different heart geometries to solve the forward and inverse problems produced a larger estimated focal excitation location. An increase of ∼2 mm in the Euclidean distance error was observed for an increase in the heart size. However, the estimation of the location of focal activity was still able to be obtained. Similarly, a Euclidean distance increase was observed when the order of regularization was reduced.

For the case of activation maps reconstructed at the same ectopic focus location but different heart rates, an increase in the errors and Euclidean distance was observed when the heart rate was increased.

Conclusions: Non-invasive cardiac mapping can still provide useful information about cardiac activation patterns for the cases when a different geometry is used for the inverse problem compared to the one used for the forward solution; rapid pacing rates can induce order-dependent errors in the accuracy of reconstruction.

Keywords: ECGi, non-invasive mapping, body surface potential, heart rate, cardiac hyperthrophy

INTRODUCTION

Cardiovascular disease is a major contributor to reduced quality of life and mortality worldwide (Benjamin et al., 2017). Cardiac conditions such as heart failure, myocardial infarction, and hypertrophic/dilated cardiac myopathy are related to electrical dysfunction (i.e., arrhythmia) and typically result in reduced cardiac output. Diagnosis and treatment of these conditions presents a significant healthcare challenge, in part due to their dual electrophysiological-structural components. Short- and long-term adaptation of cardiac structure and ion channel expression, which includes reversible and irreversible remodeling associated with disease, further compounds the challenge. For example, cardiac hypertrophy, which is an important risk factor of heart failure and sudden cardiac death (Vriesendorp et al., 2015), is characterized by abnormal thickening of the heart muscle, usually resulting from increases in cardiac cell size, in order to compensate for inhibited contractile performance (Shimizu and Minamino, 2016). The particular manifestation of electrical dysfunction may therefore vary over the time-course of the condition; the ability to accurately map the electrical activity of the heart non-invasively over this whole period can offer significant advantages for the long-term management of such conditions.

Electrocardiographic imaging (ECGi) is a novel, painless and (relatively) economic method to map the electrical activation and repolarization patterns of the heart (Ghosh et al., 2011; Alday et al., 2016; Bear et al., 2016; Perez Alday et al., 2016; Zhang et al., 2016), and presents the possibility to better understand cardiac excitation patterns and provide *a priori* information to guide invasive surgical procedures, improving success rates and reducing procedure time (Silva et al., 2009; Dubois et al., 2015; Zhang et al., 2016). Based on solving the inverse problem of electrocardiography, with the heart acting as an electrical source inside the volume conductor of the body, ECGi aims to reconstruct the electrical activity on the surface of the heart using body surface potential (BSP) maps obtained from torso surface multi-array electrocardiogram (ECG) systems (Macfarlane et al., 2010; Rudy, 2013; Perez-Alday et al., 2017b). It depends on 3D heart and torso structures and therefore requires reconstructions of patients' cardiac and torso anatomy, which are typically acquired using the clinical imaging technologies of Magnetic Resonance Imaging (MRI) or Computed Tomography (CT). Due to the expense of these modalities, it may not be desirable to attain structural information from a patient repeatedly over the course of structural adaptions. However, the potential impact of using out-of-date structural information when performing ECGi is unclear.

In addition, previous studies have shown the influence of clinical variables, such as respiration (Langley et al., 2010; Baumert et al., 2013), body composition, (Zemzemi et al., 2015), and heart rate and body position (Appel et al., 1989; Goldenberg et al., 2006) on the ECG measurement. Based on these insights, adjusted ECG parameters (e.g., corrected QT interval) have improved the detection of patients at increased risk of cardiac arrhythmias (Kabir et al., 2016). It follows that such variables may also influence interpretation of BSP and ECGi data, but the nature of these relationships have yet to be systematically investigated.

The aim of this study was therefore to assess the effect of varying cardiac structure and electrical pacing rate on the accuracy of ECGi reconstructions. An *in silico* approach was used to provide clean and controllable data to compare reconstructions attained at multiple pacing rates and with underlying hypertrophic and dilated cardiac anatomy under sinus rhythm and ectopic focal excitation.

METHODS

The *in silico* approach utilized idealized, electrophysiologically heterogeneous human bi-ventricle models to simulate electrical excitation in control, dilated and hypertrophied conditions (sections "Virtual Bi-ventricle Models" to "Ventricular Simulation Protocols"). Ventricular activation was then combined with a heterogeneous torso model and the forward problem was solved to produce simulated BSP maps (section "Simulated Body Surface Potential"). The inverse solution, using multiple regularization approaches, was applied to the simulated BSP maps in order to produce ECGi epicardial potential reconstructions and compute activation patterns (section "Inverse Solution"). Multiple measures were used to quantify and compare results obtained under the different conditions (section "Analysis Methods").

Virtual Bi-Ventricle Models

Idealized human bi-ventricle geometries were constructed as structured finite difference grids, wherein the left and right ventricles (LV and RV, respectively) were modeled as thick- and thin-walled truncated ellipsoids, respectively. A control (normal) geometry was constructed in order to have physiologically-accurate ventricular wall thicknesses (12–15 and 3–5 mm for LV and RV, respectively; Ho and Nihoyannopoulos, 2006; Ho, 2009) and volumes (∼150–210 mL for the LV in human males; Alfakih et al., 2003; Clay et al., 2006), and the overall size and ventricular curvature were qualitatively matched against multiple

existing human ventricle datasets (Seemann et al., 2006; Benson et al., 2011; Keller et al., 2011). From this, two more geometries were created by increasing either the wall thickness or the short axis diameter by 50%. In total three cases were considered: (i) normal, (ii) thick-walled (hypertrophied), and (iii) dilated ventricles (**Figure 1A**). A spatial resolution of $\Delta x = \Delta y = \Delta z = 0.5$ mm was used, which gave $\sim 2 \times 10^6$ nodes in tissue, to facilitate high-throughput generation of multiple datasets for BSP and ECGi analysis. Measurements of the LV volume, LV wall thickness, and RV wall thickness from the developed geometries are given in **Table 1**.

In each case, a simple ruled-based model was implemented to assign myocardial fiber orientations (**Figure 1Ci**) using a standard approach based on rules proposed by Streeter et al. (1969). A value of the helix angle, α, was assigned to each node of the grid, given by

$$\alpha = R(1 - 2d)^n, \quad (1)$$

where R is the transmural rotation (varying from $+R$ at the endocardium to $-R$ at the epicardium), d is the normalized transmural depth (varying from 0 at the endocardium to 1 at the epicardium), and n determines the transmural variation in helix angle (e.g., $n = 1$ is linear, $n = 3$ is cubic). For all simulations in this study, R was set to 60°, giving a transmural rotation in helix angle of 120°, similar to that observed in existing human ventricular datasets (Seemann et al., 2006; Benson et al., 2010), and n was set to 1 (Benson et al., 2008). The transverse angle was assumed to be 0° as it has been shown to be constantly around 0° throughout the ventricles (Seemann et al., 2006), and no sheetlet structure was incorporated, as this has been suggested to show great variability between hearts (Benson et al., 2008). A small degree of smoothing was applied where the right ventricle joins the ventricular septum, to ensure a smooth transition in helix angles.

Single Cell Model of Human Ventricles

To simulate the action potential (AP) of human ventricular myocytes, the 2006 version of the Ten Tusscher et al. model was used (Ten Tusscher and Panfilov, 2006), which accounts for distinct electrophysiological differences in cells from the

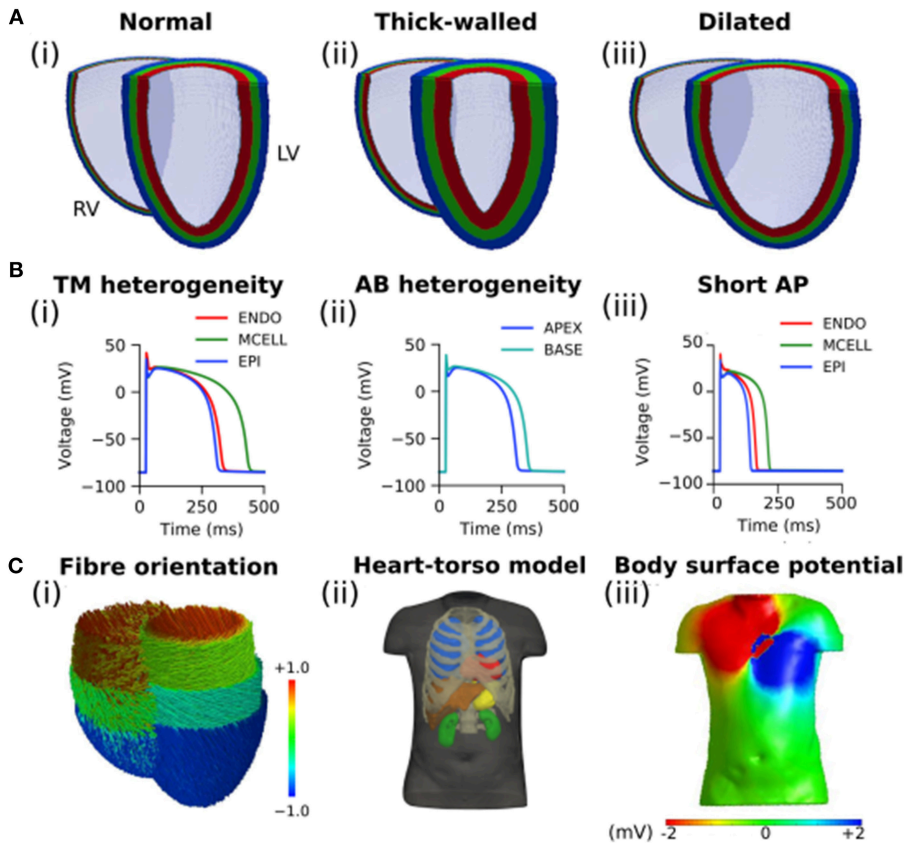

FIGURE 1 | Computational models of the human ventricles and torso. **(A)** An open view of geometries representing (i) normal/control, (ii) thick-walled, and (iii) dilated human ventricles with the epicardial (blue), mid-myocardial (green), and endocardial (red) segmented regions shown. **(B)** Single cell ventricular action potentials representing (i) transmural (TM) heterogeneity in cells from the endocardium (ENDO), mid-myocardium (MCELL), and epicardium (EPI), (ii) apico-basal (AB) heterogeneity (shown for EPI cells), and (iii) short single cell action potentials used in this study. All models are uncoupled single cells paced at a cycle length of 1,000 ms. **(C)** (i) Fiber orientation (normalized z component of primary fiber; red and blue indicate parallel to the long axis of the heart from apex to base, green indicates perpendicular to the long axis of the heart); (ii) Heart-torso model used to compute the (iii) body surface potential.

TABLE 1 | A summary of dimensions in developed idealized ventricular geometries.

	Control	Thick-walled	Dilated
LV wall volume (mL)	196.56	249.77	255.29
LV wall thickness (mm)	12.00	18.00	12.00
RV wall thickness (mm)	4.00	6.00	4.00

ventricular endocardium (ENDO), mid-myocardium (MCELL), and epicardium (EPI; **Figure 1Bi**). The bi-ventricle models were segmented into 40% ENDO, 30% MCELL, and 30% EPI cells (**Figure 1A**), similar to previously used ratios (Adeniran et al., 2011, 2017). The existing transmural heterogeneity was increased by adjusting the ENDO:EPI:MCELL ratio of rapid delayed rectifier potassium current, I_{Kr}, maximal conductance to 1.0:1.6:1.0 (Adeniran et al., 2011; Whittaker et al., 2017). This was based on transmural measurements of hERG mRNA expression (Szabó et al., 2005), and was necessary to reproduce the longer AP of ENDO compared to EPI cells (Glukhov et al., 2010; Boukens et al., 2015). Furthermore, a linear gradient in the conductance of transient outward potassium current, I_{to}, and slow delayed rectifier potassium current, I_{Ks}, was introduced along the apex-base (AB) axis (Keller et al., 2011; Alday et al., 2016). Briefly, maximal conductance of I_{to} and I_{Ks} were reduced by a maximum of 50% in basal cells relative to apical cells in order to reproduce apico-basal heterogeneity (**Figure 1Bii**), giving a roughly 50 ms longer AP duration in basal cells than in apical cells (Szentadrassy et al., 2005). The maximal conductance of current x from cell type y, $g_{x,y}$, was given by

$$g_{x,y} = g_{Base,y} + \left(g_{Apex,y} - g_{Base,y}\right) \cdot f_{AB}, \tag{2}$$

$$f_{AB} = \frac{z - z_{Base}}{z_{Apex} - z_{Base}}, \tag{3}$$

where $g_{\mathrm{Apex},y}$ and $g_{\mathrm{Base},y}$ are maximal values of the conductance of cell type y at the apex and base, respectively, f_{AB} is a gradient factor which depends linearly on the value of the z co-ordinate which lies along the AB axis (varying from 1 at the apex to 0 at the base), and z_{Base} and z_{Apex} are the values of the z coordinate at the apex and base, respectively. No electrophysiological differences were incorporated between the LV and RV (Keller et al., 2011).

Modeling Action Potential Propagation

The monodomain equation was used to describe the propagation of APs in the bi-ventricle geometries:

$$\frac{\partial V}{\partial t} = \nabla\left(\boldsymbol{D}\nabla V\right) - \frac{I_{\mathrm{ion}}}{C_{\mathrm{m}}}, \tag{4}$$

where V is the transmembrane voltage, $\mathbf{D}$ is the global conductivity tensor, I_{ion} is the total ionic current, and C_{m} is the membrane capacitance. Equation (4) was solved numerically using a finite-difference PDE solver based on the explicit forward Euler method, using an operator splitting technique and an adaptive time step with minimum and maximum time steps of Δt_{min}=0.02 ms and Δt_{max}=0.2 ms, respectively (Benson et al., 2010). As axially-symmetric anisotropy was assumed, two principal values of the diffusion coefficient were required: $D_{||}$, the longitudinal value of the conductivity which describes propagation in the fiber direction, and $D_{\perp}$, the transverse value, which describes propagation orthogonal to fibers. The diffusion tensor can thus be written as

$$\mathbf{D} = D_{\perp}\mathbf{I} + (D_{||} - D_{\perp})\mathbf{A}\mathbf{A}^{\mathrm{T}}, \tag{5}$$

where $\mathbf{I}$ is the identity matrix, $\mathbf{A}$ is a unit vector giving the fiber direction, and $\mathbf{A}^{\mathrm{T}}$ is the transpose of $\mathbf{A}$.

The longitudinal value of the conductivity, $D_{||}$, was set to 0.18 $\mathrm{mm^2ms^{-1}}$ in this study, which gave a conduction velocity of 70 $\mathrm{cms^{-1}}$ in the fiber direction (Benson et al., 2007), in agreement with experimental measurements of conduction velocity along fibers in human ventricular tissue (Taggart et al., 2000). An anisotropic conductivity ratio of $D_{||}$:$D_{\perp}$ = 4:1 was used (Benson et al., 2007; Whittaker et al., 2017).

Ventricular Simulation Protocols

Sinus rhythm activation of the ventricles was elicited by stimulating a series of 28 localized patches (with diameters of ∼9–12 mm) in quick succession along the endocardial wall (stimulus amplitude and duration −52 pA/pF and 1 ms, respectively, where the wavefront was initiated in the intra-ventricular septum before spreading from apex to base throughout the left and right ventricles. This gave a total activation time of ∼65 ms in the control geometry, in good agreement with the classic results of Durrer et al. (1970). For studying the effects of ectopic activity in the ventricles, four prescribed locations which could be easily identified in each of the geometries were chosen as "ectopic stimulus" sites: (i) the right ventricular lateral wall (RV-LAT), (ii) the intra-ventricular septum (SEP), (iii) the left ventricular lateral wall (LV-LAT), and (iv) the left ventricular apex (LV-Apex). In each case, localized −52 pA/pF stimuli of 1 ms duration were applied over 5 mm.

Simulated Body Surface Potential

The ventricular model was placed into a previously developed biophysically-detailed computational three-dimensional heart-torso model which accounts for the distinct structures of the lungs, liver, blood masses, stomach, spleen, kidneys, ribs and spinal cord, and the respective electrical conductivities (Perez-Alday et al., 2015) (**Figure 1Cii**). This model has been previously used to develop an algorithm to diagnose atrial ectopic origin from multi lead ECG systems and ventricular ischemia (Alday et al., 2016; Perez-Alday et al., 2017a). Details of the torso model development, validation and simulation protocols can be found in Perez-Alday et al. (2015). Briefly, the heart-torso algorithm previously developed was used to solve the forward problem and obtain BSP maps (**Figure 1Ciii**) in each of the cases. The potential on the surface of the body was obtained from the 3D ventricular model using Salu's approach (Salu, 1980), utilizing the Boundary Element Method and Green's identities to solve the Poisson equation (Macfarlane et al., 2010).

Inverse Solution

An inverse solution was developed, extending previously published preliminary work (Alday et al., 2016). Briefly, and based on prior work from Ramanathan and Rudy (2001), surface to surface torso-heart matrix was calculated using Barr's approach, where an equivalent potential distribution on a closed surface is used to build the homogenous heart-torso matrix (Barr et al., 1977); note therefore that, whereas the forward problem is solved on a heterogeneous torso, the inverse solution is provided on a homogeneous torso model. From the BSP maps, a previously developed inverse problem algorithm using Tikhonov regularization using Generalized Single Value Decomposition (GSVD) numerical approach was used to obtain the activation on the surface of the heart (Hansen, 1998). The potentials on the surface, x, were obtained by solving Equation (6):

$$x = \min_{x} \{ \left|\left|Zx - y\right|\right|_2 + \lambda^2 ||Rx|| \}, \quad (6)$$

where Z is the transfer matrix, y represents the BSP vector, λ is the regularization parameter obtained using the L-curve (Hansen, 1992), and R is the regularization operator. Zero (Identity matrix, $R = \mathrm{I}$), First (Gradient operator, $R = \nabla$), and Second (Laplace operator, $R = \Delta$) order Tikhonov were used to regularize the solution. The GSVD technique was used to solve Equation (6) in each case.

As an ill-posed problem, noisy signals can have an important effect on the reconstructed maps. Whereas it is common in modeling studies of ECGi to include additional white noise, this was not performed in this study for the bulk of our analysis. Please see "Discussion: Limitations" for further details on the inclusion of noise and its impact.

Analysis Methods

Epicardial potentials were reconstructed from the BSP obtained at each instant of time for each geometry and activation case. Activation maps were calculated by computing maximal negative slope at each node at each time step (Gage et al., 2017). An example of original and reconstructed epicardial potential snapshots and the corresponding activation maps is shown in the Section S1 in **Supplementary Material**. To quantify the differences between the BSP and reconstructed activation maps for each of the geometry cases, three difference methods were used (Bear et al., 2015, 2018b):

1) Voltage root mean squared (RMS):

$$RMS = \sqrt{\frac{\sum_{i=1}^{N} \varnothing_i^2}{N}};$$

2) Relative RMS error (rRMSe):

$$rRMSe = \sqrt{\frac{\sum_{i=1}^{N} (\varnothing_i' - \varnothing_i)^2}{\sum_{i=1}^{N} (\varnothing_i')^2}};$$

3) Pearson correlation coefficient (PCC):

$$PCC = \frac{\sum_{i=1}^{N} (\varnothing_i' - \varnothing_i)(\varnothing_i' - \varnothing_i)}{\sqrt{\sum_{i=1}^{N} (\varnothing_i' - \varnothing_i)^2 (\varnothing_i' - \varnothing_i)^2}},$$

where N is the number of elements in the mesh (torso or epicardial elements), $\varnothing$ is the potential reconstructed or measured and $\varnothing'$ is the original simulated potential, while $\overline{\varnothing}$ and $\overline{\varnothing}'$ are the mean potential values across all elements of the mesh. RMS gives an estimation of the variability of the signal. rRMSe gives an estimation of the variability between two methods. PCC is the measure of the correlation between two variables. The analysis was performed at each temporal snapshot of the ventricular activation.

To investigate the focus location accuracy of the inverse solutions, the Euclidean distance (ED) was calculated at the center of the earliest activation: $||ED|| = \sqrt{(r' - r)^2}$, where r is the center of activation of the reconstructed potential in the 3D Euclidean space and r' is the center of activation of the original simulated data. The Euclidean distance was calculated for all the ectopic cases and a median value is reported in this study.

Investigating the Effect of Using the Incorrect Geometry for ECGi

The impact of using only an initial patient anatomical reconstruction when performing ECGi, which doesn't capture any structural remodeling which may have occurred between the time of the scan and any present measurements, was investigated: Ectopic ventricular activation was simulated on all three geometries (control, thick-walled, and dilated; section "Virtual Bi-ventricle Models") and used to solve the forward problem and produce BSP maps; the ECGi reconstruction was performed using only the control geometry, representing the initial patient scan. Quantification of errors and correlations were performed by comparing the reconstruction with the control geometry activation for each matched ectopic location, such that geometrical differences don't have to be accounted for.

Investigating the Effect of Heart Rate on ECGi

The effect of heart rate on the epicardial reconstructions obtained using the three Tikhonov regularization methods was assessed for focal excitations using the control geometry paced at basic cycle lengths (BCL) of 1,000, 750, 500, 300, and 150 ms [corresponding to pacing rates of 60, 80, 120, 200, and 400 Beats per Minute (BPM), respectively]. Shortening of the AP (**Figure 1Biii**) induced by a five-fold increase in the conductance of I_{Kr} and I_{Ks} was employed to sustain the most rapid excitation rate (BCL = 150 ms). All other data were produced using the control AP models.

RESULTS

First, the impact of the different geometries (control, thick-walled, and dilated) on simulated BSP under control pacing conditions were compared to illustrate recapitulation of activation pattern and ECG differences observed under these conditions in the *in silico* framework (section "Simulated Body Surface Potential Under Different Conditions"). Then, the potential errors induced by using out-of-date and inaccurate cardiac anatomical reconstructions when performing ECGi was

assessed (section "Effects of Wall Thickness and Heart Size on Non-invasive Cardiac Maps"). Finally, we investigated the effect of heart rate on the accuracy of reconstructed activation patterns using the different regularization approaches (section "Effects of Heart Rate on Non-invasive Cardiac Maps").

Simulated Body Surface Potential Under Different Conditions

The effects of the different geometries on the BSP were quantified by comparing the thick-walled and dilated geometries vs. the control during ventricular activation (**Figure 2**). Small differences were observed in the BSP maps at different instants of time (**Figure 2A**), quantitative measurements are plotted for comparison. A similar RMS was obtained for the three cases which produced relatively small rRMSe values (**Figure 2B**). However, the largest values were observed early during the activation sequence (first 75 ms). A good agreement between the signal was observed for both cases (average PCC > 0.8), however, at mid activation time (between 125 and 175 ms) the values dropped significantly, with the dilated condition resulting in the smallest correlation.

Effects of Wall Thickness and Heart Size on Non-invasive Cardiac Maps

Data are illustrated for a single ectopic site only (RV-LAT—**Figure 3**) and summarized for all sites (**Table 2**). During the initial excitation phase (75 ms), similar small RMS and rRMSe values were observed for the three cases (**Figure 3**). During the mid and later activation times, RMS and rRMSe values were more dependent on the order of the regularization than the geometry, with First and Second order giving the smallest errors. Similarly, PCC values were considerably larger using First and Second order compared to the Zero order, and the Zero order displayed the most unique and geometry-dependent temporal evolution. The general increase in correlation over the time of the activation sequence is attributed to the increase in area of active tissue. RMS, rRMSe, and PCC were similar for all three heart geometries, although in general the control geometry exhibited the smallest errors and largest correlation and the dilated geometry exhibited the largest errors and smallest correlation (**Figure 3**; **Table 2**).

The calculated ED, measuring the error in correlation between real and identified focus location, varied for each geometry using the three Tikhonov methods (**Figure 4A**). Smaller values were observed for the Second order method (compared to Zero and First) and the control geometry (compared with thick and dilated, with dilated giving the largest values). However, the differences observed between geometries was less significant than that between methods.

Effects of Heart Rate on Non-invasive Cardiac Maps

The ED was calculated and compared for each different heart rate and Tikhonov method (**Figure 4B**). The Second order method in all the cases produced the smaller ED values. A marked increase in the ED was observed when the heart rate was increased for all methods, which also resulted in convergence of the solutions obtained using the different methods at the most rapid rate.

The reconstructed activation patterns were compared across the different pacing rates; illustrative data for the LV-LAT site are shown in **Figure 5** and data from all ectopic sites are summarized in **Table 3**. At the slowest pacing rates (BCL = 1,000 and 750 ms), corresponding to normal heart rates in healthy patients (60 and 80 BPM, respectively), the Zero order method resulted in the larger rRMSe values and lower PCC values and contained the most noise. Both the First and Second order methods resulted in lower rRMSe values and larger PCC values over the temporal range of excitation (**Figure 5**—BCL = 1,000 and 750 ms), with the Second order in general performing the best, in congruence with the ED values (**Figure 4B**). The PCC for all methods in general increased over the time of the activation. At the most rapid rates (**Figure 5**—BCL = 300 and 150 ms), the temporal evolution of the PCC for First and Second order reversed, decreasing over the activation time, whereas the Zero order remained largely flat. The initial larger correlation for First and Second order compared to the slow pacing rates did not correspond to small ED and therefore was not a result of accurate reconstruction of the initial phase of excitation. The differences between the methods decreased at these rapid rates, largely due to an increase in the errors associated with First and Second order with no corresponding change to the Zero order solution (**Figure 5**, BCL = 150 and 300 ms). In all conditions, the Zero order approximation presented the most noise, but the reconstruction at the rapid excitation rates was more stable and comparable with the Second and First order (**Table 3**).

DISCUSSION

Summary

In this study, we used an *in silico* approach to evaluate the impact of different ventricular anatomical morphologies and heart rate on the accuracy of epicardial reconstructions attained through the application of the inverse solution to the BSP. We have demonstrated that the different cardiac anatomical states resulted in small but measurable differences in the BSP (**Figure 2**). Furthermore, we demonstrated that differences between actual underlying cardiac anatomy (i.e., the heart model on which electrical activation was simulated) and the reconstructed anatomy (i.e., the heart model on which the inverse solution was applied) led to errors in the reconstruction of both epicardial potential maps and activation patterns (**Figure 3**; **Table 2**). However, the location of the ectopic focal excitation was still largely correctly estimated, even with the incorrect geometry used for reconstruction (**Figure 4**). Moreover, we have demonstrated an important heart rate dependency of the correlation coefficients and reconstruction errors (**Figure 5**; **Table 3**). In general, the Second order regularization approach produced the smallest errors and largest correlation.

Clinical Importance

ECGi is a powerful and rapidly developing approach to non-invasively map patients' cardiac electrical activity in the clinic. The method aims to overcome some of the numerous challenges

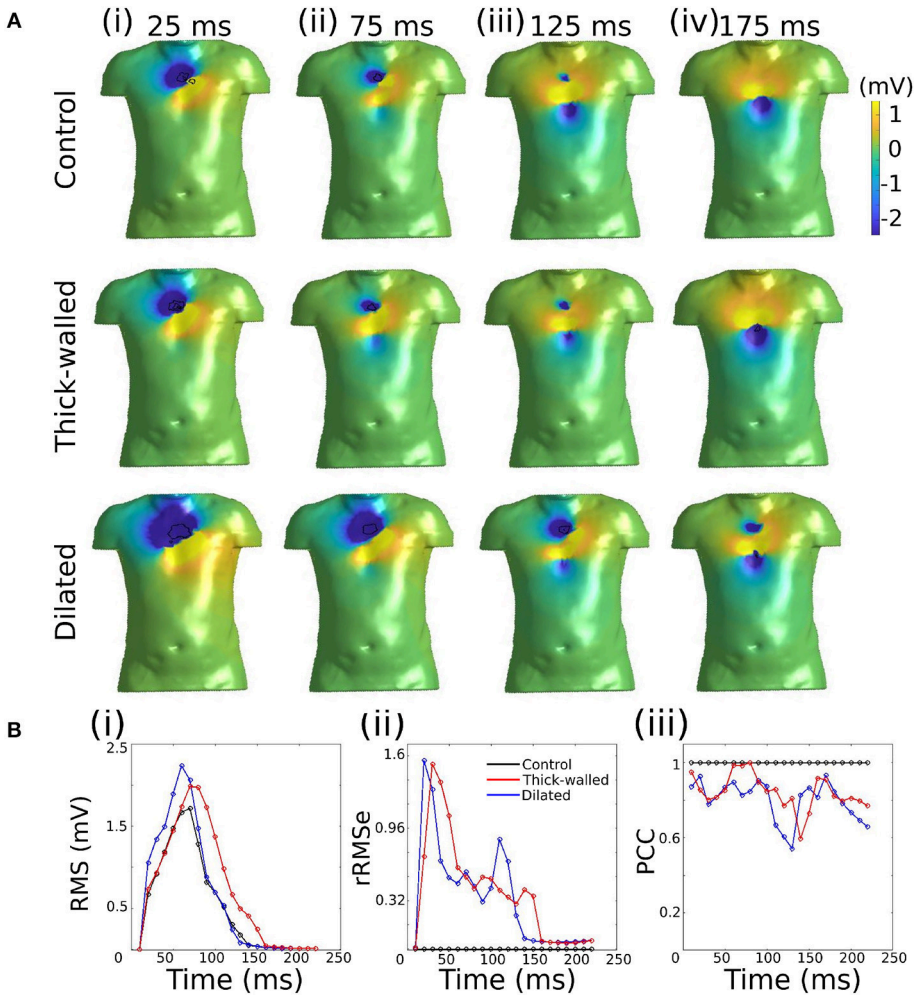

FIGURE 2 | Comparison of simulated BSP obtained from the three different geometries during ventricular activation. **(A)** BSP obtained for control case, the thick-walled and dilated geometry during simulated ectopic activation initiated in the right ventricular lateral wall (RV-LAT) at different instants of time: (i) 25 ms, (ii) 75 ms, (iii) 125 ms, and (iv) 175 ms. **(B)** (i) RMS for each case and (ii) rRMSe and (iii) PCC calculated vs. the control case.

related to effective non-invasive characterization of human anatomy and electrophysiology. Previous studies have shown the usefulness of this non-invasive method to provide information to guide ablation procedures (Dubois et al., 2015; Rodrigo et al., 2017) and identify potential patients for whom cardiac resynchronization therapy would be successful (Silva et al., 2009; Rudy, 2013; Bear et al., 2018a). In addition, current studies have merged this ECGi technology with computational models to provide patient-specific models in order to predict the efficacy of specific therapies (Boyle et al., 2018; Huntjens et al., 2018). Due to the influence of inhomogeneities inside the torso on the BSP, recent studies have also focused on the understanding of the forward problem and its relation with the inverse solution (Bear et al., 2015, 2018b; Zemzemi et al., 2015). Furthermore, the ill-posed nature of the problem requires different mathematical constraints and regularization methods to be used to find the most accurate physical and physiological solution (Oster and Rudy, 1992); recent studies have investigated the accuracy of these inverse methods (Bear et al., 2018b).

Despite these important works, there are still many questions in the field of ECGi which must be addressed in order to further develop the approach and improve its clinical and research impact. In this study, we provide analysis of the impact of electro-anatomical variability pertaining to differences in cardiac anatomy and heart rate on the accuracy of ECGi reconstructions obtained using different regularization methods. These analyses provide important insights for the interpretation of clinically obtained ECGi reconstructions over the time-course of an electro-anatomically dynamic condition such as heart failure.

Wall Thickness and Heart Size

Previous studies have investigated the influence of tissue inhomogeneities on the BSP and reconstructed solution, which were shown to have a small impact on the reconstructed signal (Ramanathan and Rudy, 2001; Zemzemi et al., 2015).

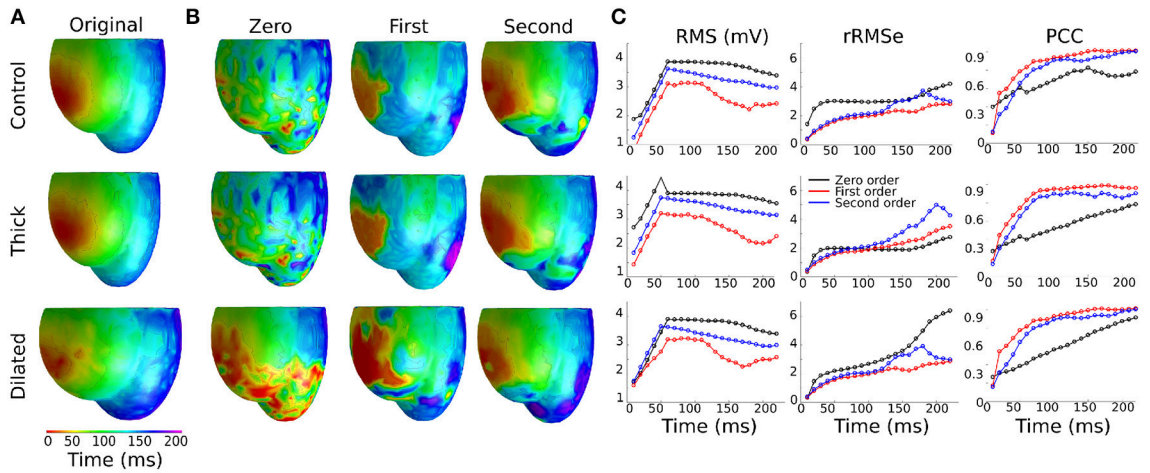

FIGURE 3 | Effects of heart geometry on the reconstructed epicardial potentials. **(A)** Original simulated ectopic activation initiated in the right ventricular lateral wall (RV-LAT) on all three geometries. **(B)** Reconstructed activation maps using Zero, First and Second order Tikhonov regularization using different geometries for the forward problem but the control/normal geometry for the inverse problem. Activation patterns were computed as the time of maximum negative first derivative d*V*/d*t* at each location. **(C)** RMS, rRMSe, and PCC calculated to quantify the differences between the reconstructed activation patterns using Zero (black), First (blue) and Second (red) order Tikhonov regularization.

TABLE 2 | A summary of the effects of geometry on RMS, rRMSe, and PCC of reconstructed activation maps using the three different regularization methods.

Tikhonov order	Metrics	Control – mean (SD)	Dilated – mean (SD)	Thick – mean (SD)
Zero order	RMS	3.45 (0.60)	3.74 (0.43)	3.65 (0.62)
	rRMSe	3.09 (0.57)	3.94 (0.45)	3.33 (0.63)
	PCC	0.673 (0.108)	0.570 (0.152)	0.603 (0.120)
First order	RMS	3.03 (0.59)	3.27 (0.46)	3.12 (0.45)
	rRMSe	2.34 (0.87)	2.77 (0.78)	2.98 (0.64)
	PCC	0.794 (0.210)	0.754 (0.213)	0.773 (0.120)
Second order	RMS	2.48 (0.59)	2.68 (0.48)	2.63 (0.44)
	rRMSe	1.97 (0.64)	2.65 (1.26)	2.39 (0.93)
	PCC	0.869 (0.106)	0.769 (0.121)	0.778 (0.140)

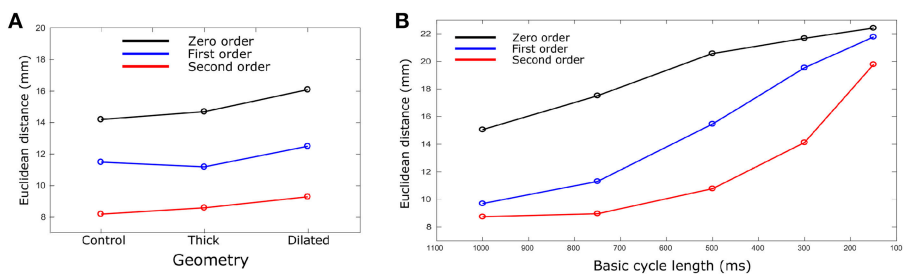

FIGURE 4 | Euclidean distance vs. **(A)** geometry and **(B)** BCL. Euclidean distances were calculated for each geometry case and BCL for Zero (black), First (Blue), and Second (red) order Tikhonov regularization. For **(B)**, only control geometry was used. Data are the mean for all ectopic sites.

Effects such as an enlargement of the heart and thickening of the cardiac wall (associated with various disease states, e.g., heart failure) are not necessarily included in the geometrical transfer matrix, and have not been fully studied. In this study, we first compared the BSP activation maps obtained by modifying the size of the ventricles. This was used as the baseline comparison between BSP prior to obtaining the inverse solution. Using RMS, rRMSe, and PCC to quantify the similarity or differences between the BSP observed under these different conditions demonstrated that cardiac anatomy

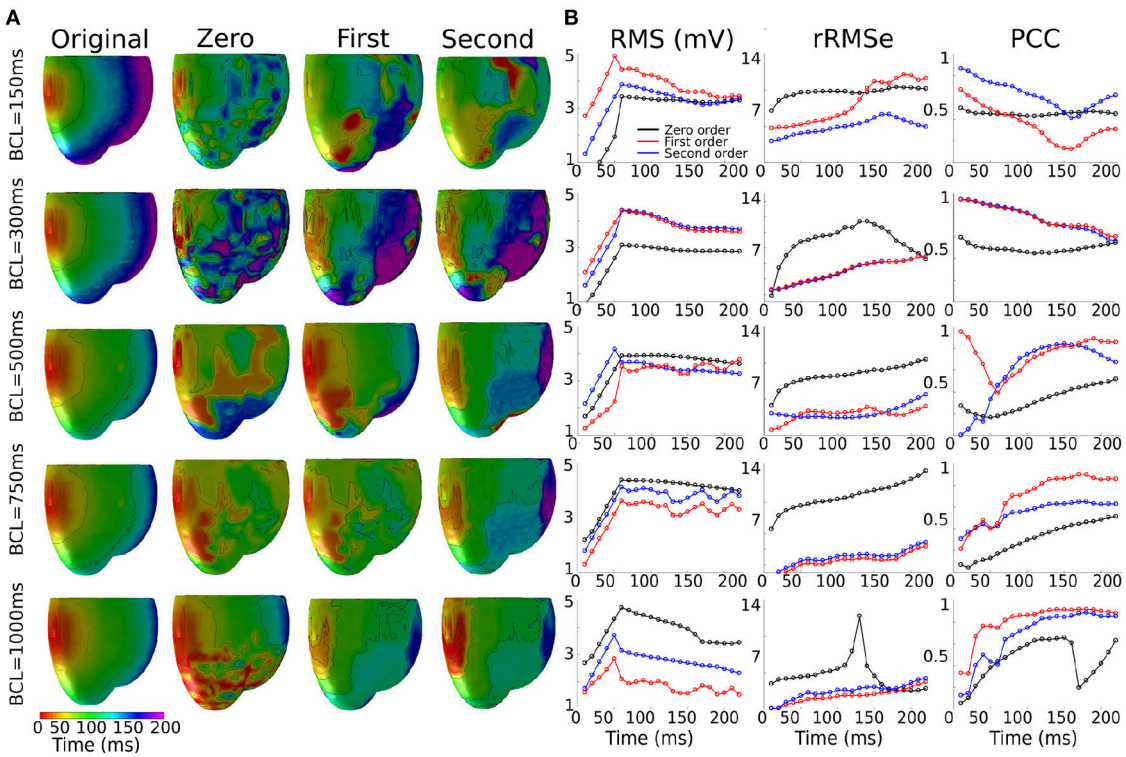

FIGURE 5 | Effects of the heart rate on the reconstructed activation maps. **(A)** 3D activation maps at different basic cycle lengths (BCLs): 150, 300, 500, 750, and 1,000 ms; activation time is given as the maximum negative slope of each local membrane potential. **(B)** RMS, rMSe and PCC measure calculated using Zero (black), First (blue), and Second (red) order Tikhonov regularization of an ectopic activation starting on the middle of the left ventricle (LV-LAT).

TABLE 3 | A summary of the effects of heart rate on reconstructed activation maps using the three different regularization methods.

Tikhonov order	Metrics	BCL 1,000 ms	BCL 750 ms	BCL 500 ms	BCL 300 ms	BCL 150 ms
Zero order	RMS	3.85 (0.55)	3.96 (0.62)	3.53 (0.65)	3.67 (0.59)	3.78 (1.02)
	rRMSe	7.64 (2.3)	7.81 (1.75)	8.31 (1.41)	8.77 (2.23)	8.70 (0.71)
	PCC	0.646 (0.190)	0.628 (.154)	0.626 (0.119)	0.629 (0.103)	0.623 (0.107)
First order	RMS	2.74 (0.39)	3.61 (0.61)	4.16 (0.66)	4.59 (0.63)	4.20 (0.61)
	rRMSe	2.82 (0.96)	2.94 (1.01)	3.14 (0.93)	4.91 (1.46)	4.92 (1.06)
	PCC	0.820 (0.169)	0.789 (0.106)	0.757 (0.280)	0.713 (0.122)	0.686 (0.130)
Second order	RMS	1.89 (0.31)	2.11 (0.61)	2.20 (0.62)	2.68 (0.55)	2.82 (0.51)
	rRMSe	2.43 (1.06)	2.44 (1.01)	2.92 (0.83)	3.98 (1.40)	4.17 (1.89)
	PCC	0.862 (0.138)	0.839 (0.213)	0.813 (0.148)	0.789 (0.107)	0.705 (0.160)

had a measurable effect on the details of the BSP but did not significantly alter the primary spatio-temporal features of normal activation (**Figure 2**).

Then, we observed how modifying the anatomy of the ventricles in the forward solution but not in the inverse approach had an effect on the accuracy of reconstructed ectopic activation. Larger RMS and rRMSe values were observed when comparing BSP error values vs. reconstructed error values (**Figure 3**; **Table 2**). Mostly, the first part of the activation (first 75 ms) produced the most significant differences. However, it was still possible to identify the origin of ectopic activation, albeit with a small error (**Figure 4A**).

These results therefore indicate that it may not be necessary to repeat a cardiac CT/MRI when repeating ECGi in a patient who has undergone anatomical remodeling since their first ECGi procedure, which could significantly reduce the cost of long-term treatment. Some consideration may still be required to determine appropriate electrode positions—especially if the torso, as well as the heart, has undergone anatomical changes.

Heart Rate

Heart rate had a regularization approach-dependent effect on the accuracy of reconstructed activation patterns: In the case of the First and Second order the PCCs were larger at slow rates

but significantly decreased when the heart rate was increased, exhibiting a negative temporal evolution over the activation period. In the case of Zero order, the values, even though not larger than the First or Second order in any case, remained similar when the heart rate increased and stable over the activation time at rapid rates (**Figure 5**; **Table 3**). The ED also showed an important dependency on the heart rate, increasing when the heart rate increased (**Figure 4B**). Therefore, these data indicate that the accuracy of inverse solutions in general decreases at rapid pacing rates. The underlying cause of this order-dependent difference in the rate-dependence of the solution is discussed in the next section, "On the Rate-Dependence of Time-Independent Solutions."

Differences in the quality of reconstruction at fast rates may have particular clinical importance: higher rates may present the most clinically interesting results, for example exposing concealed abnormalities (Leong et al., 2018), yet produce the poorest reconstructions using ECGi. This may also indicate that rapid arrhythmias such as tachycardia or fibrillation could present the greatest challenges for reconstruction, additional to the spatial complexity of the excitation pattern itself.

On the Rate-Dependence of Time-Independent Solutions

We observed that the accuracy of the solution using both First and Second order methods was rate-dependent, resulting in larger errors and smaller correlations at rapid rates; a feature not observed using the Zero order method (**Figures 4**, **5**; **Table 3**). This rate dependence raises an interesting question: given that the solutions to the inverse problem of electrocardiography use a quasi-static approximation, how does a temporal effect such as pacing rate modify the quality of the solution?

This can be explained by examining the differences between the regularization methods: A primary difference between the Zero order and First and Second order approaches is that the Zero order approach does not include any neighbor interaction (as it uses the identity matrix as the regularization operator) whereas the First and Second order do account for this interaction and result in smoothed signals (due to the use of the Gradient and Laplace operator for First and Second order, respectively). Spatial heterogeneities in voltage will therefore be smoothed using First and Second order but not Zero. Following that this approach distinction correlates with whether or not the reconstruction exhibits rate-dependence, we propose that spatial gradients observed at rapid rates, not present at slower pacing rates, may account for this observation.

In a previous preliminary study in the atria (Alday et al., 2016) we presented the hypothesis that this was primarily due to shortening of the AP morphology at rapid rates, resulting in a short excitation wavelength and therefore the simultaneous presence of both depolarization and repolarization wavefronts from a single excitation, significantly enhancing spatial gradients at temporal snapshots during the activation. An alternative explanation is that it is the presence of regions of tissue still active from the previous excitation at the time of the stimulus which lead to these enhanced spatial gradients. We tested which of these hypotheses was more likely to underlie the observation by comparing the control data at pacing cycle lengths of 300 and 1,000 ms with new simulations at those cycle lengths in which the AP duration has been significantly shortened (**Figure 1Biii**): this captures the shorter wavelength associated with rapid control pacing while simultaneously imposing that the previous excitation is no longer or only minimally present in the tissue at the time of excitation.

The RMS and PCC of First and Second order reconstructions associated with both the pacing rates using the short AP model were comparable to the slow pacing rate using the control AP model, and differed from the rapid pacing rates (**Figure 6**; Section S2 in **Supplementary Material**). In particular, the shorter AP models did not reproduce the negative temporal evolution and general lower PCC observed at the rapid rates using the control AP. These data indicate that, contrary to our original hypothesis, these increased errors were not caused by the short excitation wavelength (where it would be expected that all short AP models reproduced these features) but were rather caused by the presence of the previous excitation; the only condition which reproduced the lower correlation and large errors was the one in which large areas of still active tissue remained at the time of excitation (**Figure 6C**). The temporal evolution of the PCC also indicates that it is the presence of two large and distinct regions of active tissue, rather that multiple depolarization and repolarization wavefronts, which induces the reconstruction errors: the initial large PCC observed at rapid rates for control, which contrasts with the less accurate estimation of the focal location (i.e., increased ED), is a result of accurate reconstruction of the large area of active tissue from the previous excitation; as the area of active tissue from the present excitation grows, the correlation decreases due to inaccurate reconstruction of two large regions. There is no large impact on the PCC at the time the previous excitation's depolarization wavefront terminates at full activation; rather, the lower correlation remains until the tissue repolarizes.

Limitations

These types of studies are key to fully translate ECGi technology into clinical settings. However, they are difficult or impossible to perform in control and experimental settings, and the accuracy of the forward and inverse solution is still under study (Bear et al., 2015, 2018b). Computational modeling offers an important tool to study, understand and provide insights into the effects of cardiac arrhythmias and clinical variables (Colman et al., 2013, 2017). Unfortunately, there are still several limitations that need to be addressed. The forward model lacks several inhomogeneities which may have an important effect on the BSP measured and therefore in the reconstructed signal, as we used a homogeneous torso approach for the inverse reconstruction. However, previous studies have shown that the effects of inhomogeneities in the inverse solution are small (Ramanathan and Rudy, 2001); (Zemzemi et al., 2015).

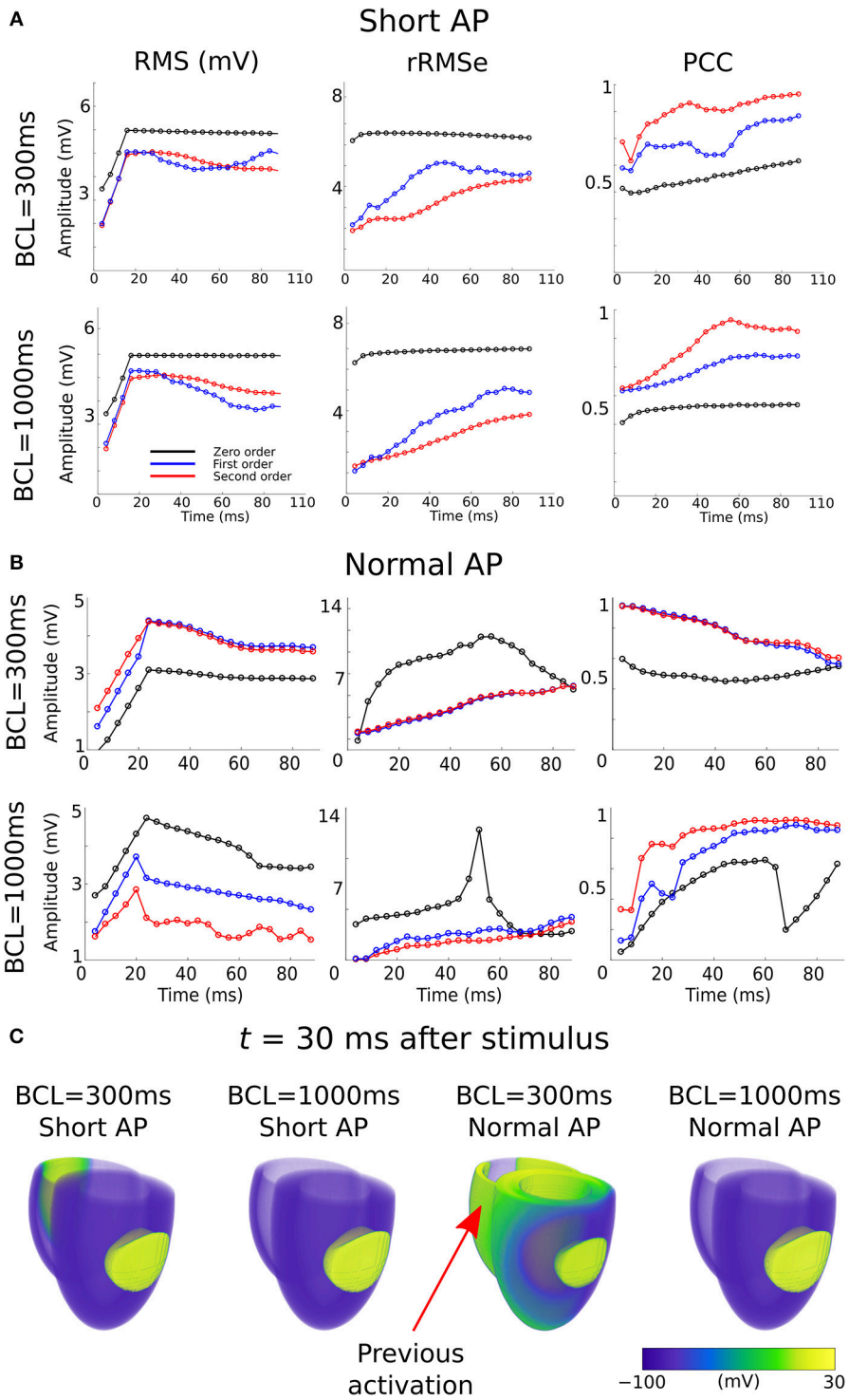

FIGURE 6 | RMS, rRMSe, and PCC of the reconstructed activation maps using **(A)** short and **(B)** normal AP durations at fast (BCL = 300 ms; upper panel) and slow (BCL = 1,000 ms; lower panel) pacing rates, for the Zero (black), First (blue), and Second (red) order Tikhonov regularization methods. **(C)** Corresponding snapshots of propagation at time $t = 30$ ms after stimulus of the LV-LAT ectopic site. The control geometry was used in all cases.

Another limitation is the idealized ventricular models used, which lacked the complex anatomy and microstructure of the real human ventricles (Stephenson et al., 2017). However, these were implemented to facilitate investigation of the effects of changing the size and wall thickness of the ventricles on non-invasive mapping. We used standard approaches to model cellular and

ventricular electrophysiology, the general limitations of which have been addressed in detail elsewhere (Benson et al., 2011).

Due to both the BSP and inverse solution being computed using simulations, it is important to ensure that "inverse crime," where the inverse method exactly inverts the forward method, is avoided. We ensure that this is the case through the use of Salu's method for the forward problem and Barr's for the inverse solution; thus, whereas the forward problem is solved by computing the electric field which arises as a result of currents in the cardiac tissue, the inverse solution uses an equivalent potential distribution on a closed surface. These independent methods, utilizing two different matrices, ensure that it is not possible for the inverse solution to exactly invert the forward solution.

Only ventricular activation was considered for comparison between different rates and geometries, disregarding potential analysis of the repolarization patterns, which may themselves provide substantial diagnostic information. Future investigation of the effects of anatomical reconstruction inaccuracies and heart rate on the reconstruction of repolarization patterns may therefore provide valuable information. However, the present study was focused on identifying the location of ectopic pacing sites, relevant in particular for guiding ablation therapy, and therefore requires only activation patterns to be reconstructed.

There are multiple further factors which will be relevant for clinical studies but not accounted for in the idealized and controlled *in silico* experiments of the present study. Whereas the geometry of the heart was considered, this was not combined with analysis of its location, its mechanical movement, or electrode location errors, all of which have been previously shown to be important factors influencing the accuracy of the reconstruction (Swenson et al., 2011; Cluitmans and Volders, 2017; Cluitmans et al., 2017; Coll-Font and Brooks, 2018). Furthermore, we did not investigate whether the effect of heart rate was influenced by the geometry, treating these analyses as separate; such investigation may provide further important insight.

In addition, the inverse problem of electrocardiography is an ill-posed problem and therefore noisy signals can have an important effect of the reconstructed maps. Whereas, the simulated data in this study and used for our analyses did not include noise, we performed further simulations in which white noise was included. These data demonstrated that noise increased ED and decreased correlation, but the differences between conditions were maintained, indicating that whereas noise has an important impact on the activation maps and ED, our observations about different geometries and pacing rate are maintained (Section S3 in **Supplementary Material**; **Figures S4–S7,** and **Tables S1**, **S2**). Also, the results obtained in this study are of the same order of magnitude observed in previous studies (Wang et al., 2010; Bear et al., 2018b); (Tate et al., 2018).

CONCLUSION

The systematic analysis revealed that the effect of size, thickness, and heart rate can manifest in the BSP and ECGi in different ways, with varying sensitivities and success rates in inferring the clinical variables from non-invasive information. We observed a rate dependence in the ability of different Tikhonov regularization methods to successfully reproduce cardiac electrical activity. Our results show that the ECGi approach gives the most accurate results when used with geometries depicting the current state of the patient's heart, but if a single image of the patient's heart is obtained, for example at the start of treatment, the ECGi approach still gives useful and reasonably accurate information relating to underlying electrophysiological abnormalities. In addition, clinical variables such as heart rate need to be accounted for when solving the inverse solution, in particular due to the increase in errors observed at rapid pacing rates.

AUTHOR CONTRIBUTIONS

EP conceived the study. EP and MC designed the study. DW developed, applied, and analyzed data associated with the bi-ventricle cardiac excitation model. EP developed, applied, and analyzed data associated with the forward problem, inverse solution, ECG, and error analysis. EP and all other authors interpreted the data. EP and DW prepared the figures. EP and MC prepared, and all authors edited, the drafts of the manuscript. All authors approve the final version of the manuscript and agreed to be accountable for all aspects of the work in ensuring that questions related to the accuracy and integrity of the work are appropriately investigated and resolved.

FUNDING

This work is supported by a Wellcome Trust ISSF Fellowship to DW (204825/Z/16/Z) (Wellcome Trust ISSF Fellow-University of Leeds account), a British Heart Foundation project grant to AB (PG/16/74/32374) and a Medical Research Council Strategic Skills Fellowship to MC (MR/M014967/1).

ACKNOWLEDGMENTS

Parts of this work were undertaken on ARC3, part of the High Performance Computing facilities at the University of Leeds, UK.

SUPPLEMENTARY MATERIAL

The Supplementary Material for this article can be found online at: https://www.frontiersin.org/articles/10.3389/fphys.2019.00308/full#supplementary-material

REFERENCES

Adeniran, I., McPate, M. J., Witchel, H. J., Hancox, J. C., and Zhang, H. (2011). Increased vulnerability of human ventricle to re-entrant excitation in hERG-linked variant 1 short QT syndrome. *PLoS Comput. Biol.* 7:e1002313. doi: 10.1371/journal.pcbi.1002313

Adeniran, I., Whittaker, D. G., El Harchi, A., Hancox, J. C., and Zhang, H. (2017). *In silico* investigation of a KCNQ1 mutation associated

with short QT syndrome. *Sci. Rep.* 7:8469. doi: 10.1038/s41598-017-08367-2

Alday, E. A., Ni, H., Zhang, C., Colman, M. A., Gan, Z., and Zhang, H. (2016). Comparison of electric- and magnetic-cardiograms produced by myocardial ischemia in models of the human ventricle and torso. *PLoS ONE* 11:e0160999. doi: 10.1371/journal.pone.0160999

Alfakih, K., Plein, S., Thiele, H., Jones, T., Ridgway, J. P., and Sivananthan, M. U. (2003). Normal human left and right ventricular dimensions for MRI as assessed by turbo gradient echo and steady-state free precession imaging sequences. *J. Magn. Reson. Imaging* 17, 323–329. doi: 10.1002/jmri.10262

Appel, M. L., Berger, R. D., Saul, J. P., Smith, J. M., and Cohen, R. J. (1989). Beat to beat variability in cardiovascular variables: noise or music? *J. Am. Coll. Cardiol.* 14, 1139–1148. doi: 10.1016/0735-1097(89)90408-7

Barr, R. C., Ramsey, M., and Spach, M. S. (1977). Relating epicardial to body surface potential distributions by means of transfer coefficients based on geometry measurements. *IEEE Trans. Biomed. Eng.* 24, 1–11. doi: 10.1109/TBME.1977.326201

Baumert, M., Javorka, M., and Kabir, M. M. (2013). Joint symbolic analyses of heart rate, blood pressure, and respiratory dynamics. *J. Electrocardiol.* 46, 569–573. doi: 10.1016/j.jelectrocard.2013.07.009

Bear, L., Huntjens, P., Coronel, R., Bernus, O., Dallet, C., Walton, R., et al. (2016). "Detection of incomplete left bundle branch block by non-invasive electrocardiographic imaging," in *Computing in Cardiology Conference (CinC), 2016* (Vancouver, BC: IEEE), 389–392.

Bear, L. R., Cheng, L. K., Legrice, I. J., Sands, G. B., Lever, N. A., Paterson, D. J., et al. (2015). Forward problem of electrocardiography: is it solved? *Circ. Arrhythm. Electrophysiol.* 8, 677–684. doi: 10.1161/CIRCEP.114.001573

Bear, L. R., Huntjens, P. R., Walton, R. D., Bernus, O., Coronel, R., and Dubois, R. (2018a). Cardiac electrical dyssynchrony is accurately detected by noninvasive electrocardiographic imaging. *Heart Rhythm* 15, 1058–1069. doi: 10.1016/j.hrthm.2018.02.024

Bear, L. R., Legrice, I. J., Sands, G. B., Lever, N. A., Loiselle, D. S., Paterson, D. J., et al. (2018b). How accurate is inverse electrocardiographic mapping? A systematic *in vivo* evaluation. *Circ. Arrhythm. Electrophysiol.* 11:e006108. doi: 10.1161/CIRCEP.117.006108

Benjamin, E. J., Blaha, M. J., Chiuve, S. E., Cushman, M., Das, S. R., Deo, R., et al. (2017). Heart Disease and Stroke Statistics-2017 update: a report from the American Heart Association. *Circulation* 135, e146–e603. doi: 10.1161/CIR.0000000000000485

Benson, A., Gilbert, S., Li, P., Newton, S., and Holden, A. (2008). Reconstruction and quantification of diffusion tensor imaging-derived cardiac fibre and sheet structure in ventricular regions used in studies of excitation propagation. *Math. Modell. Nat. Phenomena* 3, 101–130. doi: 10.1051/mmnp:2008083

Benson, A. P., Al-Owais, M., and Holden, A. V. (2011). Quantitative prediction of the arrhythmogenic effects of *de novo* hERG mutations in computational models of human ventricular tissues. *Eur. Biophys. J.* 40, 627–639. doi: 10.1007/s00249-010-0663-2

Benson, A. P., Bernus, O., Dierckx, H., Gilbert, S. H., Greenwood, J. P., Holden, A. V., et al. (2010). Construction and validation of anisotropic and orthotropic ventricular geometries for quantitative predictive cardiac electrophysiology. *Interface Focus*. 1, 101–116. doi: 10.1098/rsfs.2010.0005

Benson, A. P., Halley, G., Li, P., Tong, W. C., and Holden, A. V. (2007). Virtual cell and tissue dynamics of ectopic activation of the ventricles. *Chaos* 17:015105. doi: 10.1063/1.2404634

Boukens, B. J., Sulkin, M. S., Gloschat, C. R., Ng, F. S., Vigmond, E. J., and Efimov, I. R. (2015). Transmural APD gradient synchronizes repolarization in the human left ventricular wall. *Cardiovasc. Res.* 108, 188–196. doi: 10.1093/cvr/cvv202

Boyle, P. M., Hakim, J. B., Zahid, S., Franceschi, W. H., Murphy, M. J., Vigmond, E. J., et al. (2018). Comparing reentrant drivers predicted by image-based computational modeling and mapped by electrocardiographic imaging in persistent atrial fibrillation. *Front. Physiol.* 9:414. doi: 10.3389/fphys.2018.00414

Clay, S., Alfakih, K., Radjenovic, A., Jones, T., and Ridgway, J. P. (2006). Normal range of human left ventricular volumes and mass using steady state free precession MRI in the radial long axis orientation. *Magn. Reson. Mater. Phys. Biol. Med.* 19, 41–45. doi: 10.1007/s10334-005-0025-8

Cluitmans, M. J., Bonizzi, P., Karel, J. M., Das, M., Kietselaer, B. L., De Jong, M. M., et al. (2017). *In vivo* validation of electrocardiographic imaging. *JACC Clin. Electrophysiol.* 3, 232–242. doi: 10.1016/j.jacep.2016.11.012

Cluitmans, M. J., and Volders, P. G. (2017). Influence of body-surface geometry accuracy on noninvasive reconstruction of electrical activation and recovery in electrocardiographic imaging. *Computing* 44:1. doi: 10.22489/CinC.2017.243-189

Coll-Font, J., and Brooks, D. (2018). Tracking the position of the heart from body surface potential maps and electrograms. *Front. Physiol.* 9:1727. doi: 10.3389/fphys.2018.01727

Colman, M. A., Aslanidi, O. V., Kharche, S., Boyett, M. R., Garratt, C., Hancox, J. C., et al. (2013). Pro-arrhythmogenic effects of atrial fibrillation-induced electrical remodelling: insights from the three-dimensional virtual human atria. *J. Physiol.* 591, 4249–4272. doi: 10.1113/jphysiol.2013.254987

Colman, M. A., Perez Alday, E. A., Holden, A. V., and Benson, A. P. (2017). Trigger vs. substrate: multi-dimensional modulation of QT-prolongation associated arrhythmic dynamics by a hERG channel activator. *Front. Physiol.* 8:757. doi: 10.3389/fphys.2017.00757

Dubois, R., Shah, A. J., Hocini, M., Denis, A., Derval, N., Cochet, H., et al. (2015). Non-invasive cardiac mapping in clinical practice: application to the ablation of cardiac arrhythmias. *J. Electrocardiol.* 48, 966–974. doi: 10.1016/j.jelectrocard.2015.08.028

Durrer, D., Van Dam, R. T., Freud, G., Janse, M., Meijler, F., and Arzbaecher, R. (1970). Total excitation of the isolated human heart. *Circulation* 41, 899–912. doi: 10.1161/01.CIR.41.6.899

Gage, R. M., Curtin, A. E., Burns, K. V., Ghosh, S., Gillberg, J. M., and Bank, A. J. (2017). Changes in electrical dyssynchrony by body surface mapping predict left ventricular remodeling in patients with cardiac resynchronization therapy. *Heart Rhythm* 14, 392–399. doi: 10.1016/j.hrthm.2016.11.019

Ghosh, S., Silva, J. N., Canham, R. M., Bowman, T. M., Zhang, J., Rhee, E. K., et al. (2011). Electrophysiologic substrate and intraventricular left ventricular dyssynchrony in nonischemic heart failure patients undergoing cardiac resynchronization therapy. *Heart Rhythm* 8, 692–699. doi: 10.1016/j.hrthm.2011.01.017

Glukhov, A. V., Fedorov, V. V., Lou, Q., Ravikumar, V. K., Kalish, P. W., Schuessler, R. B., et al. (2010). Transmural dispersion of repolarization in failing and nonfailing human ventricle. *Circ. Res.* 106, 981–991. doi: 10.1161/CIRCRESAHA.109.204891

Goldenberg, I., Moss, A. J., and Zareba, W. (2006). QT interval: how to measure it and what is "normal". *J. Cardiovasc. Electrophysiol.* 17, 333–336. doi: 10.1111/j.1540-8167.2006.00408.x

Hansen, P. C. (1992). Analysis of discrete ill-posed problems by means of the L-curve. *SIAM Rev.* 34, 561–580. doi: 10.1137/1034115

Hansen, P. C. (1998). *Rank-Deficient and Discrete Ill-Posed Problems: Numerical Aspects of Linear Inversion.* SIAM.

Ho, S., and Nihoyannopoulos, P. (2006). Anatomy, echocardiography, and normal right ventricular dimensions. *Heart* 92, i2–i13. doi: 10.1136/hrt.2005.077875

Ho, S. Y. (2009). Anatomy and myoarchitecture of the left ventricular wall in normal and in disease. *Eur. J. Echocardiogr.* 10, iii3–iii7. doi: 10.1093/ejechocard/jep159

Huntjens, P. R., Ploux, S., Strik, M., Walmsley, J., Ritter, P., Haissaguerre, M., et al. (2018). Electrical substrates driving response to cardiac resynchronization therapy: a combined clinical–computational evaluation. *Circ. Arrhythm. Electrophysiol.* 11:e005647. doi: 10.1161/CIRCEP.117.005647

Kabir, M. M., Sedaghat, G., Thomas, J., Waks, J. W., Sitlani, C. M., Biggs, M. L., et al. (2016). Electrocardiographic beat-to-beat QT interval is affected by phases of respiration: the atherosclerosis risk in communities study. *Am. Heart Assoc.* 134, A12224–A12224. Available online at: https://www.ahajournals.org/doi/abs/10.1161/circ.134.suppl_1.12224

Keller, D. U., Jarrousse, O., Fritz, T., Ley, S., Dossel, O., and Seemann, G. (2011). Impact of physiological ventricular deformation on the morphology of the T-wave: a hybrid, static-dynamic approach. *IEEE Trans. Biomed. Eng.* 58, 2109–2119. doi: 10.1109/TBME.2011.2147785

Langley, P., Bowers, E. J., and Murray, A. (2010). Principal component analysis as a tool for analyzing beat-to-beat changes in ECG features: application to ECG-derived respiration. *IEEE Trans. Biomed. Eng.* 57, 821–829. doi: 10.1109/TBME.2009.2018297

Leong, K. M., Ng, F. S., Roney, C., Cantwell, C., Shun-Shin, M. J., Linton, N. W., et al. (2018). Repolarization abnormalities unmasked with exercise in sudden cardiac death survivors with structurally normal hearts. *J. Cardiovasc. Electrophysiol.* 29, 115–126. doi: 10.1111/jce.13375

Macfarlane, P. W., van Oosterom, A., Pahlm, O., Kligfield, P., Janse, M., and Camm, J. (eds) (2010). *Comprehensive Electrocardiology*. London: Springer Science & Business Media.

Oster, H. S., and Rudy, Y. (1992). The use of temporal information in the regularization of the inverse problem of electrocardiography. *IEEE Trans. Biomed. Eng.* 39, 65–75. doi: 10.1109/10.108129

Perez Alday, E. A., Michael, A. C., and Henggui, Z. (2016). "Reconstruction of atrial ectopic focal and re-entrant excitations from body surface potentials. Insights from 3D virtual human atria and torso," in *2016 Computing in Cardiology Conference (CinC)*, (Vancouver, BC: IEEE). doi: 10.23919/CIC.2016.7868839

Perez-Alday, E. A., Colman, M. A., Langley, P., Butters, T. D., Higham, J., Workman, A. J., et al. (2015). A new algorithm to diagnose atrial ectopic origin from multi lead ECG systems–insights from 3D virtual human atria and torso. *PLoS Comput. Biol.* 11:e1004026. doi: 10.1371/journal.pcbi.1004026

Perez-Alday, E. A., Colman, M. A., Langley, P., and Zhang, H. (2017a). Novel non-invasive algorithm to identify the origins of re-entry and ectopic foci in the atria from 64-lead ECGs: a computational study. *PLoS Comput. Biol.* 13:e1005270. doi: 10.1371/journal.pcbi.1005270

Perez-Alday, E. A., Thomas, J. A., Kabir, M., Sedaghat, G., Rogovoy, N., Van Dam, E., et al. (2017b). Torso geometry reconstruction and body surface electrode localization using three-dimensional photography. *J. Electrocardiol.* 51, 60–67. doi: 10.1016/j.jelectrocard.2017.08.050

Ramanathan, C., and Rudy, Y. (2001). Electrocardiographic imaging: II. Effect of torso inhomogeneities on noninvasive reconstruction of epicardial potentials, electrograms, and isochrones. *J. Cardiovasc. Electrophysiol.* 12, 241–252. doi: 10.1046/j.1540-8167.2001.00241.x

Rodrigo, M., Climent, A. M., Liberos, A., Fernández-Avilés, F., Berenfeld, O., Atienza, F., et al. (2017). Technical considerations on phase mapping for identification of atrial reentrant activity in direct-and inverse-computed electrograms. *Circ. Arrhythm. Electrophysiol.* 10:e005008. doi: 10.1161/CIRCEP.117.005008

Rudy, Y. (2013). Noninvasive electrocardiographic imaging of arrhythmogenic substrates in humans. *Circ. Res.* 112, 863–874. doi: 10.1161/CIRCRESAHA.112.279315

Salu, Y. (1980). Implementing a consistency criterion in numerical solution of the bioelectric forward problem. *IEEE Trans. Biomed. Eng.* 338–341. doi: 10.1109/TBME.1980.326742

Seemann, G., Keller, D., Weiss, D., and Dossel, O. (2006). "Modeling human ventricular geometry and fiber orientation based on diffusion tensor MRI," in *Computers in Cardiology, 2006* (IEEE), 801–804. Available online at: https://ieeexplore.ieee.org/abstract/document/4511973

Shimizu, I., and Minamino, T. (2016). Physiological and pathological cardiac hypertrophy. *J. Mol. Cell. Cardiol.* 97, 245–262. doi: 10.1016/j.yjmcc.2016.06.001

Silva, J. N., Ghosh, S., Bowman, T. M., Rhee, E. K., Woodard, P. K., and Rudy, Y. (2009). Cardiac resynchronization therapy in pediatric congenital heart disease: insights from noninvasive electrocardiographic imaging. *Heart Rhythm* 6, 1178–1185. doi: 10.1016/j.hrthm.2009.04.017

Stephenson, R. S., Atkinson, A., Kottas, P., Perde, F., Jafarzadeh, F., Bateman, M., et al. (2017). High resolution 3-dimensional imaging of the human cardiac conduction system from microanatomy to mathematical modeling. *Sci. Rep.* 7:7188. doi: 10.1038/s41598-017-07694-8

Streeter, D. D., Spotnitz, H. M., Patel, D. P., Ross, J., and Sonnenblick, E. H. (1969). Fiber orientation in the canine left ventricle during diastole and systole. *Circ. Res.* 24, 339–347. doi: 10.1161/01.RES.24.3.339

Swenson, D. J., Geneser, S. E., Stinstra, J. G., Kirby, R. M., and Macleod, R. S. (2011). Cardiac position sensitivity study in the electrocardiographic forward problem using stochastic collocation and boundary element methods. *Ann. Biomed. Eng.* 39:2900. doi: 10.1007/s10439-011-0391-5

Szabó, G., Szentandrássy, N., Bíró, T., Tóth, B. I., Czifra, G., Magyar, J., et al. (2005). Asymmetrical distribution of ion channels in canine and human left-ventricular wall: epicardium versus midmyocardium. *Pflügers Arch.* 450, 307–316. doi: 10.1007/s00424-005-1445-z

Szentadrassy, N., Banyasz, T., Biro, T., Szabo, G., Toth, B. I., Magyar, J., et al. (2005). Apico–basal inhomogeneity in distribution of ion channels in canine and human ventricular myocardium. *Cardiovasc. Res.* 65, 851–860. doi: 10.1016/j.cardiores.2004.11.022

Taggart, P., Sutton, P. M., Opthof, T., Coronel, R., Trimlett, R., Pugsley, W., et al. (2000). Inhomogeneous transmural conduction during early ischaemia in patients with coronary artery disease. *J. Mol. Cell. Cardiol.* 32, 621–630. doi: 10.1006/jmcc.2000.1105

Tate, J., Gillette, K., Burton, B., Good, W., Zenger, B., Coll-Font, J., et al. (2018). Reducing error in ECG forward simulations with improved source sampling. *Front. Physiol.* 9:1304. doi: 10.3389/fphys.2018.01304

Ten Tusscher, K. H., and Panfilov, A. V. (2006). Alternans and spiral breakup in a human ventricular tissue model. *Am. J. Physiol. Heart Circ. Physiol.* 291, H1088–H1100. doi: 10.1152/ajpheart.00109.2006

Vriesendorp, P. A., Schinkel, A. F., Liebregts, M., Theuns, D. A., Van Cleemput, J., Folkert, J., et al. (2015). Validation of the 2014 European Society of Cardiology guidelines risk prediction model for the primary prevention of sudden cardiac death in hypertrophic cardiomyopathy. *Circ. Arrhythm. Electrophysiol.* 8, 829–835. doi: 10.1161/CIRCEP.114.002553

Wang, D., Kirby, R., Macleod, R. S., and Johnson, C. A. (2010). "New family of variational-form-based regularizers for reconstructing epicardial potentials from body-surface mapping," in *Computing in Cardiology, 2010* (Belfast, UK: IEEE), 93–96.

Whittaker, D. G., Ni, H., Benson, A. P., Hancox, J. C., and Zhang, H. (2017). Computational analysis of the mode of action of disopyramide and quinidine on hERG-linked short QT syndrome in human ventricles. *Front. Physiol.* 8:759. doi: 10.3389/fphys.2017.00759

Zemzemi, N., Dobrzynski, C., Bear, L., Potse, M., Dallet, C., Coudière, Y., et al. (2015). "Effect of the torso conductivity heterogeneities on the ECGI inverse problem solution," in *Computing in Cardiology Conference (CinC), 2015* (Nice: IEEE), 233–236. doi: 10.1109/CIC.2015.7408629

Zhang, J., Cooper, D. H., Desouza, K. A., Cuculich, P. S., Woodard, P. K., Smith, T. W., et al. (2016). Electrophysiologic scar substrate in relation to VT: noninvasive high-resolution mapping and risk assessment with ECGI. *Pacing Clin. Electrophysiol.* 39, 781–791. doi: 10.1111/pace.12882

Conflict of Interest Statement: The authors declare that the research was conducted in the absence of any commercial or financial relationships that could be construed as a potential conflict of interest.

The reviewer JT declared a past collaboration with one of the authors EP to the handling editor.

Advantages of publishing in Frontiers

OPEN ACCESS
Articles are free to read for greatest visibility and readership

FAST PUBLICATION
Around 90 days from submission to decision

HIGH QUALITY PEER-REVIEW
Rigorous, collaborative, and constructive peer-review

TRANSPARENT PEER-REVIEW
Editors and reviewers acknowledged by name on published articles

Frontiers
Avenue du Tribunal-Fédéral 34
1005 Lausanne | Switzerland

Visit us: www.frontiersin.org
Contact us: info@frontiersin.org | +41 21 510 17 00

REPRODUCIBILITY OF RESEARCH
Support open data and methods to enhance research reproducibility

DIGITAL PUBLISHING
Articles designed for optimal readership across devices

FOLLOW US
@frontiersin

IMPACT METRICS
Advanced article metrics track visibility across digital media

EXTENSIVE PROMOTION
Marketing and promotion of impactful research

LOOP RESEARCH NETWORK
Our network increases your article's readership